XLVI INTERNATIONAL SCIENTIFIC CONFERENCE ON INFORMATION, COMMUNICATION AND ENERGY SYSTEMS AND TECHNOLOGIES

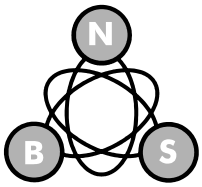

ICEST 2011

Proceedings of Papers

Volume 2

Serbia, Niš, June 29 - July 1, 2011

ICEST 2011 - XLVI INTERNATIONAL SCIENTIFIC CONFERENCE ON INFORMATION, COMMUNICATION AND ENERGY SYSTEMS AND TECHNOLOGIES, Serbia, Niš, June 29 - July 1, 2011

Proceedings of Papers - Volume 2 of 3 volumes

Editor: Prof. Dr. Bratislav D. Milovanović

Technical Editor: Dr. Zoran Ž. Stanković

Technical Co-Editor: Dr. Biljana P. Stošić

Published by: Faculty of Electronic Engineering, University of Niš, Serbia
Printed by: UNIGRAF, Niš, Serbia

Number of copies printed: 80

Printing of this edition has been financially supported by Serbian Ministry of Science

ISBN: 978-86-6125-032-3

CIP - Каталогизација у публикацији
Народна библиотека Србије, Београд

621.39(082)
621.37/.38(082)
37.02(082)
004(082)
681.5(082)
621.311(082)

INTERNATIONAL Scientific Conference on Information, Communication and Energy Systems and Technologies - ICEST (46 ; 2011 ; Niš)
Proceedings of Papers. #Vol. #2 / XLVI International Scientific Conference on Information, Communication and Energy Systems and Technologies - ICEST 2011, Niš, June 29 - July 1, 2011 ; [organized by Faculty of Electronic Engineering, Niš [and] Faculty of Telecommunications, Sofia [and] Faculty of Technical Sciences, Bitola ; editor Bratislav D. Milovanović]. - Niš : Faculty of Electronic Engineering, 2011 (Niš : Unigraf).
- XVIII, 261-570 str. : ilustr. ; 29 cm

Tiraž 280. - Bibliografija uz svaki rad. -
Registar.

ISBN 978-86-6125-032-3

a) Телекомуникације - Зборници b) Електроника - Зборници c) Образовна технологија - Зборници d) Рачунарство - Зборници e) Системи аутоматског управљања - Зборници f) Електроенергетски системи - Зборници
COBISS.SR-ID 186464012

TABLE OF CONTENTS

VOLUME 1

ORAL SESSIONS

SIGNAL PROCESSING I

SIGNAL PROCESSING II

TELECOMMUNICATION NETWORKS AND SERVICES I

TELECOMMUNICATION NETWORKS AND SERVICES II

RADIO COMMUNICATIONS, MICROWAVE TECHNIQUE AND ANTENNAS I

RADIO COMMUNICATIONS, MICROWAVE TECHNIQUE AND ANTENNAS II

METROLOGY AND REMOTE SENSING

TELECOMMUNICATION SYSTEMS AND TECHNOLOGIES

VOLUME 2

ELECTRONIC COMPONENTS, SYSTEMS AND TECHNOLOGIES I

ELECTRONIC COMPONENTS, SYSTEMS AND TECHNOLOGIES II

EDUCATION QUALITY

INTERNET TECHNOLOGIES

CONTROL SYSTEMS

COMPUTER SYSTEMS

POWER TRANSMISSION AND DISTRIBUTION SYSTEMS I

POWER TRANSMISSION AND DISTRIBUTION SYSTEMS II

STUDENT SESSIONS

STUDENT SESSION I

STUDENT SESSION II

VOLUME 3

POSTER SESSIONS

PO1 – TELECOMMUNICATION SYSTEMS AND TECHNOLOGIES

PO2 – RADIO COMMUNICATIONS, MICROWAVE TECHNIQUE AND ANTENNAS

PO3 – SIGNAL PROCESSING, METROLOGY AND REMOTE SENSING

PO4 – CONTROL SYSTEMS AND ROBOTICS

PO5 – RENEWABLE ENERGIES

PO6 – COMPUTER SYSTEMS AND INTERNET TECHNOLOGIES

PO7 – ELECTRONIC COMPONENTS, SYSTEMS AND TECHNOLOGIES

PO8 – POWER TRANSMISSION, DISTRIBUTION SYSTEM AND ELECTRICAL MACHINES

PO9 – EDUCATION QUALITY

Session EL I:

ELECTONIC COMPONENTS, SYSTEMS AND TECHOLOGIES I

Geometry Dependent Behavioral RF Model of Spiral Inductors

Elissaveta Gadjeva[1] and George Valkov[2]

Abstract – **Accurate modeling and simulation of spiral inductors are very important in RFIC design. To enable a more accurate description of the device behavior, the current flowing into the substrate is to be considered. In the present paper a computer wideband behavioral model is developed that considers the substrate losses and is geometry dependent. The model is developed using VHDL-AMS language and accepts the geometry parameters. The model is verified using measurement data in the frequency range from 1GHz to 10GHz and gives a relative error less than 5%. The VHDL-AMS version of the model is simulated in the mixed-language, mixed-signal simulation environment, provided by the Dolphin Integration SMASH simulator.**

Keywords – **Spiral inductor, Wideband behavioral model, Geometry dependent model, VHDL-AMS.**

I. INTRODUCTION

A general approach to design and simulation of electronic circuits and systems is to separate the large projects into a hierarchy of smaller modules and sub-modules. On one hand, this allows solving a complex task to be performed by solving many simple tasks, as every simple block can be designed and verified separately from the entire project. On the other hand, many of the modules in the project design can reuse sub-modules, which are already optimized and have a predetermined behavior. Some models can be geometry dependent and parameterized. In this way a given model can be instantiated with different parameters and can represent many elements from the same type, but with different geometric sizes.

Simulators based on standard behavioral languages like VHDL-AMS [1] allow the simulation of models, described at different levels of complexity. Hence a large system design can be described and simulated in low-details (system-level), to verify the functionality of the design, before spending resources to create more detailed sub-modules. Once the system-level performance is verified, additional details can be added, and for each module it is possible to switch between architectures with various levels of complexity. An important feature of the behavior languages is that models can be organized as a library and then reused in many projects, sub-projects and testing environments. Silicon factories can provide models for the most commonly used elements for the available technology processes.

With the development of the instruments for Analog Behavioral Modeling (ABM) and the simulation tools, simulators like Dolphin Integration SMASH allow mixed-signal, multi-level, multi-domain, mixed-language simulations [2]. Hence it is possible to design the various parts of the project in different languages like: *PSpice* language [3], VHDL-AMS, Verilog-AMS [1] and Behavioral-C [4], and to simulate them together.

The physical model of planar spiral inductor on silicon (1-Π) [5] is a very popular model used in microelectronic design. Its model parameter values can be expressed directly using the geometry of the spiral inductor. The skin effect at high frequencies is modeled using a frequency dependent series resistance. This frequency dependent element makes the 1-Π model incompatible with transient analysis and broad-band design. The 2-Π model taking into account the decreasing in the series resistance at higher frequencies is proposed in [6]. A wide-band spiral inductor model is proposed in [7]. Its specific feature is that the model parameters cannot be expressed as a function of inductor geometry. The substrate-coupled equivalent circuit model of an inductor based on substrate phenomena is proposed in [8]. The advantage of this model compared to the 1-Π and 2-Π models, is the prediction of the drop-down characteristic in the series resistance at higher frequencies. An enhancement of the model [8] is the scalable substrate-coupled (*SSC*) model [9] where the parameters of the model elements are expressed as monomial expressions in terms of physical geometry. As a result, the model in [9] combines the advantages of the 1-Π model and the wide-band model [7]: geometry dependence of the model parameters and high accuracy in the whole frequency range.

In the present paper, a computer model coresponding to the geometry dependent, scallable substrate-coupled spiral inductor model [9] is proposed, using the VHDL-AMS language.

II. MODEL DESCRIPTION

The equivalent electrical circuit of a simplified substrate-coupled spiral inductor is shown in Fig. 1 [9]. The model parameters are geometry dependent. The independent geometry parameters are the following: outer diameter, trace width, spacing between the traces, as well as the number of turns. The model parameters are: capacitance between terminals C_S, capacitances between the wiring and the substrate C_{OX1}, C_{OX2}, substrate capacitances C_{SI1}, C_{SI2}, wiring resistance R_S, silicon resistance R_{SI1}, R_{SI2}, substrate resistance R_{SUB}, wiring inductance L_S, L_{SUB} – representing the eddy current flowing in the substrate, coupling coefficient k of L_S and L_{SUB}, corresponding to the mutual inductance M_S.

[1] Technical University of Sofia, 8, Kliment Ohridski Blvd., 1000 Sofia, BULGARIA, e-mail: egadjeva@tu-sofia.bg

[2] Technical University of Sofia, 8, Kliment Ohridski Blvd., 1000 Sofia, BULGARIA, e-mail: gvalkov@abv.bg

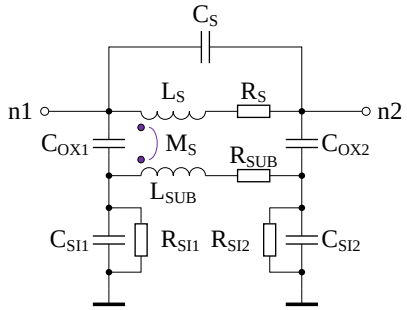

Fig. 1. Simplified substrate-coupled spiral inductor model

The equations describing the geometry dependent model parameters are in the form:

$$C_S = K_1 \cdot n \cdot w^2 \cdot 10^{-15} \tag{1}$$

$$R_S = \frac{K_2 \cdot l}{w} \tag{2}$$

$$C_{OX1} = C_{OX2} = K_3 \cdot l \cdot w \cdot 10^{-15} \tag{3}$$

$$R_{SI1} = R_{SI2} = \frac{K_4}{l \cdot w} \tag{4}$$

$$C_{SI1} = C_{SI2} = K_5 \cdot l \cdot w \cdot 10^{-15} \tag{5}$$

$$L_S = \beta_1 \cdot {d_{out}}^{a_1} \cdot w^{b_1} \cdot s^{c_1} \cdot n^{d_1} \cdot {d_{avg}}^{e_1} \cdot 10^{-9} \tag{6}$$

$$L_{SUB} = \beta_2 \cdot {d_{out}}^{a_2} \cdot w^{b_2} \cdot s^{c_2} \cdot n^{d_2} \cdot \left(L_S \cdot 10^9\right)^{e_2} \cdot 10^{-9} \tag{7}$$

$$R_{SUB} = \beta_3 \cdot n^{a_3} \cdot \left(w+s\right)^{b_3} \cdot l^{c_3} \tag{8}$$

$$k = 1 - \exp\left(\beta_4 \cdot n^{a_4} \cdot {d_{out}}^{b_4} \cdot w^{c_4} \cdot s^{d_4}\right) \tag{9}$$

$$M_S = k \cdot \sqrt{L_S \cdot L_{SUB}} \tag{10}$$

The current that flows in the substrate network composing of L_{SUB} and R_{SUB}, is in the opposite direction to the current that flows in the wiring network composing of L_S and R_S, as a result of mutual inductance M_S [9]. This effect reduces the Equivalent Terminal Resistance (ETR) of the inductor at high frequency and is an improvement over the 1-Π model, for which ETR is not restricted and may reach exceedingly high values. At low frequency, the eddy current has no impact over ETR, due to the low linkage between the wiring and substrate networks, via the high impedance of C_{OX1} and C_{OX2}.

The equations for intermediate parameters – inner diameter d_{in}, average diameter d_{avg} and conductor length l, are in the form:

$$d_{in} = d_{out} \cdot \left(n \cdot \left(s+w\right) - s\right) \tag{11}$$

$$d_{avg} = \frac{d_{in} + d_{out}}{2} \tag{12}$$

$$l = 4 \cdot d_{avg} \cdot n \tag{13}$$

The independent model parameters are: outer diameter of the coil d_{out}, conductor width w, space between the traces s, number of turns n. Additional process dependent constants required to calculate the model parameters are shown in Table I and Table II [9].

TABLE I
PROCESS DEPENDENT CONSTANTS FOR CMOS 0.35µm

i	**1**	**2**	**3**	**4**	**5**
$\boldsymbol{\beta_i}$	2.50E-4	6.18E-7	156	-4.85E+4	
$\mathbf{a_i}$	1.84	0.94	1.36	0.91	
$\mathbf{b_i}$	-0.76	4.13	0.93	-1.96	
$\mathbf{c_i}$	-0.14	-1.06	-1.40	-0.83	
$\mathbf{d_i}$	1.10	-1.90	0	0.56	
$\mathbf{e_i}$	0	1.35	0	0	
$\mathbf{K_i}$	0.0415	0.0302	4.28E-3	8.04E+6	2.10E-4

TABLE II
PROCESS DEPENDENT CONSTANTS FOR SOI 0.15µm

i	**1**	**2**	**3**	**4**	**5**
$\boldsymbol{\beta_i}$	1.00E-4	1.00E-6	39	-4.90E+4	
$\mathbf{a_i}$	2.31	0.98	1.30	2.60	
$\mathbf{b_i}$	-1.47	4.39	0.93	-2.12	
$\mathbf{c_i}$	-0.08	-0.99	-1.40	-0.98	
$\mathbf{d_i}$	1.24	-1.84	0	1.60	
$\mathbf{e_i}$	0	0.68	0	0	
$\mathbf{K_i}$	0.0895	0.0466	2.93E-3	3.03E+7	2.10E-4

III. MODEL IMPLEMENTATION IN VHDL-AMS

The VHDL-AMS description of the model has the following structure:

1. Define a list of libraries used by the model (electrical systems and mathematical functions). VHDL-AMS description is in the form:

```
library IEEE;
  use IEEE.electrical_systems.all;
  use IEEE.math_real.all;
entity inductor_pi is
```

2. Define a list of independent geometry parameters of the model: outer diameter of the coil d_{out}, conductor width w, space between the traces s, number of turns n.

```
  generic (
    dout: real := 250.0;
    w   : real :=  10.0;
    s   : real :=   5.0;
    n   : real :=   5.0
  );
```

3. Define a list of electrical terminals. The model interfaces to the external world via two general electrical terminals *n1* and *n2*. In addition, there is an internal connection to the node called *electrical_ref* (ground). It has global visibility and does not need to be explicitly declared in the port list.

```
  port (terminal n1, n2 : electrical);
end entity inductor_pi;
architecture ideal of inductor_pi is
```

4. In order to reduce the number of declarations and to make the code more readable, the process dependent constants are declared as arrays. The implementation code that follows, declares the constants for CMOS 0.35µm, Table I [1]. The constants for SOI 0.15µm fabrication process are available in Table II.

```
constant beta: real_vector(1 to 4) := ( 2.50e-4,
 6.18e-7, 156.0,  -4.85e+4   );
constant aa  : real_vector(1 to 4) := ( 1.84,
 0.94,  1.36,  0.91 );
constant bb  : real_vector(1 to 4) := (-0.76,
 4.13,  0.93, -1.96 );
constant cc  : real_vector(1 to 4) := (-0.14,
-1.06,  1.40, -0.83 );
constant dd  : real_vector(1 to 4) := ( 1.10,
-1.90,  0.00,  0.56 );
constant ee  : real_vector(1 to 4) := ( 0.00,
 1.35,  0.00,  0.00 );
constant KK  : real_vector(1 to 5) := ( 0.0415,
 0.0302,  4.28e-3, 8.04e+6, 2.10e-4);
```

5. Define and calculate the equations (11)-(13) for intermediate parameters: inner diameter d_{in}, average diameter d_{avg} and conductor length l.

```
constant din :real:=dout-2.0*(n*(s+w)-s);
constant davg:real:= 0.5*( din + dout );
constant l   :real:= 4.0*davg*n;
```

6. Define and calculate the equations (1)-(10) for schematic parameters: C_S, C_{OX1}, C_{OX2}, C_{SI1}, C_{SI2}, R_S, R_{SI1}, R_{SI2}, R_{SUB}, L_S, L_{SUB}, k and M_S.

```
constant Cs  : capacitance := KK(1)* n*w*w *1.0e-15;
constant Rs  : resistance  := KK(2)* l/w;
constant Cox1: capacitance := KK(3)* l*w   *1.0e-15;
constant Cox2: capacitance := Cox1;
constant Rsi1: resistance  := KK(4)/(l*w);
constant Rsi2: resistance  := Rsi1;
constant Gsi1: real        := 1.0/Rsi1;
constant Gsi2: real        := 1.0/Rsi2;
constant Csi1: capacitance := KK(5)*l*w    *1.0e-15;
constant Csi2: capacitance := Csi1;
constant Ls  : inductance  := beta(1)*(dout**aa(1))*
 (w**bb(1))*(s**cc(1))*(n**dd(1))*(davg**ee(1))
 *1.0e-9;
constant Lsub: inductance  := beta(2) *(dout**aa(2))
 *(w**bb(2))*(s**cc(2))*(n**dd(2))
 *((Ls*1.0e+9)**ee(2))*1.0e-9;
constant Rsub: resistance  := beta(3)*(n**aa(3))
 *((w+s)**bb(3))*(l**cc(3));
constant k   : real        := 1.0-exp(beta(4)
 *(n**aa(4))*(dout **bb(4))*(w**cc(4))*(s**dd(4)));
constant Ms  : inductance  := k*sqrt(Ls*Lsub);
```

7. Define a list of internal and external electrical nodes: *n_ox*1 between C_{OX1} and C_{SI1}, *n_ox*2 between C_{OX2} and C_{SI2}, n_s between L_S and R_S.

```
terminal n_ox1, n_ox2, n_s : electrical;
```

8. Define a list of quantities to describe the model equations: voltage U across the external nodes $n1$ and $n2$, current I_{CS} flowing through the capacitor C_S, current I_{LS} flowing through the inductor L_S and the resistor R_S, voltage U_{SUB} across L_{SUB} and R_{SUB}, current I_{SUB} through L_{SUB} and R_{SUB}, voltages U_{OX1} and U_{OX2} across capacitors C_{OX1} and C_{OX2} respectively, currents I_{OX1} and I_{OX2} through capacitors C_{OX1} and C_{OX2} respectively, voltages U_{SI1} and U_{SI2} across capacitors C_{SI1} and C_{SI2} respectively, current I_{SI1} through capacitor C_{SI1} and resistor R_{SI1}, current I_{SI2} through capacitor C_{SI2} and resistor R_{SI2}.

```
quantity U    across Ics  through n2 to n1;
quantity            Ils  through n2 to n1;
quantity Usub across Isub through
                 n_ox2 to n_ox1;
quantity Uox1 across Iox1 through n1 to n_ox1;
quantity Uox2 across Iox2 through n2 to n_ox2;
quantity Usi1 across Isi1 through
                 n_ox1 to electrical_ref;
quantity Usi2 across Isi2 through
                 n_ox2 to electrical_ref;
```

9. Define the set of equations to represent the schematic in Fig. 1. Some of the equations represent more than one schematic component, e.g. for the two parallel branches between *n_ox1* and *electrical_ref* (ground), the current I_{OX1} is a sum of two currents: one flowing through the resistor R_{SI1} and the other flowing through the capacitor C_{SI1}. This is used for better readability of the code and to reduce the number of equations.

```
begin
    Ics  == Cs  *U   'dot;
    Iox1 == Cox1*Uox1'dot;
    Iox2 == Cox2*Uox2'dot;
    Isi1 == Csi1*Usi1'dot + Usi1*Gsi1;
    Isi2 == Csi2*Usi2'dot + Usi2*Gsi2;
    U    == Ls  *Ils 'dot
          + Ms  *Isub'dot + Ils *Rs;
    Usub == Lsub*Isub'dot
          + Ms  *Ils 'dot + Isub*Rsub;
end architecture;
```

IV. Computational Results of an Example Inductor

To verify the VHDL-AMS implementation of the model, the simulation results for the quality factor have been compared to the measurement results for an example inductor fabricated on the CMOS 0.35µm process [9]. The dimensions of the inductor are shown in Table III. The simulation and measurement results for Q are shown in Fig. 2. The relative error does not exceed 5%.

TABLE III
DIMENSIONS OF INDUCTOR FABRICATED ON CMOS 0.35µm PROCESS

d_{out} [µm]	w [µm]	s [µm]	n
250	10	5	5

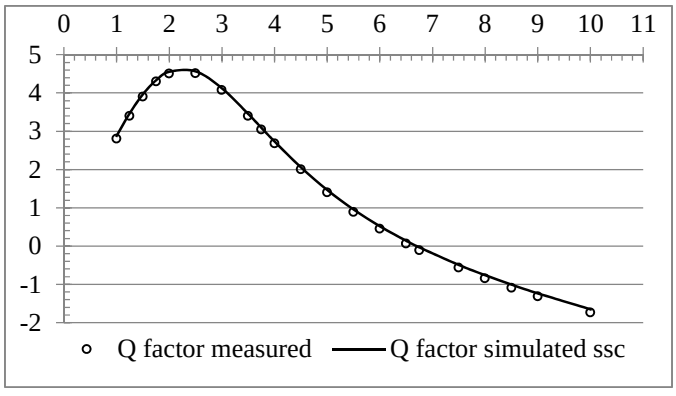

Fig. 2. Simulation and measurement results for Q

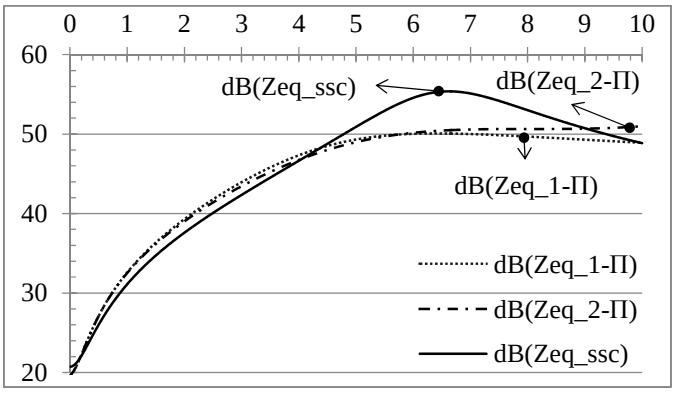

Fig. 3. Simulation results for *Zeq*

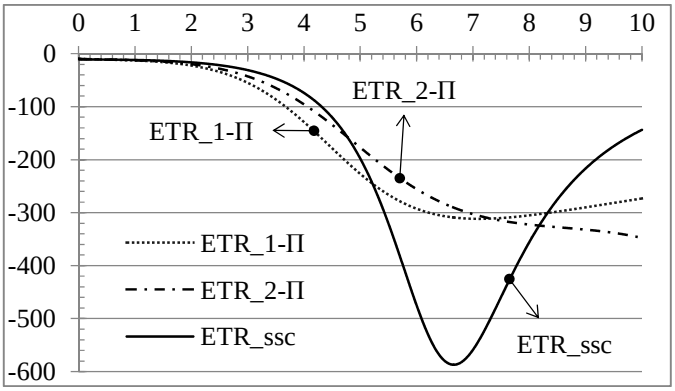

Fig. 4. Simulation results for ETR

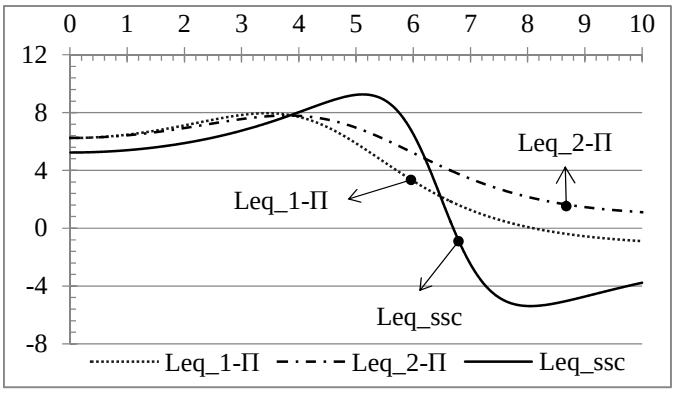

Fig. 5. Simulation results for L_{eq} for 1-Π, 2-Π, *SC* and *SSC* models

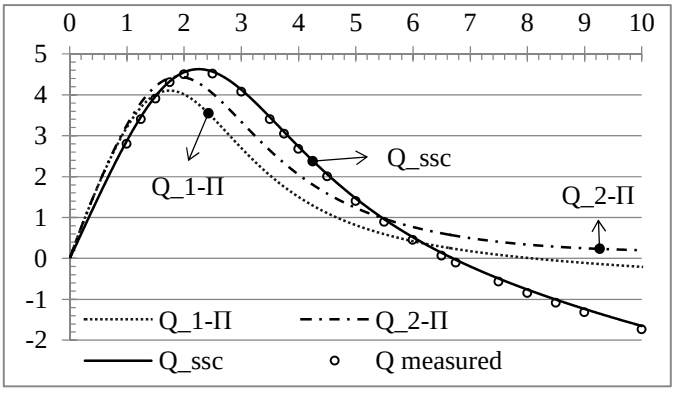

Fig. 6. Simulation results of *Q* for 1-Π, 2-Π, *SC* and *SSC* models and comparison to the measurement results

The simulation results for the module Z_{eq} of the equivalent impedance of the spiral inductor, for ETR and L_{eq} are shown in Fig. 3, Fig. 4 and Fig. 5 respectively, for 1-Π, 2-Π and scalable substrate-coupled (*SSC*) models. The simulation results of *Q* for 1-Π, 2-Π and *SSC* models are compared to the measurement data (Fig. 6). The advantages of the scalable substrate-coupled model to the other models are seen: a high accuracy in the whole frequency range, as well as its scalability.

The proposed computer realization of the behavioral scalable substrate-coupled model of the spiral inductor using VHDL-AMS language is portable and can be used in various simulation environments.

V. Conclusion

A VHDL-AMS behavioral substrate-coupled model of spiral inductor has been developed in the paper. The model considers substrate losses and is valid in a wide frequency range. It is characterized by geometry dependence of the model parameters. The proposed computer model is verified to measurement data in the frequency range of 1GHz to 10GHz and gives a relative error less than 5%. The VHDL-AMS model is simulated in the mixed-language, mixed-signal simulation environment, provided by the Dolphin Integration SMASH simulator.

Acknowledgement

The investigations are supported by the project DTK02/50/17.12.2009.

References

[1] F. Pêcheux, C. Lallement, A. Vachoux, "VHDL-AMS and Verilog-AMS as Alternative Hardware Description Languages for Efficient Modeling of Multi-Discipline Systems", Paper #1446, IEEE, ISSN 0278-0070, 2005.

[2] http://www.dolphin.fr/medal/smash/smash_overview.php

[3] *PSpice A/D Reference Guide*, Cadence Design Systems, 2009.

[4] M. Chung, S. Na, C. Kyung, "System-Level Performance Analysis of Embedded System Using Behavioral C/C++ Model", 0-7803-9060-1/05/$20.00, IEEE, pp. 178-191, 2005.

[5] C. P. Yue, C. Ryu, J. Lau, T. H. Lee and S. S. Wong, "A physical model for planar spiral inductors on silicon", Proc. IEEE Int. Electron Devices Meeting Tech. Dig., San Francisco, pp. 155-158, CA, Dec. 1996.

[6] Y. Cao, R. A. Groves, X. Huang, N. Zamdmer, J. Plouchart, R. Wachnik, T.-J. King and C. Hu, "Frequency-independent equivalent-circuit model for on-chip spiral inductors", IEEE J. Solid-State Circuits, vol. 38, no. 3, pp. 419–426, Mar. 2003.

[7] J. Gil, H. Shin, "A simple wide-band on-chip inductor model for silicon-based RF Ics", IEEE Transactions on Microwave Theory and Techniques, vol. 51, n. 9, pp. 2023–2028, Sept., 2003.

[8] Minoru Fujishima, Jun Kino, "Accurate Subcircuit Model of an On-Chip Inductor with a New Substrate Network", IEEE Symposium on VLSI Circuits, pp. 376-379, 2004.

[9] Ivan C. H. Lai, Minoru Fujishima, "A new on-chip substrate-coupled inductor model, implemented with scalable expressions", IEEE journal of solid-state circuits, vol. 41, pp. 2491-2499, 11 November 2006.

Temperature Analysis and Modeling of Voltage Regulator Circuits in PSpice

Galia Marinova[1]

Abstract – **The paper proposes a methodology for temperature analysis and modeling of voltage regulator circuits in PSpice. Six voltage regulator circuits are analyzed using temperature sweep in PSpice. Output stabilized voltages and output voltage ripples are simulated in temperature area and then temperature models are formulated for each circuit. Based on the results and the models obtained, a comparative study of the six voltage regulator circuits is performed.**

Keywords – **Voltage regulator, Temperature models, PSPICE.**

I. Introduction

The paper proposes a methodology for temperature analysis and modeling of voltage regulator circuits in PSpice. Six voltage regulator circuits are analyzed using temperature sweep in PSpice. Output stabilized voltages and output voltage ripples are simulated in temperature area and then temperature models are formulated for each circuit. Based on the results and the models obtained, a comparative study of the six voltage regulator circuits is performed.

[1]Galia Marinova is with the Telecommunications Faculty, Technical University – Sofia, bul. "Kliment Ohridski" 8, 1000 Sofia, Bulgaria, E-mail: gim@tu-sofia.bg.

II. Methodology for Temperature Analysis and Modeling of Voltage Regulator Circuits in PSpice

Table 1 presents the Methodology for temperature analysis and modeling of voltage regulator circuits in PSpice which develops the methodology for analysis of voltage regulator circuits from [3].

III. Temperature Analysis of the Voltage Regulators Carachteristics

Following the methodology described in Section II six voltage regulator circuits from Fig1a to Fig.1f are analyzed with PSpice in time area with temperature sweep for 4 temperatures: 0ºC 25ºC 40ºC 70ºC. The voltage regulator circuits from Fig. 1 are studied in details in [1,2]. Two traces are drawn for each circuit and the curves obtained are presented on Figures 2 to 7:

- Stabilized output voltage in temperature area Vout(ΔTºC) – Fig. 2a,3a,4a,5a,6a,7a
- Output voltage ripple in temperature area ΔVout(ΔTºC) – Fig. 2b,3b,4b,5b,6b,7b

IV. Analysis of the Temperature Functions for the Voltage Regulators

This section studies the temperature dependence of the circuits from Fig.1.

TABLE I
METHODOLOGY FOR TEMPERATURE ANALYSIS AND MODELING OF VOLTAGE REGULATOR CIRCUITS IN PSPICE

Characteristics of the voltage regulator circuits	**Definition of the analysis used in PSpice**	**Graphical processing of the simulation results in PSPICE**	**Definition of the voltage regulator parameters through postprocessing functions**
Temperature characteristics of the voltage regulator circuit	Temperature analysis with temperature sweep .TEMP <list of t^oC>	- Tracing a family of transient curves for the output voltage at temperatures from the list Vout(t), <list of t^oC> Extracting the curve of output voltage as a function of temperature - Vout(t°C) - Extracting the curve of output voltage ripple as a function of temperature - ΔVout(t°C) By applying the option PERFORMANCE ANALYSIS for determining the value **YatX** from the trace of output voltage **Maxr(Vout,t1,t2)-Minr(Vout, t1,t2)**	Determining the dependence: - Linear, nonlinear or constant; - Directly or inversely proportional; Determining the variation of the output voltage in the temperature interval [$\mathbf{t°_{min}}$, $\mathbf{t°_{max}}$] : **ΔVout ($t°_{min}$-$t°_{max}$) = Vout($t°_{max}$)-Vout($t°_{min}$)** and for the variation of the voltage ripple: **ΔΔVout($t°_{min}$-$t°_{max}$) = ΔVout($t°_{max}$)-ΔVout($t°_{min}$)** When linear temperature dependence is observed for the output voltage or the ripple, the temperature dependence is modeled by a linear equation.

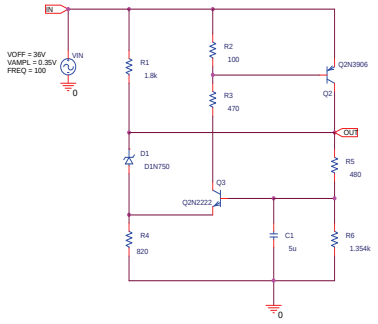

Fig. 1a. Linear voltage regulator with PNP pass transistor

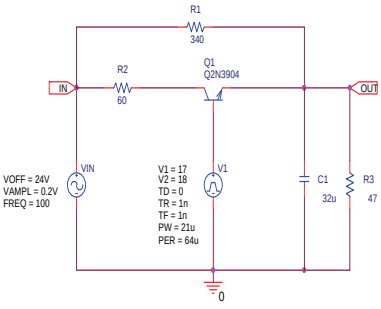

Fig. 1b. Voltage regulator with NPN pass transistor in switch mode

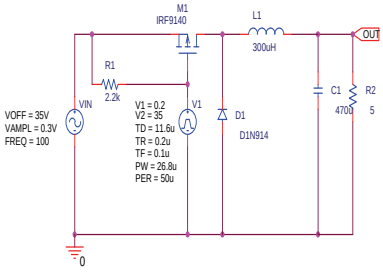

Fig. 1c. Buck DC-DC with MOS pass transistor in switch mode

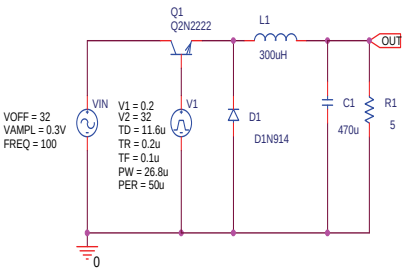

Fig. 1d. Positive buck regulator

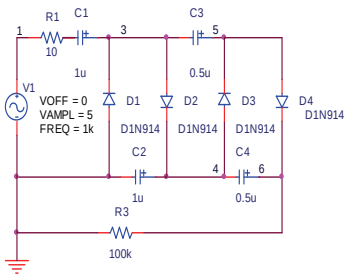

Fig. 1e. Cockcroft-Walton multiplying circuit

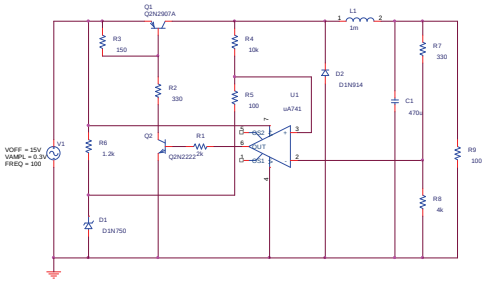

Fig. 1f. Buck switching regulator with PNP pass transistor and voltage translating circuit using op amp

Fig. 1. Six voltage regulator circuits

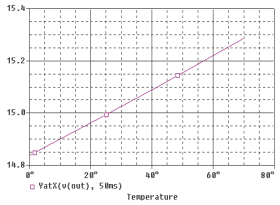

Fig.2a

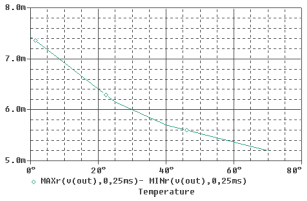

Fig.2b

Fig.2. Temperature curves for the circuit from Fig.1a

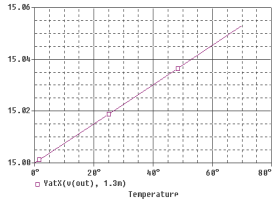

Fig.3a

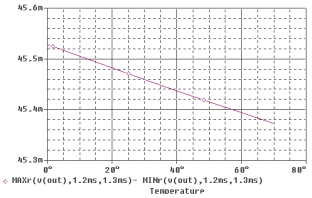

Fig.3b

Fig.3. Temperature curves for the circuit from Fig.1b

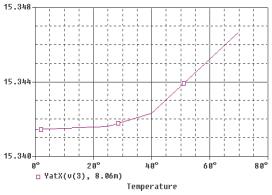

Fig.4a

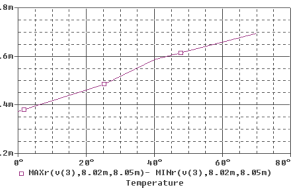

Fig.4b

Fig.4. Temperature curves for the circuit from Fig.1c

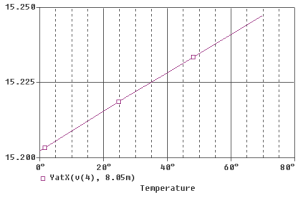

Fig.5a

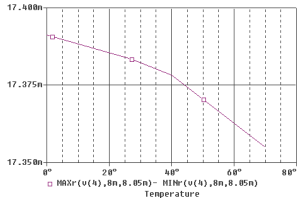

Fig.5b

Fig.5. Temperature curves for the circuit from Fig.1d

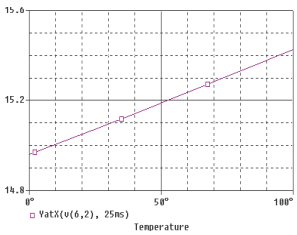

Fig.6a

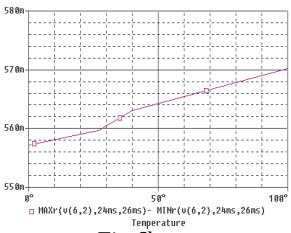

Fig.6b

Fig.6. Temperature curves for the circuit from Fig.1e

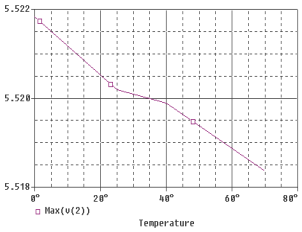

Fig.7a

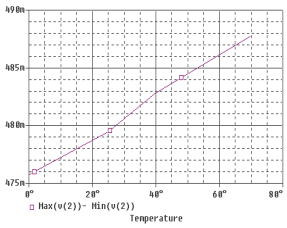

Fig.7b

Fig.7. Temperature curves for the circuit from Fig.1f

A. Temperature Functions for the Finear Voltage Regulator with PNP Pass Transistor

Considering Fig. 2a the stabilized output voltage of the linear voltage regulator with PNP pass transistor is linear and directly proportional function of temperature. The proportion observed is:

$\Delta T°C=70°C \rightarrow \Delta Vout=0.447V$

The coefficient of proportionality is determined as:

$$\frac{\Delta Vout}{\Delta T°C} = 6\frac{mV}{°C}$$

The formula of the temperature dependence for the output stabilized voltage of the circuit from linear voltage regulator with PNP pass transistor is:

$$\mathbf{V_{LIN}out(T°C)=(14.835+6.10^{-3}.T)V} \quad (1)$$

Considering Fig.2b it's determined that the dependence of the stabilized output voltage ripple from temperature is nonlinear and the ripple variation is inverse to temperature variation. When the temperature increases the ripple decreases.

B. Temperature Functions for the Voltage Regulator with NPN Pass Transistor in Switch Mode

Considering Fig.3a it's determined that the stabilized output voltage of the voltage regulator with NPN pass transistor in switch mode is linear and directly proportional function of temperature. The proportion observed is:

$$\mathbf{\Delta T°C=70°C \rightarrow \Delta Vout=5mV}$$

The coefficient of proportionality is determined as:

$$\frac{\Delta\Delta Vout}{\Delta T^{o}C} = 0.75\frac{mV}{^{o}C}$$

The formula obtained for the temperature dependence for the output stabilized voltage of the Voltage regulator with NPN pass transistor in switch mode is:

$$\mathbf{V_{SMNPN}out(T°C)=(15+0.75.10^{-3}.T)V} \quad (2)$$

Considering Fig.3b it's determined that the dependence of the output voltage ripple from temperature for the Voltage regulator with NPN pass transistor in switch mode is linear and inversely proportional.The proportion observed is:

$$\mathbf{\Delta T°C=70°C \rightarrow \Delta\Delta Vout= -0.14mV}$$

The coefficient of proportionality is determined as:

$$\frac{\Delta\Delta Vout}{\Delta T°C} = -2\frac{\mu V}{°C}$$

The formula obtained for the temperature dependence of the output voltage ripple for the Voltage regulator with NPN pass transistor in switch mode is:

$$\mathbf{\Delta V_{SMNPN}out(T°C) = (45.529 - 2.10^{-3}.T)mV} \quad (3)$$

C. Temperature Functions for the Buck DC-DC

Considering Fig.4a it's determined that the stabilized output voltage of the Buck DC-DC slightly depends from temperature:

- $\mathbf{V_{MOS}out = (15.341 \div 15.342)V, T°C=0 \div 40°C}$
- V_{MOS}out increases with 5μV for temperature variation from 40°C to 70 °C

The temperature dependence of the stabilized output voltage of the Buck DC-DC can be expressed as follows:

$$\mathbf{V_{MOS}out \approx const = 15.34V \quad , \quad T°C=0 \div 70°C}$$

Considering Fig.4b it's determined that the output voltage ripple of the Buck DC-DC depends very slightly from temperature and the dependence is close to linear and directly proportional. The proportion observed is:

$$\mathbf{\Delta T°C=70°C \rightarrow \Delta\Delta Vout= -0.14mV}$$

The coefficient of proportionality is determined as:

$$\frac{\Delta\Delta Vout}{\Delta T°C} = 2.3\frac{\mu V}{°C}$$

The formula obtained for the temperature dependence of the output voltage ripple for the Buck DC-DC is:

$$\mathbf{\Delta V_{MOS}out(T°C) = (11.39 + 2.3.10^{-3}.T)mV} \quad (4)$$

D. Temperature Functions for the Positive Buck Regulator

Considering Fig.5a it's determined that the stabilized output voltage of the positive buck regulator is linear and directly proportional function of temperature. The proportion observed is:

$$\mathbf{\Delta T°C=70°C \rightarrow \Delta Vout=45mV}$$

The coefficient of proportionality is determined as:

$$\frac{\Delta Vout}{\Delta T°C} = 0.6\frac{mV}{°C}$$

The formula of the temperature dependence for the output stabilized voltage of the Positive buck regulator is:

$$\mathbf{V_{POS}out(T°C)=(15.202+0.6.10^{-3}.T)V} \quad (5)$$

Considering Fig.5b it's determined that the temperature dependence of stabilized output voltage ripple of the positive buck regulator is nonlinear and the ripple variation is inverse to temperature variation. When the temperature increases the ripple decreases. For temperature variation from 0°C to 70°C the output voltage ripple decreases with 50μV.

E. Temperature Functions for the Cockcroft-Walton Voltage Multiplier

Considering Fig.6a it's determined that the stabilized output voltage of the Cockcroft-Walton voltage multiplier is linear and directly proportional function of temperature. The proportion observed is:

$$\mathbf{\Delta T°C=70°C \rightarrow \Delta Vout=0.328V}$$

The coefficient of proportionality is determined as:

$$\frac{\Delta Vout}{\Delta T°C} = 4\frac{mV}{°C}$$

The formula of the temperature dependence for the output stabilized voltage of the Cockcroft-Walton voltage multiplier is:

$$\mathbf{V_{MULT}out(T°C) = (14.96 + 4.10^{-3}.T)V} \quad (6)$$

Considering Fig.6b it's determined that the output voltage ripple of the Cockcroft-Walton voltage multiplier is close to linear and directly proportional function of temperature.The proportion observed is:

$$\mathbf{\Delta T°C=70°C \rightarrow \Delta\Delta Vout= 9mV}$$

The coefficient of proportionality is determined as:

$$\frac{\Delta Vout}{\Delta T°C} = 0.13\frac{\mu V}{°C}$$

The formula obtained for the temperature dependence of the output voltage ripple for the Cockcroft-Walton voltage multiplier is:

$$\mathbf{\Delta V_{MULT}out(T°C) \approx (557 + 0.13.10^{-3}.T)mV} \quad (7)$$

TABLE II
GENERALIZED DATA AND FORMULAS IN TEMPERATURE AREA FOR THE VOLTAGE REGULATORS

Voltage regulator circuit	**Stabilized output volatage as a function of temperature Vout(T°C)**	**Variation of the output voltage for temperature variation from 0°C to 70°C**	**Output voltage ripple as a function of temperature ΔVout(T°C)**	**Variation of the output voltage ripple for temperature variation from 0°C to 70°C**
Linear voltage regulator with PNP pass transistor	Linear, Direct proportional $\mathbf{V_{LIN}out(T°C)=(14.835+6.10^{-3}.T)V}$	0.447V	Nonlinear, output voltage ripple vary in inverse direction than temperature	-2.1mV
Voltage regulator with NPN pass transistor in switch mode	Linear, Direct proportional $\mathbf{V_{SMNPN}out(T°C)=(15+0.75.10^{-3}.T)V}$	5mV	Linear, Inverse proportional $\mathbf{\Delta V_{SMNPN}out(T°C) = (45.529 - 2.10^{-3}.T)mV}$	-0.14mV
Buck DC-DC	Approximately constrant $\mathbf{V_{MOS}out \approx const = 15.34V}$	6μV	Linear, Direct proportional $\mathbf{\Delta V_{MOS}out(T°C) = (11.39 + 2.3.10^{-3}.T)mV}$	0.16mV
Positive buck regulator	Linear, Direct proportional $\mathbf{V_{POS}out(T°C)=(15.202+0.6.10^{-3}.T)V}$	0.45V	Nonlinear, output voltage ripple vary in inverse direction than temperature	-50μV
Cockcroft-Walton multiplying circuit	Linear, Direct proportional $\mathbf{V_{MULT}out(T°C) = (14.96 + 4.10^{-3}.T)V}$	0.328V	Approximately linear and direct proportional	9mV
Buck switching regulator with op amp	Approximately linear, Inverse proportional $\mathbf{V_{OA}out(T°C) \approx (5.522 - 51.10^{-6}.T)V}$	-3.6mV	Linear, Direct proportional $\mathbf{\Delta V_{OA}out(T°C) = (475 + 18.6.10^{-3}.T)mV}$	13mV

F. Temperature Functions for the Buck Switching Regulator with PNP Pass Transistor and Voltage Translating Circuit using Op Amp

Considering Fig.7a it's determined that the stabilized output voltage of the buck switching regulator with PNP pass transistor and voltage translating circuit using op amp is close to linear and inversely proportional function of temperature. The proportion observed is:

$$\mathbf{\Delta T°C=70°C \rightarrow \Delta Vout = -3.6mV}$$

The coefficient of proportionality is determined as:

$$\frac{\Delta Vout}{\Delta T°C} = -51\frac{\mu V}{°C}$$

The formula of the temperature dependence for the stabilized output voltage of the circuit from Fig.1f is:

$$\mathbf{V_A out(T°C) \approx (5.522 - 51.10^{-6}.T)V} \quad (8)$$

Considering Fig.7b it's determined that the output voltage ripple of the Buck switching regulator with PNP pass transistor and voltage translating circuit using op amp is linear and directly proportional function of temperature. The proportion observed is

$$\mathbf{\Delta T°C=70°C \rightarrow \Delta\Delta Vout= 13mV}$$

The coefficient of proportionality is determined as:

The formula obtained for the temperature dependence for the output stabilized voltage ripple of the circuit from Fig.1f is:

$$\mathbf{\Delta V_{OA}out(T°C) = (475 + 18.6.10^{-3}.T)mV} \quad (9)$$

V. GENERAL FORMULAS FOR THE TEMPERATURE FUNCTIONS OF THE VOLTAGE REGULATORS

Table 2 presents the generalized models and formulas in temperature area for the voltage regulators from Fig1a,1b,1c,1d,1e,1f.

VI. COMPARATIVE STUDY OF THE VOLTAGE REGULATORS BEHAVIOR IN TEMPERATURE AREA

The comparison of the data for the 6 voltage regulators is based on the modules of variations of the output voltage and

$$\frac{\Delta\Delta Vout}{\Delta T°C} = 18.6\frac{\mu V}{°C}$$

output voltage ripple in the temperature interval from 0°C to 70°C. The comparison of the modules of the output voltage variations is:

$$\mathbf{\Delta V_{POS}out(T°C) > \Delta V_{LIN}out(T°C) > \Delta V_{MULT}ou(T°C) > \Delta V_{OA}out(T°C) > \Delta V_{SMNPN}ou(T°C) > \Delta V_{MOS}out(T°C)}$$

The positive buck regulator has the strongest temperature dependence of the stabilized output voltage and the buck DC-DC has the slightest temperature dependence.

The comparison of the variations modules of the output voltage ripples is:

$$\mathbf{\Delta\Delta V_{OA}out(T°C) > \Delta\Delta V_{MULT}ou(T°C) t > \Delta\Delta V_{LIN}out(T°C) > \Delta\Delta V_{MOS}out(T°C) > \Delta\Delta V_{SMNPN}out(T°C) > \Delta\Delta V_{POS}out(T°C)}$$

The Buck switching regulator with PNP pass transistor and voltage translating circuit using op amp has the strongest temperature dependence of the output voltage ripple and the positive buck regulator has the slightest temperature dependence.

REFERENCES

[1] G. Marinova, D. Dimitrov, "Learning optimal synthesis of voltage regulator circuits through comparative study in PSpice", XV International Symposium on Theoretical Electrical Engineering, pp. 211-215, Lubeck, Germany, 2009

[2] G. Marinova, D. Dimitrov, "Analysis of Buck switching regulator with PNP pass transistor and voltage translating circuit using op amp", Proceedings Vol. 45, 3.1. Electrotechnique, electronics, automatics, Russe University "Angel Kanchev", pp. 40-45, Russe 2006 (in Bulgarian)

[3] G. Marinova, D. Dimitrov, "Methodology for analysis of voltage regulator circuits in PSpice simulator", Announcements of Union of Scientists – Sliven, Vol. 11, №1, pp. 50-53. 2006, Sliven (in Bulgarian)

Simulation of Bulk Traps Influence on the Electrical Characteristics of VDMOS Transistor

Sanja Aleksić[1], Darko Bjelopavlić and Dragan Pantić

Abstract – **The influence of donor-like and acceptor-like bulk traps on electrical characteristics of VDMOS transistor under high electric field stress is investigated. First, the mechanisms responsible for bulk traps generation are described and the simulation model incorporated into the Silvaco TCAD software package software that takes into account the impact of bulk traps on the device electrical characteristics is given. In addition the process of sample preparation, measurement techniques and measured initial and after-stress electrical characteristics of VDMOS transistor IRF510 are presented. Finally, the influence of bulk defects simulation model parameters on the electrical characteristics is considered using Silvaco simulation tools. It is shown that bulk defects significantly affect on the device behaviour, but they are not the only mechanism responsible for the degradation of electrical characteristics of VDMOS transistor due to high electric field stress.**

Keywords – **Donor-like, acceptor-like, bulk trap, Silvaco.**

I. INTRODUCTION

Over the past six decades, high-speed and low power integrated circuits (IC) are used so widely, permeating every aspect of human life. Accordingly, high-quality circuit design is one of the most critical parts of this technology. Reducing in transistors size continually complicates the device physics and makes device modeling more sophisticated. Because of that, complete fabrication process flow and device electrical characteristics simulation programs, as well as the electronic circuit simulators are the essential tools in the procedure of ICs design.

The electrical instability of MOSFETs is usually associated with hot-carrier trapping in the oxide-semiconductor interface. In the last 30th years, so many investigation reports an experiments which determine the mechanisms leading to device degradation and propose the physical models for the instability explanations [1-3]. In most of these models, the -- presence of defects in semiconductor substrates was neglected, even though the bulk defects may significantly affect on the device electrical characteristics. As it is well known, by using the process and device simulators in the IC design procedure we have the possibility to separate the influence of different parameters, models and mechanisms on the device electrical characteristics. This ability is utilized in this paper to separate bulk and interface trap generation mechanisms due to high electric field stress (HEFS) and simulate and discuss only the bulk traps impact on the device electrical characteristics.

In order to isolate only the bulk trap generation mechanisms due to HEFS on the n-channel power VDMOS electrical characteristics (threshold voltage, transconductance, etc.), it was necessary to simulate its complete technological production process flow. After the procedure of process flow reverse engineering, the doping profile distributions in the simulation domain is obtained by using the process simulator ATHENA [4] which is an integral part of Silvaco TCAD software package. The electrical characteristics of VDMOS transistors and the influence of bulk trap generation mechanisms are simulated by using the device simulator ATLAS [5]. Comparing the obtained simulation results and measured electrical characteristics it is shown that bulk defects significantly affect on the device behaviour, but they are not the only mechanism responsible for the degradation of VDMOS electrical characteristics due to high electric field stress.

[1]Authors are with the Faculty of Electronic Engineering, Aleksandra Medvedeva 14, 18000 Nis, Serbia, E-mail: sanja.aleksic@elfak.ni.ac.rs.

II. BULK TRAPS

A. Bulk Traps Generation Mechanism

The presence of defect centers, or traps, in semiconductor substrates may significantly influence on the electrical characteristics of the device. Trap centers, whose associated energy lies in the forbidden gap, exchange charge with the conduction and valence band through the emission and capture of electrons. The trap centers influence the density of space charge in semiconductor bulk and the recombination statistics.

The donor-like hole trap (**DT**) can be either positive (ionized) when empty or neutral when filed with electron. An empty **DT**, which is positive, can capture an electron or emit hole, while a filled **DT**, which is neutral, can emit an electron or capture hole. Unlike donors, the energy levels for **DT** usually lie in energy gap near the valence band. An acceptor-like electron trap (**AT**) is neutral when empty and negatively charged (ionized) when filled with an electron. A filled **AT** can emit an electron or capture a hole, while an empty **AT** can capture an electron or emit a hole. Likewise, the energy levels for **AT** lie near the conduction band.

B. Bulk Traps Simulation Model

The net charge due to the presence of traps in semiconductor bulk is added on the right hand side of Poisson's equation. The total charge value is defined as:

$$Q_T = q(N_{tD}^{+} - N_{tA}^{-}) = Q_{tD}^{+} - Q_{tA}^{-}, \qquad (1)$$

where N_{tD}^{+} and N_{tD}^{+} are the densities of ionized donor-like and acceptor-like traps, respectively. The ionized density is equal to the product of the donor (*NTD)* and acceptor (*NTA*)

trap densities and its probability of ionization F_{tD} and F_{tA}. The probability of ionization assumes that the capture cross sections are the constant for all energies in a given band, and follows the analysis developed by Simmons and Taylor [6]:

$$F_{tD} = \frac{v_p SIGP \cdot p + e_{nD}}{v_n SIGN \cdot n + v_p SIGP \cdot p + e_{nD} + e_{pD}} \quad (2)$$

$$F_{tA} = \frac{v_n SIGN \cdot n + e_{pA}}{v_n SIGN \cdot n + u_p SIGP \cdot p + e_{nA} + e_{pA}} \quad (3)$$

SIGN and *SIGP* are the carrier capture cross sections for electrons and holes, respectively, υ_n and υ_p are the thermal velocities for electron and holes, while the electron and hole emission rates are defined by:

$$e_{nD} = \frac{1}{DEGEN.FAC} v_n \cdot SIGN \cdot n_i \cdot \exp\frac{E_t - E_i}{kT_L} \quad (4)$$

$$e_{pA} = DEGEN.FAC \cdot v_p \cdot SIGP \cdot n_i \cdot \exp\frac{E_i - E_t}{kT_L} \quad (5)$$

E_i is the intrinsic Fermi level position, E_t is the energy of the discrete trap level defined in relation to valence and conduction band edge for donor and acceptor trap, respectively, T_L is the lattice temperature and *DEGEN.FAC* is the degeneracy factor of the trap center.
In the case where the *k* donor and/or *m* acceptor trap energy levels are defined, the total charges are:

$$Q_{tD}^{+} = q\sum_{\alpha=1}^{k} N_{tD\alpha}^{+} = q\sum_{\alpha=1}^{k} NTD_{\alpha} \cdot F_{tD}^{\alpha} \quad (6)$$

$$Q_{tA}^{+} = q\sum_{\beta=1}^{m} N_{tA\beta}^{-} = q\sum_{\beta=1}^{m} NTA_{\beta} \cdot F_{tA}^{\beta} \quad (7)$$

III. Experimental Procedure

A. Sample Preparation

The devices used in the experiment were power n-channel VDMOS transistor IRF510 (TO-220), with 860 hexagonal cells, is fabricated using conventional Si-gate technology with 10Ωcm p-type <100> oriented substrate. The nominal gate oxide is 120nm thickness grown in dry oxygen ambient and annealed for 20 min in nitrogen at 1100°C. The structure of the device is shown in fabrication technology has been described in more detail in Ref. [14]. It is important to note that the current flows horizontally from the N^+ source through p-channel and then vertically through the N^- epitaxial layer to the bottom drain contact.

The HEFS was performed with the gate biases of V_{GS} = +80 V or V_{GS} = −80 V (source and drain grounded) at room temperature. The gate bias was sufficient to induce significant defect densities in the SiO_2 and at the Si/SiO_2 interface during the total stress time of 150 min. Namely, the electric field in the oxide (about 8 MV/cm) was sufficient to cause Fowler-Nordeheim tunneling of electrons into the oxide either from the silicon substrate (positive V_{GS}) or from the gate (negative V_{GS}). After the HEFS, the transistors were annealed in air at 150 °C with annealing gate bias V_{Ga} = +10 V (source and drain grounded), using the Heraeus HEP2 system of temperature chambers. In order to investigate details of defect kinetics during the repeated stress (e.g. whether some processes reach saturation during the second stress cycle), after about 3000 h of annealing time both the HEFS and thermal post-HEFS annealing were repeated under the identical experimental conditions.

B. Measurement Techniques

The equipment used for the high electric field stressing and electrical characterization consisted of Keithley 237 source-measure unit, Keithley 2400 SourceMeter, and HP8116A function generator. The HEFS and all electrical measurements were performed at room temperature and were completely automated and controlled by a PC.

Two substantially different techniques were used to determine densities of stress-induced defects in the SiO_2 and Si/SiO_2 interface – subthreshold-midgap (MG) method and charge-pumping (CP). The MG method as originally proposed uses analysis of transistor subthreshold I–V curves to determine densities of the oxide-trapped charge and interface traps created during stress and post-stress annealing. The CP technique, in our case modified for use in power VDMOSFETs uses measurements of charge-pumping current to determine number of interface traps; the technique cannot be used to reliably estimate oxide-trapped charge contribution. The CP measurements were performed with source and drain grounded, and triangular gate pulses (frequency 1 MHz, amplitude 4 V) applied to the gate.

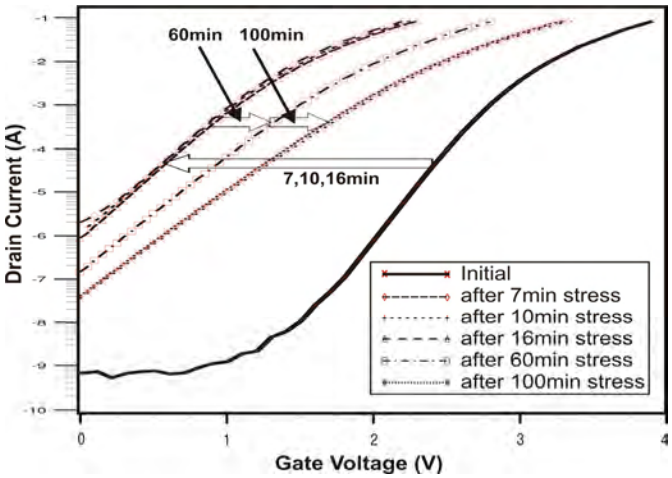

Fig. 1. The measured static electrical characteristics of VDMOS transistor before and after positive gate voltage stress.

From the measured electrical characteristics (Fig. 1) the significant transconductance degradation and subthreshold leak current increase are obvious, while the threshold voltage decreases initially and then returns to increase.

IV. Simulation Results

A. Reverse Engineering of VDMOS Production Flow

In order to simulate the influence of bulk traps formed under the influence of high electric fields, on the electrical characteristics of VDMOS transistor, it is necessary to simulate its complete technological production flow and determine the doping profiles in the simulation domain. This is a very serious problem given the fact that the VDMOS transistor production flow has more than one hundred process steps, whereby each process has dozens of process parameters that are unknown to us.

The initial data known at the beginning of the simulation procedure are the measured electrical characteristics of VDMOS transistors (threshold voltage V_T, output characteristics $I_D=f(V_{DS})$ and transport characteristic $I_D=f(V_{GS},V_{DS}=100mV)$) and basic information about the technology used for its development (type of the technology and the order of process steps). By using these data the manufacturing process flow of VDMOS transistor is reconstructed, and the values of the process parameters (implantation energies and doses, time, temperature and ambient of diffusion processes, etc.) as well as device geometry parameters are determined. After that it was possible to simulate the complete process flow using the process simulator ATHENA that is an integral part of the Silvaco TCAD software package.

The impurities profile distribution is then used as input parameter for simulation of VDMOS electrical characteristics using device simulator ATLAS, which is also a part of the aforementioned TCAD software package.

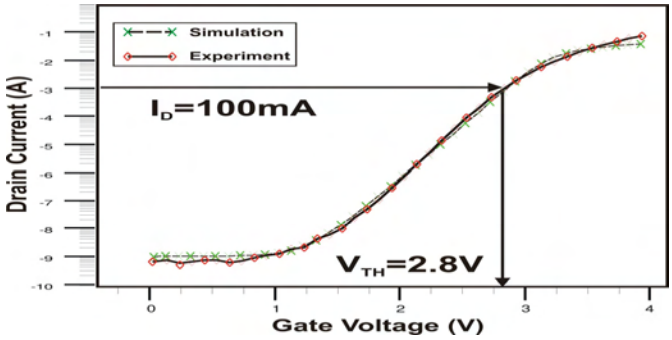

Fig. 2. Comparison of simulation results with the initial measured electrical characteristics of VDMOS transistors after device simulator ATLAS calibration.

B. Silvaco TCAD Software Package Calibration

The next very important step in the simulation of electrical characteristics of power VDMOS transistor is the calibration of device simulator ATLAS. This means that it is necessary to further fine-tuning parameters, which largely depend on the specific technology characteristics, such as: fixed oxide charge density applied at the Si/SiO_2 interface (QF), low-field electron and hole mobility (MUN, MUP), electron and hole velocity saturation (VSATN, VSATP), and electron and hale surface recombination velocities (S.N, S.P). After setting these parameters, a very good agreement of simulation results with the measured initial (unstressed) electrical characteristics of VDMOS transistor is obtained, as shown in Fig. 2.

C. Trends Caused by Vvarying Bulk Trap Ddistribution Parameters

In order to activate bulk traps in ATLAS device simulation tool and to analyze their impact on electrical characteristics of VDMOS transistor the command TRAP is used. TRAP activates donor and/or acceptor bulk traps at discrete levels within the bandgap of the semiconductor and set their parameter values:

TRAP DONOR/ACCEPTOR E.LEVEL=<r>, DENSITY=<r>, DEGEN.FAC=<r>, <capture parameters>

Parameter DONOR/ACCEPTOR specifies donor- or acceptor-type trap levels, DENSITY sets the maximum defect density states of the trap level, while DEGEN.FAC specifies the degeneracy factor of the trap level used to calculate the density. E.LEVEL sets the energy of the discrete trap level. For donors E.LEVEL value is relative to the valence band edge, while for acceptors it depends on the conduction band edge. Capture parameters specifies cross sections of the trap for electrons and holes or their lifetimes in the trap level.

Before trying to match measured electrical characteristics of stressed device with the simulation results it is worth to understand trends caused by varying the bulk trap parameters on the threshold voltage shift, the transconductance degradation and the subthreshold leakage current. The influence of maximum donor-type bulk traps and bulk trap energy level for DD=2.E16 and DD=1.E17 on the VDMOS electrical characteristics are shown on Figs. 3-5, respectively. It is obvious that the threshold voltage decreases when the the maximum concentration of donor-like bulk trap increase. On the other hand, when the donor trap energy level approaches to the bottom of conduction band edge the threshold voltage continue to decrease, while the effects of the transconductance degradation and the subthreshold leakage current increasing are more emphasized.

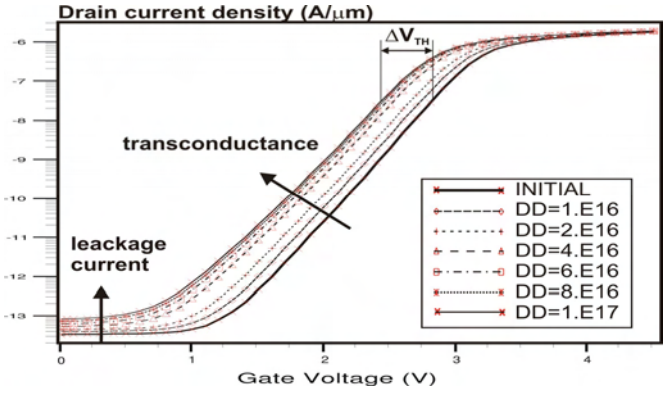

Fig. 3. The influence of maximum density donor-type bulk trap on VDMOS electrical characteristics

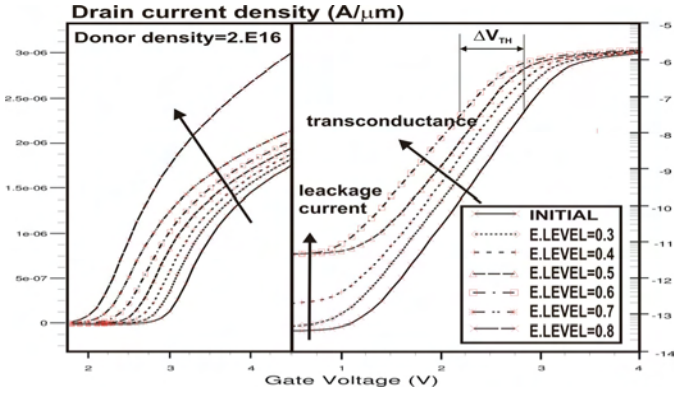

Fig. 4. The influence of donor-type bulk trap energy level on VDMOS electrical characteristics for donor density DD=2.E16

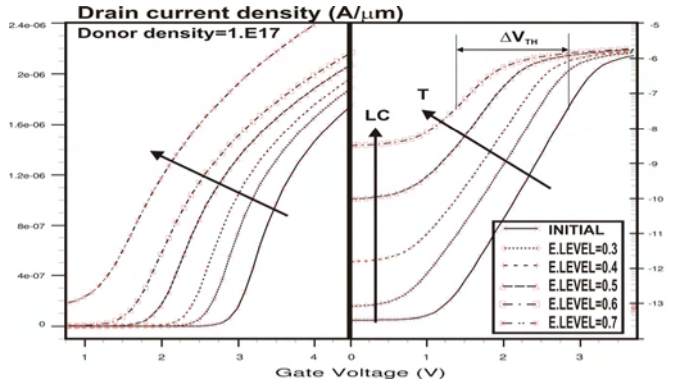

Fig. 5. The influence of donor-type bulk trap energy level on VDMOS electrical characteristics for donor density DD=1.E17

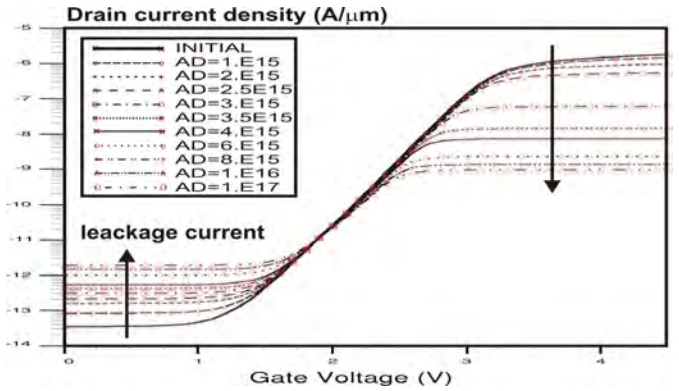

Fig. 6. The influence of maximum density acceptor-type bulk trap on VDMOS electrical characteristics

The influence of maximum density acceptor-type bulk trap on VDMOS electrical characteristics is shown on Fig. 6, and on the basis of their shape, it is clear that the acceptor-like bulk traps are not responsible for the degradation of device characteristics due to positive HFES. Finally, the values of bulk traps distribution parameters and the obtained simulation results are compared with experimentally measured characteristics of stressed VDMOS transistor (Fig. 7). It is important to note that the effects of short-term HFES could not be well simulated when only the influence of bulk traps on characteristics is taken. In that case we have to include in simulation model the influence of donor and acceptor interface traps generation mechanisms. A quite well match with electrical characteristics of longer stressed components can be explained by the fact that the current in these components flows not only through the channel but also vertically through the substrate, where the influence of bulk traps is dominated.

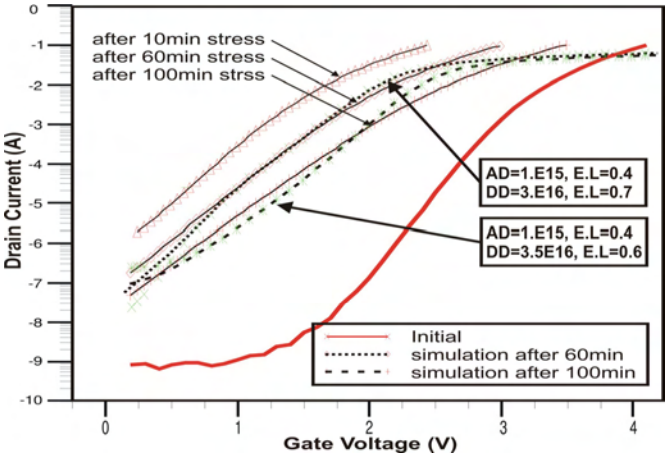

Fig. 7. The comparison of measured and simulated electrical characteristics of stressed VDMOS transistor with values of bulk traps distribution parameters.

V. Conclusion

In this paper the influence of bulk traps on the degradation of electrical characteristics of power VDMOS transistor due to positive HFES is analyzed. It is shown that the degradation effects can be quite good simulated by taking into account only the influence of bulk traps, but for the correct and precise simulation of HFES impact on device characteristics it the necessary to include in the simulation model all relevant effects and generation mechanisms.

Acknowledgement

This work has been partially supported by the Serbian Ministry for Education and Science under the projects TR-33035 and ??.

References

[1] D.J. DiMaria, J. W. Stasiak, “Trap Creation in Silicon Dioxid Produced by Hot Electrons”, J. Appl. Phys., vol. 65, pp. 2342-2346, 1989.

[2] G.S.Ristic, M.M. Pejovic, A.B. Jaksic, "Fowler-Nordheim High Electric Field Stress of Power VDMOSFETs", Solid. State. Electron., vol. 49, pp.1140-11152, 2005.

[3] N. Stojadinovic et all, "Effects of Electrical Stressing in Power VDMOSFETs", MIcroelectron. Reliab., vol. 45, pp. 115-122, 2005.

[4] *ATHENA User’s Manual*, SILVACO, Inc., CA, USA, 2010.

[5] *ATLAS User’s Manual*, SILVACO, Inc., CA, USA, 2010.

[6] J. Simmons and G. Taylor, “Nonequilibrium.Steady-State Statistics and Associated Defects for Insulators and Semiconductors Containing an Arbitrary Distribution of Traps”, Phys. Rev. B, vol. 4, p502, 1971.

Simulation and Optimization of HIT Solar Cells with Intrinsic Thin Amorphous Si Layer

Darko Bjelopavlić[1], Sanja Aleksić[1], Danijela Pantić[2], Branimir Đorđević[3] and Dragan Pantić[1]

Abstract – **Photovoltaic modules based on single crystal and polycrystalline silicon are almost 90% of the total world solar market, mainly because of its stable, robust and reliable characteristics. Therefore, great efforts are being made to improve their characteristics, especially their efficiency. One of the many approaches is HIT solar cells (hetero-junction solar cell with an intrinsic thin amorphous layer) fabricated at temperatures below 300°C. In this paper, the electrical characteristics of HIT solar cells are simulated by using the TCAD Silvaco software package. The structure of HIT solar cell is optimized in order to obtain their maximum efficiency.**

Keywords – **Solar cells, hetero-junction, amorphous/crystalline silicon, simulation, Silvaco.**

I. Introduction

Mono-crystalline, poly-crystalline and amorphous silicon solar cells are the most widely used group of the commercial solar cells. This is, primarily, based on the fact that these solar cells have stable characteristics over a long period of time, good reliability during operation, and their mass production, as developed in the microelectronics technology allows fast and relatively cheap production of solar cells based on silicon. The declining trend in the price of solar cells continues, and the technology improves so that the efficiency of solar cells produced becomes greater. One of the improvements is a combination of technologies based on single crystalline silicon (mono-crystalline silicon) layer with the addition of a thin amorphous layer. The resulting structure is known as HIT solar cell (hetero-junction with an amorphous intrinsic thin layer) produced by Sanyo Ltd., where the efficiency of commercially produced HIT solar cells is over 20%, and there is plenty of room for it to improve [1,2].

The production technologies of HIT solar cells use a thin intrinsic amorphous silicon layer (a-Si:H(i)) which is formed on both sides of wafer (Czochralski n-type c-Si), using low temperature PECVD process that takes place on 175°C or 250°C [3].In this way they avoid high temperature processes that degrade the interface surface of amorphous film and crystalline bulk. Thus obtained HIT structure has multiple advantages over the standard process. First, the width of a band gap Eg of amorphous silicon is in the range of 1.55eV to 1.87eV, which increases the efficiency at lower wavelengths, where is the most concentrated intensity of terrestrial solar radiation. Now, HIT structure shows better temperature characteristics, as well as a higher voltage V_{OC} (open-circuit voltage), because of a significant decrease in surface and interface recombination.

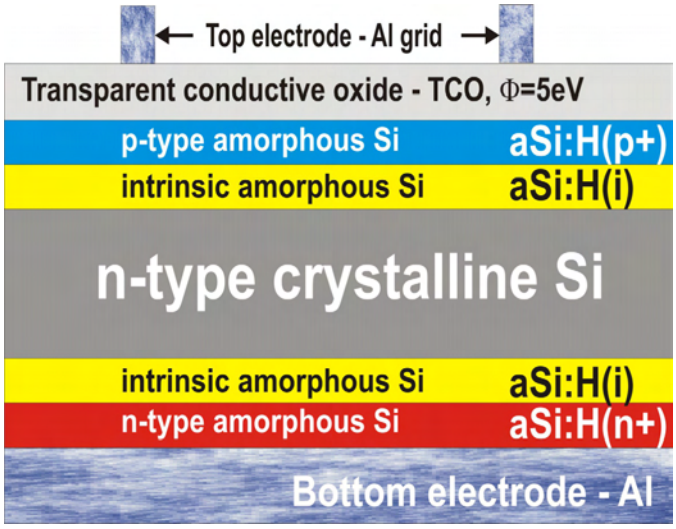

Fig. 1. HIT solar cell structure with the intrinsic amorphous Si layer.

This paper presents the results for the technology process flow and electrical characteristics of HIT solar cells simulation. Program ATHENA [4] is used for the simulation of complete production flow, while the electrical characteristics of HIT solar cell are simulated by program ATLAS [5]. Software tools ATHENA and ATLAS are an integral part of the Silvaco TCAD (Technology Computer-Aided Design) package. Initially, special attention was paid to the definition and analysis of interfacial and volume states impact on the electrical characteristics of HIT solar cells. Thereafter, the structures of the HIT cells are optimized, in order to gain V_{OC} and output power increase, taking into consideration the influence of a-Si:H(p^+) layer thickness and the level of n-type crystalline silicon supstrate doping.

II. Structure of HIT Solar Cell

The cross-section structure of HIT solar cell with a-Si:H(i) layer between the p^+ doped amorphous silicon and c-Si(n^+) from the front, and n^+ doped amorphous silicon cathode and c-Si(n^+) on the back side of solar cells is shown in Fig. 1 [6]. The TCO (transparent conductive oxide) is deposited on the front side (but it could be on both sides to provide a low serial

[1]Autors are with the Faculty of Electronic Engineering, Aleksandra Medvedeva 14, 18000 Nis, Serbia, E-mail: dragan.pantic@elfak.ni.ac.rs.
[2]Danijela Pantić is with ETŠ,"Nikola Tesla", Aleksandra Medvedeva 18, 18000 Nis, Serbia, E-mail: danijela.pantic@etstesla.ni.ac.rs.
[3]Branimir Đorđević is with the Megatrend University, Belgrade E-mail: drbranimir@gmail.com

resistance of cathode contact). An aluminum grid is deposited on the upper surface, the first electrode, and the bottom surface is aluminum metallization as a second electrode. However, the standard HIT solar cells do not have a-Si:H(i) which reduces the thickness of a-Si:H, but this layer increases the quantum efficiency of the structure, especially in the smaller wave lengths, without significant impact on the value of voltage V_{OC}. The doping profile distribution in the whole simulation domain of the HIT solar cell was obtained after simulation of the complete technology process flow by using the program ATHENA.

III. Parameters of Physical Model

To be able to simulate the electrical characteristics of HIT solar cells correctly and accurately, it is necessary to select and define properly the parameters of the physical models. This primarily refers to the definition of contacts, and to a model of the carriers generation and recombination, both in amorphous and mono-crystalline silicon, and finally the interfaces that exist in the HIT solar cell structure.

In defining the upper anode contact, it is necessary to choose carefully the material with its workfunction (*WF*), higher than 5eV. Another parameter that significantly affects the characteristics is the doping level of n-type Si crystalline layer. Less resistance, that is, higher doping ($>10^{15}$cm^{-3}) increases the value of V_{OC}, until serial resistance R_S is activated, not only due to the presence of interface states (the electronic equivalent is a parallel resistance R_P), but also due to decrease of the depletion region width, which reduces the absorption "surface" (the depletion region length).

The influence of *WF* on the HIT solar cell electrical characteristcs deals over Schottky-contact on the anode, i.e. contact potential. Klaassen's mobility model are used for the simulation, while the values of electron and hole mobilities in n^+ and p^+ a-Si:H silicon layers are μ_e=10cm^{2}V^{-1}s^{-1} and μ_h=2cm^{2}V^{-1}s^{-1}. In addition to the standard SRH, Auger and modified surface recombination model, it is necessary to define the acceptor-like and donor-like states, both at the a-Si/c-Si interface. The carriers' lifetime τ_n and τ_p are also a function of defect energy states in the bandgap.

As already mentioned, disordered materials contain a large number of defect states within the band gap of the material. To accurately model device such as HIT solar cell, which has layers of amorphous silicon, the DEFECT statement is used to specify the density of defect states (DOS) as a combination of exponentially decaying band tail states and Gaussian distributions of mid-gap states [7] in a-Si:H and c-Si regions, and on the interfaces a-Si/c-Si.

It is assumed that the total density of states (DOS) *g(E)*, is composed of four bands: two tail bands (a donor-like valence band and an acceptor-like conduction band) and two deep level bands (one acceptor-like and the other donor-like) which are modeled using a Gaussian distribution.

$$g(E) = g_{TA}(E) + g_{TD}(E) + g_{GA}(E) + g_{GD}(E) \qquad (1)$$

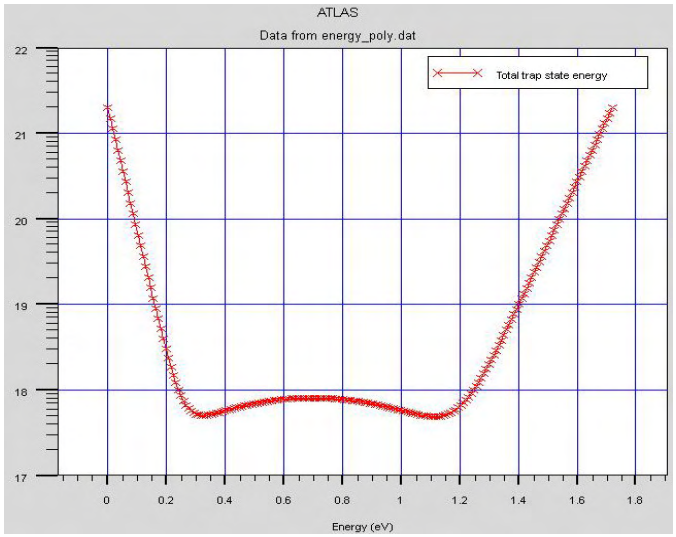

Fig. 2. The total distribution of energy states g(E) in amorphous silicon layers

The profile of energy distribution, shown on Fig. 2, has standard "U" profile. Exponential band "tail" defined for acceptor-like states and donor-like states are:

$$g_{TA}(E) = NTA \exp\left(\frac{E - E_C}{WTA}\right) \qquad (2)$$

$$g_{TD}(E) = NTD \exp\left(\frac{E_V - E}{WTD}\right) \qquad (3)$$

NTA and *NTD* are the maximum of acceptor-like and donor-like trap densities (band tail density of states), respectively (*NTA*=*NTD*=2.E+21cm^{-3}eV^{-1}). E_C is the conduction band energy, E_V is the valence band energy, while *WTA* and *WTD* are characteristic decay energy for acceptors and donors (*WTA*=0.03eV, *WTD*=0.06eV). The mid-gap traps described by Gaussian distributions of donor-like states and acceptor-like states are:

$$g_{GD}(E) = NGD \exp\left[-\left(\frac{E - EGD}{WGD}\right)^2\right] \qquad (4)$$

$$g_{GA}(E) = NGA \exp\left[-\left(\frac{EGA - E}{WGA}\right)^2\right] \qquad (5)$$

NGD and *NGA* are Gaussian maximum energy density of states in the Si doped layer (*NGD*=8.E+17cm^{-3} and *NGA*= 5.E+20cm^{-3}), while for the intrinsic Si layer *NGD*=8E+15cm^{-3} and *NGA*=5.E+17cm^{-3}. Parameters *EGD* and *EGA* are the Gaussian peak energies (*EGD*=1.22eV and *EGA*=0.7eV). The standard deviation for these functions are *WGD*=*WGA*= 0.23eV.

Capture cross-sections for the exponential "tail" distributions are *SIGTAE*=1.E-17 and *SIGTAH*=1.E-15 for the acceptor traps, and *SIGTDE*=1.E-15 and *SIGTDH*=1.E-17 for the donor traps. Electron and hole capture cross-section for

acceptor-like states of Gaussian distributions are *SIGGAE* =1.E-15, *SIGGAH*=1E-14, while for Gaussian distributions of donor-like states capture cross-sections are *SIGGDE*=1E-14 and *SIGGDH*=1E-15. These values are taken as default and they are the same for c-Si region, and also for a-Si/c-Si interface. The surface concentration of interface fixed charge is $QF=10^{10}\text{cm}^{-2}$, while the surface recombination velocity of electrons and holes are *S.N* = *S.P* =1E+3cm/s. Modeling was carried out for the life-time of carriers on the interface surface a-Si/c-Si, which is described in equations for the electrons and holes lifetimes:

$$\frac{1}{\tau_n^{eff}} = \frac{1}{\tau_n^i} + \frac{d_i}{A_i} S.N \tag{6}$$

$$\frac{1}{\tau_p^{eff}} = \frac{1}{\tau_p^i} + \frac{d_i}{A_i} S.P \tag{7}$$

where τ^i is the time specified for semiconductors bulk, and A_i and D_i are the length and area of influence for each analyzed point.

IV. Simulation Results and Discussion

The simulated HIT solar cell has two intrinsic amorphous layers on both sides of n-type mono-crystal silicon, where both of them are 10nm thick. The bulk itself is an n-type silicon. Phosphours concentration is changed in the range from $3.E+15\text{cm}^{-3}$ to $1.E+17\text{cm}^{-3}$. The doped amorphous silicon top layer a-Si:H(p+) is also a 10nm thick, doped with boron, where the doping concentration is $3E+19\text{cm}^{-3}$. The simulation results and experimental measurements showed that this concentration is a limit value for which the efficiency of HIT solar cells enters saturation. The lower doped amorphous silicon layer a-Si:H(n+) is doped with phosphorus, where the doping concentration is $1E+19\text{cm}^{-3}$. Anode electrode is 80nm thick TCO-type, while the cathode contact is made of aluminum. During the simulation it is taken into account the possible reflection of light from the lower electrode. For simulation under illumination it was used the standard AM 1.5 normalized to 0.1W/cm^2 or 100mWcm^{-2} (1sun), the wavelength vary from 0.25μm to 2.4μm. In this way the excitation of solar insolation for terrestrial systems is positioned.

As already mentioned, the workfunction value for TCO electrodes significantly affects on the open circuit voltage V_{OC} and thus on the efficiency of HIT solar cells. It is therefore important to perform the analysis of its influence.The values of *WF* are changed and the simulated output electrical characteristics for *WF* = 4.9eV, 5.1eV, 5.3eV and 5.5eV, and output power are shown in Fig. 3 and Fig. 4, respectively.

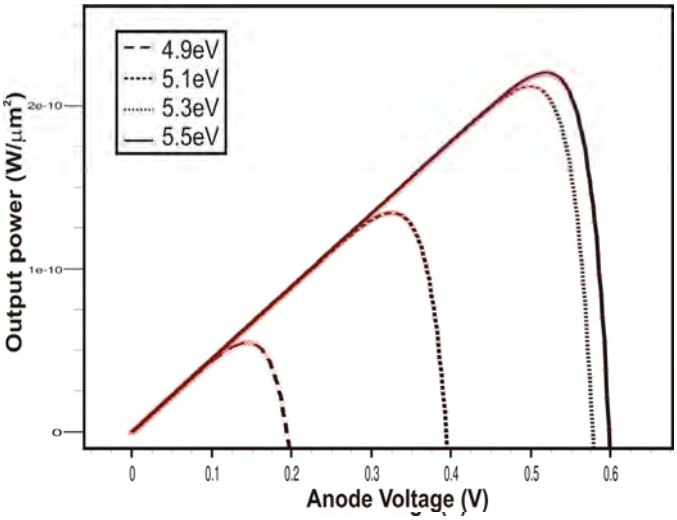

Fig. 3. I-V characteristics of HIT solar cells for different values of the parameter WF

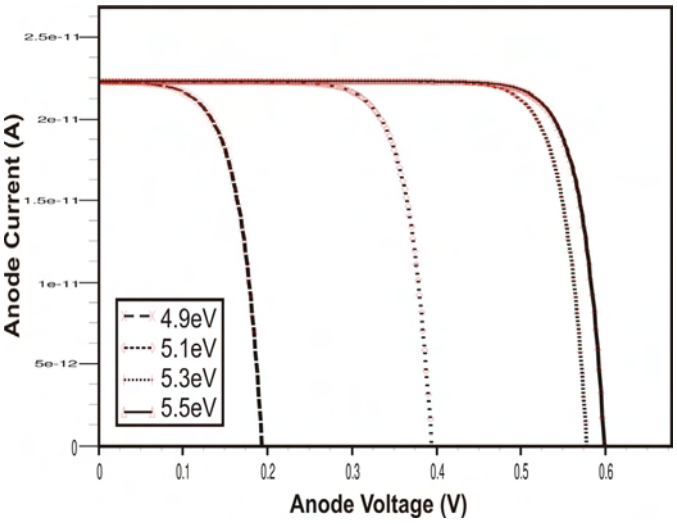

Fig. 4. Output power per μm^2 of HIT solar cell for different values of the parameter WF

Based on the simulation results it is obvious that for the *WF* values less than 5.3eV, the open circuit voltage V_{OC} rapidly changing and decreasing, while for the larger *WF* values V_{OC} saturates. The maximum value of V_{OC} = 0.6V is obtained for the *WF* = 5.5eV. For example, when the doping level of mono-crystalline Si is 1.E+16 and *WF*=5.5eV, the efficiency of HIT solar cell η=22% is obtained. It should be noted that the actual technology processes used for HIT solar cell production can make the TCO electrode with the indicated value of *WF*.

The next parameter that proved to be very important for HIT solar cell electrical characteristics is the level of mono-crystalline silicon doping. The influence of this concentration is two-fold, at least when viewed from the basic parameters. The first is the serial resistance reduction until the mobility of carriers is significantly reduced, increasing the V_{OC}, and the second is the influence on the width of the depletion region. Also, as a side effect, the relationship between the impurity concentration and interface traps could be observed.

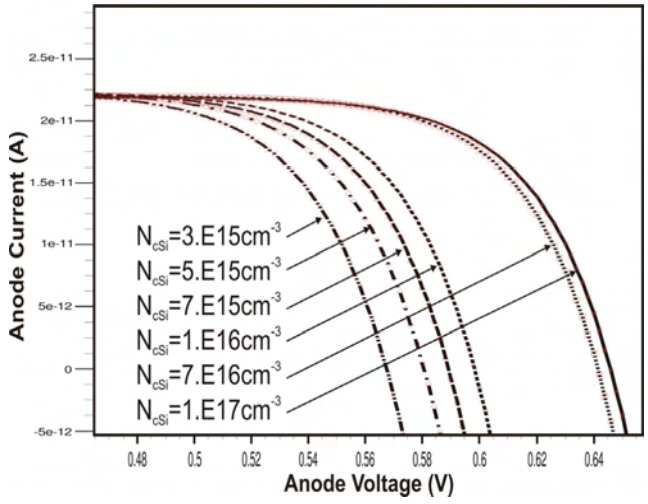

Fig. 5. Dependence of V_{OC} on doping concentration of c-Si

In Fig. 5 the dependence of V_{OC} due to doping concentration of c-Si changing is shown and V_{OC} saturation is noticed when the doping is greater than 1E+17cm^{-3}. The decrease of I_{SC} with increasing the substrate doping level can also be observed. Fig. 6 shows the dependence of output power *P*. In addition, in order to determine the coefficient of efficiency in % it is needed only to multiply the maximum value from the graphics to 10^{12} (take the absolute value).

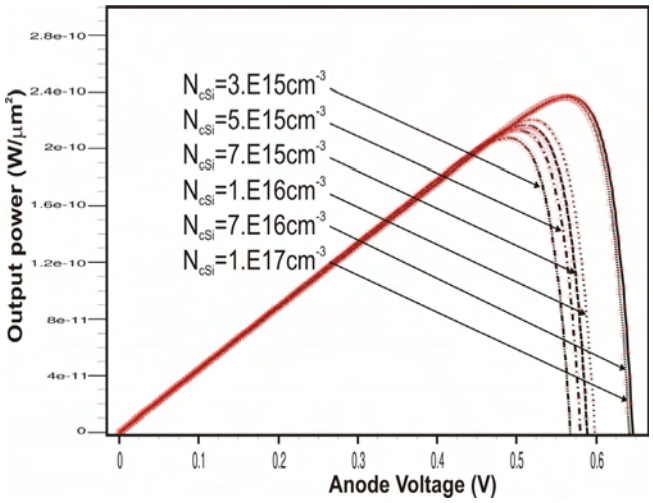

Fig. 6. Dependence of output power P (W/μm^2) on doping concentration of c-Si

Besides the saturation of the V_{OC} there is also the saturation in the HIT solar cell efficiency η. For the optimum doping level value 7.E+16cm^{-3}, gives V_{OC}=0.64V, η=23.6% and *FF*=83.48%. With further doping level increase the open circuit voltage slowly begins to decline, while the short circuit current starts to decrease significantly.

V. Conclusion

This work presents the results of simulation and optimization of the technology flow, and electrical characteristics of HIT solar cells. For the simulation of technological processes of production, ATHENA software was used, while the electrical characteristics were simulated in ATLAS software. ATHENA and ATLAS programs are an integral part of the Silvaco TCAD (Technology Computer-Aided Design) software package. It is shown that the proper choices of physical model parameters are: mobility, generation and recombination, as well as defining the contacts, and the interface can successfully and accurately simulate the electrical characteristics of HIT solar cells. The structure with the best characteristics in terms of V_{OC} and efficiency η was obtained by optimizing the most important parameters of HIT structure: the level of doping and layers thickness.

Acknowledgement

This work is partially supported by the Serbian Ministry for Education and Science under the projects TR-33035.

References

[1] S. Taira, Y. Yoshimine, T. Baba, M. Taguchi, H. Kanno, T. Kinoshita, H. Sakata, E. Maruyama, M. Tanaka, Our approaches for achieving HIT solar cells with more than 23% efficiency, in: *Proceedings of the 22nd European Photovoltaic Solar Energy Conference*, Milan, Italy, 3–7 September 2007, pp. 932–935

[2] Y. Tsunomura , Y. Yoshimine, M. Taguchi, T. Kinoshita, H. Kanno, H. Sakata, E. Maruyama, M. Tanaka, *22%-Efficiency HIT solar cell*, SANYO Electric Co., sep. 2007.

[3] L. Zhao, C.L. Zhou, H.L. Li, H.W. Diao and W.J. Wang, Design optimization of bifacial HIT solar cells on p-type silicon substrates by simulation, *Sol. Energy Mater. Sol. Cells* **92** (2008), pp. 673–681.

[4] *ATLAS User's Manual* – Device Simulation Software, SILVACO, Santa Clara, USA, 2009.

[5] *ATHENA User's Manual* – Process Simulation Software, SILVACO, Santa Clara, USA, 2009.

[6] N. Hernández-Como**,** A. Morales-Acevedo, *Simulation of hetero-junction silicon solar cells with AMPS-1D*, Solar Energy Materials and Solar Cells, Volume 94, Issue 1, Jan. 2010, pp. 62-67

[7] Kemp, A.M., M. Meunier, and C.G. Tannous, "Simulations of the Amorphous Silicon Static Induction Transistor", Solid-State Electronics, Vol. 32, No. 2 (1989): pp. 149-157.

Power Consumption Analysis of Distributed Lift System

Branislav Petrovic[1], Goran Nikolic[1] and Milica Jovanovic[1]

***Abstract* – In this paper the distributed power supply for the embedded lift processor system is analyzed, drawbacks exaggerated and solution is suggested. A basic structure of lift system and practical lift processor realization is described. Power supply requirements for the lift processor are defined accordingly industry standard classifications. Power consumption analyse of the distributed power system is analyzed. The results shown that number of floors is greater than six, a dc/dc structure of floor processor power supply is optimal solution.**

***Keywords* – Lift system, reconfigurable power supply, distributed power architecture**

I. INTRODUCTION

Most nowadays systems are highly dependent on computers for their basic day-to-day functioning. One of significant functional requirements of those systems is related to safety reliability. An aircraft and traffic control, medical devices, automated manufacturing, military systems and for appliance-type applications such as automobiles, washing machines, temperature control, and telephony, name a few for instance. The cost and consequences of these systems failing can range from mildly annoying to catastrophic, with serious injury occurring or lives lost, systems (both human-made and natural) destroyed, security breached, businesses failed, or opportunities lost. [1]

Very important aspect of system reliability in addition to the above is the segment of power supply. Today's computer-based electronic systems require power supplies that are safe and reliable as well.

Generally, a modern electric power system is a very large and complex network consisting of generators, transformers, transmission and distribution lines, buses, reactors, capacitors, and other devices. A power system has to provide high-quality electric energy to the user instantly, constantly, and exactly in the amount that is needed.

But in practice, despite significant protection, since it is impractical and not cost effective to design and build a fault-proof power system at this level, we must consider the protection, reliability at the lower levels, in order to the designed the system worked without failure.

A typical electronic system is implemented in two ways: with a central power source, and with a distributed power scheme. [2]

One of the quiet design revolutions of the 1980s was the rapid growth of distributed power architecture in a wide variety of complex electronic systems. Distributed power architectures replace multiple central power sources with a single bulk supply that is converted to the end-use voltages by dc/dc converters located at the point of need.

Distributed power networks let engineers power all the subsystems from a single bus and a central battery bank rather than running redundant wiring for each voltage level throughout the system.

Another important advantage that distributed power brought to high reliability programs is isolation. Using switching DC/DC converters that use transformers in the conversion process, they can provide electrical isolation, making it easy to build in redundancy and to protect whole systems from failure effects caused by no isolated issues.

In this paper one distributed power supply for the embedded lift processor system is analyzed, drawbacks exaggerated and solution is suggested. At the beginning a basic structure of lift system is described followed by description of the distributed lift processor realization. In the next section most of power supply requirements for the processor are defined. All demands are defined accordingly industry standard classifications. Finally, power consumption is analyzed on realized system. The results shown that number of floors is greater than six, a dc/dc structure of floor processor power supply is optimal solution.

A. Lift System

There are many types of lifts, and their classification is usually based on the principle of running the cabin. Starting cabin with ropes is usually used, and there are so-called hydraulic and lifts with vertical guides. In the following we will briefly describe the principles of each of them.

Type of lift which is most commonly used is the lift on the rope. With this type of lift cabin to move up and down with wire ropes. Domesticated is that this type of lift is called an elevator driven by electric motors. Ropes were attached to the cabin lift and wrapped around the drive pulley - sheave. A sheave has a number of grooves in the scope in which they are put ropes. Turning a sheave leads to the withdrawal of rope to one side or the other, or the cabin up or down. A sheave through the gear system mechanically linked to drive an electric motor. Nowadays, you can find solutions to drive a sheave without gear. In this case a special type of motor runs directly a sheave. Typically sheave, motor and control system located in the so-called machine room above the elevator shaft.

The systems of hydraulic lift raise the cabin that sits on the carrier. Carrier is in connection with a hydraulic piston which is built into the cylinder. The cylinder is located in the hydraulic circuit pump as uncompressed fluid used oil. Hydraulic system consists of three parts:

- Oil tank
- Electromotive pump
- Valves

[1]Branislav Petrovic, [1]Goran Nikolic and [1]Milica Jovanovic are with the University of Nis, Faculty of Electronic Engineering, Aleksandra Medvedeva 14, 18000 Nis, Serbia, Email: branislav.petrovic {goran.nikolic, milica.jovanovic}@elfak.ni.ac.rs

By activating the pump creates enough pressure to ensure insertion of oil from the tank into the main pipe cylinder. When the valve is open under the pressure of oil will go the way of least resistance and return to the reservoir of oil or cabin is lowered. When the valve is closed, the oil pressure remains the only time in the cylinder. As the amount of oil in the cylinder increases it pushes the piston upwards, thus raising the cabin lift. The valve is operated electrically by a basic solenoid switch. Variable valve timing is achieved by bringing the power solenoid which mechanically powered core and enables the opening and closing valves.

B. Standards

Standard defined guidelines for planning and building lift system, especially concentrating on network design and cabling systems [3]. It specifies minimum requirements for communications and power infrastructure of data centres' and machine rooms and proposes rules for the following segments of the system:

• Infrastructure architecture • Electrical design • Environmental and mechanical design (HVAC) • System redundancy and infrastructure • Cabling systems • Access control and security • Environmental control • Power management • Protection against physical hazards (fire, flood, windstorm)

In accordance with the standards we have the following:

a) Loading Capacity - Loading capacity is a function of the desired platform size and/or maximum weight to be moved.

b) Machine Type - Machine types in use today are the hydraulic pump, geared traction and gearless traction.

- The hydraulic pump can generate speeds of 0.25 m/s to 0.75 m/s. For high-capacity applications, more than one pump may be needed to generate the required lifting capacity and speed. Hydraulic machine rooms should be located adjacent to the elevator hoist way at the lowest landing.

- Geared traction machines are used for medium-speed applications up to 2.0 m/s. The machines are normally located overhead, directly over the hoist way, but can be mounted to the side and below

- Gearless traction machines are used for high-speed passenger elevator applications. The machines should be located over the hoist way in an overhead machine room.

c) Hoist Drive Systems

The motors in use today are either alternating current (*AC*) or direct current (*DC*).

- *AC* motors are used directly in hydraulic elevator applications. They have across-the-line starting unless they are larger than 40 hp, in which case they should be provided with wye-delta starting.

- *AC* motors for virtually all geared traction and some gearless traction machines use variable-voltage, variable frequency (*VVVF*) drives systems.

- Gearless traction machines typically use dc motors driven by motor generator (*MG*) or silicon-controlled rectifiers (*SCR*). *MG* is a better application when there is a possibility of fluctuating line voltage or the building contains very sensitive electronic equipment. *SCR* use less power and require less maintenance, however, they are currently more expensive than *MG*. By the turn of the century, virtually all new gearless traction machines are expected to use ac motors driven by the *VVVF* drive

C. Electrical Requirements

Globally a lift system, in the accordance with the classification given in the previous segment of paper, there are requirements for the power supply voltage levels as shown in Fig. 1.

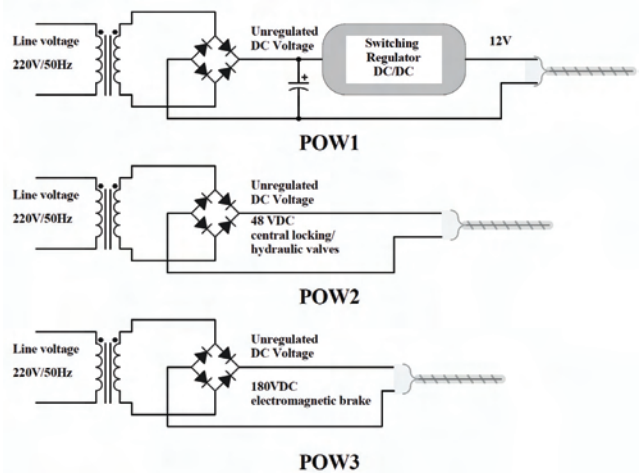

Fig. 1. Typical voltage values of the lift system

Power supply mainly consists of three parts. First, POW1 is DC power supply for lift processor electronics that have to provide supplying for all sensors and actuators also. POW2 is unregulated and unfiltered power supply for controlling a central locking system; typically drive a solenoid, in case of manual or semiautomatic doors, this power supply can be used for hydraulic lifts for driving valves. Finally, POW3 is used to drive electromagnetic brake that is energized during lift movement.

A global functional structure of the lift processor system is given in Fig. 2. Structure is composed of a number of lift processor clusters *LPCi*. Such the system is intended for controlling more lift units so-called multiplex lift system (duplex, triplex). The clusters are connected by *XNET* bus based on *RS485*. As can be seen on Fig 2, the lift processor cluster has distributed structure. Nodes are connected by *LNET* bus, also of *RS485* type. The lift processor cluster is composed of following nodes:

- Master node, M, which directly controls most of actuators in system (motor, valves, brakes, and others).

- Cabin node, *CAB*, acquire all information from moving car, and for automatic door control.

- Register box, *RB*, for collecting requests from passengers in lift and displaying all necessary information.

- A corresponding number of floor processors *FPi* on each floor.

Gateway for connecting to *XNET* bus is realized trough master node. *PNET* is a network of bus power, which is in the most practical implementation of the lift system distributed by

two pairs together with the pair communication bus LNET same cable.

The consumption of the lift system have influence two factors:

1. number of floors that cover the lift with a one cab, so called "simplex" system, where the dominant influence is that number of *FPi* and cable lengths, and

2. multiplex lift system, or different types of lift control system such as the "duplex" system with two cabs, or systems that have three or more cabins known as a "group supervisory operation" so called cluster structure.

Below paper it is interesting to consider and analyze the firstly mentioned problem.

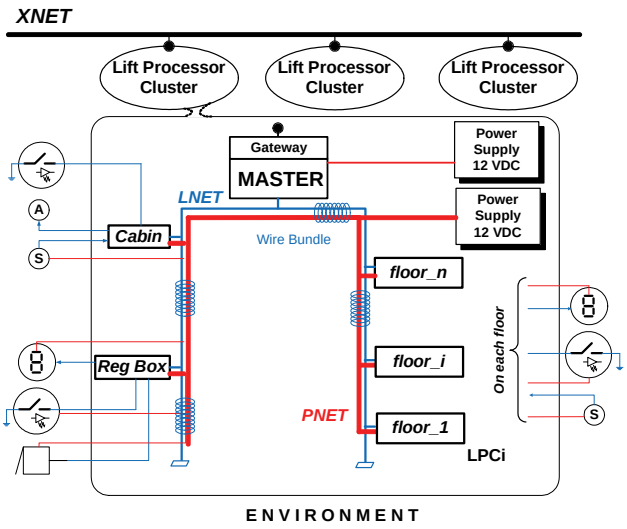

Fig. 2. Topology of the lift system (communication and distributed power supply)

As can be seen from Fig. 2, Master node has near locating power source POW1A, and is not of interest for our analysis. We can only point out that it is designed and implemented in the accordance with the functional requirements.

On the other hand, nodes *CAB*, *RB* and *FP*, in terms of power supply consist of one unit, and are connected to the POW1B through PNET bus.

II. Practical Results

The system was implemented and installed at several locations in public buildings in simplex mode with AC motors and sensors and actuators given in Fig 2.

In addition to the power block, a very important aspect in designing and implementing such a system is the cabling to communication networks and power networks. Namely, if the cable system is not designed and installed properly, the consequences could be drastic.

On the one hand, the occurrence of incomplete or dropped packets. Dropped packets are more difficult to detect because they are "lost" on the wire. When data is lost on the wire, the data is transmitted properly but, due to problems with the cabling, the data never arrives at the destination or it arrives in an incomplete format.

On the other hand we have the appearance of voltage drop. Voltage drop is the reduction in voltage in the passive elements of an electrical circuit. Voltage drops across conductors, contacts, connectors and internal source resistances are undesired as they reduce the supplied voltage.

Also, by standard, communications cables or wires shall not be placed in any raceway, compartment, outlet box, junction box, or similar fitting with conductors of any electrical power.

Generally, lift systems are located in harsh environments with extreme conditions, caused by vulnerability to external interferences from electric motors, lighting, cell phones, etc. Because of this, the performance of the cables used in lift applications is arguably more critical than that of other applications. The moving parts of the lift system (cabin) also add to the already heightened level of importance of proper cable selection. Therefore, it was necessary to perform cable system that will meet the requirements of an environment such as flexibility, low attenuation, low *EMI*, etc. The choice was *CAT3*. *UTP* Category 3 cable is usually four-pair twisted-pair cable with copper conductors, solid and *24 AWG* (*American Wire Gauge*).[4]

Practical measurement of power consumption of the system described in Fig.2, are shown in Table 1. Table shows current consumption for Register Box, Cabin and Floor controllers when no actuators is driven (led diodes, displays ...), and for peak current consumption.

TABLE 1.
LIFT ELECTRIC POWER REQUIREMENTS

Electric Load	Units	Idle Power	Peak Power
Register Box			
Microcontroller	1	6.5mA	25mA
Communications Driver	1	10µA	500µA (*receive*)
			900µA (*transmit*)
Buttons	16	0	32mA
LED Drivers	2	160µA	3.0625mA
LED7SEG	2	0	106.4mA
LED diode	5	0	60.17mA
Cabin			
Microcontroller	1	6.5mA	25mA
Communications Driver	1	10µA	500µA (*receive*)
			900µA (*transmit*)
Relay Actuator	3	0	150mA
Optocouplers	15	0	40.90mA
Floor processor			
Microcontroller	1	6.5mA	25mA
Communications Driver	1	10µA	500µA (*receive*)
			900µA (*transmit*)
Buttons	5	0	10mA
LED Drivers	2	160µA	3.0625mA
LED7SEG	2	0	106.4mA
LED diode	5	0	60.17mA

Worst-case scenario of the lift system with a two floor (*CAB*, *RB* and *FP1* and *FP2*) has a requirement for the consumption of 857mA. It is obviously that increasing number of floors adds consumption of the floor processors only, while the other variables remain constant as shown in Fig 3.

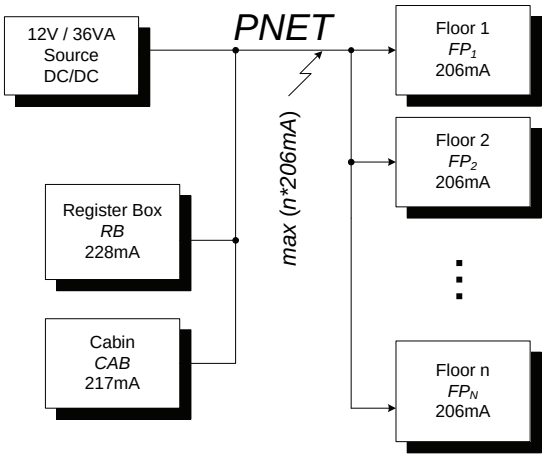

Fig. 3. Block presentation of distributed power supply with the required load

Based on characteristics of the cable [5] and requires the consumption presented in Table 1, the analysis of the voltage drop across the PNET bus conductor in the function of the number of floors served by lift (or length of cable) is performed. The resulting analyze is shown as diagram in Fig. 4.

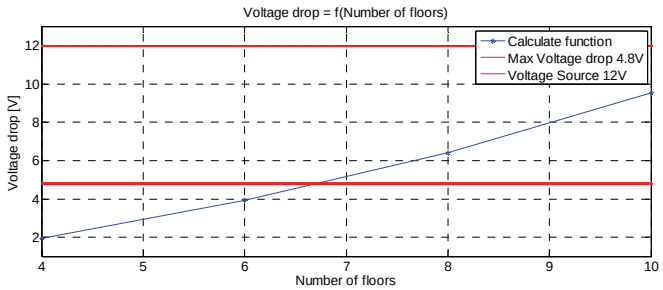

Fig. 4. Voltage drop in the function of the number of floors

Previous theoretical analysis and practical application of the system in real conditions have shown some disadvantages in the field of power supply. Initial solution with a linear voltage regulator is not optimal in situations where the building has many floors (more than 6 floors) and when there is a large fluctuation of supply voltage (spikes, surges, sags, and brownout or restore power). The main problem with linear regulators is that request minimal input voltage *7.2V@I_L=500mA* to maintain linear regulation and exhibits a large loss. But the above solution is not expensive, requires no external components and is suitable for buildings with fewer floors.

III. Conclusion

This paper describes the realization of the power block in the lift system. Power block is implemented as a distributed power architecture which achieves its simplification and eliminates the redundant wiring. In the initial phase of design and implementation of the lift system convert to the end-use voltage is achieved using a linear voltage regulator. Despite the low efficiency and sensitivity to changes of input voltage is shown that the linear voltage regulator is a good choice for small buildings, especially because its low cost, easy implementation and high reliability. Future activities would be the design and implementation of high reliability DC/DC switching power supply. Standard features of the switching power supplies, such as low voltage drop, high efficiency, low quiescent supply current, and operation with a wider input voltage range, makes it ideal for use in lift systems. Building distributed power networks with dc/dc converters offers weight, size, isolation, and power quality advantages to the designer of complex electronic systems.

Acknowledgement

This work was supported by the Serbian Ministry of Science and Technological Development, Project No. TR-32009 – “Low-Power Reconfigurable Fault-Tolerant Platforms”.

References

[1] L. L. Pullum, "Software Fault Tolerance Techniques and Implementation", Norwood, MA, ARTECH HOUSE, INC.2001

[2] "Designed with a Distributed Power Architecture", Application Note, Crane Aerospace & Electronics Power Solutions, Rev C-20061206, pp.1-7, www.craneae.com

[3] Technical Instructions, "Elevator Systems", TI 810-90, 3 August 1998, Headquarters U.S. Army Corps of Engineers Engineering and Construction Division Directorate of Military Programs, Washington, DC 20314-1000, National Institute of Building Sciences at Internet site http://www.nibs.org/ccb/

[4] "American wire gauge", from Wikipedia, the free encyclopedia, http://en.wikipedia.org/wiki/American_wire_gauge

[5] "*Cat_3_UTP_4-Pair_Cable_Cut_Sheet_(040430).pdf*", http://www.google.com or http://www.ampnetconnect.com/

FPAA Implementation of RMS-to-DC Converter for Analog Signal Processing

Ivailo Pandiev[1]

Abstract – **This paper presents a true RMS-to-DC converter employing single Field Programmable Analog Array (FPAA) device. The proposed converter is based on indirect (or implicit) computation method. The conversation circuit consists of a full-wave rectifier, a squarer/divider, low-pass active filter with two external capacitors (averaging circuit) and 8-bit analog-to-digital converter (ADC). The functional elements of the structure are realized by employing available configurable analog modules (CAMs) of the FPAA AN231E04 from Anadigm. The converter has wide-band frequency response and can operate with single supply voltage at 3,3V. Simulation and experimental results show good agreement with theoretical predictions.**

Keywords – **Analog signal processing, Root-mean-square value, Methods of RMS-to-DC conversion, True RMS-to-DC converters, FPAA.**

I. INTRODUCTION

A true Root-Mean-Square (RMS) to DC (RMS-to-DC) converter is a device that provides a dc output voltage, which is proportional to the average energy content in an ac electrical signal. These devices are useful in the fields of instrumentation, communication and medical systems. A variety of RMS-to-DC converters for analog signal processing, are available in the literature [1-7]. In [1] a bipolar RMS-to-DC converter is based on a synthesis of translinear loop squaring/ divider and current-mode low-pass filter. The main drawbacks of this proposed circuit are as follows: first, this circuit operate in only one-quadrant input current; secondly, the circuit is suitable for a voltage supply of more than $5V$. Recently, a new RMS-to-DC converter using translinear-based squarer circuit is proposed [2], where the input current can be a two-quadrant current signal. Because the full-wave rectifier is not required by this conversation scheme, the circuit exhibits a wide bandwidth. However, the implementtation of the circuit is rather complicated and bandwidth is limited to less than $5kHz$. Wider bandwidth ($>100kHz$) is achieved in the converter proposed in [3]. This RMS-to-DC converter is based on the explicit computation method. The circuit can operate with single supply voltage at $2V$ and maximum bandwidth is $60MHz$. Design techniques based on explicit computation of rms value are with limited dynamic range. In [4] is proposed a system based on Discrete Wavelet Packet Transform (DWPT) and Hilbert transform for measuring RMS value and phase angle of the fundamental harmonic of the signal. This system based on DWPT is with great precision and computationally efficient, but it is characterized by a relatively narrow bandwidth (e.g. several tens of Hz).

Many integrated forms of true RMS-to-DC converters have been proposed [5-7]. Most of these ASICs (Application Specific Integrated Circuits) used the implicit method of rms computation employing and absolute value V/I converter, a squarer/divider, low-pass filter, precision current mirror and an output buffer.

While some approaches imply the use of ASICs for the front-end circuits, which requires considerable design time and costs, FPAAs have been recently raised flexible, fast-prototyping and comparatively economical solutions for design of complex analog processing systems [8-10]. To the author's knowledge, an FPAA implementation of a true RMS-to-DC converter has not yet been reported in the literature. It is, therefore, the purpose of this paper to present a voltage-mode RMS-to-DC converter based on implicit computation method.

II. PRINCIPLE OF RMS-TO-DC CONVERTER OPERATION

The definition of the RMS value of an input signal with period of T is given by

$$U_{RMS} = \sqrt{\frac{1}{T}\int_0^T u^2(t)dt}\,, \tag{1}$$

where U_{RMS} is the rms value and $u(t)$ is the instantaneous voltage, a function of time.

Squaring both sides of this equation yields

$$U_{RMS}^2 = \frac{1}{T}\int_0^T u^2(t)dt\,. \tag{2}$$

The integral, given in Eq. (2) can be approximated as an average value

$$Avg\left[u(t)\right]^2 = \frac{1}{T}\int_0^T u^2(t)dt\,. \tag{3}$$

Then Eq. (2) simplifies to

$$U_{RMS}^2 = Avg\left[u(t)\right]^2\,. \tag{4}$$

Dividing both side of Eq. (4) by U_{RMS} yields

$$U_{RMS} = \frac{Avg\left[u(t)\right]^2}{U_{RMS}}\,. \tag{5}$$

[1]Ivailo Pandiev is with the Faculty of Electronics, Kl. Ohridski 8, 1000 Sofia, Bulgaria, E-mail: ipandiev@tu-sofia.bg.

The Eq. (5) provides the basis for the implicit computing method for U_{RMS}. The advantages of implicit rms computation over other methods are fewer components and greater dynamic range. A disadvantage of this method is that it has less bandwidth than either thermal or explicit computation method [5, 11].

Fig. 1 shows the circuit diagram of the voltage-mode true RMS-to-DC converter based on the implicit computation method. The circuit is essentially an analog signal processor that solves Eq. (5). The input stage is an absolute-value circuit that is a precision full-wave rectifier. The output signal $|u(t)|$ of the absolute-value circuit drives the cascade structure of a

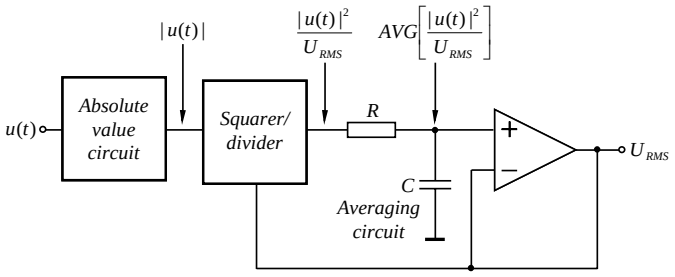

Fig. 1. Circuit diagram of the voltage-mode true RMS-to-DC converter based on implicit computation method.

squarer/driver and a low-pass filter. The squarer/driver squares the signal $|u(t)|$ and divides it by the output signal, which is the average output of the squaring circuit. By closing loop around the divider, Eq. (5) is solved continuously.

III. FPAA for RMS-to-DC Conversion

This section analyzes the suitability of FPAA for RMS-to-DC conversion and conditioning. A subsequent presentation of the Anadigm® FPAA architecture and functionalities [15] allows to link these with those required for conditioning of analog signals with small amplitude and wide bandwidth.

The synthesis of the analog system for RMS-to-DC conversion is strongly conditioned by the incoming signal features, such as amplitude, frequency and noise level. This means that the implementation of the circuit would have to allow changing the gain to cope with a variation in the amplitude of the signal, and it should be able to change the pole frequency of the low-pass filter to different noise levels. These requirements are easily achieved using a FPAA to synthesize this analog system. Moreover, programmable analog arrays offer a tradeoff between performance and system design time. The main drawback presented by the use of FPAAs could be their high power consumption, compared with that of ASICs. This drawback is affordable for implementations that are intended to be a portable instrument.

Among different devices and technologies in the market [12-14], Anadigm offers dynamically programmed Analog Signal Processors (dsASP), in particular the AN231E04 that is a reconfigurable programmable analog device based on switched capacitor (SC) technology. The AN231E04 device consists of a 2×2 matrix of fully Configurable Analog Blocks (CABs), surrounded by programmable interconnect resources and analog input/output cells with active elements. Different circuit configurations with AN231E04 are achieved through manipulation of electronic switches between various circuit components within the CABs. Each CAB contains two operational amplifiers (op amps), Successive Approximation Register (SAR), 8 variable capacitors, and a comparator. The chip has seven configurable input/output structures each can be used as input or output, 4 of the 7 have integrated differrential amplifiers. There is also a single chopper stabilized amplifier that can be used by 3 of the 7 output cells. Each configurable input/output cell contains a collection of resources that allow for high fidelity connections to and from the outside world with no need for additional external components. In order to maximize signal fidelity, all signals routing and processing within the device is fully differential. Accordingly, each input/output cell accepts or sources a differential signal. The AN231E04 devices also contain an 8-bit, 250k samples per second ADC with SAR on the FPAA, thus eliminating the potential need for an external converter.

Programming and testing analog circuits with FPAA ICs can be realized with computer-based development systems, available from the manufacturers. Such development systems include specialized *evaluation printed circuit boards* with FPAA IC sockets and the *AnadigmDesigner2* ECAD system. The ECAD system *AnadigmDesigner2* has the functionality for creating electronic circuits employing CAMs, which map onto portions of CABs, simulation testing of the resulting circuits and programming real FPAA ICs.

IV. FPAA Configuration for RMS-to-DC Conversion

Once the FPAA features have been presented, this section is focused the key qualities and elements of this device that will be used for RMS-to-DC conversion of analog signals. Moreover, the functional circuit of voltage-mode true RMS-to-DC converter based on FPAA AN231E04 is presented.

A. Interfacing of Analog Signals to the FPAA AN231E04

The FPAA AN231E04 uses analog signals that are referenced to $VMR = +1{,}5V$ (Voltage Mid-Rail − VMR) and are limited to the range from 0 to $+3{,}3V$. In Fig. 2 are shown the op amp circuits for interfacing of single-ended signals to the FPAA [16]. The single-ended input signals can be level-shifted to $+1{,}5V$ with non-inverting amplifier stage referenced to $+1{,}5V$ .This circuit can also be used to attenuate large signals or amplify small signals. The transfer function of the input stage is given by

$$U_{IN,FPAA} = (R_F / R_N)u(t) + VMR\,, \qquad (6)$$

where $R_P = R_N$.

It is recommended to keep the sum of R_F and $R_P = R_N$ to approximately $100k\Omega$.

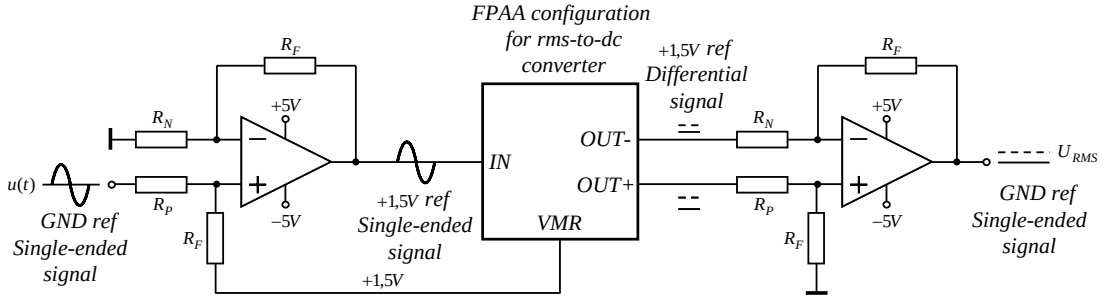

Fig. 2. Op amps circuits for interfacing analog signals to the FPAA device.

The output differential stage is used to level-shift the FPAA output signal and do a differential to single-ended conversion. Furthermore, the output stage can drive external devices with low input impedance and can be used to amplify the FPAA output voltage by any desired amount. For $R_P = R_N$ the transfer function of the output stage can be written as

$$U_{RMS} = (R_F / R_N)(U^{+}_{OUT,FPAA} - U^{-}_{OUT,FPAA}) . \qquad (7)$$

The advantages of the circuit shown in Fig. 3 are that dc information is not lost, signals of any amplitude or dc bias can be handled, and output signal can drive external devices with low input impedance. Also the FPAA output signal can both level-shifted and converted from differential to single-ended.

B. FPAA CAMs for RMS-to-DC Conversion

The RMS-to-DC converter is built by selecting among the available CAMs, shown in Table 1. The *RectifierFilter1* with low-pass filter rectifies an input signal $u(t)$ of either polarity in a manner determined by the other options. A sample input and output waveform is shown on the symbol. The switching clock for this module is set to $250kHz$. This is the highest frequency that allows setting the filter corner frequency to $25kHz$. The *Multiplier1* and *Divider1* square the signal $|u(t)|$ and divide it by the output voltage. The output signal of the squarer/driver is a product of two input voltages with multiplication and divisor factor equal to 1. The output low-pass filter that eliminates noise components over several mHz is developed using *FilterLowFreqBilinear2* with external capacitors C_{AV1} and C_{AV2}. Finally ADC produces an 8-bit digital output word proportional to the U_{RMS}.

C. FPAA Cconfiguration of RMS-to-DC Converter

By placing and routing presented above CAMs in the software interface is created a functional circuit. FPAA configuration of RMS-to-DC converter that solves Eq. (5) is shown in Fig. 3. The differential input voltage is connected to the FPAA input cell 2 (pins 09 and 08). In bypass mode, the input signals are routed directly through the cell, bypassing all active circuit elements. The output differential voltage is obtained by the output cell 6 (pins 17 and 18). In bypass mode, the cell's output pins are being driven directly by the low-pass filter connected to the output cell. The digital signals by ADC "Synch" and "Data" are routed to the upper and lower pins of the output cell 7 (pins 19 and 20). Each data bit will become valid during the SAR clock period Clock B (from pin 42). The external averaging capacitors C_{AV1} and C_{AV2}, connected between nodes *n7* and *n9* are chosen with values equal to $1{,}2\mu F$.

V. Simulation and Experimental Results

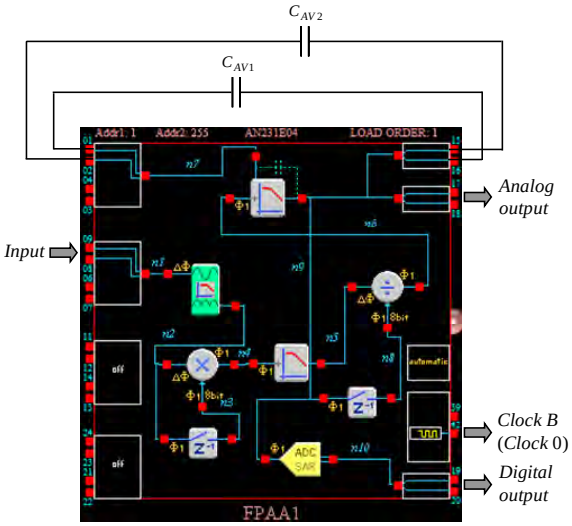

Fig. 3. FPAA configuration of RMS-to-DC converter from Fig. 1.

The workability of the proposed RMS-to-DC converter of Fig. 3 is presented through the simulation results using the simulator built in *AnadigmDesigner2* and also through the experimental results from the circuit configured on prototype board. The experimental test that has been used for validating the FPAA configuration is based on the AN231K04-DVLP3 – Development Board [17]. The AN231K04-DVLP3 is built around the AN231E04 device, biased with $+3{,}3V$ supplies. In Table 2 are presented the experimental results for the performance of the FPAA-based circuit shown in Fig. 3. The maximum error is not greater than 0,5% for the basic waveforms. The tests are performed for input signal with peak value of $1{,}5V$ and frequency $1kHz$. The bandwidth of the circuit is $20kHz$ at $1V$rms input. The high-frequency response is limited by stray capacitance in the circuit board and the finite bandwidth of the *RectifierFilter1*.

TABLE I
FPAA CAMS FOR RMS-TO-DC CONVERSION

Name		Options	Parameters	Clocks
RectifierFilter1		Rectification: full wave Polarity: non-inverting	Corner frequency [kHz]: 25 Gain: 1,00	Clock A: 250kHz (Clock 3)
Multiplier1		Sample and hold: off	Multiplication factor: 1,00	Clock A: 250kHz (Clock 3) Clock B: 4000kHz (Clock 0)
Hold 1 (2)		Input sampling phase: phase1	none	Clock A: 250kHz (Clock 3)
FilterBilinear1		Filter type: low-pass Resource usage: min. resources	Corner frequency [kHz]: 25 Gain: 1,00	Clock A: 250kHz (Clock 3)
Divider1		Sample and hold: off	Divisor factor: 1,00	Clock A: 250kHz (Clock 3) Clock B: 4000kHz (Clock 0)
FilterLowFreqBilinear2		Independent variable: Corner frequency Polarity: non-inverting	Corner frequency [mHz]: 20 Gain: 1,00 External cap value [μF]: 1,2	Clock A: 250kHz (Clock 3)
ADC-SAR1		Input phase: phase1	none	Clock A: 250kHz (Clock 3) Clock B: 4000kHz (Clock 0)

TABLE II
EXPERIMENTAL RESULTS OF THE CIRCUIT IN FIG. 3

Power requirements	
Supply voltage	$+3{,}3V_{DC}$
Power	$166mW \pm 50mW$
Input characteristic	
Input voltage	$1V\ rms$
Bandwidth of the input signal	$20kHz$
Input resistance	$\approx 10M\Omega$
Accuracy	
Crest factor ($CF = U_{PEAK} / U_{RMS}$):	
$CF = \sqrt{2}$ (undistorted sine wave),	error 0,5% ;
$CF = \sqrt{3}$ (triangle wave),	error 0,45%;
CF=1 (symmetrical square wave),	error 0,5%.

VI. CONCLUSION

In this paper a true RMS-to-DC converter trough the use of an implicit computation method has been proposed. The conversation circuit consists of a full-wave rectifier, a squarer/ divider, low-pass filter with two external capacitors (averaging circuit) and 8-bit ADC. The selected FPAA is an Anadigm AN231E04, where the analog signal processing is implemented. The experimental results, obtained for the various waveforms confirm the results of the theoretical analysis.

ACKNOWLEDGEMENT

This paper is a part of a project which is sponsored by the research program of the Technical University of Sofia, Bulgaria.

REFERENCES

[1] R. Wassenur, E. Seevinck, M. Leeuwen, C. Speelman, E. Holle, "New Techniques for High-Frequency RMS-to-DC Conversion Based on a Multifunctional V-to-I Convertor", IEEE Journal of Solid-State Circuits. Vol. 23, No. 3, pp. 802-814, 1988.

[2] E. Farshidi, S. Sayedi, "A 1.2V current-mode true RMS-DC converter based on the floating gate MOS translinear principle", Microelectronics Journal, Vol. 39, No 2, pp. 293-298, 2008.

[3] K. Kaewdang, K. Kumwachara,W. Surakampontorn, "A trans-linear-based true RMS-to-DC converter using only npn BJTs", Int. J. Electron. Commun. Vol. 63, pp. 472-477, 2009.

[4] F. Vatansever, A. Ozdemir, "A new approach for measuring RMS value and phase angle of fundamental harmonic based on Wavelet Packet Transform", Electric. Power Systems Research, Vol. 78, pp. 74-79, 2008.

[5] B. Clarke, M. Fazio, D. Scott, "RMS-to-DC Converters Easy Measurement Tasks", App. note AN-268,Analog Devices, 2000.

[6] Analog Dev., RMS to DC Converters, http://www.analog.com, last accessed March 21, 2011.

[7] Linear Tech., RMS-DC Conversion, http://www.linear.com, last accessed March 21, 2011.

[8] Е. Манолов, П. Якимов, М. Христов, "Управляеми генератори на правоъгълни импулси с FPAA", Електротехника и електроника, кн. 11-12, стр. 3-7, 2004.

[9] Zh. Georgiev, E. Manolov, T. Todorov, I. Karagineva, "Synthesis and Experimental Verification of Sinusoidal Oscillator Based on the Modified Van der Pol Equation", Inter. J. of Electronics, Vol. 96, No 5, pp. 467-478, 2009.

[10] D. Morales, A. Garcia, E. Castillo, M. Carvajal, J. Banqueri, A. Palma, "Flexible ECG acquisition system based on analog and digital reconfigurable devices". Sensors and Actuators, Vol. 165, pp. 261–270, 2011.

[11] C. Kitckin, L. Counts, *RMS to DC conversion application guide*, 2nd Edition, Analog Devices, 1986.

[12] Lattice ispPAC-POWR1014/A, http://www.latticesemi.com/documents/DS1018.pdf, last accessed March 1, 2011.

[13] Cypress PSoC® Mixed-Signal Array, http://www.cypress.com, last accessed March 21, 2011.

[14] Zetex, TRAC-S2, http://www.datasheetcatalog.org/datasheets/208/306841_DS.pdf, last accessed March 21, 2011.

[15] AN231E04 Datasheet – Dynamically Reconfigurable dpASP, http://www.anadigm.com/_doc/DS231000-U001.pdf, last accessed March 21, 2011.

[16] "Interfacing analog signals to the Anadigmvortex FPAA devices", Application note 205, Anadigm, 2003.

[17] AN231K04-DVLP3 – AnadigmApex Development Board, http://www.anadigm.com/_doc/UM231000-K001.pdf, last accessed March 21, 2011.

Compensation of the Impact of Temperature and Humidity on Gas Sensors

Zvezditza Nenova[1] and Georgi Dimchev[2]

Abstract – **The methods for gas control have been extensively developed for many applications such as monitoring the quality of air environment, in control systems of indoor gas leakages, or development and implementation of systems such as "electronic nose". In particular, metal oxide based gas sensors have been widely used. However, changes in their parameters depend, apart from changes in the controlled gas, also on temperature and humidity. That is why, compensating for these disturbances is an important problem aiming to increase the accuracy of concentration measurements of the controlled gases and the reliability of control. The present paper proposes a method for compensation of the impact of temperature and humidity on gas sensors using artificial neural network (ANN). This compensation method is applied on the control of methane pollution by gas sensor TGS813 and results are presented.**

Keywords – **Gas sensors, ANN, compensation of disturbing factors.**

I. Introduction

The methods for gas control of the air environment have been undergoing continuous improvement and development because of the importance of monitoring atmospheric pollution, which can quickly spread over large areas. A wide range of gas sensors [1-5] is offered, metal oxide semiconductor gas sensors being one of them. Different kinds of metal oxides like SnO_2, ZnO, Fe_2O_3, WO_3, Co_3O_4 , etc. [1, 6-8] are used as sensing materials. Their principle of operation is based on increasing the conductivity of the sensitive element in the surface area when the test gas is adsorbed. Depending on the composition of the sensitive material layer, the sensor responds to different gases such as carbon monoxide, carbon dioxide, ethanol, methane, propane, ammonia, hydrogen sulfide, hydrogen, etc. [1-5]. Metal oxide semiconductor gas sensors have high sensitivity, low cost and less reaction time. They are used in gas leakage control systems, monitoring the quality of indoor air environment, development and implementation of systems such as "electronic nose", etc. [9-11]. However, a typical feature of such gas sensors is the impact of temperature and humidity on their readings [2-5], which act as disturbances in the control of gas emissions into the air. To increase the accuracy of measurements and reliability of control it is very important to compensate the impact of these disturbances.

This paper proposes a method for compensating the impact of temperature and humidity on the readings of gas sensors using artificial neural network. It also shows the results of the implementation of the method for control of methane pollution by using gas sensor TGS813 [2].

[1]Zvezditza Nenova is with the Faculty of Electrical Engineering, Technical University of Gabrovo, 4, H. Dimitar Str., Gabrovo 5300, Bulgaria, E-mail: nenova@tugab.bg.

[2]Georgi Dimchev is with the Faculty of Electrical Engineering, Technical University of Gabrovo, 4, H.Dimitar Str., Gabrovo 5300, Bulgaria,

II. ANN-Based Method for Compensation of Disturbing Factors

Artificial neural networks are widely used to detect gases, characterize products, control of environmental parameters, etc. [12-14]. They are used to solve problems of sensor calibration, detection of odors in environments with different disturbing factors and approximation of sensor characteristics [15-18].

The proposed ANN-based method aims at increasing the accuracy of measurements of gas concentrations by compensation of the impact of temperature and humidity. The method is based on the training of ANN with gas sensor characteristics that relate changes in their parameters due to changes in gas concentration as well as changes in temperature and humidity. Consequently, three-dimensional approximation of the sensor characteristics is conducted, linking the output parameter of the sensor and the gas concentration, temperature and humidity of the controllable air environment. Apart from the measurement of the gas sensor parameter, the implementation the method requires measurement of temperature using a temperature sensor and air humidity using a humidity sensor. Figure 1 shows a schematic of the implementation of the ANN-based method and the respective input and output parameters for measurement and control of a gas pollutant.

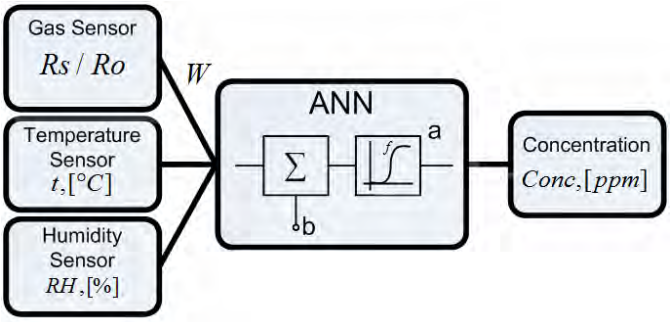

Fig. 1. Schematic of implementation of the ANN-based method for compensation of temperature and humidity on gas sensor

Thus after the training of the neural network approximated relation of the following type is obtained

$$Conc = f\left(Rs/Ro,\ t,\ RH,\ W,\ a,\ b\right) \quad , \qquad (1)$$

where Rs is the measured gas sensor resistance, $Ro-$ is resistance at pre-specified reference concentration, Rs/Ro is the relative change of the gas sensor resistance, t – is temperature measured by the temperature sensor, RH – is the relative humidity measured by the humidity sensor, W, a, b are ANN parameters.

The gas concentration measured can be determined using relation (1), which takes into account the impact of the ambient temperature and humidity.

III. Method Implementation

The method is applied to compensate the impact of temperature and humidity of TGS813 type gas sensor in the control of methane pollution. The characteristics of the sensor from the manufacturer have been used, connecting the concentration of methane with the relative change Rs/Ro of the sensor resistance at -10°C/0%RH, 20°C/65%RH, 40°C/100%RH and the characteristics of the sensor at 1000ppm for changes in temperature and relative humidity of 0, 20, 40, 65 and 100%RH [2]. Ro is resistance at pre-specified reference concentration of 1000ppm and 20°C/65%RH. Under these experimental relations in logarithmic scale the change in temperature leads only to offset these characteristics to Rs/Ro. Given this and the characteristics of the sensor at 1000ppm in case of changes in temperature and relative humidity of 0, 20, 40, 65 and 100%RH [2], the characteristics of $Rs/Ro=f(Conc)$ in the temperature range -10°C...40°C and fixed values of relative humidity 0, 20, 40, 65 and 100% RH are obtained analytically. Figure 2 shows a set of characteristics $Rs/Ro=f(Conc)$ at 65%RH, showing the impact of temperature of the air environment, and Figure 3 – a set of characteristics $Rs/Ro=f(t)$, indicating the impact of humidity in case of basic concentration of 1000 ppm.

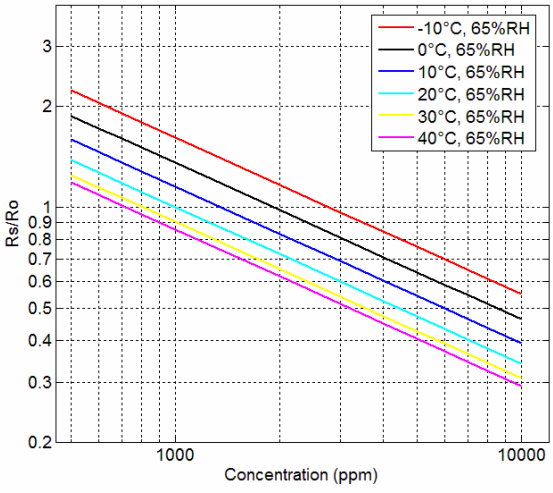

Fig. 2. Impact of temperature on the characteristics $Rs/Ro=f(Conc)$ at 65% RH

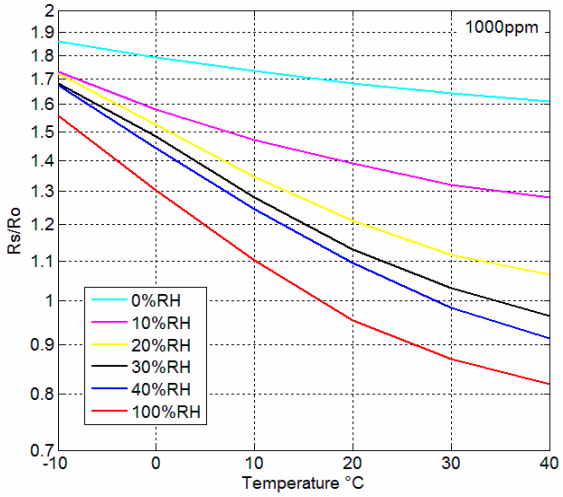

Fig. 3. Impact of humidity on the characteristics $Rs/Ro=f(t)$ in case of basic concentration of 1000 ppm

The entire range of characteristics obtained was used for training of backpropagation ANN. Experiments were conducted with different algorithms for training. The best convergence for the lowest number of neurons was obtained by training with Levenberg-Marquardt (LM) backpropagation algorithm. Moreover, the resulting backpropagation ANN has three layers - two hidden and one output. The number of neurons is determined by trading off the training time and the approximation error [19]. Thus it is established that the first layer is composed of three neurons - one for each input variable, the second layer is composed of five neurons, and the third layer has one neuron (Figure 4).

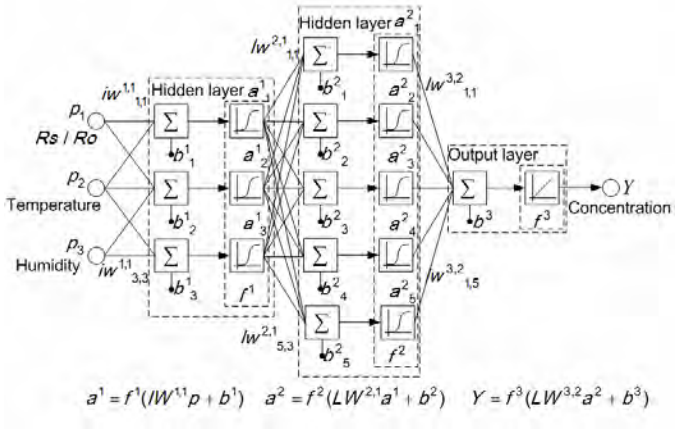

Fig. 4. ANN for approximation of gas sensor characteristics

In the first and second layer transfer function of neurons (f^1) and (f^2) is sigmoid and the third layer (f^3) - linear.

The neural network has the following form

$$Y=f^3\left(LW^{3,2}f^2\left(LW^{2,1}f\left(IW^{1,1}p+b^1\right)+b^2\right)+b^3\right), \qquad (2)$$

where $Y=Conc$, $p_1=Rs/Ro$, $p_2=t$, $p_3=RH$.

Figure 5 shows the results of the output of the trained neural network. Thus based on three-dimensional

approximation of the characteristics of the sensor obtained as a result of training of ANN, the value of the concentration of methane can be obtained while compensating the impact of temperature and relative humidity.

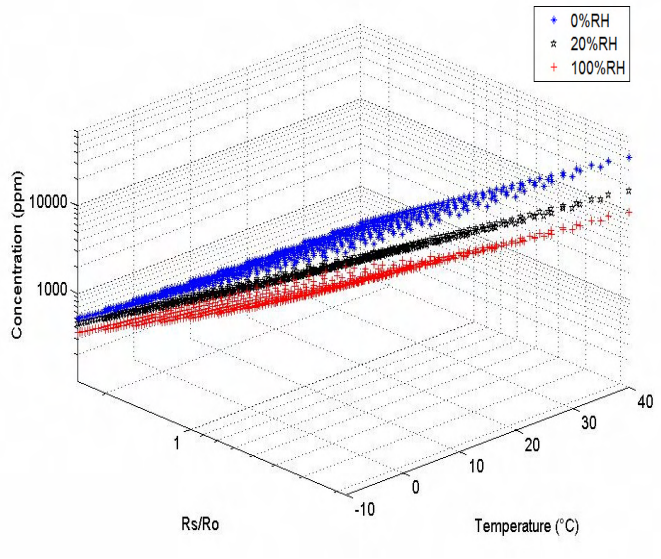

Fig. 5. Results of output of the trained ANN

Figure 6 shows the algorithm to compensate the impact of temperature and humidity on the reading of the gas sensor through the ANN.

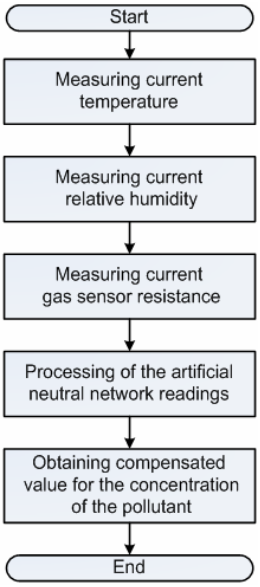

Fig. 6. Algorithm for ANN-based compensating method

Using the trained neural network after compensating the impacts of temperature and humidity the methane concentration values $Conc_{ANN}$ are obtained. Based on them the absolute error from the approximation is

$$\Delta Conc_{appr} = Conc_{ANN} - Conc \qquad (3)$$

and the normalized error from the approximation

$$\varepsilon_{n\ appr} = \frac{\Delta Conc_{appr}}{Conc_{\max} - Conc_{\min}} \cdot 100\% \ , \qquad (4)$$

where $Conc$ is the measured value of the concentration for given temperature and humidity; $Conc_{\max} - Conc_{\min}$ is the concentration measurement range.

Figure 7 shows the actual and ANN-approximated characteristics at different values for temperature and relative humidity.

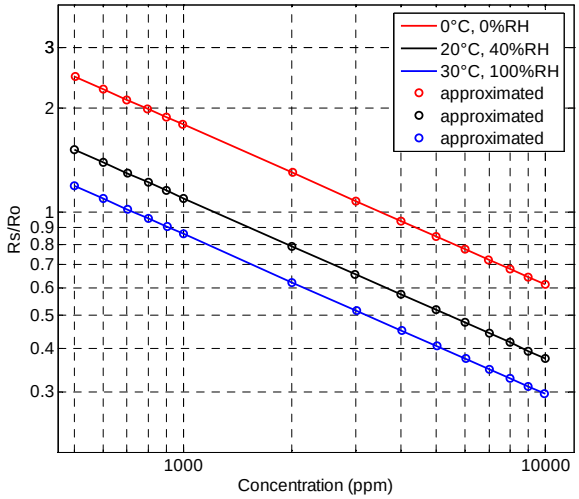

Fig. 7. Real and ANN-approximated characteristics of the gas sensor

The normalized error from the approximation has been calculated for all points obtained by ANN and the values of this error do not exceed ±0.05%.

For comparison the errors without compensation of the impact of disturbing factors has been determined when a reference characteristic for the sensor is used. The absolute and normalized errors are determined by

$$\Delta Conc = Conc_{ref} - Conc \qquad (5)$$

and

$$\varepsilon_n = \frac{\Delta Conc}{Conc_{\max} - Conc_{\min}} \cdot 100\% \ , \qquad (6)$$

where $Conc_{ref}$ is the concentration from the reference characteristic.

For the TGS813 gas sensor the characteristic at 20°C/65%RH is taken as the reference. The normalized error is 2,1% and -3,5% respectively for a temperature change of ±10°C and 0,4% and -0,6% for relative humidity change of ±10%RH. For a simultaneous change of both temperature and relative humidity from 20°C/65%RH to 30°C/75%RH and 10C/55%RH, the normalized error is 2,5% and -4,1% respectively, and at 40°C/100%RH and -10°C/0%RH it is 3,7% and -28,7 % respectively.

This confirms the need to perform compensation of the disturbing factors and increase the accuracy of measurements through the described method of the compensation using ANN.

IV. CONCLUSION

The following conclusions can be drawn based on the investigations made:

- temperature and humidity have significant impact on the readings of metal oxide gas sensors;
- a method is proposed to compensate the impact of temperature and humidity on the readings of gas sensors by using ANN;
- to compensate the impact of the disturbing factors on TGS813 gas sensors used for measurement and control of methane, a backpropagation ANN with two hidden and an output layer is obtained;
- three-dimensional approximation of TGS813 gas sensor characteristics with the trained neural network allows for compensation of the temperature and humidity impact, with the normalized error from the approximation of around ±0,05%.
- the proposed ANN based compensating method can be used with other types of gas sensors as well.

REFERENCES

[1] Nenov, T., P.Panteleev, "Gas sensors for environmental monitoring", Automatica&Informatics, No 1, pp.16-19, 2010.

[2] FIGARO Engineering Inc. Products - Gas Sensors (www.figaro.co.jp/en/product/)

[3] SYNKERA Technologies Inc. Products (www.synkera.com)

[4] E2v Technologies. Products (www.e2v.com)

[5] Sencera. Products (www.sencera.com)

[6] Ning Han, Linyu Chai, Qi Wang, Yajun Tian, Pingye Deng, Yunfa Chen, "Evaluating the doping effect of Fe, Ti and Sn on gas sensing property of ZnO", Sensors and Actuators B, No 147, pp.525–530, 2010.

[7] Chia-Yu Lin, Yueh-Yuan Fang, Chii-Wann Lin, James J. Tunney, Kuo-Chuan Ho, "Fabrication of NO_x gas sensors using In_2O_3–ZnO composite films", Sensors and Actuators B, No 146, pp.28–34, 2010.

[8] G. Korotcenkov, B.K. Cho, "Thin film SnO_2-based gas sensors: Film thickness influence", Sensors and Actuators B, No 142, pp.321–330, 2009.

[9] Ivanov, S., Z. Nenova, "Sensor module for gas control", International scientific conference UNITECH'10, November 19-20, 2010, Gabrovo. Proceedings, Vol. I, pp.I-524 – I-527, 2010.

[10] Hyung-Ki Hong, Hyun Woo Shin,Dong Hyun Yun, Seung-Ryeol Kim, Chul Han Kwow, Kyuchung Lee, Toyosaka Moriizumi, "Electronic nose system with micro gas sensor array", Sensors and Actuators B 35-36, pp.338-341, 1996.

[11] B.A. Botre, D.C. Gharpure, A.D. Shaligram, "Embedded Electronic Nose and Supporting Software Tool for its Parameter Optimization", Sensors and Actuators B 146, pp.453–459, 2010.

[12] Hines E. L., J. W. Gardner, "An artificial neural emulator for an odor sensor array", Sensors and Actuators B, 18-19, pp.661-664, 1994.

[13] Hyung-Ki Hong, Chul Han Kwon, Seung-Ryeol Kim, Dong Hyun Yun, Kyuchung Lee, Yung Kwon Sung, "Portable electronic nose system with gas sensor array and artificial neural network", Sensors and Actuators B 66 2000. pp.49–52, 2000.

[14] Dehan Luo,, H. Gholam Hosseini, John R. Stewart, "Application of ANN with extracted parameters from an electronic nose in cigarette brand identification", Sensors and Actuators B 99, pp.253–257, 2004

[15] Nenov T., Ivanov, S, "Linearization of characteristic of relative humidity sensor and compensation of temperature impact", Sensors and Materials, vol. 18, No 2, pp.95-106, 2007.

[16] Ivanov, S., "LabVIEW Virtual Instruments for Sensor Linearization and Calibration", ISAC 2006 International Study in Automatic Control, Koshice, Slovakia, 2006, pp.111-116.

[17] Singh A.P, S. Kumar, T.S. Kamal, "Virtual compensator for correcting the disturbing variable effect in transducers", Sensors and Actuators A 116, pp.1-9, 2004.

[18] Singh A.P., T.S. Kamal, S. Kumar, "Development of a virtual curve trace for estimation of transducer characteristics under the influence of a disturbing variable", Sensors and Actuators A 120, pp.518-526, 2005.

[19] Zhou Kaili, Kang Yaohong, "Model of neural network and MATLAB simulation program design," M. Tsinghua University Press, Beijing, 2005.

Session EL II:

ELECTONIC COMPONENTS, SYSTEMS AND TECHOLOGIES II

Total Power Consumption in Modern VLSI Circuits

Bojan B. Jovanović and Milun Jevtić[1]

Abstract – **In this paper various design methods applicable on different stages of system design and aimed to minimize the power consumed by the system are presented. Along with the overview of the power minimization techniques, as an example, the circuit of binary divider is implemented in various FPGAs to demonstrate technology as well as placement and routing influence on total power consumption.**

Keywords – **Power consumption, Power minimization techniques, binary dividers.**

I. INTRODUCTION

During the past years the progress of silicon process technology marches on relentlessly. According to Moore's law, silicon process technology continues improvement at an astonishing pace. Every 2 years the number of transistors that can be integrated on a single IC approximately doubles. Despite a strong relationship between the consumed power and the performance of CMOS circuits, the power of early circuits remained within the allowable power envelope due to various heat dissipation techniques. In this scenario, designers focused primarily on achieving the needed performance. However, as the density and size of the chips and systems continue to increase, the difficulty in providing adequate cooling might either add significant cost to the system or provide a limit on the amount of functionality. Also, having in mind many high-volume battery-powered portable and wireless consumer devices, power minimization should be treated very carefully. Starting from 0.18μm technologies, static power consumption due to leaky "off" transistors, is now a non negligible source of power dissipation even in running mode. Thus, the total power consumption (i.e. dynamic plus static power) has to be optimized instead of simply reducing dynamic power. Design methods that explore true power optimization need to work in a large dimension search space, where power and performance of different solutions are compared. This includes system architecture optimization (outer loop), block-level optimization (intermediate loop), and fixed topology optimization (inner loop).

II. THE SOURCES OF POWER CONSUMPTION

The two main sources of power dissipation in CMOS VLSI's are the dynamic power dissipation due to charging and discharging of load capacitance, and the static power dissipation due to subthreshold leakage. There may be short-circuit power dissipation (V_{DD} to ground) as the third source of power dissipation. This power source is due to non-zero rise and fall time of input waveforms and it is less than 10% in total power dissipation.

The expression for dynamic power consumption is widely known. It depends on squared power supply, V_{DD}, operating frequency, load capacitance of the node, and the average number of $0 \rightarrow 1$ transitions within one clock cycle.

Leakage currents consists of two main components: subthreshold leakage (I_2), and gate leakage current (I_3) as shown in Fig. 1. There are some other leakage current components that have started to gain interest recently due to an excessive scaling of the transistor dimensions. They occur due to the short channel-lenght (I_4, I_6), the thinner oxide thickness (I_5), and due to high doping concetracions (I_1) [1].

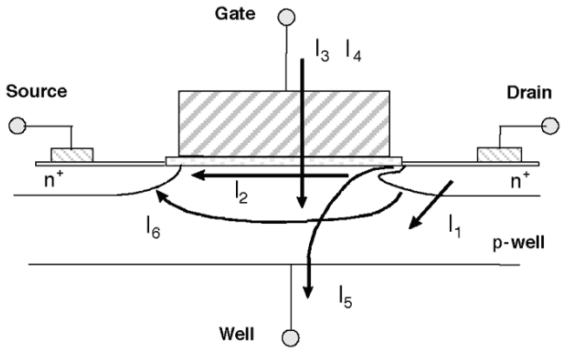

Fig. 1. Leakage current components

However, the largest amount of static power is still owed to subthreshold leakage current. It is the most temperature-dependent leakage component, and thus, every increase in dynamic power produces an increment of the chip temperature, which in turn, increase the leakage current. This leakage component is also one of the main reasons why the scaling process is facing difficulties. Four tunneling mechanisms (the gate to channel, bulk, source, and drain) as well as analytical expressions for gate leakage current can be found in [1,2].

III. FIXED TOPOLOGY OPTIMIZATION

Power optimization techniques in this level do not alter the circuit topology, so the principle variables they affect are transistor sizes, supply voltages, and the threshold voltages. Some of the authors investigate the impact of single variable on circuit power consumption and delay while other perform thorough analysis considering mutual influence of two or even more variables on design power consumption. There are a few commonly used power minimization techniques: gate-sizing, variable supply-voltage, variable threshold-voltage, multi voltage design, power gating, clock gating, stack forcing, on-chip optical interconnect, nano devices etc.

[1]Bojan B. Jovanović and Milun Jevtić are with the Faculty of Electronic Engineering, Aleksandra Medvedeva 14, 18000 Niš, Serbia,
E-mail: {bojan.jovanovic, milun.jevtic}@elfak.ni.ac.rs.

A. Gate Sizing and Supply Voltages in Power Minimization

Decreasing transistor sizes enables higher densities of transistors on a chip. In order to control the power of the circuit, the power supply voltage is also reduced with each transistor scaling. Due to quadratic relationship between dynamic power consumption and power supply, this supply voltage reduction is the most effective way to lower the dynamic power. For CMOS circuits, a lower supply voltage means lower performance. This problem is solved by reducing the threshold voltage (V_{TH}) of a transistor. V_{TH} is defined as a gate-source voltage of MOSFET transistor, above which, the transistor is turned on. Ideally, if the gate voltage is below the threshold voltage, the transistor is not conducting any current. However, in practice there is still some current flowing from the drain to the source of a transistor. This is the subthreshold current. Its most important feature is that it increase exponentially with any V_{TH} decrease. That's why this leakage current is one of the main limiting factors to scaling process. SIA Roadmap [3] forecast supply voltage as low as 0.8 to 0.5 V in year 2018. Predicted threshold voltages are up to 0.1 V.

It is sure that between all the combinations of V_{DD}/V_{TH} guaranteeing the desired speed only one will result in the lowest power consumption. The location of this optimal working point and its associated total power consumption are tightly related to architectural and technology parameters. Authors in [4] give the equation of total power consumption for circuits working at their optimal supply and threshold voltages, while in [5] authors present closed-form formula for optimum supply and threshold voltages that minimize power dissipation when technology parameters and required speed are given.

The techniques of variable supply or/and threshold voltages continuously adapt their values in the design (during the design run on) so the power dissipation is reduced and the critical-path delay is not changed. Instead of using variable voltages power minimization techniques with dual or multiple V_{DD} or/and V_{TH} can be applied. The gates on critical paths operate at higher V_{DD} or lower V_{TH}, while those on non-critical paths operate at the lower V_{DD} or higher V_{TH}, thereby reducing overall power consumption without performance degradation.

Among the leakage power reduction techniques power gating is commonly used to disconnect idle logic blocks from power network to curtail sub-threshold leakage [6]. The similar clock gating technique is used to prevent clock signal to give a pace to non-active gates. Stack forcing is another technique to tackle the ever-increasing leakage power. It has been shown that stacking of two off transistors can significantly reduce leakage power than a single one [7]. In 90nm technologies and beyond gate oxide leakage current has become comparable to subthreshold leakage. It is, therefore, necessary to develop methods for oxide leakage reduction, which unlike subthreshold leakage, occurs only in transistors that are ON as shown in Fig. 2. Increasing the oxide thickness will decrease gate oxide leakage current but this will be payed with substantial transistor delay. So, thick-oxide transistors in non-critical path will not speed down the circuit but will reduce static power consumption.

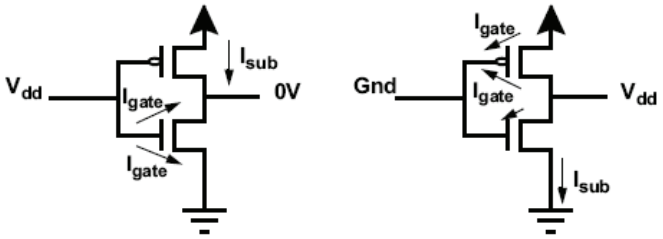

Fig. 2. Gate oxide leakage in CMOS inverter

B. On-chip Optical Interconnections for Power Minimization

Global interconnect performance required for future generations of ICs cannot be achieved with metal. Using optical instead of electrical interconnections lead to decrease in power consumption, enormous bandwidth increase, immunity to electromagnetic noise, and reduced sensitivity to temperature variations. However, there are some difficulties in obtaining a large enough optical-electrical conversion efficiency [8].

Another power minimization technique is on-chip wavelength division multiplexing. For example, a single waveguide could be used to replace a 64-bit bus, where each individual signal makes use of a distinct wavelength.

C. Technology Influence on Total Power Consumption

In order to practically demonstrate the influence on design's technology parameters on total power consumption the 12-bit binary divider logic circuit is described in VHDL and implemented in Xilinx FPGA devices from different families (Virtex-4, Virtex-5, Virtex-6, and Virtex-6 Lower Power). For binary division Radix-2 non-restoring algorithm with non-fractional remainder is used [9].

XPower CAD tool (within ISE 12.4 software) was utilized for power consumption measurements. Divider inputs were generated in MATLAB as signals with Gaussian distribution (1000 values for both dividend and divisor). Mean value, auto-correlation and cross-correlation of these signals are all equal to zero. Implementation results are presented in Fig. 3.

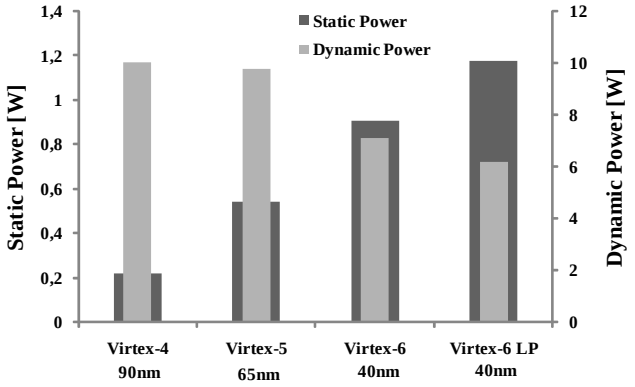

Fig. 3. Power consumption of binary dividers implemented in FPGAs

Technology process variations (from 90nm to 40nm), supply voltage variations (from 1.2 to 0.9 V), threshold voltage and transistor sizes variations obviously influence

both static and dynamic power consumption. There is a clear increase in static power consumption when moving toward newer generation FPGA families. Static consumption increases due to increase in leakage currents as a consequence of shrink in transistor sizes. The shorter channel lengths and thinner gate oxides generally used at the new process node make it easier for current to leak, either across the channel region or through the gate oxide of the transistor. Concerning dynamic power, the core FPGA supply voltage and node capacitance generally reduce with each new process node, providing substantial dynamic power savings over previous generation FPGAs. The new 28nm Xilinx-7 series FPGAs will enable a 50% overall power reduction compared to previous 40nm generation [10].

IV. Placement and Routing Influence on Power Consumption

Mandatory part of each integrated circuit (ASIC, FPGA, custom IC etc.) design flow is the process of physical implementation. This process is usually iterative and divided into several stages. In each iteration, design must be firstly partitioned into groups or blocks small enough to fit into a single unit (ASIC standard cells, FPGA configurable logic blocks etc). Secondly, these units are assigned specific location on the chip. This stage is usually called placement. Finally, placed blocks are interconnected by wires. Assigning paths, or routes, to the wires is usually done in two stages. After rough or global wiring, in detailed wiring (also called exact embedding) each wire is given a unique complete path. In the case of ASIC or custom IC design, from the detailed wiring results, masks can be generated and chips fabricated. At each stage of physical implementation process one tends to optimize the eventual performance of the system (to minimize chip area, power consumption and delay) without compromising the feasibility of the subsequent design stages. The major focus in placement and routing (PAR) is on minimizing the length of interconnections since this translates into the time required for propagation of signals and thus into the speed of the entire design. Also, minimal interconnection length leads to less capacitive interconnects and consequently to decrease in dynamic power consumption. However, the presence of regions in which the wiring is too congested for the packaging technology should be anticipated and minimized during the PAR process. Besides, the sources of noise such as crosstalk between adjacent wires should be eliminated.

From the above mentioned one can conclude that PAR are very important phases in system design influencing overall system performance. Furthermore, placement and routing phases have both equal influences on the system features. Consequently, for the best results, both place and route phases need to be considered since the benefits from high quality placement might impose low quality routing decreasing overall system performances [11].

In theory, PAR problem is an NP-complete problem and require iterative algorithms capable of efficiently searching for a near optimal solution in a large solution space. Some of widely used ones are generic arithmetic, tabu search and simulated annealing [12]. Many authors investigate power-aware placement and routing. Vorwerk et al. introduce two techniques for minimizing power during the FPGA placement [13]. The first aspect discussed in their work is a power-aware objective function for placement. In particular, a capacitance model for global nets allowing net power reduction is described. The second technique permits area and power reduction by optimizing the number of combinational and sequential cells. The results are quantified across a suite of 119 industrial benchmarks targeting Actel Igloo FPGA architecture. Power is reduced by 13% on average with a 6.7% average improvement in timing performance across the suite. Cheon et al. [14] present power-aware placement method that simultaneously performs activity-based register clustering for clock power reduction and activity-based net weighting for net switching power reduction. In [15] Xilinx's engineers consider dynamic power dissipation and present CAD techniques for dynamic power reduction in Xilinx Virtex-5 FPGA. The proposed techniques, comprising power-aware placement, routing, and a novel post-routing transformation are applied to optimize the industrial designs power consumption. Board level measurements show that the techniques reduce power by 10%, on average. There are also researches on leakage-aware PAR. Gupta et al. [16] introduce LEAF – a novel tool for leakage-aware PAR for SoCs. Up to 190% difference in the leakage power between leakage-unaware and leakage aware PAR is observed. The similar tool called TPAP intended for FPGAs is presented in [17]. It is also known that temperature variations across a chip (thermal non-uniformities) are an issue that threatens chip performance and reliability. The correlation between the total power consumption and the temperature variations across a chip is investigated in [18]. As a result, PAR guidelines are proposed that uses the correlation to efficiently optimize the chip's total power. It is demonstrated that optimizing a floorplan to minimize either the leakage or the peak temperature can lead to a significant increase in the total power consumption. The experimental results show that lowering the temperature variations across a chip not only addresses performance degradation and reliability concerns, but also significantly contributes to chip power reduction.

To demonstrate PAR influence on overall system performance already mentined 12-bit binary divider circuitry is implemented in Xilinx Virtex-5 FPGA device. In each implementation of the same logic design the only changing parameter was PAR design goal. Three different design goals were Area Reduction, Power Optimization and Timing Performance. Xilinx PAR tool runs in ten iterations and at different effort levels (1-5). This effort levels indicate the amount of time the tool spends searching for a better quality solution. In the fourth case Xilinx IP core divider (using the same division algorithm) [19] was implemented. Fig. 4 shows implementation results.

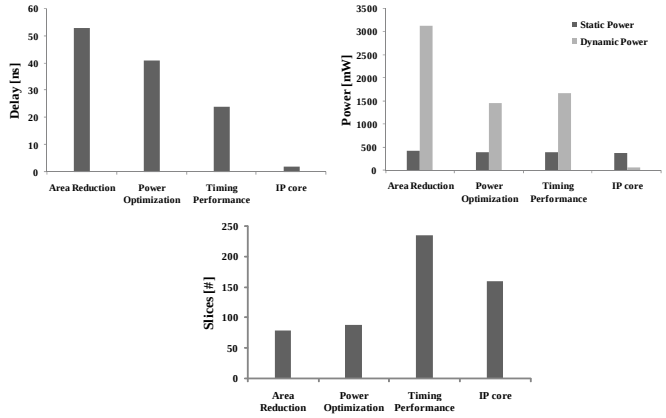

Fig. 4. Delay, power consumption and size of the same design with the different PAR goals

Implementation of Xilinx IP core divider ensures the best design performances. It is expected, having in mind utilization of hard IP blocks (circuitry dedicated to commonly used functions) which contain only the transistors necessary to implement the required function. Furthermore, there are no programmable interconnects, so routing capacitance is as small as possible. On the other hand, three remaining designs are implemented in the general-purpose FPGA logic. Changing of the PAR objective function can lead to obvious design performance variation. So, speed and dynamic power fluctuations are about 55 % while design size varies about 65 % (compared to the worst case). Static power consumption insignificantly changes.

V. CONCLUSION

Some power-aware system design methods are presented in this paper. These methods take into account static power consumption as more and more dramatic issue in very deep submicron technologies. The influence of technology parameters on design power consumption is demonstrated through implementation of binary dividers in FPGAs with the different technological properties. With the improvements of the technology parameters, there is an obvious trend in decreasing dynamic and increasing static power consumption of the design. Various placement and routing design goals during the design implementation also influence design power consumption.

ACKNOWLEDGEMENT

This paper is supported by Project Grant III44004 (2011-2014) financed by Ministry of Education and Science, Republic of Serbia.

REFERENCES

[1] K. Roy, S. Mukhopadhyay, and H. Mahmoodi-Meimand, “Leakage Current Mechanisms and Leakage Reduction Techniques in Deep-submicrometer CMOS circuits”, in Proc. of the IEEE, vol. 91, no. 2, pp. 305-327, 2003.

[2] R. Inagaki, N. Sadachika, D. Navarro, M.M. Mattasch, and Y. Inoue, “A Gate-Current Model for Advanced MOSFET Technologies Implemented in HiSIM2”, ICCCAS, pp. 1057-106, Kokura, Japan, 2007.

[3] http://public.irts.net

[4] C. Schuster et al.,“Architectural and Technology influence on the Optimal Total Power Consumption“, DATE, pp. 13-19, Munich, Germany, 2006.

[5] K. Nose, T. Sakurai, “Optimization of V_{DD} and V_{TH} for Low-Power and High-Speed Applications“, ASP-DAC, pp. 469-474, Yokohama, Japan, 2000.

[6] S.Y. Chen et al.,”Power gating design for standard-cell-like structured ASICs”, DATE, pp. 514–519, Germany 2010.

[7] S. Narendra et al.,”Scaling of Stack Effect and its Application for Leakage Reduction”, ISLPED, pp. 195–200, USA, 2001.

[8] C. Piguet et al.,“Extremely Low-Power Logic”, DATE, pp. 656–661, Paris, France 2004.

[9] R. Jevtić, B. Jovanović, C. Carreras,”Power Estimation of Dividers Implemented in FPGAs”, GLSVLSI, Lausanne, 2011.

[10] Xcell Journal, Fourth Quarter 2010, Issue 73, pp. 65, www.xilinx.com/xcell

[11] C. Mulpuri, S. Hauck, “Runtime and Quality Tradeoffs in FPGA Placement and Routing”, ASM/SIGDA, pp. 29–36, San Jose, USA, 2001.

[12] M. R. Minhas, “Iterative Algorithms for Timing and Low-Power Driven VLSI Standard Cell Placement”, Master’s thesis, Department of Computer Engineering, King Fahd University of Petroleum and Minerals, Saudi Arabia, Dhahran 31261, 2001.

[13] K. Vorwerk et al., “Power minimization during field programmable gate array placement”, IET Journ. on Computers&Digital Techn., vol. 4, no. 3, pp. 170–183, 2010.

[14] Y. Cheon et al., “Power-aware placement”, ASP-DAC, pp. 795–800, Shanghai, China, 2005.

[15] S. Gupta, J. Anderson, L. Farragher, Q. Wang,“CAD Techniques for Power Optimization in Virtex-5 FPGAs”, CICC pp. 85–88, San Jose, USA, 2007.

[16] A. Gupta et al., “LEAF: A System Level Leakage-Aware Floorplanner for SoC”, ASP-DAC, pp. 294–297, Yokohama, Japan, 2007.

[17] B. Salami, “Chip-dependent leakage Power-Aware Placement algorithm for FPGAs”, ELECO, pp. 350–360, Bursa, 2010.

[18] K. Haghdad, M. Anis, Y. Ismail, “Floorplanning for low power IC design considering temperature variations”, Microelectronics Journal, vol. 42, no. 1, pp. 89–95, 2011.

[19] Xilinx IP Core Divider Datasheet, www.xilinx.com, Jan. 2006

Comparison of Filters with Film Bulk Acoustic-Wave Resonators (FBAR)

Dobromir Gaydajiev[1] and Ivan Uzunov[2]

Abstract – **The paper compares different architectures of FBAR filters: ladder filters, ladder filters with added extra components, lattice filters, modifications of the lattice filters. The goal of the comparison is to give an approximate estimation of the effect of different approaches in the filter design. The considerations are based on computer simulations and the main focus is on the filter frequency response: relative passband bandwidth and stopband attenuation.**

Keywords – **analog filters, RF filters, piezo-rezonators, Film Bulk Acoustic Resonators (FBAR), frequency response.**

I. INTRODUCTION

Due to their high quality factors, low losses, good temperature stability and high power handling capabilities, the bulk acoustic-wave resonators (FBAR) became widely used in the past few years in analog front-ends for realizing stable bandpass filters with good selectivity [1],[2]. Initially FBAR have been used primarily in duplexers and their success in this application caused attempts to incorporate them in other communication devices. This leads to diversification of the filter requirements: passband bandwidth extension, passband tuning, higher stopband attenuation, creating of transmission zeros at desired positions, etc.

One of the challenges of these filters is that the above requirements must be achieved with a limited set of components. In fact, FBAR filters consist of two sets of identical resonators and rarely few capacitors or inductors are added. This limitation is due to the specifics of the FBAR technology where usually the values of the parameters of both sets of resonators differ by few percent only. Usually bonding wires are used as extra inductors and sometimes these inductors are on the surface of the integrated circuit (IC) – in both cases their number is limited. The extra capacitors are connected in series to the resonator in the form of dielectric, formed on top of the piezoelectric layer. These limitations do not allow direct application of the known methods for design and synthesis of classic *LC* or quartz crystal filters. Two basic architectures for FBAR filters are known: ladder and lattice. Each of them has its advantages and disadvantages. In conclusion, the FBAR filters have limited circuit and parameter variability.

The limited filter architectures and the similarity of the FBAR parameters lead to similarity of their frequency responses. Their comparison can be done by considering of the passband bandwidth; stopband attenuation and slope steepness; existence and positioning of transmission zeros; and tunability. The goal of this paper is to do such comparison based on computer simulation of the most common filter architectures. Section II presents the used FBAR model and sections III and IV review the ladder and lattice architectures.

[1]Dobromir Gaydajiev is with Smartcom Bulgaria AD, BIC IZOT, 7th km, Tzarigr. Chausse, 1784 Sofia, Bulgaria, E-mail: dobromir_gaydajiev@smartcom.bg.

[2]Ivan Uzunov is with the Faculty of Telecommunications, Technical University of Sofia, 8 Kl. Ohridski blvd., 1000 Sofia, Bulgaria, E-mail: iuzunov@tu-sofia.bg.

II. FBAR: PARAMETERS AND MODELS

FBAR, as every piezo-resonator, features a series followed by a parallel resonance. It is modeled by the modified Butterworth – van Dyke model, shown in Fig. 1(a) [1],[3]. The elements C_m and L_m define the series resonance and the ratio C_0/C_m determines the distance between series and parallel resonance frequencies (typically 2-3% of the series resonance frequency). Both resonances define also the effective coupling factor k_{eff}^2 [1], which is typically few percents. The resistances are very small (around 1 Ω) which constitutes high quality factors in the range of 500 to 2000 [1]. Therefore the FBAR equivalent impedance depends primarily on its reactance, which frequency response is given in Fig. 1 (b). The basic FBAR parameters are its resonance frequencies, one of the reactive components in the mBVD model, basically C_0, and its quality factor.

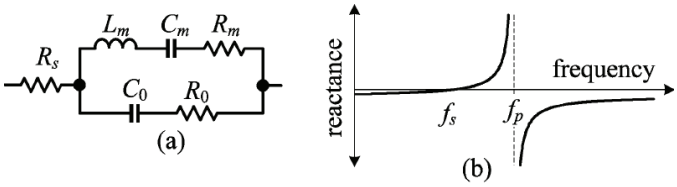

Fig. 1. (a) Modified Butterworth - Van Dyke (mBVD) model of FBAR; (b) FBAR reactance vs. frequency.

The simulations below are based on the model data given in [4]: f_s = 2.1506GHz; f_p = 2.207GHz; L_m = 69.59nH; C_m = 78.7fF; C_0 = 1.48pF; R_m = 1.027Ω; R_s = 0.8Ω; R_0 = 0.2Ω; Q≈500. These values are used for the resonators in one of the sets (set '*b*'). The parameters for the resonators from the other group (set '*a*') are determined partly artificially: their series resonance must be equal to the parallel resonance of set '*b*', C_0 and Q are the same. The corresponding parameters of set '*a*' are: f_s = 2.207GHz; f_p = 2.26496GHz; L_m = 66.08nH; C_m = 78.7fF; C_0 = 1.48pF; R_m = 1.001Ω; R_s = 0.8Ω; R_0 = 0.195Ω; Q≈500. Both sets of resonators have the same effective coupling coefficient k_{eff}^2 = 6.15%.

III. LADDER FILTERS

The basic ladder architecture with 5 resonators is shown in Fig. 2(a). It consists of Γ-type sections and Fig. 2(a) has 2½ sections. A single Γ-type section has very low stopband

attenuation, which is the reason for cascading multiple sections to meet the filter specifications. It is clear intuitively that the higher number of sections increases also the attenuation at the passband edges, i.e. it shrinks the passband bandwidth. Therefore it is reasonable to investigate the effect of increased number of sections on the stopband attenuation and on the passband bandwidth. This is done by using PSpice and the results in Fig. 3 confirm the shrinking of the passband bandwidth when the number of sections is larger. The transfer function is calculated in the usual way for passive filters: square root from the power in the load divided by the maximum available power from the source [5]. The terminal resistances in all simulations are 48Ω.

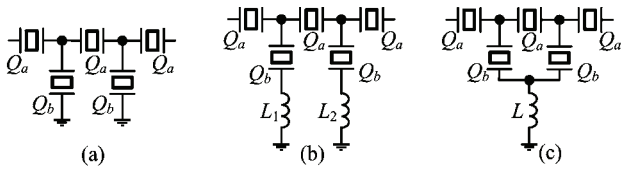

Fig. 2. (a) Basic ladder structure with 2½ Γ-type sections; (b) adding inductors in each shunt branch; (c) adding common inductor for all shunt branches.

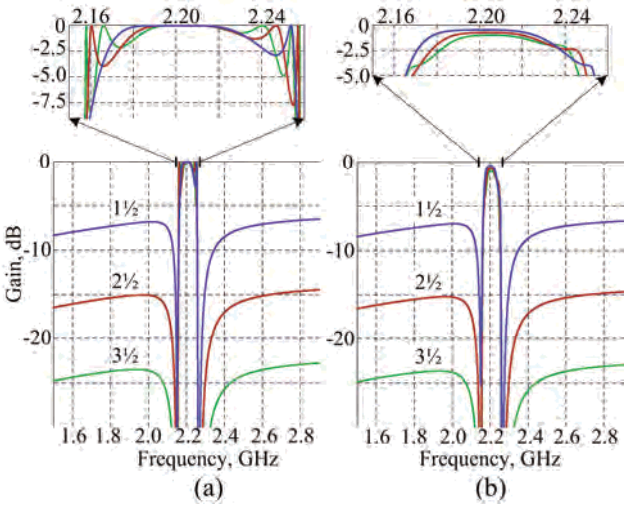

Fig. 3. Frequency response of the basic ladder filter with 1½, 2½ and 3½ sections: (a) neglected FBAR losses; (b) included FBAR losses.

The first conclusion from the simulation results is that each Γ-type section adds around 7.5–8dB attenuation in the stopband. The transmission zeros at both sides of the passband are defined by f_{sb} and f_{pa} and they do not depend on the number of sections. The simulation of the lossless circuits in Fig. 3(a) helps to clarify an interesting phenomenon in the passband: appearance of extra gain maxima beside the central passband maximum at $f_{sa} = f_{pb}$. They are due to new resonances between the resonators in the series and shunt branches. Unfortunately they are very narrow with deep gaps between them and they do not contribute for extending of the passband – their effect is just opposite. When losses are included (Fig. 3(b)) the resonance peaks are suppressed to stairs, which only extend the transition region between the stop- and passbands. This behavior is observed also in the measured filter characteristics [1].

Ladder filters can be complicated by adding of inductors in series to the shunt resonators. Connection of individual inductors to each shunt resonator (Fig. 2(b)) causes extension of the passband. The series inductor shifts the equivalent series resonance downwards, which causes the extension of the passband. A side effect is appearance of second series resonance in the upper stopband, since the order of the equivalent impedance increases [5]. The second series resonance introduces a transmission zero in the upper stopband. The shunt branch behaves as inductor above this zero, causing appearance of second passband. This is illustrated in Fig. 4(a). The higher the inductance is, the closer to the passband is the extra zero. This limits the values of the extra inductors and usually they are less than 1nH [1],[6]. Fig. 4(b) illustrates the effect of extra inductors on ladder filters with different number of sections. It is small in the stopband (the attenuation increases by approx. 1 dB). The effect on the passband is larger, when the number of the sections is bigger: for example the passband is extended by 10% for the filter with 3½ sections.

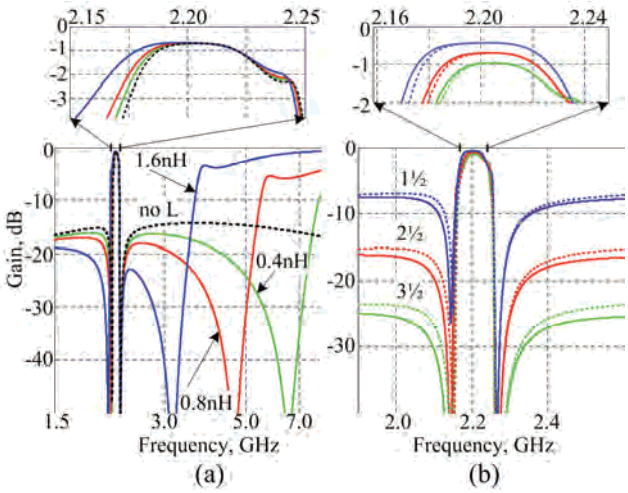

Fig. 4. Frequency responses of filters with individual series inductors (FBAR losses are included): (a) 2½ section filter with different values of the inductors; (b) filters with different number of sections and 0.4nH inductors in each shunt branch (dotted lines are for corresponding filters without inductors).

The circuit on Fig. 2(c) suggests the use of a common mode inductor that is series resonant with the set of shunt resonators [1]. It slightly increases the passband, due to the same reason as in the previous case, but its major effect is the increasing of the attenuation in the upper stopband. A second transmission zero in the stopband is introduced by this inductor, which effect is similar to the effect of the individual inductors. However a single inductor is used in this case and the simulation shows that now the reasonable value of this inductor is smaller. Fig. 5(a) compares the frequency responses of 2½ section filters without inductors, with individual 0.4nH inductors and with common 0.2nH inductor. The effect is obvious: 0.2nH common inductor gives better attenuation in the stopband of interest than two 0.4nH individual inductors. Fig. 5(b) compares 2½ and 3½ section filters with common 0.2nH inductors: evidently the effect of the inductor increases when the number of sections is bigger.

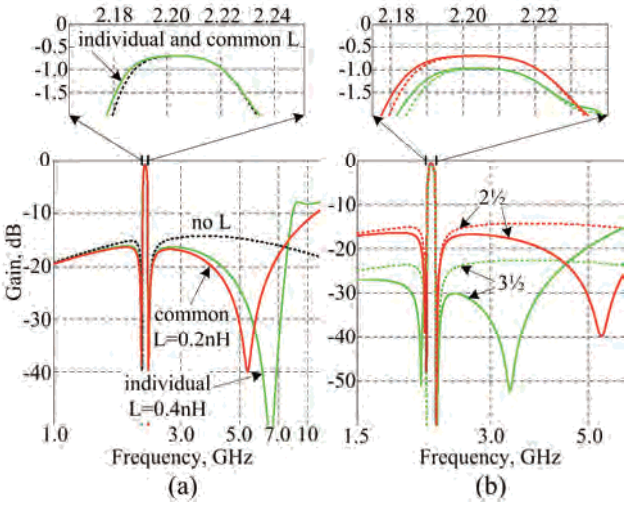

Fig. 5. (a) Comparison of 2½ section filters without inductor, with individual 0.4nH inductors and with common 0.2nH inductor. (b) Comparison of 2½ and 3½ section filters with 0.2nH common inductor (dotted lines are the frequency responses of filters without inductors).

Some numerical data are summarized in Table 1.

IV. Lattice Filters

The other common architecture for FBAR filters is the lattice structure shown in Fig. 6(a) [1],[2]. It consists of two pairs of identical resonators, for which a similar requirement as for the ladder filters is valid: the series resonance frequency of one of the pairs must be equal to the parallel resonance of the other (for example $f_{sa} = f_{pb}$). Also, the relationship $R^2 = Z_a Z_b$ is satisfied at certain frequency f_0 in the passband, where R is the value of the terminating resistors at both sides of the lattice, Z_a and Z_b are the impedances of the corresponding resonators. Theoretically there are two frequencies of maximum gain in the passband: f_0 and the frequency $f_{sa} = f_{pb}$.

Fig. 6(b) shows a modification of the lattice filter proposed in [7]. It has similar properties as the original lattice filter, when the resistances R_a and R_b are equal to the lattice terminating resistors. However R_a and R_b could differ slightly, which allows creating and tuning of transmission zeros. The first amplifier is transconductance amplifier and the second one is transresistance amplifier.

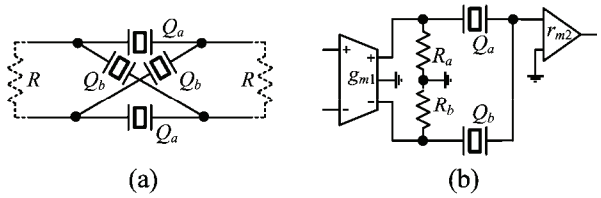

Fig. 6. (a) Lattice FBAR filter; (b) its modifications with less number of resonators.

The simulations of both lattice filters in Fig. 6 are done for two values of the resistors R (R_a and R_b in Fig. 6(b)). The first value 48Ω ensures coinciding of the frequencies f_0 and $f_{sa} = f_{pb}$ – then the frequency response in the passband has flat behavior. The other value is 96Ω. Then f_0 is far from $f_{sa} = f_{pb}$ and close to f_{pa}. The whole passband is moved upwards and it has two ripples: one at $f_{sa} = f_{pb}$ and another at f_0. The frequency responses are shown on Fig. 7. When the losses are not taken into account the frequency responses of both circuits in Fig. 6 are identical. Their difference in Fig. 7(b), when the losses are included, is due to the input impedance of the second amplifier in Fig. 6(b), which is taken to be 5Ω. For comparison, the corresponding frequency responses of 3½ stage ladder filter taken from Fig. 3 are given in Fig. 7 also.

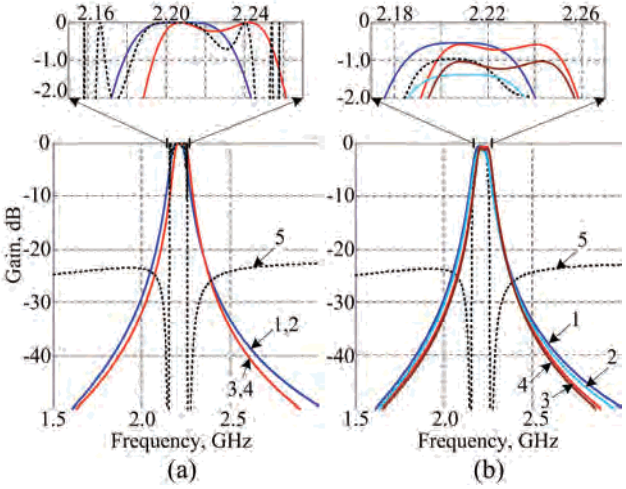

Fig. 7. Frequency responses of the lattice filters: (a) without FBAR losses; (b) with losses. Curve enumeration: 1 – the filter from Fig. 6(a) with flat passband; 2 – Fig. 6(a) with ripples in the passband; 3 – the filter from Fig. 6(b) with flat passband; 4 – Fig. 6(b) with ripples in the passband; 5 – the ladder filter from Fig. 2(a) with 3½ sections.

The comparison of the characteristics of the considered basic filter structures shows that the ladder filters have significantly narrower passband. The ladder filter ensures steeper slopes and very high attenuation close to the passband, which is due to the multiple transmission zeros in that region. This high attenuation is in narrow bands at both sides of the passband and the attenuation degrades very fast away from them. The width of the bands with high attenuation is approximately the same as the passband bandwidth. The lattice filters have opposite behavior. Their attenuation increases monotonically and not far from the zeros of the ladder filter exceeds the ladder filter attenuation.

The FBAR losses in lattice filters have the same effect as in the ladder filters. Their influence is relatively small in the stopband and the major effect is in the passband. The passband insertion loss in the lattice filters is approximately the same as in the ladders, but the shrinking of the passband bandwidth is much less. There is an increase of the insertion loss in the modified lattice filter in Fig. 6(b) due to the input impedance of the transresistance amplifier. However this could be compensated by the amplifiers.

Transmission zeros can be also created in the lattice filters. It can be done via changing of the capacitance C_0 in the mBVD model of one of the resonators (technologically this resonator should have larger area). The same effect could be achieved in Fig 6(b) by making R_a and R_b different. Examples of the corresponding frequency responses are shown in Fig. 8.

The position of the transmission zeros could vary depending on the relative difference between R_a and R_b.

Table I makes a brief comparison between both basic FBAR filter architectures, based on numerical data extracted from the frequency responses shown in the pictures above.

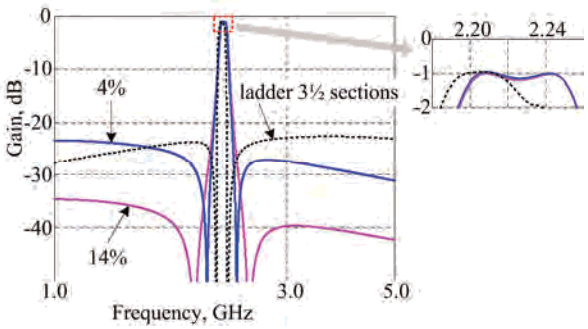

Fig. 8. Frequency responses of the filter in Fig. 6(b) when R_a and R_b are different. The percentage values give the relative difference between R_a and R_b.

TABLE I
SOME NUMERICAL DATA EXTRACTED FROM THE SIMULATED FREQUENCY RESPONSES.

	Min. attenuation in lower stopband, dB	Min. attenuation in upper stopband, dB	Min. attenuation in passband, dB	Passband width at 0.3dB, MHz
Fig. 3(a), 1½ / 2½ /3½ sections	6.8 / 15.0 / 23.5	6.1 / 14.0 / 22.3	0 / 0 / 0	45.7 / 36.7 / 32.3
Fig. 3(b), 1½ / 2½ /3½ sections	6.6 / 14.5 / 22.7	5.9 / 13.6 / 21.6	0.45 / 0.72 / 0.99	40.6 / 32.4 / 26.5
Fig. 4(b), 1½ / 2½ /3½ sections	7.1 / 15.5 / 24.0	7.1 / 15.7 / 24.5	0.42 / 0.69 / 0.96	42.8 / 34.5 / 30.4
Fig. 5(b), 2½ / 3½ sections	15.5 / 25.9	16.1 / 29.1	0.69 / 0.96	34.6 / 31.1
Fig. 7(a), flat passband	30.2*	28.4*	0	42.4
Fig. 7(a), passband with ripples	31.7*	31.1*	0	51.9
Fig. 7(b), flat passband, lattice	29.9*	28.2*	0.54	40.3
Fig. 7(b), passband with ripples, lattice	31.3*	30.6*	0.58	50.37
Fig. 7(b), flat passband, modified lattice	29.8*	28.4*	1.39	41.2
Fig. 7(b), passband with ripples, modified lattice	31.5*	30.8*	1.04	51.4

* The stopband attenuation of the lattice and modified lattice circuits is measured at frequencies, which are at ±10% from the passband center frequency.

V. CONCLUSION

The comparison of the characteristics of the two major FBAR filter architectures, done in the paper, allows to outline their pros and cons. The ladder filter features better rectangularity of the frequency response around the passband, especially when multiple Γ-type sections are used. However the positions of their transmission zeros depend strongly on the used resonators and their change can be very small using the proposed techniques. Outside of narrow bands around the passband the attenuation quickly returns to moderate values. Also the passband bandwidth is typically less than that of a lattice filter. The lattice filters also have steep slopes and they may have monotonically increasing attenuation in the stopband. In addition, it is possible to create transmission zeros in the stopband, which can be positioned everywhere. The modified lattice filter in Fig. 6(b) allows also easy tuning of these zeros.

Of course, "the best filter" does not exist and every application requires its own filter. The results reported in the paper can be used for making the proper choice. These results are extracted by using a particular example. However it is not difficult to extend the conclusions for other cases. For example, different coupling coefficient will change proportionally the bandwidths and the distances between basic filter frequencies; different values of the capacitances require typically different loads; etc. Thus the reported results are not limited only to the considered examples.

ACKNOWLEDGEMENT

This work is supported by contract No. DDVU02/6 from 17.12.2010 funded by National Science Fund of the Ministry of Education, Youth and Science of Bulgaria.

REFERENCES

[1] K.-ya Hashimoto, ed., "*RF Bulk Acoustic Wave Filters for Communications*", Artech House, 2009.

[2] R. Ruby, "Review and comparison of bulk acoustic wave FBAR, SMR technology", *Proc. 2007 IEEE Int. Ultrasonic Symposium*, pp. 1029-1040.

[3] R.Larson III, P. Bradley, S. Wartenberg, R. Ruby, "Modified Butterworth – Van Dyke circuit for FBAR resonators and automated measurement system", *Proc. 2000 IEEE Ultrasonic Symposium*, pp. 863-868.

[4] K. Östman, S. Sipilä, I. Uzunov, N. Tchamov, "Novel VCO architechture using series above-IC FBAR and parallel LC resonance", *IEEE J. Solid-State Circuits*, vol. 41, No. 10, pp. 2248-2256, Oct. 2006.

[5] R. Schaumann, M. E. Van Valkenburg, "*Design of Analog Filters*", Oxford University Press, 2001.

[6] Y.-D. Kim et al, "Highly miniaturized RF bandpass filter based on thin-film bulk acoustic-wave resonator for 5-GHz-band application", *IEEE Trans. Microwave Theory Techniques*, vol. 54, No. 3, pp. 1218-1228, March 2006.

[7] I. Uzunov, R. Bradvarov, P. Statev, B. Boyanov, "Easy adjustable FBAR filter circuit", *Electronics Letters*, vol. 46, No. 9, pp. 657-658, Apr. 29th, 2010.

The Hall Voltage Nonlinearity: a Surface Layer Formation with the Lorentz Force

Ivelina Cholakova[1], Siya Lozanova[2], Tihomir Takov[1], Chavdar Roumenin[2]

Abstract – **A new galvanomagnetic source for the Hall voltage nonlinearity related to conductive surface layer formation by the Lorentz force is experimentally proved. This nonlinearity appears as tendency saturation in output characteristics. This behaviour occurs under certain values of the magnetic induction depending on the bias current and the magnetic-field polarity.**

Keywords – **Hall effect, Orthogonal Hall microsensor, Nonlinearity, Conductivity surface layer formation, Device performance.**

I. INTRODUCTION

Sensor output characteristics, magnetotransducers including, are a functional dependence of the output parameter, for example the Hall voltage $V_H(\boldsymbol{B})$ related to the input influence, in this case the magnetic field $\boldsymbol{B}$, defined in steady-state conditions. In most of the cases in control-measurement technologies, the output signal is preferred to be a straight line in order to use a constant sensitivity S = const. The voltage $V_H(\boldsymbol{B})$ of Hall elements with finite sizes is not an ideal straight line, as it is theoretically said about this phenomenon, $V_H(I_s,\boldsymbol{B}) = GR_HI_sB/t$, where $R_H = -1/qn$ or $R_H = 1/qp$ is the Hall coefficient, I_s is the bias current, t is the thickness of the structure in direction of the magnetic field $\boldsymbol{B}$, and G is the geometrical correction factor [1], [2], [3], [4], [5]. The reasons for the non-linearity of the Hall output V_H have different origin. One of the possible sources is the dependence of G parameter from the induction B. Another reason is the influence of the field $\boldsymbol{B}$ on the Hall coefficient R_H by modulation of the carrier concentration n or p, etc. These negative factors in the common case exert quadratic influence on the voltage $V_H(B) \sim B^2$. In the CMOS Hall sensors, especially parallel-field CMOS Hall devices, the cause for the non-linearity is the dependence of the effective thickness t_{eff} confining the transducer zone with p-n junction by the field $\boldsymbol{B}$ [4]. Other factors, disturbing the linearity, are the high values of the magnetic induction ΔB, working temperature range ΔT and the dependence of the sensitivity S from the strength and strain of the field $\boldsymbol{B}$. The highest linearity is achievable when the magnetic induction has small values $B \leq 1$ T and the temperature T is near to room conditions, $15 \leq T \leq 40$ °C. In this cases the nonlinearity NL, defined as NL = $(V_H(B) - V_{Hideal})/V_{Hideal}$, is up to 0.2 - 0.4 % for silicon Hall sensors, where $V_H(B)$ is the actual measured Hall voltage on the output with fixed current I_{s0} and induction B_0, and V_{Hideal} is the point (with the same current I_{s0} and field B_0) of the best linear fit to the experimentally measured values [2], [4].

In Hall sensors, it is often observed a typical, well reproducible nonlinearity, manifested as a tendency of saturation of the characteristic $V_H(\boldsymbol{B})$ at one polarity of the magnetic field $\boldsymbol{B}$, and in the other direction of the vector $\boldsymbol{B}$ this peculiarity is missing [6]. This irregularity is strongly visible at high values of the magnetic inductance B. It makes worse the metrological qualities of the signal $V_H(\boldsymbol{B})$, so a software linearization is needed when it is electronically processed at the next step. In our opinion the main cause for this negative property of the Hall sensor output is a galvanomagnetic process, which is not sufficiently clarified so far. The present publication extends the scope of investigations of this regularity with samples of batch fabricated Hall devices.

II. SAMPLES AND MEASUREMENT METHODS

Figure 1 illustrates a sketch of the Hall sensor fabricated by one corporation. The substrate semiconductor material is n-type silicon with majority carriers' concentration $n \sim 10^{15}$ cm^{-3}. The design is symmetrical with quadratic shape and the bias contacts C_1 and C_2, and Hall terminals H_1 and H_2 are in the middle of the four sides and are electrically interchangeable.

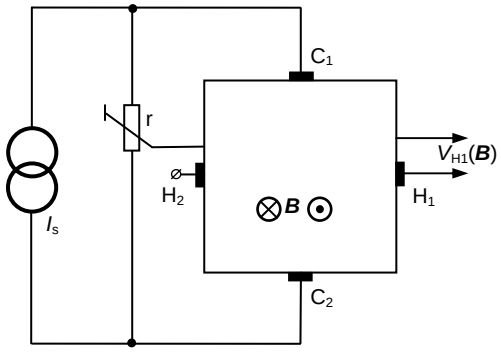

Fig. 1. Sketch of the investigated orthogonal Hall device, the circuitry containing a trimmer r for compensation of the quadratique magnetoresistance is shows too.

[1]Ivelina Cholakova is with the Faculty of Electronic Engineering and Technologies, TU, Kliment Ohridski 8, 1000 Sofia, Bulgaria, E-mail: inch@ecad.tu-sofia.bg

[2]Siya Lozanova is with the Institute of Systems Engineering and Robotics, BAS, Acad. G. Bonchev 2, 1113 Sofia, Bulgaria, E-mail: slozanova@icsr.bas.bg.

[1]Tihomir Takov is with the Faculty of Electronic Engineering and Technologies, TU, Kliment Ohridski 8, 1000 Sofia, Bulgaria

[2]Chavdar Roumenin is with the Institute of Systems Engineering and Robotics, BAS, Acad. G. Bonchev 2, 1113 Sofia, Bulgaria

The Si chips are fixed on four terminal packages with a plastic coverage. The power-supply of the samples is accomplished in mode of operation constant current I_s = const. The output voltage $V_{H1,2}$ ($\boldsymbol{B}$) is measured with both high quality voltmeter, type Hewlett Packard, and with a curve tracer, too. The inevitable offset $V_{H1,2}(B = 0) \neq 0$ can be compensated by trimming. This approach is described in [1], [2], [3], [7]. The controlled external magnetic field $\boldsymbol{B}$ is generated by an electromagnet with water cooling. When the supply power is 1.2 kW and the distance between the poles is 20 mm, the value of the magnetic inductance is B = 2 T. The vector $\boldsymbol{B}$ is normal to the sensor plane, Fig. 1. According to the results in [6], the effect of nonlinear behavior of the output signal is better visible in Hall element with minimal design complexity [7], [8]. These devices have only three contacts: two bias electrodes and one output contact. The Hall effect and the magnetoresistance coexist at the output terminal H. Because the Hall voltage is the parameter of interest, the sensors are investigated as three contacts, as shown in Figure 1. The overall measurement error is no more than 2 %.

The inevitable geometrical quadratic magnetoresistance MR ~ B^2 between the supply contacts C_1 and C_2 introduces on terminal H a MR-component, which value is the half of the whole $V_{C1,2}(\boldsymbol{B})$ voltage on electrodes C_1 and C_2. Hence, on the terminal H sinergetically attend a Hall voltage V_H and a MR signal. The circuitry in Fig. 1 realizes precise extraction of the Hall voltage V_H only at a fully compensation of the magnetoresistance MR. The main conclusion of this analysis is that the half of the Hall voltage $V_H = 0.5\ V_{Hall}$ generated in the sensor from Fig. 1 posses the same physical and metrological characteristics as the well known classical Hall devices. This circuitry gives the opportunity the Hall signal to be investigated without the so called "differential contamination". The differential Hall voltage $V_{H1,2}(\boldsymbol{B})$ to a great extend disguises details about the galvanomagnetic processess in the structures.

III. Experimental Results. Interpretation

Figure 2 illustrates a typical behaviour of the investigated Hall sensors, registered with the arrangement from Fig. 1. For one polarity of the magnetic field $\boldsymbol{B}$, depending on the bias current $I_{C1,2}$ and after a fixed value of the magnetic induction B_0, the Hall signal goes to saturation. For the other polarity of the field - $\boldsymbol{B}$, the linearity of the dependence $V_H(\boldsymbol{B})$ remains the same, by analogy with [6]. It is clearly established by a further experiment, that the nonlinearity NL at a field $\boldsymbol{B} > 0$ appears when the Lorentz force $\boldsymbol{F}_L$ deflects the carriers to the respective side with contact H. For the other direction of the force $\boldsymbol{F}_L$, when the carriers are deflected to the substrate bulk, the linearity is maintained. Figure 3 shows the experimental dependence of the threshold induction $B_0(I_{C1,2})$ as a function of the bias current $I_{C1,2}$. The resulting curve can be approximated as $B_0 \sim 1/I_{C1,2}$. As bigger the bias current $I_{C1,2}$ is, as earlier the nonlinearity NL is visible for the Hall voltage $V_H(\boldsymbol{B})$.

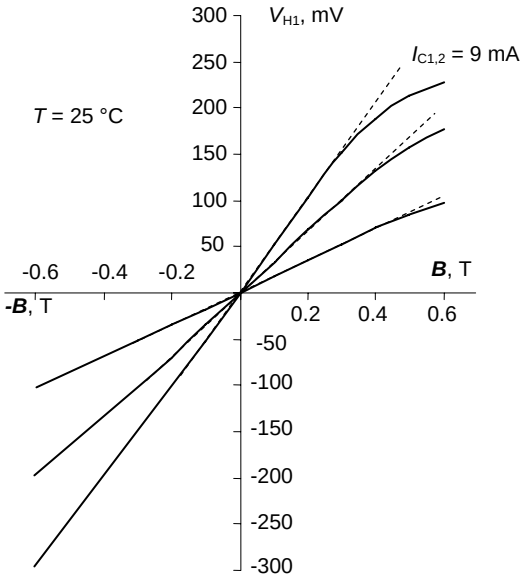

Fig. 2. Output sensor characteristics $V_H(\boldsymbol{B})$, the bias current is as a parameter, T = 25 °C. The nonlinearity occurs when the Lorentz force deflects the carriers toward the surface with the Hall contact H.

Comparing our results with these in [6], we can conclude that the nonlinear behavior of the Hall voltage V_H has a regular character. Such nonsymmetrical behavior of the Hall voltage is not a consequence of the existing theory of this phenomenon [2], [3], [4], [5], [9], [10], [11], [12], [13].

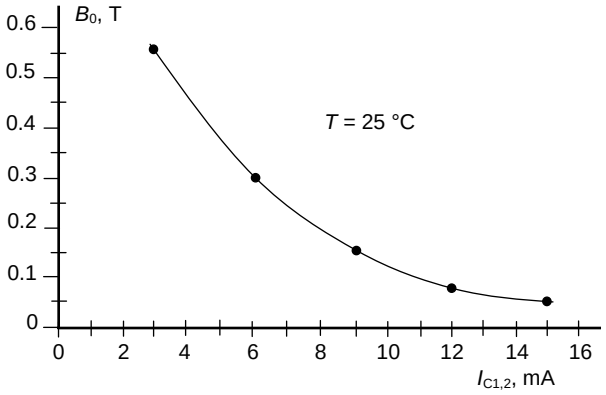

Fig. 3. Dependence of the threshold induction B_0 as a function of the bias current $B_0(I_{C1,2})$.

Therefore the interpretation of this property is based on a new physical mechanism. We think that in the theory of the Hall effect, there are essential gaps. It is believed that the charges which are accumulated by the Lorentz force $\boldsymbol{F}_L$ to the respective boundary with Hall contact H are immovable and generate a Hall field $\boldsymbol{E}_H$ and voltage $V_H(\boldsymbol{B})$. This clearly contradicts to the fact that the supply voltage V_s is applied not only to the bulk of the structure, but also to its surface! Therefore, the additional electron concentration to the side

with contact H increases the conductivity of the surface layer. So, after a concrete value of the field B_0, i.e. of the additional electrons of the boundary, the Hall voltage V_H on contact H is shunted from the reduced surface resistance. At the dependence $V_H(\boldsymbol{B})$ this is observed as a saturation. For the opposite direction of the field - $\boldsymbol{B}$, the Lorentz force $\boldsymbol{F}_L$ impoverishes the boundary with contact H from movable electrons. Thus, positive donor ions remain and generate positive potential, directly proportional to the induction B [14].

Especially, the stronger is the bias current $I_{C1,2}$, the higher the Lorenz deflection, and the shunting role of the formed high-conductive surface n^+ layer, depending on the voltage $V_H(\boldsymbol{B})$ is better expressed. The saturation behavior of the curve $B_0(I_{C1,2})$, Fig. 3, is most probably related to an upper limiting density value of the electrons on the Hall surface caused by the repulsing Coulomb forces. For the opposite direction of the magnetic field -$\boldsymbol{B}$, the depletion of the surface region from moving carriers is proportional to the Lorentz force $\boldsymbol{F}_L$ value. In this case a tendency of saturation within the magnetic fields range used is not experimentally observed. We can presume that the dimension of the depletion zone, induced by the Lorentz force with respect to the thickness of the structure is negligible. Therefore, for +$\boldsymbol{B}$ field, the generated by the Hall effect high-conductive surface layer directly exert a shunting action on the voltage $V_H(\boldsymbol{B})$. This is accompanied by a tendency of saturation on the dependence $V_H(+\boldsymbol{B})$. The new property is better experimentally pronounced at a field $\boldsymbol{B} > 0$ when a high-conductive surface n^+ - layer under the interface Si-SiO_2 already exists. This effect arises when in the oxide SiO_2 positive charge exists, emerging there during technology realization. This initial n^+-layer at a field polarity $\boldsymbol{B} > 0$ grows and its influence on the surface conductivity becomes decisive after induction $B > B_0(I_{C1,2})$, Fig. 2. At negative polarity $\boldsymbol{B} < 0$ the n^+-layer remains unchanged like at induction $B = 0$ and the dependencies $V_H(-\boldsymbol{B})$ remain linear. The behavior of the samples with linear characteristics $V_H(\boldsymbol{B})$ at two magnetic-field polarities is most probably caused by the higher quality of technology realization. In this case, for the asymmetry of the Hall contact dependencies to be observed, substantially higher magnetic-field inductions are necessary [14]. Consequently the linear character of the Hall voltage remains the same. The described sensor's effect undoubtedly explains the reason for this polar nonlinearity in the investigated batch fabricated Hall devices.

IV. Conclusion

The main question, related to the metrology of Hall effect sensoric is the possibility to eliminate the reason for this drawback. We consider that it can be done with an appropriate gate, located on the surface with the Hall contact. Applying negative voltage we can maintain the Fermi level in flat bands mode, analogously to MOST. In such a way the accumulation of carriers from the Lorentz force will not dominate, and the linearity will be maintained in two polarities of the magnetic field.

Acknowledgement

This work was financially supported by grant DTK02/50/17.12.2009 of Ministry of Education and Science, Bulgaria.

References

[1] R. Thiel, *Elektrisches Messen Nichtelektrischer Grossen*, Stuttgart, B.G. Teubner, 1983.
[2] C. Roumenin, *Solid State Magnetic Sensors*, Amsterdam, Elsevier, 1994.
[3] T. Takov, *Semiconductor Sensors*, Sofia, Technika, 1986.
[4] R. Popovic, *Hall Effect Devices*, Bristol, IOP Bubl., 2004.
[5] P. Ripka, *Magnetic Sensors and Magnetometers*, Boston, London, Artech House, 2001.
[6] I. Cholakova, S. Lozanova, T. Takov, C. Roumenin, "Hall Contact's Asymmetrical Dependencies of Silicon Sensors: Experimental Evidence for High-Conductive Surface Layer Formation by the Hall Effect", CR de l'Acad. Bulg. Sci, vol. 62, no 11, pp. 1455-1460, 2009.
[7] S. Lozanova, Three-Contacts Silicon Parallel-Field Hall Sensors, PhD Dissert., Sofia, BAS, Techn. Univ. Press, 2006, (in bulg.).
[8] S. Lozanova, C. Roumenin, "Parallel-Field Silicon Hall Effect Microsensors with Minimal Design Complexity". IEEE Sensors J., vol. 9, no 7, pp. 761-766, 2009.
[9] J.M. Ziman, *Principles of the Theory of Solids*, Cambrdge Univ., 1972.
[10] R.A. Smith, *Semiconductors*, Edinburgh, Cambridge Univ. Press, 1978.
[11] K. Seeger, *Semiconductor Physics*, Wien, New York, Springer Verlag, 1973.
[12] F.J. Blatt, *Physics of Electronic Conduction in Solids*, McGraw-Hill Book Comp., 1968.
[13] E. Putley, *The Hall effect and Semiconductor Physics*, New York, Dover, 1960.
[14] C. Roumenin, S. Lozanova, S. Noykov, "Magnetic-Induced Surface Current: Experimental Evidence of an Unexpected Galvanomagnetic Effect in Solids", Appl. Phys. Lett., 2011 (to be publ.).

Development of Pulse and Digital Circuits for Industrial Applications

Elena Koleva[1]

Abstract – **Have been developed in practice the main pulse and digital circuits, shapers, multivibrators, monostable multivibrators, flip – flop, sawtooth generator, frequency dividers with the possibility of starting, stopping, control and maintaining galvanic decoupling between the control signals and outputs schemes for most developments. To build the circuits using different types of optocouplers and elements with negative resistance – tunnel diodes and unijunction transistors. Here are formulas for determining basic parameters of the circuits and developed methods for sizing of sawtooth and pulse generator.**

Keywords – **Pulse and Digital Circuits, Optrons, Tunnel Diodes, Unijunction Transistors.**

I. Development of Pulse and Digital Circuits with Optocouplers and Tunnel Diodes

The tunnel diode (TD) is an element with negative resistance (with N – shaped volt – ampere characteristic). Other elements with a negative resistance in the volt – ampere characteristic are Gunn diode, avalanche transistor, unijunction transistor, dinistor, diak, thyristor, simistor and etc. [1].

Characteristic of TD is that it is low voltage and fast low – current element. For developments choosing TD type АІ301Г (3І301Г) – Russia with the following parameters – Table 1:

TABLE I

Current in peak	I_{max} = 10 mA
Current in minimum	$I_{min} \approx$ 1,25 mA
Ratio	I_{max}/ I_{min} = 8
Voltage in maximum	U_{max} = 0,18 V
Voltage in minimum	U_{min} = 0,55 V
Voltage nominal	$U_{ном}$ = 0,8 V
Current nominal	$I_{ном}$ = 5 mA
Switching time	50 ns

Volt – ampere characteristic of TD is shown in Fig. 1.

The section 1-2 is section with a negative differential resistance.

Persistent areas of the characteristic are 0-1and 2-3.

The capacitor C_1 is charged by the U_{CC}, the resistors R_2 and R_3 as a phototransistor optocouplers is blocked.

The TD is in the first ascending section of the volt – ampere characteristic – section 0-1.

Gradually increase the voltage of the TD and it switches to the second ascending section of the volt – ampere characteristic (p. 3).

Phototransistor VT_1 opens up.

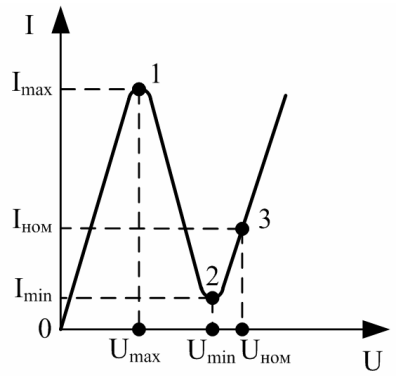

Fig. 1. Volt – ampere characteristic of TD

Circuit of controllable oscillating multivibrators with TD VD_1 and phototransistor optocouplers O_1 – Fig. 2, [3].

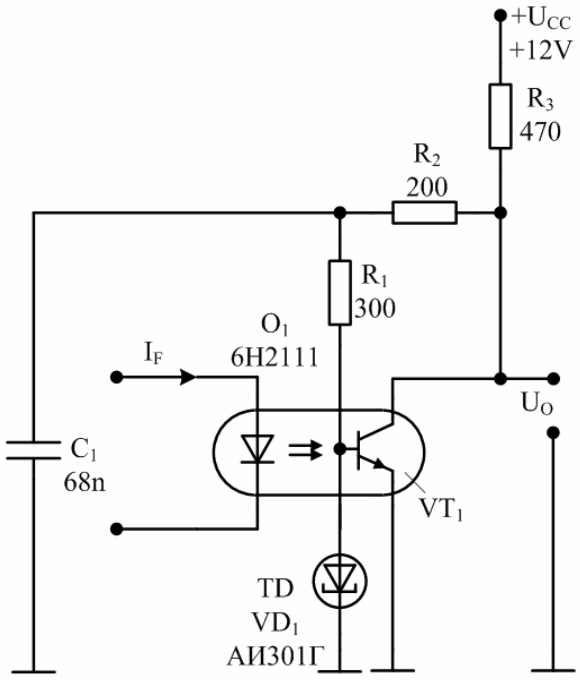

Fig. 2. Controllable oscillating multivibrator

The frequency of the generator can be operated in galvanically separated channel by the current through the LED I_F.

[1]Elena N. Koleva is Ph. D., Department of Electronics, Technical University – Gabrovo, Street "Hadji Dimitar" No. 4, 5300 Gabrovo, Bulgaria, phone: +359 898 226 464,
e-mail: elena_ndpt@yahoo.com

Principle of operation of the circuit:

The capacitor C_1 is discharged through the resistor R_1, TD, the resistor R_2 and phototransistor.

TD and switches back to section 0-1, the phototransistor is closed and capacitor C_1 begins to charge again of the power supply through the resistors R_2 and R_3.

When the C_1= 68 nF, the times of charge and discharge capacitor C_1 are respectively t_3 = 8 μs, t_p ~ 5 μs, f ≈ 77 kHz (I_F = 0).

By the LED current I_F can adjust the frequency of the generator to 10 %. The period T is Eq. 1:

$$T = t_3 + t_P \quad (1)$$

$$T \approx C_1.(R_3 + R_2 + R_1 // R_2).\ln\frac{U_{CC} - R_1.I_{\max}}{U_{CC} - R_1.I_{\min}} =$$

$$= 68.10^{-9}.(470 + 200 + 300 // 200).$$

$$.\ln\frac{12 - 300.10.10^{-3}}{12 - 300.1{,}25.10^{-3}} = 13{,}75\ \mu s$$

TD can be used for the formation of pulses with steep fronts for controlled of the LEDs of the optocoupler – Fig. 3.

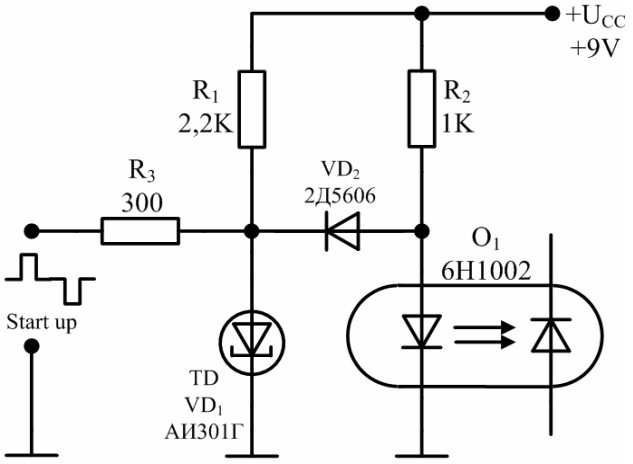

Fig. 3. Control of the LED of the optocoupler by formatting pulses tunnel diode

The circuit consisting of resistor R_1, resistor R_3 and TD form trigger, which is controlled (on and off) with two – pole pulse with amplitude a few volts.

The work of the circuit is to switching tunnel diode by section 0-1 in section 2-3 of the volt-ampere characteristic (see Figure 1) and back in the section 0-1 by the input pulses.

The supply voltage U_{CC} of the circuit is selected in the range – Eq. 2 and Eq. 3:

$$U_{CC\min} > U_{\min} + I_{\min}.R_1 = 0{,}55 + 1{,}25.10^{-3}.2.2.10^3 \geq 3{,}3\ V \quad (2)$$

$$U_{CC\max} < U_{\max} + I_{\max}.R_1 = 0{,}18 + 10.10^{-3}.2.2.10^3 \leq 22{,}18\ V \quad (3)$$

The amplitude of input pulses positive inlet is Eq. 4:

$$U_{(+)} > U_{\max} + I_{\max}.R_3 = 0{,}18 + 10.10^{-3}.300 = 3{,}18\ V \quad (4)$$

Then the current through the LED of the optocoupler is Eq. 5:

$$I_F = \frac{U_{CC} - U_F}{R_2} = \frac{9 - 1{,}2}{1000} = 7{,}8\ mA \quad (5)$$

Fig. 4 is a circuit of monostable multivibrator with TD and phototransistor optocouplers O_1, [4].

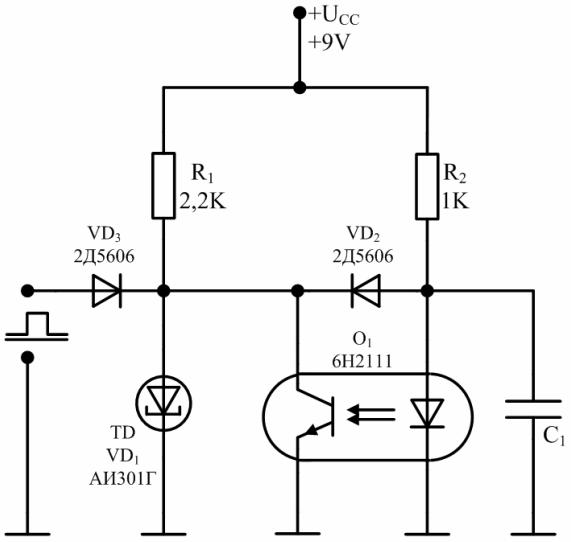

Fig. 4. Circuit of monostable multivibrator with TD and phototransistor optocoupler O1

The monostable multivibrator to restart with a single positive pulse with amplitude of few volts.

Positive input pulse switches TD in section 2-3.

The duration of the output pulse is determined by the charging time of capacitor C_1 through resistor R_2.

Discharge of the capacitor C_1 be made in the unclog diode VD_2 and the tunnel diode, where TD returns in section 0-1 of the volt-ampere characteristic. The amplitude of the starting pulse is:

$$U_{(+)} > U_{F3} + U_{\text{HOM}} = 0{,}7 + 0{,}8 = 1{,}5\ V \quad (6)$$

Application of the developed circuits: forming controls the LEDs and laser diodes, for the development of pulse and digital circuits, oscillators and monostable multivibrators, triggers, frequency dividers and more.

Conclusion – when using TD as shapers of pulse for control of the light sources is obtained controlling pulses with steep fronts. At construction of the main pulse and digital circuits with TD and optocouplers enables a galvanically separated channel to be controlled circuits (switching, on and off switch, regulating the period and duration of the pulse and so on).

II. Development of Pulse and Digital Circuits with Optocouplers and Unijunction Transistors

For basic optocouplers of the developments is used the classic optocouplers – photoresistor, photodiode, phototransistor and photothyristor optocouplers.

For unijunction transistor (two base diode) is used transistors KT117B (Russia) with the following parameters:

- resistance between base 1 and base 2 $R_{B1B2} = (6 \div 9)$ kΩ;
- emitter on current $I_{Emax} \leq 20$ μA;
- emitter off current $I_{Emin} \geq 1$ mA;
- transfer factor – Russia, coefficient of neutralization – USA) $\eta = 0{,}5 \div 0{,}7$;
- voltage emitter - base 1 in the saturation mode – $U_{EB1sat} \leq 1{,}5$ V.

In the input volt – ampere characteristic of unijunction transistor has an area of negative resistance (section AB) – Fig. 5.

The volt – ampere characteristic is the dependence of current of the emitter PN junction I_E emitter – base 1 (E – B_1) as a function of the voltage emitter – base 1 - U_{EB1}.

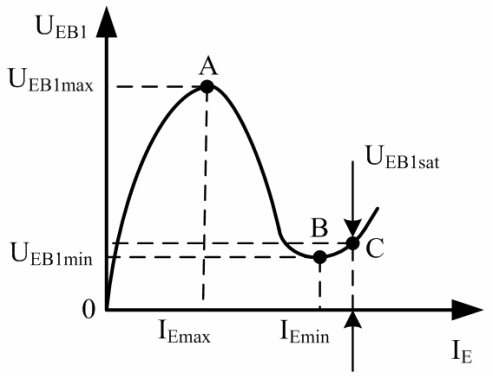

Fig. 5. Volt – ampere characteristic of unijunction transistor

The section OA is blokced condition of the unijunction transistor, and the section BC saturation is deep state of unijunction transistor. On volt – ampere characteristic in flicked characteristic points.

It appears that unijunction transistor is a threshold element.

Aplications of unijunction transistor are generators of linear, pulse and step voltage.

Controlled generator of asymmetric rectangular pulses (Fig. 6), implemented with a photodiode optocouplers O_1 and FET phototransistor -VT_1, [2].

Principle of the work:

The capacitor C is charged by the supply voltage in the resistor R and the photodiode of optocouplers O_1.

When the voltage reached a threshold voltage of the FET phototransistor it opens and the capacitor is discharged through it.

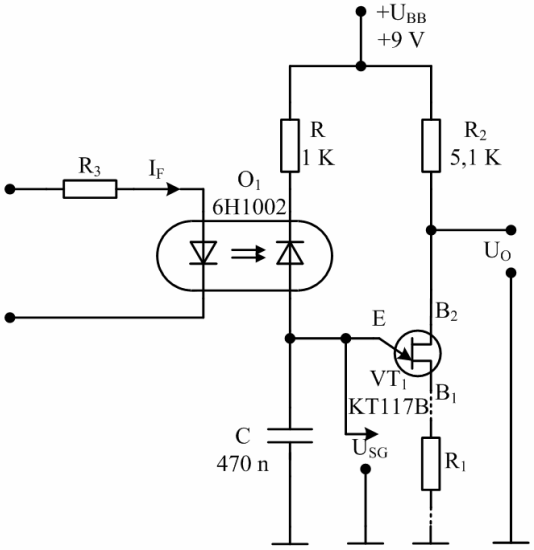

Fig. 6. Generator of asymmetric rectangular pulses

The photodiode optocoupler has a large differential resistance and determination of time capacitor is charged by linear law.

Charge time constant is Eq. 7:

$$\tau = \left[R + R_{PD}(I_F)\right].C \qquad (7)$$

Where R_{PD} is the resistance of the photodiodes of optocoupler O_1.

From expression (7) shows that by the current through the LED I_F can adjust the period of the generator in a wide range (up to 5 times in amending the current I_F 10 mA). The circuit can be realized with photoresistor optocoupler or optocoupler with FET phototransistor.

Circuit of controlled oscillator multivibrator with blocking generations by phototransistor optocouplers O_1 – Fig. 7.

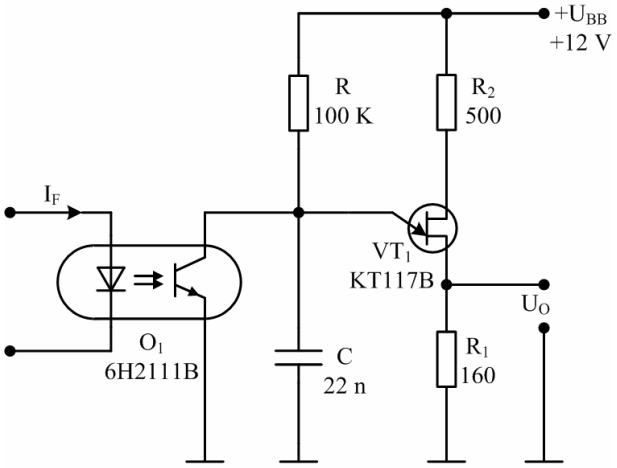

Fig. 7. Circuit of controlled oscillator multivibrator with blocking generations

When the I_F = 0, the controlled oscillator multivibrator operates in a continuous generations. For I_F > 0,5 mA, unijunction transistor maintain blocked, capacitor C is discharged and no generations.

Methodology for sizing the generator of Fig. 7:

1. Determination of transmission coefficient η of the unijunction transistor is Eq. 8:

$$\eta = \frac{U_{EB1\max} - E_{EB1sat}}{U_{B1B2}} = \frac{6V - 1{,}5\,V}{9\,V} = 0{,}5 \qquad (8)$$

2. Determination of the resistors R_1 (R_{B1B2} = 6 ÷ 9 kΩ for KT117V, choose an average value R_{B1B2} = 7500 Ω) is Eq. 9:

$$R_1 \approx \frac{0{,}2.R_{B1B2}}{U_{B1B2}} = \frac{0{,}2.7500}{9} = 166\ \Omega \qquad (9)$$

Choose the resistor R_1 = 160 Ω.

3. Determination of the resistor R_2 is Eq. 10:

$$R_2 \approx 0{,}015.U_{B1B2}.R_{B1B2}.\eta = 0{,}015.9.7500.0{,}50 = 506\ \Omega \qquad (10)$$

Choose the resistor R_2 = 500 Ω.

4. Determination of the voltage turn U_{EB1max} of the unijunction phototransistor is Eq. 11:

$$U_{EB1\max} \approx U_{B1B2}.\frac{\eta + \frac{R_1}{R_{B1B2}}}{1 + \frac{R_1}{R_{B1B2}} + \frac{R_2}{R_{B1B2}}} \approx 5{,}75\ V \qquad (11)$$

Here U_{B1B2} be replaced by U_{BB} = 12 V.

5. Determination of time of the resistor R are Eq. 12 and Eq. 13:

$$R < \frac{U_{B1B2} - U_{EB1\max}}{I_{E\max}} = \frac{9 - 5{,}75}{20.10^{-6}} = 162\ k\Omega \qquad (12)$$

$$R > \frac{U_{B1B2} - U_{EB1\min}}{I_{E\min}} = \frac{9 - 1{,}2}{1.10^{-3}} = 7{,}8\ k\Omega \qquad (13)$$

7,8 kΩ <R <162 kΩ, choose R = 100 kΩ.

6. Determining the period of generations T, where C = 22.10^{-9} F – Eq. 14:

$$T \approx R.C.\ln\frac{1}{1-\eta} = 100.10^3.22.10^{-9}\ln\frac{1}{1-0{,}50} = 1{,}52\ ms \qquad (14)$$

(f = 655 Hz)

To maintain blocked generator emitter voltage of the unijunction phototransistor should be 1,2 V – Eq. 15:

$$\frac{U_{BB}}{R + R_{CE(I_F)}}.R_{CE(I_F)} = 1{,}2\ V \qquad (15)$$

In U_{BB} = 12 V, R = 100 kΩ by the Eq. 16 is given.

Photocurrent of the phototransistor of the oprocoupler is Eq. 17:

$$I_{ph}(I_C) = \frac{U_{B1B2}}{R + R_{CE(I_F)}} = \frac{12}{100.10^3 + 11.10^3} \approx 108\ \mu A \qquad (17)$$

The photocurrent 108 μA is obtained at I_F > 0,5 mA.

Few companies produced optocouplers with unijunction phototransistors such series AOT102A ÷ Г (Russia).

III. CONCLUSION

The combination of the optocouplers and the unijunction phototransistors significantly increases the functionality of the generators implemented with these elements. Control by external galvanic channel – start, stop, control of the period (frequency) in wide ranges and more.

REFERENCES

[1] Kolev, I. S and E. N. Koleva. Infrared Optoelectronics. 2nd Edition. Gabrovo, Univ. publ. „Vasil Aprilov", 2008.

[2] Kolev, I. S. and E. N. Koleva. Coherent Optoelectronics. Plovdiv, Autospectar, 2008.

[3] Kolev, I. S and E. N. Koleva. Noncoherent Optoelectronics. Gabrovo, Univ. publ. „Vasil Aprilov", 2007.

[4] Kolev, I. S. and E. N. Koleva. Optoelectronics and Optical Communications. 2nd Edition. Gabrovo, Univ. publ. „Vasil Aprilov", 2008.

[5] Iliev T. , Plamen Danailov, "An Optical Method of Electrical Machines Diagnostics", Journal of the University of Applied Sciences Mittweida Wissenschaftliche Zeitschrift der Hochsule Mittweida (FH) , Nr. 10, page 96, Germany, Mittweida, 2002.

Computer Simulation of the PV – Boost Converter System Working at MPPT Mode of Operation

Georgi Kunov[1], Elissaveta Gadjeva[2] and Deyan Zhelev[3]

Abstract – **A PV – Boost converter system working at hysteresis MPPT mode of operation is proposed in the present paper. A computer model of the system is developed and simulated. Behavioral parameterized *PSpice* macromodels are developed for the single photovoltaic element and for series connection of single cells. The PV model is used to simulate a concrete electrical circuit, which optimizes the mode of operation of the Boost converter in order to achieve maximum transmitted power from the photovoltaic element (maximum power point tracking - MPPT). The computer models are realized in the *Cadence Capture* and *Cadence PSpice* environment.**

Keywords – **Photovoltaic element, Boost converter, Maximum power point tracking, PSpice model.**

I. INTRODUCTION

Recently, the problem for non-polluting energy production using renewable energy sources is of significant importance. In this respect, the direct converting of the solar energy in electrical energy takes an important place. At present, the cost of the photovoltaic (PV) panels is a determining factor to the cost of the produced using this method electricity. Therefore, the obtaining of maximum amount of energy from PV is of significant importance, despite of climate working conditions. The PV panel has a highly nonlinear I-V characteristic, which in turn, varies depending on the intensity of solar irradiation and the temperature. The maximum power point tracking (MPPT) control of the PV system is therefore critical for the PV system efficiency. A number of methods are developed for MPPT control [1-4] such as:

– Perturb and Observe (P&O) (hill climbing) method;
– Modified Perturb and Observe (MP&O) method;
– Estimate Perturb-Perturb (EPP) method;
– Constant Voltage Method (CV);
– Increment Conductance (Inc Cond) method;
– Fuzzy Logic or Artificial Neural Network Control method.

The disadvantage of these control methods is the high cost of implementation as a result of complex algorithms that usually need a DSP as their computing platform. In the work [1], for instance, the microcontroller TMS320F2812 of TI is used. A relatively simple method for MPPT control is proposed in [5], [6]. Later, other researchers are involved in the investigations based on this method and develop the Ripple Correlation Control technique [4], [7]. The adequate computer modeling of the photovoltaic (PV) element is of significant importance for the computer simulation of MPPT control systems. *PSpice* models of the photovoltaic element are developed in [8], [9].

A PV – Boost converter system working at hysteresis MPPT mode of operation is proposed in the present paper. A computer model of the system is developed and simulated. Behavioral parameterized *PSpice* macromodels are created for the single photovoltaic element and for series connection of single cells. Two variants of PV models are developed – in schematic view, as well as in the form of a subcircuit in accordance to the input language of the *PSpice* simulator. The models are used to simulate a concrete electrical circuit, which optimizes the mode of operation of the Boost converter in order to achieve maximum transmitted power from the photovoltaic element. The computer models are realized in the *Cadence Capture* and *Cadence PSpice* environment.

II. PSPICE MODEL OF PV – BOOST CONVERTER SYSTEM

PSpice simulation model of the system consisting of photovoltaic source, Boost converter, together with the proposed control system, is shown in Fig. 1. The power and I-V characteristics of the solar cell are presented in Fig. 2a and Fig. 2b correspondingly. The waveforms illustrating the principle of the hysteresis MPPT are shown in Fig. 3. The following waveforms are presented in Fig. 3a: Vpv_fb – voltage feedback from the PV output, Ipv_fb – current feedback from the PV output, as well as Ppv – resulting power, obtained by multiplication of Vpv_fb and Ipv_fb. The following waveforms are presented in Fig. 3b: Ppv_fb – scaled power, Ppv_max – upper threshold of the power hysteresis, obtained by a peak detector realized by the capacitor C1 and the switch S1, Ppv_min – lower threshold of the power hysteresis at the output of the scaling amplifier GAIN4. In the moment when Ppv_fb goes to the left of the power maximum, (Fig. 2a), hold by capacitor C1 (Ppv_max), the comparator E1 changes its state and the pulse Reset is produced for the R-S trigger U3A_U4A (Fig. 3c). The transistor Qsw is turned off and the power decreases to the right of the maximum (Fig. 2a). In the moment, when Ppv_fb becomes less than Ppv_min, the comparator E2 changes its state and the pulse Set is produced for the R-S trigger (Fig. 3c).

[1]Georgi Kunov is with the Faculty of Electronic Engineering and Technologies, Technical University of Sofia, 8, Kliment Ohridski Blvd., 1000 Sofia, BULGARIA, e-mail: gkunov@tu-sofia.bg.

[2]Elissaveta Gadjeva is with the Faculty of Electronic Engineering and Technologies, Technical University of Sofia, 8, Kliment Ohridski Blvd., 1000 Sofia, Bulgaria, e-mail: egadjeva@tu-sofia.bg.

[3]Deyan Zhelev is with the Mantov Ltd, 133 Tzarigradsko shosse Blvd., 1784 Sofia, Bulgaria, e-mail: deyan.zhelev@mantov.com.

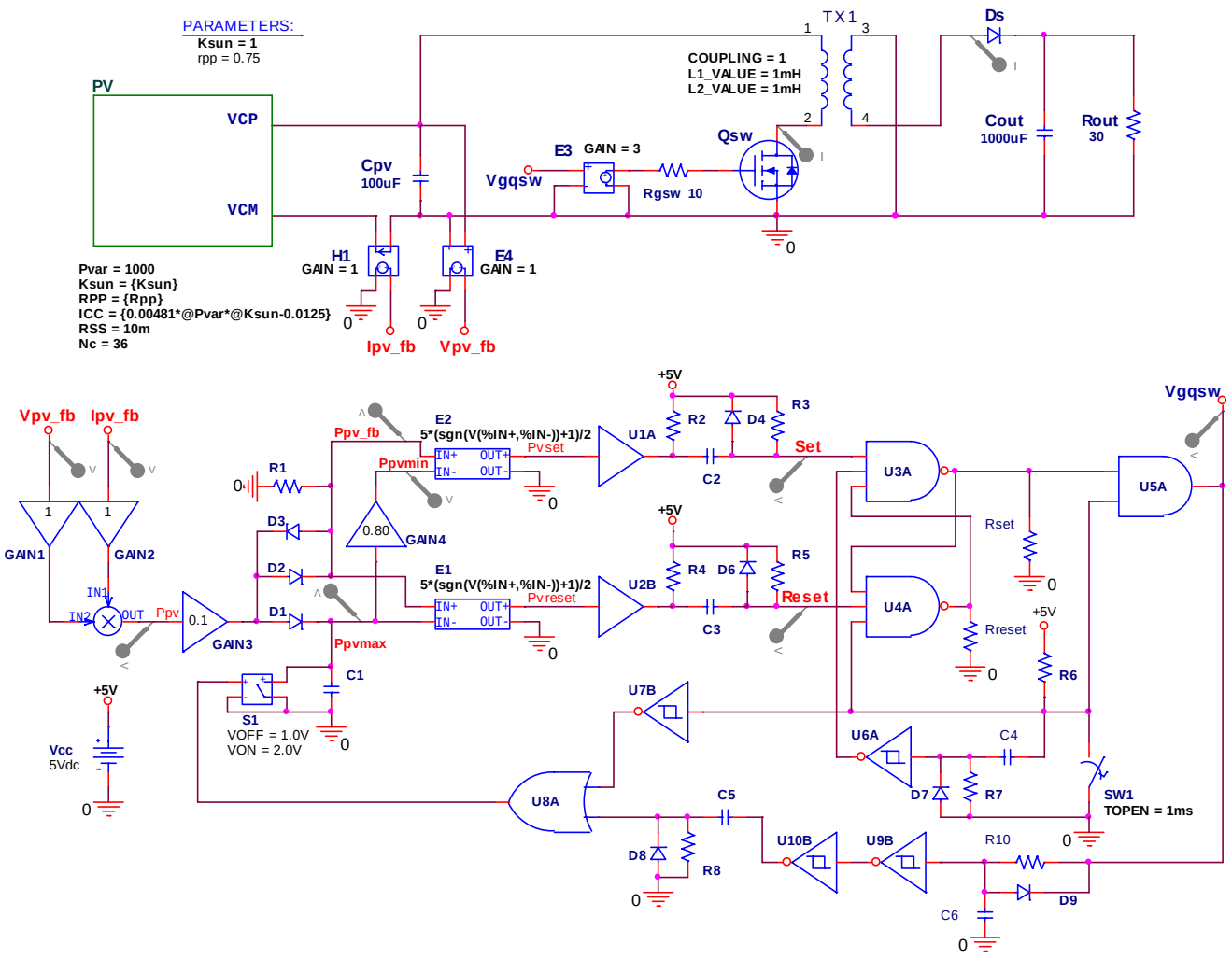

Fig. 1. *PSpice* simulation model of the system consisting of photovoltaic source, Boost converter, together with its control system

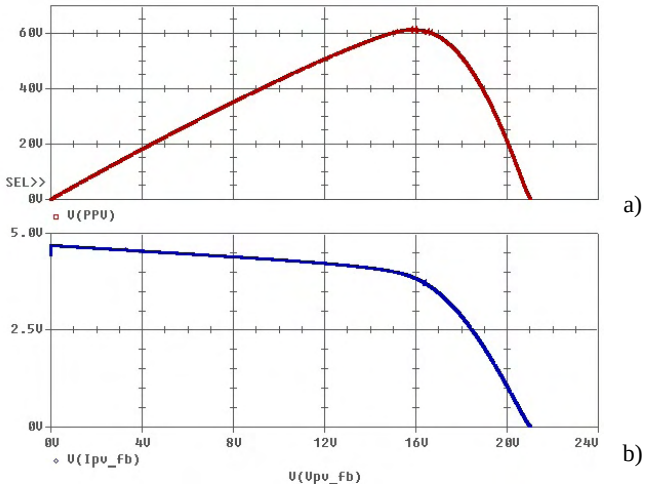

Fig. 2. The power and I-V characteristics of the solar cell

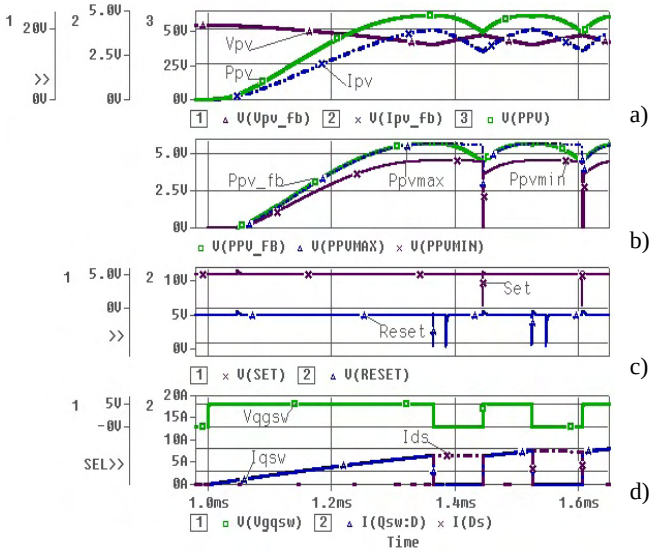

Fig. 3. Waveforms illustrating the principle of the hysteresis MPPT

The transistor Qsw is turned on again. The peak detector is reset and the MPPT process starts again.

The following waveforms are presented in Fig. 3d: Vgqsw – pulses applied to the gate of the transistor Qsw, Iqsw – current through the transistor Qsw, as well as Ids – current through the diode in the secondary winding of the transformer.

III. Computer Model of the Solar Cell

A. PSpice Model of a Single Solar Cell

The macromodel of single solar cell is created in the form of a hierarchical block as shown in Fig. 4. *Icc* is a DC current source which is a function of the solar irradiation P_{var} according to the equation [8] :

$$I_{CC} = aP_{var}K_{sun} + b \quad (1)$$

where *a* and *b* are constants depending on the PV cell.

The behavior of the cell under reduced light conditions is simulated using the shading coefficient K_{sun} . It is defined in the range [0,1], where K_{sun} = 1 for unshaded cell. D1 is a diode with parameters given for the solar cell. R_s and R_p model the corresponding series and shunt resistance losses. The parameters (Icc, Rss and Rpp) are preceded by "@" in the hierarchical block. The symbol and the block properties of the single cell are presented in Fig. 5.

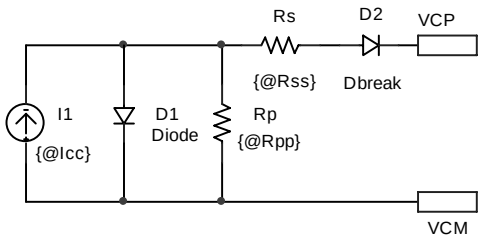

Fig. 4. Macromodel of the single solar cell

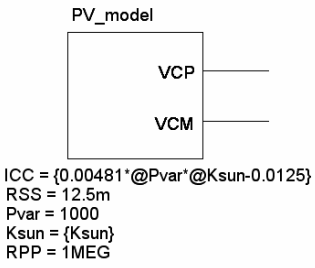

Fig. 5. Symbol representation of the single cell

B. PSpice Model of Series Connected Solar Cells

Based on the single cell model, the series connection of N_C cells is represented using the macromodel shown in Fig. 6. Using the voltage controlled voltage source (VCVS) E1 the voltage $V_{VCP,VCM}/N_C$ is applied to the single cell model consisting of the elements I_1, D_1, R_{P1} and R_{S1}. The voltage controlled current source (VCCS) G1 defines the current through the series connection of the cells, equal to the current of the single cell. The source E1 is of EVALUE type and the source G1 is of GVALUE type in order to ensure parameterization of the block elements.

The block properties of the of series connection of N_C cells are presented in Fig.7. The corresponding symbol is shown in Fig. 8.

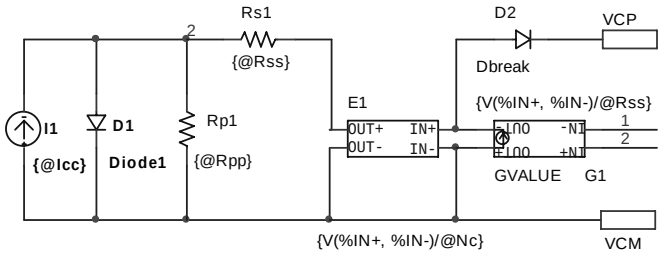

Fig. 6. Macromodel of series connection of *Nc* cells

	A
ICC	{0.00481*@Pvar*@Ksun-0.0125}
Ksun	{Ksun}
Name	PV
Nc	36
Pvar	1000
RPP	{Rpp}
RSS	10m

Fig. 7. Block properties of series connection of N_C cells

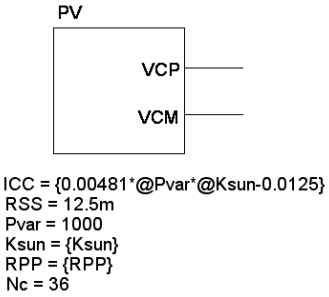

Fig. 8. Symbol representation of series connection of *Nc* cells

The parameterized library PV model of series connection of N_C cells is developed in accordance to the input language of the *PSpice* simulator [10] in the form:

```
.subckt PV VCP VCM PARAMS: Rss={Rss}, Rpp={Rpp},
+ Nc={Nc}, Pvar={Pvar} Ksun={Ksun}
I1 VCM 2 DC {0.00481*Pvar*Ksun-0.0125}
D2 3 VCP Dbreak
D1 2 VCM diode
Rp1 VCM 2 {Rpp}
Rs1 1 2 {Rss}
E1 1 VCM VALUE {V(3, VCM)/Nc}
G1 VCM 3 VALUE { V(2, 1)/Rss}
.model diode D (Is=100pA, Rs=3m, Ikf=.3227, N=1, Xti=0,
+ Eg=1.11, Cjo=302.5p, M=.7206, Vj=.50, Fc=.5, Isr=1.2u,
+ Nr=1.426)
.ends PV
```

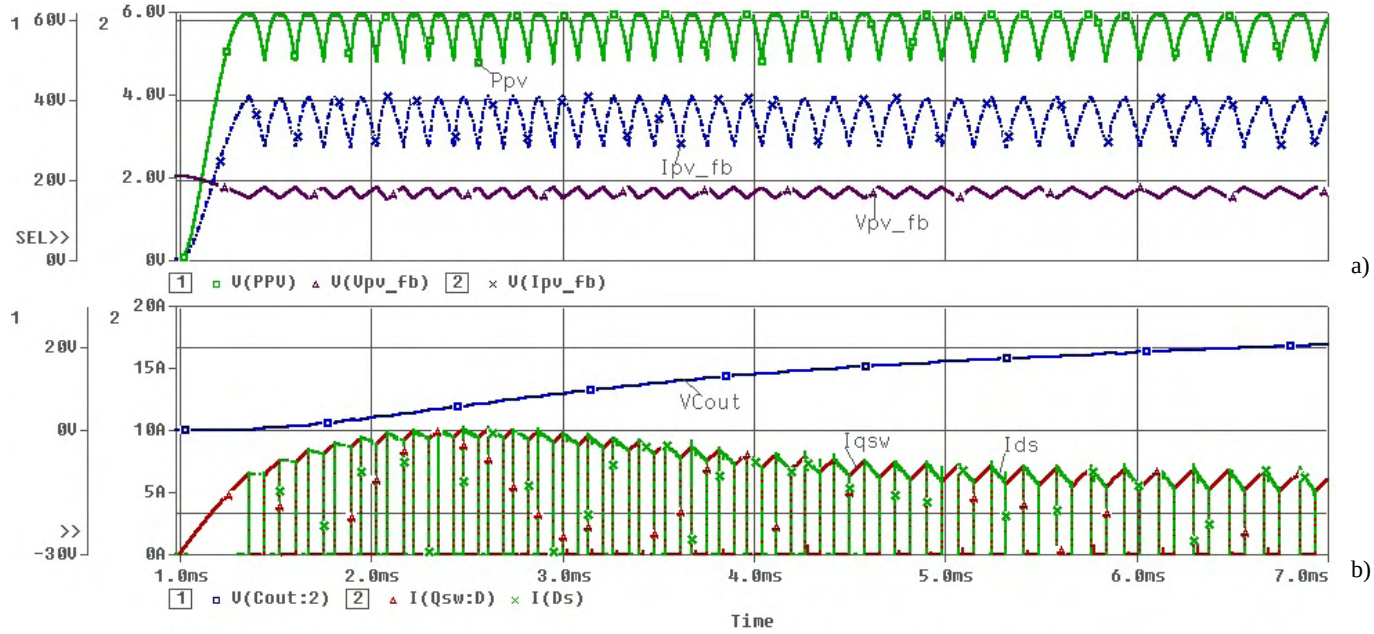

Fig. 9. Simulation in the time domain of the system

IV. Simulation in the Time Domain of the System

The waveforms presented in Fig. 9a show that the quantities Ppv, Vpv_fb and Ipv_fb have constant average value with pulsations defined by the MPPT hysteresis. The results for the currents Iqsw and Ids, as well as for the voltage VCout are shown in Fig. 9b. As the voltage on Cout during the transients increases from 0 to the nominal value, the values of the currents Iqsw and Ids in this interval are greater than the nominal ones.

V. Conclusion

A PV – Boost Converter System Working at hysteresis MPPT mode of operation has been proposed. The system optimizes the mode of operation of the Boost converter in order to achieve maximum transmitted power from the photovoltaic element. A computer model of the system is constructed and simulated. Behavioral parameterized *PSpice* macromodels are created for the single photovoltaic element and for series connection of single cells in schematic view, as well as using subcircuit definition in the form of *PSpice* model. The computer models are realized in the *Cadence Capture* and *Cadence PSpice* environment.

Acknowledgement

The investigations are supported by the project D002-126/15.12.2008.

References

[1] A. Yafaoui, B. Wu and R. Cheung, “Implementation of Maximum Power Point Tracking Algorithm for Residential Photovoltaic Systems”, 2nd Canadian Solar Buildings Conference Calgary, June 10 – 14, 2007.

[2] C. Liu, B. Wu and R. Cheung, “Advanced Algorithm for MPPT Control of Photovoltaic Systems”, Canadian Solar Buildings Conference Montreal, August 20-24, 2004.

[3] Yen-Jung Mark Tung, Aiguo Patrick Hu, Nirmal-Kumar Nair, “Evaluation of Micro Controller Based Maximum Power Point Tracking Methods Using dSPACE Platform”, Australian University Power Engineering Conference, 2006.

[4] T. Ersam, J. Kimball, P. Krein, P. Chapman and P. Midya, “Dynamic Maximum Power Point Tracking of Photovoltaic Arrays Using Ripple Correlation Control”, IEEE Transactions on Power Electronics, Vol. 21, No. 5, pp.1282-1291, Sept. 2006.

[5] Y. H. Lim and D.C. Hamill, “Simple Maximum Power Point Tracker for Photovoltaic Arrays” Electronics Letters, vol. 36, No. 11, pp. 997–999, 25th May 2000.

[6] Yan Hong Lim and D.C. Hamill, “Synthesis, Simulation and Experimental Verification of a Maximum Power Point Tracker from Nonlinear Dynamics”, 32nd Annual IEEE Power Electronics Specialists Conference, pp. 199-204, 2001.

[7] M. Savenkov and R. Gobey, “A Simple Maximum Power Point Tracker Utilizing the Ripple Correlation Control Technique”, ISES-AP - 3rd Intern. Solar Energy Society Conf. – Asia Pacific Region, Incorporating the 46th ANZSES Conference, 2008.

[8] A. Aziz, K. Kassmi, F. Olivié, A. Martinez, “Symbolization of the Electric Diagram of the Marketed Solar Panels in the OrCAD- PSpice Environment”, M. J. CONDENSED MATER, Vol. 7, No. 1, January 2006.

[9] L. Castaner and S. Silvestre, “*Modelling Photovoltaic Systems using PSpice*”, John Wiley & Sons Ltd, 2002.

[10] *PSpice User’s Guide*, Cadence PCB Syst. Division, USA, 200

Influence of the Snubbers over the Work of a Transistor Resonant DC/DC Converter

Nikolay D. Bankov[1]

Abstract **- The work of a transistor resonant DC/DC converter is analyzed using the phase plane method, taking into consideration the influence of the snubbers, which are connected in parallel to the transistors. The author has obtained the equation of the frontier line after which are not observed the conditions for switching the transistors by zero voltage (ZVS). The frontier of the natural commutation is drawn in the plane of the output characteristics of the converter.**

Keywords **- transistor resonant DC/DC converter, snubbers**

I. INTRODUCTION

Theoretical analysis of a transistor resonant DC/DC converter, operating at frequencies, higher than its resonant frequency, is performed in a number of publications [1÷5]. Usually the influence of the protective capacitors (snubbers), connected in parallel, is neglected. The analyses describe accurately the operation of the converter but they do not allow clearing out an important fact: the increase in the load resistance leads to breakage in the conditions for natural switching the transistors on at zero voltage (ZVS) as well as to stopping the converter. The bigger the capacity of the snubbers, the earlier this failure of the commutation is observed.

The present paper clears out this phenomenon. A transistor resonant DC/DC converter is analyzed using the phase plane method, taking into consideration the influence of the snubbers.

II. ANALYSIS OF THE CONVERTER

Fig.1 presents the principal electric circuit diagram of the converter under consideration. It is assumed that all circuit elements are ideal, and the pulsations of the input and output voltages are neglected. The matching transformer Tr is also an ideal one and it has a coefficient of transformation **k**.

The following quantities in relative units are introduced:

$x = U'_C = u_C / U_d$ - voltage of the capacitor C;

$U'_0 = kU_0 / U_d$ - output voltage;

$I'_0 = \dfrac{I_0 / k}{U_d / Z_0}$ - output current;

$U'_{Cm} = U_{Cm} / U_d$ - maximum voltage of the capacitor C;

$\nu = \omega / \omega_0$ - distortion of the resonant circle

where ω is the operating frequency, and $\omega_0 = 1/\sqrt{LC}$ and $Z_0 = \sqrt{L/C}$ - are the resonant frequency and the characteristic impedance of the oscillating circuit.

All snubbers $C_1 \div C_4$ are theoretically equivalent to just one condenser with capacity C_1 (drawn by dotted line in fig. 1), connected in parallel to the input of the converter. This can be physically realized, since the semiconductor switches do not have a command for opening. They close by force but open naturally at zero voltage (ZVS).

The operation of the converter under an established mode per cycle can be divided into six consecutive stages, whose equivalent diagrams are shown in fig. 2.

The commutations of the output voltage are not instantaneous, due to the availability of the capacitor C_1. During these commutations the transistors are closed and the current in the oscillating circuit closes through the capacitor C_1 (stages 2 and 5). Then the capacitors C and C_1 are connected in series and the sinusoidal quantities have angle frequency $\omega'_0 = 1/\sqrt{LC_E}$, where $C_E = CC_1/(C + C_1)$.

It is known [3, 4] that in a phase plane only sinusoidal quantities with the same angle frequency can be presented. In order to carry out an analysis of the transistor converter, two phase planes must be used – the first one to show the operation of the converter during the intervals between the commutations of the inverter output voltage (stages 1, 3, 4 and 6), and the second one to show the operation of the converter during these commutations (stages 2 и 5).

However, the investigation of one of these commutations (stage 2) shows that it is possible to use just one phase plane to illustrate the whole period of the converter operation.

The following notations are made:

$$a = C_1 / C\,; \qquad k = \sqrt{(a+1)/a} \tag{1}$$

By the index **(B)** all quantities at the beginning of the commutation are denoted ($p.M_{(B)}$), while the same quantities at the end of the commutation are denoted by the index **E.**

The voltages of the capacitors C_S and C can be expressed by:

$$U_{Cs_{(E)}} = U_{Cs_{(B)}} + 2U_d \tag{2}$$

$$U_{C(_E)} = U_{C_{(B)}} + 2aU_d \tag{3}$$

[1] Nikolay Dimitrov Bankov is with the University of Food Technologies, 26 Maritza Blvd., 4002 Plovdiv, Bulgaria, E-mail: nikolay_bankov@yahoo.com

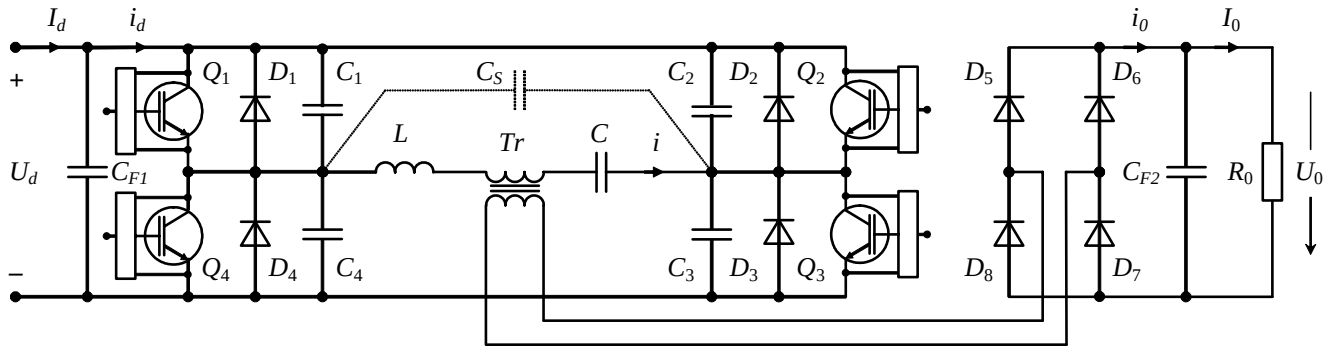

Fig.1. Circuit of the transistor DC/DC converter

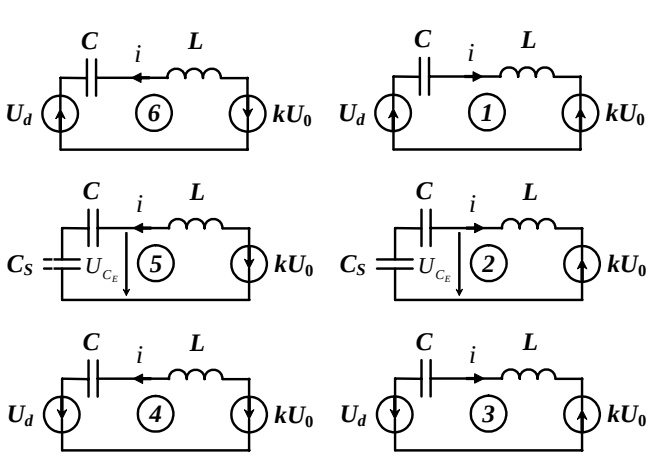

Fig.2. Equivalent circuits

The following equation is valid for stage 2:

$$\left(U_{C_E(B)}+U_0\right)^2+\left(i_{(B)}\sqrt{L/C_E}\right)^2=\left(U_{C_E(E)}+U_0\right)^2+ \\ +\left(i_{(E)}\sqrt{L/C_E}\right)^2 \tag{4}$$

From (2), (3) and (4) it is obtained:

$$\left(U_{C(B)}+U_0\right)^2+\left(i_{(B)}\sqrt{L/C}\right)^2=\left(U_{C(E)}+U_0\right)^2+ \\ +\left(i_{(E)}\sqrt{L/C}\right)^2 \tag{5}$$

or in relative units:

$$\left(U'_{C(B)}+U'_0\right)^2+I'^2_{(B)}=\left(U'_{C(E)}+U'_0\right)^2+I'^2_{(E)} \tag{6}$$

Equation (6) shows that in the phase plane $\left(x=U'_C;y=I'\right)$ the points, corresponding to the beginning ($p.M_{(B)}$) and the end ($p.M_{(E)}$) of the commutation, belong to the same arc from a circle with its center in point $\left(-U'_0;0\right)$.

It is important to note that only the ending points matter on this arc. Its central angle does not matter, as during the commutation the electric quantities change with angle frequency $\omega'_0=1/\sqrt{LC_E}$, not with $\omega_0=1/\sqrt{LC}$.

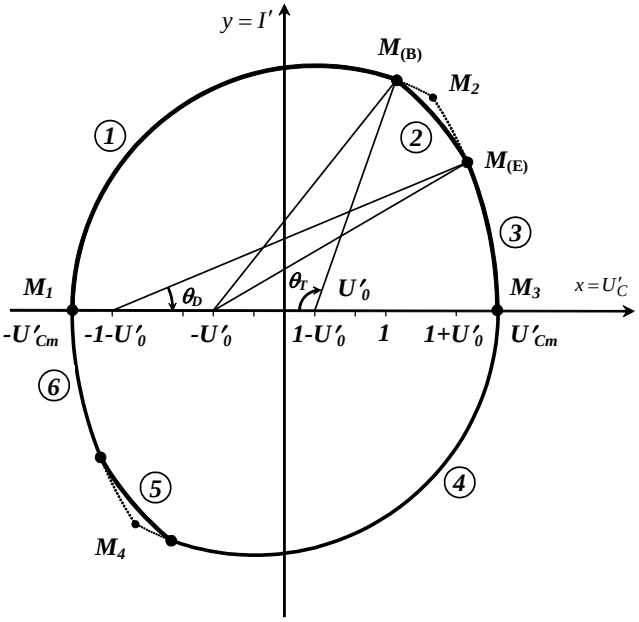

Fig.3. Trajectory of the depicting point in the phase plane

The trajectory of the depicting point in the phase plane $\left(x=U'_C;y=I'\right)$ is shown in fig.3, considering the influence of the protective capacitors on the performance of the converter. The following correlations are valid for it:

$$\left(U'_{C(B)}-1+U'_0\right)^2+I'^2_{(B)}=\left(-U'_{Cm}-1+U'_0\right)^2 \tag{7}$$

$$\left(U'_{C(E)}+1+U'_0\right)^2+I'^2_{(E)}=\left(U'_{Cm}+1+U'_0\right)^2 \tag{8}$$

Equation (3) is presented in relative units as it follows:

$$U'_{C(E)}=U'_{C(B)}+2a \tag{9}$$

From (6) and (9) it is obtained:

$$I'^2_{(E)}=I'^2_{(B)}-4a\left(U'_{C(B)}+a+U'_0\right) \tag{10}$$

The expressions (9) and (10) for $U'_{C(E)}$ are substituted in (8), then (8) is subtracted from (7) and it is obtained:

$$U'_{C(B)}=U'_0\cdot U'_{Cm}-a \tag{11}$$

$$U'_{C(E)} = U'_0 \cdot U'_{Cm} + a \qquad (12)$$

These two results are in conformity with the fact that when the protective capacitors are decreased, i.e., a→0, then p. $M_{(B)}$ and p. $M_{(E)}$ tend to p. M_2, and $U'_{C(B)}$ and $U'_{C(E)}$ tend to $U'_0 U'_{Cm}$ [3, 4].

According to fig.3 it follows:

$$U'_{Cm} = \frac{a + (1 - U'_0) \cdot (1 - \cos\theta_T)}{U'_0 + \cos\theta_T} \qquad (13)$$

$$I'_{(B)} = (U'_{Cm} + 1 - U'_0)\sin\theta_T \qquad (14)$$

$$\theta_C = \frac{1}{k}\left(arctg \frac{kI'_{(B)}}{U'_{C(B)} + U'_0 - 1} - arctg \frac{kI'_{(E)}}{U'_{C(E)} + U'_0 + 1} \right) \qquad (15)$$

$$\theta_D = arctg \frac{I'_{(E)}}{U'_{C(E)} + U'_0 + 1} \qquad (16)$$

Where θ_C is the angle of commutation, θ_T and θ_D are correspondingly the angles of conductivity of the transistors and reverse diodes in the inverter.

The average current value through the load is:

$$I'_0 = 2\nu U'_{Cm} / \pi \qquad (17)$$

where

$$\nu = \frac{\pi}{\theta_T + \theta_D + \theta_C} \qquad (18)$$

Switching the transistors Q2 and Q4 on at zero voltage is ensured if after switching Q1 and Q3 off, the protective capacitors C_2 and C_4 manage to discharge completely (the equivalent C_1 manages to recharge from $-U_d$ to $+U_d$) before the current in the oscillating circuit becomes zero. It means that p. $M_{(E)}$ (fig. 3) has to be located always above the abscissa or, in the border case, on it. From (12) the condition for natural commutation of the transistors can be written:

$$U'_{Cm} \geq U'_{C(E)} = U'_0 \cdot U'_{Cm} + a \qquad (19)$$

or $$U'_{Cm} \geq a/(1 - U'_0).$$

By substituting (19) in (17) it is obtained:

$$I'_0 \geq 2\nu a / \pi(1 - U'_0) \qquad (20)$$

Equation (20) allows for drawing the border line, after which the conditions for switching the transistors on at zero voltage are broken and the converter stops. The border of the natural commutation can be drawn in the plane of the output characteristics of the converter $I'_0 = f(U'_0, \nu)$. The equation of the output characteristics is known from [3, 4]:

$$\left(U'_0 \sin\frac{\pi}{2\nu}\right)^2 + \left[\left(\frac{\pi}{2\nu} \cdot I'_0 + 1\right)\cos\frac{\pi}{2\nu}\right]^2 = 1 \qquad (21)$$

A family of output characteristics of the converter is shown in fig.4, together with two border lines – at a=0,1 and a=0,02. It can be seen that the bigger the capacity of the snubbers, the bigger the limitations in the output characteristics. It causes difficulties in the operation of the converter with high-ohm loads (close to the real idle running mode). The increase in the snubbers, however, leads to a decrease in the commutation losses in the transistors as well as to limiting the electromagnetic interferences of the converter.

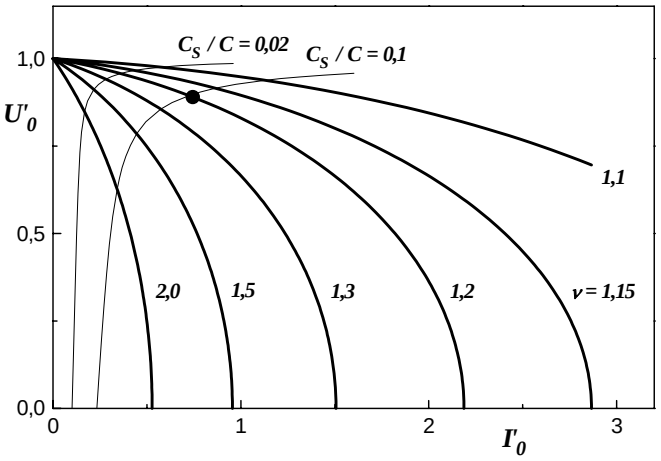

Fig.4. Output characteristics of the converter

III. SIMULATION RESULTS

Following a methodology, known from [1] and [3], a transistor resonant DC/DC converter has been designed, working at frequencies, higher than its resonant one at these input data: P = 3 kW; f = 100 kHz; U_d =300 V. For the nominal mode of work it has been chosen that ν = 1,15. The values of the elements in the resonant circuit are as it follows: C =46,157 nF, L =72,577 μH. In order to prove the obtained theoretical results the coefficients a=0,1 and k=1, have been chosen, which corresponds to the values $C_1 \div C_4$=4,6157 nF.

The model of computer simulation by means of the software package OrCAD PSpice is shown in fig. 5. Individual schemes for controlling the transistors $Q_1 \div Q_4$ have been introduced. These schemes supply controlling voltage to the gate of the corresponding transistor if at the input of the individual scheme there is a controlling signal and the voltage drain-source of the transistor is practically equal to zero (ZVS).

Computer simulation at ν=1,2 and load resistance R_T=41 Ω has been realized. Fig.6 illustrates the voltage on the transistor Q_4 – V(Q_4:d, Q_4:s), its controlling voltage - V(Q_4:g, Q_4:s), as well as the current in the resonant circuit - $I(L)$.

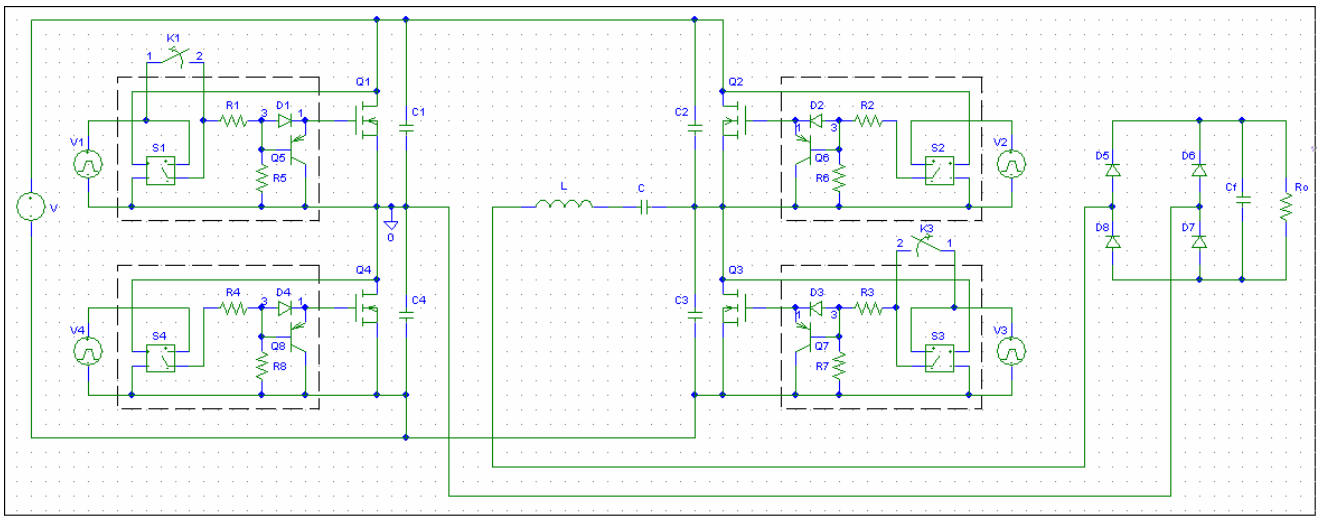

Fig. 5. Computer model of the DC/DC converter

It can be seen that the protective capacitor C_4, connected in parallel to Q_4 does not manage to discharge from $+U_d$ to 0 before the current in the oscillating circuit becomes zero. Then the individual controlling scheme does not supply controlling voltage to the gate of Q_4 and the converter stops working. Fig. 6 shows the failure of commutation which corresponds to the crossing point of the output characteristic at ν=1,2 and the border line at a=0,1 (fig.4).

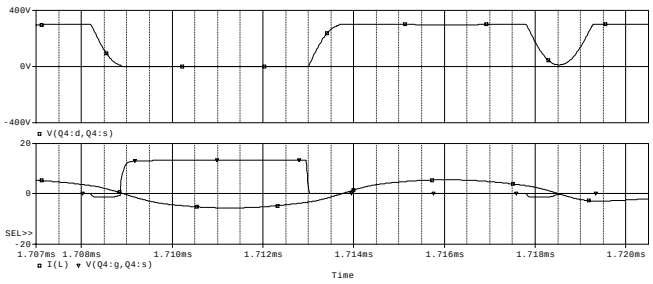

Fig. 6. Result from the simulation of the converter

IV. Conclusions

Analysis of a transistor resonant DC/DC converter working at frequencies, higher than its resonant one, has been carried out by the method of the phase plane. During the analysis the influence of the protective capacitors (snubbers), connected in parallel to the transistors, has been taken into consideration. Equation of the border line after which the conditions for switching the transistors on at zero voltage (ZVS) are broken, has been obtained. The border line of the natural commutation has been drawn in the plane of the output characteristics of the converter. The obtained results can be used in designing wide range of power supply sources for the needs of the electrical power technologies.

References

[1]. Al Haddad, K., Y.Cheron, H.Foch, V.Rajagopalan, “Static and dynamic analysis of a series resonant converter operating above its resonant frequency”, SATECH'86 Proceedings, Boston, 1986, pp.55-68.

[2]. Bankov, N.D., S.E. Tabakov, C.V. Gavrovski. - Analysis of a transistor series-resonant inverter operating at frequencies higher than the resonance. Proceedings, Faculty of Electrical Engineering, Skopje, Vol.21, No.1-2, December 2001, pp. 37-43.

[3]. Cheron, Y. La commutation douce dans la conversion statique de l'energie electrique. Technique et Documentation - Lavoisier, 1989.

[4]. Cheron, Y., H.Foch, J.Salesses. Study of resonant converter using power transistors in a 25-kW X-Rays tube power supply. - IEEE Power Electronics Specialists Conference, ESA Proceedings, 1985, pp. 295-306.

[5]. Valtchev, St.S., J.B. Klaassens. Efficient resonant power conversion. - IEEE Transactions on Industrial Electronics, vol.37, №6, December 1990, pp. 490-495.

Study of System Power Supply Source – the Galvanic Bath with Pulse Plating Deposition of Nickel Coating

Mincho Peev

Abstract: - **This article presents common work of MOSFET key converter from constant voltage into pulse voltage, and galvanic bath for the deposition of metal layers by regime of pulsed electrolysis. Parameters of substitute electric circuit of the galvanic bath are defined with a specific composition of electrolyte and wide range of cathode current density. Experimental simulation studies were performed in the program environment MicroSim DisignLab for polarization of the cathode and anode. For different frequencies is determined impulse and pause durations, for which pulse current of the supply source corresponds to the Faraday current. The experimental studies that are made by real system power supply source - galvanic bath confirmed he results from simulation. The determined parameters of power supply source ensure high efficiency of the process of electroplating. The presented analysis and results can be used in laboratory and industrial conditions to determine the working parameters of the power supply source on the application of pulsed electrolysis.**

Keywords – **Pulse electrodeposition, Pulse plating source**

I. INTRODUCTION

The study of pulse electrolysis, as a method for increasing the technological parameters of the coatings obtained in DC electrolysis is presented in some publications from about 20-30 years [1,2]. The development of electronics and improvement of management systems is a prerequisite for development and improvement of supply sources and for new surveys of pulse electroplating technology [3-5]. Galvanic deposition of metal coatings in pulse mode allows improving operational capacities of the coating: better adhesion to the substrate, less internal mechanical tensions, less porosity, higher hardness and straight resistance, better electrical conductivity; and also magnetic properties [4].

In known literature sources, however, is not represented the relationship between process efficiency with change of electrode potential, which change of electrode potential, which substantially affect the electrochemical processes of the cathode.

The purpose of this work is to present researches, allowing optimization of the electrodeposition regime by regulating the pulse current value, frequency and duty cycle of pulses for the most widely used rectangular pulse. Based on theoretical analysis, simulations and experimental studies using of developed specialized programmable source, [5] it is represented the relationship between the cathode potential and current pulse value at different frequencies.

Mincho Peev is with the Technical University of Sofia, Branch Sliven, 59 Burgasko shose Blvd., 8800 Sliven, Bulgaria, E-mail: mfpeev@abv.bg.

II. BASIC CHARACTERISTICS OF PULSE ELECTROLYSIS

Electrodeposition of metal coatings by the application of rectangular pulses (Fig.1) allows simultaneous the control of three typical parameters of pulse electrolysis: pulse current density (j_p), pulse duration (t_{ON}) and pause duration (t_{OFF}). The application of high pulse current density determines the high cathode polarization [1, 2]. The ultra high cathode potential influences the speed of electrochemical reactions.

The useful range for regulation of parameters (j_p, t_{ON}, t_{OFF}) is determined by the theoretical aspects of pulse electrolysis [1,2]. Great pulse duration (t_{ON}) and pause duration (t_{OFF}) creates conditions similar to DC regime of electrodeposition.

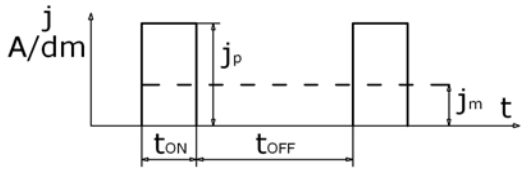

Fig.1. Pulse regime

Very little pause and pulse durations are limited by the capacity of the double electric layer [1]. Double electric layer arises at the border electrode – electrolyte. It has a large capacity and specifies active - capacitive nature of the electrode – electrolyte system (and generally of the galvanic bath). For this reason, in pulse regime, the current in the external electrical chain (i_{REC}) for time of charging double electric layer differs from the current for electrodeposition (i_F-Faraday current). In Fig.2a is presented time-chart at the electrical output of the power source for rectangular pulse. If pulse duration is longer from the time of charging double

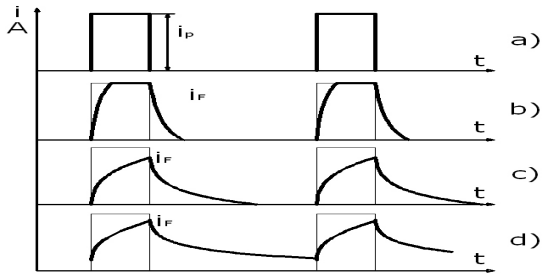

Fig.2 .Damping of Faraday current

electric layer, than Faraday pulse current reaches the source current value (fig.2b). Accordingly, the polarization of the cathode reaches a high value. If pulse duration is shorter

towards the charging time of the double layer, than electrodeposition current value (i_F) is below the current value of the power source (fig.2c and fig.2d).

III. Replacement Scheme of the Galvanic Bath. Determination of Parameters.

The replacement scheme of the galvanic bath is made in order to study its joint work with power supply source of pulses during nickel electro deposition developed in [5].

A. Mathematical Model

During the electrodeposition of metals most limiting stage is the discharge of metal ions on the surface of the cathode The creation of a mathematical model of the galvanic bath for electrochemical processes with delayed stage of ion's discharge is possible by the following assumptions [2]: It is assumed that the cathode process involves two parallel electrochemical reactions with the following substances - metal that deposits on the cathode and hydrogen. Dependencies between the partial current density and electrode overvoltage is expressed by the emergence of electrode polarization, the separation of oxygen to the anode is ignored; the electrolyte is homogeneous; the surface of the electrodes is plane; the migratory movement of ions at cathode electrolyte layer is ignored.

Under these conditions, the dynamic processes in galvanic bath are described by the following nonlinear differential equations system [2]:

$$j_k(t) = \frac{i}{S_k} = j_{мк}(t) + j_H(t) + j_{ck}(t) \quad (1)$$

$$j_a(t) = \frac{i}{S_a} = j_{ма}(t) + j_{ca}(t) \quad (2)$$

$$j_{мк}(t) = j_{мк}^0 \left\{ \exp\left[-\alpha_м \frac{z \cdot F}{R \cdot T}\left(E_k - E_{рм}\right)\right] - \exp\left[(1-\alpha_м)\frac{z \cdot F}{R \cdot T}\left(E_k - E_{рм}\right)\right]\right\} \quad (3)$$

$$j_{ма}(t) = j_{ма}^0 \left\{ \exp\left[\beta \frac{z \cdot F}{R \cdot T}\left(E_a - E_{рм}\right)\right] - \exp\left[-(1-\beta)\frac{z \cdot F}{R \cdot T}\left(E_a - E_{рм}\right)\right]\right\} \quad (4)$$

$$E_k - E_{pH} = \begin{cases} R_n \cdot j_H(t) \to npu \left| E_k - E_{pH} \right| \le \dfrac{RT}{F} \\ a + b \cdot \lg j_H(t) \to npu \left| E_k - E_{pH} \right| > \dfrac{RT}{F} \end{cases} \quad (5)$$

$$u(t) = E_a(t) - E_k(t) + \frac{d}{\gamma \cdot \sqrt{S_k \cdot S_a}} i(t) \quad (6)$$

Where: E_k is the cathode electrode potential, V; - E_a - electrode potential of the anode, V; - $E_{рм}$ - equilibrium potential of reaction of the discharge and ionization of the metal ions, V; - E_{pH} - equilibrium potential of the reaction of discharge of hydrogen ions, V; - J_k - the current value of cathode current density, A.dm^{-2}; - J_a - current value of anode current density, A.dm^{-2}; - $J_{мк}$ - partial current density of discharge of metal ions on the cathode, A.dm^{-2}; - J_H - partial current density of discharge of hydrogen ions on the cathode, A.dm^{-2}; - $J_{ма}$ - partial current density of ionization of metal ions on the anode A.dm^{-2}; - $j_{мк}^{\ 0}$ - density of the current exchange of the cathode, A.dm^{-2}; -$j_{ма}^{\ 0}$- density of the current exchange of the anode A.dm^{-2}; - J_{ck} - capacitive current density of cathode A.dm^{-2}; - J_{ca} - density capacitive current rating, A.dm^{-2}; - a, b - constants determined experimentally; - $\alpha_м$ - activity of metal ions on the cathode; - β - activity of metal ions on the anode; - F - Faraday number, F = 96486,7 C.mol^{-1};- R - gas constant, R = 8,31434 J.K^{-1}.mol^{-1}; - T - absolute temperature, K; - z - valence (charge of ions); - γ - specific conductivity of the electrolyte, Ω^{-1}.m^{-1}; - d - distance between electrodes, m; - $S_к$, S_a – surface of cathode and anode.

Under System of equations corresponds to electrical replacing scheme of the galvanic bath shown in Figure 3.

In the replacing scheme $R_{electrolyt}$ is the resistance of the electrolyte in the space between anode and cathode. R_a is the resistance of the anode surface during the transmission of

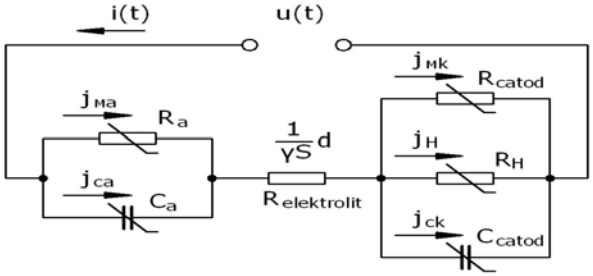

Fig.3 Electrical replacing scheme of the galvanic bath

electrical charges between the anode and electrolyte. R_{cathod} is the resistance on the cathode surface during transmission of electrical charges (electrons) from the cathode to the metal ions of the electrolyte. C_a and C_{cathod} are the capacities of electric double layer on the anode and cathode surfaces. The elements of the replacement scheme have nonlinear character as their values depend greatly on current density.

B. Determination of Parameters

The parameter's determination of the replacing scheme was made for galvanic deposition of nickel coating trough following electrolyte deposition: $NiSO_4.7H_2O$ – 145 g/l; $Na_2SO_4.10H_2O$ – 45 g/l; H_3BO_3 – 25 g/l; NaCl – 7 g/l. During the process the maintaining temperature of electrolyte is T=25 ^oC (298 K); pH = 5,5. Recommended current density in a constant current mode j_{DC} = (0,8 to 2,0) A.dm^{-2} [2]. In a pulse mode the average current density j_m (Figure 1) must correspond to the current density in a constant current mode. The average current density is determined by the expression:

$$j_m = j_p \frac{t_{ON}}{t_{ON} + t_{OFF}} \qquad (7)$$

The constants in the equations for the used electrolyte composition have the following values [1]: $j^0_{мк} = 3{,}1.10^{-5}, A.dm^{-2}$; $j^0_{ма} = 7{,}94.10^{-6}, A.dm^{-2}$; $\alpha_м$=0,3; β=0,4; $E_{рм}$=-0,25,V; $E_{рН}$=-0,226,V; $C^*_{Ni} = 80.10^6, F.dm^{-2}$; $\gamma_{ел} = 12.7, \Omega^{-1}.m^{-1}$; S_a=2S_k.

Determination of the values of the elements of the replacing scheme was made by the following sequence:

- Elaboration of polarization curves $E_k = f(j_{мк})$ $E_a = f(j_{ма})$ (Fig.4 and Fig.5).

The elaboration is done with calculations by equations (3) and (4).

- Determination of the cathode's area value for the performed experiment;
- Determination the duty cycle of pulses value

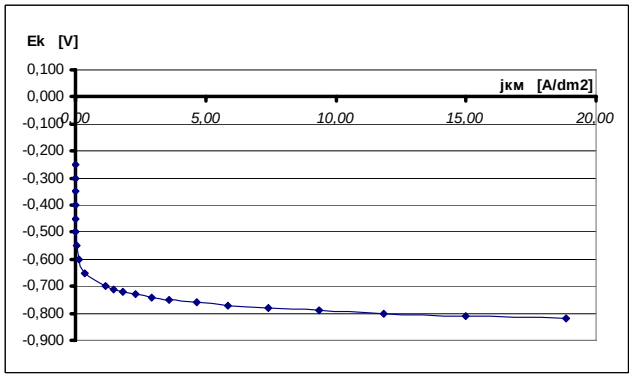

Fig.4 Polarization curve of nickel cathode

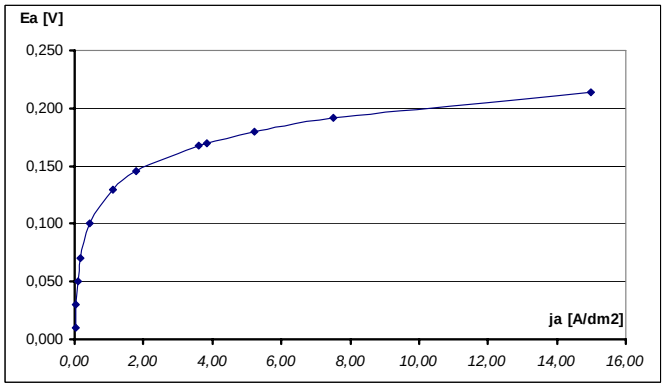

Fig.5 Polarization curve of nickel anode

$$k_з = \frac{t_{ON}}{t_{ON} + t_{OFF}}$$

and calculation of the pulse current density value $j_p = \frac{j_m}{k_з}$

- Determination the value of pulse current of the external circuit (the current of power source)

$i_{REC} = j_p \cdot S_к$

- Determination of the pulse current density of cathode $j_{мк} = \frac{i_{REC}}{S_k}$ and of anode $j_{ма} = \frac{i_{REC}}{S_a}$

- Determination of polarization of the cathode E_k and anode E_a from polarization curve by received values of $j_{мк}$ and $j_{ма}$;

- Calculation of the replacing scheme elements by dependencies:

$$R_{catod} = \frac{E_k - E_{рм}}{j_k.S_k}, \Omega \qquad (8)$$

$$R_a = \frac{E_a - E_{рм}}{j_a.S_a}, \Omega \qquad (9)$$

$$C_{catod} = S_k \cdot C_{Ni}, \mu F \qquad (10)$$

$$C_a = S_a \cdot C_{Ni}, \mu F \qquad (11)$$

$$R_{electrolit} = \frac{d}{\gamma_{ел} \cdot \sqrt{S_k \cdot S_a}}, \Omega \qquad (12)$$

In order to carry out the simulation study during producing nickel coating with cathode surface S_k = 0,1 dm^2, duty cycle pulse k_z = 0,1 and average current density j_m = 1 $A.dm^{-2}$ are obtained the following values for the elements of the replacing scheme: R_{cathod} = 0.543 Ω, C_{cathod} = 800 μF, R_a = 0.428 Ω, C_a = 1600 μF, $R_{electrolyt}$ = 5,57 Ω.

IV. Simulation Studies

Current state of the theory of galvanic deposition of metals by pulsed currents is not yet possible to give a definite answer to the question of rational choice of form and parameters of the polarizing pulses [2]. Therefore, for each metal deposition processes in the laboratory have tried many variations of the current forms and regimes of work. Mathematical modeling has significant opportunities and advantages over laboratory tests.

In the programming environment PSpice is created a simulation model of the system MOSFET key converter pulses - galvanic bath (Fig. 6).

The galvanic bath's replacement scheme is represented with ignoring of hydrogen separation at the cathode (cathode current utilization in nickel electrodeposition is about 97%). The equilibrium potential of the electrodes (anode and cathode) is represented by constant voltage souses E_{pNi_a} and E_{pNi_c}. R_{cathod} is the resistance on the cathode surface during transmission of electrical charges from the cathode to the metal ions of the electrolyte. R_a is the resistance of the anode surface during the transmission of electrical charges between the anode and electrolyte. $R_{electrolyt}$ is the resistance of the electrolyte in the space between anode and cathode. C_a and C_{cathod} are the capacities of electric double layer on the anode and cathode surfaces.

The key converter is able to set the pulse and pulse reverse mode of galvanizing. Through transistors M5 and M7 it is possible to set a positive impulse. By M8 and M6 it is possible to set the reversible impulse. A study of cathode electric regimes (E_k, i_F,, i_{ck}) for frequencies from 10 Hz to 10000 Hz at average current density j_m = 1 $A.dm^{-2}$ and $k_з$ = 0,1 is done using this model. Measurement of Faraday current (i_F) is not possible in real conditions but it determines the character of the processes flowing on the cathode.

Fig.7 and fig.8 of presents the results of simulation for cathode: current of the power source; the potential of the cathode; Faraday current; current of the electric double layer. These results are received at the duty cycle $\kappa_з$=0,1 and frequencies 10 Hz and 10000 Hz.

The received results from the simulation studies for cathode potential values and current pulse value at low frequencies correspond to these, received in real conditions. For frequency

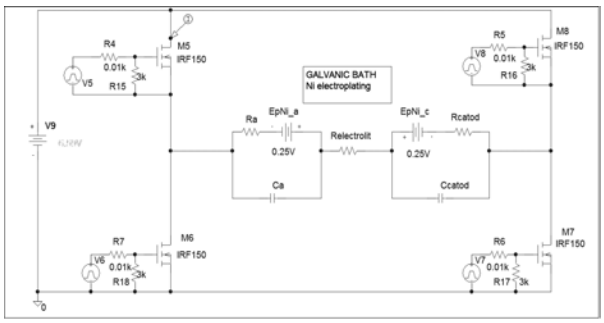

Fig.6 Replacing scheme MOSFET transistor switch - galvanic bath

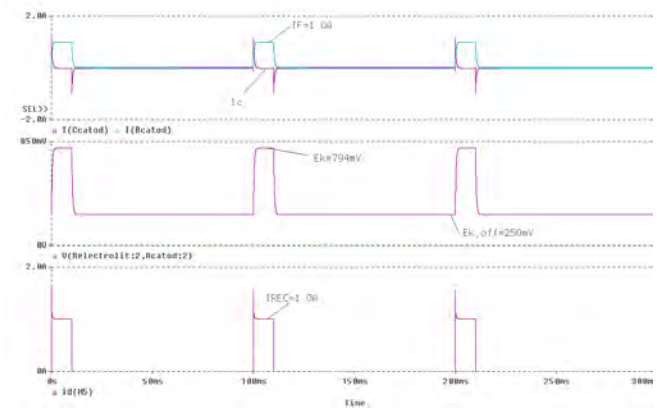

Fig.7 Pulse mode $k_з$ = 0,1; f=10 Hz

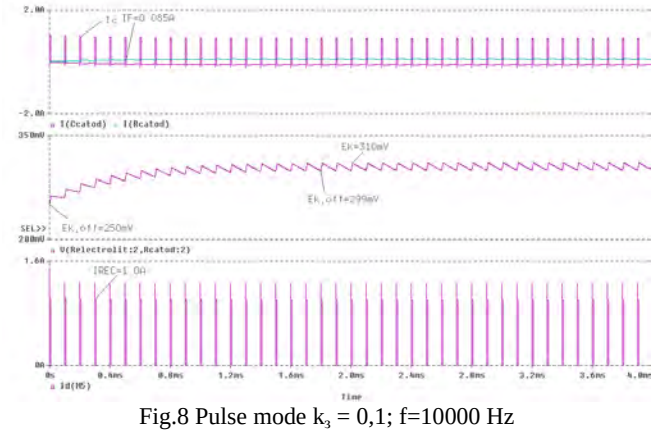

Fig.8 Pulse mode $k_з$ = 0,1; f=10000 Hz

10 Hz (fig.7) the value obtained for E_k is 0.79V (at calculated 0,79V), Faraday current also corresponds to the calculated - 1A. For frequency 100Hz cathode potential does not reach the estimated value (E_k = 0,75 V - 95% of the set one), Faraday current reached 93% (i_F = 0,93). With increasing frequency Faraday current decreases because during the pulse electric double layer was unable to be charged up to the established value and thus current from the power source is distributed between the capacitive current of the electric double layer (i_c) and Faraday current (i_F).

At frequencies above 2000 Hz Faraday current strongly decreases and the cathode potential reduces too. The resulting effect is rectification of Faraday current. This effect is greatly expressed at a frequency of 10000 Hz (fig8): current from the power source is a pulse, but Faraday current fluctuates around an average of 0.09 A. Cathode potential fluctuates around an average of 0,3 V. The regime is similar to DC electrodeposition.

V. Conclusion

A simulation model of the system MOSFET key converter from dc to pulse voltage - galvanic bath is developed in the programming environment PSpice; thus the electrical replacing scheme of the galvanic bath is reported.

The systematization of sequence for calculations to determine the electrical parameters of the galvanic bath was made. For specific parameters of galvanic coating deposition in pulse mode are defined the parameters of electrical circuit replacing scheme of the galvanic bath.

Simulation researches in PSpice for the polarization of cathode, current of the electrodeposition and current of the electric double layer on the cathode for a nickel coating under pulse mode and under range of frequency variation from 10 Hz to 10000 Hz were carried out.

The proposed survey approach can be used in laboratory and industrial conditions to determine the operating parameters of the power source for pulse electrolysis (current density, duty cycle pulse, frequency of pulses).

References

[1] J. Cl. Puippe, N. Ibl, Influence of charge and discharge of electric double layer in pulse plating, J. of Applied Electrochem. 10 (1980) 775-784

[2] Костин Н.А., В.С. Кублановский, В.А. Заблудовский, Импульсной электролиз, Киев, Науковая думка, 1989.

[3] M.S.Chandrasenar, Malathy Pushpavan, Pulse and pulse reverse plating – Conceptual, advantages and applications, Electrochemica Actaq 53 (2008), pp 3313-3322.

[4] M. Lindblom, H.M. Hertz, A. Holmberg, Pulse reverse plating for uniform nickel height in zone plates, Vac. Sci. Technology, Vol. 24, Nr.6, Nov/Dec 2006, pp 2848-2851.

[5] Анастасия Кръстева, Минчо Пеев, Йовчо Стоянов, Георги Кънов, Реверсивен програмируем източник на импулси за нанасяне на галванични покрития, Електротехника и Електроника, 2005, бр 5-6 стр. 10-16.

Session EQ:

EDUCATION QUALITY

Development of Collaborative Learning Environment Combining with Web2.0 Functionalities

Boyka Gradinarova[1]

Abstract – **Collaborative learning is a kind of group learning mode where members of group learn any concept or topic through communication and discussions. Current researches on collaborative learning paid little attention to the functionalities of group members. In order to solve this problem, this paper utilizes a Learning Blog (LBlog) to share experience and viewpoints of group members, and achieve learning goals together in the end. The LBlog also integrates Learning Management System (LMS) to manage the group members' profiles to evaluate the learners' learning efficiency. This paper considered an integrated framework which combined the personal learning blog functionalities to LMS by using the Tools Interoperability (TI) architecture in order to develop the suitable learning functionalities and interface in LMS for learners.Our initial experiments with the LBlog indicate that it is an useful educational tool to support collaborative learning..**

Keywords – **Learning Management System, Collaborative Learning, Blog, E-learning**

I. INTRODUCTION

In With the emergence of Internet technologies, web-based learning as an increasing acceptable learning approach makes interesting and possible. The concept of web-based learning totally differs from classroom-based method by online communications and powerful computer technologies. This pedagogical mode offers many possibilities, such as approaching new groups of students [3], the freedom of choosing the time to learn anywhere and the way learners prefer, and collaborative learning environment [2]. Many recent studies show that Computer-Supported Collaborative Learning (CSCL) is a promising paradigm for research in web-based education that focuses on the use of Information and Communications Technology (ICT) as a mediation tool within collaborative methods of learning [9] and provides advanced activities, necessary functionalities and learning resources to all participants to enable the collaborative learning experience in open, dynamic, large-scale and heterogeneous environments. However, one of the main challenges in the development of CSCL systems is to overcome important non-functional requirements arisen in distributed environments such as scalability, flexibility, availability, interoperability, and integration of different, heterogeneous, and legacy Collaborative Learning Systems. In order to overcome these issues, we propose an LBlog that combines with the Web2.0, weblog, and LMS technologies to improve the quality of collaborative learning and life-long learning. Our proposed LBlog is the first one to extend blog functionalities with LMS based on IMS Tools Interoperability (TI) architecture to manage learning course materials and learners' learning processes [12]. IMS organization has recently announced the Common Cartridge specification [1] in draft version. This specification mainly focuses on providing the framework in order to integrate SCORM (Sharable Content Object Reference Model) and QTI (Question and Test Interoperability) standards, and also provide Tools Interoperability architecture which aims at the LMS functionalities expanding part. All LMSs can possibly utilize the tools or functionalities based on TI architecture in order to improve the lack of functionalities for LMSs. We mainly focus on TI architecture and the Web2.0-based blog functionalities to make suitable learning interface for LMS. We hope it can improve the usability of LMS in order to fulfill the learners' needs and improve the utility rate of LMS. Our experiences indicate that collaborative learning at LBlog mechanism may give as good results as CSCL or even better.

[1]Boyka Gradinarova is with the Faculty of Computing and Automation, Technica university of Varna, 1, Studentska Str., Varna, Bulgaria, E-mail: BGradinarova@hotmail.com

II. RELATED WORK

Collaborative learning has presented a pedagogical mode around a long time. It is a student-centered approach that interacts with one or more collaborating peers to accomplish a given problem. In [4], authors explore the strengths and weaknesses of CSCL, including the viewpoints of the repositioning of the responsibility of learning in which the lecturer's role has been transferred to that of facilitator and resource guide as CSCL requires that the student take a more active role in his or her own learning [10]. [11] states vicarious learning that points out the knowledge is formed from others' experience. [13] proposes a concept of distributed constructive learning that explains knowledge comes from "doing", not "receiving." The author [2] builds a web-based collaborative learning environment via a web-based course to indicate that collaborative learning work and draws some conclusion. at web-based environment may give as good as results as classroom learning. owever, the weblog has been widely accepted in use in e-learning during the past four years, it not only provides the personal web vision, but also facilitates the command post function for learner to provide the opportunity to make a discussion with each other [5]. This rapid growth reflects attempts to circumvent the constraints of centralized authorship [6] and increase needs for instant communication on knowledge-building community [7], as it allows alternative forms of learning, such as self-reflection, student-student and student-tutor different to the conventional ways. Besides, with the concept of Web2.0, the weblog is much easy to develop a suitable personal learning interface for LMS in order to fulfill the construction of the collaborative learning environment. If we can design the blog

functionalities which can be utilized by other LMSs, it can not only reduce functionalities development time but also make the functionalities popularize in other LMSs. One issue herein is how to implement such kind of tools or functionalities. The IMS proposed the Common Cartridge draft in 2007. The Common Cartridge specification have three parts, it respectively includes IMS Tools Interoperability Guideline, IMS Common Cartridge Authorization Web Service and IMS Common Cartridge Profile. IMS Tools Interoperability Guideline specification focuses on the LMS functionalities developing architecture, runtime environment and related concept. It also resolves the reusable problems of functionalities for multiplatform LMS. Therefore, we propose a LBlog with the integration of weblog and LMS to illustrate that the LBlog has great potential to become one of the effective groupware in collaborative education.

II. IMS TOOLS INTEROPERABILITY ARCHITECTURE

Fig. 1 shows the IMS Tools Interoperability architecture. On the left-hand side is the LMS, and the right-hand side contains the related tools. We utilize the web services to serve the connection. This architecture mainly contains two parts. One is Proxy Tool and the other is Tool Interoperability Runtime (TIR).

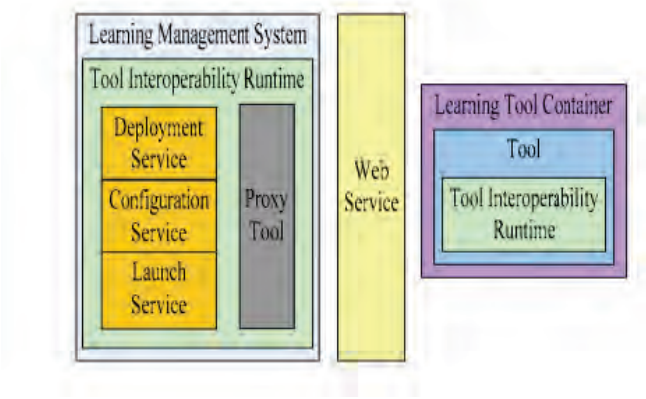

Fig. 1. Tools Interoperability Logical Architecture-revised by [1]

- Proxy Tool - LMS takes advantage of the tool to make communication with exterior Tools.
- Tool Interoperability Runtime (TIR) - TIR is a set which contains a series of services and provides a series of different services to manage Proxy Tool (Ex, deployment, configuration, initiation and so on).

In TIR part, it includes several kinds of services:

- Deployment Service: The TIR deploys the service. Tools are deployed under the LMS environment by Proxy Tool and become the part of LMS.
- Configuration Service: This service ensures the normal deployment and initial operation in the middle of LMS. Launch Service: In the Host part, this service must be able to produce related proxy tool and related security mechanism. In the end, this service can utilize the web service to receive the initial message which transmits by LMS TIR, and then understand and use this security mechanism to make the correlation response.
- Outcome Service: Outcome profile which produces by Tool will transmit to LMS TIR, but LMS TIR must be able to receive, understand this profile and make responds for Tool TIR.
- Security Management: To guarantee an elastic authentication mechanism, TIR can provide Security Management to make the security profile and utilize the proxy tool to transmit the authentication information to LMS.
- Session Management: When the user uses new Tool, LMS can provide the user a URL to open a new browser. At this time, it will use session to manage its transmission data. Therefore, TIR must provide session management to do the session control.

This framework utilizes the Service-Oriented Architecture (SOA)/web services to do the data transmission. Fig. 2 shows the related TI components and interaction relations between the user, tool and LMS. The operation steps are as follows:

Step 1: When the tool editors or the learners use the tools, LMS produces the Proxy Tool URL related to the particular Tool in order to provide user choice links. After LMS accepts the request, it will be sent to Launch Service in TIR and then to coordinate Configuration Service to produce related configuration data. This Launch message will then be sent to the Proxy Tool.

Step 2: The Security Manager in TIR will process the data which is provided by Configuration Service and Launch message in order to produce the identity authentication data and Security Header. And then the Security Header will put into the Launch message.

Step 3: The Launch Message produced by step 2 will be sent to Tool TIR by the way of Proxy Tool. This message will be received and processed by Launch Service in Tool's TIR. In this message, the Security Header will assure the identity authentication process by way of Tool's TIR. The identity authentication's result and related message processed by Launch Service will be returned to LMS.

Step 4: When finishing identity authentication, the LMS will receive the Tool feedback message, then the user will open new browser and operate the Tool directly. And at this stage, it has no interaction between LMS and Tool.

Step 5: After the user completes the particular work, Outcome Service will possibly produce some data and then send it to LMS. At this time, Tool's TIR will do the coordination between the Security Service and Outcome Service in order to produce the Outcome Profile. The Outcome Profile includes the Security Header which will be sent from Proxy Tool to LMS's Outcome Service in order to

do the process. LMS Outcome Service will return the outcome message to Tool in order to inform the processing result.

Step 6: After the user finishes the interaction with the Tool and returns to the LMS's delivery context, the LMS will close the new browser window opened by step 4 and then remove the related Proxy connected with the Tool.

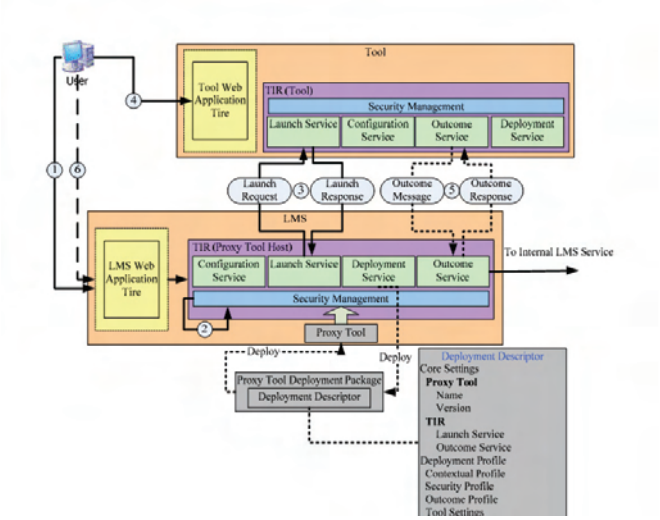

Figure 2. Tools Interoperability Interaction Diagram – revised by [1]

III. Constructing a Collaborative Learning Environment with Learning Blogs

According to the features of the weblog, it is easy to provide collaborative workspace, where the learners can exchange information in a synchronous or asynchronous manner and support primitive activities and resources in collaborative learning, such as dialogue channel, shared workspace, technologically mediated remote communication, and personal workspace [8]. In order to emphasize these characteristics, we propose an LBlog integrating with LMS to share knowledge or interaction when a learner faces a problem that he/she cannot solve, he/she can exchange meaningful information.

- First of all, in order to process the collaborative learning in the open learning workspace, it is very important to find out the suitable group members. It consists of two ways to manage the searching method.
- Searching for mentors
  - Searching for course materials: browsing members' blogs and realizing their learning statuses and interests.
  - Learning goal: utilizing members' learning goal records and course scheduling strategy to learn the similar knowledge courses.
- Building study forum: The forum is used to construct a more get-together and affinity group such that it is easy to the same learning goal.
  - Grouping members
  - Scheduling the same goal and time
  - Monitoring each other
  - Displaying status
  - Synchronizing multiple discussion
  - Delivering messages

Personal LBlog architecture encompasses two functions-traditional blog function and e-learning function. The former presents the personal operation and interface to exchange and retrieve the learning contents. The latter compliments the features of the pedagogical learning to promote the learners' interests and to motivate their self-learning potentiality. The architecture consists of three managers shown in Fig. 3.

Learning Schedule Manager: providing the functions of learners' self-scheduling courses, making the learning goals, and then saving as XML documents in the blog learning database.

Learning Process Monitor: Monitoring and recording the learners' learning status and behavior, including the beginning time, the reading ID, and time duration.

Learning Note Manager: Notating the learners' experience and thought and saving the learners' IDs and courses' IDs to database.

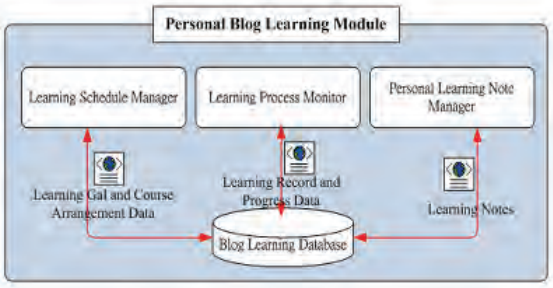

Fig. 3. Personal Learning Blog Framework

In the meanwhile, in order to manage the learners' own blogs, this system provides a Learning Object Operation Module to control the learning resources. It consists of two functions shown in Fig. 4.

- eLarning Object Navigator: Having a responsibility to view all kinds of learning objects. It parses course files, loads and shows the course architecture, retrieves the course metadata, and represents the course contents.
- Learning Object Manager:
  - Learning Object Subscribing and Collection: Assigning the name and ID of the courses which are stored in the repository.
  - Learning Object Uploading: Authoring self course contents and uploading to course repository.
  - Learning Object Deletion: Deleting learners' collecting courses names and IDs.

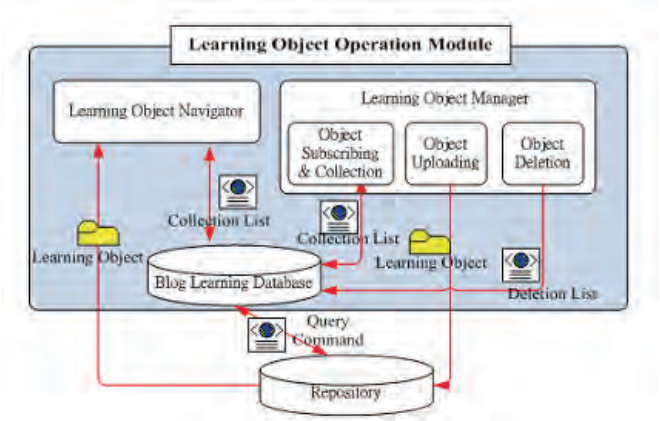

Fig. 4. Learning Object Operation Module

IV. CONCLUSION

In the case this paper showed that the LBlog has been proved to be an efficient environment that enables group members to achieve the learning goal in a collaborative learning. Besides, in the system architecture, we utilized the multiplatform tools designing architecture proposed by IMS Tools Interoperability Guideline to develop our integrated system and took advantage of the Technical University of Varna do the system design issues. This collaborative learning environment combining with proposed LMS and Web2.0 functionalities observes as a very important mechanism for motivating students' continuous communication, discussion or participation and sharing their learning experiences in the e-learning field.

REFERENCES

[1] IMS Global Learning Consortium, "IMS Tools Interoperability Guidelines Version 1.0", February 28, 2006.

[2] Yi Jia, "Building a Web-Based Collaborative Learning Environment", Proceedings of the 6th Annual International Conference on Information Technology Based Higher Education and Training, Juan Dolio, Dominican Republic, pp. F2D-7-F2D-9, July 7-9, 2005.

[3] Rune Pettersson, Gary Svensson, Yvonne Warn, "On Web Based Learning-Experiences from Teaching and Learning Online", Proceedings of the 34th Annual Conference of the International Visual Literacy Association, Breckenridge, Colorado, USA, October 1-5, 2002.

[4] Sallyanne Williams and Tim. S. Roberts, "Computer Supported Collaborative Learning: Strengths and Weaknesses", Proceedings of the International Conference on Computers in Education 2002, Auckland, New Zealand, pp. 328-331, December 3-6, 2002.

[5] Wei-Jane Lin, Hsiu-Ping Yueh, Yi-Ling Lu, Masayuki Murakami, Koh Kakusho, and Michihiko Minoh, "Blog as a tool to develop e-learning experience in an international distance course", Proceedings of the 6th International Conference on Advanced Learning Technologies (ICALT 2006), Kerkrade, the Netherlands, pp. 290-292, July 5-7, 2006.

[6] B.Gradinarova, "Importance of Web 2.0-Mediated Competence for the Educational Demends on Learners", Proceedings of the 11th IC on Computer Systems and Technologies (CompSysTech'10), pp.455-460, June 17-18, 2010

[7] M. Divitini, O. Haugalokken, and E.M. Morken, "Blog to support learning in the field: lessons learned from a fiasco", Proceedings of the Fifth IEEE International Conference on Advanced Learning Technologies (ICALT 2005), pp. 219-221, July 5-8, 2005.

[8] Toshio Okamote, Muzue Kayama, and Alexandra Cristea, "Proposal of a Collaborative Learning Standardization", Proceedings of the Fifth IEEE International Conference on Advanced Learning Technologies (ICALT 2001), pp. 267-268, August 6-8, 2001.

[9] Zhengyou Wang and Jianhua Ming, "A Web Collaborative Learning System Based on Multi-agent", Proceedings of the 3rd International Conference on Natural Computation (ICNC 2007), pp. 305-309, August 24-27, 2007.

[10] D.W. McMurray and M.E. Dunlop, "The collaborative aspects of online learning: A pilot study", Proceedings of the 6th International Literacy & Education Research Network Conference on Learning, Bayview Beach Resort, Penang, Malaysia, September 27-30, 1999.

[11] A. Bandura, Social learning theory, Englewood Cliffs, NJ:Prentice Hall, 1997.

[12] Jui-Hung Chen, Timothy K. Shih, Chun-Chia Wang, Shu-Wei Yeh, and Chen-Yu Lee, "Combine Personal Blog Functionalities with LMS using Tools Interoperability Architecture", Proceedings of 22ndInternational Conference on Advanced Information Networking and Applications (AINA 2008), pp. 146-151, March 25-28, 2008.

[13] M. Resnick, "Distributed Construction", Proceedings of the International Conference on the Learning Science, 1997.

Permanent Education of High School Teachers Through Corporate-Academic Joint Venture E-Learning

Martin Jovanović[1] , Dušan Vučković[2] and Dragan Janković[3]

Abstract – **In this paper the experiences and lessons learned from the 6 year nationwide permanent continuous teachers' education programme, performed as e-learning joint venture of Microsoft Software d.o.o. and Faculty of Electronic Engineering Niš are given. The Microsoft Partners in Learning programme and its implementation by the Faculty of Electronic Engineering have been descripted and the outcomes, lessons learned and guidelines for further similar initiatives discussed. The paper is intended to serve as a resource for any individual or institution with upcoming projects in permament education of K-12 personnel.**

Keywords – **Life long education, e-learning, Microsoft, Faculty of Electronic Engineering Niš.**

I. Introduction

Partners in Learning is a 10-year ongoing international project of Microsoft Corporation, initiated in 2003, as a five-year $250 million funded initiative. In 2008 it was renewed for another five-year span, with additional $235 million funding [1]. The PiL initiative revolves around three fundamental concepts: professional development, including training and technical support, of education staff; development of professional collaborative networks od educators; and innovation through research in the domain of education. Partners in Learning is a collaborative project, aimed at institutions that provide service in the three aforementioned areas, the Faculty of Electronic Engineering being the one since 2005 [2].

II. Project Overview

A. Recognition of need

According to the current legislation in the area of K-12 (elementary and high-school) education [3], teachers are licensed for 5-year periods. One of the conditions for renewing the license is the minimum of 100 hours of professional training (60 hours mandatory and 40 hours optional courses), as defined in the Rulebook on Permanent Professional Training and Vocations of Teachers [4]. According to this policy, the Ministry of Education's Education Advancement Center [5] serves as the accreditation body for independent permanent-education course providers. There is an ongoing contest for courses [6] and each year a catalogue of accredited courses is published [7] for educators to choose from. The catalogue encompasses both live and e-courses. One of course providers listed is Microsoft d.o.o. Belgrade with courses developed and shipped through the Partners in Learning program.

Faculty of Electronic Engineering joined the PIL initiative in the fall of 2006, initially with a live course in Visual Basic .Net. The premier course was not accredited and served as a pilot-course for testing the options for cooperation. Main payload consisted of Microsoft learning material localization. After initial success (97% positive feedback from users), the e-learning stage followed.

TABLE I
PROJECT PHASES IN SHORT

Year	Fall	Spring
2005/06	VB.Net Live	
2006/07	VB.Net eLearning	Web Design
2007/08	Net Security	Digital Video
2008/09	Net Maintainance	Social Software
2009/10	eLearning - Admin	eLearning – Instr Design
2009/11	C#	eComm and eCollab

B. E-learning Discussed

Even though a vastly used notion, the e-learning still seems to skip precise and comprehensive definition. Lexically similar to e-mail, it was coined by relatively marginal electronic learning guru Jay Cross and used in large variety of meanings, forming white noise of partial definitions. However, this flexibility seem to foster comprehensive research in the area(s) worldwide. Vaguely formulated by [8] as delivery of personalized, comprehensive, individualized, dynamic learning material in real time, supporting the development of knowledge communities and connecting learners with experts. Other than the term e-learning, various aspects of technology-aided learning introduce respective terms, such as CAI (Computer-Aided Instruction), CBT (Computer-Based Training), distance education, online learning etc. These terms predominantly refer to several historical aspects of e-learning, or its partial implementations. Driven by certain inflated expectations from purely technology-based instruction (that led to a crisis in this domain in 2002-2003), knowledge providers resorted to a less technological approach labeled *blended learning* – a loosely defined mixture of computer-based and live teaching. The approach chosen by the Faculty of Electronic Engineering fits best in this frame.

[1]Martin Jovanović, [2]Dušan Vučković and [3]Dragan Janković are with the University of Niš, Faculty of Electronic Engineering, Aleksandra Medvedeva 14, P.O. Box 73,18000 Niš, Serbia, E-mails, respectively: martin.jovanovic@elfak.ni.ac.rs, dusan.vuckovic@elfak.ni.ac.rs and dragan.jankovic@elfak.ni.ac.rs.

C. Modes of implementation

After initial, well accepted, live course on Visual Basic .Net in 2005, the online approach was chosen immediately, primarily aiming at widening the course scope. In 2006/07, same course was set up online, followed by the course on fundamentals of Web development. Courses will not be accredited by the Education Advancement Center until the following academic year.

Methodology of knowledge delivery is closest to the blending learning concept, materials being weekly published, consumed online, and participants being web-tested fixed number of days after lesson publication. Moreover, discussions have been encouraged on forums – which in turn facilitated development of community that produced moderators-volunteers, still actively participating in courses. Final exams, at the end of each course (semester) are conducted in person, in cities of Niš, Belgrade and Novi Sad. These exams are mandatory, but not sufficient for certification. Roughly up to 50% of credits are obtained throughout the course, while final exams carry additional minimum of 15% required for certification. In the course of semester, 30% of credits are gained through weekly tests, while 20% are gained via forum activities.

Starting from the first online course, constructionist element has been introduced through programming tasks. Participant were expected to build their own solutions and upload the source code, and were assessed by both course teachers and peer moderators.

The element of collaboration has been achieved both through communities around discussion forums and, especially, through peer review of not only assignment solutions but also questions and answers on forums. Motivation for forum activity has been increased by leaving certain small percentage of concepts and facts deliberately open (incomplete or somewhat ambiguous) in order to provoke cognitive dissonance in participants. This strategy proved to generate desired outcome and was used regularly in courses.

Significant interference of live teachers and traditional teaching methods is obvious in this project. One of the reasons for this conception is the very aim of the project: professional development of teaching staff as primary and uncompromised goal, to which the choice of methodology and the experimental component being fully subdued. Another reason for the live teaching component were the requirements imposed by the Education Advancement Center. In the year 2010, in the C# programming course, this condition has been met through synchronous multi-user video conference (webinar with active involvement of participants, enabled and invited to interact in the course of the lecture). This way the gap between classical, location-dependent education and distance learning has been overcome and this mode of teaching has been recognized and accepted by the Education Advancement Center. This is a significant step in State's institutions' acceptance of distance learning mechanisms and a leap forward in the introduction of more machine-sided e-learning in the State education system.

III. PROJECT PHASES

A. 2005/06

One live pilot course in Visual Basic .Net in the fall semester. Primary task – localization of official training material and probing the potential market. This course was aimed at schoolchildren and has sparked off the rest of the project. From this point on all the courses are web-based.

B. 2006/07

FALL: The material has been uploaded and web-based course was set up. This course was aimed at teachers (to train them to teach Visual Basic .Net to schoolchildren previously targeted). 378 participants, out of which 81 took and 81 passed the final exam. This course was not accredited.

SPRING: Fundamentals of Web Presentations. 828 participants, out of which 404 took and 404 passed the final exam. No accreditation. This academic year peer-reviewing of participants' activities was introduced.

C. 2007/08

FALL: Computer Networks Security. 427 participants out of which 165 took and 165 passed the final exam. Learning material has already been used in PIL project in Croatia, only localized to Serbian. Accredited to 16 hrs.

SPRING: Digital Video in Teaching. 557 participants, out of which 130 took and 130 passed the final exam. Course has been set up and led by one of the previous participants (a high school Informatics teacher) and supervised by the Faculty staff. No accreditation.

C. 2008/09

FALL: Computer Network Maintenance. 878+292 participants, out of which 320+292 took and 320+ passed the exam.[1] First number represents fall semester targeted at technical school staff. Second number represents re-run of the course in the following spring semester, targeted at gymnasium staff (held in parallel with the following course). The course is accredited to 20 hrs.

SPRING: Social Software in Teaching. 1046 participants, out of which 550 took and 445 passed the final exam. In this course moderators (volunteer participants) were engaged in the development of instructional material. Accredited to 20 hrs.

C. 2009/10

FALL: The course title was E-learning (System Administration). 1272 participants, out of which 160 took and 153 passed the final exam. Large number of applications is thought to be inertial, while vast majority was actually

[1] Exact number currently unavailable.

interested in instructional design (to which all the previous courses were dedicated) and not the administrative side. These participants were proposed to wait for the spring semester. Course was accredited to 20 hrs.

SPRING: The course title was E-learning (Instructional Design). 1541 participants, out of which 730 took and 721 passed the final exam. This was the first massive course, attended by a large number of non-technical teachers. Course was accredited to 20 hrs.

C. 2010/11

FALL: Modern Programming Concepts. 539 participants, out of which 130 took and 103 passed the final exam. Acredited to 20 hrs.

SPRING: E-communication and E-collaboration Within the K-12 Educational Teaching and School Procedures Support System. 1616 participants. The course is currently in progress and other statistics pending. It is accredited to 20 hrs.

IV. LESSONS LEARNED

The evaluation of each course was performed within final exams and results were submitted to the Education Advancement Center as a requirement. The statistics is the Center's internal document and is not publicly available. The Faculty of Electronic Engineering's own evaluation began in this academic year, primary results are pending and will be published as soon as they show statistical validity. Nonetheless, the six-year experience yielded several significant points that motivated this paper. These points are intended to serve as auxiliary guidelines to any course designer/administrator involved in the State-governed or other e-learning activities.

The main impression can be summed up as: pressure must be maintained at all times. This refers to a positive, motivating pressure; nonetheless it must contain certain portion of force. This is best achieved through two approaches: constant human presence and challenge. First of all, this project (in the way it was implemented) strongly suggests that autonomous, machine-based e-learning is still unable to produce better or equal results as human-driven instruction. For example, in the C# course one group of participants was deliberately "left alone with the machine" to establish a self-paced learning, while the other group was closely monitored. The motivation of the first group decreased significantly in the first two weeks of the course, and the number of participants that even took the final test was significantly lower. The group seemed to have been "left without custody" and the intrinsic motivation was not sufficient. The fall of motivation appears quickly upon the absence of live instructors (primarily as moderators on forums), so the presence must be kept constant. The second aspect is the challenge. Whatever time constraint being assigned to tests, majority of participants will procrastinate until the deadline. Shortening of deadlines didn't lower the results in general (deadlines were not shortened to more than 3 days after lesson publication). Other type of challenge was introduced by peer reviewing in forums. Gaining points in discussion was the primary factor for attracting and keeping participants in forums, i.e. active in the process of learning throughout the course. Another means of activation of participants was deliberate incompleteness in instructional material. This provoked desire to learn more in order to gain full picture of lessons, thus ask and respond in discussions. This experience only emphasizes the aspect of motivation in schooling, often neglected in technologically-driven approaches. Teacher equally serves as the knowledge provider and a motivator/moderator of students' behavior; and behavioral component is crucial for the success of any instruction. In that sense, no e-course can succeed without both sides of the role.

Procrastination issue led to another important observation. In courses that had no time-bind for testing, nearly all participants took the test just before the closing. This led to the server overhead and test crash in a large number of participants, which put extra overhead to moderators, since not all the tests crashed, so those that did needed be restarted manually. Multiplied by several hundreds of participants, this overhead was large and unnecessary. The solution was found in pipelined approach to testing; certain time overlapping of tests was permitted, but no tests were closed simultaneously. This was only one test was largely occupied at any given moment, and the overload was prevented.

Sloppy decrease of active participants in the first week of all courses was noticed. Through feedback, it was established that participants usually had wrong expectations from courses and that it was only when they had immediate contact with the material that they were able to decide whether or not they want to participate further. This brings about two issues. Firstly, each course need have appropriate preview/summary that gives sufficient information about the type of knowledge offered, use cases etc. Secondly, this situation can be viewed as a micro-case of State education in general. It is common that students get disappointed by the material/methodology in Universities, and a need for efficient high-school level professional orientation services is present.

Discrepancy between traditional and electronic teaching is perhaps best seen in the participants' feedback regarding the number of professional development hours accredited to courses. Most of the courses are accredited to 16 hours, while participants claim that they took them more to complete. Almost all courses last 6 weeks and, hours estimated, last longer. In traditional education, number of hours is easily measured; nonetheless, this number shows little about the actual learning process that takes place. Time measure is a blunt and obsolete instrument. However, e-courses still don't have any widely-accepted means of metrics, which puts them into even a worse position, especially in a rigid system such as State education.

Finally, it was noticed that a number of teachers volunteered to help moderate courses. This self-motivated moderator base still actively participates and takes on a large portion of workload from the Faculty moderators. These moderators are not materially rewarded and operate only driven by intrinsic motivation and, partially, challenge. Each moderator is assigned three 50-person groups and given assessment privileges. This phenomenon shows that service to

community, coupled with certain degree of technological challenge (just slightly less than competencies), can and does serve as a sufficient motivation factor.

V. Conclusion

In this paper the experience and lessons learned from an ongoing, 6-year long Microsoft Software d.o.o. Belgrade and Faculty of Electronic Engineering Niš joint venture within the Partners in Learning project have been summarized. It is intended to serve as an addition to guidelines to any institution to be involved in a State governed or supervised e-learning project. Experience gained through this blended-learning project can be shortly stated in the following fashion: at the current state of electronic (blended) learning, especially within slowly-changing systems such the State education, requires constant active participation of human resources in the instruction process. Moreover, the participants need be constantly challenged in order to be kept active and learning. Efficient metrics of course value (adequate to time measure in traditional education) is still unclear in e-courses, and any accreditation assigned to them may be understated.

References

[1] Microsoft Partners in Learning Homepage can be found at http://www.microsoft.com/education/pil/ (URL retrieved on April 14th, 2011).

[2] The official website/LMS of PiL at the Faculty of Electronic Engineering: http://www.pil-vb.net (in Serbian - URL retrieved on April 14th, 2011).

[3] Serbian National Law on Fundamentals of the Educational Systems, available on the Ministry of Education official page: http://www.mp.gov.rs/propisi/dokumenti/propis-9-Zakon_o_osnovama_sistema_obrazovanja_i_vaspitanja.doc (in Serbian - URL retrieved on April 14th, 2011).

[4] Rulebook on Permanent Professional Training and Vocations of Teachers, available on the Ministry of Education official page: http://www.mpn.gov.rs/propisi/propis.php?id=17 (in Serbian - URL retrieved on April 14th, 2011).

[5] Education Advancement Center – Zavod za unapređenje obrazovanja i vaspitanja (ZUOV), official web page at: http://www.zavod.edu.rs/ (in Serbian – URL retreived on April 14th, 2011).

[6] http://www.zavod.edu.rs/index.php?option=com_content&view=article&id=111:2010-09-30-13-19-25&catid=4:2009-02-19-11-16-58&Itemid=59 (in Serbian – URL retreived on April 14th, 2011).

[7] The Catalogue in PDF format can be retrieved from: http://www.zavod.edu.rs/index.php?option=com_docman&task=doc_download&gid=7&Itemid= (in Serbian – URL retrieved on April 14th, 2011).

[8] Drucker, P. - Need to Know: Integrating e-Learning with High Velocity Value Chains, A Delphi Group White Paper, http://www.delphigroup.com/whitepapers/pdf/20001213-e-learning-wp.pdf

User-generated Semantic Content Framework for E-learning

Martin Jovanović[1]

Abstract – **This paper presents a framework for collaborative or individual user-generated semantic content gathering and markup, with primary application in e-learning. This framework is a part of the ongoing research at the Faculty of Electronic Engineering Niš and is a follow-up to the previously designed and developed semantic layer framework for online learning material.**

Keywords – **E-learning, Semantic Web, Ontology, Web 2.0.**

I. Introduction

This paper describes a conceptual model of a framework for collecting user-generated content in e-learning systems. Though the notion of e-learning, established in 1998, still lacks precise definition, its convergence towards autonomous, adaptable, intelligent systems is obvious. Design of these systems imply that there is, in general, physical distance (spacial and/or temporal) between the tutor and the student, that students use some version of technology to access the material (as well as for the interaction with peers) and that some form of student support exists [1]. Opposite to the traditional education paradigm, which uses *push* delivery of knowledge that might be applied in student's future (and that is largely over-quantified), e-learning is aimed at *just-in-time* and *just-enogh* knowledge delivery [2], which makes it particularly suitable for continuous education in business environment. To achieve this goal, e-learning systems need to be adaptible and dynamic by nature. Adaptibility is achieved through student modeling, while the dynamic trait requires a repository of fine-grained learning material (learning objects, LO) that are agregated in lessons and courses on demand, personalized for each individual user and for any particular use case. LO repositories are universal and reusable resources, which are dependant on metadata (LO meta-tags) – data that enables the system to determine rules of sequencing and navigation, and other stages of course aggregation. Global initiatives like [3] support this aspect of LO, though global consensus (or "killer application") hasn't been achieved yet. Aggregation mechanisms can benefit from ontologies as means for structuring LO and building dynamic instruction materials – which is the main link between Semantic Web technologies and e-learning. This paper presents a prototype of a semantic-based textual e-learning markup tool aimed at user-generated small-scale learning objects. This prototype is in development at the Faculty of Electronic Engineering, and it is based on the previously developed system for supplemental semantic layering of the online text material [4].

[1]Martin Jovanović is with the University of Niš, Faculty of Electronic Engineering, Aleksandra Medvedeva 14, P.O. Box 73,18000 Niš, Serbia, E-mail: martin.jovanovic@elfak.ni.ac.rs.

II. Drag-and-Drop Semantic Interface

A. Introduction

Existing system, labeled Drag-and-Drop Semantic Interface (DSi) adds semantic layer to any digital textual material. This is achieved through coupling drag-and-drop funcionality with a graph (or ontology) of relations between key notions/terms in the text, enabling the user to graphically interconnect different terms and, by doing so, querry the ontology. If the link between chosen terms is defined, system will return all possible relations. This way the tools of Semantic Web have been applied for e-learning purposes.

B. Conceptual Details

If we assume that learning means acquisition of new knowledge, behavior, skill, value, preference or understanding [5], and define understanding as a psychological process connected with and abstract or concrete object where a person is able to use concepts to meaningfully interact with this object [6], we can conclude that learning means the acquisition of a concept about a new object. If a concept is defined as something that determines all entities and/or *relations* in a given category/class, by means of definitions [7], we can conclude that learning essentially implies acquisition of *facts* and *relations* (links between facts), if we leave behavioral learnings out of this discussion (these learnings cannot be delivered through textual material in focus here). Simply put – a new notion can only be explained/taught by defining its relations to other, known notions. These relations are central to the system described.

B. Implementation Details

On the implementation side, DSi solution has two key components: human-computer interface, implemented with a Scriptaculous JavaScript framework [8], and the interface to an RDF graph (in XML serialization) through the Simple JavaScript RDF Parser and Query Thingy framework [9]. This two-sided solution enables the user to graphically interact with a relation base stored as XML. Instructional design can be separated in two - textual and semantic development, and these can be performed by different authors. Semantic layer, carrying relations between terms, can be applied to any textual material (and vice versa), having in mind that relations are context-dependant. Primary focus in design of DSi was on the simple and intuitive user interface to the relatively complicated semantic storage.

III. User-Generated Content Interface

After implementation and testing, previously invisible aspects emerged. The user interface is single-sided. Semantic layer needs to be prepared in advance, using appropriate RDF editor like Protégé [10]. This requires domain experts to understand basic notions of ontologies/graphs which severely limits the author base. The only way to harness the infinite potential of non-IT users is to make the knowledge acquisition automated through the simplest possible user interface. This interface is already present in the current version of DSi.

Reversing the process realized in DSi, a semantic editor concept model is developed. User interaction is identical as in current DSi, for example the user takes the word "iskrivljavanje":

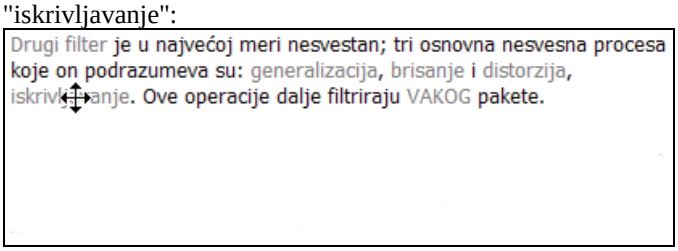

Then they drag it over the text:

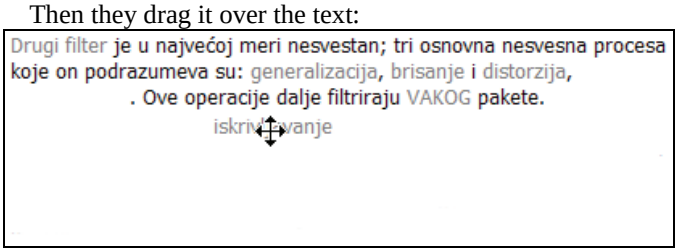

Finally, they drop it onto the word "distorzija". These two words may and may not be synonyms, depending on the context. In the context of Neuro-Linguistic Programming [11], out of which the example has been retreived, these words are synonimical. After dropping the word "iskrivljavanje" onto the word "distorzija", the system interacts with the user through an appropriate GUI element.

In the current conceptual model, the interaction is performed through a simple text field, so the relations is purely textual.

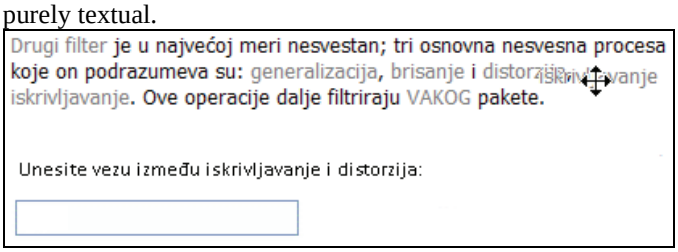

The system searchs the RDF for duplicate relations. If the duplicate is found, newly entered relation is ignored. If the input is correct, new RDF triplet is formed with the new relation. In XML format, for the illustrated example (and if the user's input is "same_as", source code will look as follows:

```
<dsi:Primer rdf:nodeID="generalizacija">

   <dsi:name>generalizacija</foaf:name>
   <eg:same_as rdf:nodeID="distorzija"/>

</dsi:Primer>
```

An interface like this enables any user of the textual material to generate their own connections between notions. These connections can be immediately visible to other users accessing the same material or other materials within the same domain (in the area of validity of entered connections), enabling collaboration between peers.

IV. Directions for Further Development

Primary direction for further development of the system is the introduction of an automated reasoner that can infer hidden (implicit) relations. This is even more important in collaborative environments, where users can create relations that can be bound to form compound relations (for example, any transitive relation between X and Y and between Y and Z will lead the reasoner to infer a new relation between X and Y; in this example, different users may have entered the same transitive relation to X-Y and Y-Z, but may not have been aware of the existence all three elements in material).

Secondly, a form of peer-review mechanism will be added. With every query, a user will be prompted with the existing relations and offered to choose the one they agree upon the most (or other forms of marking may be used, like a classical 1-5 star rating for all existing connections). This way the most popular connections as voted by users will "bubble-up" the system. This is, however, not a guarantee of the truthfulness of those connections; still, the wiki approach, counter to the initial doubts, proved to yield quality material. Peer-review proposed will benefit from the very similar concept.

Further development may include tagging of relations (according to domains/scopes of validity) and/or providing a framework for users to moderate the connection base development (for example by allowing them to detect and mark synonymic or antonymic relations in the RDF, thus enabling them to "purify" the RDF).

V. Conclusion

This paper describes a conceptual model of a semantic editor with a user-friendly interface, aimed at collecting user-generated content as an underlying semantic layer in systems for e-learning. Conjunction between Semantic Web and e-learning is an area of wide and extensive research, since it is the Semantic Web that truly provides tools for dynamic and personalized on-demand learning material delivery. Nevertheless, instructional design of these materials requires Semantic Web skilled domain experts. Conceptual model proposed in this paper emphasizes the user input and conjunction between e-learning, Semantic Web and Web 2.0 concepts. Though this compound isn't new, sometimes called e-learning 2.0 [12], the particular implementation, especially the user interface, is the author's original contribution.

References

[1] Ally, M. – Foundations of Educational Theory for Online Learning, u Anderson, T. (editor) - The Theory and Practice of

Online Learning, Athabasca University Press, 2008, ISBN 1897425082, pp. 15-44.
[2] Horton, W. – Leading E-Learning: Here is how You Can Chart your Course, Champion Implementation, Ensure Success, American Society for Training and Development, 2001, ISBN 1562862987.
[3] IEEE LTSC LOM Draft Document can be retrieved from http://ltsc.ieee.org/wg12/20020612-Final-LOM-Draft.html.
[4] Jovanović, M. - Semantička nadgradnja nastavnog sadržaja u sistemima za elektronsko učenje, magistarska teza, Univerzitet u Nišu, Elektronski fakultet, 2009.
[5] http://en.wikipedia.org/wiki/Learning
[6] http://en.wikipedia.org/wiki/Understanding
[7] http://en.wikipedia.org/wiki/Concept
[8] http://script.aculo.us/
[9] http://www.jibbering.com/rdf-parser/
[10] http://protege.stanford.edu/
[11] http://en.wikipedia.org/wiki/Neuro-linguistic_programming
[12] Downes, S – E-Learning 2.0, ACM eLearn Magazine (online), http://www.elearnmag.org/subpage.cfm?section=articles&article=29-1

Modelling Adaptive Distance Learning Course Using Petri Nets

Pavlina Vladimirova[1] and Daniela Ilieva[2]

Abstract – **This paper considers the modelling of interactive education and adaptation process. A model of interactive adaptive tutoring course, using coloured Petri nets is offered. The transitions are connected with predicate functions, which give the rules for firing the transitions.**

Keywords – **modeling, Petri nets, learning course, adaptive**

I. INTRODUCTION

Distance education has opened the gates of "Learning Anytime and Anywhere". The constantly increasing requirements to these courses and cost of the development and deployment is a fact, therefore it is important their preliminary design and testing. Some of the important requirements for an e-learning course are:

• Adaptability - the ability to provide educational material for each student individually;

• Possibility of restructuring - the updating of the product to be convenient and law costing. It is often necessary because of change and development of the topics or improving the quality of the course;

• Ability to research - it is very important to examine the training system in the development, implementation and operation in order to improve its quality and learning outcomes;

The mathematical model description of the learning course is essential to meet these requirements.

II. COLORED PETRI NETS

CPN (Colored Petri Net) have much more modelling power and have better structuring facilities as types and modules. CPN are hierarchical because they contain facilities for representing a model as a hierarchical structure. CPN use basic data types that can be used for building composite data types.

Colored Petri net is defined as a tuple [1]

CPN = (Σ, P, T, A, N, C, G, E, I) satisfying the requirements:

Σ is a finite set of non-empty types, called color sets;
P is a finite set of places;
T is a finite set of transitions;
A is a finite set of arcs such that

$A \subseteq (P \times T) \cup (T \times P), P \cap T = P \cap A = T \cap A = \varnothing;$
N is a node function, where N: $A \rightarrow (P \times T) \cup (T \times P)$;
C is a color function. It is defined as C: $P \rightarrow \Sigma$;
G is a guard function. It is defined from T into expressions such as:

$$\forall t \in T : [Type(G(t)) = Bool \wedge Type(Var(G(t))) \subseteq \Sigma]$$

E is an arc expression function. It is defined from A into expression such as:

$$\forall a \in A:[Type(E(a)) = C(p(a))_{MS} \wedge Type(Var(G(t)) \subseteq \Sigma],$$

where p(a) is a place of N(a);

I is an initialisation function. It is defined from P into closed expression such as:

$$\forall p \in P:[Type(I(p)) = C(p)_{MS}] .$$

CPN provides typing data (color sets) and sets of values from specified types for each place. The expression E (p, t) is the variable name associated with an incoming arc from place p to transition t, and the expression E (t, p) is associated with transformation (action), which transition t performed on incoming to it data to obtain outcome data for the place p. The so-called guard is a logical expression associated with transition t, which must be true to enable transition t.

Consideration and modeling of the system in terms "condition-event", allows visualization of the passage of the training course, possibility to study the dynamics and the different properties of the modeling system and establishing the simulation algorithms. Colored Petri nets allow introducing additional conditions for activation of the transitions, to link places with certain data types and tokens to be associated with some of these tips.

III. FORMULATION OF THE PROBLEM

Let us consider a course that consists of a number of modules (m), corresponding to the topics of the course. Each of these modules covers a certain amount of theoretical and reference material on the subject and problems for independent work. To design adaptive learning course on the volume and complexity of the material is required for each of the modules to develop several levels of complexity. Experience shows that it is appropriate to develop three levels of complexity:

1st level - covering the minimum required to pass the course;

[1]Pavlina St. Vladimirova is from Technical University – Varna, Faculty of Computer Sciences and Technology, 1 Studentska str., 9010 Varna, Bulgaria, E-mail: pav_varna@yahoo.com

[2]Daniela D. Ilieva is from Technical University – Varna, Faculty of Computer Sciences and Technology, 1 Studentska str., 9010 Varna, Bulgaria, E-mail: ilievadaniela@abv.bg

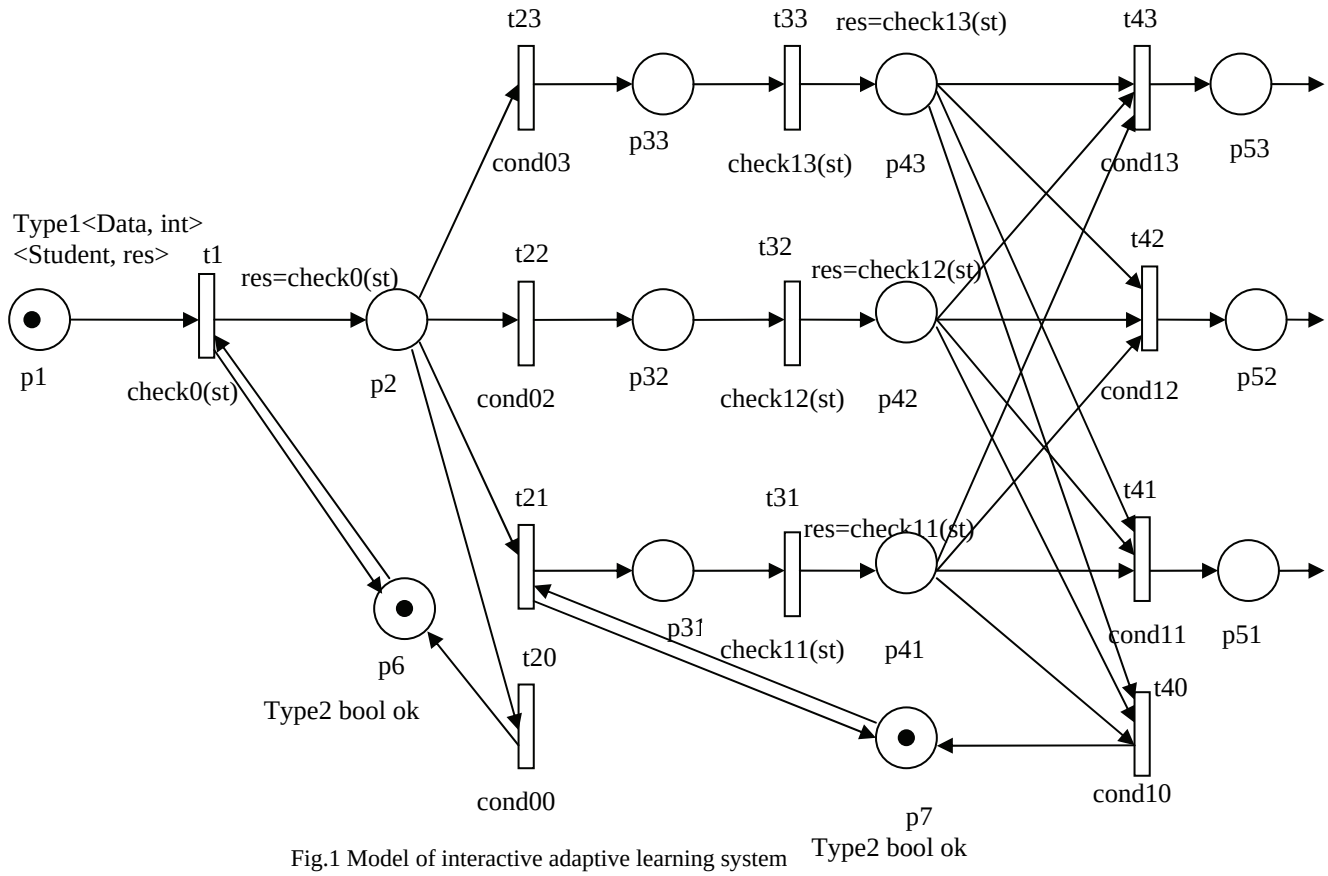

Fig.1 Model of interactive adaptive learning system

2nd level - covering 80% of material aimed at good or very good students;

3rd level - for excellent students, where the basic material is added with additional practical problems, requiring in-depth and analytical thinking.

For each of these components and their levels is necessary to develop tests (questions, problems), checking the degree of understanding the material. Regardless of the initial level of complexity, the student is able to change it depending on the results of tests on the previous modules. Adaptability of the course lies on the fact that every student can choose a suitable path of training, i.e. individual sequence of modules, depending on the recorded knowledge and skills.

IV. Interactive Model of Adaptive Learning System with Colored Petri Nets

Model of interactive adaptive learning system is given on Fig.1.

Places p_i correspond to the different states of the student during his passage through the training course, which most often are: ready to start a new training module, completion of a module and a readiness to verify his knowledge on this module, completing the verification of knowledge and readiness to continue training the same or another level.

Transitions t_i correspond to the student activities such as: training on specified module, testing of knowledge, conducting additional training. Some transitions are associated with predicate functions and activation of the transition is executed only if the predicate function is true and if tokens are available in all input places.

Description of the developed model training system:

All the places p_i can store tokens (data) of type ordered pair (Student, res), where Student is a class/data structure for student and res is a variable of integer type holding current result of the reported knowledge of the student. Student class stores the following data:

```
class Student
{string name; / / name of student
string facnumber; / / faculty / ID number
string speciality; / / speciality
string path; / / path of the course
int totalresult; / / total score for knowledge of  the course
};
```

Places p6, p7 can store and data logical type {1,0}.

p1 - ready for starting the course and passing the entrance test reviewing the necessary basic knowledge for this course;

p2 - ending of the entrance test and moving to training on the material of module 1;

p3i - completion of the i-th level of the module 1 and readiness to check knowledge on it (i = 1, 2, 3);

p4i - completion of test 1 and ready to start module 2 (i = 1, 2, 3);

p5i - completion of the i-th level of module 2 and readiness to check knowledge on it (i = 1, 2, 3);

p6, p7 - completion of additional training to the last module and a readiness to re-pass the last test. In these places there is always a token which is constant readiness for further training;

t1 - execution of entrance tests, verifying basic knowledge required;

t2i - learning the material of module 1, level i (i = 1, 2, 3);

t20 - additional training due to insufficient knowledge for starting the course;

t3i – executing the test 1 checks knowledge on module 1, level i (i = 1, 2, 3);

t4i - learning the material of module 2, level i (i = 1, 2, 3);

check0 (st) - function related to transition t1, forming the value of variable res;

check1i (st) - function related to transition t3i, forming the value of variable res;

cond01 - logical condition (guard) associated with the transition t21 to switch to study the material from module 1 level 1 (res$\in$ [40, 60));

cond02 - logical condition (guard) associated with the transition t22 to switch to study the material from module 1, level 2 (res $\in$[60, 80));

cond03 - logical condition (guard) associated with the transition t23 to switch to study the material from module 1, level 3 (res $\in$[80, 100));

cond00 - logical condition (guard) associated with the transition t20 to return to study additional material (res <40);

cond1i - logical condition (guard) associated with the transition t4i to switch to study the material of module 2, level i (i = 1, 2, 3 and corresponding logical conditions res $\in$[40, 60), res $\in$[60, 80), res $\in$ [80, 100));

cond10 - logical condition (guard) associated with the transition t40 to return to study additional material for module 1 (res <40);

The model extends beyond the places p5i by analogy to the network from t2i to p5i, i.e. test on another module follows, with subsequent adaptive guidance to the appropriate level to the next module and these iterations continue according to the number of the modules in the course.

The model allows adding the additional variable of time for the tokens and duration to transitions, which would increase the criteria for analysis and evaluation of the system. Also, the network can be considered as hierarchical, i.e. some of the transitions are represented as macros that the next level can be presented in a more detailed look.

V. CONCLUSION

1. The developed model of adaptive learning system allows testing, evaluation and quality management of the system during the development, deployment and its operation.
2. Using Colored Petri nets as a mathematical model allows using variables and data accumulation about statistical information of system performance which will be used for analysis and subsequent modifications of the learning course in order to enhance the effectiveness of training.
3. The model allows easy and comfortable transition to program implementation.

REFERENCES

[1] K. Jensen, “Colored Petri Nets: Basic Concepts, Analysis Methods and Practical Use” – New York, NY: Springer-Verlag, Vol.1 – 1996, Vol.2 – 1997, Vol.3 – 1997.

[2] P. Vladimirova, D. Ilieva,” Fuzzy based approach for decision support system”, ICEST 2010, Conference Proceedings, pp. 743-746, Ohrid, Macedonia, 2010.

[3] M. Mitev, P. Vladimirova,” Graph - Based Analytical Approach to Testing Programs”, ICEST 2010, Conference Proceedings, pp. 719-722, Ohrid, Macedonia, 2010.

Analysis of Internet Use among College Students

Svetlana Čičević,[1] Marjana Čubranić-Dobrodolac, [1] Milkica Nešić[2]

Abstract – **The purpose of this study was to gather information about college students' Internet use. The results indicated that two most frequent and time-consuming activities were browsing the Internet and checking email. Internet is used more on weekends than during weekdays. For educational purposes most of the students use Internet daily.**

Keywords – ***Internet use; college students; educational purposes*.**

I. INTRODUCTION

Since the mid-1990s, the Internet has experienced unprecedented growth in both its size and number of users. The Internet has become one of the most popular communication channels among college students worldwide.

With the advent of Internet, a significant transition can be seen in the academic communities' approach and the way they seek information and the methods they employ for teaching and learning activities. This has become possible as Internet provides a wealth of current information and delivers text, graphics, images, audios and videos at the same time. It acts as a powerful supplement to the traditional ways of studying and learning. The Internet can provide access to essentially unlimited resources of information, not conventionally obtainable through other means. There have been a number of research studies on the use of Internet, especially in the developed countries. Some of these studies measure usefulness, some have focused on accessibility, while others have combined all these. A review of literature reveals that the teachers and students are the most frequent users of Internet. They use Internet for teaching, learning and for research purposes.

An increasing number of studies have examined how college students, and youth more generally, use ICTs (Information and communications technologies) [1-4]. Salaway, Caruso, and Nelson (2007) found that students spent an average of 18 hours per week on online activities [5], while Junco and Mastrodicasa (2007) found that college-age instant messaging users typically spent an hour and 20 minutes each day actively chatting [6]. Social networking websites are one of the most popular online activities for college students [2,7,8]. Quan-Haase (2007) found that 65 % of the students spent more than 3 hours per day online, 62 % used e-mail weekly, 67 % used IM (instant messaging) daily, and most students had been using IM for 4 years or more [9]. Morgan and Cotten (2003) found that students spent an average of 3.9 hours using e-mail, 16.3 hours of chatroom and IM use, and almost 12 hours using the Internet for noncommunication-related activities per week, such as surfing or playing games [10]. Hargittai (2007) found that 82 % of students reported using chat features of digital media, and almost 84 % went online more than once a day [11].

In terms of their daily lives, college student schedules provide them with a lot of flexibility and free time resulting in the flexibility to spend long epochs on various Internet applications. Moreover, college students have easy access through direct Internet connections in dorms, libraries, and computer labs.

As students use of the Internet continues to increase, so does the need for institutions to understand the role the Internet is playing on the college. The evaluation of this question is complex and derives through understanding the activities students engage in online. Bearing the above mentioned in mind, the purpose of this pilot study was to gather descriptive information about college students' Internet use.

II. METHOD

The current investigation describes Internet use and patterns of online behavior among students at the Faculty of Transport and Traffic Engineering in Belgrade.

The sample consisted of 35 college students (60% male and 40% female; with the mean age 21.68 years). Students in an introductory psychology course were invited to complete a self-reported questionnaire on patterns of Internet use. The survey consisted of 45 multiple- choice items. Besides demographical information, general internet usage data was collected including amount of experience, time spent online, type of usage, etc.

III. RESULTS

Students generally use the Internet center in the dorm. Due to the gradual introduction of ADSL in student dormitories, as well as the growing popularity of wireless modems, many of the respondents access the Internet from the room. Also, many students access the Internet from an Internet center at the University or from some other Internet centers.

The results have shown that most of the respondents had extensive experience in using the Internet, about half of participants (46%) have 3 or more years experience using the Internet. Only 11% of them use the Internet less than a year. The analysis clearly indicates that on an average, majority of the respondents used Internet weekly. The two most frequent

[1]Svetlana Čičević is with the Faculty of Transport and Traffic Engineering, Vojvode Stepe 305, 11000 Beograd, Serbia, E-mail: s.cicevic@sf.bg.ac.rs.;

Marjana Čubranić-Dobrodolac is with the Faculty of Transport and Traffic Engineering, Vojvode Stepe 305, 11000 Beograd, Serbia, E-mail: marjana@sf.bg.ac.rs.;

[2]Milkica Nešić is with the Faculty of Medicine, Blvd. Dr Zorana Djindjica 81, 18000 Nis, Serbia, E-mail: milkica@medfak.ni.ac.rs.

and time-consuming activities were browsing the Internet and checking email. 43% of the students were checking their mails weekly or daily (40%), 5% of them every few hours, and only 6% very rare. To find the necessary information over half of the students (54%) used the Internet weekly, and daily 26%. The participants do not buy online, in general (86%), while 14% rarely. Most of the students use Internet for educational purposes daily (62%) or weekly (26%) (Table I).

TABLE I.
FREQUENCY OF GENERAL INTERNET ACTIVITY ENGAGEMENT

How often you participate in the following activities on the Internet (%)	1	2	3	4	5	6
Email	5	40	43	6	6	0
Instant Message	8	26	54	3	9	0
Find Information	8	40	40	6	6	0
Make Purchases	0	0	0	0	14	86
Academic Research	6	62	26	3	3	0

*1 - Hourly | 2 - Daily | 3 - Weekly | 4 - Monthly | 5 – Rarely | 6 -1 don't do this

Although web sites and magazines provide a great source of information, almost equal to the number of students who read the internet sites / magazines is the number of those who do not read. Due to lack of interest, or lack of time most students (74%) do not play online games (Fig. 1).

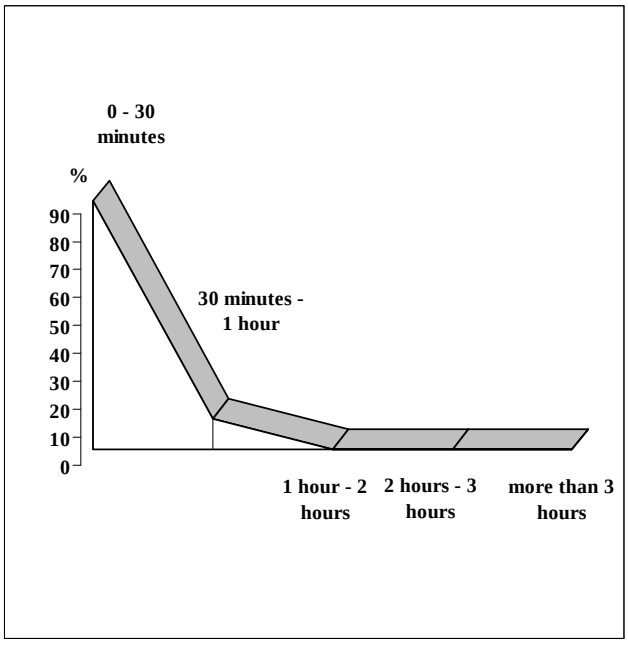

Fig. 1. Time spent playing games online on weekdays and weekends

The respondents use the Internet less on weekdays (Monday – Friday) and more on weekends (Saturday and Sunday). This result was expected because of lower engagement in educational activities on weekends, but not in accordance with the findings from literature (Figs. 2 and 3).

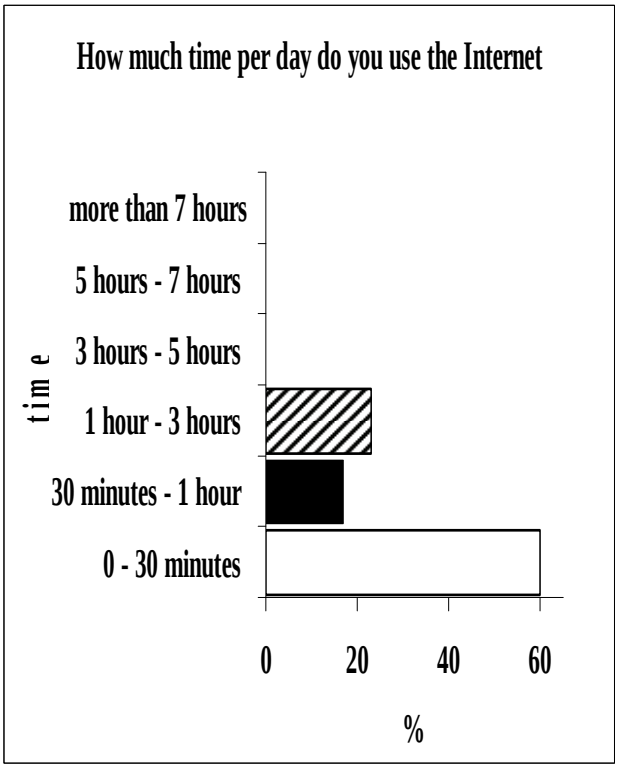

Fig. 2. Frequency of Internet Use on weekdays

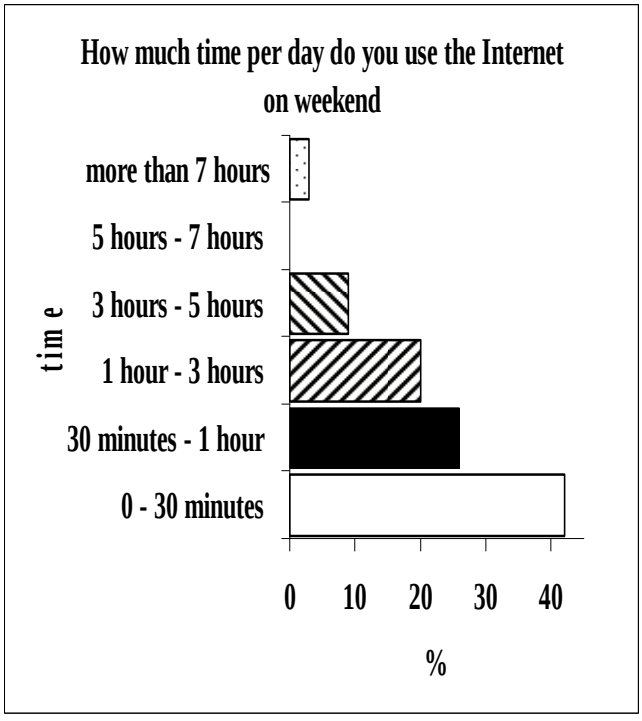

Fig. 3. Frequency of Internet Use on weekends

66% of respondents have opened a Facebook account. On Facebook, 57% spent up to 30 min, 22% up to an hour and 17% by 2 h, still only 4% between 2 and 3 h (Fig. 4).

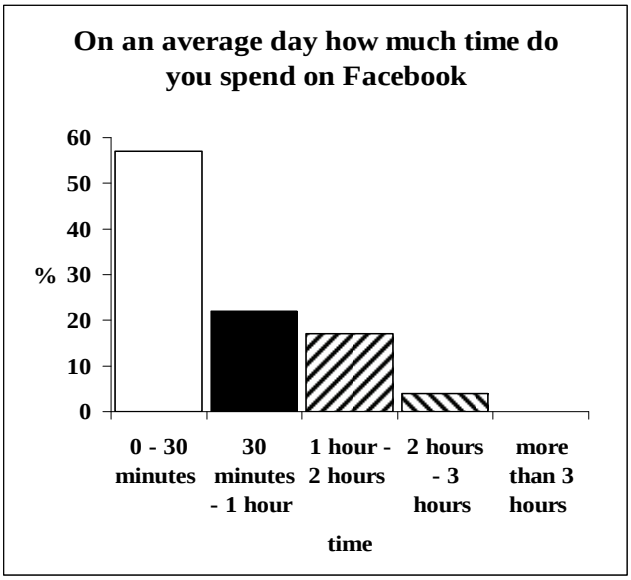

Fig. 4. Frequency of Facebook Daily Use

Mainly (48%), students agree to strongly agree with the statement: "I was excited to join Facebook." The majority of participants (82%) agree to strongly agree with the statement: "I use Facebook to stay connected to friends from high school". Only 21% of respondents use Facebook to make social connections they could not find in person (Table II).

TABLE II.
ACTIVITIES THAT PARTICIPANTS WERE ENGAGED IN ON FACEBOOK

Being involved on Facebook (%)	1	2	3	4	5
I was excited to join Facebook.	4	44	26	13	13
I use Facebook to meet new people.	4	52	9	35	0
I use Facebook to stay connected to friends from high school.	0	9	9	69	13
I use Facebook to keep track of what my friends are doing.	4	26	30	40	0
I feel connected to my friends on Facebook.	4	44	9	39	4
I use Facebook to make social connections that I couldn't find in	17	49	13	17	4
I am addicted to Facebook.	35	35	17	4	9

*1 - Strongly Disagree | 2 - Disagree 3 - Neither Agree Nor Disagree | 4 - Agree | 5 - Strongly Agree

Respondents usually read its own wall at least once a day, some more frequently. Very often the respondents read the wall of their friends, probably because of the need to see what they are doing, or to comment on something. Students also often set the "status", place links to other web pages, pictures or the "like". They rarely seek for new friends, because most have a profile on Facebook for a very long time and have a lot of "friends" and groups in almost all areas, so the creation of new groups and areas of interest is almost rare. The majority of our students didn't feel addicted to Facebook (Table III).

TABLE III.
FREQUENCY OF FACEBOOK WALL USE

How often you participate in the following activities on Facebook(%)	1	2	3	3	5	6
Read my wall	26	39	31	0	4	0
Read my friend's wall	17	36	30	13	0	4
Write on my own wall	22	26	40	4	4	4
Write on my friend's wall	0	39	35	13	9	4
Search for new friends to add	9	4	9	30	35	13
Update my profile	13	53	22	4	4	4
Create groups	0	0	4	13	35	48
Create parties	0	0	0	9	26	65

*1 - Hourly | 2 - Daily | 3 - Weekly | 4 - Monthly | 5 – Rarely 6 - 1 don't do this

The results, in general showed that the two most frequent and time-consuming activities were browsing the Internet and checking email. About two-thirds of the students use the Internet for educational purposes.

From the results of our research it is obvious that our students use ICTs to a lesser extent in comparison with their peers in other countries. This fact could be explained, on the one hand, with the fact that, for example, Facebook, is much more popular among adolescents in secondary schools, and on the other hand, due to the large students' workload during the work week, lacking of their own personal computers, as well as smaller capacities for Internet access.

Approximately 1 / 3 of our students avoided to be engaged in Facebook. The main reasons respondents indicated not participating in Facebook were that they were simply not interested and they didn't want to put personal information online. Other reasons, respectively, included that their friends don't do that, they had no time to participate in it, and that it was too much of a fad (Fig. 5).

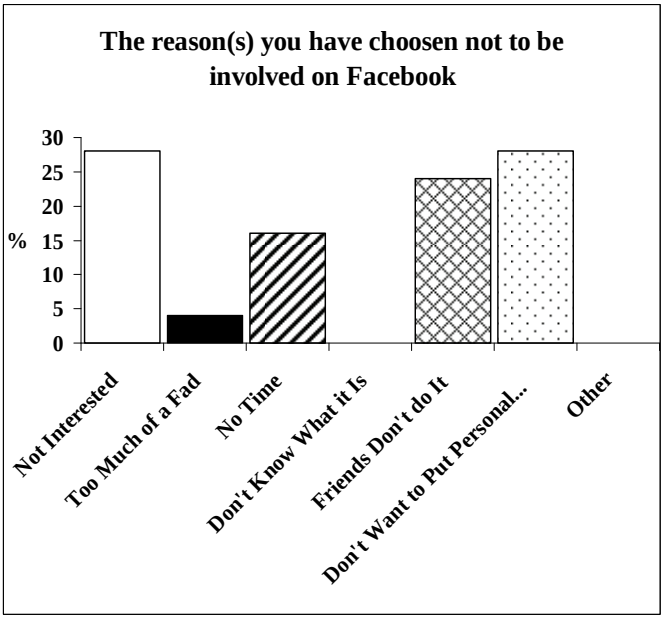

Fig. 5. Reasons why not to be involved on Facebook

IV. CONCLUSION

In the drive in higher education to promote the use of information and communications technology (ICT), the role of the Internet cannot be over emphasized. It has introduced new concepts of the teaching process and is recasting the roles played by the participants of the educational process. Still, while many undergraduates use the Internet, there are many who may not. It is encouraging to note that the respondents were making maximum use of the Internet and were aware of its benefits for educational purposes as well as other purposes.

Several questions remain unanswered in the literature, as well as in current study, on the impacts of ICT use among students and young adults [12]. For example, we know little about the use of multiple technology devices, multitasking with these and other devices, and the impacts of use on well-being. A wide range of activities can be conducted online, among them Web surfing, e-mail, live chatting, IM, list-servs, wikis, blogging, and gaming, and these activities can be social or solitary in nature.

Because modes of online communication differ, researchers need to make distinctions between their various uses. It is important for higher education faculty and staff to be aware of how their students are using technology [13]. Lifelong learners must be equipped with skills to effectively and intelligently find, evaluate, manage, apply, create, publish and store, and retrieve information using both conventional research resources as well as digital tools, such as the Internet, that access very diverse databases of information. Still, there remains a paucity of research on the subject, including the types and reasons for use, and their consequences.

It would be even more fruitful to examine the linkage between Internet use and academic achievement. Such a comparative perspective would further identify the extent to which the current findings can be applied in various social and cultural contexts.

The current research provided, is a starting point at beginning to understand how our students are engaging in online communities.

ACKNOWLEDGEMENT

This study was supported by The Ministry of Science and Technological Development of Serbia (project 36022 and 36006).

REFERENCES

[1] S. R. Cotten, “Students’ technology use and the impacts on well-being”, In R. Junco, & D. M. Timm (Eds.), *Using emerging technologies to enhance student engagement.* New directions for student services issue #124 (pp. 55–70). San Francisco, CA: Jossey-Bass, 2008.

[2] S. Jones, S. Fox, “Generations online in 2009”, Washington, DC: Pew Internet and American Life Project. Retrieved from. http://www.pewinternet.org/w/media/ /Files/ Reports /2009/ PIP_Generations_2009.pdf.

[3] J. Pasek, E. More, and E. Hargittai, “Facebook and academic performance: reconciling a media sensation with data”, First Monday, vol.14, no.5, 2009.

[4] D. F. Roberts, U. G. Foehr, “Trends in media use”, The Future of Children, vol.18, no.1, pp. 11–37, 2008.

[5] G. Salaway, J. B. Caruso, and M. R. Nelson, “The ECAR Study of Undergraduate Students and Information Technology, 2007”, Boulder, Colo.: EDUCAUSE, 2007. Retrieved from http://connect.educause.edu/library/abstract/TheECARStudyof Underg/45075.

[6] R. Junco, J. Mastrodicasa, “Connecting to the Net Generation”, Washington, D.C.: National Association of Student Personnel Administrators, 2007.

[7] A. Lenhart, S. Arafeh, A. Smith, and A. R. Macgill, “Writing, technology, and teens”, Washington, DC: Pew Internet and American Life Project. Retrieved from http://www.pewinternet.org /w/media // Files /Reports /2008 /PIP _ Writing_Report_FINAL3.pdf.pdf.

[8] New Media Consortium, “The horizon report”, Retrieved from http://www.nmc.org/ pdf/2007_Horizon_Report.pdf.

[9] A. Quan-Haase, “College Students’ Local and Distant Communication: Blending Online and Offline Media”, Information, Communication and Society, vol.10, pp. 671–693, 2007.

[10] C. Morgan, S. R. Cotten, “The relationship between Internet activities and depressive symptoms in a sample of college freshmen”, Cyberpsychology and Behavior, vol. 6, no. 2, pp. 133–142, 2003.

[11] E. Hargittai, “A Framework for Studying Differences in People’s Digital Media Uses.” In N. Kutscher and H.-U. Otto (Eds.), *Cyberworld Unlimited.* VS Verlag für Sozialwissenschaften /GWV Fachverlage GmbH, 2007.

[12] S. R. Cotton, “Students’ Technology Use and the Impacts on Well-Being”, In: New Directions for Student Services, no. 124, Winter 2008 © Wiley Periodicals, Inc. Published online in Wiley InterScience (www.interscience.wiley.com) DOI: 10. 1002 /ss. 295, 55-70, 2010.

[13] R. Junco, S. R. Cotton, “Perceived academic effects of instant messaging use”, Computers and Education, vol. 56, no. 2, pp.370–378, 2011.

Mining Student Data Using Clustering Expectation-Maximization Algorithm

Gabrijela Dimic[1], Petar Spalevic[2] and Kristijan Kuk[3]

Abstract – **In this paper data mining technique named clustering is applied to analyze student's learning behavior u e-learning system Moodle. Study showed what kind of data can be collected, how to perform the previous data preparation, how to apply appropriate methods on the data, and how to apply the discovered knowledge.**

Keywords – **Data mining, Educational data mining, Clustering, Moodle, E-learning**

I. INTRODUCTION

Over the past years, several thousand e-learning systems have been developed, which represents a basis of the modern learning technology concept [1].

E-learning systems enables autoidentification of the user, access and use of learning material, simple editing and layout of documents, leading of discussions and communication with other participants of the course, carrying out of exercises, testing and surveying of users, grades recording etc. These systems provide database in which all system information on users is being recorded.

The analysis of activity data and user interaction e-learning system can be measured its effectiveness and then used as a support for decision making in the organization of online courses for distance learning. Majority of analysis and evaluation of e-learning system based on the use of questionnaires and surveys that are widely used to assess the impact and usability of interactive systems [2].

An alternative to traditional data analysis is the use of data mining as an inductive approach for automatic detection of hidden information present in the data. Data mining, unlike the traditional analysis, is based on discovering knowledge in the sense that an assumption is automatically derived from data, i.e. that it is driven by data rather than based on research or driven by a man.

Data mining is a process of extracting samples or models from observed data. It is defined as a process of identifying valid, new, potentially useful and understandable patterns in data [3]. Data mining techniques can be applied to a wide range of data. It is often used as a method for discovering knowledge on commercial websites for identification of key buyers and increasing efficiency of online sale on commercial websites.

These aspects can be transmitted to the field of knowledge and management systems. The use of data mining in education implies integration of data discovery processes and methods for knowledge discovery in educational environment, i.e. development of methods for extracting a unique type of data coming from the educational environment, and the use of those methods in order to better understand students. This new developing field, known as Educational Data Mining, refers to selection of best methods for discovery of knowledge on the basis of data available in the educational environment.

The data needed for research in this field are collected from operational data that are kept in databases of educational institutions and represent personal and academic data on students, and from the systems that support electronic learning and have a huge quantity of information.

On the basis of discovered knowledge an analytical model is constructed, which reveals interesting patterns and guidelines based on student user information that the teacher uses to improve the course performance and efficiency, and thus students' learning, their results and final marks as well. The use of data mining in e-learning systems is a constant cyclical process in which the discovered knowledge should realize and record the cyclical loop of the system, and on the basis of that state, enable and improve learning as a whole, not only by putting data into knowlegde but also by filtering the discovered knowlegde for making a final decision.

II. CASE STUDY

For the purpose of this study we collected and analyzed students data in the course Computer graphics, held in the summer semester of the school year 2009/2010 at the College of Electrical Engineering and Computer Science Applied Studies in Belgrade. The course was chosen by 130 students from different study programs. Students were not obliged to attend the lectures, and the lecture material was also available in the Moodle course. Before every laboratory exercise, students took a knowledge check test referring to the current exercise in Moodle, which contained questions from the theoretical part needed for performing tasks from the exercises.

[1]Gabrijela Dimic is with the College of Electrical Engineering and Computer Science Applied Studies, Vojvode Stepe 283, 11000 Belgrade,Serbia, E-mail: gdimic@viser.edu.rs.

[2]Petar Spalevic is with the Faculty of Technical Sciences, Kneza Miloša 7, 38000 Kosovska Mitovica, Serbia,
E-mail: petarspalevic@yahoo.com

[3]Kristijan Kuk is with the College of Electrical Engineering and Computer Science Applied Studies, Vojvode Stepe 283, 11000 Belgrade,Serbia, E-mail: kkristijan@viser.edu.rs.

The course user environment was organized in the following way:

- Forum: Notifications by which students were delivered information related to lectures by the course teacher.
- Learning material: Lessons, Self-check tests, Interactive tasks.
- Knowledge check tests for each laboratory exercise.
- Final knowledge check tests.

The main objective of this study was grouping students into clusters according to their characteristics and analyzing of their activities. In order to perform the necessary research, was identified set of basic questions for the analysis course e-learning system:

- What materials do they access most often?
- Is there a connection between activities and results?
- How do results of data mining methods correspond to final marks?
- How to form the groups – on the basis of what characteristics and activities of students?
- What are the main characteristics within a group, and what are differences between them?

III. APPLICATION OF DATA MINING METHODS

A data mining process comprises the following stages [4]:

- collection of data to be analyzed,
- preparation and pre-procession of data,
- usage of data mining algorithms,
- interpretation and evaluation of results.

A.Data collection

For this study, we collected the information activities of students in the Computer Graphics course from Moodle database. We collected information on students access to the course and excluded the students who didn't access the course at all, and thus the number of analyzed students decreased from 130 to 123. Data were collected about usage of learning material, results of the tests for individual knowledge evaluation, reading of messages sent via forums.

B. Data preprocessing and discretization

This phase implies gathering of relevant and exlusion of irrelevant data, transformation of original data to an adequate form for implementation data mining algorithm and discretization and adjustment of data in regard to usage of data mining algorithm. All information on access to the Moodle system are recorderd into database and log file on the server where Moodle is installed. Anyway, the database is much more reliable and powerful data source about all activities in comparison to log file and data gathered from the e-learning system database require less clean up and less processing.

In the preprocessing phase, data are prepared for the application of data mining techniques. This phase implies previous procession and cleaning of data, removal of inapplicable and unimportant information, collection of information necessary for modelling, selection of methods for handling the missing data fields, and finally discretization.

Atributes are determined in a way to integrate information regarding all student activities at the analyzed course and namely number of lessons read, number of interactive tasks performed, number of read forum posts, number of self-check tests, an average result achieved on self-check for all try outs and all of these in a single record.

By the application of discretization method [5] numerical values of an atribute have been transformed into discrete thus becoming more comprehansive and clearer for further analysis. Analysis report about all student's activities was showed key parameters on which the new table is created with the appropriate attributes (see Table I).

TABLE I
USED ATTRIBUTES FOR EACH INSTANCE OF STUDENT

n_lessons	Number of read lessons	Low/ Medium/High
n_int_tasks	Number of solved interactive tasks	Low/ Medium/High
n_read_forum_post	Number of read forum posts	Low/ Medium/High
n_self_check_tests	Number of taken self-check tests	Low/ Medium/High
mark_ self_check_tests	An average result achieved on tests	Failed/ Passed
mark_exam	Mark obtained in the exam	Failed/ Passed/ Excellent

Percentage of usage of learning material has been established (lessons, interactive tasks, read forum posts, self_check_tests) and labeled like this:

- Usage of up to 25% – Low
- Usage of up to 55% – Medium
- Usage of up to 100% – High

After the use of dicretization filter, the resulting file with data has all nominal attributes, and it is transformed into a text file of the ARFF format (Attribute-Relation File Format), which is an ASCII text file and describes the list of instances assigned within the collection of attributes [4] and is ready for the use of data mining methods.

C. Clustering

Clustering is one of the basic techniques often used in analyzing data sets. The main task of this method is to put items into groups so that the similarity of items within a group is maximized, while similarity of items in various groups is minimized [4]. With the use of clustering in e-learning systems the implemented algorithms can find clusters of students with similar learning characteristics, group students

in order to obtain various environments based on their capabilities and other characteristics [6].

There are a lot of algorithms for generating clustering methods and in this case study was applied Expectation-Maximization (EM) algorithm . The EM algorithm is a mixture of the basic algorithm that finds maximum probabilities of parameter evaluation in a possible model [7].

This method is an efficient iterative procedure to compute the Maximum Likelihood estimate in the presence of missing or hidden data [8]. Generally, this is an optimization approach, which had given some initial approximation of the cluster parameters, iteratively performs two steps: first, the expectation step computes the values expected for the cluster probabilities, and second, the maximization step computes the distribution parameters and their likelihood given the data. It iterates until the parameters being optimized reach a fixpoint or until the log-likelihood function, which measures the quality of clustering, reaches its maximum.

In this study, we used data mining EM algorithm for predicting the final grade on the basis of analyzing the behavior of students in the course. Students were grouped into three clusters according to their learning activities. The algorithm assigned to attributes the maximum probability of affiliation with each cluster (see Table II).

TABLE II
RESULTS OF GROUPING WITH THE USE OF EM ALGORITHM

Attribute	Cluster 1	Cluster 2	Cluster 3
n_lessons			
Low	1.2397	6.9088	**21.8515**
Medium	9.232	**25.5078**	1.26
High	**33.2252**	7.7296	1.0552
n_int_tasks			
Low	2.0727	**19.8781**	**16.0491**
Medium	11.1044	13.7918	6.1038
High	**30.5152**	6.4762	2.0138
n_read_forum_posts			
Low	15.1014	**25.9356**	**18.9629**
Medium	10.8257	6.907	3.2673
High	**17.76**	7.3035	1.9365
n_self_check_tests			
Low	3.9294	**19.7804**	**20.2902**
Medium	3.3961	9.6714	1.9324
High	**36.3616**	10.6943	1.9441
mark_ self_check_tests			
Failed	1.0001	1.005	**13.9949**
Passed	**41.687**	**38.1411**	9.1719
mark_exam			
Failed	1.0278	2.1752	**21.797**
Passed	4.2375	**36.407**	1.3555
Excellent	**38.4219**	1.5639	1.0143

Observation of maximum values of the probability of affiliation of the atribute mark_exam, in Cluster 1 we have grouped students which achieved excellent results at the exam, in Cluster 2 those who passed the exam and in Cluster 3 those who failed it.

Cluster 1 constists of 21% of students which in large extens used all kinds of offered learning material and had mostly passed self-check tests of knowledge. Grade of students in this cluster is *excellent.* Cluster 2 consists of 40% of students which moderately used lessons, interactive tasks, read forum posts and self-check tests in less extent, but on average have passed self-check tests. Students are grouped in this cluster achieved the grade *passed*. Cluster 3 has 39% of students which poorly used learning material and have in average failed self-check tests. Final grade of students in this cluster is *failed*.

How to use results from application EM algorithm? The biggest issue are definately students from Cluster 3 (failed). By following student activities in Moodle, during semester, teacher can certainly mark students which do not use any of learning materials, to give them timely warning, or to organize some other model of learning which will be more efficient for them.

For students in Cluster 2 teacher could create new learning material which will be combination of lessons, interactive tasks and self-check tests. That way these students can prepare and achieve even better results at the exam.

IV. CONCLUSION

This paper describes application one of data mining methods for analysis of behavior and activities of students in the e-learning systems. An advantage of data mining methods lies in the fact that a student's low mark can be predicted on time. The teacher can predict what students have a tendency to fail the exam and can work with them on improvement of their characteristics and achievements prior to the end of semester and the final exam.

Based on the detected information from the student activities, the teacher can create a new kind of activities and learning materials from which the students receive higher grades, decide to eliminate some of the activities related to the low grade or to offer a new way of learning, which will improve passing the exam.

Continuation of work in this field will refer to Establishing a model of student knowledge in the e-learning systems using data mining methods.

ACKNOWLEDGEMENT

This paper was produced under the research project TR35026 funded by the Ministry of Education and Science Republic of Serbia.

REFERENCES

[1] B. Erol , Y. Li, "An overview of technologies for e-meeting and e-lecture", IEEE International Conference on Multimedia and Expo, pp. 6 pp, 2005.

[2] P. Zaharias and A.Poylymenakou, "Developing a usability evaluation method for e-learning applications: Beyond Functional Usability", *International Journal of Human Computer Interaction*, Vol. 25, Issue 1, 76-79, 2009.

[3] U.Fayyad, "Data mining and knowledge discovery in databases: implications for scientific databases", 9th International Conference on Scientific and Statistical Database Management, 1996.

[4] I.H. Witten and E. Frank, "Data mining: practical machine learning tools and techniques", Morgan Kaufmann, 2005.

[5] J. Dougherty, M. Kohavi and M. Sahami, "Supervised and unsupervised discretization of continuous features", Internacional Conference Machine Learning Tahoe City, CA, 194–202, 1995.

[6] W. Hamalainen, J. Suhonen, E. Sutinen and H. Toivonen, "Data mining in personalizing distance education courses", World Conference on Open Learning and Distance Education, Hong Kong , 1-11, 2004.

[7] D. Frank, "The Expectation-Maximization algorithm", Technical Report GIT-GVU-02-20, Georgia Institute of Technology, 2002.

[8] B.Sean, "The Expectation Maximization Algorithm - A short tutorial", Last updated, January, 2009.

Quality Estimation Model of Higher Education Institutions

Suzana Savic [1], Goran Janackovic [2] and Miomir Stankovic[3]

Abstract – **This paper presents quality indicators and performances of higher education institutions and a model for evaluating the quality of higher education institutions based on the application of the methods of analytical hierarchy process and trends of quality indicators changing.**

Keywords – **higher education, quality indicators, quality performances, quality assessment.**

I. INTRODUCTION

In the last decades of the twentieth century there was the internationalization of economic trends in production, market development and education. It was a period of constant change in technology, business and politics, working and living environment and integration of the organization and integration technologies. This led to the transformation of systems form traditional to systematic organization.

These changes are closely related to knowledge and education. Education is a dynamic system that tracks and initiates any changes in society, such as changes in technology, engineering, organization, management, regulation and standardization, quality policy, and examples of good practice [1].

Education and knowledge are increasingly becoming primary development resources for creating competitive advantage of any organization (companies, nations, states, the regions or economic integration).

Therefore, the challenges of higher education in the twenty-first century can be understood as a threat or an opportunity. If they are treated as a threat to universities, that will put emphasis on the preservation of the past. Otherwise, when seen as a chance, the emphasis is on the future, which requires the use of best practices from the past and the development of higher education institutions of high quality [2].

When evaluating of the quality of higher education institutions it is necessary to use a systems approach, where higher education institutions must be analysed as complex systems that are parts of a dynamic, changing environment with complex interactions between education, scientific research and support processes exist. This paper presents a model for evaluating the quality of higher education institutions based on a modified AHP method.

[1]Suzana Savic is with the University of Nis, Faculty of Occupational Safety, Carnojevica 10a, 18000 Nis, Serbia, E-mail: suzana.savic@znrfak.ni.ac.rs.

[2]Goran Janackovic is with the University of Nis, Faculty of Occupational Safety, Carnojevica 10a, 18000 Nis, Serbia, E-mail: goran.janackovic@znrfak.ni.ac.rs.

[3]Miomir Stankovic is with the University of Nis, Faculty of Occupational Safety, Carnojevica 10a, 18000 Nis, Serbia, E-mail: miomir.stankovic@gmail.com.

II. QUALITY OF HIGHER EDUCATION

The main tasks of higher education in the XXI century are the continuous provision, improvement and quality assurance of higher education. The implementation of these tasks influences the competitiveness of not only higher education institutions, but also a national system of higher education in general.

In the academic community there are two approaches to quality: (1) Approach to quality as measure of values, which means striving to be the best according to some criterion; (2) Approach to quality as the extent of reaching the threshold, which means compliance with minimum standards (of competence and burden on teaching staff, facilities, technical equipment, library holdings, etc.).

Research undoubtedly shows that the standards of quality with the minimum requirements are not sufficient to create a unique position of higher education institutions in the knowledge economy. It is essential for higher education institutions to have something that makes it different from their competitors. It can be: the quality of their curricula, technology and teaching process and extra-curricular activities, organizational culture, strategy, promotions, branding and the ability to build the public image, the quality of human resources, technical equipment, facilities and library facilities, but also the quality system and philosophy of Total Quality Management [3].

Higher education institutions (HEIs) are very complex systems for management, security and quality improvement and quality management. They are characterized by high level personnel, complexity of the process of education, high social importance of performance, long cycle process of education and training, the historical independence and freedom in the choice of lecturers teaching methods, the complexity of identifying the beneficiaries of higher education, their requirements, desires and expectations [2]. They are also characterized by various forms of education (traditional, electronic, lifelong learning), and different standards for different types and forms of basic processes and support processes.

The activity of higher education is described by three main areas: education, scientific research and application. Therefore, three basic processes can be defined in the institutions of higher education [4]:

- Educational process, through which the main purpose of higher education institutions is fulfilled;
- Scientific process, which, besides its basic role in raising the level of general and applied scientific knowledge, generates inputs into the educational process and

• The process of applying the results in practice, primarily necessary to check the quality of research and educational process and achievement of feedback on these processes.

Way of organizing, implementation and management of these processes and support processes (administration, finance, and publishing) fully determine the quality of higher education institutions.

The quality of higher education is formed in accordance with the following requirements [2]:

• User requirements,
• International requirements,
• Requirements of national standards for accreditation,
• Standards requirements of higher education institutions,
• Requirements of technological standards,
• Quality management system requirements.

In estimating the quality special emphasis is given to users' satisfaction. Users of higher education are internal (teachers and staff) and external (students, parents, students, employers, society, state). Their demands are very different. Students sometimes want to get a grade more easily, while the employer always wants a professional who is ready to solve particular practical problems, and who also has the skills of communication, teamwork, planning and organization, writing and using numbers, and decision-making [5].

International requirements refer to the requirements of the Bologna process, the requirements of international standards of quality in higher education, as well as the requirements of international organizations dealing with issues of quality in higher education. Bologna process emphasizes flexibility as a core performance quality, which refers to the same standards, mobility and exchange of students and teachers in the wider educational area. International standards are based on the following basic principles [6]:

• Interests of students as well as employers and the society more generally in good quality higher education;
• Central importance of institutional autonomy, tempered by a recognition that this brings with it heavy responsibilities;
• Need for external quality assurance to be fit for its purpose and to place only an appropriate and necessary burden on institutions for the achievement of its objectives.

The main objectives of these standards are [6]:

• To encourage the development of higher education institutions which foster vibrant intellectual and educational achievement;
• To provide a source of assistance and guidance to higher education institutions and other relevant agencies in developing their own culture of quality assurance;
• To inform and raise the expectations of higher education institutions, students, employers and other stakeholders about the processes and outcomes of higher education;
• To contribute to a common frame of reference for the provision of higher education and the assurance of quality within the European Higher Education Area.

National standards for accreditation define requirements related to higher education institutions, curricula, internal assessment and external quality assurance.

The requirements of higher education institutions work are related to the organization and technology of work, educational context, human, material and information resources, while technological requirements of standards are related to technology and pedagogical subsystem [2].

A large contribution to the quality of higher education is made by the introduction and compliance with the requirements of quality management systems (planning, managing, securing and improving the quality of) the TQM model.

III. Quality Performance Indicators

Key performance indicators (KPI) are non-financial and financial measures which, on the basis of quantifiable targets, reflect strategic performance of higher education institutions. KPIs are used to assess the current situation and define the main directions of development. Originally, KPIs are applied in order to determine the strategy of the institution and evaluate the progress in achieving goals. The essential application of KPIs is reflected in the establishment of standards for their own control over the parameters of the quality of higher education institutions [4].

The purpose of Performance Indicators is to [7]:

• provide reliable information on the nature and performance of higher education sector
• allow comparison between individual institutions of a similar nature, where appropriate
• enable institutions to benchmark their own performance
• inform policy developments
• contribute to the public accountability of higher education.

In a quality-driven and never ending improvement environment, the following are some of the main reasons why measurement is needed and why it plays a key role in quality and accountability improvement [7]:

• To ensure that customer (internal, external) requirements have been met.
• To be able to set sensible objectives and comply with them.
• To provide standards for establishing comparisons (not ranking) for continuous improvement
• To provide transparency and provide a ‘score-board’ for people to monitor their own performance levels.
• To highlight quality problems and determine which areas require priority attention.
• To give an indication of the costs of poor quality
• To justify the use of resources.
• To provide feedback aimed at improving quality, healing the weak points and updating the strong ones.

Performance indicators, therefore, are the means by which performance will be evaluated. To be meaningful, they must be measurable, relevant and important.

KPIs are of interest to a wide range of bodies, including Government, universities and colleges, and the higher education funding bodies. The indicators are also relevant to schools, prospective students and employers.

IV. Assessment Model of HEI Performance

The model is based on combination between AHP, trend analysis and comparative data [8]. It consists of: (1) Key

success factors identification, (2) Key performances identification, (3) KPIs identification, (4) Building KPIs tree, (5) Trend and comparison based scoring.

(1) *Key success factors identification*. Three key success factors (KSFs) of HEI are: achievement of education activities, achievement of research activities quality and achievement of community services and supporting activities.

(2) *Key performances identification*. Identification of key performance is based on standards. In the Republic of Serbia that are the standards for accreditation of institutions. Each standard can be regarded as a performance of quality: 1-objectives of the institution, 2-planning and control, 3 - organization and management, 4-studies, 5-scientific and artistic work; 6-teaching staff; 7-non-teaching staff, 8 students, 9-workspace and equipment, 10 -library, textbooks and information support; 11-funding; 12-QA, 13-transparency of its operations. HEI has to choose the key performances.

(3) *KPIs identification*. Based on the above criteria and key performances, it is necessary to identify a list of KPIs related to each performance. The selected KPIs were analysed by experts group in a Delphi Forum. The experts used the three-point scale of "not important", "somewhat important" and "very important". The result is the selected KPIs according to their degree of importance. In this case, we have to find first the most important KPIs from list of KPIs. This list is completed by experts who are more aware of the problems that HEI have to cope with.

(4) *Building KPIs tree*. KPIs tree is basically composed by four levels: 1st level - the goal: total score of HEI performance; 2nd level - the criteria: education, research and supporting; 3rd level - the key performances; the rating scale (4th level) contains KPIs related to each performance, and its rating scale (Figure 1).

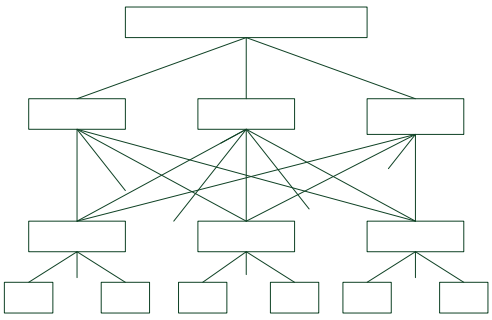

Fig. 1. Hierarchy of KPIs tree

(5) *Trend and comparison based scoring*. In the second level (criteria), the three criteria (education, research, supporting) are weighted using pairwise comparison proposed by AHP approach [9]. The expert group compared relative importance of each criterion in the pairwise manner using 1-9 comparison scale, where 1 means that importance of two criteria is the same, while 9 means that one criterion is extremely more important that the other, as shown on Table I.

TABLE I
SCALE FOR AHP PAIRWISE COMPARISON [10]

Level	Importance	Explanation
1	Equal	The equal contribution of two factors to the objective
3	Moderate	Experience and judgment slightly favor one factor over another one
5	Strong	Experience and judgment strongly favor one criterion over another one
7	Very strong	A factor is favored very strongly over another; its dominance demonstrated in practise
9	Extreme	The evidence favoring one factor over another is of the highest possible of affirmation

Assumption is that if criterion A is extremely more important than criterion B and is rated at 9, then B must be absolutely less important than A and is valued at 1/9.

Each expert has to compare elements of the same hierarchy level. Results of these judgments are summarized in pair-wise comparison judgement matrices. An example of a pair-wise comparison for the first hierarchical level is shown in Table II.

The procedure for obtaining a priority vector is:

1. Calculate the sum of all elements in each column;
2. Divide elements of each column with sum of the values of the column, which was obtained in the previous step;
3. Calculate the sum quotient obtained for each species and determined the average value of each species.

Column consisting of the average value is normalized by its own vector.

TABLE II
PAIR-WISE COMPARISON JUDGEMENT MATRIX

Criterion	E	R	S	Priority vector
Education (E)	1	3	3	0,6
Research (R)	1/3	1	1	0,2
Supporting (S)	1/3	1	1	0,2
∑	5/3	5	5	1,0

The consistency value is determined as follows:

1. Pairwise comparison judgement matrix is multiplied by the priority vector:

$$\begin{bmatrix} 1 & 3 & 3 \\ 1/3 & 1 & 1 \\ 1/3 & 1 & 1 \end{bmatrix} \cdot \begin{bmatrix} 0,6 \\ 0,2 \\ 0,2 \end{bmatrix} = \begin{bmatrix} 1,8 \\ 0,6 \\ 0,6 \end{bmatrix} \quad (1)$$

2. The calculated matrix Eq. (1) is divided by priority vector:

$$\begin{bmatrix} 1.8 \\ 0,6 \\ 0,6 \end{bmatrix} \div \begin{bmatrix} 0,6 \\ 0,2 \\ 0,2 \end{bmatrix} = \begin{bmatrix} 3 \\ 3 \\ 3 \end{bmatrix} \quad (2)$$

3. Further, eigenvalue $\lambda_{\max}$ is calculated as maximum value of elements in Eq. (2) matrix:

$$\lambda_{\max} = 3 \tag{3}$$

4. The consistency index is calculated as follows:

$$CI = (\lambda_{\max} - n)/(n-1) = 0 \tag{4}$$

5. A value of a random index, RI, is selected according to the matrix size, as shown on Table III. For a 3x3 matrix selected value is RI= 0.52.

TABLE III
RANDOM INDEX

n	1	2	3	4	5	6	7	8
RI	0	0	0.52	0.89	1.11	1.25	1.35	1.4

6. The consistency ratio is calculated as follows:

$$CR = CI / RI = 0 \tag{5}$$

If CR ≤ 0.10, it means that judgment is consistent. If it is more, the judgment matrix is inconsistent. To obtain a consistent matrix, judgments should be reviewed and improved.

Key performances and KPIs are weighed using the same method as the criteria described above.

KPIs are measured based on the principles of trends and comparison dimensions. Trends consist of the current level and last year performances. The following decision making rule has been suggested in [7]:

(1) If KPI trend is growing and current level is higher than competitor/benchmark, then the score is 100.

(2) If KPI trend is growing and current level is lower than competitor/benchmark, or if KPI is declining and current level is higher than competitor/benchmark, then the score is 50.

(3) If KPI trend is declining and current level is lower than competitor/benchmark, then the score is 0.

The total score of Higher Education Institution performance (TPS) is calculated as follows:

$$TPS = \sum_{i=1}^{n} W_{i,I} \sum_{j=1}^{m} W_{j,II} \sum_{k=1}^{r_j} s_{jk} w_{jk} \tag{6}$$

where, *i* is index for criteria; *j* is index for performances; k is index for KPIs; $W_{i,I}$ is weight of criterion-i (1st level); $W_{j,II}$ is weight of performance-j (2nd level); w_{jk} is weight of KPI-k related to performance-j (3rd level); s_{jk} is score of KPI-k related to performance-j.

V. CONCLUSION

The best model ensuring the quality of higher education institutions is introducing the concept of total quality management and continuous improvement. This requires the use of tools and techniques for monitoring, measuring and evaluating quality. The proposed model for quality assessment, based on the AHP method and the development trends of key performance indicators, provides higher education institutions with a real picture of their comparative advantages, and their positions in higher education.

ACKNOWLEDGEMENT

The research presented in this paper was partially supported by Serbian Ministry of Science and Environment (projects III44006 and III42006).

REFERENCES

[1] S. Savic, M. Stankovic, “Systems Engineering - Education Framework for Safety Management, Occupational and Environmental Safety in National and European Educational System“, Conference Proceedings, pp 157-164, Nis, 2005.

[2] M. Lazic, “Quality System – QMS in Higher Education“, Quality festival 2007, Conference Proceedings on CD, Kragujevac, 2007.

[3] B. Masic, “Quality and Differentiation Strategy in High Education: Path to European Integration”, www.singipedia.com/655-Kvalitet-i-strategija-diferenciranja-u-visokom-obrazovanju-Put-ka-Evropskim-integracijama, 2010.

[4] R. Maksimovic, “High Education Institution Quality Parameters”, Development Trends: Bologne Studies Acreditation”, Conference Proceedings, pp 47-51, Kopaonik, 2007.

[5] W. Archer, J. Davison, “Graduate Employability: What do Employers Think and wont”, How to educate economists for labor market, Conference Proceedings on CD, Belgrade, 2009.

[6] ENQA report, “Higher Education Area”, European Association for Quality Assurance in Higher Education, Helsinki,3rd edition, 2009, www.enqa.eu/pubs.lasso

[7] S. Kaplanis, D. Talaba, D. Nanoussi, “ Measuring Quality and Improvement: Quality Indicators”, www.lib.teipat.gr/ JeanMon/ Papers/15_MEASURING QUALITY AND IMPROVEMENT - 2.pdf.

[8] K. Suryadi, “Framework of Measuring Key Performance Indicators for Decision Support in Higer Education Institution”, Journal of Applied Sciences Research”, 3(12), pp. 1689-1695, 2007.

[9] T. L. Saaty, *The Analytic Hierarchy Process*, New York, McGrawl-Hill, 1980.

[10] T. L. Saaty, L. G. Vargas, *Decision Making in Economic, Political, Social, and Technological Environments with the Analytic Hierarchy Process*, Pittsburgh, RWS Publications, 1994.

FSO System for Students Training

Kalin Dimitrov[1], Tsvetan Mitsev[2], Nikolai Kolev[3]

Abstract – **A specialized optical communication system for students training is designed. The system gives the opportunity to do exercises at short distances in a laboratory and also at longer distances in the corridors of some of the Technical University blocks. Problems related to the alignment and adjustment of the optical blocks are solved. In this paper we discuss the problems which arise with the using of cheap fixing of the photoreceiver to the walls of the box.**

Keywords – **Free Space Optics, Engineering Education.**

I. Introduction

The free space optic communication systems (FSO) typically use two transceiver blocks with line of sight between them [1-3]. Usually in each of these blocks there is an analog transmitter and receiver and a module for respective converting of the signals to a form suitable for existing digital computer networks. With FSO systems, a strong fluctuation of the atmosphere transparency as well as spot movements in the receiver plane are observed. It is very important for the system to have a good alignment and adjustment of the optical blocks. To implement the latter is necessary a relatively expensive fixing of the photoreceiver, the light source and the boxes as a whole.

II. General Setting of the Analysis

Some of the physical parameters of the FSO systems are relatively weakly determined. It turns out that the significant changes of the intensity of the optical radiation in the receiver aperture are one of their major problems.

The performance of a FSO link is primarily dependent upon the climatology and the physical characteristics of its installation location. In general, weather and installation characteristics that impair or reduce visibility also affect FSO link performance.

One of the key challenges with FSO systems is maintaining transceiver alignment. FSO transceivers transmit highly directional and narrow beams of light that must reach the receiver aperture of the transceiver at the opposite end of the link. For a FSO link to function, it is very important that both the transmitted beam of light and the receiver cone encompass the transceiver at the opposite end of the link.

It is very important to have a clear methodology in order to create a coupled structure of a receiver and a transmitter rather than a separate receiver and a separate transmitter. This is important for a further mounting and alignment.

[1]Kalin Dimitrov is with the Faculty of Telecommunications at Technical University of Sofia, 8 Kl. Ohridski Blvd, Sofia 1000, Bulgaria, E-mail: kld@tu-sofia.bg.

[2]Tsvetan Mitsev is with the Faculty of Telecommunications at Technical University.

[3]Nikolai Kolev is with the Faculty of Telecommunications at Technical University.

III. Experimental Setup

To able to illustrate the methodology for alignment and adjustment we have made an experimental setup shown with a photo in fig.1 and schematically in fig.2.

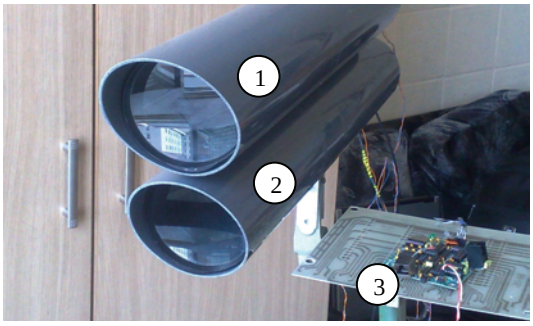

Fig. 1. Experimental setup - photo
(1 – transmitter box; 2 – receiver box; 3 – interface)

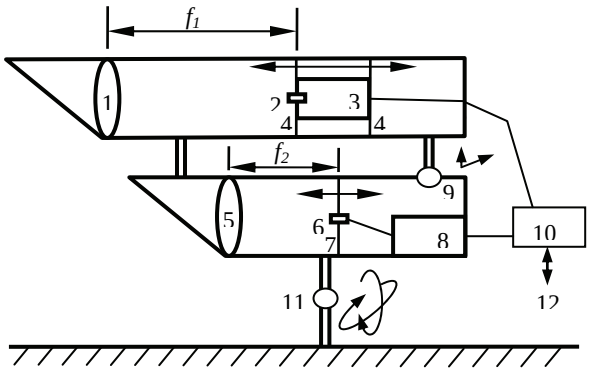

Fig. 2. Experimental setup - schematic
(1 – lens of receiver; 2 – photodiode; 3 – analog amplifier; 4 – fixation; 5 – lens of transmitter; 6 – transmitter; 7 – fixation; 8 – transmitter driver; 9 – adjustment bolt with two degrees of freedom; 10 – interface; 11 – mounting; 12 – computer network device)

We have prepared models in boxes resistant to the atmosphere, so that we can make outdoor experiments.

IV. Experimental Procedure for Students

In this section we will present an example step by step algorithm for a student Lab experiment. Described in this way, the task is suitable for practical work with students in the corridors of block 2 of the Technical University of Sofia. There the distance with line of sight is of a suitable order.

The measuring of the optical power in 1,2 and 3 is done by using the receiver - item 2 and 3 in fig. 2 without the lens. During the measuring is used modulated light to avoid the influence of the background light.

Algorithm:

1. The focal length of the transmitter lens f_1 is determined by using some of the popular methods [4]

2. The transmitter is placed near the focal point and is fixed (to make the system simpler and cheaper we do not use high precision X,Y translation and Z rotation mounts)

3. The profile of the optical beam is checked at several distances from the transmitter head and corrections are made if necessary. It must be ensured that a collimated beam is derived. If it is necessary, we correct the fixing in 2.

4. The same type of optical system is used (with the same type of lens $f_2 = f_1$) for the receiver too. The photodiode is placed in the probable focus.

5. A second system like the one in fig. 2 is placed at several meters and the level in its receiver part is checked. If, despite the alignment (which we apply with item 11 in fig. 2) there is a low power level, we move the receiver along the optical axis until the derivation of a sufficient level. It is possible, during this moving, for the photodiode not to be exactly at the focus distance. This is a compromise which is made in order to fix the receiver in the box more simply. In the next section has been made an evaluation of the influence of this over the attenuation.

6. 1 to 5 are repeated for the transmitter of the second couple of optical systems. The alignment with the first couple is made with item 9 in fig. 2.

7. The distance is increased to several tens of meters, now using only item 11 in fig. 2.

8. If the experiments from 7 are successful, the performance of the system is checked respectively at 100 and 200 meters.

V. Experimental and Simulation Results

With the real setup shown in fig. 1 (lens diameter 100 mm) and using the algorithm in the previous section we derive a focal length of 380 mm and diameter of the lightspot 400 and 900 mm respectively at 100 and 200 meters distance.

To evaluate the added losses due to incorrect placing of the receiver, we have created a simulation program evaluating the overlapping of the photodiode aperture with the lightspot formed by the lens. At the same time we have taken into account the decreasing of the power density during movement along the optical axis (fig. 3).

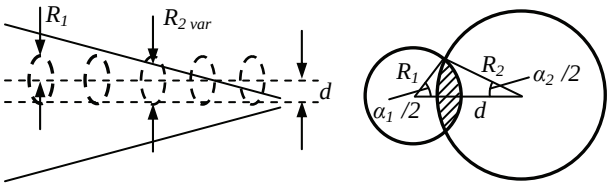

Fig.3.Change of the photodiode location on the optical axis

From the law of cosines we derive respectively the angles

$$\alpha_1 = 2\arccos\frac{R_1^2 + d^2 - R_2^2}{2R_1 d}\ ,\ \alpha_2 = 2\arccos\frac{R_2^2 + d^2 - R_1^2}{2R_2 d} \quad (1)$$

We derive the overlapping by the formula

$$J = \frac{R_1^2}{2}\left(\alpha_1 - \sin\alpha_1\right) + \frac{R_2^2}{2}\left(\alpha_2 - \sin\alpha_2\right) \quad (2)$$

We present the attenuation resulting from the moving in dB, and at the same time we take into account the decreasing of power density

$$Attenuatio\ n[dB] = 10\lg\frac{\pi R_2^2}{J}\ . \quad (3)$$

Using (1), (2), (3) we can easily present the attenuation as a function of R_2 and d. The results from the numerical experiment for intervals of light spot radius change from 2,5 mm to 7,5 mm and the interval of the distance between the centers from 3 mm to 4mm with photodiode radius 2,5 mm have been shown in fig.4.

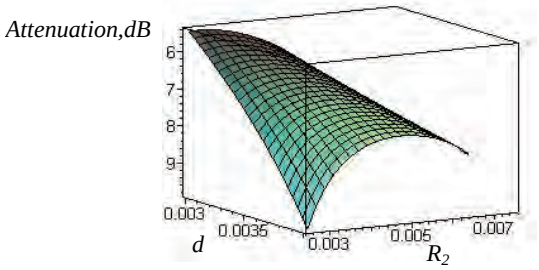

Fig.4. Simulated data for the attenuation in dB as a function of the light spot radius and the distance between the light spot center and the photodiode aperture center

VI. Conclusion

The research we have conducted can be useful for the creation of cheap and simple FSO systems. Our work has shown that when we use specific methodology for pointing and aligning, we can evaluate the deviation of the geometrical path loss. This paper would also be useful in that it provides concrete experimental guidelines.

The scientific research in this paper has been funded by the Internal competition of the Research and Development Sector of TU-Sofia-2011.

References

[1] H. Willebrand, B. Ghuman, *Free Space Optics: Enabling Optical Connectivity in Today's Networks*, Indianapolis, SAMS, 2001.

[2] E. Ferdinandov, B. Pachedjieva, K. Dimitrov, *Optical Communication Systems*, Sofia, Technika, 2007.(in bulgarian)

[3] L. Andrews, R. Phillips, C. Hopen, *Laser beam scintillation with applications*, SPIE Press, 2001.

[4] Freeman M, C. Hull, Optics, Elsevier Health Sciences, 2003.

Session IT:

INTERNET TECHOLOGIES

HTML5 Web Sockets

Aleksandar Kotevski[1], Gjorgi Mikrovski[2] and Ilija Jolevski[3]

Abstract – **The HTML5 Web Sockets specification defines the Web Sockets API that enables web pages to use the Web Socket protocol for full-duplex communication with a remote host. HTML5 Web Sockets defines a channel for full-duplex communication that operates through a single socket over the Web and represents a colossal advance, especially for real-time, event-driven web applications - significantly reduction in unnecessary network traffic and latency compared to legacy polling and long-polling solutions that are often used to push real-time data to clients. Through this paper should be present benefit from using Web socket in HTML5 and practical realization on several examples.**

Keywords- ***HTML5 Web Sockets, communication, traffic network, protocol***

I. INTRODUCTION

In the existing technologies that enable pushing of data from a server to a subscribing client are not using true asynchronous communication. Instead they emulate this using long polling where the client polls the server for data. If no data exists for the client, the server does not immediately respond but rather, he waits for data to be available and then sends it to the client. This technique of delayed responses relies on always having an outstanding client request that the server can respond to. What might look like a server initiated communication actually relies on the client making requests to the server.

II. IMPLEMENTING HTML5 WEB SOCKET

HTTP was originally designed for document transfer, but, this protocol is half-duplex (Figure 1 shows the half-duplex architecture), so it can't be use in real-time communications. It that situation, Ajax (Asynchronous JavaScript and XML) can be use to build interactive Web applications, so content can be changed without refreshing the entire page. But, Real-time often achieved through polling and long-polling, which is reason for lots of complexity.

The latest HTML version, HTML5, introduce elements that integrate web front-end much tighter with server back-end. Most importantly, web sockets are now being introduced and thereby allowing browser applications to receive asynchronous updates from the server side, so called server push. Web sockets define a full-duplex communication channel that operates over a single socket using HTML5 compliant browsers. Web sockets allow for true low latency applications and put less strain on the server.

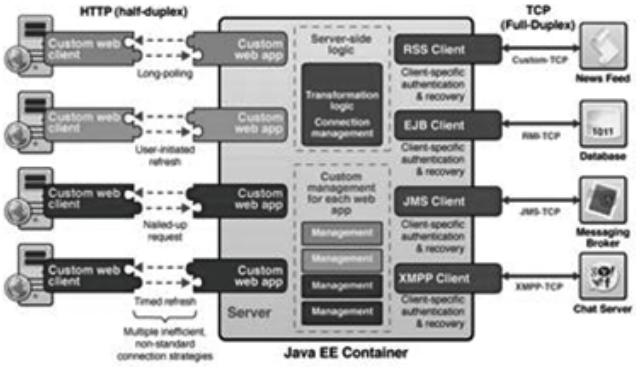

Figure 1: Half – duplex architecture

.

The goal with this paper is to implement the HTML5 web socket protocol for presenting real time data. Data will be pushed to the client without any explicit request from the client allowing for true asynchronous updates from the server. HTML5 Web Sockets is not just another incremental enhancement to conventional HTTP communications; it represents a colossal advance, especially for real-time, event-driven web applications. In simple words the web application client can maintain an always open connection with the server and data can be sent and received at the same time.

It runs via port 80/443, the TCP handshakes are HTTP compatible and it also integrates with cookie based authentication. The message headers have been kept small (only 2 bytes overhead per frame) and latency from establishing new connection every time as in HTTP have been dealt with by using a single persistent connection.

All these result in impressive network throughput. Apart from that Websockets API is much simpler to code than the XmlHttpRequest(). Bottomline, you can make the process of web application developmentmore responsive and interactive with lesser effort.

Today's Web applications demand reliable, real-time communications with near-zero latency, not just broadcast, but bi-directional communication. Examples: financial applications, social networking applications, online games, smart power grid etc.

Implementing WebSocket into the HTML5 is really useful, because he is full-duplex, enables web pages to communicate with a remote host, traverses firewalls, proxies and routers seamlessly. HTML5 WebSocekt API has a following structure:

1 Aleksandar Kotevski is with the Faculty of Law, Partizanska BB, 7000 Bitola, Macedonia
E-mail: aleksandar.kotevski@uklo.edu.mk.
2 Gjorgi Mikarovski is with the Faculty of Technical science, Ivo Lola Ribar BB, 7000 Bitola, Macedonia
E-mail:gjorgi.mikarovski@tfb.uklo.edu.mk.
3 Ilija Jolevski is with the Faculty of Technical science, Ivo Lola Ribar BB, 7000 Bitola, Macedonia
E-mail:ilija.jolevski@uklo.edu.mk.

```
interface WebSocket {
  readonly attribute DOMString URL;
// ready state
const unsigned short CONNECTING = 0;
const unsigned short OPEN = 1;
const unsigned short CLOSED = 2;
readonly attribute unsigned short readyState;
readonly attribute unsigned long bufferedAmount;
// networking
attribute Function onopen;
attribute Function onmessage;
attribute Function onclose;
boolean send(in DOMString data);
void close();
}
```

III. USING HTML5 WEB SOCKET

HTML5 WebSocket should be use in situation where web application has data that must flow bi-directional simultaneously, when web application is used by huge number of users simultaneously, in situation where the web application must extend TCP-based protocols to the browser. Also, HTML5 WebSocket should be use when web application developers need an API that is easy to use or when web application must extend SOA over the Web and in the Cloud.

Connection established by upgrading from the HTTP protocol to the WebSocket protocol using the same TCP connection. Once upgraded, WebSocket data frames can be sent to both client and server in full-duplex mode.One possible WebSocket architecture is shown on figure 2.

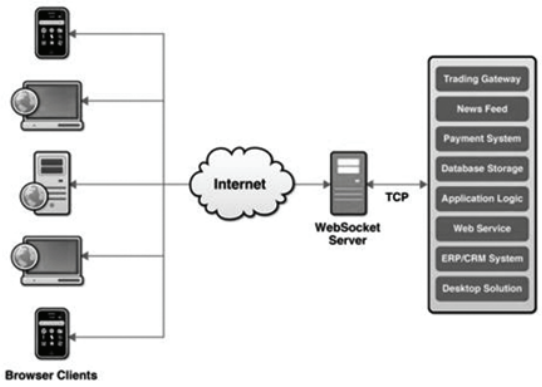

Figure 2: WebSocket architecture

To establish a WebSocket connection, the client sends a WebSocket handshake request, and the server sends a WebSocket handshake response, as shown in the following example**:**

Client

GET /demo HTTP/1.1
Upgrade: WebSocket
Connection: Upgrade
Host: example.com
Origin: http://domain.com
Sec-WebSocket-K1: 4 @1 56846xW%3l 1 2
Sec-WebSocket-K2: 12548 5 Y3 1 .P20

^n:df[4R

Server

HTTP/1.1 101 WebSocket Protocol Handshake
Upgrade: WebSocket
Connection: Upgrade
Sec-WebSocket-Origin: http://domain.com
Sec-WebSocket-Location: ws://domain.com/test
Sec-WebSocket-Protocol: sample

8j&S'y:G*To,:xa-

After receiving the response HTTP header, data will be transmitted according to the WebSocket protocol. This means at this point only WebSocket frames will be transferred over the wire. A frame can be sent at each time in each direction. The WebSocket protocol defines two types of frames: a *text frame* and a *binary frame*. The text will be transferred UTF8-encoded between the start and the end byte. A text frame requires only 2 additional bytes for packaging purposes. Figure 3 shows a text frame for the string "Today" and the string "Sat April 25 11:20:005 2011".

Text frame of "Today":
0x22 0x47 0x65 0x73 0x44 0x61 0x41 0x65 0xFF

Text frame of "Sat April 25 11:20:005 2011":
0x00 0x53 0x61 0x74 0x20 0x4D 0x34 0x72 0x20 0x31
0x33 0x98 0x31 0x23 0x3A 0x30 0x30 0x3A 0x34 0x35
0x68 0x95 0x45 0x54 0x30 0xFF

If the handshake was successful, then the data transfer starts.

This is a two-way communication channel where each side can, indeendently from the other, send data.

Data is sent in the form of UTF-8 text. Each frame of data starts with 0x00 byte and ends with a 0xFFbyte, with the UTF- text in between. The protocol is designed to support other frame types in future. Instead of the 0x00 byte, other bytes might in future be defined. Frames denoted by bytes that have the high bit set (0x80 to 0xFF) have a leading length indicator.

The Sec-WebSocket-Key1 and Sec-WebSocket-Key2 fields and the 8 bytes after the fields are random tokens which the server uses to construct a 16-byte token at the end of its handshake to prove that it has read the client's handshake.

The handshake is constructed by concatenating the numbers from the first key, and dividing by the number of spaces. This is then repeated for the second key. The two resulting

numbers are concatenated with each other, and with the last 8 bytes after the fields. The final result is an MD5 sum of the concatenated string.

The handshake looks like HTTP but actually isn't. It allows the server to interpret part of the handshake request as HTTP and then switch to WebSocket.

Once established, WebSocket data frames can be sent back and forth between the client and the server in full-duplex mode. Text frames can be sent full-duplex, in either direction at the same time. Binary frames are not supported yet in the API. WebSocket text frames use a terminator, while binary frames use a length prefix.

The following listing is example of JavaScript using the WebSocket interface:

```
<html>
  <head>
    <script type='text/javascript'>
      var ws = new WebSocket('ws://domain.com/test');
      ws.onmessage = function (message) {
        var messages = document.getElementById('messages');
        messages.innerHTML += "<br>[in] " + message.data;
      };
      sendmsg = function() {
        var message =
document.getElementById('message_to_send').value
        document.getElementById('message_to_send').value =
"
        ws.send(message);
        var messages = document.getElementById('messages');
        messages.innerHTML += "<br>[out] " + message;
      };
    </script>
  </head>
  <body>
    <form>
      <input type="text" id="message_to_send" name="msg"/>
      <input type="button" name="btn" id="sendMsg"
value="Send" onclick="javascript:sendmsg();">
      <div id="messages"></div>
    </form>
  </body>
</html>
```

Next listing present one more example of using the WebSocket:

Step 1:
Create a new WebSocket connection to WebSocket server at test.example.com.

```
var stockTickerWebSocket = new
WebSocket("ws://test.example.com");
```

Step 2: Attach JavaScript Callback Functions
Associate event listeners to handle each phase of the connection life cycle.

```
stockTickerWebSocket.onopen = function(evt) {
alert("Connection open...");
};
stockTickerWebSocket.onmessage = function(evt) {
alert( "Update: " + evt.data);
};
stockTickerWebSocket.onclose = function(evt) {
alert("Connection closed.");
};
```

Step 3: Send and Receive Data
To send a message to the server, simply call the postMessage method on the webocket with the content you wish to send to the server.

```
stockTickerWebSocket.postMessage("MSG:
GOOG,100@200.25″);
```

This will send the MSG message to the server. Any message coming from the server will be delivered to the onmessage callback registered in step #2.

Step 4: Disconnect When Done
When completed, call the disconnect() method to close the WebSocket connection.

```
stockTickerWebSocket.disconnect();
```

As demonstrated in the example above, there are no HTTP requests made to the server from the client side to retrieve data, instead the data was pushed to the client from the server - when it becomes available.

When a new WebSocket connection is established the browser opens an HTTP connection to the server first and then negotiates with the server to upgrade the connection to a dedicated and persistent WebSocket connection. This process automatically sets up a tunnel through to the server - passing through all network agents (proxies, routers, and firewalls) in the middle (very much like HTTPS establishing a secure, endtoend connection), solving numerous issues that the various Comet programming techniques encountered. Once established the WebSocket is a fullduplex channel between the client and the server.

IV. Compatibility

Currently all browsers do not support the Websockets API. List of browsers that support them are:

- Chrome 4.0
- Firefox 4.0 beta
- Opera 11
- Safari 5.0.3
- IE9

For other browsers it’s not so clear but support will come as major browsers are already in line.

Overall things appear exciting as web applications will become realtime and allow better resource utilization allowing developers to build interactive and responsive applications.

V. Conclusion

By using HTML5 WebSockets, writing highly interactive *real-time web* applications becomes very easy and practical. The WebSocket API is very easy to understand andn

also to use. The underlying WebSocket protocol is high efficient: there is a minimal overhead involved in managing a WebSocket. Due the fact that the WebSocket protocol runs on the top of TCP, the WebSocket protocol does not have to deal with "hacks" as do popular Comet protocols like Bayeux or BOSH. Simulating a bidirectional channel over HTTP leads to complex and less efficient protocols. Especially if only a small amount of data will be transferred, such as tiny notification events, the overhead of the classic Comet protocols is very high. This is not true for WebSockets. To establish a new WebSocket connection, the WebSocket protocol makes use of the connection management capabilities of the HTTP protocol.

On the other hand, WebSockets do less for reliability. This has to be done on the application (sub-protocol) level. In contrast to Server-Sent events, the WebSocket protocol does not include reconnect handling or guarantee message delivery. The current WebSocket protocol represents a low-level communication channel only.

REFERENCES

[1] W3C, 2009. Html 5 specification, canvas section. http://dev.w3.org/html5/spec/Overview.html#the-canvas-element

[2] HTML5–A vocabulary and associated APIs for HTML and XHTML. http://www.w3.org/TR/html5/

[3] HTML5 Demos and Examples. http://html5demos.com

[4] How HTML5 Will Change the Way You Use the Web. http://lifehacker.com/5416100/how-html5-will-change-the-way-you-use-the-web

[5] Pushing real time data using HTML5 Web Sockets, Nikolai Qveflander

[6] Harnessing the Power of HTML5 WebSocket to Create Scalable Real-time Applications - Brian Albers & Peter Lubbers, Kaazing

[7] Using the HTML5 WebSocket API,Peter Lubbers, Brian Albers and Frank Salim

[8] Using the HTML5 Web Workers API, Peter Lubbers, Brian Albers and Frank Salim

[9] The Extensible HyperText Markup Language. Steven Pemberton et al.W3C, 2000

[10] http://eziniearticles.com/?expert=Eric_D_Rowell

[11] Web sockets now available in google chrome, December 2009. http://blog.chromium.org/2009/12/web-sockets-now-available-in-google.html.

[12] Ian Hickson. Google Inc. The web socket api, June 2010. http://dev.w3.org/html5/websockets/

[13] Ian Hickson. Google Inc. The web socket protocol, May 2010.http://tools.ietf.org/html/draft-hixie-thewebsocketprotocol-75

[14] HTML5, W3C Working Draft, 24 June 2010, Ian Hickson, http://www.w3.org/TR/html5/

[15] The Web Sockets API, W3C Working Draft, 22 December 2009, Ian Hickson, http://www.w3.org/TR/websockets/

[16] HTML Device, Editor's Draft, 15 June 2010, Ian Hickson,http://dev.w3.org/html5/html-device/#peer-to-peer-connections

General Architecture for Semantic Querying of Heterogeneous Data Sources*

Ivo Marinchev[1]

***Abstract* – In this paper we propose a general architecture for semantic querying of heterogeneous data sources. The general idea is to introduce semantic descriptions in the forms of base ontologies to the legacy data sources containing structured data. All base ontologies are mediated to a general ontology that describes the whole domain knowledge against which all end user applications are created. The advantages of this approach are twofold. First – all applications are written independent of the physical and logical representation of processed data. And second – at any time data sources can be added/removed to the application stack by additions/removal of only the corresponding transformation and data access mapping rules that are part of the data mediator layer.**

***Keywords* – Data integration, Ontology, Heterogeneous data sources, OWL, RDF, SPARQL.**

I. Introduction

In recent years the need to process data from heterogeneous data sources becomes widespread. It is the result of integration of many legacy databases that were developed for use in proprietary applications but later (sometimes many years after they were created) data integration becomes a central issue in many areas to facilitate the access and manipulation of highly distributed, heterogeneous and dynamic collection of information sources.

Integrating and querying data from heterogeneous sources is a hot research topic in database research field. The goal of data integration is to provide user a uniform access to multiple heterogeneous data sources. This problem is known in the literature as query rewriting and query answering using views, and has been studied very actively in the recent years [10]. However, with the use of ontology, these former research works are not applicable.

In this paper, an ontology-based approach for heterogeneous data source integration is proposed. We deal with several ontologies. A specific ontology is created for every data source and it corresponds to the data logical structure. Then all base ontologies are generalized to a domain ontology that serves the purpose of semantic data model against which all end user applications are implemented.

II. General Architecture

Fig. 1 depicts the general architecture for semantic querying of heterogeneous data sources. At the bottom is a data source layer where all external heterogeneous data sources are represented. They provide data to the data mediation layer with the help of base ontologies and semantic lifting. The data mediation layer uniforms different base ontologies to a single semantic model that is exported for use by end-user applications. Above all is the application layer that represents all end-user applications created against the domain model. Application layer utilizes semantic repositories, reasoners and SPARQL [24] query language to build queries against the domain model and infer results.

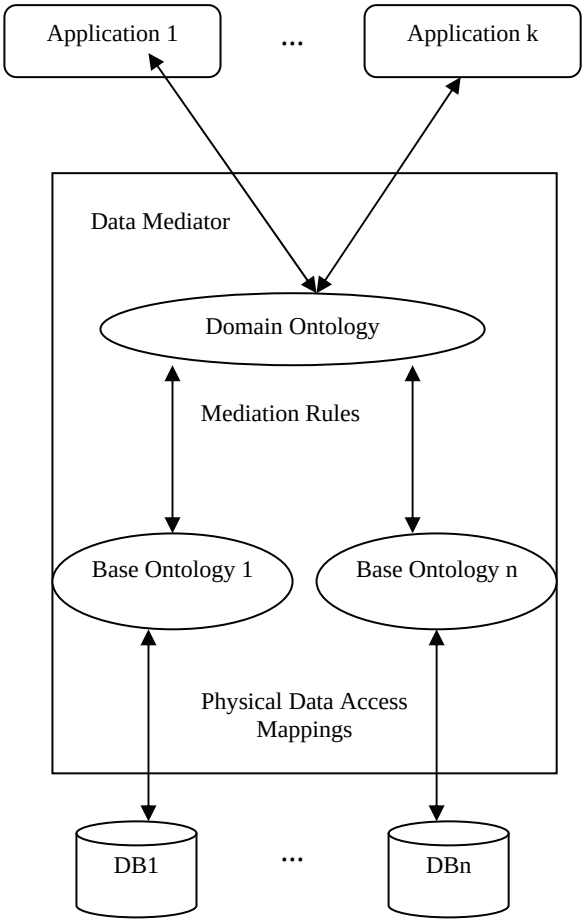

Fig. 1: General Architecture of semantic querying system.

III. Data Source Layer

Data source layer can be any data source that is accessible over the network and available to external applications. It can be standard relational databases, object databases, enterprise information systems, web feeds, web services, etc. For every data source a XML schema is created that describes logical

[1]Ivo Marinchev is with the Institute of Information and Communication Technologies, Bulgarian Academy of Sciences, Acad. G. Bonchev Str., Bl. 2, Sofia 1311, Bulgaria, E-mail: ivo@iinf.bas.bg

*This work was partially supported by Research Project No. D-002-189 funded by the National Science Fund of Bulgaria

structure of the corresponding data. On top of this XML schema a base ontology is created that is a semantic description/explanation of the data source. The ontology is encoded in OWL [25]. Based on the XML schema and the ontology (semantic schema) a transformation rules are created that transforms between physical representations of the data and its form as ontology instances and vice versa. Transformation between the physical representations of the data and its form as ontology instance is named lifting in the semantic web literature. The opposite transformation is named lowering. Both are required during execution time for communication between semantic and non-semantic layers of the system as almost all data that exist today are not semantically annotated. Hence pure semantic practical system can not be build at the moment and in the near future and every such system will require some form of lifting.

One example for lifting data from the SINUS project [23] is given the fragment of XML instance file

```
<?xml version="1.0" encoding="utf-8" ?>
……
<Identification>
   <Location>
        <Area>Sofia</Area>
   </Location>
<Identification>
……
```

it is lifted to the following fragment of ontology instance

```
<owl:Thing rdf:about="#OWLClass_Province_65">
   <rdf:type rdf:resource="#OWLClass_Province" />
   <rdfs:label>Sofia</rdfs:label>
</owl:Thing>

<sinus:OWLClass_ObjectLocationAddress
   rdf:about="#OWLClass_ObjectLocationAddress35”>
   <rdf:type
      rdf:resource="http://www.w3.org/2002/07/owl#Thing" />
   <sinus:OWLObjectProperty_has_Province
      rdf:resource="#OWLClass_Province_65" />
</ sinus:OWLClass_ObjectLocationAddress>
```

Note that on the semantic level the lifting produces two instances. One is the province of Sofia that is an instance of the ontology class OWLClass_Province and the other one is the instance of the class OWLClass_ObjectLocationAddress that has object property has_Province that refers to the province instance. On the semantic level we have two instances because the Sofia is lifted from String to the instance of ontology class. Hence it is no longer just sequence of characters but inherits all the semantics that stem from its corresponding class.

The last thing that is part of the physical data access mapping subsystem is the information about communication protocols. It is required so that the data mediation layer can communicate with corresponding data management software.

IV. Data Mediation Layer

Different data sources are expected to use different base ontologies for the annotation and interpretation of their data. Such differences hamper interoperation between applications and hamper reuse of data and ontologies across data bases. Reuse of data and interoperation between applications on the Semantic Web can be achieved by ontology merging, ontology mapping, and ontology alignment.

A. Ontology merging

In areas where ontologies do not overlap ontology merging can be implemented. As a side effect of ontology merging the newly created ontology can be shared between legacy applications which used the original ontologies. This ontology can now be used to enable interoperation between applications on the Semantic Web.

Ontology merging is the creation of a new ontology from two or more source ontologies. The new ontology will unify and in general replace the original source ontologies.

There are many different approaches to ontology merging found in the scientific literature. Some of them are [15], [20], [4] also different research tools are implemented PROMPT [17], OntoMerge [6], FCA-Merge [9] based on Formal concept analysis [4], OntoMorph [11].

B. Ontology mapping

In the case of ontology mappings, semantic overlap between ontologies needs to be detected and described using a formal language. Such a mapping can then be used for querying across ontologies, transforming data between representations, etc. The mappings are used to integrate autonomous heterogeneous applications over the Semantic Web.

An ontology mapping M is a (declarative) specification of the semantic overlap between two ontologies Os and Ot . This mapping can be one-way (injective) or two-way (bijective). In an injective mapping we specify how to express terms in Ot using terms from Os is a way that is not easily invertible. A bijective mapping works both ways, i.e. a term in Ot is expressed using terms of Os and the other way around [21].

Some tools the facilitate ontology mappings are MAFRA [1] and [19], OntoMap [3], RDFT [5].

One practical consideration related to mapping language is that it is better to be part of the ontology language itself or at least the widespread reasoners to be able to interpret it out of the box. Then any third part software as semantic repositories, reasoners, etc, can be reused without costly modifications.

C. Ontology matching/alignment

Ontology matching is the process of discovering similarities between two source ontologies. The result of a matching operation is a specification of similarities between two ontologies. Ontology matching is done through application of the Match operator [7].

Some approaches to ontology alignment are described in AnchorPROMPT [17], [18] and GLUE [2], Semantic Matching [8], QOM -Quick Ontology Mapping [13] and [14]

In our architecture we need a special case of ontology mapping, merging and alignment where the source ontologies remain, alongside of mappings to the domain ontology. In this case, the source ontologies can maintain their instance stores.

All the semantic information on this layer of the system is stored in some semantic repository as OWLIM [16], Sesame [22], or Jena [12].

Semantic repositories are engines similar to other database management systems (DBMS). Their main function is to support efficient storage, querying, and management of formal knowledge and semantically annotated data. The main functionalities of semantic repositories that distinguished them from other data management systems are:

- use ontologies as semantic schemata, which allows them to automatically reason about the data;
- work with generic physical data models, which allow them to easily adopt updates and extensions to the schemata, i.e. in the structure of the data;
- can be described as RDF-based column stores with inference capabilities.

V. Application Layer

This layer consists of all end user applications created against the domain model. They access the data with the help of SPARQL [24] query language against the used semantic repository. As mentioned above semantic repositories support inference capabilities. Thus using the semantics of the schemata/ontologies, semantic repositories can infer implicit information and return it during query evaluation. To illustrate the benefit of automated interpretation (or reasoning), consider a query about telecom companies in Europe: If an ontology describes the nesting of industry sectors and geographical areas, then a semantic repository would know to return mobile operators in the UK even though it has not been explicitly told that any particular UK mobile operator is also a European telecoms company.

VI. Querying Heterogeneous Data Sources

Mediation between ontologies is established in order to solve a particular problem in interoperability between ontologies. The most important use case for ontology mediation throughout this paper is querying.

Mediation between ontologies enables querying of one ontology in terms of another. This type of querying needs to be supported by the mediation component.

Such querying can be achieved in two principled ways: (1) by loading the source and target ontologies, together with the mapping rules, in the reasoner and then posing queries and (2) by rewriting queries in terms of the target ontology to queries in terms of the source ontology and then querying the source knowledge base, after which the query answers must be transformed to the target ontology.

Both ways have advantages and disadvantages. In case all ontologies along with the mapping rules are loaded in the reasoner, one can pose simple queries and immediately retrieve the answers in terms of the target ontology. The additional steps of rewriting the query and transforming the answers are not required. Disadvantage is that the reasoner must have access to the instance store which corresponds with the source ontology. Such an instance store would typically be a relational database and thus the reasoner must be aware how to translate queries on the ontology concepts to queries in the relational database and have access to the database to execute the queries.

In the second case, the additional steps of query rewriting and transformation of the query results are required. Especially query rewriting is a very complicated and costly task. This scenario is appropriate in case the source knowledge base exposes only a simple query interface and there is no access to the instance store.

VII. Conclusion

In this paper we presented general architecture for semantic querying of heterogeneous data sources. Important part of every implementation of this architecture is ontology mediation. We enumerated several approaches to ontology mediation that can generally be classified in three groups – ontology merging, ontology mapping, and ontology alignment. Our architecture require a special case of ontology mapping, merging and alignment where the source ontologies remain, alongside of mappings to the domain ontology. In this case, the source ontologies can maintain their instance stores.

References

[1] Alexander Maedche, Boris Motik, Nu no Silva, and Raphael Volz. *Mafra a mapping framework for distributed ontologies.* In Proceedings of the 13th European Conference on Knowledge Engineering and Knowledge Management EKAW-2002, Madrid, Spain, 2002.

[2] AnHai Doan, Jazant Madhaven, Pedro Domingos, and Alon Halevy. *Ontology matching: A machine learning approach.* In Ste_en Staab and Rudi Studer, editors, Handbook on Ontologies in Information Systems, pages 397 - 416. Springer-Verlag, 2004.

[3] Atanas Kiryakov, Kiril Iv. Simov, and Marin Dimitrov. Ontomap: *The upper-ontology portal.* In Proceedings of "Formal Ontology in Information Systems", Ogunquit, Maine, 2001.

[4] Bernhard Ganter and Rudolph Wille. *Formal concept analysis: Mathematical Foundations.* Springer, Berlin-Heidelberg, 1999.

[5] Borys Omelayenko and Dieter Fensel. *A two-layered integration approach for product information in B2B e-commerce.* In Proceedings of the Second Intenational Conference on Electronic Commerce and Web Technologies (EC WEB-2001), Munich, Germany, 2001. Springer-Verlag.

[6] Dejing Dou, Drew McDermott, and Peishen Qi. *Ontology translation by ontology merging and automated reasoning.* In Proc. EKAW2002 Workshop on Ontologies for Multi-Agent Systems, pages 3 - 18, 2002.

[7] Erhard Rahm and Philip A. Bernstein. *A survey of approaches to automatic schema matching.* VLDB Journal: Very Large Data Bases, 10(4):334 - 350, 2001.
[8] Fausto Giunchiglia and Pavel Shvaiko. *Semantic matching.* The Knowledge Engineering Review, 18(3):265 - 280, 2004.
[9] Gerd Stumme and Alexander Maedche. *Fca-merge: Bottom-up merging of ontologies.* In 7th Intl. Conf. on Artificial Intelligence (IJCAI '01), pages 225 - 230, Seattle, WA, USA, 2001.
[10] A. Y. Halevy, *Answering queries using views: a survey.* In: VLDB Journal. Vol.10, No.4, pp. 270-294, 2001.
[11] Hans Chalupsky. OntoMorph: *A translation system for symbolic knowledge.* In Anthony G. Cohn, Fausto Giunchiglia, and Bart Selman, editors, KR 2000, Principles of Knowledge Representation and Reasoning Proceedings of the Seventh International Conference, pages 471 - 482, Breckenridge, Colorado, USA, 2000. Morgan Kaufmann Publishers.
[12] Jena http://jena.sourceforge.net/
[13] Marc Ehrig and Steffen Staab. *QOM - quick ontology mapping.* In Frank van Harmelen, Sheila McIlraith, and Dimitris Plexousakis, editors, Proceedings of the Third International Semantic Web Conference (ISWC2004), LNCS, pages 683 - 696, Hiroshima, Japan, 2004. Springer.
[14] Marc Ehrig and York Sure. *Ontology mapping - an integrated approach.* In Proceedings of the First European Semantic Web Symposium, ESWS 2004, volume 3053 of Lecture Notes in Computer Science, pages 76 - 91, Heraklion, Greece, May 2004. Springer Verlag.
[15] Michel Klein. *Combining and relating ontologies: an analysis of problems and solutions.* In Asuncion Gomez-Perez, Michael Gruninger, Heiner Stuckenschmidt, and Michael Uschold, editors, Workshop on Ontologies and Information Sharing, IJCAI'01, Seattle, USA, August 4 - 5, 2001.
[16] OWLIM http://www.ontotext.com/owlim/
[17] Natalya F. Noy and Mark A. Musen. *Anchor-prompt: Using non-local context for semantic matching*. In Proceedings of the Workshop on Ontologies and Information Sharing at the Seventeenth International Joint Conference on Artificial Intelligence (IJCAI-2001), Seattle, WA, USA, 2000.
[18] Natalya F. Noy and Mark A. Musen. *Prompt: Algorithm and tool for automated ontology merging and alignment.* In Proc. 17th Natl. Conf. On Artificial Intelligence (AAAI2000), Austin, Texas, USA, July/August 2000.
[19] Nuno Silva and Jo ao Rocha. *Service-oriented ontology mapping system.* In Proceedings of the Workshop on Semantic Integration of the International Semantic Web Conference (ISWC2003), Sanibel Island, USA, 2003.
[20] Pepijn R. S. Visser, Dean M. Jones, T. J. M. Bench-Capon, and M. J. R. Shave. *An analysis of ontological mismatches: Heterogeneity versus interoperability*. In AAAI 1997 Spring Symposium on Ontological Engineering, Stanford, USA, 1997.
[21] Scharffe F. and Bruijn J.D., *A language to specify mappings between ontologies* In Proceedings of SITIS, 2005, pp.267-271.
[22] Sesame http://www.openrdf.org/
[23] SINUS project http://sinus.iinf.bas.bg/
[24] SparcQL query language http://www.w3.org/TR/rdf-sparql-query/
[25] Web Ontology Language (OWL) http://www.w3.org/TR/owl2-overview/

Structural Organization of Anatomical Data Using XML Technologies

Goran S. Krstic[1], and Zoran Z. Stanković[2]

Abstract - **This paper describes the basics necessary for building an educational system in the field of anatomy using XML technologies. It contains the original XML schema for hierarchical structuring of anatomical data. It also contains a discussion on the possibilities of implementation.**

Keywords - **XML, XML Schema, XPath, XSL, SVG, Anatomical Data.**

I. Introduction

XML (*Extensible Markup Language*) is able to represent any kind of structured and semi-structured data. As a meta-signifying language, it has enabled the development of many other new signifying languages (vocabularies). These vocabularies are defined by XML schemas (*XML Schema Language*). XML schemas are used to specify the structure of XML documents and requests that need to be answered. The wide range of XML's possibilities mostly stem from the strict rules under which the documents can be created. Languages based on XML are independent from the platform, simple for lexical analysis, with well-defined syntax, easily read by people, and there are a lot of tools for lexical analysis and manipulation of XML data.

Furthermore, xml belongs to a family of technologies which rapidly develop. Today, XML technologies have a wide range of appliance, from document development, through developing multi-layer (*n-tier*) applications and Web services, to semantic Web, in all areas of human functioning (business, medicine, education, government organizations etc.)

This paper gives the basics needed for the realization of educational system in the field of anatomy. XML is considered to be a mature technology, which helps realize an advanced educational system. At the end of the paper, the analyzed possibilities and ways of implementation are summed up. We have also pointed out some conceptual advantages that the displayed solution is expected to have in relation to the existing programs in this area, which primarily rely on the multimedia aspect.

[1]Goran Krstic is with the College of Agriculture and Food Technology, Cirila and Metodija 1, Prokuplje, Serbia, E-mail: gorca@ni.ac.rs.

[2] Zoran Stankovic is with the Faculty of Electronic Engineering, Aleksandra Medvedeva 14, 18000 Nis, Serbia, E-mail: zoran.stankovic@elfak.ni.ac.rs.

II. XML Schema

All living systems are hierarchically organized [1]. The human organism is composed of organ systems, nine of them altogether. Organic systems, as indicated by the term, are composed of several organs, which are composed of various tissues built of one or more types of cells. The human organism, anatomically seen, may represent the best example of hierarchical organization and order in nature (Figure 1). Therefore, it is the best to represent anatomical data by a hierarchical structure provided by XML.

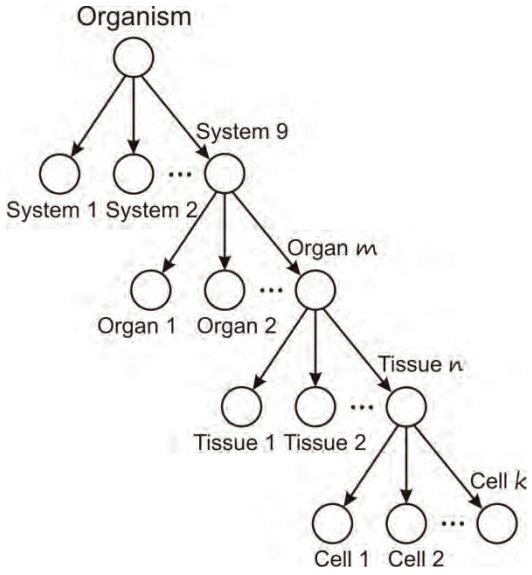

Fig.1. *Hierarchical organization of human organism.*

The numbers *m*, *n*, *k* relate to the number of types of entities, instead of their total number.

XML schema language is able to model any hierarchy that is generally plausible to specify [2, 3, 4]. The XML *Anatomy* schema follows the hierarchical structure of an organism:

```
<?xml version="1.0"?>
<xsd:schema xmlns:xsd="http://www.w3.org/2001/XMLSchema">
    <!-- XML Schema Anatomy.xsd -->
    <xsd:element name="Organism">
        <xsd:complexType>
            <xsd:sequence>
                <xsd:element ref="Latin-name"/>
                <xsd:element ref="English-name"/>
                <xsd:element ref="Serbian-name"/>
                <xsd:element ref="Description"/>
                <xsd:element ref="System" maxOccurs="9"/>
            </xsd:sequence>
        </xsd:complexType>
    </xsd:element>
    <xsd:element name="System">
```

```
        <xsd:complexType>
            <xsd:sequence>
                <xsd:element ref="Latin-name"/>
                <xsd:element ref="English-name"/>
                <xsd:element ref="Serbian-name"/>
                <xsd:element ref="Description"/>
                <xsd:element ref="Organ"
                 maxOccurs="unbounded"/>
            </xsd:sequence>
        </xsd:complexType>
    </xsd:element>
. . .
    <xsd:element name="Cell">
        <xsd:complexType>
            <xsd:sequence>
                <xsd:element ref="Latin-name"/>
                <xsd:element ref="English-name"/>
                <xsd:element ref="Serbian-name"/>
                <xsd:element ref="Description"/>
                <xsd:element ref="Part" minOccurs="0"
                 maxOccurs="unbounded"/>
            </xsd:sequence>
        </xsd:complexType>
    </xsd:element>
    <xsd:element name="Part">
        <xsd:complexType>
            <xsd:sequence>
                <xsd:element ref="Latin-name"/>
                <xsd:element ref="English-name"/>
                <xsd:element ref="Serbian-name"/>
                <xsd:element ref="Description"/>
                <xsd:element ref="Sub-part" minOccurs="0"
                 maxOccurs="unbounded"/>
            </xsd:sequence>
        </xsd:complexType>
    </xsd:element>
. . .
    <xsd:element name="Latin-name" type="xsd:string"/>
    <xsd:element name="English-name" type="xsd:string"/>
    <xsd:element name="Serbian-name" type="xsd:string"/>
    <xsd:element name="Description" type="xsd:string"/>
</xsd:schema>
```

Elements of the schema correspond to the entities composing the organism. The *Description* element is used as the container element and is supposed to embody the main part of the educational content. Moreover, the *Description* element should include links to other elements in the document, which provides a mixed structured of this element and an XML oriented towards (*document-centric*, *document-oriented)*. This brings about new issues in the implementation phase. For example, relational data bases can only accept a data-oriented XML. More about it at the end of work.

The role of the *Part* element is dual. On the one hand, it includes parts of entities which comprise the hierarchical structure, and on the other hand it includes all the macroscopically visible elements that are not directly incorporated in the hierarchical structure (upper part, lower part, front, back).

For reasons of clarity and visibility, in the first illustration, the schema is not burdened with details. In the implementation phase, it is possible to add various restrictions, which provides better control and validity of the document. For example, it can be ensured that an element is not left empty during the insertion of data into the XML document, i.e. – that it contains at least one character.

```
<xsd:element name="Latin-name">
    <xsd:simpleType>
        <xsd:restriction base="xsd:string">
            <xsd:minLength value="1"/>
        </xsd:restriction>
    </xsd:simpleType>
</xsd:element>
```

Needless to say, the schema is not final; it is open to development and upgrading before implementation, as well as in the implementation phase itself.

III CREATING A DOKUMENT

In XML terminology, there are two terms related to the accuracy of the document, i.e. the XML document can be well-formed and valid. A well-formed document fulfills the basic XML syntax. A valid document is a well-formed document that also responds to the structure defined by the XML schema.

All documents must be well-formed, but not necessarily valid. However, a valid document has certain advantages. Checking the validity ensures that the document responds to a certain structure and satisfies the standards demanded. If a part of the document does not respond to the specification in the schema, the processor shows an error notification, and therefore the necessary corrections can be made. The following document is a valid one that fulfills the standards specified by XML *Anatomy* schema:

```
<?xml version="1.0"?>
<?xml:stylesheet type="text/xsl" href="Anatomy.xsl"?>
<!-- Dokument Anatomy.xml -->
<Organism xmlns:xsi="http://www.w3.org/2001/XMLSchema-instance"
xsi:noNamespaceSchemaLocation="Anatomy.xsd">
    <Latin-name>Human</Latin-name>
    <English-name>Man</English-name>
    <Serbian-name>Čovek</Serbian-name>
    <Description>The most perfect organism on earth
...</Description>
    <System>
        <Latin-name>Sceletus</Latin-name>
        <English-name>Skeletal system</English-name>
        <Serbian-name>Koštani sistem</Serbian-name>
        <Description>Every living thing has its own form and
          structure. The skeletal system is ...</Description>
        <Organ>
            <Latin-name>Femur</Latin-name>
            <English-name>Femur</English-name>
            <Serbian-name>Butna kost</Serbian-name>
            <Description>Femur is the largest bone in the human
            body. Belongs to ...</Description>
            <Part>
                <Latin-name>Trochander major</Latin-name>
                <English-name>Big wheel</English-name>
                <Serbian-name>Veliki kotur</Serbian-name>
                <Description>Forms part of ...</Description>
            </Part>
            <Part>
                <Latin-name>Trochander minor</Latin-name>
                <English-name>Smal wheel</English-name>
                <Serbian-name>Mali kotur</Serbian-name>
                <Description>Forms part of ...</Description>
            </Part>
            <Tissue>
                <Latin-name>Bone tissue</Latin-name>
                <English-name>Bone tissue</English-name>
                <Serbian-name>Koštano tkivo</Serbian-name>
```

```
                <Description> Falls into the category of connective
                 tissue... </Description>
                <Cell>
                    <Latin-name>Osteocit</Latin-name>
                    <English-name>Osteocyte</English-name>
                    <Serbian-name>Osteocit</Serbian-name>
                     <Description>Osnovna ćelija koštanog tkiva...
                      </Description>
                </Cell>
                <Cell>
                    <Latin-name>Osteoblast</Latin-name>
                    <English-name>Osteoblast</English-name>
                    <Serbian-name>Osteoblast</Serbian-name>
                    <Description>Mlade ćelije koje ...</Description>
                </Cell>
            </Tissue>
        </Organ>
    </System>
</Organism>
```

XML is not only a signifying language; it also represents an almost ideal way of structuring data. The given document is barely larger that the minimal one that satisfies the rules specified in the schema. In the realization phase, a far larger XML document is given, perhaps even the largest one so far.

IV. ADVANTAGES OF USING XML TECHNOLOGIES

The existing educational programs in this area have relatively good possibilities of visualization and animation. The disadvantage is bad organization of data, which does not follow the hierarchical structure of organism. Their crucial disadvantage is the lack of browsing possibilities by using a questioning language. The data is organized into lessons accessed from a formerly established menu.

Once we have structured data in XML format, huge possibilities are achieved. Here is an attempt to systematize them and point out each of the advantages of using XML technologies:

Data storage. Even though an XML document can basically be placed in a relational or object-relational database, the Native XML Database should be primarily considered.

The source XML databases are also appropriate for *data-centric* and *document-centric* applications. They have an XML document for a fundamental unit of logical data storage, just like the relational database has syllable tables as its fundamental unit of logical storage. This group of databases includes Tamino, Ipedo, dbXML, etc. With these databases, there is no conversion, the data remain in XML format, which in this case makes them the best choice for storage of XML coded anatomical data.

Searching. The languages currently existing used in commercial products are SQL and Xpath (*XML Path Language*). It is evident that relational products will be browsed using SQL, while XML data will be browsed with XPath. In relation to this, their possibilities are to be considered.

If requests are to be made over the recursive data structure, XPath is more suitable than the "syllabic" RDBMS and SQL. For example, if we need to find out which parts (ingredients), sub-parts, or even sub-sub parts a certain element contains, languages based on XPath will handle this kind of data better than SQL-based languages. On the other hand, SQL has a far richer collection of operators for manipulating data than XPath languages. In the particular case discussed here, there are no mathematical operations with the elements, so XPath tends to be the language that is more suitable for data browsing.

Supposing we are not using XML and we want to place the data in a relational database. A relational representation could be achieved by *master-detail* organization of tables that would follow the hierarchical structure of organism in Illustration 1. However, on the lowest level, there would be a plethora of tables ($m*n*k$), which would result in too many contactenations, making the requests too long and practically unworkable. For example, if we wanted to select all types of cells in the organism, we would generally have the following situation:

$table_1.key = table_2.key$ and $table_2.key = table_3.key$ and ... and $table_{n-1}.key = table_n.key$

Xpath expression is far simpler:

```
//Cell
```

Selects all the elements in the document named *Cell*.

Data display. Not presuming the final solution, it is clear that the most natural way of displaying XML data is by using XSL stylesheets (*Extensible Stylesheets language*). By using Xlink (*XML Linking Language*) for referring and SVG (*Scalable Vector Graphics*) picture format, the use of XML technologies would be fully encompassed. SVG has the advantage over other formats, because it uses XML syntax for inscription of geometrical shapes. This provides various possibilities for working with images, such as interactivity, animation, reaction to different events, etc. [5]. Apart from that, it the data are placed in an XML database, the solutions these bases offer for storage and working with images are also available.

Application. Using the potentials of a database in which XML data are placed, it is also easy to construct a Web application, which would provide an *on-line* anatomy and enable e-learning. The vision goes so far as to also enable a *stand-alone* application that would provide a three-dimensional display of elements, their rotation and interaction. We agree that this is not so easy to achieve at the moment, but this possibility should be pursued.

Level of detailisation. It is important to notice that XML data are separated from display. The same XML document can be displayed in several ways, without making any changes in the document itself. In relation to that, it is possible to determine the level of detail of the display, where one level or degree of details would be used for students, and another one for specialists, for example - i.e., it would show even the smallest details. It is possible to further separate the sub-documents and get histology (the branch of anatomy dealing with tissues), or cytology (the branch of anatomy dealing only with cells)

Semantic upgrading. It is possible to use one of the languages of semantic Web (RDF and RDFS) to build classes that would correspond the hierarchical structures of the organism (metaphorically seen, of course, since an organ is not precisely a sub-class of the organism. XML data can be used to fill instances, which would form an information base. If RDF(S) were to be used, it would be possible, using GSS (*Graph Stylesheets Language*), to get a certain diagram display of the organism. It is also possible to further improve the system by developing ontology. By the implementation of knowledge, certain aspects of organism functioning, i.e. physiology, could be enveloped.

Multilinguality. It is possible to efficiently organize the educational content and implement multilinguality in an entirely uniform way.

The best results would be achieved by using: an XML database for storing XML documents, XPath question language for browsing, XSL stylelist to display data and SVG format for the images.

V. CONCLUSION

This paper lays out the original XML schema for hierarchical structuring of anatomical data. The basics necessary for the realization of an advanced educational system in the field of anatomy by using the advantages of XML technology are laid out. It is our opinion that the recommended solution will enable efficient structuring of content and implementation of multilinguality.

REFERENCES

[1] G. Tortora, Principles of Human Anatomy, 6th ed., HarperCollins Publishers, New York, 1992.

[2] A. Skonnard, "Designing XML Schema Libraries", http://msdn.microsoft.com/library/

[3] XML Schema Part 1: Structures, W3C Recommendation 2 May 2001, http://www.w3.org/TR/xmlschema-1/

[4] XML Schema Part 2: Datatypes, W3C Recommendation 02 May 2001, http://www.w3.org/TR/xmlschema-2/

[5] Scalable Vector Graphics (SVG) 1.1 Specification, W3C Recommendation *14 January 2003* http://www.w3.org/TR/SVG11/

Architecture of Adaptive Geospatial Data Visualization

Danilo Vulović[1], Miloš Bogdanović[2] and Leonid Stoimenov[3]

Abstract – **This paper presents our research in the area of Geographic Information Systems (GIS) and adaptive geospatial data visualization. As a result of this research, we have developed architecture of the system that enables adaptive geospatial data visualization according to context-relevant information. This architecture is provisioned as open, scalable and interoperable environment. It is based on SOA and follows the architectural principles of the most prominent SOA examples. Also, our proposal was designed to be highly modular and mainly built-up of service instances developed according to Open Geospatial Consortium (OGC) specifications.**

Keywords – **context, adaptive visualization, GIS, Web.**

I. INTRODUCTION

The increasing presence of Internet in all fields of life and business led to mass usage of GIS tools. Nowadays, contemporary GIS tools are used by average users via their computers, smart phones or tablets. A majority of spatial data transfer is accomplished through the Internet via standardized Web Services which sometimes offer large quantities of spatial data. In order to solve the problem of large quantities of spatial data, services need to efficiently and appropriately filter provided data for a single user or a particular situation according to user-defined and/or situation-driven visualization preferences.

In addition to the ability of geospatial data filtering, contemporary GIS tools need to enable control of graphical representation of geographic objects by GIS users. The control of graphical representation is usually accomplished by defining styles that will be used to display the group or individual geographic objects and maps. Different styles used for geospatial data representation are created according to user needs and demands.

Nowadays, GIS tools are able to perform adaptive geospatial data visualization on the basis of the description of the situation and preferred user style. This type of a description usually consists of information that should affect application running and appearance and is referred to as context [3].

Contextual information enables users to indirectly affect geospatial data appearance. Contemporary GIS should be able to receive contextual information and perform the adoption of geospatial data representation according to contextual information. According to Open Geospatial Consortium (OGC) standards, this process is effectively delegated to multiple Web services. As a consequence, a retrieval of the contextual information and a determination of the user context are often implemented as functions of a separate Web service [12]. This service is used as a proxy between users and geospatial data visualization services and is responsible for selecting an appropriate symbology. In order to enable systems for adaptive geospatial data visualization, during design process of system architecture, it is necessary to enable the usage of such service.

The rest of this paper will propose architecture of adaptive geospatial data visualization using Service Oriented Architecture paradigm. This architecture introduce services that are able to perform adoption of geospatial data using existing services designed according to Open Geospatial Consortium (OGC) standards and specifications. These services are specified in accordance with OGC Web Service Common Standard [10]. The proposed architecture enables the usage of distributed geospatial data style repositories [2] and their integration with user contexts. OGC Web Map Context Documents implementation specification [6] has been used for the development of context documents. After presenting adaptive geospatial data environment, these services will prove to be capable of supporting the adaptation of geospatial data representation on both server (such as Web Map Service) and client (desktop, Web, mobile GIS) side.

II. RELATED WORK

In the process of Geo-Information System (GIS) development the importance of visual identification of geospatial data cannot be ignored [7][8]. Significant effort has been made towards developing styles used for visualization of geographic objects and maps. As a result, different styling languages and catalogues of styles have been proposed. OGC proposed Geography Markup Language (GML) [9] which was combined with Scalable Vector Graphics (SVG) [16] and XSL Transformation [15] for the purpose of geospatial data visualization, mostly within Web GIS clients [5, 14]. Styled Layer Descriptor (SLD) [8] and Symbology Encoding (SE) [7] styling language specifications have also been proposed by OGC. Aside from languages coupled with specific systems, such as Cartographic Markup Language (CartoML) [1] and Diagram Markup Language (DiaML) [13], OGC SLD and SE have been broadly accepted and used. Recent research has shown that usage of these styling languages, in combination with information regarding GIS user context, can highly improve usability of GIS [4, 11, 12]. This is one of the reasons

[1]Danilo Vulović is with the Faculty of Electronic Engineering, Aleksandra Medvedeva 14, 18000 Nis, Serbia, E-mail: danilo.vulovic@elfak.ni.ac.rs

[2]Miloš Bogdanović is with the Faculty of Electronic Engineering, Aleksandra Medvedeva 14, 18000 Nis, Serbia, E-mail: milos.bogdanovic@elfak.ni.ac.rs

[3]Leonid Stoimenov is with the Faculty of Electronic Engineering, Aleksandra Medvedeva 14, 18000 Nis, Serbia, E-mail: leonid.stoimenov@elfak.ni.ac.rs

why an effort has been made in order to make GIS able to adapt geospatial data visualization according to user needs, e.g. towards performing adaptive (contextual) cartographic visualization [4, 11, 12].

A majority of solutions that support adaptive (contextual) cartographic visualization is based on client–server architecture. [11] proposed a solution for adaptive visualization of geospatial information on mobile devices. Partially because of the limitations that this environment introduces, adaptive cartographic visualization was performed on the server side while client side was only responsible for presentation of geospatial data. This solution uses a set of predefined context types. Similar solution can be found in GiMoDig project [12], which is also based on client-server architecture. GiMoDig architecture introduces extensions of WMS and WFS specification used for the purpose of establishing communication between server and client side. Context types used in this architecture are invariant.

Probably the most similar solution to one presented in this paper and one of the best implementation we encountered is named Sissi – Contextual Map Service. This solution was designed in 2007 [4]. Sissi is also based on client-server architecture. However, compared to previously described solutions, Sissi differs in more that few characteristics which are, in our opinion, very significant. Unlike mentioned solutions, Sissi does not have a predefined set of elementary context types. Therefore, it is capable of supporting different contexts. Its specification is based on WMS specification with extending requests – GetElementaryContextType and GetMapWindows. Also, WMS GetCapabilities request has been modified in order to include additional context parameter. Context parameter is used for user context encoding in the form comma-separated context values. Symbology of the adaptive (contextual) maps is an integral part of Sissi and is defined using SLD specification.

However, Sissi context types are not developed according to Web Map Context Documents specification. Since it extends WMS specification, Sissi is capable of performing rendering functions in terms of merging images from different WMS services. This can multiply request towards existing WMS services. Further, Sissi environment does not involve the usage of WFS services. If clients are capable of adapting geospatial data presentation according to style provided on the bases of the context, than the usage of WFS services is more than legitimate. Also, it is our opinion that the symbology should not be restricted to SLD and that it should be provided by independent services, e.g. style repositories [2].

The purpose of the previous discussion is to indicate the advantages that our proposed architecture introduces. The architecture of adaptive geospatial data visualization introduces new stand-alone services (Web Map Context Service and Context Proposal Service) which are able to a perform adoption of geospatial data according to user requirements. These services perform adaptation in combination with existing services which provide geospatial data and styles and do not require any extension of these services in terms of additional functions or modification of the existing one. The basis for development of introduced services is OGC Web Service Common Standard (Open Geospatial Consortium). Styles that are used for adaptation of geospatial data are acquired from previously developed remote repositories [2]. Styling document is created according to Symbology Encoding [7] or Styled Layer Descriptor [8] specifications. User context used by services within proposed architecture is developed according to Web Map Context Documents [6] implementation specification.

III. ARCHITECTURE

The main objective of the proposed architecture and its components is to provide GIS users with appropriately visualized geospatial data according to user-relevant information, e.g. user context. The system is built on the basis of Service Oriented Architecture (SOA) principles and contains services which provide geospatial data, perform visualization and maintain user contexts.

The architecture of adaptive geospatial data visualization uses existing services that provide geospatial data and style documents. These services are developed according to available OGC standards and specifications. Furthermore, proposed architecture introduces new services which are responsible for maintaining context documents and the adaptation of requested geospatial data according to user-defined visualization preferences.

The architecture consists of several layers that include components responsible for adaptive geospatial data visualization, as shown in Fig. 1:

- **Geospatial Data Repositories** – This layer consists of any available data repository which provides geospatial data: legacy RDBMS, DBMS with spatial extension or file system.
- **Data Access Services** – Services that provide geospatial data (WFS) and perform their visualization (WMS) are the components of data access layer. The proposed architecture enables the usage of WMS services which support SLD styling as well as WMS services which do not support SLD styling. Data access services provide geospatial data which can be used in different contexts. In order to be available to system users, these services have to be registered within Web Map Context Service. Users use layer information from any of the registered services to create context documents according to their needs.

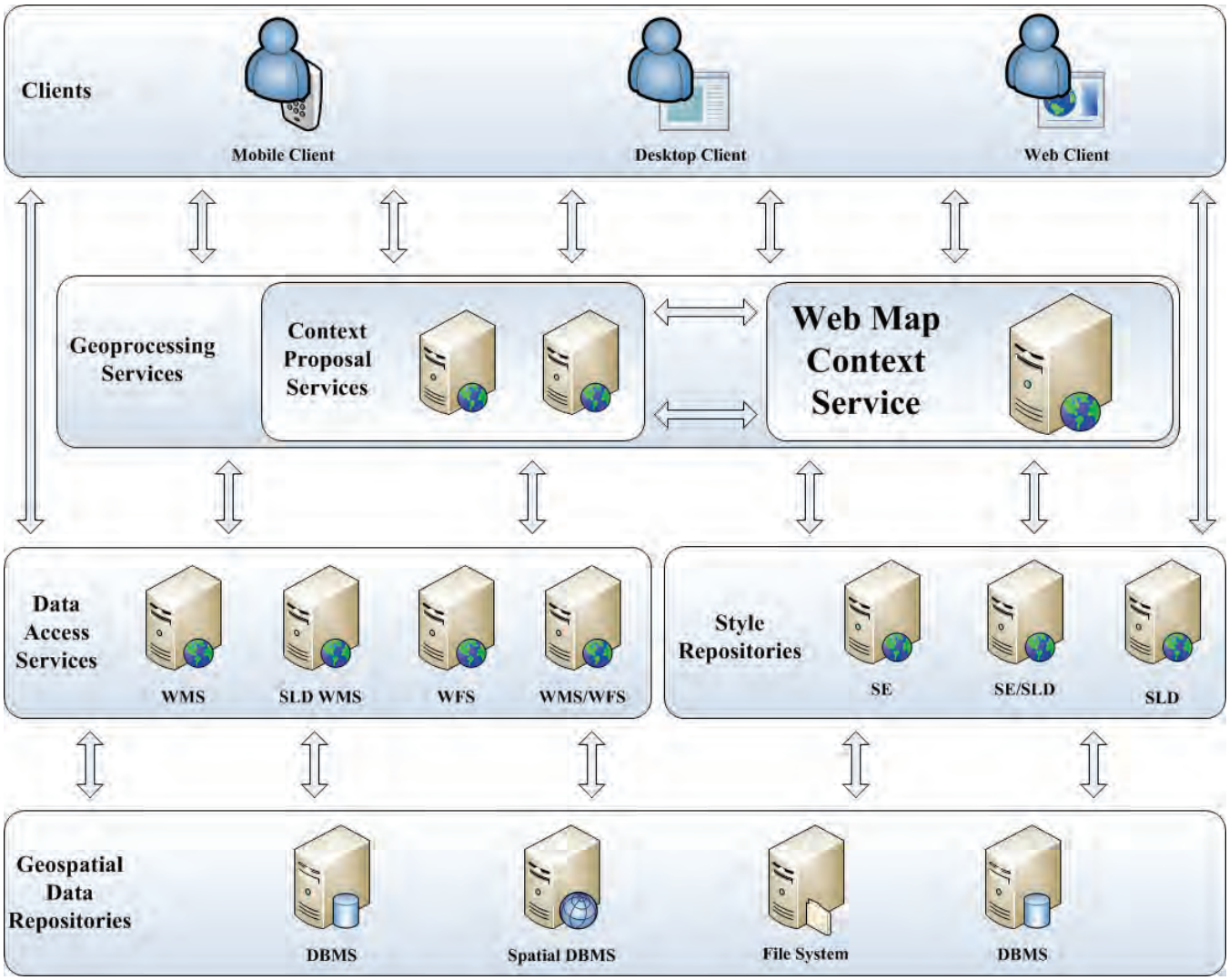

Figure 1. Layered architecture capable to perform adaptation of geospatial data

- **Style Repositories** – Services that provide styling document developed using Styled Layer Descriptor or Symbology Encoding styling language. Styling documents contain information used for appropriate geospatial data visualization. These documents are used in order to create and register contexts within Web Map Context Services. These services also have to be registered within Web Map Context Service.
- **Geoprocessing Services** – The geoprocessing services layer is responsible for the maintenance of the user context and represents the foundation for the adaptive visualization processes. This layer uses user context information stored in context document created according to OGC Web Map Context Documents implementation specification. Furthermore, this layer consists of two main services: Web Map Context Service (WMCS) and Context Proposal Service (CPS). WMCS maintains information considering all registered services and style repositories in the system, maintains information considering registered user contexts and provides them to the clients. CPS is an open, customizable service that can be implemented by a third-party according to their needs. The purpose of this service is to enable users to obtain specific context that describes the situation that is of users' interest, e.g. probably similar to the situation the user is currently in.
- **Clients** – Platform independent GIS applications capable of displaying geospatial data according to user's context. These applications have to be able to understand context documents received from one of the geoprocessing components. Also, these applications have to be able to create requests to data access components or style repositories and properly display received data. If the context consist layers from the WMS services, the client creates an appropriate GetMap request with information from context document, sends request to the WMS and displays the resulting image. Client is responsible for embedding SLD document into WMS request if the SLD styling is supported by the WMS service. In order to visualize geospatial data acquired from the WFS service, clients need to have a mechanism which enables visualization of data acquired from WFS according to styles obtained from one of the Style Repository Services.

Architecture of adaptive geospatial data visualization was designed to be highly modular and mainly built-up of service instances developed according to Open Geospatial

Consortium (OGC) specifications. The system developed according to the presented architecture is capable of adapting large quantities of geospatial data based on different users' needs without changing its internal structure. This ability illustrates the level of system's modularity. Another advantage of our proposal is introduced through the usage of WMCS instances and reflected by the fact that WMCS instances do not require any extension or modification of the existing service instances developed according to OGC specifications. Therefore, any existing service oriented GIS architecture can easily adopt WMCS instances and become capable of performing adaptive geospatial visualization.

IV. Conclusion

In this paper we have presented architecture which is starting point for the development of GIS environment capable of supporting adaptive geospatial data visualization. Through the presented architecture we introduce new services developed according to OGC Web Service Common Standard. These services are responsible for efficient and appropriate geospatial data filtering. Presented environment does not require any further modifications of the existing services developed in accordance with OGC specification which means that this architecture design can be used for the extension of an existing interoperable GIS environment. Furthermore, symbology used for adaptation of geospatial data visualization is delegated to styling documents repository services used by WMCS in combination with appropriate contexts.

Future research and development of the presented architecture should cover development and extension of Web Map Context Service in term of new operations. WMCS will be able to transform styling documents developed according to third-party styling languages into styling documents developed according to OGC specification. Each styling language developer should be able to register a XSLT or procedural transformation of its styling language into SLD or SE.

Since the Context Proposal Service allows obtaining of already-existing similar contexts, future research should cover development of different methods for context similarity according to situation the user is currently in.

It is our opinion that these improvements would lead WMCS and the proposed system towards becoming a solution highly applicable within any adaptive geospatial data visualization environment.

Acknowledgement

Research presented in this paper were partially funded by the Ministry of Science of the Republic of Serbia and PD Jugoistok Niš, within the project in the field of technological development "Intelligent integration of geo-, business and technical information on the company level", ev. No. 13003.

References

[1] Baer H.R. (2003) iMap Documentation. Institute of Cartography, ETH Zurich, Zurich, http://www.ika.ethz.ch/statlas/imap/index.htm

[2] Bogdanović M., Vulović D., Stoimenov L. (2010) Symbology Encoding Repository, in Proceedings of 13th AGILE International Conference on Geographic Information Science 2010, Guimaraes, Portugal, 10.-14. May, ISBN: 978-989-20-1953-6, http://agile2010.dsi.uminho.pt

[3] Kozel J., (2007) Open Contextual Cartographic Visualization, in Proceedings of GI-Days, pp. 223-227, Munster, Germany, ISBN: 978-3-936616-48-4

[4] Kozel, J., Stampach, R. (2010): Practical Experience with Contextual Map Service. In Konecny, M., Zlatanova, S., Bandrova, T.: Geographic Information and Cartography for Risk and Crisis Management. London : Springer. ISBN: 978-3-642-03441-1.

[5] Mathiak B., Kupfer A., Neumann K. (2004) Using XML languages for modeling and Web-visualization of geographic legacy data, GeoInfo, Campos do Jordão. Sociedade Brasileira de Computação

[6] Open Geospatial Consortium, Inc. (2005) OGC Web Map Context Documents Implementation Specification, 05-005, Version 1.1.0, http://www.opengeospatial.org/standards/wmc

[7] Open Geospatial Consortium, Inc. (2006) OpenGIS Symbology Encoding Implementation Specification, 05-077r4, Version 1.1.0, http://www.opengeospatial.org/standards/symbol

[8] Open Geospatial Consortium, Inc. (2007a) OpenGIS Styled Layer Descriptor Profile of the Web Map Service Implementation Specification, 05-078r4, Version 1.1.0

[9] Open Geospatial Consortium, Inc (2007b) OpenGIS Geography Markup Language (GML) Encoding Standard. 07-036. Version 3.2

[10] Open Geospatial Consortium, Inc. (2010) OGC Web Service Common Standard, 06-121r9, Version 2.0.0, http://www.opengeospatial.org/standards/common

[11] Reichenbacher, T. (2004) Mobile Cartography-Adaptive Visualisation of Geographic Information on Mobile Devices. Dissertation submitted at the Institute of Photogrammetry und Cartography, Technical University, Munich

[12] Sarjakoski T., Sester M., Sarjakoski L. T., Harrie L., Hampe M., Lehto L., Koivula, T. (2005) Web generalisation services in GiMoDig – Towards a standardised service for real-time generalisation, in Proceedings of 8th AGILE International Conference on Geographic Information Science 2005, Estoril, Portugal, 26.-28. May, pp. 509-518, ISBN: 972-8093-13-6, http://plone.itc.nl/agile_old/Conference/estoril/themes.htm

[13] Schnabel O., Hurni L. (2007) Diagram Markup Language - A New Model for Symbolization in Internet Maps, Proceedings of the International Cartographic Conference, Theme 12, Oral 2, Moscow

[14] Tennakoon W.T.M.S.B. (2003) Visualization of GML data using XSLT, Msc Thesis, ITC, Emschede, 60 pp., http://www.itc.nl/library/papers_2003/msc/gim/tennakoon.pdf

[15] World Wide Web Consortium (W3C) (1999) XSL Transformations (XSLT), Version 1.0., http://www.w3.org/TR/1999/REC-xslt-19991116

[16] World Wide Web Consortium (W3C) (2009) Scalable Vector Graphics (SVG) 1.0 Specification. http://www.w3.org/TR/2000/WD-SVG-20000629/

Web Service Based Modular Architecture for 3D Web Visualization of Geo-referenced Data

Igor Antolović[1], Miroslav Milivojević[2], Dejan Rančić[3], Vladan Mihajlović[4]

Abstract – **This paper presents a service based architecture for 3D Web visualization of geo-referenced data which relies on the GinisVis library. The GinisVis visualization library combines server .NET and client AJAX/WebGL technology as well as modular workflow approach in order to efficiently visualize geo-referenced data obtained from geospatial Web services like WFS and WMS. As a proof of concept a prototype Web application for 3D visualization of terrain and geo-referenced objects is created. It is shown that this architecture presents a flexible and stable platform for future rapid development of 3D Web GIS applications.**

Keywords – ***Modular, 3D Web visualization, Web service***

I. Introduction

Web service based architectures are becoming increasingly popular in the past few years. Applications of existing Web services are various ranging from language translation, word search, weather information, 2D geo-referenced map rendering etc. Communication with Web services is accomplished using open standards such as SOAP (Simple Object Access Protocol) which defines the XML data message format as well as WSDL (Web Services Description Language) which was designed with the aim to provide Web service description.

Availability and standardization of Web services has greatly influenced the migration of existing desktop architecture based applications into the Web environment.

Existing solutions for client-server based 3D data visualization rely mostly on thin Web clients. These are simple Web clients which are able to display a 3D model image which is entirely generated on the server side. This approach has shown to be very reliable in the past since Web technologies did not allow 3D rendering on the client side. Other existing alternatives require installation of additional plug-ins which would lead to many problems in terms of compatibility and usability.

In this paper, special attention will be devoted to Web applications for 3D data visualization which have become practically possible with the recently introduced WebGL standard [1] which provides hardware support for OpenGL ES 2.0 within the standard Web browsers.

The aim of this paper is to consider a Web service architecture, which should serve as a solid and flexible platform for efficient development of 3D Web GIS (Geographic Information Systems) applications [2,3] that would enable geo-referenced 3D object rendering using open standard Web technologies. It is important to emphasize that the starting point in designing this architecture is based on a workflow methodology. The basic concept of this idea is shown in Fig. 1.

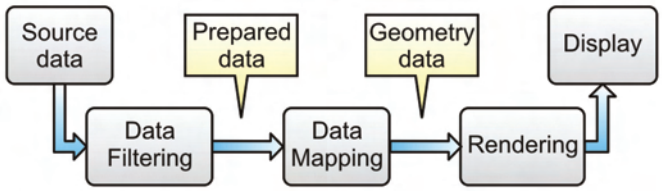

Fig. 1. Basic workflow graph

The data from the source domain is first filtered and then mapped on geometric primitives which can be rendered and than displayed. Within this kind of system the data can pass through one or more filters. Each filter usually implements a relatively simple function which processes the input data by additionally taking into account various input parameters.

This paper first gives an overview of existing 3D Web data visualization solutions followed by a description of the GinisVis client-server architecture. Finally a minimum set of modules is introduced in order to enable modeling of a 3D terrain as well as 3D geo-referenced buildings.

II. Related Work

There are many examples of desktop environments that provide a user interface for interactive workflow creation in order to obtain rather complex data visualizations. Among such applications one example is VisTrails[4] which is a scientific workflow management system that provides rich support for data exploration and visualization and relies on the VTK[5] (Visualization Toolkit) library that implements a wide set of algorithms for 3D data processing. This and similar environments have influenced the development of various Web based data visualization applications in the past several years. Among existing 3D Web visualization solutions ParaviewWeb[6] is distinguished by its robustness and capabilities. This environment is based on a thin client which provides 3D data display as well as an intuitive user interface, while the rendering is done on the server side. Paraview also relies on VTK thus offering a wide set of data visualization

[1]Igor Antolović is with the Faculty of Electronic Engineering, Aleksandra Medvedeva 14, 18000 Nis, Serbia, E-mail: igor.antolovic@elfak.ni.ac.rs.

[2]Miroslav Milivojević is with the Faculty of Electronic Engineering, Aleksandra Medvedeva 14, 18000 Nis, Serbia, E-mail: miroslav.milivojevic@elfak.ni.ac.rs.

[3]Dejan Rančić is with the Faculty of Electronic Engineering, Aleksandra Medvedeva 14, 18000 Nis, Serbia, E-mail: dejan.rancic@elfak.ni.ac.rs.

[4]Vladan Mihajlović is with the Faculty of Electronic Engineering, Aleksandra Medvedeva 14, 18000 Nis, Serbia, E-mail: vladan.mihajlovic@elfak.ni.ac.rs.

algorithms which can be somewhat observed as a kind of a downside of this and similar environments. Namely the user must choose between great number of algorithms in order to get the best output results thus making his task sometimes time-consuming. Another solution which is designed to work in a client-server environment and deals with the previously described problem is Envision[7]. What is distinctive about this solution is that it provides the user the ability to describe the basic features of the input data hence enabling the system to offer only a reduced set of visualization algorithms. In this way, the user is greatly relieved because he does not have to choose manually between hundreds of available algorithms. Unlike previous solutions, [8] describes a Web service that is based on the IRIS Explorer system. The described architecture relies on a Web service which generates VRML (Virtual Reality Modeling Language) models hence the client side needs a VRML viewer application that can be installed as a browser plugin.

What is common for most of this solutions is that they rely on thin clients therefore providing the highest level of compatibility with existing Web browsers. However, as WebGL API is becoming the leading standard for 3D Web visualization on the Web it is now possible to create true Web 3D applications capable of fully using modern graphic acceleration hardware.

The combined concepts of workflow based data visualization and WebGL enabled clients directly influenced the design of the GinisVis Web service architecture.

III. GINISVIS ARCHITECTURE

The GinisVis Web client-server architecture is built on top of the server side GinisVis.NET as well as the client side GinisVis AJAX library. Both of this libraries are in fact a migration of the GinisVis C++ library described in [9].

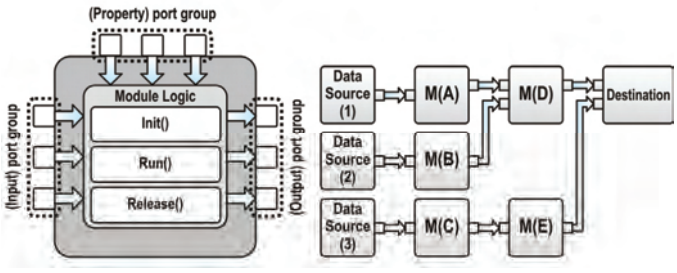

a) b)

Fig. 2. a) Single module architecture, b) Basic workflow example

The GinisVis library supports a workflow methodology which is based on assigning parts of the visualization process to smaller functional units in the form of modules. In the process of visualization, every module should execute a relatively simple processing of the input data and generate an appropriate output. A simplified architecture of a single module is shown on Fig.2.a).

The real advantage of this modular approach lies in the possibility of module linking as shown in Fig.2.b). It is important to note that the corresponding output ports of module M(A) and M(B) must be compatible with the corresponding input ports of module M(D). Also in the process of execution of modules, M(D) can be executed only after executing the modules M(A) and M(B). After execution off all modules a final destination output is created. More precisely the described architecture is designed to generate outputs in a form of 3D models.

A detailed view of the client-server architecture is shown in Fig.3.a), where we clearly distinguish three parts:

- **Data sources** – they can be various but standard OGC (*Open Geospatial Consortium*) Web services are preferred like WMS (*Web Map Server*) which provides geo-maps for requested regions and WFS (*Web Feature Server*) which provides geo-feature information,
- **GinisVis Web Service** – relies on the GinisVis.NET library, contains a set of module implementations and descriptions and provides an engine for module workflow creation and execution,
- **GinisVis Client** – relies on the GinisVis AJAX library and provides rich 3D rendering of models retrieved from the service.

The GinisVis Web service consists of the following components:

- **Modules –** a set of DLL libraries and corresponding XML descriptions where each module can implement data filter, data source or an algorithm,
- **Module Manager –** is a component that performs registration of all available modules,
- **Module Graph –** is a structure that represents the current data flow graph that is executed,
- **Module Graph Manager –** is a component that performs workflow graph execution.

The client retrieves generated 3D models in a two step procedure. The first step is to obtain only the geometry of the model that contains texture URLs, resulting in an additional texture download request. These problems can be solved by introducing Image Buffer and Buffer model components as shown in Fig.3.b). The Image buffer is a component that provides temporary storage of textures on the server side allowing them to download through sequential call to the GinisVis Web service. More precisely, this component assigns each image a unique ID which is used to link with the corresponding 3D model. After the texture is retrieved it is been automatically deleted from the buffer. On the other hand the Model Buffer component has an identical role as the Image Buffer but it handles geometry instead. This two components form an efficient buffering mechanism which overcomes the inability to send both the model and all textures at once.

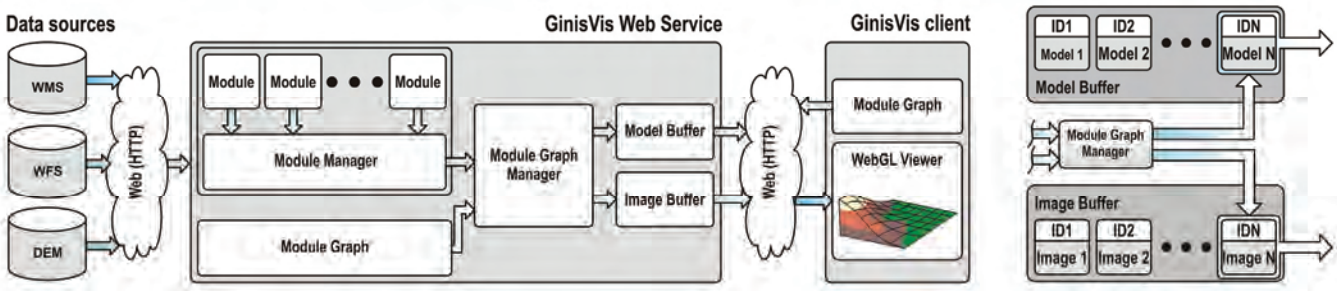

a) b)

Fig. 3. a) GinisVis client-server arhitecture, b) GinisVis buffering subsystem

Considering all service side components the communication between the GinisVis client and the GinisVis Web service can be described as follows:

1. The client invokes the *GetCapabilities* service side method.
2. The Web service responds with a list of available modules.
3. The client invokes the *RunModuleGraph* Web method sending a XML workflow configuration of linked modules.
4. The service receives the request, initializes dynamic module loading, performs module linking, executes the workflow and sends back the generated XML output in a form of a 3D model list.
5. The client retrieves the generated output and starts model downloading by invoking the *GetModel* Web method. After model retrieving the client invokes subsequent *GetImage* requests in order to obtain model textures.

In order to test the concept of the described architecture, necessary modules for terrain and 3D building modeling are considered below. As already stated, our primary motivation of is to design a platform that will provide efficient future development of 3D Web GIS applications.

IV. VISUALIZATION

Visualization of 3D terrain models has always been the first and foremost requirement in GIS applications. This resulted in a great number of algorithms (both static and dynamic [11]) for 3D terrain visualization. However, it is not our goal to create a fully optimized algorithm for terrain visualization but rather to transpose the process of terrain modeling into a workflow graph.

Basically a terrain model consists of a height matrix based mesh overlayed with a geo-referenced texture for a given region. The starting point for generating such a mesh is the data flow graph shown on Fig.4.a) (bottom).

This data flow graph consists of the following modules:

- **WMS proxy** – a proxy module that retrieves a geo-referenced image from a WMS service.
- **DEM (Digital Elevation Map) proxy** – a proxy module that retrieves a height matrix from a DEM service.
- **Terrain Modeler** – a module that generates a simple 3D triangle geometry based on a input height matrix.
- **Mesh 3D** – a module that combines both texture and geometry and produces a textured 3D.
- **Project** – a module that converts geo-spatial coordinates into Cartesian coordinates.
- **ColladaExporter** – a module that exports 3D Mesh into XML COLLADA [10] models.

In contrast to terrain models, 3D buildings can have a moderately complex structure which can make the process of their modeling a rather difficult task, but one of the most practical ways of modeling is based on contour elevation as shown on Fig.4.a) (top).

Some of the modules required for building modeling are reused but also additional modules were created:

- **WFS proxy** – a proxy module retrieves a collection of features from a WFS service by invoking a *GetFeature* request. What is important is that every feature consists of great number of attributes among which the *Geometry* attribute represents a 2D geo-referenced contour.
- **Building modeler** – a module that generates a 3D building model based on a input contour geometry obtained from WFS features.

In both cases the **Project** module has a very important role since it converts the model from geo-referenced space into Cartesian space. The input models can have geometries which are positioned in one of the standard geo-coordinate systems (e.g. WGS84 where every point is determined by a longitude, latitude and height value) while the output model has standard Cartesian (x,y,z) coordinates. There are two types of models which can be handled by this module:

- **Multipoint geo-referenced –** these are the models that are geo-referenced for every point in their geometry. The terrain for example is one such model.
- **Singlepoint geo-referenced –** these are the models that are geo-referenced with a single point usually the center of mass. In our case 3D buildings belong to this category.

The final result in a form of a combined 3D model of a terrain and buildings is shown on Fig.4.b) where the rendering is performed using the WebGL based GinisVis AJAX client which enables interactive visualization of COLLADA models.

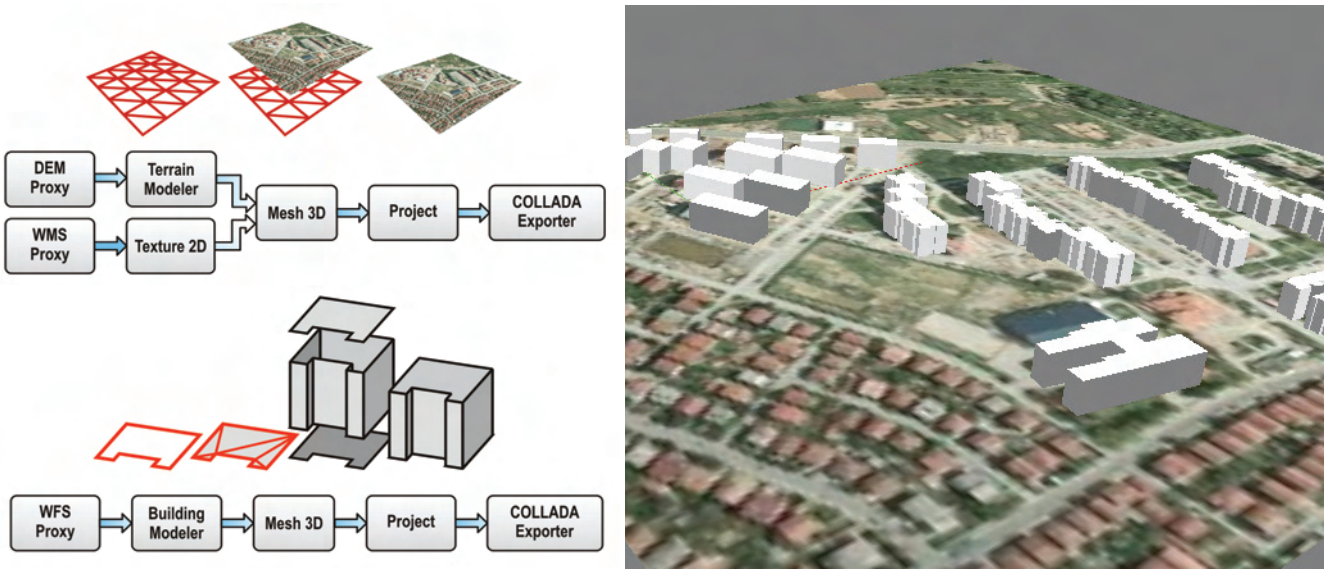

a) b)

Fig.4.a) Terrain and building workflows b) Final result rendered using the GinisVis AJAX WebGL based client

V. Conclusion

The lack of proper support for 3D visualization within the Web browsers has resulted in Web data visualization solutions that rely mainly on thin clients which are able to show images of 3D models that are fully rendered on the server side. The recently introduced WebGL standard that provides support for OpenGL ES 2.0 enables hardware rendering within Web browsers. This technology enables the design of more powerful Web based 3D model rendering clients eliminating the need to install additional browser plug-ins.

In this paper, we introduced the GinisVis Web client-service architecture that takes advantage of both current Web open-source standards and workflow graph methodology. The idea of a workflow approach is that the Web service handles a collection of modules which individually perform rather simple functions but connected within a workflow graph they can produce rather complex 3D models. Also, the GinisVis client server architecture emphasizes the advantage of Web technologies and the usage of standard OGC services as data sources (WMS, WFS, etc.) as these services play an important role in GIS applications.

A proof of concept was provided by creating a minimum set of modules that allow 3D terrain and geo-referenced buildings modeling by using a WMS service as a source of aerial photographs and WFS service as a data source for building contours.

The main advantage of the GinisVis Web service is that it forces open standard protocols as well as technologies, and furthermore, it is based on a modular workflow architecture thus it can be easily extended with new modules. All this features make this architecture an ideal platform for building future rich 3D Web GIS applications.

References

[1] http://www.khronos.org/webgl/

[2] D. Rančić, D. Dačić, “Ginis web 3D modeler - a framework for 3D terrain visualisation on web”, 8th AGILE Conference on GIScience, May 26-28, 2005, Estoril Congress Center, Estoril, Portugal

[3] D. Rančić, A. Dimitrijević, V. Mihajlović, "GIS and Virtual Reality Systems Integration", ICEST 2004, Bitola, Macedonia, pp. 313-316, 2004.

[4] Steven P. Callahan , Juliana Freire , Emanuele Santos , Carlos E. Scheidegger , Cláudio T. Silva , Huy T. Vo, „VisTrails: visualization meets data management“, Proceedings of the 2006 ACM SIGMOD international conference on Management of data, June 27-29, 2006, Chicago, IL, USA

[5] William J. Schroeder , Kenneth M. Martin , William E. Lorensen, „The design and implementation of an object-oriented toolkit for 3D graphics and visualization“, Proceedings of the 7th conference on Visualization '96, p.93-ff., October 28-29, 1996, San Francisco, California, United States

[6] K.M. Martin, B. Geveci, J. Ahrens, C. Law, „Large Scale Data Visualization Using Parallel Data Streaming “. IEEE Computer Graphics & Applications, (July 2001)

[7] G. P. Johnson, S. Mock, B. Westing, G. S. Johnson, EnVision: „A Web-Based Tool for Scientific Visualization“, CCGRID '09 Proceedings of the 2009 9th IEEE/ACM International Symposium on Cluster Computing and the Grid IEEE Computer Society, Washington, DC, USA, 2009

[8] J. Wood, K. Brodlie, J. Seo, D. Duke, „A Web Service Arhitecture for Visualization“. ESCIENCE '08 Proceedings of the 2008 Fourth IEEE International Conference on eScience IEEE Computer Society, Washington, DC, USA, 2008

[9] I. Antolović, V. Mihajlović, D. Rančić, M. Milivojević, “GinisVIS: Data flow control graph based 3D visualization framework”, YUINFO 2010, Kopaonik

[10] Dejan Rancic, Aleksandar Dimitrijevic, Bratislav Predic, "Spatial Coherency and Parallelism in Blocks Reorganization of RINGO Algorithm for Large Terrain Rendering", WSEAS Transaction on Computers, Vol. 5, No. 12, pp. 3073-3079, December 2006,

[11] http://www.khronos.org/collada/

Using COLLADA and X3D for WebGL Based 3D Data Visualization

Miroslav Milivojević[1], Igor Antolović[2], Dejan Rančić[3]

Abstract **- This paper describes the evaluation of *COLLADA* and *X3D* with the GinisVis *WebGL* based library for *3D Web* data visualization. These standard formats are very similar but they are quite different in their design goals and intended use. This paper describes a universal parser that was developed with a goal to provide uniform interface for both formats. The results of this study are comparisons of COLLADA and X3D parser performance in the form of tables.**

Keywords **– COLLADA, X3D, WebGL, 3D Web, visualization**

I. INTRODUCTION

WebGL[1] based 3D data visualization is the goal of a large number of organizations that develop advanced 3D Web applications. This is a substitute for desktop environments for 3D visualization[2,3]. The 3D Web applications provide a visualization of complex scenes, whose rendering is accelerated with graphics hardware. These have a major impact on research and development of Web visualization in the scientific fields such as Computer graphics, Astronomy, Physics, Chemistry, Medicine and etc. WebGL[1] is derived from OpenGL ES 2.0 and provides similar rendering functionality. It extends the capability of the JS (JavaScript) programming language to allow it to generate interactive 3D Web applications. This technology uses the HTML5 canvas element which is accessed using DOM (Document Object Model). A large number of functionality and 3D scene description is contained in portable formats such as COLLADA[4,5], VRML and X3D[5,6].

This paper describes a universal parser that was developed with a goal to provide uniform interface for both formats such as COLLADA and X3D. This parser is part of the GinisVis Ajax library[7], together allow a 3D interactive Web visualization as well as full compatibility with the well known Web browsers such as Firefox 4.0, Chrome 11, Opera 11 and Safari 5.

The goal of this paper is to present a set of capabilities of these two formats, their purpose, as well as similarities and differences. The possibilities of these formats are great and some of them allow users of CAD (Computer aided design), GIS (Geographic Information Systems)[8] and automation applications to enjoy the benefits of open standard royalty free content formats. The COLLADA and X3D section describes their feature set is expanding to incorporate technologies such as packaging programmable shader[9] effects and controlling real-time physics engines.

Next section describes the parsers architecture, as well as their common interface and strategy to the selection one of them. The results of this study are 3D data visualization in a Web browsers as well as values comparisons of both formats in tabular form. The conclusion section describes the analysis of the both formats, their comparison, the intersection features as well as their purpose values based of research results.

[1]Miroslav Milivojević is with the Faculty of Electronic Engineering, Aleksandra Medvedeva 14, 18000 Niš, Serbia, E-mail: miroslav.milivojevic@elfak.ni.ac.rs.

[2]Igor Antolović is with the Faculty of Electronic Engineering, Aleksandra Medvedeva 14, 18000 Niš, Serbia, E-mail: igor.antolovic@elfak.ni.ac.rs

[3]Dejan Rančić is with the Faculty of Electronic Engineering, Aleksandra Medvedeva 14, 18000 Niš, Serbia, E-mail: dejan.rancic@elfak.ni.ac.rs.

II. COLLADA AND X3D

COLLADA and X3D are two open standards that use XML schema technology to fully describe 3D scenes. These formats can be used together as a powerful tool set for developing interactive Web and enterprise applications.

A. COLLADA format

COLLADA (Collaborative Design Activity) defines an interchange file format to enable interactive 3D applications. This format is developed by the non-profit consortium, the Khronos Group[10]. COLLADA is an intermediate format that is focused on describing 3D models and bringing content and assets from different authoring tools to an 3D application or an another tool. This is useful for DCC (Digital Content Creation) tools, conditioning tools and for data storage. Rich data representation that fully describes one or more 3D scenes is stored in files with the ***.dae*** extension. This XML format contains a large number of elements that on mathematical or physical way describe the scene models as well as their interaction. Some of these elements are: **geometry**, **node**, **material**, **effect**, **image**, **scene**, **dynamic, controller, density**, **mass**, **inertia**, **imager** (image sensor), **bind, texcombiner** (texture combiner) **etc.** Mathematical model and design model are presented with the first five elements respectively. Element **geometry** contains the position coordinates, texture coordinates, colours and normals. Element **node** can contain the geometry and the other nodes. The COLLADA file can contain one **scene** that is composed of tree nodes and cameras. Element **dynamic** contains a Boolean value that indicates whether a physical model is movable or not. Element **controller** is a generic mechanism to describe active or dynamic content and it contains an element that describes control data. This is a very important element that manages the operations of another object with a control data. The following elements such as mass and density describe the

model more clearly. Total mass of the physical model is described in the floating-point value of the **mass** element. Diagonal elements of the moments of inertia are presented with three floating-point numbers of the **inertia** element. The **imager** element is an image sensor of camera and defines how camera sensor transforms light colour and intensities into numerical values. The **bind** element allows the mapping of parameters to uniform inputs at run time. Parameters such as material, texture, and etc. can be forwarded to a shader allowing the FX (framework) runtime but they can also be the shader programs. The **texcombiner** element allows the specification of different commands for combiner-mode texturing. Extra tags allow definition of user information and provide additional information about or related to its parent element. The **instance_node** element refers to an element in the node tree or in another COLLADA file using the **url** attribute. This is especially convenient for GIS[8] applications for example when the city visualization requires that each object or building is stored in one COLLADA file.

B.X3D format

X3D is the successor to the VRML (Virtual Reality Modeling Language) standard. This format fully describes the 3D scene, physics, interactions and collisions between objects on the scene. Described 3D data are stored in files with ***.x3d*** and ***.x3dv*** (X3D VRML) extensions. Because the file is encoded in XML it can be easily extended thus making X3D more flexible than its predecessors. Developers use other technologies such as DOM and XPath for X3D data access. Unlike other formats X3D describes 3D models in a very simple way even without the uses of specification. This is not a binary format and not designed as an intermediary format.

X3D is a delivery format that contains the information needed for interactive applications and includes behaviors such as picking, viewing, navigation and scripting. This format is used in many applications and it is applied in the following areas: virtual worlds, social networks, GIS, military simulation, medical visualization, industry engineering (oil and gas, automotive, virtual training), mobiles and etc. X3D data can be created from DTD (Document Type Definition) or XML schemas and transformed using XSLT (Extensible Stylesheet Language Transformations). There are a large numbers of elements in X3D format such as geometry, grouping, appearance, material, textures, viewing, environment, navigation, animation, lightning, sound, interaction and etc. This format contains a 2D geometry that includes following elements **arcs**, **closed**, **circles**, **polylines**, **rectangles**, **triangles** and as 3D geometry includes **cones**, **cylinders**, **elevation grids**, **extrusion**, **boxes**, **spheres**, **indexed face sets** and **indexed line sets**. Defining following elements such as terrain, water and skies is provided by the **GeoElevationGrid** element**.** Information of physical characteristic description of the viewer's avatar and models are stored in the navigation info element. Full 3D navigation of X3D format is supported with the following types: walk, any, examine, look-at, none, slide, pan and fly. 3D environment experience in the X3D scene is enabled by the following elements such as lightning, sound, background and fog element. For example describing the earth and sky is allowed by the background element with a set of colors or image textures. Sound and audio clip element allow the identification and management of sound in the X3D scene. X3D supports following compressed and uncompressed formats such as wavefile (***.wav***), MIDI (***.midi***) and MP3 (***.mp3***). Element **inline** embeds an X3D scene into another scene using the **url** attribute. Url refers to another X3D file that contains data for the scene such as a list of children nodes, prototypes etc. This element is important for the development of GIS applications. Behaviors in the run-time X3D environment is allowed by the events. Some events are initiated by the time sensor and for other events the following sensors are responsible: touch sensor, key sensor, picking sensor, visibility sensor, plane sensor, sphere sensor, geo touch sensor and so on. Main purpose of sensors is to control the animations and user interactions. For example when the user clicks or drags a geometry followed by a series of activities. First the touch or plane sensor is activated, then it activates the time sensor which sends values to an interpolator node and interpolation of result allows the modification of current geometry in the scene.

III. PARSER ARCHITECTURE

This section describes the similarities and differences between COLLADA and X3D formats, the design goals and the communication between objects of developed classes.

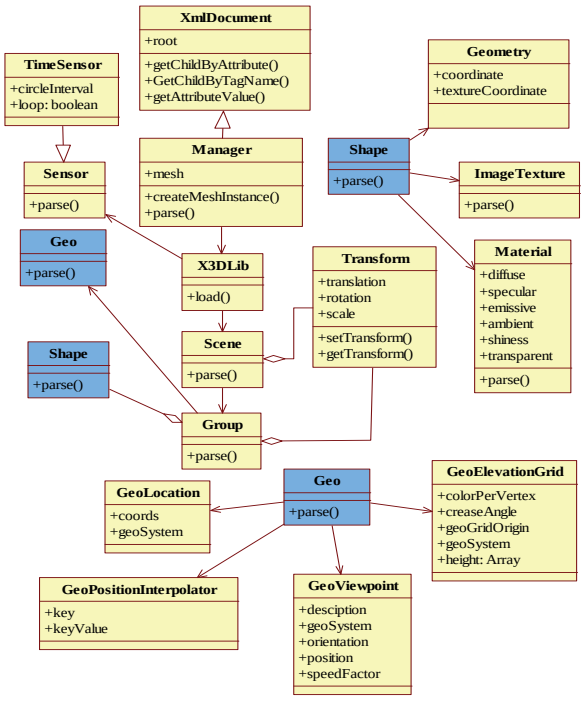

Fig.1. X3D parser architecture

A library that allows you to select one of X3D and COLLADA parsers is developed in this study. Decision on the choice of a parser is made using the file extension.

XmlDocument class is the basic XML parser. This parser consists of methods to search and return value of the attribute

node, then methods for searching nodes and return of the node based on their tag name, as well as methods for searching nodes and return of the node based on attribute name or based on attribute values.

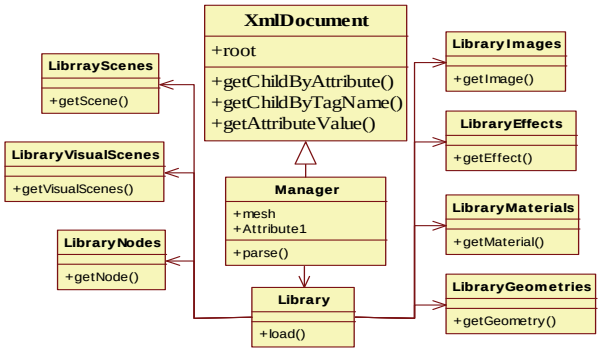

Fig.2. COLLADA parser architecture

Manager class initiates the main parse method. This method runs load method of the X3Dlib class. These classes are common for both COLLADA and X3D parsers.

Scene class contains all the scene elements covered in the X3D format such as group, shape, viewpoint and so on. Unlike the COLLADA parser where there is an class (LibraryVisualScenes) which refers to the instance of several scenes in the file X3D parser contains only one Scene instance, because each X3D file can only include one X3D scene according to XML principles.

Group class of the X3D parser is very similar to the LibraryNodes class of COLLADA parser but it's easier for the parsing. LibraryNodes class contains a list of nodes that one node has a geometry and material or refers to another node in this class. Group class contains a tree of nested nodes and consequently reduces the parsing time or the time for access to nodes. Nodes in Group class can refer to other group instances or may have an instance of Shape class.

Shape class is similar to the node that contains geometry and doesn't contain other nodes. This class contains a reference to Geometry class and Material class.

Transform class allows the transformation of the Group object, such as translation, rotation and scaling.

Geometry class contains information about vertices, indices, normal and texture coordinates. Unlike COLLADA parser where the material is related with geometry using material ID attribute, Geometry and Material are embedded in the Shape class and X3D parser doesn't contain attributes to connect them. Common features of both formats are to include the field indices of points, normals and texture coordinates. Otherwise, the graphics hardware for visualization uses OpenGL ES 2.0 that supports a unique index field common to all types of coordinates. The parsers allow the creation of a unified field of all indices.

GeoViewpoint class provides a perspective view of the scene using a geospatial data. This class contains several attributes such as **geoSystem**, **geoOrigin**, **position, orientation**, **navType** and **speedFactor**. The geoSystem attribute contains a combination of the following fields of strings that define which ellipsoid is used and how. The position attribute defines the actual coordinate of the viewpoint. The speedFactor attribute is a multiplier to the elevation-based velocity.

GeoElevationGrid class presents a uniform grid of elevation values and GeoLocation class allows the georeferencing of object whose is parent node.

GeoPositionInterpolator class allows interpolation of geographical coordinates using the key values and information about the specified coordinate system. Classes that allow the description of georeferenced objects are integral part of the X3D parser because only X3D format has specialized nodes for this purpose.

TimeSensor class represents a timer in the scene and allows the construction of events based on time. Object of this class provides information that can be used for many purposes and some of them are: using it for simulation and animation, use it as a trigger for periodic events, use it as an as alarm clock and so on. In this case the TimeSensor class is used for animation of georeferenced objects.

IV. RESULTS

This paper describes the realized sub-library for 3D data visualization based on the WebGL technology using COLLADA and X3D standards. This sub-library is an universal parser that allows the extraction of 3D content from the described formats. The universal parser consists of the COLLADA and X3D parser where both are advanced XML parsers. Parser classes are implemented using the COLLADA and X3D formats as well as their methods that successfully provide the necessary information such as geometry, material, normal and colors for 3D visualization to the Web browser. In addition, support for georefrenced objects is implemented. Parsers are implemented using the JavaScript API. There are several limitations of the used technology and some of them are: OpenGL | ES2.0 and WebGL do not support 32-bit values for the vertex indices. WebGL supports identifier names of no more than 256 characters. The maximum number of vertices per chunk is 64K. 3D data visualization is provided on several best-known Web browsers. Rendering of complex 3D scenes is executed on the graphics hardware without having to install additional plug-in components. Result of the 3D data Web visualization is an imported 3D model from the COLLADA file, shown in Fig.3. The values shown in Table 1 are the results of comparing parsing time and download time. Testing is performed with the same 3D models for the COLLADA and X3D parser.

Fig.3. Health Center[11]

Table 1 COMPARISON OF FORMATS

Format	COLLADA		X3D		COLLADA and X3D		
Model/Parameters	download time(s)	parsing time(ms)	download time(s)	parsing time(ms)	number of faces	number of vertices	framerate (fps)
Health Center	3	81	1.38	67	80	40	6.5
Hotel Ambasador	4	186	1.85	155	1628	1648	6.5
Court	2	376	0.92	336	2586	1712	6.5
Niški cvet	11	2381	5.08	2198	7954	11757	4.25
Federation	32	2060	14.77	1895	1357	550	7
Post Office	18	2185	8.31	1908	1096	525	7.5
Mileševa	20	20528	9.23	20100	4804	3223	7
Colosseum	4	1637	1.85	1520	9988	5104	7

V. CONCLUSION

COLLADA and X3D are two very similar XML based open standards. Their goals, design and purpose are very different but both are used in tools for data visualization.

COLLADA is an intermediate and interchange file format. This format is used to describe 3D models in the following fields: computer graphics, visual simulation, animation, virtual reality, Medicine, GIS and so on. COLLADA was designed for the interchange applications and for transporting data from one tool to another including: **Maya, 3D Studio Max, Sketchup, Blender** etc. COLLADA file can contain more than one scene and can contain only one **scene_instance** tag within **scene** tag. This information is stored in the element as libraryVisualScenes. In COLLADA file, nodes have a reference to other nodes or contain rich information about geometries and materials. Materials effect allows the use of color or texture or both. This format contains sensors and one of them is the imager that describes the camera sensor characteristics. Described 3D content of the COLLDA does not support the ECMA script which would allow the interactive features.

X3D is a delivery format and open standard based on XML schema technology. This is a good format for interactive 3D Web applications. X3D supports shaders and the following techniques such as **CSM** (Cascade Shadow Maps), **SSAO** (Screen Space Ambient Occlusion), as well as reflection and lightning in the real-time. X3D can contain only one scene nodes and the tree nodes. Nodes are embedded in each other so that it reduces the time while moving through the tree nodes. X3D format supports many sensors that allow animation, simulation and interaction in the 3D scene. Scripting is another good feature of this format that is allowed by the X3DScriptNode element. This allows the browser to execute the program in the Script node's url field. The Script node's url field allows the following scripts: Java, ECMA Script and inline ECMA Script. There are many purposes of this format and some of them are for the following fields: CAD, Chemistry markup language, GIS, Networking, Humanoid Animation, Medical and etc.

COLLADA and X3D can be used for developing powerful tools or 3D Web applications using modular Web services[12]. Both formats allow the insertion of user information and import of the other COLLADA and X3D files. This is very important for GIS applications because it is possible to combine several files of these formats and provide a textual description of the 3D scenes.

REFERENCES

[1] WebGL, Khronos Group: http://www.khronos.org/

[2] Igor Antolović, Vladan Mihajlović, Dejan Rančić, Miroslav Milivojević, "GINISVIS: DATAFLOW CONTROL GRAPH BASED 3D VISUALIZATION FRAMEWORK", YU INFO 2010, Kopaonik, pp. 1-6, March 2010, Proceedings

[3] Igor Antolović, Miroslav Milivojević, Dejan Rančić, Vladan Mihajlović, "3D Object modeling and Visuallization using Modular Web services", YUINFO 2011, Kopaonik

[4] COLLADA: http://www.khronos.org/files/collada_spec_1_4.pdf

[5] COLLADA, X3D: http://www.khronos.org/collada/presentations/Developing_Web_Applications_with_COLLADA_and_X3D.pdf

[6] Craig Anslow , Stuart Marshall , James Noble , Robert Biddle, "Evaluating X3D for use in software visualization", Proceedings of the 2006 ACM symposium on Software visualization, September 04-05, 2006, Brighton, United Kingdom

[7] Miroslav Milivojević, Igor Antolović, Dejan Rančić, "AJAX LIBRARY FOR THE VISUALIZATION OF 3D DATA ON THE INTERNET USING WEBGL TECHNOLOGY", YUINFO 2011, Kopaonik

[8] D. Rančić, A. Dimitrijević, V. Mihajlović, "GIS and Virtual Reality Systems Integration", ICEST 2004, Bitola, Macedonia, pp. 313-316, 2004

[9] Shader: http://www.opengl.org/documentation/glsl

[10] Khronos Group: http://www.khronos.org/

[11] Health Center: http://sketchup.google.com/3dwarehouse/details?mid=56bdbc35d9a2e3f2369024cdcd1746d&prevstart=0

[12] Igor Antolović, Miroslav Milivojević, Dejan Rančić, Vladan Mihajlović, Marko Kovačević, "3D terrain models generating using modular web service", 18. Telekomunikacioni forum TELFOR 2010, Sava Centar Beograd, pp. 1-4, November 2010, Proceedings on CD

Session CNS:

CONTROL SYSTEMS

The Concept of Quasi Orthogonality Applied in Technical Systems

Dragan Antić[1], Marko Milojković[2], Saša Nikolić[3], Darko Mitić[4] and Staniša Perić[5]

Abstract – **In this paper we introduce quasi-almost orthogonal filters, as a new class of filters, based on Legendre type quasi-almost orthogonal polynomials. These filters are generators of quasi-almost orthogonal signals for which we have derived and presented important properties and relations. Our work is based on classical theory of orthogonality, and orthogonal rational functions, and also on new results in this field of research. Quasi-almost orthogonal filters can be successfully used for signal approximation as well as for modeling, identification, and analysis of dynamical systems. Based on mathematical results, we have designed schemes for practical realization of these filters.**

Keywords – **Quasi orthogonality, Almost orthogonality, Quasi-almost orthogonal filters.**

I. Introduction

Orthogonal polynomials have been in the focus of the research for the last two centuries. One of the most important applications of orthogonal polynomials is designing orthogonal filters. Today these filters provide an efficient tool for identification, modeling and control of dynamical systems.

Concept of quasi orthogonality is introduced for the first time in 1923 [1] as a tool for solving the problem of moments in mechanics. Quasi orthogonal functions and especially quasi orthogonal polynomials as well as numerous applications are discussed in many papers [2-5]. It is important to notice that classical orthogonal filters and orthogonal signal generators have transfer functions with the order of numerator polynomial for one less then denominator. In practice there is often need for filters of more general type i.e., filters with difference in orders of transfer functions polynomials higher then one. This can be accomplished by using quasi orthogonal filters.

The components that are used for designing any real (practical) system are not perfect and their parameters values vary in the range of allowed tolerance. The reasons can be various: imperfect manufacturing, systems exploitation conditions (environment temperature, pressure, moisture, electromagnetic fields, variations in voltage)… With respect to that fact, every real system is in some way imperfect, so the models of these systems should reflect this fact. Almost orthogonal filters designed in earlier papers [6-8] can be successfully used for modeling and analysis of the systems with imperfections.

In this paper we consider quasi-almost Legendre type orthogonal polynomials. Based on these polynomials, we have designed first order quasi-almost Legendre type orthogonal filter. For the first time, here, we combine two theories into new class of filters. These filters can be used as generators of functions sequence, suitable for modeling and analysis of appropriate imperfect systems that can be described with transfer function with difference in polynomials orders higher that one.

II. Almost Orthogonal Polynomials – A New Approach

Our design of orthogonal filters, is based on shifted Legendre polynomials orthogonal over interval (0, 1). On the other side, technical systems operate in the real time, so we need the corresponding approximation over interval (0, ∞). The solution is to use the substitution $x = e^{-t}$. In this manner polynomial sequence orthogonal over (0, 1), become exponential polynomial sequence orthogonal over interval (0, ∞).

Consider the orthogonal Legendre polynomials in their explicit form:

$$P_n(x) = \sum_{i=0}^{n} A_{n.i} x^i \tag{1}$$

where:

$$A_{n.i} = \frac{1}{n!}(-1)^{n-i}\binom{n}{i}\frac{(n+i)!}{i!} \tag{2}$$

The first few members of the sequence are:

$$\begin{aligned} P_0(x) &= 1, \\ P_1(x) &= 2x-1, \\ P_2(x) &= 6x^2-6x+1,\ldots \end{aligned} \tag{3}$$

These polynomials are orthogonal over interval (0, 1), with weight function $w(x)=1$, i.e.:

[1]Dragan Antić is with the University of Niš, Faculty of Electronic Engineering, Aleksandra Medvedeva 14, 18000 Niš, Serbia, E-mail: dragan.antic@elfak.ni.ac.rs

[2]Marko Milojković is with the University of Niš, Faculty of Electronic Engineering, Aleksandra Medvedeva 14, 18000 Niš, Serbia, E-mail: marko.milojkovic@elfak.ni.ac.rs

[3]Saša Nikolić is with the University of Niš, Faculty of Electronic Engineering, Aleksandra Medvedeva 14, 18000 Niš, Serbia, E-mail: sasa.s.nikolic@elfak.ni.ac.rs

[4]Darko Mitić is with the University of Niš, Faculty of Electronic Engineering, Aleksandra Medvedeva 14, 18000 Niš, Serbia, E-mail: darko.mitic@elfak.ni.ac.rs

[5]Staniša Perić is with the University of Niš, Faculty of Electronic Engineering, Aleksandra Medvedeva 14, 18000 Niš, Serbia, E-mail: stanisa.peric@elfak.ni.ac.rs

$$\int_0^1 P_m(x)P_n(x)dx=\begin{cases}0, & m\neq n\\ N_i, & m=n\end{cases} \tag{4}$$

and they can be successively used for modeling [9], and control [10] of dynamical systems as well as for identification of specific systems parameters [11].

Corresponding almost orthogonal polynomials $P_n^{(\varepsilon)}(x)$ can be defined as [6]:

$$\int_0^1 P_m^{(\varepsilon)}(x)P_n^{(\varepsilon)}(x)dx=\begin{cases}\varepsilon, & m\neq n\\ N_n^{(\varepsilon)}, & m=n\end{cases} \tag{5}$$

where ε represent a very small positive constant $(0<\varepsilon<<1)$.

The connection between classical orthogonal and almost orthogonal polynomials is proved in [7] with following relation:

$$P_n^{(\varepsilon)}(x)=P_n(x)+\sum_{k=1}^{n-1}\frac{b_k}{\|P_k\|^2}P_k(x) \tag{6}$$

where $\|P_k\|^2$ represents the square of the norm and b_k are polynomials dependent on ε.

The first few members of the Legendre almost orthogonal polynomial sequence are:

$$\begin{aligned}&P_0^{(\varepsilon)}(x)=1,\\ &P_1^{(\varepsilon)}(x)=2x-(1-2\varepsilon),\\ &P_2^{(\varepsilon)}(x)=6x^2-6\left(1-12\varepsilon+12\varepsilon^2\right)x+\left(1-30\varepsilon+36\varepsilon^2\right),\ldots\end{aligned} \tag{7}$$

Complete mathematical background for designing almost orthogonal filters based on polynomials given by Eq. (6) can be found in [6, 7]. These filters represent generalization of the Legendre type orthogonal filters [7, 10]. Obviously, for ε=0 almost orthogonal filter becomes strictly orthogonal filter. Practical realization of almost orthogonal filters defined in such way is elaborated in [8].

In this paper, we will define almost orthogonality in different manner in order to accomplish further simplifications in filters design. First, we define almost orthogonal Legendre polynomials $P_n^{\delta}(x)$:

$$P_n^{\delta}(x)=\sum_{i=0}^{n}A_{n,i}^{\delta}x^i \tag{8}$$

where:

$$A_{n,i}^{\delta}=(-1)^{n+i}\frac{\Gamma(n\delta+i+1)}{\Gamma(n\delta+1)i!(n-i)!} \tag{9}$$

In Eq. (9), δ represents constant: δ=1+ε≈1 and Γ represents gamma function.

Now, we can define almost orthogonality in the other way:

$$\int_0^1 P_m^{\delta}(x)P_n^{\delta}(x)dx=\begin{cases}(1-\delta)\sum_{k=1}^{n}kQ_k, & m\neq n\\ N_n^{\delta}, & m=n\end{cases} \tag{10}$$

where:

$$Q_k=\frac{\prod_{j=1}^{m}(k-j\delta)\prod_{j=1}^{n}(k+j\delta)}{k^2\prod_{j=1}^{m}(k+j)\prod_{j=1}^{n}(k-j)} \tag{11}$$

The first few members of the Legendre almost orthogonal polynomial sequence defined with Eq. (8) are:

$$\begin{aligned}&P_0^{\delta}(x)=1,\\ &P_1^{\delta}(x)=(\delta+1)x-\delta,\\ &P_2^{\delta}(x)=(\delta+1)(\delta+2)x^2-(\delta+1)(2\delta+1)x+\delta^2,\ldots\end{aligned} \tag{12}$$

After applying the substitution $x=e^{-t}$ to Eq. (8) and Laplace transform, we have:

$$W_n^{\delta}(s)=\frac{\prod_{i=1}^{n}(s-i\delta)}{\prod_{i=0}^{n}(s+i)}=\frac{(s-\delta)(s-2\delta)\cdots(s-n\delta)}{s(s+1)(s+2)\cdots(s+n)} \tag{13}$$

III. QUASI-ALMOST ORTHOGONAL POLYNOMIALS

The following definition of quasi orthogonality for polynomial set $P_n(x)$ can be found in papers [4, 5]:

$$\int_a^b P_n^k(x)P_m^k(x)w(x)dx=\begin{cases}=0, & 0\le m\le n-k-1\\ \neq 0, & n\ge k+1\end{cases} \tag{14}$$

where k represents the order of quasi orthogonality, a and b - quasi orthogonality interval and $w(x)$ - the weight function.

A large number of papers consider quasi orthogonal polynomials in classical manner, analogous to the classical orthogonal polynomials. One approach [4] is based on known theorem that every polynomial $R_n(x)$ that can be represent as linear combination of classical orthogonal polynomials given by:

$$R_n(x)=P_n(x)+c_1P_{n-1}(x)+\cdots+c_kP_{n-k}(x) \tag{15}$$

is itself quasi orthogonal with order k of quasi orthogonality. Coefficients c_i can be dependent on n. The second approach [4] is based on the fact that every orthogonal polynomial with weight $w(x)$ is quasi orthogonal with some other weight. For example, in the case of Legendre polynomials orthogonal over interval (-1, 1) with weight $w(x)=1$, we can introduce different weight: $w(x)=x^k$, and obtain quasi orthogonal, Legendre type, polynomials over same interval. Many papers

also analyze in details configuration of the zeroes in quasi orthogonal polynomials [5, 12].

If we apply definition of quasi orthogonality on almost orthogonal polynomials given with Eq. (8), we obtain quasi-almost orthogonal Legendre type, polynomials over interval (0, 1) with weight function $w(x)=1$:

$$P_n^{k,\delta}(x)=\sum_{i=0}^{n}A_{n,i}^{k,\delta}x^i \tag{16}$$

where:

$$A_{n,i}^{k,\delta}=(-1)^{n+i+k}\frac{\prod_{j=1}^{n-k}(i+j\delta)}{i!(n-i)!} \tag{17}$$

Starting first order (k=1) quasi-almost orthogonal polynomials of this sequence are:

$$\begin{aligned}
&P_1^{1,\delta}(x)=-x+1,\\
&P_2^{1,\delta}(x)=-\frac{(\delta+2)}{2}x^2+(\delta+1)x-\frac{\delta}{2},\\
&P_3^{1,\delta}(x)=-\frac{(\delta+3)(2\delta+3)}{6}x^3+\\
&+(\delta+1)(\delta+2)x^2-\frac{(\delta+1)(2\delta+1)}{2}x+\frac{\delta^2}{3},\cdots
\end{aligned} \tag{18}$$

After applying the substitution $x=e^{-t}$ to Eq. (18) and Laplace transform, we have:

$$W_n^{1,\delta}(s)=\frac{\prod_{i=1}^{n-1}(s-i\delta)}{\prod_{i=0}^{n}(s+i)}=\frac{(s-\delta)(s-2\delta)\cdots(s-(n-1)\delta)}{s(s+1)(s+2)\cdots(s+n)} \tag{19}$$

Transfer function given in form of Eq. (19) is very suitable for practical design of quasi-almost orthogonal filters.

IV. Quasi-Almost Orthogonal Filters

First order (k=1) quasi-almost orthogonal polynomials can be generated by a filter whose analogue scheme is given in Fig. 1. This filter has been directly designed using relation (19). Signals labelled as $\varphi_i^{1,\delta}(t)$ in Fig. 1 represent the sequence of exponential quasi-almost orthogonal functions.

Obtained filter analogue scheme given in Fig. 1 is very simple and suitable for practical realization. Simulation in MATLAB, based on Fig. 1, was performed and few quasi-almost orthogonal signals (chosen value for δ was 1.02) are shown in Fig. 2. In this simulation we have applied input step signal with amplitude of 2V.

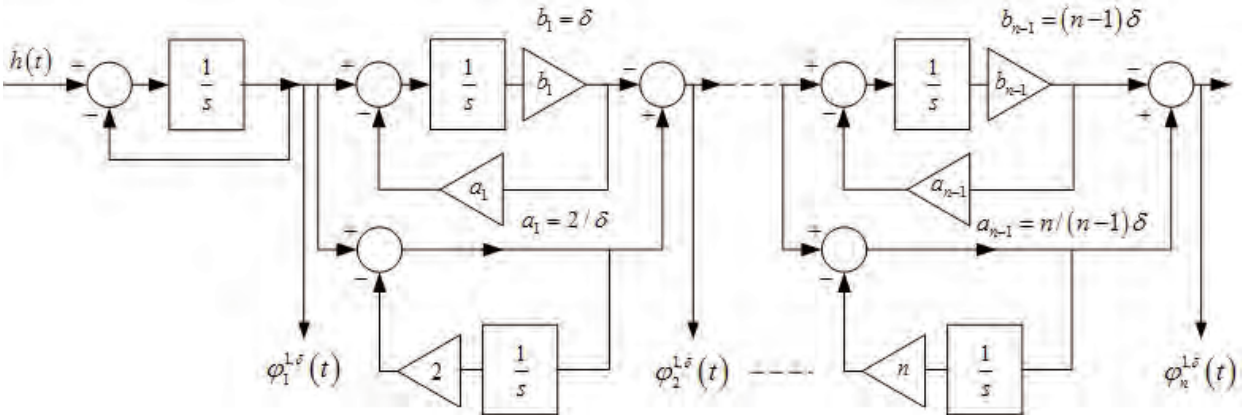

Fig. 1. Analogue scheme for the first order quasi-almost orthogonal filter adjusted for practical realization

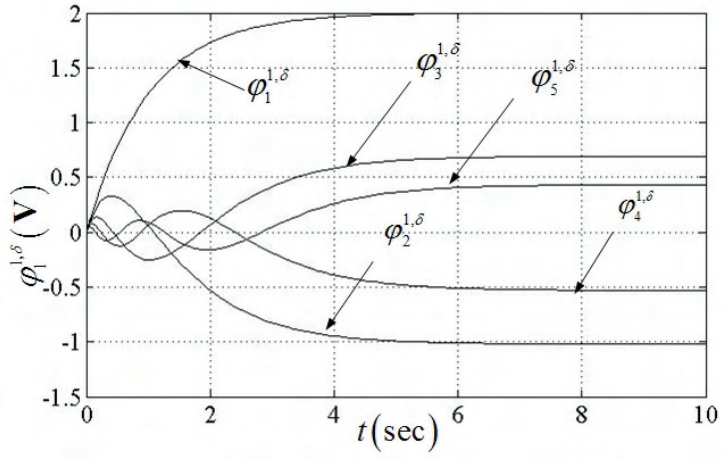

Fig. 2. First order quasi-almost orthogonal filter signals simulated in MATLAB

V. CONCLUSION

In this paper we have defined almost orthogonal polynomials, as well as quasi-almost orthogonal polynomials of Legendre type. Main relations valid for those polynomials are also given. Using these relations, we proposed a method for designing quasi-almost orthogonal filters of arbitrary order. Designed filter can be successfully used for modeling, identification, simulation, and analysis of different dynamical systems as well as for designing adaptive systems.

ACKNOWLEDGEMENT

This paper was supported in part by the Serbian Ministry of Science and Technology within the projects II 43007, II 44006 and TR 35005.

REFERENCES

[1] M. Riesz, "Sur le Probleme des Moments", Troisième Note, Arkiv för Matematik, Astronomi och Fysik, vol. 17(16), pp. 1-52, 1923.

[2] T.S. Chihara, "On Quasi-orthogonal Polynomials", Proceedings of the American Mathematical Society, vol. 8, pp. 765-767, 1957.

[3] S. Dehesa, F. Marcellan and A. Ronveaux, "On Orthogonal Polynomials with Perturbed Recurrence Relations", Journal of Computational and Applied Mathematics, vol. 30, pp. 203-212, 1990.

[4] C. Brezinski, K.A. Driver and M. Redivo-Zaglia, "Quasi-orthogonality with Applications to Some Families of Classical Orthogonal Polynomials", Applied Numerical Mathematic, vol. 48, pp. 157-168, 2004.

[5] M. Alfaro and L. Moral, "Quasi-orthogonality on the Unit Circle and Semi-classical Forms", Portugaliae Mathematica vol. 51, pp. 47-62, 1991.

[6] M. Milojković, S. Nikolić, B. Danković, D. Antić and Z. Jovanović, "Modelling of Dynamical Systems Based on Almost Orthogonal Polynomials", Mathematical and Computer Modelling of Dynamical Systems, vol. 16, no. 2, pp. 133-144, 2010.

[7] B. Danković, S. Nikolić, M. Milojković and Z. Jovanović, "A Class of Almost Orthogonal Filters", Journal of Circuits, Systems, and Computers, vol. 18, no. 5, pp. 923-931, 2009.

[8] S. Nikolić, M. Milojković, D. Antić, B. Danković, Z. Jovanović and S. Perić, "Almost Orthogonal and Quasi-orthogonal Filters", TEHNIKA-Elektrotehnika, vol. 59, no. 5, pp. 1-6, 2010.

[9] B. Danković, D. Antić, Z. Jovanović, S. Nikolić and M. Milojković, "Systems Modeling Based on Legendre Polynomials", SACI 2009, Timisoara, Romania, May 28.-29., pp. 241-246, 2009.

[10] S. Nikolić, D. Antić, B. Danković, M. Milojković, Z. Jovanović and S. Perić, "Orthogonal Functions Applied in Antenna Positioning", Advances in Electrical and Computer Engineering, vol. 10, no. 4, pp. 35-42, 2010.

[11] D. Antić, B. Danković, Z. Jovanović and S. Perić, "Legendre Orthogonal Functional Network Applied in Modeling of Dynamical Systems", ICEST 2010, Ohrid, Macedonia, June 23.-26., vol. 1, pp. 449-452, 2010.

[12] A. Bultheel, P. González-Vera, E. Hendriksen and O. Njastad, "Separation of Zeroes of Para-orthogonal Rational Functions", Acta Mathematica Hungarica, vol. 96, pp. 169-186, 2002.

Adaptive Control of System for Rubber Transportation

Zoran Jovanović[1], Nikola Danković[2], Miodrag Spasić[3], Stanko Stankov[4] and Zoran Ićić[5]

Abstract – **A new method of adaptive control for cascade-connected transporter systems is suggested in this paper. The main goal of this control is to neutralize the oscillations which could appear due to unappropriate system parameters. Laboratory rubber cooling system has been practically realized and used for experimental purposes. Genetic algorithm has been applied for parameters adjustment in order to minimize the steady state error.**

Keywords – **Adaptive optimization, Transportation system, Genetic algorithm.**

I. INTRODUCTION

In every tyre factory in the world, there are one or more tyre strip cooling systems. That tyre strip is used to form external (stripped) part of a tyre. It is estimated that there are about 2500 systems, like that, all over the world, mostly in China, India, USA and Brasil. These systems consist of a large number (4-24) of cascade-connected transporters along which the tyre strip moves, passing from one transporter to another. Thereby, the rubber is cooled by the water which flows in opposite direction. The velocities of individual transporters are adjusted using local controllers which determine the velocity of the next transporter according to the length of rubber between two consecutive transporters. In this manner, a dynamic system with a lot of cascades is obtained (Fig. 1).

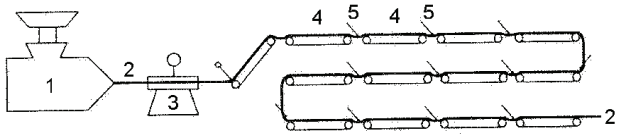

Fig. 1. Cascade system for the rubber strip transportation (1-extruder 2-rubber strip 3-balance 4-transporters 5-transitions)

[1]Zoran Jovanović is with the University of Niš, Faculty of Electronic Engineering, Aleksandra Medvedeva 14, P.O. Box 73 18000 Niš, Serbia, E-mail: zoran.jovanovic@elfak.ni.ac.rs.

[2]Nikola Danković is with the University of Niš, Faculty of Electronic Engineering, Aleksandra Medvedeva 14, P.O. Box 73 18000 Niš, Serbia, E-mail: nikola.dankovic@elfak.ni.ac.rs.

[3]Miodrag Spasić is with the University of Niš, Faculty of Electronic Engineering, Aleksandra Medvedeva 14, P.O. Box 73 18000 Niš, Serbia, E-mail: miodrag.spasic@elfak.ni.ac.rs.

[4]Stanko Stankov is with the University of Niš, Faculty of Electronic Engineering, Aleksandra Medvedeva 14, P.O. Box 73 18000 Niš, Serbia, E-mail: stanko.stankov@elfak.ni.ac.rs.

[5]Zoran Ićić is with the University of Niš, Faculty of Electronic of Electronic Engineering, Aleksandra Medvedeva 14, P.O. Box 73 18000 Niš, Serbia, E-mail: zoran.icic@elfak.ni.ac.rs.

Following properties of these systems impact dynamics, stability and system quality:

- Tyre strip accumulates at transition places (points 5 in Fig. 1), because of integration of velocities difference.
- Nonlinear dependencies are formed at the cascade transitions, between transporters.
- During the tyre strip movement along a transporter, rubber runs cold and contracts. Because of that, velocity at transporter's end is less than velocity at transporter's beginning, with contraction coefficient μ. Coefficient μ is stochastic because it depends on rubber quality and environment temperature which are stochastic parameters. Influence of stochastic parameters μ_i on cascade systems stability is analized in [1].

Due to cascade structure and nonlinearities, the system is prone to oscillations [2], [3]. Under certain conditions, deterministic chaos may appear in the system [4], [5]. Because of the stated properties, the referred system is very complex and difficult to control [6]. The only way for successful control is local control of transporters velocities at every transition (points 5 in Fig. 1) and also a compensation for the entire system using adjustable parameters. Until now, these parameters have been adjusted manually. Compensational parameters adjustment has been applied in [7] in order to minimize the steady state error. To avoid these oscillations, we propose adaptive control of the system, i.e. adaptive adjustment of all parameters independently. Thus, genetic algorithm, apllied in [7] for simultaneous optimisation of n parameters, is devided into n consecutive operations where each one is used for only one's parameter optimisation. The same goal is achived, but the algorithm is being executed n times faster which prevents the appearing of oscillations.

II. CASCADE-CONNECTED SYSTEM FOR THE RUBBER STRIP COOLING

Figure 1 shows a cascade-connected transporters for the rubber strip cooling.

The rubber strip comes from extruder (point 1 in Fig. 1), pass through the balance (point 3 in Fig. 1) and goes to the cooling system. It is necessary to cool down the rubber strip to the room temperature. When rubber runs through the cooling system, it is beeing cooled and contracts with contraction coefficent $\mu < 1$. During that contraction, rubber velocities at transporter ends are not equal to the transporter velocities, producing the effect of rubber slipping relatively to transporter.

The length change of the rubber strip between two transporters is described with the following equations:

$$\frac{dl_i}{dt} = V_{g,i-1}^{(2)} - V_{g,i}^{(1)}, i = 1,2,...,n, \quad (1)$$

$$V_{g,i-1}^{(2)} = V_{i-1}, \quad V_{g,i}^{(1)} = \frac{1}{\mu_i} V_i \quad (2)$$

$$\frac{dl_i}{dt} = V_{i-1} - \frac{1}{\mu_i} V_i \quad (3)$$

$$\Delta l_i = \frac{1}{s}\left(V_{i-1} - \frac{1}{\mu_i} V_i \right) \quad (4)$$

where: l_i is the length of rubber strip between *i*-th and (*i*+1)-th transporter, $V_{g,i-1}^{(2)}$ is rubber velocity at the end of the *(i*-1)-th transporter, $V_{g,i}^{(1)}$ is rubber velocity at the beginning of the *i*-th transporter, *n* is the number of transporters, Δl_i is length change of rubber strip between two consecutive transporters, V_{i-1} is the velocity of the (*i*-1)-th transporter, V_i is the velocity of the *i*-th transporter, μ_i is the rubber contraction coefficient for the i-th transporter.

Figure 2 shows a transition between two transporters. To regulate transporter velocities, it is necessary to measure the lenghts of rubber between transporters (Δl_i). These measurements are being done by special sensors (potenciometers – *P* in Fig. 2). Measurer (potenciometer) angle β_i satisfies the following relation:

$$\beta_i = \Phi(\Delta l_i) = \mathrm{sgn}(\Delta l_i) \frac{\pi}{6}\left(1 - e^{-0.01|\Delta l_i|}\right) \quad (5)$$

where Φ represents nonlinear dependency.

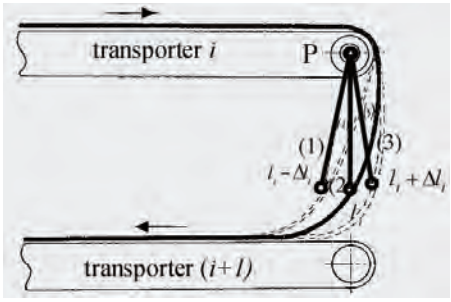

Fig. 2. The length measuring of the rubber between transporters

The value of β_i is between 0 and 90 degrees.

Potenciometer voltage is:

$$u_i = K_P \beta_i \quad (6)$$

where K_P is the potenciometer coefficient [V/rad].

Real coefficent value μ_i, $i = 1,2,3,4$ is in a range of (0.9042 - 0.9620), and when there are 13 transporters, this coefficent is in range of (0.9042 - 1). It is posible to determine the contraction coefficient for every cascade separately, using the next relation which was experimentally derived:

$$\eta_i = \frac{0.7 + 0.3e^{-\frac{i}{2.6}}}{0.7 + 0.3e^{-\frac{i-1}{2.6}}} \quad (7)$$

Potenciometer voltage is being amplified and, through thyristor regulators, the velocities of drive motors are being controled. Dynamics of *i*-th transporter can be described with following well known equation:

$$T_1 T_2 \frac{dV_i^2}{dt^2} + (T_1 + T_2)\frac{dV_i}{dt} + V_i = u_i \quad (8)$$

where T_1 and T_2 are mechanical and electrical time constants of electromechanical drive.

The transfer function with controller, drive motor, tachogenerator and reductors has the following form:

$$W(s) = \frac{V_i(s)}{u_i(s)} = \frac{k}{s^2 + as + b} \quad (9)$$

where *k*, *a*, *b* are gain functions and functions of time constants, respectively:

$$k = \frac{2\pi R k_r k_m k_t}{T_1 T_2}, \quad a = \frac{T_1 + T_2}{T_1 T_2}, \quad b = \frac{1 + k_t k_m k_{tg}}{T_1 T_2} \quad (10)$$

Constants in previous functions: k_r, k_m, k_t, k_{tg} are thyristor regulator, drive motor, transporter and tachogenerator gain, respectively; and *R* is drive drum radius.

Using stated equations (1)-(10), the block diagram of the entire system, given in Fig. 3, is obtained.

Integration of velocity between transporters can cause steady state error when parameter μ changes (change of used rubber quality or change of ambience temperature). In Fig. 2, middle position of the sensor (position (2)) correspondes to normal operating. If μ magnifies, sensor comes in positon (1) and steady state error $-\Delta l_i$ occures (the rubber streches). If μ decreases, sensor comes to positon (3) and steady state error $+\Delta l_i$ occures (the rubber accumulates). Compensational potenciometers (K_{ri} in Fig. 3) are introduced in order to compensate steady state errors, so their adjustement bring system back to normal operating (position (2) in Fig. 2). Today, these parameters are being adjusted manually (manual system adaptation). This paper presents a new method, based on genetic algorithms for automatic adaptation and optimization of disscused systems.

III. Experimental Results

The principles of genetic algorithms were first published by Holland in 1962 [8]. Genetic algorithms are optimization techniques based on simulating the phenomena that takes place in the evolution of species and adapting it to an optimization problem.

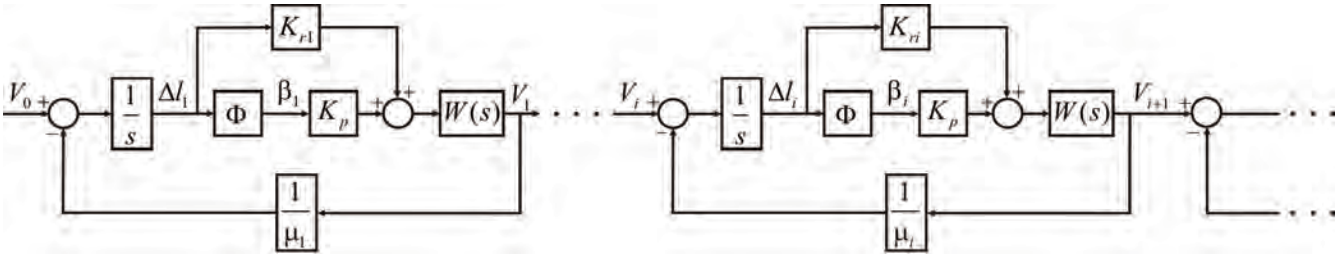

Fig. 3. Block diagram of the cascade-connected system in the tyre industry

Genetic algorithms have been used in many areas such as function optimization, image processing, system identification, etc. They have demonstrated very good performances as global optimizers in many types of applications [9], [10].

MATLAB model of the cascade-connected system with four transporters, based on block diagram in Fig. 3, is made.

For experimental purposes, cascade-connected system with four transporters (Fig. 4) has been practically realized in our Laboratory for modeling, simulation and systems control. Our system is capable for imitating real factory systems in all above-mentioned aspects.

The purpose of genetic algorithm is to optimize parameters K_{ri} on the bases of measured Δl_i .

Compensational parameters adjustment has been applied in [10] in order to minimize the steady state error. Steady state error is defined as deviation of rubber strip position between two transporters in steady and working state. It has been proven that this method is very slow, because a large number of parameters should be optimized at the same time. This could lead to temporary poor rubber quality at the end of the transporter. A poor rubber quality is a consequence of oscillations which are appearing during genetic algorithm execution. To avoid these oscillations, we propose adaptive control of the system, i.e. adaptive adjustment of all parameters independently. Thus, genetic algorithm, apllied in [10] for simultaneous optimisation of n parameters, is devided into n consecutive operations where each one is used for only one's parameter optimisation. The same goal is achived, but the algorithm is being executed n times faster which prevents the appearing of oscillations.

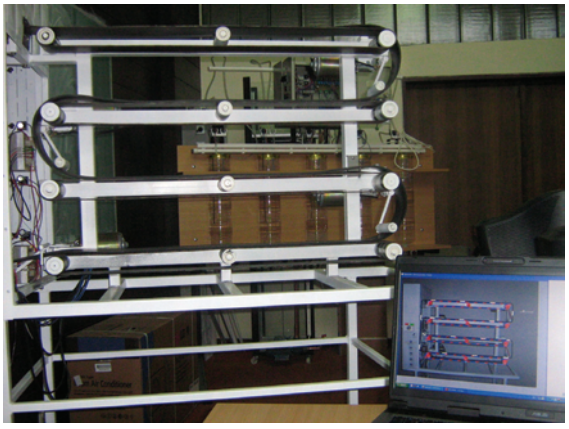

Fig. 4. Laboratory system with four transporters for experimenting

Fitness function is the sum of the mean square errors at all transporters (11). Smaller fitness fuction means lower error and, therefore, better chromosome.

$$J = (\Delta l_1)^2 + (\Delta l_2)^2 + (\Delta l_3)^2 + (\Delta l_4)^2 \qquad (11)$$

Algorithm converges very fast to the set of K_{ri} parameters which are optimal for the system and give the lowest fitness function. Genetic algorithm used in simulation has the following parameters: initial population of 150, number of generations 100, stochastic uniform selection, reproduction with four elite individuals, Gaussian mutation with shrinking and scattered crossover. In this way we obtained the following parameter values:

$$\begin{aligned} K_{r1} &= 1.786 \\ K_{r2} &= 1.588 \\ K_{r3} &= 1.401 \\ K_{r4} &= 1.207 \end{aligned} \qquad (12)$$

Velocities (normalized values) of individual transporters, for a given step input, are shown in Fig. 5.

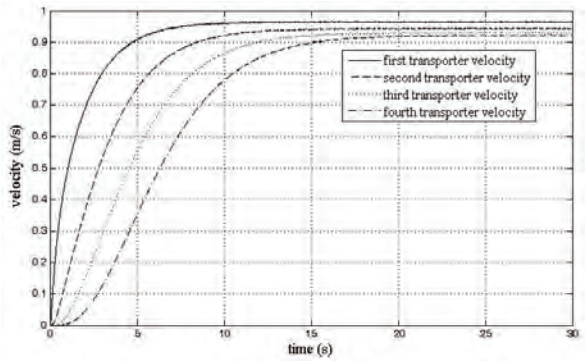

Fig. 5. Step response of laboratory cascade-connected system

IV. Conclusion

The new method for parameter optimization in systems for rubber strip cooling is presented in this paper. In this purpose, genetic algorithm is used. Parameters are being adjusted in discrete-time intervals and that gives good results for inert systems like the one considered in this paper. The gained results are better than those which are obtained by [10] in the sense of better speed and adaptation accuracy.

ACKNOWLEDGEMENT

The work presented here was supported by the Serbian Ministry of Education and Science (projects III 43007, III 44006 and TR 35005).

REFERENCES

[1] B. Danković, Z. Jovanović, "On the Reliability of Discrete-Time Control Systems with Random Parameters", Quality Technology and Quantitative Management, vol. 2, no 1, 2005.

[2] B. Danković, "On the Oscillations in the automated cascade systems for rubber threades transport", Jurema, Zagreb, 1989.

[3] D. Trajković, B. Danković, "Analyzing, Modeling and Simulation of the cascade Connected Transporters in Tyre Industy using Signal and Bond Graphs", Machine Dynamics Problems, vol. 29, No3, Warsaw University, 2005.

[4] B. Danković, M. Stanković, B. Vidojković, "On the Appearance of Chaos in the Automatic Control Cascade Systems", Proc. 7th Symposium of Mathematics and its Applications, Univ. of Timisoara.

[5] B. Danković, B. Vidojković, "On the Chaos in Cascade Systems for Rubber Strip Transportation", Proc. HM 2002, 4th International Conference, Heavy Machinery, pp. A97-A100.

[6] B. Danković, B. Vidojković, Z. Jovanović, "Dynamical Analysis of the Protector Cooling System in Tyre Industry", Proc. ICMFMDI 2002, XVII International Conference on Material Flow, Machines and Devices in Industry, pp. 56-59.

[7] B. Danković, D. Antić, Z. Jovanović, M. Milojković, "Genetic Algorithms Applied in Parameter Optimization of Casacade Connected Systems", ICEST 2007, Ohrid, Macedonia, June 24-27, 2007, pp. 557-560.

[8] J. H. Holland, "Outline for a logical theory of adaptive systems," J. ACM, vol. 3, pp. 297-314, July 1962; also in A. W. Burks, Ed., Essays on Cellular Automata, Univ. Illinois Press, 1970, pp. 297-319.

[9] D. Antić, M. Milojković and S. Nikolić, "Fuzzy sliding mode control with additional fuzzy control component", FACTA UNIVERSITATIS Series: Automatic Control and Robotics, vol. 8, no. 1, pp. 25-34, 2009.

[10] D. Antić, M. Milojković, S. Nikolić and S. Perić, "Optimal fuzzy sliding mode control with a time-varying sliding surface", Proceedings of the 8th International Conference on Computational Cybernetics and 9th International Conference on Technical Informatics, ICCC-CONTI 2010, Timisoara, Romania, May 27.-29., pp. 149-153, 2010

Sliding Mode Control of Anti-lock Braking System based on Reaching Law Method

Darko Mitić[1], Dragan Antić[2], Staniša Perić[3], Marko Milojković[4] and Saša Nikolić[5]

Abstract – **To improve the performances of anti-lock braking system, sliding mode control with constant plus proportional reaching law method is discussed in this paper. The proposed approach is verified through digital simulation and experimental results showing good system characteristics.**

Keywords – **Antilock braking system, Wheel slip, Sliding mode control, Reaching law method.**

I. INTRODUCTION

In order to prevent the wheels to stop completely during a sudden braking, an anti-lock braking system (ABS) is used as a standard equipment in modern vehicles. In the absence of ABS, during the braking phase, when the wheels are completely locked, the control over vehicle could be lost and it can skid in an undesirable direction. ABS does not allow the wheels to be stiffened and thus enable driver to normally operate with the vehicle.

The main objective of the ABS controller is to ensure the best adhesion of a wheel to a surface. This is performed by controlling the road adhesion coefficient representing the proportion between the friction force, generated during the acceleration and braking phase, and the normal load of the vehicle. It is shown that this coefficient is in nonlinear dependence on the wheel slip, defined as the relative speed difference between the wheel and vehicle. ABS controller is usually designed to regulate the wheel slip so that the road adhesion coefficient has a maximum value. The optimal value of wheel slip should be in the range from 0.08 to 0.3 [1].

ABS is a nonlinear system whose nonlinearities are reflected in unknown parameters of vehicle environment and nonlinear characteristics of braking dynamics. Besides that, the system parameters vary, which is caused by components deterioration, and many external disturbances cannot be predicted in advance. That is why sliding mode control (SMC) methods seem to be the right choice in the control of ABS.

SMC belongs to the well-studied class of discontinuous nonlinear control systems [2-4]. Sliding mode is of particular interest in these systems and it occurs when the system state is forced to move along a predefined sliding surface, determined by the so-called switching function. The switching function dynamics can be defined by using the so-called reaching law method [3]. The constant plus proportional variant of this control approach is used in this paper. If sliding mode exists, a system becomes robust to parameter variations and external disturbances, and its dynamics is known in advance and usually of the low order. The shortcoming of SMC is the existence of the chattering phenomenon. It occurs as the consequence of the high frequency control signal, which can excite the system's unmodelled dynamics.

Traditional SMC enhanced by a grey system theory is proposed in [5, 6]. Digital simulation results of ABS with conventional SMC, where hydraulic brake dynamics is neglected during the design, is shown in [7]. The combination of SMC and the sliding mode observer is elaborated in [8]. In [9], the SMC, allowing the maximum value of the wheel–road friction force during the braking phase, without *a priori* knowledge of optimal slip, is discussed. The adaptive SMC of vehicle traction is considered in [10]. The integration of SMC and pulse width modulation (PWM) method, realized by using computer software as opposed to hardware, is given in [11, 12]. For overall vehicle stability enhancement, the traditional SMC is also used in wheel slip control [13].

II. ANTI-LOCK BRAKING SYSTEM MODEL

We consider the system shown in Fig. 1 [14] with two rolling wheels: the lower car-road wheel and the upper car wheel which is in a rolling contact with the lower wheel. Two optical encoders are installed on both of the wheels to measure the angles with the resolution of $2\pi/2048 = 0.175°$. The wheel angular velocities are not measured and they are estimated by Euler formula with the sample time period of 0.5 ms.

The upper wheel is equipped in the disk brake system driven by the small *DC* motor. The lower wheel is coupled to the big flat *DC* motor using to accelerate the wheel and its power supply is switched off during the braking phase. Both *DC* motors are controlled by 3.5 kHz pulse-width modulation (PWM) signals.

The Fig. 1 shows the simple quarter vehicle model treating only longitudinal motion of the vehicle and angular motion of the wheel, while the lateral and the vertical motions are neglected. There is no influence of other vehicle wheels.

The car velocity is equal to the angular velocity of the lower wheel multiplied by the radius of this wheel, while the angular velocity of the wheel is equal to the upper wheel angular velocity. According to Fig. 1, x_1 represents the angular velocity of the upper wheel, x_2 is the angular velocity of the lower wheel and r_1, r_2 represents the radius of the upper and lower wheel, respectively.

A braking torque is applied to the upper wheel during braking phase causing wheel speed to decrease. Introducing the auxiliary variables:

$$s = \operatorname{sgn}\left(r_2 x_2 - r_1 x_1\right),\ s_1 = \operatorname{sgn}\left(x_1\right),\ s_2 = \operatorname{sgn}\left(x_2\right). \qquad (1)$$

[1,2,3,4,5]All authors are with the University of Niš, Faculty of Electronic Engineering, A. Medvedeva 14, 18000 Niš, Serbia, E-mail:{darko.mitic, dragan.antic, stanisa.peric, marko.milojkovic, sasa.s.nikolic}@elfak.ni.ac.rs.

The equation of the upper wheel motion is given in the following form:

$$J_1\dot{x}_1 = F_n r_1 s\mu(\lambda) - d_1 x_1 - s_1 M_{10} - s_1 M_1, \quad (2)$$

by using the Newton's second law, where: J_1 is the moment of inertia, d_1 is the viscous friction coefficient and M_{10} is the static friction of the upper wheel. According to (2), the friction force is assumed to be proportional to the normal pressing force F_n, where $\mu(\lambda)$ is the coefficient of proportion called the road adhesion coefficient.

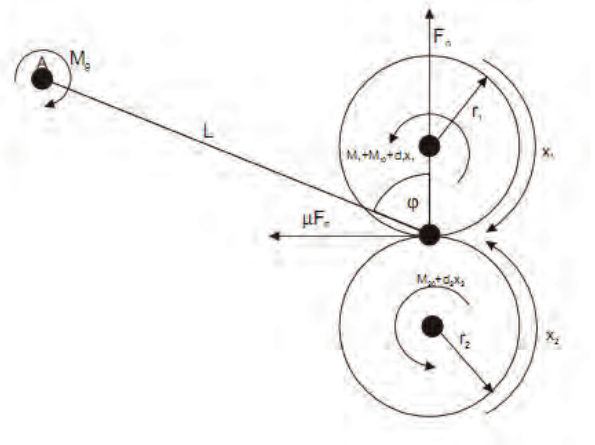

Fig. 1. ABS model (graphical presentation)

The lower wheel motion can be described by:

$$J_2\dot{x}_2 = -F_n r_2 s\mu(\lambda) - d_2 x_2 - s_2 M_{20}, \quad (3)$$

where J_2 is the moment of inertia, d_2 is the viscous friction coefficient and M_{20} is the static friction of the lower wheel. To derive the normal force F_n, we write the sum of torques corresponding to the point A in Fig. 1 as:

$$F_n L(\sin\varphi - s\mu(\lambda)\cos\varphi) = M_g + s_1 M_1 + s_1 M_{10} + d_1 x_1, \quad (4)$$

yielding:

$$F_n = \frac{M_g + s_1 M_1 + s_1 M_{10} + d_1 x_1}{L(\sin\varphi - s\mu(\lambda)\cos\varphi)}, \quad (5)$$

where M_g represents gravitational and shock absorber torques acting on the balance lever, L is the distance between the contact point of the wheels and the rotational axis of the balance and φ is the angle between the normal in the contact point and the line L.

Replacing F_n from (5) in (2) and (3), the model becomes:

$$\begin{aligned} J_1\dot{x}_1 &= \frac{M_g + s_1 M_1 + s_1 M_{10} + d_1 x_1}{L(\sin\varphi - s\mu(\lambda)\cos\varphi)} r_1 s\mu(\lambda) - s_1 M_1 - d_1 x_1 - s_1 M_{10}, \\ J_2\dot{x}_2 &= -\frac{M_g + s_1 M_1 + s_1 M_{10} + d_1 x_1}{L(\sin\varphi - s\mu(\lambda)\cos\varphi)} r_2 s\mu(\lambda) - d_2 x_2 - s_2 M_{20}. \end{aligned} \quad (6)$$

While the wheel angular velocity would match the forward car velocity in the normal operating conditions, in the course of the braking and the acceleration phases these velocities differs one from other. Their difference is called a wheel slip λ, defined as:

$$\lambda = \begin{cases} \frac{r_2 x_2 - r_1 x_1}{r_2 x_2}, r_2 x_2 \geq r_1 x_1, x_1 \geq 0, x_2 \geq 0, \\ \frac{r_1 x_1 - r_2 x_2}{r_1 x_1}, r_2 x_2 < r_1 x_1, x_1 \geq 0, x_2 \geq 0, \\ \frac{r_2 x_2 - r_1 x_1}{r_2 x_2}, r_2 x_2 < r_1 x_1, x_1 < 0, x_2 < 0, \\ \frac{r_1 x_1 - r_2 x_2}{r_1 x_1}, r_2 x_2 \geq r_1 x_1, x_1 < 0, x_2 < 0, \\ 1, x_1 < 0, x_2 \geq 0, \\ 1, x_1 \geq 0, x_2 < 0. \end{cases} \quad (7)$$

for all model operating conditions. A zero wheel slip represents the equality of the wheel and the vehicle velocities, while the slip value equal to one tells us that the tire is not rotating and the wheels are skidding on the road surface, meaning that the vehicle is no more steerable.

The road adhesion coefficient $\mu(\lambda)$ is a nonlinear function of wheel slip and other physical variables, and one of its model can be given by:

$$\mu(\lambda) = \frac{w_4 \lambda^p}{a + \lambda^p} + w_3\lambda^3 + w_2\lambda^2 + w_1\lambda. \quad (8)$$

Equation (6) can be rewritten as:

$$\begin{aligned} \dot{x}_1 &= S(\lambda)(c_{11}x_1 + c_{12}) + c_{13}x_1 + c_{14} + (c_{15}S(\lambda) + c_{16})s_1(x_1)M_1, \\ \dot{x}_2 &= S(\lambda)(c_{21}x_1 + c_{22}) + c_{23}x_1 + c_{24} + c_{25}S(\lambda)s_1(x_1)M_1. \end{aligned} \quad (9)$$

where:

$$\begin{aligned} S(\lambda) &= \frac{s\mu(\lambda)}{L(\sin\varphi - s\mu(\lambda)\cos\varphi)}, c_{11} = \frac{r_1 d_1}{J_1}, \\ c_{12} &= \frac{(s_1 M_{10} + M_g) r_1}{J_1}, c_{13} = -\frac{d_1}{J_1}, c_{14} = -\frac{s_1 M_{10}}{J_1}, \\ c_{15} &= \frac{r_1}{J_1}, c_{16} = -\frac{1}{J_1}, c_{21} = -\frac{r_2 d_1}{J_2}, c_{22} = -\frac{(s_1 M_{10} + M_g) r_2}{J_2}, \\ c_{23} &= -\frac{d_2}{J_2}, c_{24} = -\frac{s_2 M_{20}}{J_2}, c_{25} = -\frac{r_2}{J_2}. \end{aligned} \quad (10)$$

In the braking phase, the wheel speed will be lower than vehicle speed, i.e. $r_2 x_2 \geq r_1 x_1$ and $x_1 > 0$, $x_2 > 0$, so that the wheel slip is determined by:

$$\lambda = \frac{r_2 x_2 - r_1 x_1}{r_2 x_2} \quad (11)$$

In that case, since $s = s_1 = s_2 = 1$, (9) is rewritten as:

$$\begin{aligned} \dot{x}_1 &= S(\lambda)(c_{11}x_1 + c_{12}) + c_{13}x_1 + c_{14} + (c_{15}S(\lambda) + c_{16})M_1, \\ \dot{x}_2 &= S(\lambda)(c_{21}x_1 + c_{22}) + c_{23}x_1 + c_{24} + c_{25}S(\lambda)M_1. \end{aligned} \quad (12)$$

ABS controller is designed to regulate the vehicle slip at the desired value, where the friction force, i.e. road adhesion coefficient, reaches its maximum value. That is why we determine vehicle model with wheel slip as a controlled variable. Differentiating (11) results in:

$$\dot{\lambda} = -\frac{r_1}{r_2 x_2}\dot{x}_1 + \frac{r_1 x_1}{r_2 x_2^2}\dot{x}_2 . \quad (13)$$

Putting (12) in (13) finally yields and taking into account that:

$$\lambda = 1 - \frac{r_1 x_1}{r_2 x_2} \Rightarrow x_1 = \frac{r_2}{r_1}(1-\lambda)x_2 , \quad (14)$$

yields:

$$\dot{\lambda} = f(\lambda, x_2) + g(\lambda, x_2) M_1 ,\ x_2 \neq 0 , \quad (15)$$

where

$$f(\lambda, x_2) = -\left(\begin{array}{l}\left(S(\lambda)c_{11} + c_{13}\right)(1-\lambda) + \\ + \frac{r_1}{r_2 x_2}\left(S(\lambda)c_{12} + c_{14}\right)\end{array}\right) + \\ + \frac{(1-\lambda)}{x_2}\left(\begin{array}{l}\left(S(\lambda)c_{21}\frac{r_2}{r_1}(1-\lambda) + c_{23}\right)x_2 + \\ + S(\lambda)c_{22} + c_{24}\end{array}\right) \quad (16)$$

$$g(\lambda, x_2) = -\frac{r_1}{r_2 x_2}\left(c_{15}S(\lambda) + c_{16} - \frac{r_2}{r_1}c_{25}S(\lambda)(1-\lambda)\right). \quad (17)$$

III. Sliding Mode Control Based on Constant Plus Proportional Reaching Law

Since the system is of first order, the switching function is selected as:

$$\sigma = \lambda - \lambda_r , \quad (18)$$

where λ_r is the constant reference wheel slip. The main control design objective is to find control providing $\sigma = 0$ and consequently $\lambda = \lambda_r$. The switching function dynamics is defined via the constant plus proportional reaching law [3]:

$$\dot{\sigma} = \dot{\lambda} = -M_k \sigma - M_Q \operatorname{sgn}(\sigma), M_k > 0, M_Q > 0 , \quad (19)$$

enabling the finite reaching time determined by:

$$t_r < \ln\left(\left(M_k|\sigma| + M_Q\right)/M_Q\right)/M_k . \quad (20)$$

By substituting (19) in (15), the control torque becomes:

$$M_1 = -g(\lambda, x_2)^{-1}\left(f(\lambda, x_2) + M_k\sigma + M_Q \operatorname{sgn}(\sigma)\right). \quad (21)$$

Since the nominal values of f and g are $\hat{f}$ and $\hat{g}$ respectively, the control torque implemented in real control is:

$$M_1 = -\hat{g}(\lambda, x_2)^{-1}\left(\hat{f}(\lambda, x_2) + M_k\sigma + M_Q \operatorname{sgn}(\sigma)\right). \quad (22)$$

For the sake of simplicity, we denote $g(\lambda, x_2) = g$, $\hat{g}(\lambda, x_2) = \hat{g}$, $f(\lambda, x_2) = f$ and $\hat{f}(\lambda, x_2) = \hat{f}$. We assume that $|\hat{f}| < \hat{F}$, $|f - \hat{f}| < \varepsilon_f$ and $|1 - g/\hat{g}| < \varepsilon_g < 1$, where $\hat{F}$, ε_f and ε_g are the positive real constants, as well as $g/\hat{g} > 0$.

The implementation of (22) in (15) gives:

$$\dot{\sigma} = f - \hat{f} + \hat{f}\left(1 - \frac{g}{\hat{g}}\right) - \frac{g}{\hat{g}}M_k\sigma - \frac{g}{\hat{g}}M_Q \operatorname{sgn}(\sigma). \quad (23)$$

The existance conditions of sliding mode is fulfilled:

$$\sigma\dot{\sigma} = \frac{g}{\hat{g}}\left(\frac{\hat{g}}{g}\left(f - \hat{f}\right)\sigma + \frac{\hat{g}}{g}\hat{f}\left(1 - \frac{g}{\hat{g}}\right)\sigma - M_k\sigma^2 - M_Q|\sigma|\right) < 0 , \quad (24)$$

if M_Q is chosen in accordance with:

$$M_Q > \max\left(\left|\frac{\hat{g}}{g}\left(f - \hat{f}\right) + \frac{\hat{g}}{g}\hat{f}\left(1 - \frac{g}{\hat{g}}\right)\right|\right), \quad (25)$$

which is satisfied if

$$M_Q > \frac{\varepsilon_f + \hat{F}\varepsilon_g}{1 - \varepsilon_g} , \quad (26)$$

since $1 - \varepsilon_g < g/\hat{g} < 1 + \varepsilon_g \Rightarrow 1/(1+\varepsilon_g) < \hat{g}/g < 1/(1-\varepsilon_g)$. M_k is selected to make the reaching phase as faster as possible.

IV. Experimental Results

For the practical verification of the proposed control method, the ABS produced by Inteco [14] is utilized. The ABS framework is previously described in Section II and it represents the open-architecture software environment for real-time control experiments on the basis of MATLAB and Simulink tools.

Both simulation and real-time experiments are performed and results are given in Figs. 2 and 3. Each figure consists of three subplots representing the responses of wheel and vehicle velocities (speeds), the wheel slip and the control brake torque, respectively. The reference wheel slip is considered to be constant and $\lambda_r = 0.2$.

Firstly, the digital simulation is done. Fig. 2 shows the case with $M_k = 2$ and $M_Q = 1$. The sliding mode exists, but the chattering is not too large since the constant component of reaching law control is taken to be as small as possible. The

proportional term, ensuring existence of sliding motion with faster reaching time, enables such selection of M_Q .

Figure 3 presents the experimental results performed in the previous described real-time framework. To cope with unmodelled dynamics, M_k and M_Q are chosen to be 10 and 4, respectively. It can be notice that experimental results are similar to the simulation ones, despite the presence of noise and the fact that the control input is more limited than in the case with digital simulation. The proposed control approach slightly improves the system accuracy in comparison with the results given in [15].

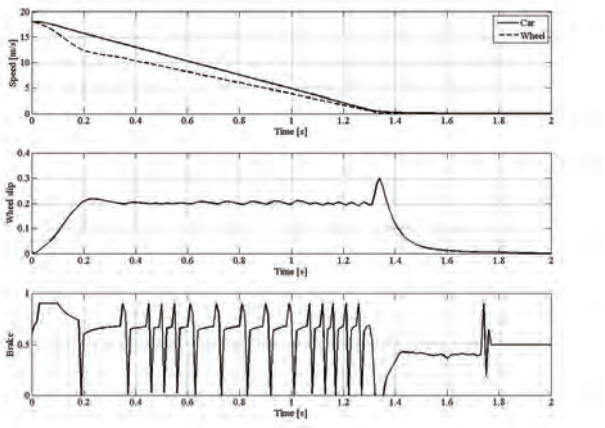

Fig. 2. ABS responses: SMC with constant plus proportional reaching law (simulation results)

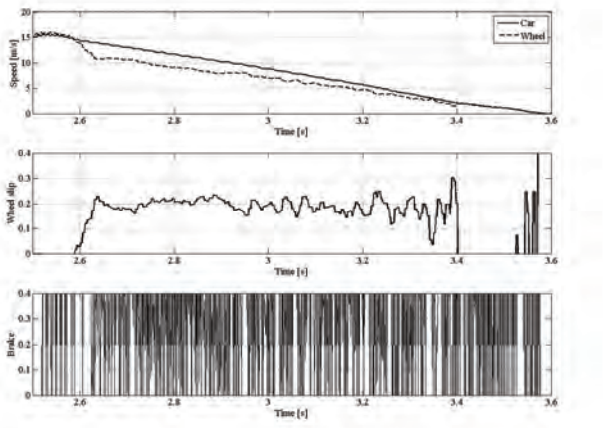

Fig. 3. ABS responses: SMC with constant plus proportional reaching law (experimental results)

V. Conclusion

This paper treats the sliding mode control of anti-lock braking system on the basis of constant plus proportional reaching law method. Both digital simulation and experimental results shows good performances in relation to traditional sliding mode control concepts.

Acknowledgement

This work was supported in part by the Serbian Ministry of Science and Technology within the projects II 43007, II 44006 and TR 35005.

References

[1] A. Zanten, R. Erhardt and A. Lutz, “Measurement and Simulation of Transients in Longitudinal and Lateral Tire Forces”, SAE Paper, vol. 99, no. 6, pp. 300-318, 1990.

[2] J. Y. Hung, W. Gao and J. C. Hung, “Variable Structure Control: A Survey”, IEEE Transactions on Industrial Electronics, vol. 40. no. 1, 1993.

[3] W. Gao and J. C. Hung, “Variable Structure Control of Nonlinear systems: A New Approach”, IEEE Transactions on Industrial Electronics, vol. 40, no. 1, 1993.

[4] V. I. Utkin, “Sliding Mode Control Design Principles and Application to Electric Drives”, IEEE Transactions on Industrial Electronics, vol. 40, no. 1, 1993.

[5] Y. Oniz, E. Kayacan and O. Kaynak, “Simulated and Experimental Study of Antilock Braking System Using Grey Sliding Mode Control”, ISIC. IEEE International Conference on Systems, Man and Cybernetics, pp. 90-95, 7-10 October 2007.

[6] E. Kayacan, Y. Oniz and O. Kaynak, “A Grey System Modeling Approach for Sliding-Mode Control of Antilock Braking Systems”, IEEE Transactions on Industrial Electronics, vol. 56, no. 8, pp. 3244-3252, 2009.

[7] N. Hamzah, M.Y. Sam and A. A. Basari, “Enhancement of Driving Safety Feature via Sliding Mode Control Approach”, Fourth International Conference on Computational Intelligence, Robotics and Autonomous Systems, pp. 116-120, November 28-30, 2007.

[8] C. Unsal and P. Kachroo, “Sliding Mode Measurement Feedback Control for Antilock Braking Systems”, IEEE Transactions on Control Systems Technology, vol. 7, no. 2, pp. 271-281, 1999.

[9] S. Drakunov, U. Ozguner, P. Dix and B. Ashrafi, “ABS Control Using Optimum Search via Sliding Modes”, IEEE Transactions on Control Systems Technology, vol. 3, no. 1, pp. 79-85, 1995.

[10] A. El Hadri, J. C Cadiou and N. K. M’sirdi, “Adaptive Sliding Mode Control of Vehicle Traction”, 15th Triennial World Congress, July 21-26, 2002.

[11] M. Wu and M. Shih, “Using the Sliding-Mode Pwm Method in an Anti-lock Braking System”, Asian Journal of Control, vol. 3, no. 3, pp. 255-261, 2001.

[12] M. Wu and M. Shih, “Simulated and Experimental Study of Hydraulic Anti-lock Braking System Using Sliding-mode PWM Control”, Mechatronics, vol. 13, no. 4, pp. 331-351, 2003.

[13] S. Zheng, H. Tang, Z. Han and Y. Zhang, “Controller Design for Vehicle Stability Enhancement”, Control Engineering Practice, vol. 14, no. 12, pp. 1413-1421, 2006.

[14] Inteco, “The Laboratory Anti-lock Braking System Controlled from PC”-User’s Manual, (2008) available at www.inteco.com.pl.

[15] D. Antić, V. Nikolić, D. Mitić, M. Milojković and S. Perić, “Sliding Mode Control of Anti-lock Braking System: An Overview”, Facta Universitatis Series: Automatic Control and Robotics, vol. 9, no. 1, pp. 41-58, 2010.

Secure Data Transmission Approach with Two-stage Chaotic Protection

Dragomir Chantov[1]

***Abstract* – In this paper an approach for chaotic data protection, applicable to different types of secure communication systems, is proposed. The essence of the proposed method is in combining two independent principles of chaotic data protection – chaotic masking and chaotic parameter modulation, together in order to obtain a higher security level. The method implies the usage of two different pairs of synchronized chaotic systems, integrated in the transmitter and in the receiver of the communication system. The binary information signal modulates a particular parameter of the first system in the transmitter in such way, that the system switches between two different chaotic attractors. The synchronizing chaotic signal, containing and hiding the information signal, is then not directly fed to the identical chaotic system in the receiver as by the standard chaotic parameter modulation approach, but is added to the synchronizing chaotic signal of the second synchronization scheme. In such way the chaotic masking technique is applied, but the masked signal is not the information signal, but the synchronizing signal of the first synchronization scheme. By masking a chaotic signal with another chaotic signal, produced from two different systems, a higher degree of information protection is achieved.**

***Keywords* – Chaotic synchronization, Chaotic masking, Chaotic sswitching**

I. INTRODUCTION

Chaotic systems are a specific class of nonlinear systems, characterized with high sensitivity to the initial conditions and a positive Lyapunov exponent(s), which determines the exponential setting apart of the nearby trajectories and the forming of a strange attractor in the phase space. Due to their properties, which put the chaotic systems neither in the class of the determined nor in that of the stochastic systems, they are used in communication systems with chaotic data protection, where the specific features of the chaotic signal are used to hide the transmitted information signal.

These communication systems are based on a phenomenon, called chaotic synchronization. To synchronize two or more chaotic systems means to design a proper coupling between them in such way that the motion of the systems to be in some aspect synchronized. After achieving stable synchronization between two chaotic systems, the coupling chaotic signal between them can be used to bear and hide some kind of useful signal, for example the information signal of a communication system. Different approaches of chaotic data protection are offered so far, the most popular are the chaotic masking technique [1] and the chaotic parameter modulation [2]. However, some research works have shown, that not always these techniques can guarantee the desired level of security.

The chaotic synchronization data protection method, proposed in this paper, implies a two-level structure with synchronized chaotic systems in the transmitter and in the receiver of the communication system. The chaotic parameter modulation technique is used in the first pair of systems to encode a binary information signal. Instead of directly transmitting the chaotic coupling signal through the transmission channel, as with the basic method, it is added to the synchronization chaotic signal of the second pair of completely different chaotic systems. In this way a chaotic signal is masked with another chaotic signal, enhancing the security level of the whole system.

The remaining sections of the paper are organized as follows. In Section II the basic chaotic synchronization definitions are given. In Section III the proposed technique for secure data transmission with two-stage chaotic protection is defined. In Section IV the numerical results with the Van der Poll - Duffing and Rossler chaotic systems, used for the two levels of data protection, are presented.

II. CHAOTIC SYNCHRONIZATION WITH COMBINED DECOMPOSITION-TYPE AND FEEDBACK COUPLING

The main task of chaotic synchronization is to design a coupling scheme between two or more chaotic systems in such way, that their dynamics to be synchronized. Two uni-directionally coupled continuous chaotic systems, called *Master* system and *Slave* system, defined with:

$$Master\ \dot{\mathbf{x}} = \mathbf{f}(\mathbf{x}, t),\ Slave\ \dot{\tilde{\mathbf{x}}} = \tilde{\mathbf{f}}(\tilde{\mathbf{x}}, \mathbf{x}, t) \qquad (1)$$

where $\mathbf{x} \in \Re^n$ and $\tilde{\mathbf{x}} \in \Re^n$, are called *synchronized* in terms of a given function $Q_t = Q_t[\mathbf{x}(t), \tilde{\mathbf{x}}(t)]$, if $\lim_{t\to\infty} Q_t = 0$. By the most common case of two identical chaotic systems, subjected to synchronization, this function usually is $Q_t = \|\mathbf{e}(t)\|$, where $\mathbf{e}(t)$ is the difference (the error) between the states of the two systems:

$$\mathbf{e}(t) = \mathbf{x}(t, \mathbf{x}(t_0)) - \tilde{\mathbf{x}}(t, \tilde{\mathbf{x}}(t_0)). \qquad (2)$$

The Master and Slave systems are *identically synchronized*, if:

$$\lim_{t\to\infty} \mathbf{e}(t) = 0. \qquad (3)$$

Different approaches to design the coupling are proposed so far. In this paper the combined synchronization approach, proposed in [3], is used. This approach is a combination of the well-known *Partial Replacement* (PR) and *Feedback-coupling* (FB) synchronization methods and implies a double connection between the systems of the type:

$$\dot{\mathbf{x}} = \mathbf{f}(\mathbf{x}, x_i) \rightarrow \dot{\tilde{\mathbf{x}}} = \mathbf{f}(\tilde{\mathbf{x}}, x_i) + \alpha \mathbf{E}(\mathbf{x} - \tilde{\mathbf{x}}). \qquad (4)$$

[1]Dragomir Chantov is with the Department of Automation, Technical University of Gabrovo, Hadji Dimitar 4, 5300 Gabrovo, Bulgaria, E-mail: dchantov@yahoo.com.

This technique gives the possibility to design a far greater number of coupling variants than the basic PR and the FB methods.

III. Method for Secure Data Transmission with Two-stage Chaotic Protection

Two of the most popular methods for chaotic data protection in communication systems are the chaotic masking and the chaotic parameter modulation (chaotic switching) techniques.

By the first one, the data signal is simply added to the chaotic synchronization signal, generated from the master chaotic system at the transmitter. If the amplitude of the data signal is significantly lower than that of the chaotic signal, the synchronization scheme remains stable and the re-construction of the system's variables in the Slave system in the receiver (after achieving stable synchronization) allows the extraction of the data signal.

The chaotic parameter modulation method is characterized with the coding of a binary information signal by different chaotic attractors, obtained for different values of a system parameter at the transmitter. Although more reliable than the chaotic masking technique, this approach also has some limitations and in some cases the desired security level can not be achieved.

The proposed two-stage chaotic data protection method, which implies the consecutive application of the afore-mentioned principles, is illustrated on Fig. 1. The system consists of two synchronization schemes – Master 1 – Slave 1 and Master 2 – Slave 2, which are based on *different chaotic systems*. The chaotic parameter modulation is applied to the Master 1 system at the transmitter. Instead of transmitting the chaotic coupling signal x_i directly to the Slave 1 system at the receiver, it is then masked with a second chaotic signal y_l, generated from a completely different chaotic system at the transmitter. In such way the transmitted signal through the transmission channel is $s(t) = y_l(t) + x_i(t)$, which is a combination of two different chaotic signals. If the level of $x_i(t)$ is sufficiently lower than that of the bearing signal $y_l(t)$ and if a stable synchronization scheme is designed for the pair Master 2 – Slave 2, the signal $x_i(t)$ can be recovered at the receiver - $x_{ir}(t)$. If the level of $x_i(t)$ is such, that it hampers the synchronization of the second pair of systems, it can be scaled down to $x_{isc}(t)$ by the gain k and after extracting the recovered signal $x_{iscr}(t)$ at the receiver it is re-scaled to its original level.

The recovered chaotic signal $x_{ir}(t)$ drives the Slave 1 system at the receiver. according to the preliminarily designed coupling scheme with stable synchronization. After detecting the moments of synchronized and de-synchronized behavior of the pair Master 1 – Slave 1 by the accessible error functions, the original information signal is recovered at the receiver - i_r.

Both synchronization schemes can be designed using the combined method, defined in Section II, to take advantage of the great variety of coupling variants, offered by this approach. The Master 1 – Slave 1 scheme is then defined with:

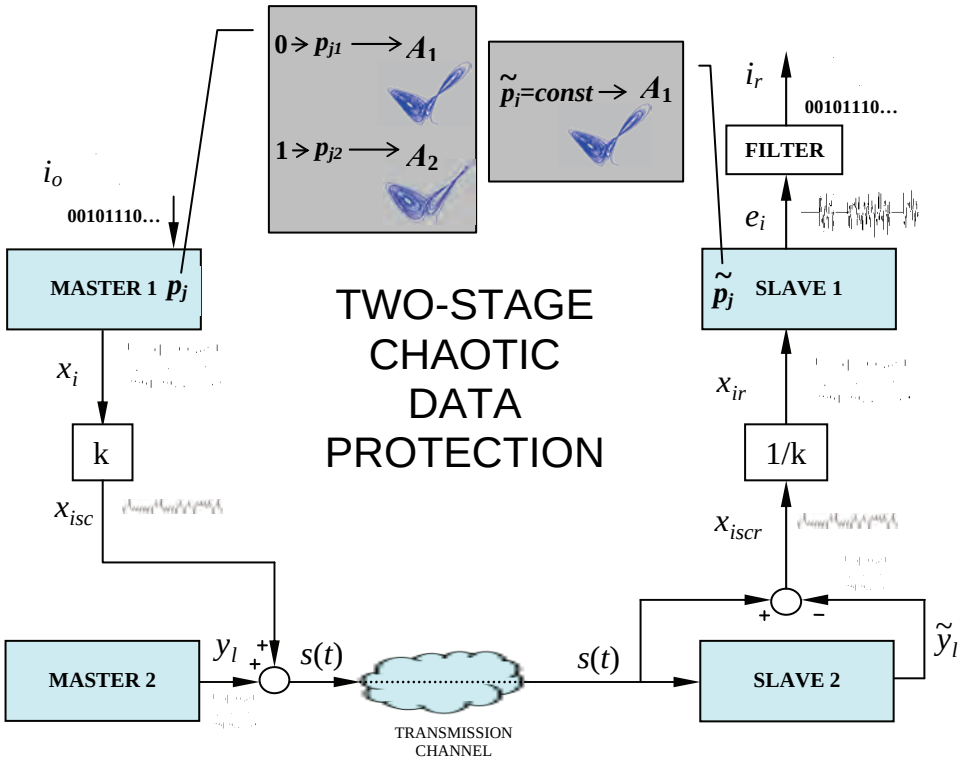

Fig. 1. Two-stage data protection technique with chaotic parameter modulation and chaotic masking

$$\dot{\mathbf{x}} = \mathbf{f}(\mathbf{x}, x_i, p_j) \rightarrow \dot{\tilde{\mathbf{x}}} = \mathbf{f}(\tilde{\mathbf{x}}, x_{ir}) + \alpha_x \mathbf{E}_x (\mathbf{x} - \tilde{\mathbf{x}}), \quad (5)$$

where p_j is the parameter, modulated by the information signal $i_o(t)$.

The Master 2 – Slave 2 scheme is defined with:

$$\dot{\mathbf{y}} = \mathbf{g}(\mathbf{y}, y_l) \rightarrow \dot{\tilde{\mathbf{y}}} = \mathbf{g}(\mathbf{y}, s(t)) + \alpha_y \mathbf{E}_y (\mathbf{y} - \tilde{\mathbf{y}}), \quad (6)$$

where $s(t) = y_l(t) + x_{isc}(t)$ is the signal, transmitted through the channel.

The recovered scaled synchronizing signal of the first pair at the receiver is:

$$x_{iscr}(t) = s(t) - \tilde{y}_l(t). \quad (7)$$

Apparently, the reconstruction of this signal can be achieved after the second pair of chaotic systems synchronizes, i.e. after $y_l(t) = \tilde{y}_l(t)$.

The main advantage of the proposed approach is that in fact one chaotic signal is masked by another one, produced from different system, and the combined chaotic signal is the only signal, transmitted through the channel of the communication system. In such way, by combining the advantages of two known approaches for secure data transmission with chaotic protection, the security level of the system is enhanced.

IV. Numerical Experiments

To test the proposed two-stage chaotic data protection approach, two well-known chaotic models are chosen for designing the two separate synchronization schemes.

The Master 1 – Slave 1 synchronization scheme is designed on the basis of the Van der Pol – Duffing (VPD) third-order continuous chaotic model [4], which is described by the equations:

$$\begin{aligned} \dot{x}_1 &= -\nu(x_1^3 - \sigma x_1 - x_2), \\ \dot{x}_2 &= x_1 - x_2 - x_3, \\ \dot{x}_3 &= \beta x_2, \end{aligned} \quad (8)$$

where the nominal parameter values are: $\nu = 100$, $\sigma = 0.35$, $\beta = 300$. The VPD attractor, obtained by computer simulation with Matlab, is shown on Fig. 2(a).

As the first synchronization scheme is used for the parameter modulation data transmission technique, one of its parameters has to be selected for the modulating procedure. The experiments with the three parameters of the VPD system show, that the parameter β is an appropriate candidate for this task. The p_{j1} value, used to code the zeros of the information signal, can be the nominal value $\beta = 300$. After some simulations, the p_{j2} value, used to code the ones, is set to $\beta = 350$. The VPD attractor for $\beta = 350$ is shown on Fig. 2(b). Obviously, it occupies the same area of the state space as the basic attractor, but is slightly different. In such way the switching moments between the two attractors will be unidentifiable by observation of the time-series of the state variables, as the transitions between the two attractors are commensurable with the transitions between the unstable periodic orbits within the basic attractor. On the other hand, as it will be shown further, the difference between the two attractors is enough the two systems to de-synchronize when the ones of the information signal are transmitted.

The Master 2 – Slave 2 scheme is designed on the basis of the Rossler third-order continuous chaotic model [5], which is described by the equations:

$$\begin{aligned} \dot{y}_1 &= -y_2 - y_3, \\ \dot{y}_2 &= y_1 + a y_2, \\ \dot{y}_3 &= b + y_1 y_3 - c y_3, \end{aligned} \quad (9)$$

where the nominal parameter values are: $a = 0.2$, $b = 1$, $c = 9$. The Rossler attractor is shown on Fig. 2(c).

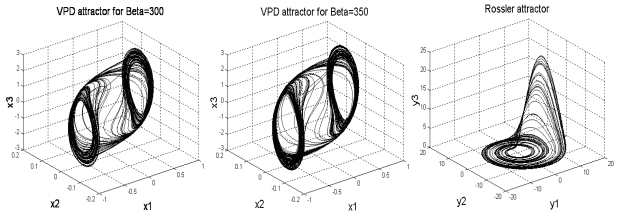

(a) (b) (c)

Fig. 2. (a) - VPD attractor for $\beta = 300$; (b) - VPD attractor for $\beta = 350$; (c) - Rossler attractor

At first, both synchronization schemes are designed and simulated independently to find the most appropriate type of the couplings. After testing the different possible variants of the combined synchronization approach over the Van der Pol – Duffing model and assuming only a one-variable coupling, the Slave 1 system is designed in the following way:

$$\begin{aligned} \dot{\tilde{x}}_1 &= -\nu(\tilde{x}_1^3 - \sigma \tilde{x}_1 - \underline{x_2}), \\ \dot{\tilde{x}}_2 &= \tilde{x}_1 - \tilde{x}_2 - \tilde{x}_3 + \underline{\alpha_x (x_2 - \tilde{x}_2)}, \\ \dot{\tilde{x}}_3 &= \beta \tilde{x}_2, \end{aligned} \quad (10)$$

where the coupling gain is $\alpha_x = 20$.

The Slave 2 Rossler system is designed according to the same principles as the previous one. The most appropriate variant of the combined synchronization approach, again implying the self-imposed limitation of one-variable coupling to get the most "economic" coupling, is defined with the equations:

$$\begin{aligned} \dot{\tilde{y}}_1 &= -\tilde{y}_2 - \tilde{y}_3, \\ \dot{\tilde{y}}_2 &= \tilde{y}_1 + a \underline{y_2} + \underline{\alpha_y (y_2 - \tilde{y}_2)}, \\ \dot{\tilde{y}}_3 &= b + \tilde{y}_1 \tilde{y}_3 - c \tilde{y}_3, \end{aligned} \quad (11)$$

where the coupling gain is $\alpha_y = 2$.

After designing the two stable synchronization schemes, the two-stage chaotic data protection system can be built according to the scheme, shown on Fig. 1. To imitate the information signal i_o in the simulation scheme, a pulse generator with period of 20*s* and 50% duty cycle is used. It modulates the β parameter of the Master 1 VPD system at the transmitter between the values $\beta = 300$ and $\beta = 350$.

The time series of the modulated parameter $\beta(t)$ is shown on Fig. 3(a).

The experiments have shown that no additional scaling of the synchronization signal of the first synchronization scheme is necessary as the level of the VPD x_2 coupling variable is significantly lower than the y_2 Rossler synchronization signal. The time series of the modulated by the information signal VPD coupling variable x_{2MOD} is shown on Fig. 3(b).

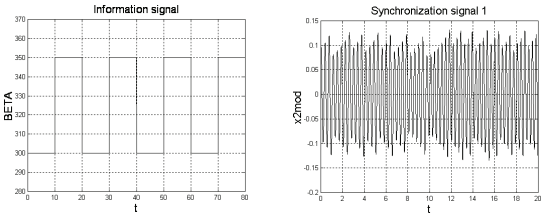

(a) (b)

Fig. 3. (a) – Information signal; (b) – Synchronization signal of the first synchronization scheme

The combined chaotic signal $s(t) = y_2(t) + x_{2MOD}(t)$, transmitted over the channel, is shown on Fig. 4(a). One of the zero-to-one transition moments of the information signal is magnified on Fig. 4(b). It is obvious that the switching remains undetectable by observing the time series of $s(t)$. After the two Rossler systems are synchronized, the recovered VPD synchronization signal $x_{2rMOD}(t)$ at the receiver is approximately equal to the original signal $x_{2MOD}(t)$ at the transmitter. Consequently, $x_{2rMOD}(t)$ can be used to synchronize the Slave 1 VPD system with the MASTER 1 system at the transmitter. Then the observation of the second error function $e_2(t) = x_{2MOD}(t) - \tilde{x}_2(t)$ at the receiver, shown on Fig. 4(c), allows to restore the original information signal after the initial synchronization of the two Rossler systems.

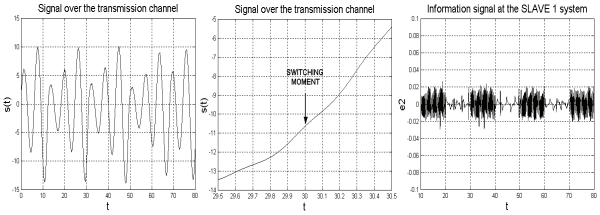

(a) (b) (c)

Fig. 4. (a) – Signal over the transmission channel $s(t)$; (b) – One of the switching moments over $s(t)$; (c) – Error function $e_2(t) = x_{2MOD}(t) - \tilde{x}_2(t)$

The de-synchronization moments (the ones of the information signal) are clearly visible on the figure. The experiments show that the variance of $e_2(t)$ is about $1.2e-4$ in the de-synchronization windows (a "one" transmission) and about $1.7e-5$ in the synchronization ones (a "zero" transmission). A simple filter can then be designed in the receiver module to track the changes in the variance of the error function in order to restore the original information signal.

V. CONCLUSION

A method for secure data transmission with chaotic protection of the information signal was presented in this paper. The proposed method combines the advantages of chaotic masking and chaotic parameter modulation techniques and at the same time it ensures a higher rate of data security by transmitting only a chaotic signal, generated by one chaotic system, masked with another chaotic signal, generated by completely different chaotic system, over the transmission channel. The reconstruction of the information signal at the receiver is achieved by application of a simple algorithm, assuming stable synchronization schemes are designed for the chaotic parameter modulation and chaotic masking procedures. To facilitate the design of such schemes, a synchronization approach implying a combination of partial replacement and feedback coupling synchronization methods is used. It allows to design a large number of coupling schemes for any particular pair of chaotic systems and it was proven empirically, that some of these schemes achieve faster synchronization than the fastest variant of the basic synchronization methods. This permits a faster rate of data transmission if a chaotic data protection system is designed on the basis of the given synchronization scheme.

REFERENCES

[1] U. Parlitz, *et all*, "Encoding messages using chaotic synchronization", Physical Review E, Vol.53, No.5, pp.4351-4361, 1996.

[2] M. Ogorzalek, "Taming chaos – part I: Synchronization", IEEE Transactions on Circuits and Systems-I, Vol.40, No.10, pp.693-699, 1993.

[3] R. Radev, D. Chantov, "Control of chaotic system by combined synchronization", Proc. of International Scientific Conference ICEST 2005, 29 June - 1 July 2005, Nis, Serbia, pp.490-493.

[4] G. King and T. Saito, "Bistable chaos. I. Unfolding the cusp", Physical Review A, Vol.46, No.6, pp.3092-3099, 1992.

[5] O. Rossler, "An equation for continuous chaos", Physics Letters, Vol.57A, No.5, pp.397-398, 1976.

A Practical Approach to Control of an Overhead Crane

Plamen Petrov[1] and Lubomir Dimitrov[2]

***Abstract* – This paper proposes a trajectory tracking controller for a two degree of freedom (2-DOF) overhead crane. First, a dynamic model of the crane suitable for feedback control is developed using robotic methodology. A desired trajectory for the trolley motion is generated using a reference differential equation. The proposed control law is based on collocated partial feedback linearization combined with trajectory tracking and linear feedback control which achieves local asymptotic stability of the closed-loop system. Simulation results illustrate the effectiveness of the proposed controller.**

***Keywords* – Overhead crane, Dynamic modelling, Feedback control, Perturbed systems.**

I. Introduction

In the last decades, the overhead cranes have been widely used for transportation in many industrial applications and become an interesting issue from automatic control point of view. The goal is to transport the payload quickly and in the same time to reduce the rope swing angle. Recently, different techniques been proposed for the design of Linear Quadratic [1, 2], adaptive [3], nonlinear coupling control [4] controllers for overhead cranes. The overhead cranes belong to the class of underactuated mechanical systems, which have fewer control inputs than degrees of freedom. One of the complexities of these systems is that they are not feedback linearizable. Due to the positive definiteness of the inertia matrix of this class of systems, the so-called collocated partial feedback linearization property [5] holds, which refers to the control that linearizes the equations associated with the actuated degrees of freedom of the system. Available control design methods mainly include approximate linearization [6] and saturation control [7].

In this paper, we propose a simplified control strategy based on collocated partial feedback linearization of the dynamic model combined with trajectory tracking and linear feedback control law, which achieves local asymptotic stability of the closed loop system. The organization of the paper is as follows: In Section II, a dynamic model of the crane suitable for feedback control applications is derived. The Problem formulation is given in Section III. In Section IV, a control law is designed. Section V contains simulation results. Conclusions are presented in Section VI.

[1]Plamen Petrov is with the Faculty of Mechanical Engineering, Technical University of Sofia, 8, Kl. Ohridski str., 1797 Sofia, Bulgaria (E-mail: ppetrov@tu-sofia.bg).

[2]Lubomir Dimitrov is with the Faculty of Mechanical Engineering, Technical University of Sofia, 8, Kl. Ohridski str., 1797 Sofia, Bulgaria (E-mail: lubomir_dimitrov@tu-sofia.bg).

II. Dynamic Model

A schematic view of an overhead crane is shown in Fig. 1. In order to derive a dynamic model suitable for control applications, we make the following assumptions: the payload mass is considered as a point-mass, and the mass and stiffness of the hoisting rope are neglected. The system has two degree-of-freedom and the associate generalized coordinates are

$$q = \begin{bmatrix} d & \theta \end{bmatrix}^T \in \Re^2 \tag{1}$$

where d is the displacement of the trolley and θ is the swing angle of the load, (Fig. 1).

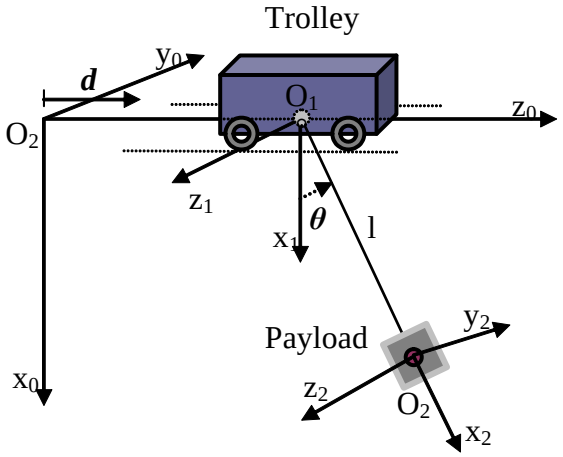

Fig. 1. Schematic of the overhead crane

We use the Denavit-Hartenberg convention [8] for the description of the crane kinematics. An inertial coordinate system $O_0x_0y_0z_0$ is assigned in the work space where the z_0 axis is in direction of the trolley displacement. The z_1 axis of a moving together with the trolley coordinate frame $O_1x_1y_1z_1$ is the axis of revolution of the rope. The z_2 axis of the coordinate frame $O_2x_2y_2z_2$ which is attached to the payload is parallel to z_1. The link parameters are given in Table I where the four quantities a_i, d_i, α_i, and θ_i are parameters of link i and joint i, (i = 1,2).

TABLE I
PARAMETERS FOR A 2-DOFS OVERHEAD CRANE

Parameters	Link 1	Link 2
a_i [m]	0	l
d_i [m]	$d=var$	0
α_i [rad]	$\pi/2$	0
θ_i [rad]	0	$\theta = var$

The corresponding transformation matrices which define the relative position and orientation between the adjacent coordinate systems are

$$A_1 = \begin{bmatrix} 1 & 0 & 0 & 0 \\ 0 & 0 & -1 & 0 \\ 0 & 1 & 0 & d \\ 0 & 0 & 0 & 1 \end{bmatrix}, \quad A_2 = \begin{bmatrix} \cos\theta & -\sin\theta & 0 & l\cos\theta \\ \sin\theta & \cos\theta & 0 & l\sin\theta \\ 0 & 0 & 1 & 0 \\ 0 & 0 & 0 & 1 \end{bmatrix}. \quad (2)$$

Using the transformation matrices (2), the coordinates of point O_2 with respect to $O_0x_0y_0z_0$ are

$$\begin{aligned} z_{O_2} &= d + l\sin\theta \\ x_{O_2} &= l\cos\theta \end{aligned}. \quad (3)$$

The dynamic equations of motion of the crane are derived using Lagrange formalism

$$\frac{d}{dt}\frac{\partial L}{\partial \dot{q}_i} - \frac{\partial L}{\partial q_i} = Q_i \text{ , } i = 1,2 \quad (4)$$

where the Lagrangian L represents the difference between the kinetic and potential energy of the system, and Q_i are the generalized forces associated with the generalized coordinates.

The kinetic energy of the system is obtained as follows

$$T = \frac{1}{2}(M+m)\dot{d}^2 + \frac{1}{2}m(2l\cos\theta\dot{d}\dot{\theta} + l^2\dot{\theta}^2) \quad (5)$$

where M and m are the mass of the trolley and the load, respectively and l is the length of the rope.

The potential energy of the system is given as

$$U = -mgl\cos\theta . \quad (6)$$

Using Eqs. (3), (4), (5) and (6), the dynamic equation of motion of the overhead crane are obtained in the form

$$D\ddot{q} + C\dot{q} + G = Q \quad (7)$$

where

$$D = \begin{bmatrix} M+m & ml\cos\theta \\ ml\cos\theta & ml^2 \end{bmatrix}, \quad C = \begin{bmatrix} 0 & -ml\sin\theta\dot{\theta} \\ 0 & 0 \end{bmatrix},$$
$$G = \begin{bmatrix} 0 \\ mgl\sin\theta \end{bmatrix}, \quad Q = \begin{bmatrix} F \\ 0 \end{bmatrix} \quad (8)$$

where F is the control force acting on the trolley.

Remark 1: It should be noted that the matrix D is positive definite and the matrix $1/2\dot{D} - C$ is skew-symmetric.

III. Problem Statement

In this paper, we consider the problem of position control of the overhead crane. The goal is to transport the payload quickly with high precision, and in the same time to reduce the swing angle which does not exceed 5^0 through the entire trajectory of the trolley. The desired trajectory for the trolley motion is proposed in the integral form

$$z^d(t) = z_0^d\left[1 - (1+\rho t)e^{-\rho t}\right] \quad (9)$$

where z_0^d is the desired distance which has to be traveled by the trolley, and ρ is a double root of a desired linear differential equation describing the trolley motion, (a larger ρ leads to a faster motion of the trolley and as a consequence, a bigger swing of the payload).

We make the following change of coordinate

$$z_e = d - z^d . \quad (10)$$

and input

$$w = u - \ddot{z}^d \quad (11)$$

where, due to the collocated partial feedback linearization property, u is obtained in the form

$$u = \frac{1}{M + m\sin^2\theta}\left[F + m\sin\theta(l\dot{\theta}^2 + g\cos\theta)\right]. \quad (12)$$

Finally, using (10)-(12), after some work, the dynamic equations (7) for the crane can be written in error coordinate form as

$$\begin{aligned} \ddot{z}_e &= w \\ \ddot{\theta} &= -\frac{1}{l}\left[(w + \ddot{z}^d)\cos\theta + g\sin\theta\right] \end{aligned}. \quad (13)$$

We assume that $e = \left[z_e \quad \dot{z}_e \quad \theta \quad \dot{\theta}\right]^T \in \Re^4$ are measurable. Given the crane dynamics in error coordinates described by (13), the control objective is to asymptotically regulate $z_e(t)$ to zero (transportation of the payload) and minimize the swing angle $\theta(t)$ of the payload.

IV. Feedback Control Design

The overhead crane is an underactuated single-input (w) two-output (z_e, θ) system. The control problem consists in finding a feedback control law for the system (13) such that

$$\lim_{t\to\infty}(z_e(t)) = 0 \quad \text{and} \quad \lim_{t\to\infty}(\theta(t)) = 0 . \quad (14)$$

Consider the linear control

$$w = -k_1 z_e - k_2\dot{z}_e + k_3 l\theta + k_4 l\dot{\theta} \quad (15)$$

where k_i, ($i = 1,2,3,4$) are positive gains.

The resulting closed-loop system becomes

$$\begin{aligned} \ddot{z}_e &= -k_1 z_e - k_2\dot{z}_e + k_3 l\theta + k_4 l\dot{\theta} \\ \ddot{\theta} &= -\frac{1}{l}\left(\left(\left(-k_1 z_e - k_2\dot{z}_e + k_3 l\theta + k_4 l\dot{\theta}\right) + \ddot{z}^d\right)\cos\theta + g\sin\theta\right) \end{aligned}. \quad (16)$$

Denoting $\dot{z}_e = v_{ze}$ and $\dot{\theta} = \omega$, for small swing angles, the tangent linearization of Eqs. (16) about $\theta = 0$ can be written in state-space form as

$$\dot{x} = f(x) + g(t,x) \tag{17}$$

where

$$x = \begin{bmatrix} z_e & v_{ze} & \theta & \omega \end{bmatrix}^T \tag{18}$$

$$f(x) = \begin{bmatrix} v_{ze} \\ -k_1 z_e - k_2 v_{ze} + k_3 l\theta + k_4 l\omega \\ \omega \\ \frac{k_1}{l} z_e + \frac{k_2}{l} v_{ze} - \left(k_3 + \frac{g}{l}\right)\theta - k_4 \omega \end{bmatrix}; \quad g(t,x) = \begin{bmatrix} 0 \\ 0 \\ 0 \\ -\frac{1}{l}\ddot{z}^d \end{bmatrix}. \tag{19}$$

The system (17) can be viewed as a perturbation of the nominal system $\dot{x} = f(x)$, which has exponentially stable equilibrium point at the origin $x = 0$, and $\ddot{z}^d(t)$ is a uniformly bounded disturbance that satisfies $\left|\ddot{z}^d\right| \le \frac{z_0^d \rho^2}{l} = \delta$. Furthermore, $\ddot{z}^d(t) \to 0$ as $t \to \infty$. Using Lemma 4.9, [9, p. 208], for the perturbed system (17), it can be shown that $x(t) \to 0$ as $t \to \infty$. Based on Lyapunov's linearization (indirect) method [9], one can be concluded that the corresponding nonlinear system is locally asymptotically stable.

V. Simulation Results

Several simulations using MATLAB were carried out in order to illustrate the performance of the proposed controller. The desired trajectory of the trolley is given by (9) where the desired distance to travel is $z_0^d = 7m$ and $\rho = 0.5$. The overhead crane is tested with a mass of 200kg and 300kg for the trolley and the payload, respectively. The length of the rope was chosen to be $l = 5m$. In the first simulation, from Fig. 2, we can see the evolution in time of the swing angle θ during the displacement of the trolley. Fig. 3, presents the evolution in time of the movement of the trolley d according to desired trajectory $z^d(t)$. The results of the simulations confirm the validity of the proposed controller.

VI. Conclusion

In this paper, a trajectory tracking controller for a 2-DOF overhead crane has been proposed. A dynamic model of the crane was developed using robotic methodology. A desired trajectory for the trolley motion was generated using a reference differential equation. The proposed control law was based on collocated partial feedback linearization combined with trajectory tracking and linear feedback control and achieved local asymptotic stability of the closed-loop system. Simulation results were carried out and confirmed the effectiveness of the proposed controller.

Acknowledgments

This work is a part of the Project "University scientific and research complex for innovations and transfer of knowledge in the fields of micro/nano-technologies, energy effectiveness, and virtual engineering",Contract DYNK-01/3 from 29/12/2009 with the National Ministry of Science and Education of Bulgaria.

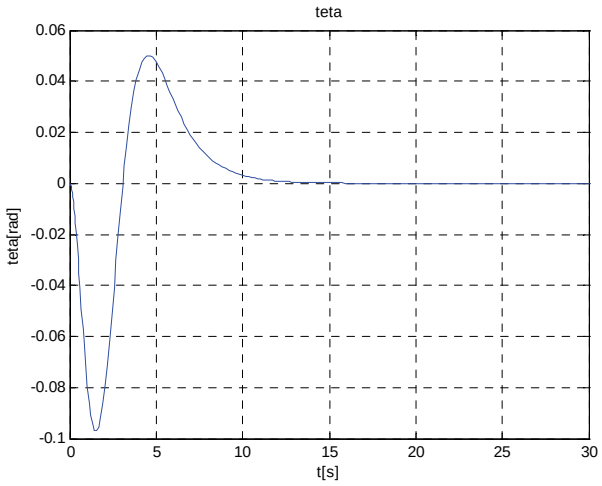

Fig. 2. Time history of the swing angle of the payload

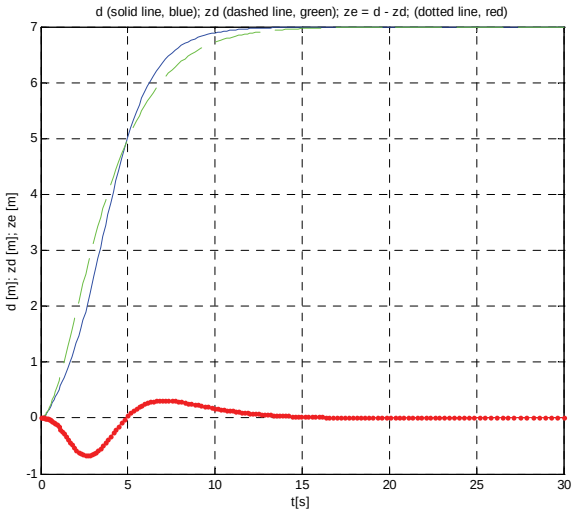

Fig. 3. Time history of the trolley displacement (solid line), desired trajectory (dashed line), and tracking error (dotted line)

References

[1] Z. Wang, B. Surgenor, A problem with the LQ control of overhead cranes, *Trans. ASME J. Dyn. Syst. Meas. Control*, vol. 128, 2006, pp. 436-440.

[2] K. Prommaneewat, P. Roengruen, V. Kongratana, Anti-sway Control for Overhead Crane, in *Proc. Int. Conf. Contr. Autom. Systems*, 2007, pp. 1954-1957.

[3] B. Ma, Y. Fang, X. Zhang, Adaptive tracking control for an overhead crane system, in *Proc. 17th IFAC World Congress*, 2008, pp. 12194-12199.
[4] Y. Fang, E. Zergeroglu, W. Dixon, D. Dawson, Nonlinear coupling control laws for an overhead crane system, in *Proc. IEEE Int. Conf. Contr. Applications*, 2001, pp. 639-644.
[5] M. Spong, Underactuated mechanical systems, Lecture Notes in Control and Information Sciences, Springer, vol. 230, 1998, pp. 135-150.
[6] N. Bedrossian, Approximate feedback linearization: the cart-pole example, in *Proc. Rob. Automation*, 1992, pp. 1987-1992.
[7] A. Teel, Using saturation to stabilize a class of single-input partially linear composite systems, in *IFAC Symp. Nonlinear Control Design*, 1992, pp. 224-229.
[8] M. Spong, S. Hutchinson, M. Vidyasagar, Robot modeling and control, John Wiley and Sons, Inc., 2005.
[9] H. Khalil, Nonlinear systems, Macmillan Publishing Company, 1992.

Analysis of the Inertial MEMS Sensor Parameters for Navigation Applications

Emil Iontchev[1], Ivaylo Simeonov[2] and Rossen Miletiev[3]

Abstract – **The paper discuss the analysis of the MEMS sensor parameters, which are important in the different control and navigation systems, where the sensor bias offset could significantly degrade the system performance. The axes bias offset and standard deviation are analyzed for ADIS16405 inertial sensor. Also distance and angular error is calculated according to the measured values.**

Keywords – **MEMS sensor, offset, standard deviation**

I. Introduction

Interest in the development of microelectro-mechanical systems (MEMS) has mushroomed during the past decade [1,2]. In the most general sense, MEMS attempts to exploit and extend the fabrication techniques developed for the integrated circuit (IC) industry to add mechanical elements to the electrical circuits to make integrated microsystems for perception and control of the physical world. MEMS devices are already being used in a number of commercial applications [3,4] and the new applications are emerging as the existing technology is applied to the miniaturization and integration of conventional devices. MEMS sensors allow the implementation of a lot of different functions, as free-fall detection, car navigation, map browsing, gaming, menu scrolling, motion control, vibration monitoring, antitheft and many others.

The current paper discusses the sensor offset and standard deviation of the output signal due to their significant role for the inertial system accuracy and different control and measurement devices and systems, which use integration with time to calculate the speed and the movement according to the measured acceleration [5,6]. The integrative nature of this approach has both positive and negative aspects. On the positive side, integration will smoothed out the high-frequency errors (e.g., sensor noise). On the negative side, integration of low frequency errors due to biases, scale factor error, or misalignment will cause increasing error between the true and estimated vehicle state [1]. Bias offset drift exhibited in the acceleration signal is accumulative and the accuracy of the distance measurement could degrade with time due to the integration [7].

[1]Emil Iontchev is with the Higher School of Transport "T. Kableshkov" 158 Geo Milev Street, Sofia 1574, Bulgaria, E-mail: e_iontchev@yahoo.com

[2]Ivaylo Simeonov is with the Faculty of Telecommunications at Technical University of Sofia, 8 Kl. Ohridski Blvd, Sofia 1000, Bulgaria, E-mail: ivosim@abv.bg

[3]Rosen Miletiev is with the Faculty of Telecommunications at Technical University of Sofia, 8 Kl. Ohridski Blvd, Sofia 1000, Bulgaria. E-mail: miletiev@tu-sofia.bg

II. Inertial MEMS Sensors Description

The analyzed inertial MEMS sensors are recognized as ADIS16405 - Triaxial Inertial Sensor with Magnetometer, produced by Analog Devices. The ADIS16400/ADIS16405 combine industry-leading *i*MEMS® technology with signal conditioning that optimizes dynamic performance. ADIS16405 sensor is a member of ADIS16400 inertial sensor family, but each sensor has its own dynamic compensation for correction formulas that provide accurate sensor measurements over a temperature range of −40°C to +85°C.

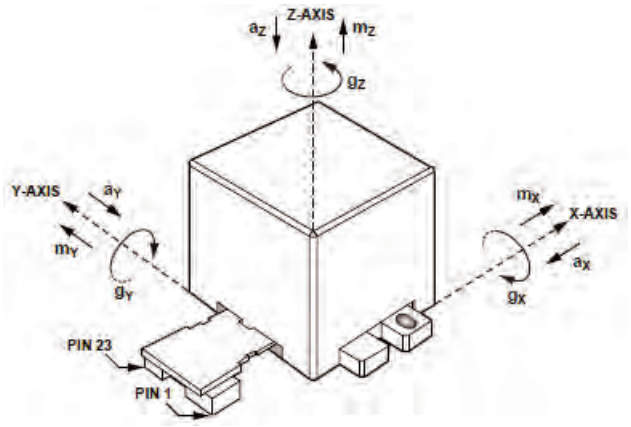

Figure.1. Inertial sensor ADIS16405

The ADIS16405 parameters are defined as follows [8]:

- Triaxial, digital gyroscope with digital range scaling - ±75°/sec, ±150°/sec, ±300°/sec settings
- Triaxial, digital accelerometer, ±18 *g*
- Triaxial, digital magnetometer, ±2.5 gauss
- Autonomous operation and data collection
- Calibrated temperature range: −40°C to +85°C
- Software configuration of the sampling rate, digital filtering and offset
- Autocalibration option available

III. Analysis of the Inertial Sensor Parameters

The analysis of the inertial sensor parameters is accomplished by a measurement of the output signal (linear and angular rate registers for the ADIS1640 sensor) without motion. The sampling rate of the ADIS sensor is set to 819.2Hz and 901056 samples are recorded.

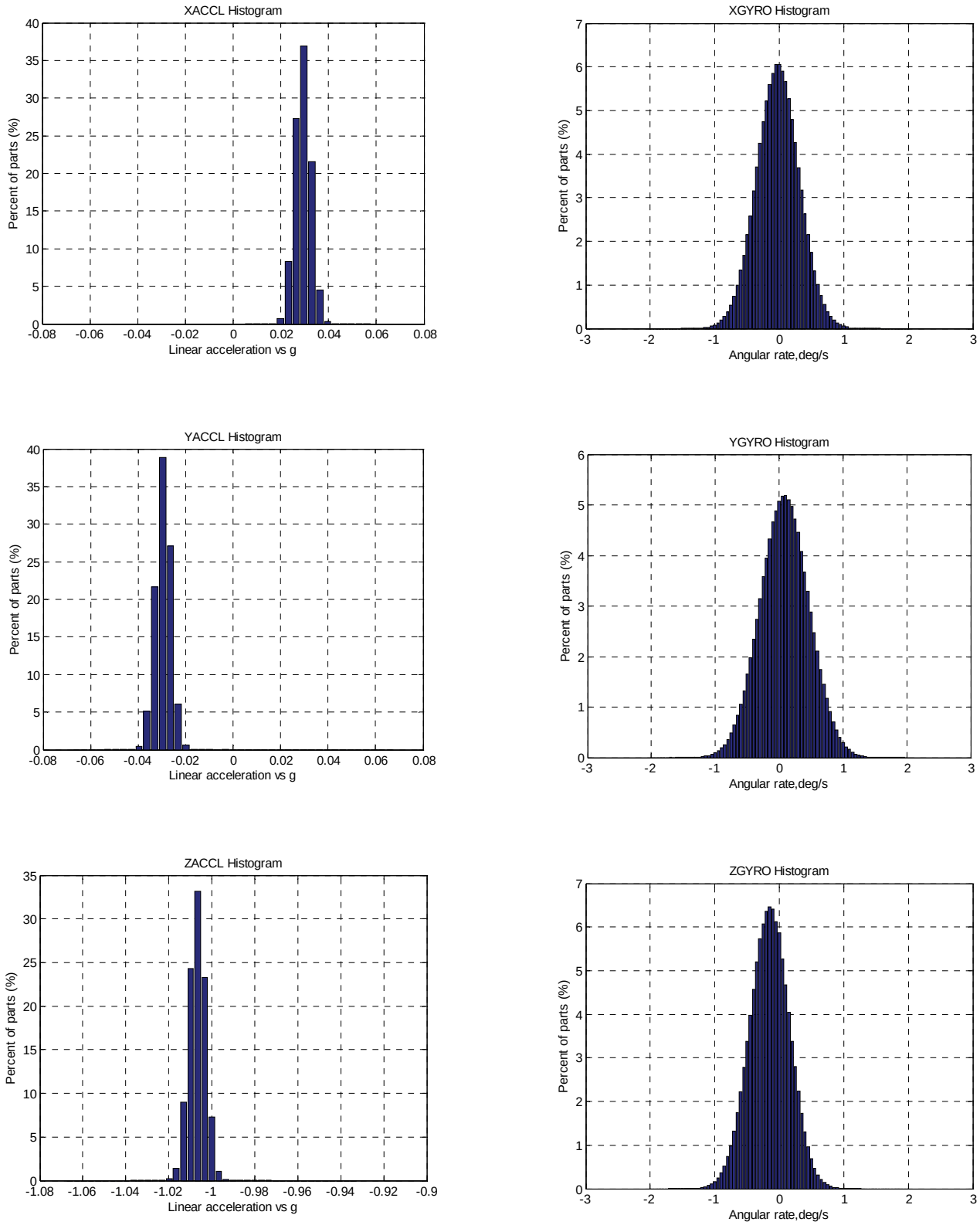

(a) (b)

(a) – linear accelerometers
(b) – angular rate sensors

Figure 4. ADIS16405 histograms

The measurement time duration is calculated as 901056 / 819.2 = 1100s. The measurements are accomplished by ADISUSBZ evaluation system and iSENSOR Evaluation Tool. The obtain data for ADIS16405 sensor are processed by MATLAB routine and the results are shown at Figure 4a and Figure 4b for linear accelerometers and gyroscopes respectively. The calculated mean value and standard deviation are shown at Table 1 and Table 2 for gyroscopes and accelerometers respectively.

Table 1. Analyzed parameters of the gyroscope sensor

Parameter	Mean value, °/sec	Standard deviation, °/sec
gyroX	-0.0236	0.3314
gyroY	+0.0838	0.3833
gyroZ	-0.1515	0.3096

Table 2. Analyzed parameters of the linear accelerometer sensor

Parameter	Mean value, g	Standard deviation, g
acclX	+0.0295	0.0035
acclY	-0.0297	0.0034
acclZ	-1.0059	0.0040

The calculated results show that the ADIS16405 inertial sensor is distinguished with a maximum gyroscope bias offset of 0,15°/s for the Z axis and standard deviation 0.3÷0,4°/s, while the corresponding values for the accelerometers are equal respectively to 0,03g and 3÷4mg. The calculated bias offset of the axes degrades the accuracy of the navigation systems, because the error is accumulated. Therefore it has to be compensated.

The shown figures (Fig.5 – Fig.7) represent the numerical integration of the linear accelerations using the trapezoidal rule according to the X, Y, Z axis after bias compensation. The calculated distance error for each axis does not exceed 3 meters. This error could not significantly degrade the inertial navigation system performance in the integrated GPS/INS navigation systems, but it is unacceptable value for the precise systems such as robotic ones. The calculated distance error with offset compensation is much smaller than the calculated one without offset compensation, which is equal to $S=a_{x,0}.t+1/2.a_{x,0}.t^2=1.6236.10^5$m!

The estimated mean values and standard deviation of the velocity of each axis are given at Table 3.

Table 3. Calculated parameters of the accelerometer sensor after one stage integration

Parameter	Mean value, m/s	Standard deviation, m/s
Vx	$2.154.10^{-4}$	$5.232.10^{-5}$
Vy	$6.196.10^{-5}$	$5.493.10^{-5}$
Vz	$2.170.10^{-4}$	$5.152.10^{-5}$

Theoretically, the integration of the zero offset acceleration data could not produce an offset bias of the velocity data, according to the following expressions:

$$a(t)=\sum_{i=1}^{N} A_i \cos(\omega_i t+\varphi_i) \quad (1)$$

$$v(t)=\int a(t)\,dt=\sum_{i=1}^{N} A_i \int \cos(\omega_i t+\varphi_i)\,dt= \quad (2)$$

$$=\sum_{i=1}^{N} \frac{A_i}{\omega_i}\cos\left(\omega_i t+\varphi_i-\pi/2\right)$$

But the numerical integration always produces an error E_n, which value may be calculated according to equation [9]:

$$\frac{(\Delta t)^3}{12}.\min\left(\left|a''(x)\right|\right)\le\left|E_n\right|\le\frac{(\Delta t)^3}{12}.\max\left(\left|a''(x)\right|\right), \quad (3)$$

where $t_{k-1}\le x\le t_k$.

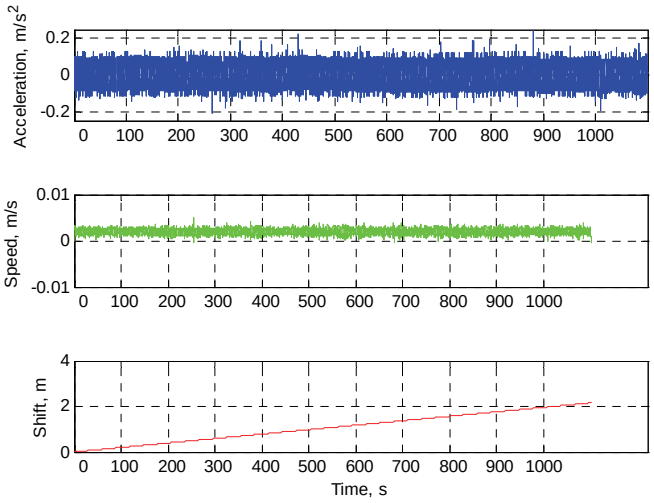

Figure 5. Numerical integration of X acceleration

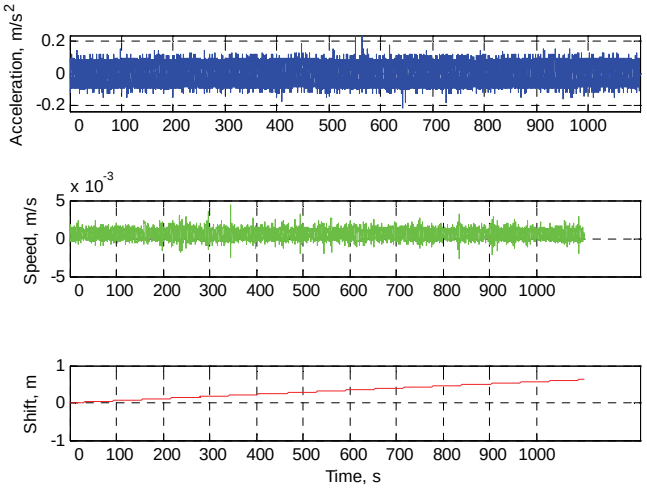

Figure 6. Numerical integration of Y acceleration

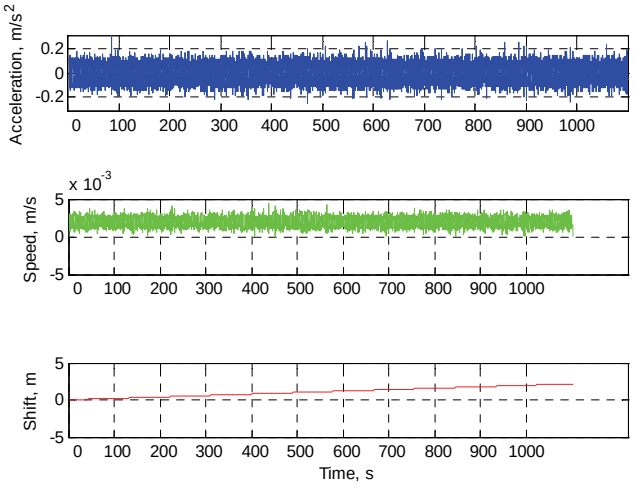

Figure 7. Numerical integration of Z acceleration

It is clearly visible, that the distance error is generated due to the speed offset and the distance error is proportional to the integration time.

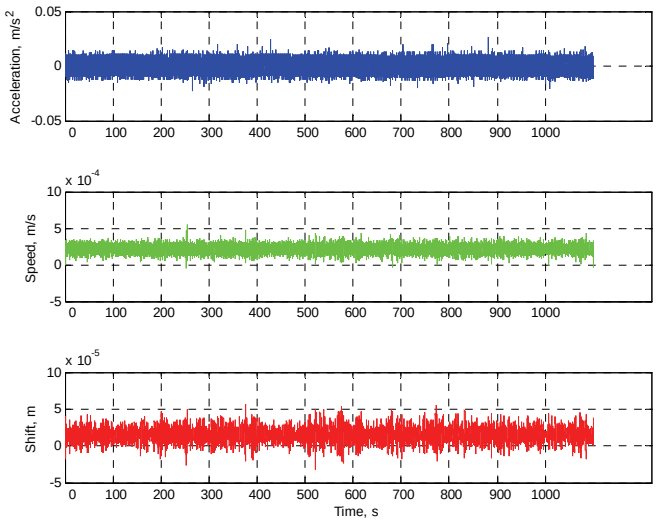

Figure 8. Distance error after velocity offset compensation (X axis)

If the velocity bias offset is also compensated, the distance error is reduced to 5.10^{-5}m, while the mean value of the distance offset is equal to $1.473.10^{-5}$m.

The proposed example and results show that the bias offset compensation is a critical part of the double integration of the acceleration data. The high pass filter could not be used to remove the offset because it will reject the steady acceleration or velocity data. Therefore the mean value of the acceleration and velocity data have to be measured for each sensor and their values have to be compensated for the sensitive applications such as mechanics or robot part moving calculation.

IV. Conclusion

In this paper we discuss the parameters of the ADIS16405 inertial sensor and distance and angular errors are calculated to analyze the sensor performance to be built in the different type of navigation and control systems. It is shown that the analyzed sensor is distinguished with a small bias offset which have to be compensated in the precise systems like robotics, vibration measurement systems, long range inertial navigation systems, etc., but also could be remain uncompensated in the short range GPS/INS navigation systems where the system could lost the GPS signal for several seconds.

The estimated mean and standard deviation value of the output signal also could be used as initial parameters for Kalman filters in the different navigation or control systems.

Acknowledgement

This paper was prepared and supported by the National Fund under contract number No.DTK02/2-2009.

References

[1] Jay Farrell - Aided Navigation GPS with High Rate Sensors, *McGraw-Hill Inc., 2008*

[2] Grewal M.S., Weil L.R., Andrews A.P., Global Positioning Systems, Inertial navigation, and Integration, *John Willey & Sons, Inc., 2001*

[3] Favre-Bulle B., An inertial navigation system for robot measurement and control, *Second IEEE Conference on Control Applications, 1993*

[4] Barbour N., Schmidt G., "Inertial Sensor Technology Trends", *IEEE Sensors Journal, Vol. 1, No. 4, December 2001*

[5] Walchko K. J., Low Cost Inertial Navigation: Learning To Integrate Noise And Find Your Way, *A Master Of Science Thesis, University Of Florida, 2002*

[6] Sukkarieh S., Nebot, E.M., Durrant-Whyte H.F., Achieving integrity in an INS/GPS navigation loop for autonomous land vehicle applications, *IEEE International Conference on Robotics and Automation, 1998, page(s): 3437-3442 vol.4*

[7] G. Artese, A. Trecroci – Calibration of a low cost MEMS INS sensor for an integrated navigation system, *The International Archives of the Photogrammetry, Remote Sensing and Spatial Information Sciences. Vol. XXXVII. Part B5. Beijing 2008,* pp.877-882

[8] http://www.analog.com/static/imported-files/data_sheets /ADIS16400_16405.pdf - *datasheet of ADIS16400/ADIS16405 inertial sensor family*

[9] *www.mathcs.emory.edu/ccs/ccs215/integral/node3.html*

Models and Resources for Analysis and Accuracy of Instruments for Measurement of Parameters on Moving Objects

Dimitar Dichev[1], Stefan Nachev[2]

Abstract - **In the report are presented basic models, which are supposed to investigate of dynamical error, mistakes by measuring devices, determent parameters of movable objects. Developed are schemes and settlements for experimental determination of basic characteristics of dynamical error. By virtue of package Sim-Mechanics from the program complex Matlab and on the base of developed structural schemes are modulated necessarily mechanical systems for theoretical investigation of dynamic accuracy. Structural schemes is presented, stend apparatus for investigate metrological accuracy of measuring instruments was used. On the base of structural schemes was developed. Software for automatically engineering projects Solid-Works was used. Consumer user interface was involved for connection are complete in LabVIEW domain.**

Keyword s- **imitation model, modeling, dynamical error.**

I. INTRODUCTION

The contemporary stage in development of the measuring techniques is characteristic with the fast transition of instruments, measuring static quantity to measuring devises, reacting to dynamic of real quantities. Measurement of quantity in the proper dynamic gives the possibility to measure better to determine characteristics of the quantity, in there to dynamic and to establish more-considerable properties and condition of the objects.

All that require though established of the measuring resources and methods of measuring in two directions. The first is connected with the development of new measurement instrumentation like technical modules possessing broad early convenience at the first opportunity for following and measuring its dynamics. In the contemporary, that direction is extremely and developed extremely, rapidly, thanks to the nanotechnology, microprocessors and computer technique. The second direction is connected with improving accuracy of measurement. The improving of that indicator is increasing reliability of the results, give possibility for precise management and control of the processes. The quantity indicator of the accuracy of measurement is the total error, accented in the measurement process.

The basic share by formation of the recapitulation of the error is occupied from the dynamic component. The last is a consequence of operation, plenty of factories, but not all of them are connected with the coordinate of the time. For example, inertial component of dynamical error is owed to the second derivate of measured quantity or perplexity influences against the time.

Theoretical and experimental investigation of the dynamical error is connected with rank of difficulty. From one side to the present moment do not exists sufficient etalons for measurement for measuring of dynamical quantity, from anode- theoretical argumentation of the dynamical error do not response to the contemporary request in the engineering science and need of perfection. In that direction is the purpose of the present work, namely to present the basic structures scams for analysis of the dynamical error, its programs models for theoretical investigation, to produce measuring apparatus with metrological regulation of standards, with normalized indicator for investigation of dynamical accuracy characteristics by measuring instruments and system for measuring of kern and different on ships' vessel.

II. STRUCTURAL SCHEMES FOR INVESTIGATION OF THE DYNAMICAL ERROR

In the ground of theoretical and experimental investigation of dynamical accuracy is the pawnbroker's the model of Fig. 1.for formation of the error. On that bases could be create different structural schemas for analysis of dynamical error dependant of the kind of the measuring instrument, characteristics of the transmission function, metrological qualitative and quantitive displayed of the instrument, all-embracing of the exploration characteristics and so forth.

By some cases the more successful use of models with open structural schemes to define and investigation of dynamical error. Such a schema is presented on Fig. 1. The last is a structure on the base on generator for etalon signal. In that case, the metrological chain is relatively short; this diminishes possibly sources of distortion of the signal.

The scheme on Fig. 2 an etalon measuring device is placed on the same condition, to the investigated measuring instrument. By the dynamical measurements, however for small part of the quantities have been created etalon for checking and calibration, which in considerable degree it embarrass the implementation of that scheme.

[1]Dimitar Andonov Dichev is with the Faculty of Mechanical and Precision Engineering, Hadji Dimitar 4, 5300, Gabrovo, Bulgaria, e-mail: dichevd@abv.bg

[2]Stefan Atanasov Nachev is with the Faculty of Mechanocal and Precision Engineering, Hadji Dimitar 4, 5300, Gabrovo, Bulgaria, e-mail: stefnach@directbox.com

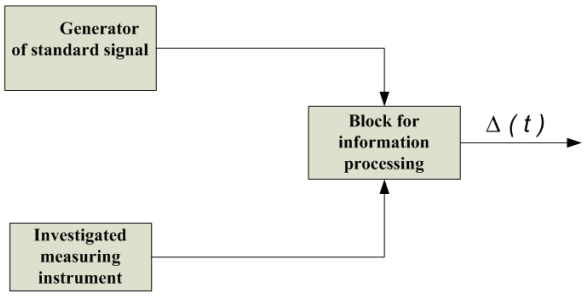

Fig. 1. Open structural schema for generator of etalon signal

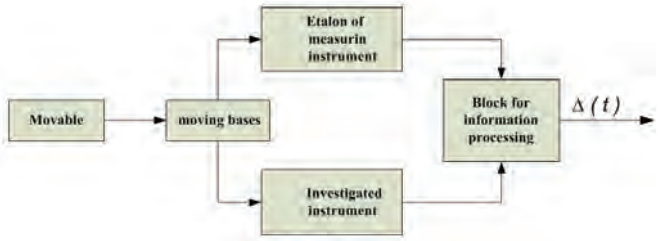

Fig. 2. Structural schema with etalon of measuring instrument

With the development of the micro processing and computer technique, and appearing of programmed instruments like LabVIEW, Matlab as well, which offer broadly possibility for automation of physical investigation, become possible to exceed the limit to closed schemes for determination and investigation of the dynamical error. Those kinds of schemes are shown on Fig. 3 and Fig. 4.

By means the structural schemes from Fig. 3 could be investigated the influence of the constitute of the generalization additive influence *G(t)* on the input of the investigated measuring instrument. For the purpose of foreseeing possibility for moving-on the ground, towards the basic coordinate, diversion from the measured one. By projection of stand apparatus of that kind should realize factual compatibility in constrictive, program and metrological attitude with the compound modules.

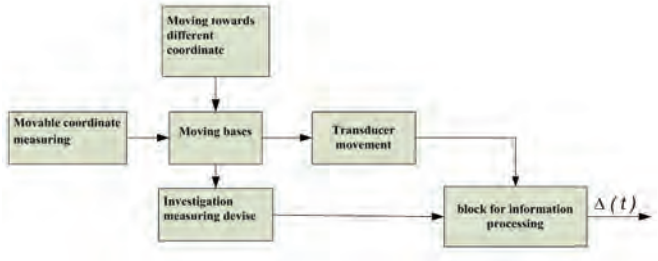

Fig.3. Locked structural scheme

Investigation of the influences on the divergence of nominal sensibility and compatibility of the generalization disturbance *U(t)* the output of the instrument could realise by scheme decision on Fig. 4.

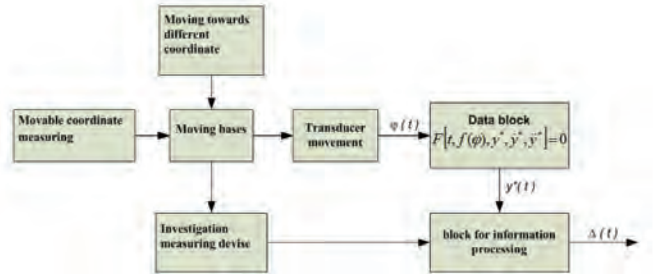

Fig.4. Locked structural scheme with computation block

Computing block is constructed on the base of mathematical model of the measuring instrument. Usually dynamic of the instrument is define by means of non-homogeneous differential equation of the kind of $F\left[t, f(\varphi), y^*, \dot{y}^*, \ddot{y}^*\right] = 0$. The right part of the differential equation is function with generalize coordinate of φ , which is receiving in real time from the transducer, registration shifting of the stand towards measuring coordinate.

III. Modeling of a System for Investigation of the Dynamical Accuracy

The construction and investigation of concrete system for investigation dynamical accuracy is impossibility without mathematical model, adequately decrypting functionality; property and characteristics. The process of constitute the mathematical models simplify to considerably degree with use of such a powerfully contemporary programs complexes lice MatLab.

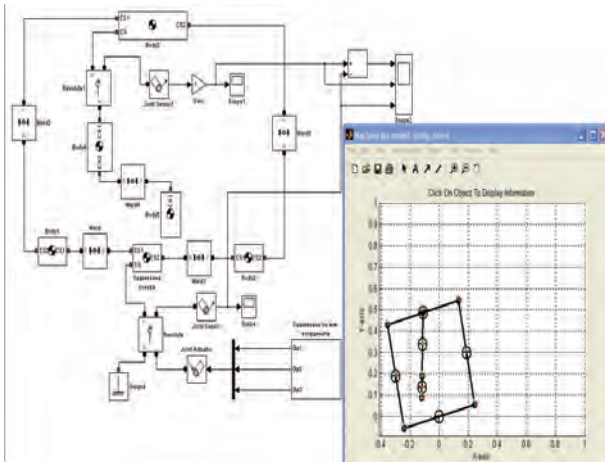

Fig.5. Sim-Mechanics model

In fact, that case it is expressional useful for implication of so cold imitation modeling by introducing SimMechanics package. Imitation model is a formal description of the logic of functionality of the system and interaction of the initial elements in time, give an account the most essential causatively-inquest connection, inherent to the system and ensure conduct of statistical experiment.

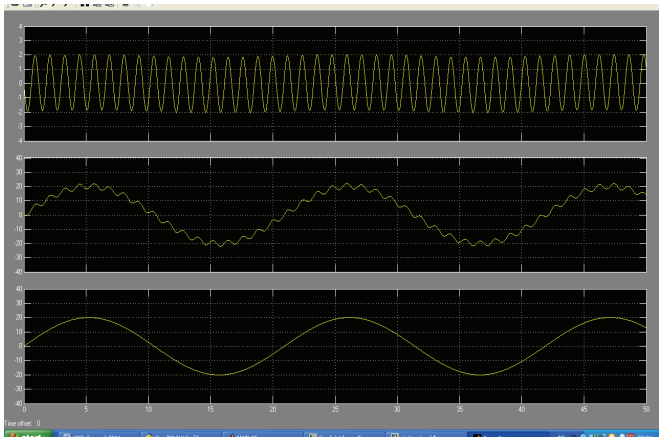

Fig.6. Numerical solutions

IV. Structural Scheme with Etalon Measuring Instrument

Structure schemes is shown on Fig. 7 is developed on the base of defined for this reason, characteristic of the investigated measuring instruments and measured from them physical quantity and structural scheme as well. It is presented in [1] for formatting and investigation of the dynamical error.

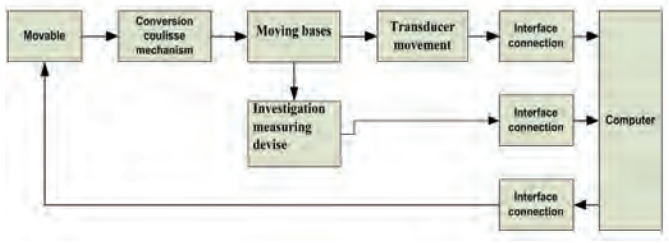

Fig.7. Structural scheme of the stand apparatus

The structural chemes is composed on three channels. The first is used for delivering of etalon information from the stand apparatus, the second is give transmission of devices of measuring information from the controlled measuring instrument, and the third channel is used for control of the parameters from the assignment of parameters from moving of the computer.

By the use of transformed sinus-function of movement on the base was controlled. The stend is following the function of rotation of the input lever, which is connecting with the transmission of the aperture. The transducer for shifting presents measuring scale with nominated metrological pointers, registration the actual angular movement of the base sinusoidal wave with frequency, which ken be given using programmable and amplitude, chancing by transforming module.

V. Apparatus Module of Stand

As far the construction attitude the stend apparatus is divided conditionally in two modules. Apparatus module included mechanical knots and elements, transducer for shifting. The second module was marked as interface and includes the interfaces for connection towards the three informational channels of structural scheme and program insurance as well using the data and to governing of the system.

In fact the constructing implementation of the apparatus module is presented on Fig. 8. By the project of that module, important task for realizing of contracture was realized. Metrological and exploitation compatibility between the initial knots and elements of the module was done.

Constricting compatibility ensure co-ordination with the constrictive parameters and mechanical and mechanical goings of separate knots and elements, by solution of measuring chains as well, influencing on instrumental accurate of the module.

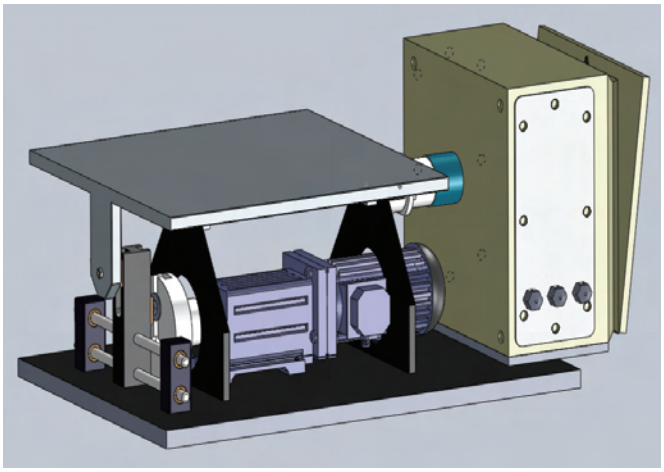

Fig.8. 3D appearance of the stend apparatus

The metrological compatibility includes recessional chose against accuracy precision characteristic and legal regulation of the metrological indicatives between separate knots and elements.

The main goal of metrological point of view by projecting and producing of the stend apparatuses is to reach accuracy, which definite with stipulation the summery error to be les then the hirer one division of the transducer for movement, which should be realize in the stipulation of the metrological compatibly. In the case transducer for movement of photo electrical raster angular transducer with 2500 imp./revolution which allowed after interpolation of 10 000 disserts per revolution.

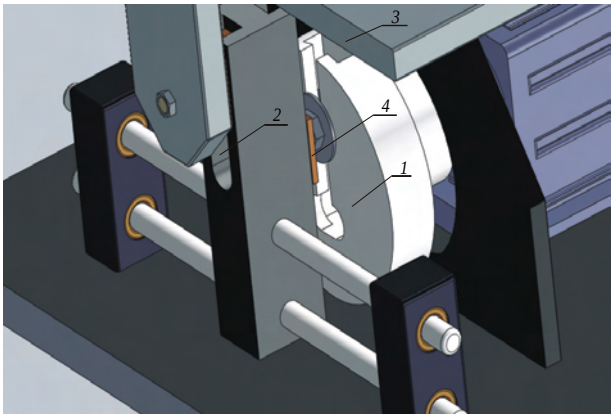

Fig. 9. Transformation block

Transformation block (Fig. 9) is fulfillment in appearance of coulisses mechanism. The last transform rotation movement of the cylindrical eccentric cam-shaft 1 in reflexive-translational movement of the coulisses mechanism 2. The base 3 is connected with coulisses mechanism 2, which formed sinusoidal angular movement on the base. The coulisses stone 4 can be faxed in different positions along the coordinate of the radial channel of the cylindrical eccentric. That gives possibility for change the amplitude of the moving by sinusoidal angular movement.

VI. Interface of Connection and Steer

The control of the stend, measuring of the parameters of investigated instruments was realized by means of the module NI USB-6211, presenting poly-punctually analog to digital devise.

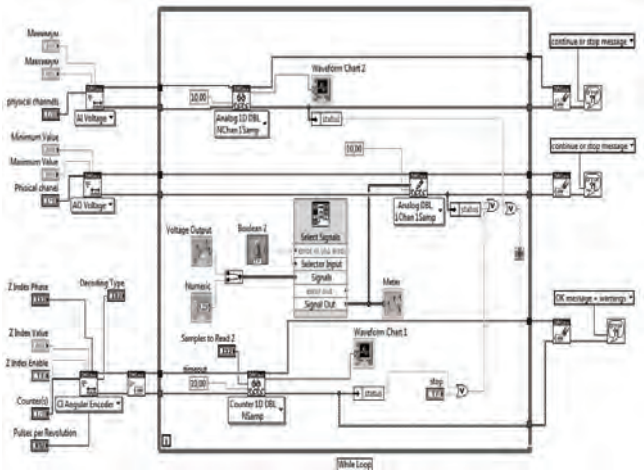

Fig.10. Block scheme of the program

By means of analogue output channel and frequency control the revolution of asynchrony electrical motor and respectively frequency of sinusoidal angular movement of the platform of the stend. Input digital channel is insurance the etalon measurement of angular translation of the base with the use of incremental transducer with 10 000 discretes per revolution. Possibility for include devices with analog output.

The program for control and measuring is realized in the LabVIEW domain, and the block scheme is shown on Fig. 10.

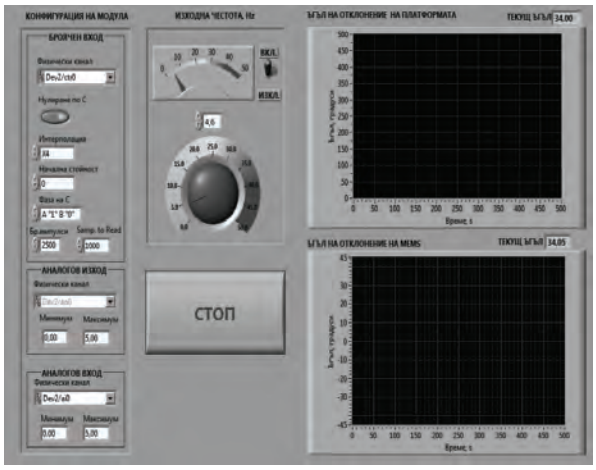

Fig.11. Panel for control and measurements

The Interface was build in effective and visible displaces forms and control elements in format “virtual panel”. The basic panel for control and measurement is presented on Fig.11. With the last one can have additional virtual instruments for information processing. In the use of additional bibliotheca in LabVIEW for analysis of measuring signals are possible.

VII. Conclusions

• Structural schemes of open and closed type for investigation of dynamical error foe instruments measuring are developed.

• By means of the package of SimMechanic is modeling systems for investigation of dynamical error of concrete type measuring devices.

• Theoretical base and imitation models allowed to be obtained optimal quantity of functional parameters to be optimized quantity of function parameters and the apparatus part as well.

• Structural scheme of measuring apparatus for investigated dynamical characteristics of instruments for parameters of movable objects.

• Constructed decision of apparatus module of the stend, for the purpose of software for the automation for engineering projects in Solid Works was done.

• On the base of program in LabVIEW domain and the module NI USB-6211, are realized with interface for connection and control in all three channels.

References

[1] Дичев, Д., Хр. Коев. Модели за изследване на динамичната грешка. XX МНТК „АДП-2011”. Созопол, 2011.

[2] Коев, Хр., Д. Дичев. Стендова апаратура за изследване на динамичните характеристики на уреди за измерване на параметри на подвижни обекти. XX МНТК „АДП-2011”. Созопол, 2011.

Investigation of Dynamic Characteristic of Sensor Elements of Micromechanical System

Dimitar Dichev[1], Stefan Nachev[2]

Abstract – **Sensor Elements of Micromechanical systems (SEMS) find out more and more application by measurement in the kinematical parameters of moving objects. In the study structures and schemes for investigation of accurately characteristics on known MEMS systems. On the base of structures systems are developed mathematical model to be investigated. Numerical determination model by the use of Simulink models on differential equation, description of dynamical characteristics.**

Keywords – **dynamic characteristics, structural schemes, imitation model, measurement accuracy.**

I. INTRODUCTION

The development of contemporary techniques in different domains requires formation of more quality and different information in measurement systems. Requirements for reduction of the mass and the measures of the systems are already of importance, because one of the sides of the objects have tendency for diminishing its proper characteristic and the other grow bigger in different points of already investigated objects in attends to achieve better accuracy, as well to measure more quantity, characterizing the object in its proper dynamic.

The wide development and application of gyroscopic systems and instruments for navigation and orientation in the aircraft systems, ships, automobiles, robots and other moving objects is connected with inherent autonomy, which consist in devises and systems, based on principle of gyroscopes and accelerometer. In contrast of radio-location and optical systems determine location of moving objects without using indispensably whatever physical connection with a stationary on-aground. Thanks the MEMS- technology become possible the contraction of those types of miniature dimensions. The last could propose possibility for simple decision before its complicated systems solutions in the field of measurements and management of dynamical quantities and processes thanks to there metrological characteristics, bud also in easy integration of that miniature component to each dynamic system.

On the other hand it is especially important to guarantee indispensability compatibility between the dynamic characteristics of the components and systems and the dynamical quantities, characterizing the measurement surroundings. The absent of such of compatibility could provoke appearance of dynamic error with unthinkable large value. Unfortunately in the catalogues of leading producers do not offer sufficient information on the dynamical characteristics of the systems, which in considerable extent diminish possibility for normalization of the dynamical accuracy.

That why the aim of the present is to work up a model of a system for investigation of a model of a system for investigation of the dynamical characteristics for MEMS-acceleration.

II. STRUCTURAL SCHEME OF A SYSTEM FOR INVESTIGATION OF DYNAMICAL CHARACTERISTICS OF MEMS-ACCELEROMETER

The structural scheme is contracted on the base of already developed in the department of "Mechanical and precision engineering" of TU-Gabrovo: apparatus and machinery for investigation of dynamical characteristics of devises for measurements of parameters of moving objects [1].

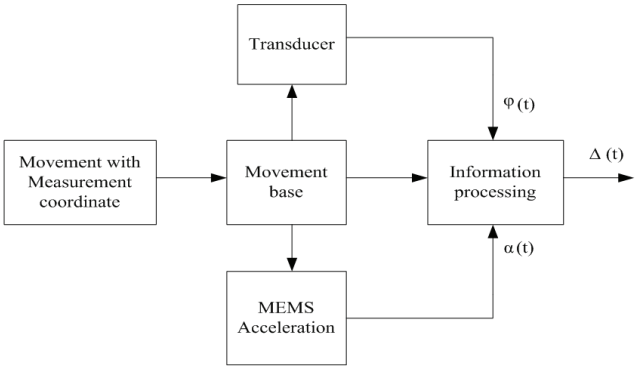

Fig. 1. Structural scheme

The Fig.1 presents a structure is a locked-tipped scheme. It consists of two channels for data transfer. The first channel is used for information transfer of standard, scheme movement on the base of the platform. On the second, the corps of MEMS-acceleration is mounted. The information from it proceeds to the processing block on the second channel.

The scheme is developed in attempt to solve problems of two basic directions. The first is used for investigation of dynamical deposition of micro-electro-mechanical systems, and the second for analysis of dynamic errors. For the purpose

[1]Dimitar Andonov Dichev is with the Faculty of Mechanical and Precision Engineering, Hadji Dimitar 4, 5300, Gabrovo, Bulgaria, e-mail: dichevd@abv.bg

[2]Stefan Atanasov Nachev is with the Faculty of Mechanocal and Precision Engineering, Hadji Dimitar 4, 5300, Gabrovo, Bulgaria, e-mail: stefnach@directbox.com

of standardize dynamical aracteristics of measuring instruments, mostly complete characteristics like transition, transmission, impulse, transitional functions. Also some cases could be used and specific private dynamic characteristics, like coefficient of damping, time-constant "and so forth". Composition of structural scheme is conformed according to the model, determine the formations of the dynamical error Δ(t), presented at [2]. That gives possibility for experimental study on the characteristics of that particular error: both on the temporal and the frequency coordinate.

III. Mathematical Model of the System in Examination

The investigation of the dynamical indicators of the measuring devises are unbearable without there mathematical models, adequate description of the basic property and characteristics. Even the results from the experimental investigation do not be analyzed exactly and precision towards the reason in separate formation of the dynamic error.

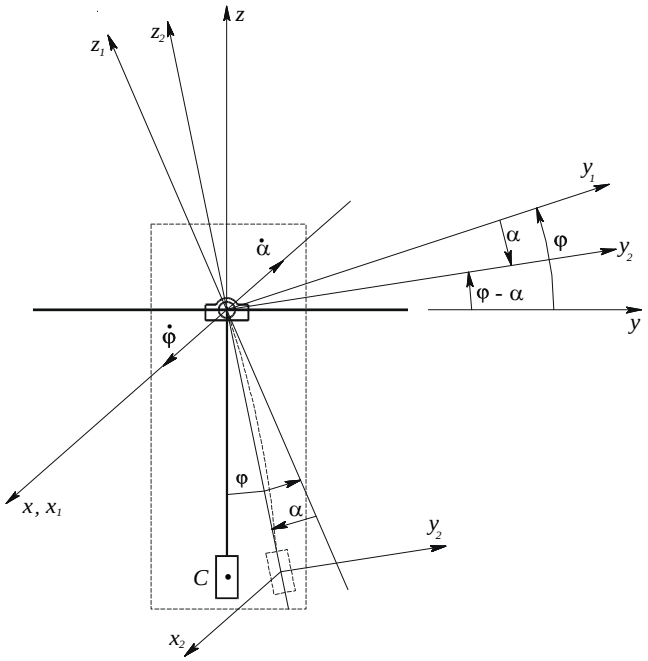

Fig.2. Dynamic systems

On the base of each mathematical model of dynamical system stands the differential equation, decrypting mostly the inertial properties of the system. In the concrete cause differentially equations of motion are composed on the base of the dynamical scheme from Fig. 2. Accepting the corps of the MEMS-accelero-meter is fastened firmly on the plate of the platform.

The measuring sensor of the instrument is determined as a physical pendulum, fixed by means of a plane spring on the corps of the accelerometer. That is generalizing of the sensors in known constriction and it could be accepted as a based model by investigation of the dynamic of the devises.

Then a generalized coordinate, could be assign by means of an angular quantityα. The last define the declination of the pendulum. Coordinate α is accepted as a generalization; bear the information changing of the measured quantity from MEMS-accelero-meter. In the schemes of the Fig. 2., dynamic system are introduced the followed coordinates systems: xyz, which coincide with inertial coordinate scheme and is immovable; x1y1z1 - is a movable coordinate, connected with the plate of the platform: x2y2z2- system, whose commencement coincide with the center of gravity C of the pendulum and move together with it.

In that instance the corps accomplishes rotation movement and consequently, kinetic energies will be:

$$E_к = \frac{1}{2}.J_x.\omega_x^2 \quad . \tag{1}$$

Mass inertial moment of the sensing element towards the access x is determined from the theory of Steiner,:

$$J_x = J_C + M.l^2 = M.\left[1/12.\left(a^2 + b^2\right) + l^2\right] \tag{2}$$

where, the JC – moment of insertion of the sensing element towards the mass center C ; l- the arm of the sensing element: a and b – constructing parameters of the sensing arm.

The projection of the vector of the angular velocity of the sensing element over the action x will be:

$$\omega_x = \dot{\varphi} - \dot{\alpha} \tag{3}$$

where $\dot{\varphi}$ is the angular velocity of the plate of the platform.

Substituted (2) and (3) in (1), obtained the definitive formulae of the kinetic energy of the sensing element:

$$E_к = \frac{1}{2}.M.\left[\frac{1}{12}.\left(a^2 + b^2\right) + l^2\right].\left(\dot{\varphi} - \dot{\alpha}\right)^2 \tag{4}$$

The potential energy Eп could finish the active forces, then:

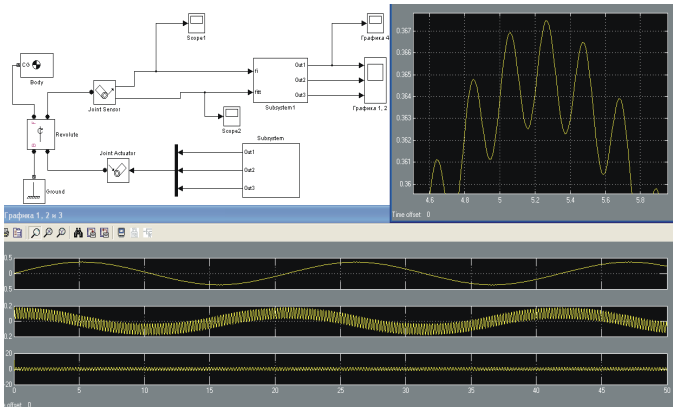

Fig.3. Sim Mechanics model of the investigated system

$$E_n = M.g.[l.\cos\varphi - l.\cos(\varphi - \alpha)] - \frac{1}{2}.c.\alpha^2 \quad (5)$$

where c is the spring constant.

After adduce of (4) and (5) in the usual form and substitution in the equation of Lagrange of second order, one obtained the following differential equation:

$$M.\left[\frac{1}{12}(a^2 + b^2) + l^2\right].\ddot{\alpha} + c.\alpha - M.g.l.\sin(\varphi - \alpha) =$$
$$= M.\left[\frac{1}{12}(a^2 + b^2) + l^2\right].\ddot{\varphi} \quad (6)$$

In the equation (6) are not take in foreseeing the damping forces, because do not exists sufficient data of them. The definite of the quantitative values of those forces for the concrete instruments could be able to perform such an experiment on the bases of the system of investigation.

IV. Imitation Model of the System for Investigation of Dynamical Characteristics

Imitation model is completed on the base of the structural scheme of Fig.1.1 and the mathematical model of the system, of investigation. That give possibility for adduce the real system to its mathematical analog on the base of the programming forms of its realization.

On that manner could be investigated as follows: compatibility of the theoretical and experimental model of the system; the influence of the functionality parameters on the instrument over the dynamic characteristics; the influence of the functional parameters; the influence of the embarrass quantity, definite in a format, which do not be suffocated experimentally.

On the Fig. 3 is presented Sim-Mechanics, the model of the dynamical system, the graphical results from the quantity solutions as well. On the block-schema of Fig. 3 the apparatus part is presented by the plate (block type Body), which offer rotational movement around the axes x, coincide with access x1 (Fig. 2). The ensure that motion of the plate is fulfilled by the block “Revolute”, determent the direction of the coordinate access, toward the body fulfilled rotational movement. The signals, defended the parameters of motion of the plate are registries using the block Joint Sensor and send to the Subsystem 1.

The moving apparatus are supposed to modeling of the block Subsystem. The Library Smolensk offer perfect possibility for choosing the parameters of the signals, formatting the moving system of the stand. Usually choosing of signals, determinate or accidental function in time with practically illimitable diapason of values of its functional parameters, which in practice is not possible to realize in experimental circumstances.

Numerical integrate of equation (6) towards summaries coordinate $\alpha(t)$ is realizing in a block Sub-System 1 (Fig. 4). In the base of the block-scheme are two pawnshops integrates. To the input of the first integrator is moved a signal, incorporate the functional mutual assistance between the constrictive parameters of the investigated instrument and the signal, characterizing the influence of the movements of the plate and the platform, which is definitude of the function on the right part of the differential equation (6).

Fig. 3 (Graphics: 1, 2 and 3) are shown graphical solutions, illustrated the movement of the sensing element of the MEMS- accelerometer, and its derivatives. The last are indispensable by the dynamical investigation because on the output of the real instrument, obtained signal, proportional to the second derivate. In the imitation model is foreseeing possible change of the scale graphics (Graphic 4). That offer possibility for analysis of its proper vibrations of the measuring instrument. That is illustrated by the example of Fig. 3, where the plenty of leers are seen on the measuring instrument again the constraint.

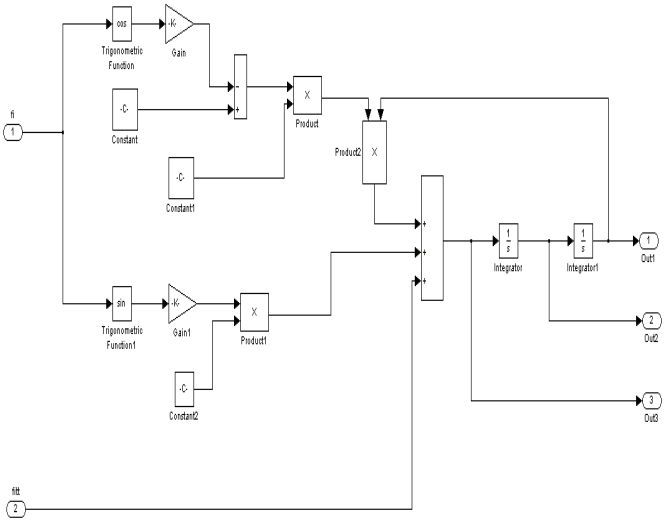

Fig. 4. Subsystem for solving the differential equations

The obtained results offer possibility for investigation of influence on the functional constructive parameters of the measuring instruments on the formation of the dynamical characteristics for analysis of the experimental results, for investigating conditions, usually are not obtaining experimentally, which increasing the affectivity of the model.

V. Conclusion

Structural scheme is constructed for the purpose of dynamical characteristics of MEMS-accelerometer, on the bases of developed in the Department of “Mechanical and Precision Engineering”, Technical University of Gabrovo.

Mathematical model of the concrete measuring instrument, investigated system is deduced.

On the base of the structural scheme differential equations imitation model for investigation of the dynamical model MEMS-accelerometer is developed.

REFERENCES

[1] Hr.Koev, D.Dichev,. Стендова апаратура за изследване на динамичните характеристики на уреди за измерване на параметри на подвижни обекти. XX МНТК „АДП-2011”. Созопол, 2011.

[2] D.Dichev,Hr. Koev,. Модели за изследване на динамичната грешка. XX МНТК „АДП-2011”. Созопол, 2011.

Simulation Modeling of Railway Technology in Dry Port Concept

Ivan Belošević[1], Sanjin Milinković[1], Miloš Ivić[1], Milan Marković[1], Slavko Vesković[1]

Abstract – **As maritime containerized transport continues to increase, relocation of port facilities inland is one way to achieve efficiency of the transportation chain as a whole. *The* dry port concept is based on creating direct railway linkages between seaport and inland intermodal terminals. This provides increasing productivity, modal shift from road to rail, resulting in reduced congestion at the seaport gates and along the routes. The subject of this paper is comparison between ports with work technology of a conventional container yard and work technology of a port within dry port concept.**

Keywords – **Railway, Container Yard, Dry port concept, Technology, Simulation.**

I. Introduction

Dynamic growth of the world trade, especially its liberalization and globalization, has had great influence on transport sector development. On the other hand, transport enables fast and efficient linkage, thus increasing competitiveness, one of the basic characteristics of the modern trade. Container transport has especially important place in all of this, nowdays representing a leading service for linking transcontinental destinations.

Container transport influences see fleet, ports and terminals, its facilities, and even continental transport system.

Trend in today's development of maritime transport demands intensive research in transshipment sphere. Development of transshipment facilities traditionally steps back from shipbuilding. This causes poor compatibility of maritime service and facilities and terminal capacity. Also, new systems that will enable better compatibility in transport chain.

Relocation of port facilities inland is one way to achieve efficiency of the transportation chain as a whole. Inland intermodal terminals are important nodes in the transport network and have attracted considerable attention. The dry port concept is based on creating direct railway linkages between seaport and inland intermodal terminals.

This paper is primarily focused on comparison of characteristics between conventional port concept applied so far and new concepts, such as dry port. Holding of ships in ports for handling operations and holding containers in container yards have high costs, and it is important to decrease them as much as possible.

[1]University of Belgrade, Faculty of Transport and Traffic Engineering, 11000 Belgrade, Vojvode Stepe 305, Serbia, Email: i.belosevic@sf.bg.ac.rs

II. Analysis of Container Transport

With the aim of satisfying needs of mega container flows, maritime operators engage ever larger ships to cope with increasing transport demand and for facilitating lower unit costs. Contemporary ships reaching over then 10 000 TEU and ships on order over 15 000 TEU. Increase of ship capacities has enabled a decrease in transport marginal price. Progress in ports and hinterland operations must improve similarly to fully realize the economies of scale. Huge advantage in increase of ship dimensions raised many problems for ports and terminals regarding handling and reduction of time ships spend in port [2]. This caused increase in port costs (Fig. 1.).

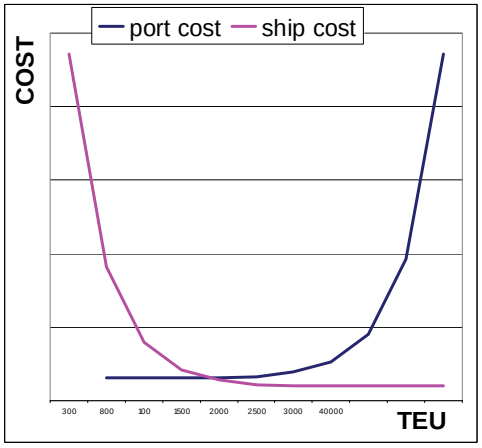

Fig. 1. Transportation costs

III. Ports as Transshipment Points

Nowdays there are many ports with dominant transshipment operations. Their main function is serving container ships of high capacity. Ships of high capacities are much more sensitive to values of transshipment norms. For those reason container ships of capacities higher than 2000 TEU demand very high transshipment norms.

Many subjects look for its place in container terminals. Those are maritime operators on one hand and continental transporters that are directly dependent on its location from technological and financial aspect, on the other hand. Both tend to minimize the time of transport elements flow and increase the flow in main transport directions.

Transshipment ports have two subsystems (Fig. 2.)

1. Anchorage – Vessels – Apron area
2. Apron area – Container yard – Continental transport.

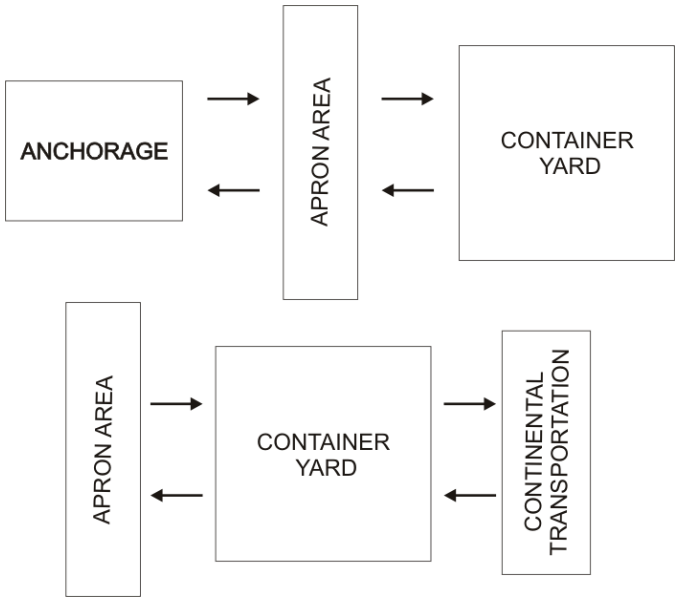

Fig. 2. Port subsystems

Primary function of transshipment ports are enabled by basic manipulation operations [4]. Container mechanisation exploited in operational parts of terminals is used for their realization. Technological process in transshipment ports provides realization of the following operations:

- Manipulation on relation ship-apron area (Gantry cranes)
- Manipulation on relation apron area - ship (Gantry cranes)
- Manipulation on relation apron area - container yard (flexible facilities)
- Manipulation on relation container yard - apron area (flexible facilities)
- Manipulation on relation container yard - continental transport (flexible mechanisation)
- Manipulation on relation continental transport - container yard (flexible mechanisation)

In seaport interface with railway and road transport is preformed directly or indirectly [5].

Direct transshipment demands less investment in facilities and takes up less space. It is possible to perform where railway network with large operational wagon fleet is developed. In terminals, broad-scaled gantry cranes that serve tracks and roads are installed. Container yard is in the function of synchronization of operational mechanisation cycle of continental transporters' arrivals and departures.

Indirect transshipment is more used in exploitation. Container yard has a dominant role mostly serving for realization of technological terminal processes. Ship linkages with continental transport are performed indirectly. Flexible mechanisation serves for both continental transporters and gantry cranes. Indirect transshipment terminals are faced with the problem of inefficient mega carriers serving. This stems from long holds in container yard and space limitation preventing further expansion.

IV. Dry Port Concept

Dry port concept successfully reduces additional infrastructure in ports, as well as operations that are parts of transport chains, not related to container ships operations. This concept keeps indirect transshipment via transit container yard. Transit container yard tends to minimize container hold in ports and functions as arrival and departure spot for block system trains. Block system trains link ports with inland terminals. At inland terminals shippers can leave and collect their goods in intermodal loading units as directly at the seaport [3]. Main activity in dry ports is handling with intermodal loading units. In addition to this activity, an array of other activities necessary to realize ''door to door'' transportation process shall be made in dry ports. These activities include customs clearance, handling of information, short term storage and storage of empty containers, containers maintenance and cleaning. Terminal itself can be connected to one or more ports, one port can be connected to one or more inland terminals and dry port can be part of network for supply chains. According to distance from the coast, dry ports are categories as close, mid-range and distant [3].

All participants in transport chain, maritime operators, ports, railways, road operators, local authority and citizens have advantages of dry port concept application. Advantage for maritime operators is reduction of ship hold in ports. Trough inland terminal construction, port's authority obtains increased participation in transport chain and control on hinterland. Dry port may be considered as ''extended gates'' for sea ports. Increased participation in transport scope represents advantage of dry port concept for railway also. Road transport has positive effect by focusing on and utilizing on shorter hauls. Benefits for local community are traffic intensity and pollution reduction on highway network in hinterland and in city road network in the seaport zones. This concept directly decrease negative impact on environment and increases the quality of life for the citizens.

V. Simulation Model

Simulation models gives opportunity to show certain system behavior in real conditions relatively easily. Simulation models enable comparison of different system solutions. Such analysis is easy to perform changing conditions in which the system functions, system surrounding, service rate, arrival rate, and so on [1]. Modern computers allow few-minute notification of all relevant parameters of functioning even in very complex systems. Complex mathematical equations and various measurements in a system are avoided in application of these models.

This paper provides simulation model of work technology of a port with a conventional container yard and work technology of a port within dry port concept. In formed simulation models gantry cranes, flexible mechanisation, portal cranes and loading bay with inland transport represent servers. Anchorage, container yards, parking lots for lorries and railway sidings can be represented as lines where objects accumulate during the simulation process. Objects are containers, lorries and trains as transport units. There are two

simulation models given, one of a conventional port operations and another within dry port terminal concept. In the first simulation model, it is presumed that containers are further transported by lorries only (Fig. 3.). In the second simulation model, the possibility of block trains usage is considered (Fig. 4.).

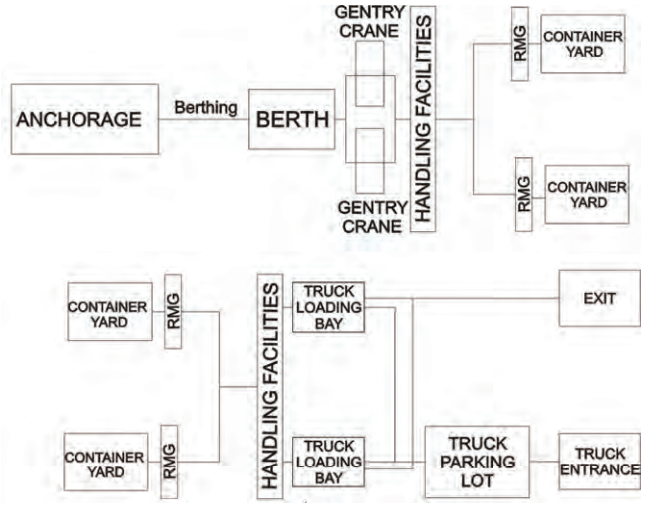

Fig. 3. Block shame of conventional port technology

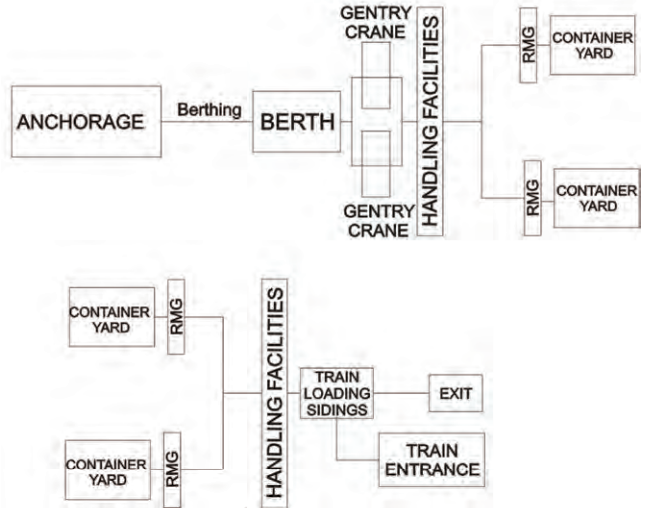

Fig. 4. Block shame of dry port concept technology

Input data that represent intensity of object's flow and intensity of server operations are provided by expert surveys and from available parameter values of port facilities.

VI. Results of Simulation Model

For simulation model creation, Flexsim 5.1.2 simulation software is used.

Quality of work technology in the container terminal can be observed within average container holding time in the terminal. Fig. 5. presents comparison of average container holding time in the container yard in the function of arrival vessels capacity. By application of dry port concept, holding time is decreased comparing to a conventional port. Containers departure by bock trains and transferring additional activities regarding container manipulation to inland terminal, holding time in ports is considerably decreased.

Port capacity is directly dependent upon container holding time. Fig. 6. presents comparison of container yard capacity also in the function of arrival vessels capacity. Dry port concept enables container yard capacity increase without additional investment in facilities and further port expansion.

The simulation model encompassed the research of the port system that can handle ships up to 1500 TEU capacity. Apart from the container yard adaptation, larger ships of Panamax generation would demand adaptation of other terminal parts as well. Analysis and optimization of port facility's capacities do not represent the research subject of this paper, therefore it is not considered in the paper.

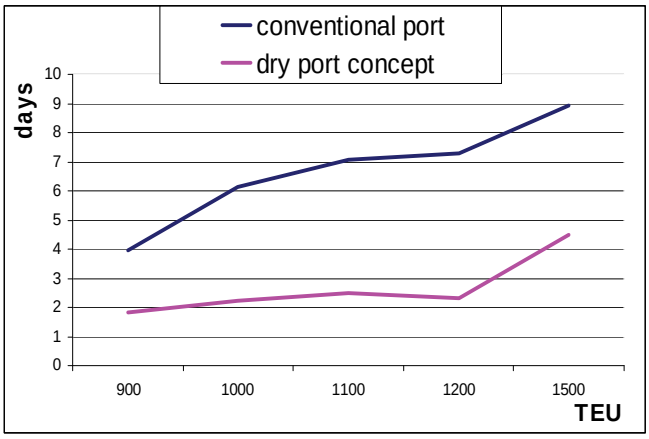

Fig. 5. Container holding time in container yard

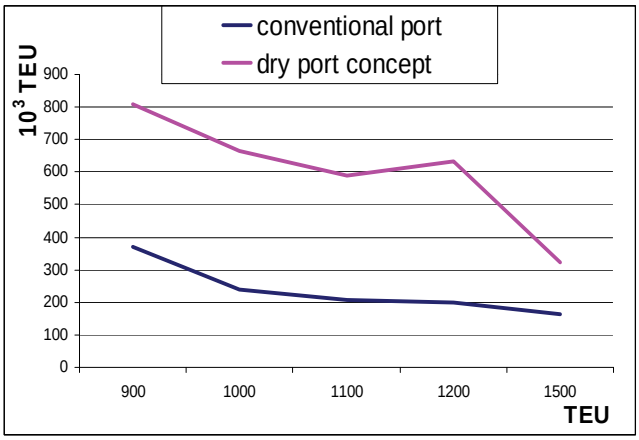

Fig. 6. Container yard capacity

VII. Conclusions

With expected increase in the scope of maritime transport, ports will face the problem of efficient handling with mega carriers. Apart from improving apron area facilities (gantry cranes) it is necessary to develop container yards and technologies of their operations.

Increase in port capacities can be succeeded by further expansion or work technology improvement. Due to land limitations that almost all ports face, great attention is given to new concepts that can solve this problem technologically. Dry port concept, as one of these concepts, enables considerable container holding time decrease in port terminals. Therefore, an opportunity of improved operations inland and port capacity increase is given.

ACKNOWLEDGMENTS

This paper is supported by Ministry of Science and Technological Development of the Republic of Serbia (no. project 36012).

REFERENCES

[1] A. Law, *Simulation Modeling and Analysis*, New York, McGraw-Hill Inc, 2007.

[2] J. P. Rodrigue, "Globalization and the synchronization of transport terminals", Journal of Transport Geography, vol. 7, pp.255-261, 1999.

[3] V. Roso, J. Woxenius and K. Lumsden "The dry port concept: connecting container seaports with the hinterland", Journal of Transport Geography, vol. 17, pp. 338-345, 2009.

[4] Z. Radmilović, *Planiranje i razvoj luka i pristaništa*, Belgrade, Faculty of Transport and Traffic Engineering, 2002.

[5] Z. Radmilović, B. Dragović, *Rečni i pomorski transport u intermodalnim sistemima Jugoistočne Evrope*, Belgrade, Faculty of Transport and Traffic Engineering, 2003.

Session CS:

COMPUTER SYSTEMS

Analysis of Possibilities to Overcome the Transient Faults in Real-time Systems with Time Redundancy

Sandra Djosic[1], Milun Jevtic[2] and Milunka Damnjanovic[3]

***Abstract* – In this paper we analyze timing constrains of one fault tolerant real-time system. Our goal is to estimate a probability of overcoming a transient fault detected during tasks executions. The faults are overcoming using technique of executing task again and time redundancy. Response time analysis (RTA) is the basis of our research and it is used to find minimum time between two consecutive faults which real-time system can tolerate. We have modified RTA to get more reliable real-time system.**

***Keywords* – Real-time system, Fault tolerance, Time redundancy.**

I. INTRODUCTION

A system is said to be real-time if the total correctness of an operation depends not only upon its logical correctness, but also upon the time in which it is performed, [1]. Real-time systems play an important role in many areas of the daily life: robotics, cosmic research, automotive industry, process control, factory automation….

Those systems have been designed in order to be safe and extremely reliable. Reliability in a real-time system means that it can run continuously for extended periods of time: typically for years without any failures, [2]. They are usually realized as real time systems with the ability of tolerating some faults, [3]. A fault-tolerant system has to ensure that faults in the system do not lead to a failure.

The focus of our research is transient faults. Transient faults are temporary malfunctions of the computing unit or any other associated components, and cause an incorrect result to be compute. Transient faults can be caused by a variety of sources, such as atmospheric nuclear particles (alpha-particles, protons and neutrons) or electrical noise (power supply noise or electromagnetic interference), [3].

The key to fault tolerance is redundancy. It can be said that redundancy is the addition of information, resources, or time beyond what is needed for normal system operation [4]. There are of three kinds: hardware redundancy, software redundancy and time redundancy. Hardware redundancy is the addition of extra hardware to the system, such as spare processors which are used if one of the running processors fails. Software redundancy is the use of extra software modules to verify the result, or to use multiple versions of a program. Time redundancy is the use of additional time to perform the functions of a system. This time might be used to re-execute a faulty task or to execute a different version of the task. We are particularly interested in time redundancy techniques, since they are cost-effective as well as more suitable to applications where there are severe constraints on space and weight.

So, if a fault occurs during real-time task execution then it is necessary to overcome that fault and satisfies all timing constraints. We assume that the faults are overcoming using time redundancy and technique of executing task again. Our first analysis of transient fault tolerance in hard real-time systems with time redundancy was presented in [5]. In this paper we analyze possibilities to overcome the transient faults using response time analysis (RTA). More about RTA can be found in [6].

We use response time analysis to find minimum time (period) between two consecutive faults which real-time system can tolerate. For that period RTA guaranties that analyzed real-time system will be fault tolerant. If new fault occurs during that calculated period of time then RTA cannot guaranties overcoming of that fault. We saw that as a problem and our task was to modify RTA in order to obtain a guarantee for the case that extra fault occurs.

During modification we started with assumption to provide enough time redundancy for re-execution of the highest priority (the most critical) for the case of fault tolerance. Consider added extra time we modify the base RTA equation and present it in the paper. Our goal is to analyze how added time redundancy can be used for tolerance some new (extra) faults in the RTS. We use MATLAB for all calculations related to the RTA and the modify RTA.

The rest of the paper is organized as follow: Section II deals with the existing RTA applied on non-faulty RTS (part A) and faulty RTS (part B). Part C of Section II presents the research problem and our modification of RTA. Section III offers our conclusion.

II. ANALYSIS OF REAL-TIME SYSTEMS TIMING CONSTRAINS

A. Non-faulty RTS

In this paper we consider only a uniprocessor system where algorithm for scheduling real-time tasks could be Rate Monotonic, Deadline Monotonic [7] or any other priority assignment algorithm. We assume that each task is assigned a unique priority and that a task can be immediately preempted by a higher priority task. At run time, the highest priority task from the set of runnable tasks is allocated processor time.

[1]Sandra Djosic is with the Faculty of Electronic Engineering, Aleksandra Medvedeva 14, 18000 Nis, Serbia, E-mail: sandra.djosic@elfak.ni.ac.rs.

[2]Milun Jevtic is with the Faculty of Electronic Engineering, Aleksandra Medvedeva 14, 18000 Nis, Serbia, E-mail: milun.jevtic@elfak.ni.ac.rs.

[3]Milunka Damnjanovic is with the Faculty of Electronic Engineering, Aleksandra Medvedeva 14, 18000 Nis, Serbia, E-mail: milunka.damnjanovic@elfak.ni.ac.rs.

We assume a set of n tasks, $\Gamma=\{\tau_1,..., \tau_n\}$ in which tasks are ordered according to the assigned priorities, where 1 denotes the highest priority and n denotes the lowest priority. Each task τ_i is assumed to have a minimum inter-arrival time T_i, worst case execution time (WCET) C_i and deadline D_i. We assume that $D_i \le T_i$, for $i = 1, 2, \ldots, n$. We use hp(i) to denote the set of tasks with higher priorities than i, hp(i)=$\{\tau_j \in \Gamma \mid p_j > p_i\}$.

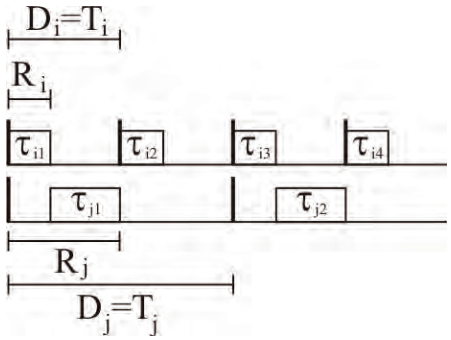

Fig. 1. Response time of tasks when there are no faults in the system

If there are no faults in the system then the response time of task τ_i can be evaluated using Eq. (1). Here the response time R_i, of a task τ_i, is expressed as the sum of its WCET C_i and interference due to preemption by higher priority tasks. If we can find $R_i \in [0, D_i]$, which satisfies the Eq. (1):

$$R_i = C_i + \sum_{j \in hp(i)} \left\lceil \frac{R_i}{T_j} \right\rceil C_j \qquad (1)$$

then task τ_i is feasible. The smallest value of R_i which satisfies the Eq. (1) is the worst case response time of task τ_i. Since R_i appears on both sides solutions can be obtained using the following recurrence relation:

$$R_i^{n+1} = C_i + \sum_{j \in hp(i)} \left\lceil \frac{R_i^n}{T_j} \right\rceil C_j \qquad (2)$$

Iteration starts with $R_i^0 = C_i$. When $R_i^{n+1} = R_i^n$ we have found a minimum solution, that is R_i. If $R_i^{n+1} > D_i$ then task τ_i is infeasible and iteration is terminated.

TABLE I
TASK SET - CASE I

Task	Task characteristics				R_i
	C_i	T_i	D_i	p_i	
τ_1	30	100	100	1	30
τ_2	35	175	175	2	65
τ_3	25	200	200	3	90
τ_4	30	300	300	4	150

Fig. 1 presents scheduling of two periodic real-time tasks τ_i and τ_j when there is no fault in the system. System of these two tasks are schedulable i.e. both tasks execute before their deadlines, D_i and D_j. Response time of tasks τ_i and τ_j are the output results of RTA and they are also shown on Fig. 1.

We illustrate this procedure for a task set consisting of four periodic tasks. Timing characteristics for these four tasks are shown in Table I. Using Eq. (2) we found the value for the response times of the complete task set (last column in Table I). For all four tasks we got that $R_i < D_i$, for i = 1, 2, 3 and 4, which means that all tasks finished before their deadlines. It can be concluded that the real-time task set – case I is schedulable.

B. Faulty RTS

The fault-free assumption for one RTS is in fact not realistic because "non-faulty systems hardly exist, there are only systems which may have not yet failed", [6]. So, if a fault occurs during real-time task execution then it is necessary to overcome that fault and satisfy all timing constraints of real-time tasks. We consider transient fault and assume that the effects of a fault can be eliminated by simple re-execution of the affected task at its original priority level. Now, the response time analysis can be describe using Eq. (3):

$$R_i = C_i + \sum_{j \in hp(i)} \left\lceil \frac{R_i}{T_j} \right\rceil C_j + \left\lceil \frac{R_i}{T_F} \right\rceil \max_{j \in hp(i) \cup i} (C_j) \qquad (3)$$

Eq. (3) has one more addend (then Eq. (1)) due to possible faults in the system. If we assume that inter-arrival time between faults is T_F then there can be at most $\left\lceil \frac{R_i}{T_F} \right\rceil$ faults during the response time R_i of task τ_i. Since these faults could occur during the execution of task τ_i or any higher priority task which has preempted τ_i, each fault may add $\max_{j \in hp(i) \cup i} (C_j)$ to the response time of task τ_i. So, the third addend in Eq. (3) presents an extra time needed tasks recovery due to faults.

Since R_i appears on both sides we need again recurrence relations:

$$R_i^{n+1} = C_i + \sum_{j \in hp(i)} \left\lceil \frac{R_i^n}{T_j} \right\rceil C_j + \left\lceil \frac{R_i^n}{T_F} \right\rceil \max_{j \in hp(i) \cup i} (C_j) \qquad (4)$$

Eq. (4) calculates the response times of tasks in the presence of faults if the interval between two faults is T_F. Recurrence relations also starts with $R_i^0 = C_i$. When $R_i^{n+1} = R_i^n$ we have found a minimum solution, that is R_i. If $R_i^{n+1} > D_i$ then task τ_i is infeasible and iteration is terminated. Minimum value for T_F which satisfies Eq. (4) presents minimum time between two consecutive faults which real-time system can tolerate.

Fig. 2 illustrates RTA applied on faulty RTS. It can be seen scheduling of the same real-time tasks τ_i and τ_j when two faults occur in the system. Time between two consecutive faults T_F is long enough and real-time system can tolerate these faults. First fault occurs just a little bit before the end of tasks τ_{j1} execution. Real-time system overcomes this fault by executing task τ_{j1} again. Output results of RTA, response time

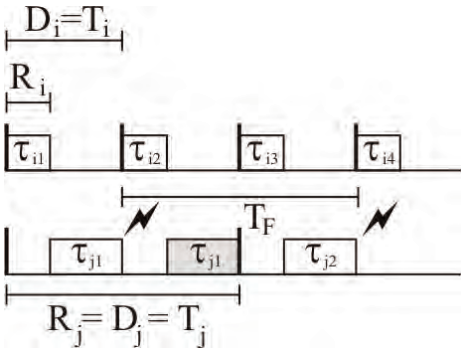

Fig. 2. T_F is long enough and RTS is fault tolerant

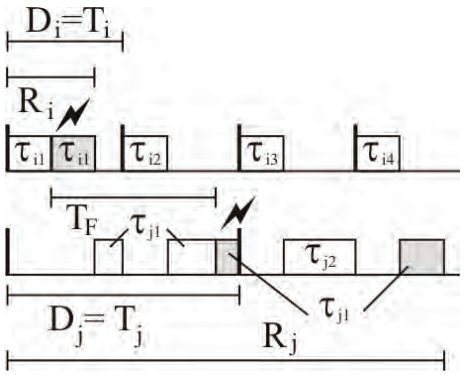

Fig. 3. T_F is not long enough that RTS stays fault tolerant

of tasks τ_i and τ_j, for the assumed value T_F are shown on Fig. 1.

Fig. 3 presents scheduling of the same real-time tasks τ_i and τ_j when two faults occur in the system. Now, time between two consecutive faults T_F is not long enough and real-time system cannot tolerate these faults. First fault occurs just a little bit before the end of tasks τ_{i1} execution. Real-time system can overcomes this fault by executing task τ_{i1} again. Second fault occurs just a little bit before the end of tasks τ_{j1} execution. Now time redundancy is not enough to tolerate this fault. Systems starts procedure for overcoming fault by executing task τ_{j1} again but timing characteristics of tasks τ_{j1} cannot be satisfied and τ_{j1} missing its deadline i.e. $R_j > D_j$. This is not acceptable in one hard real-time system, so in this case real-time system is not fault tolerant.

TABLE II
TASK SET - CASE I

Task	Task characteristics				T_F=300	T_F=200	T_F=275
	C_i	T_i	D_i	p_i	R_i	R_i	R_i
τ_1	30	100	100	1	60	60	60
τ_2	35	175	175	2	100	100	100
τ_3	25	200	200	3	155	155	155
τ_4	30	300	300	4	275	**340**	275

In Table II, we present the response times of the task set used in Table I for two different fault inter-arrival times. With a minimum fault inter-arrival time of T_F = 300 the task set is schedulable, but it is not schedulable with T_F = 200.

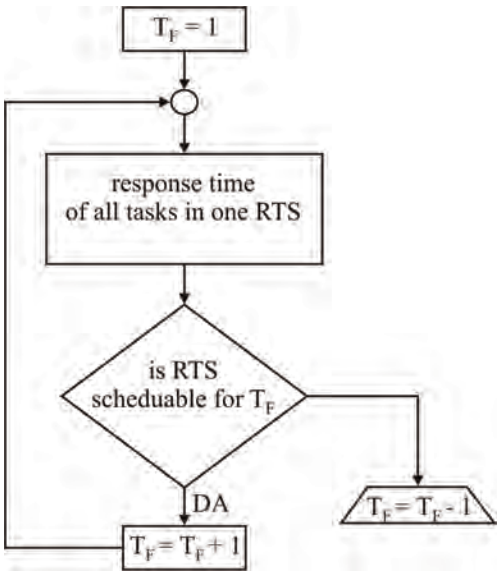

Fig. 4. Algorithm for finding minimum T_F

Based on Eq. (4) we realized algorithm (Fig. 4) for finding minimum time between two consecutive faults which real-time system can tolerate. We start from the minimum possible value for T_F and for that value we calculate response time for each task. After that, it is necessary to check is the real-time system fault tolerant. Depends on answer we continue process with increment value of T_F ("true" answer) or finish it ("not true") finding minimum T_F.

Using presented algorithm we calculated minimum T_F for the same task set – case I. The value for T_F is 275 and the response time of the tasks is shown in the last column of Table II.

C. Modification of RTA

Using RTA and our presented algorithm we can find minimum time (period) between two consecutive faults which one real-time system can tolerate. If minimum time between two faults is equal or greater then T_F then RTA can guaranty that this real-time system will be fault tolerant. But if minimum time between two faults is less then T_F then RTA cannot guaranties tolerance of that fault. For that case we have modified RTA to get fault tolerant RTS. The basic idea for modification was to ensure enough redundancy for the highest priority task and to use this extra spare time for potentially less priority tasks re-execution.

Let's illustrate idea with one simple real-time task set shown in Table III. If we apply presented algorithm on task set from Table III we can conclude that RTS is fault tolerant if T_F is 60 time units.

Let's ensure 100% redundancy for the task τ_1, doubling his execution time. New WCET for task τ_1 is:

$$C_1 = C_{1task} + C_{1extra} = 20+20 = 40$$

where C_{1task} is WCET of tasks τ_1 and C_{1extra} is an added time needed for tasks τ_1 re-execution. We applied presented algorithm with new input parameters and have got the result shown in Table IV.

TABLE III
TASK SET - CASE II

Task	Task characteristics				T_F=60
	C_i	T_i	D_i	p_i	R_i
τ_1	20	100	100	1	40
τ_2	25	175	175	2	95
τ_3	20	200	200	3	160
τ_4	25	300	300	4	300

Now, response time for task τ_1 is R_1 = 80. This value is not correct because we already doubling WCET for task τ_1 for fault tolerant case. More correct value for R_1 is 40 time units, even in the worst case. Time period of 40 units is long enough for executing task τ_1 and to re-execute it in the presence of fault.

TABLE IV
TASK SET - CASE IIMOD

Task	Task characteristics				T_F=275	T_{Fmod}=143
	C_i	T_i	D_i	p_i	R_i	R_{imod}
τ_1	40	100	100	1	80	40
τ_2	25	175	175	2	145	90
τ_3	20	200	200	3	165	175
τ_4	25	300	300	4	275	285

To get more correct result we needed to modify Eq. (3) and we got new equation:

$$R_{i\,mod} = C_i + \sum_{j \in hp(i)} \left\lceil \frac{R_{i\,mod}}{T_j} \right\rceil C_j + \left\lceil \frac{R_{i\,mod}}{T_{F\,mod}} \right\rceil \max_{j \in hp\,mod(i)} (C_j) \qquad (5)$$

The main difference between Eq. (3) and Eq. (5) is within the third addend. We needed to eliminate the possibility that fault can occurs within task τ_1. Because of that we have new task set for the third addend hpmod(i)=$\{\tau_j \in \Gamma_{mod} | p_j \geq p_i\}$ where is $\Gamma_{mod}=\{\tau_2,..., \tau_n\}$.

Appropriate recurrence relation for Eq. (5) is:

$$R_{i\,mod}^{n+1} = C_i + \sum_{j \in hp(i)} \left\lceil \frac{R_{i\,mod}^{n}}{T_j} \right\rceil C_j + \left\lceil \frac{R_{i\,mod}^{n}}{T_{F\,mod}} \right\rceil \max_{j \in hp\,mod(i)} (C_j) \qquad (6)$$

Initial and ending conditions are the same as for Eq. (4). Using Eq. (6) and algorithm for finding minimum T_F we realized application in MATLAB which can help us to analyze timing constrains of one fault tolerant real-time system.

We applied the realized application on the task set Case IImod and the results are shown in the last column of Table IV. It can be concluded that response time for τ_1 is 40 time units what is in accordance with our starting assumption. Also, value for T_{Fmod} = 143 is less then T_F = 275 what is good for one RTS. If minimum time between two consecutive faults, which real-time system can tolerate, is less then the RTS is more faults tolerant. Because of that the modified analysis gave us better result then original.

III. CONCLUSION

The modify RTA gave us more precise analysis results which show us that RTS can tolerate more faults then unmodified RTA was given. For the tasks set – case IImod (Table IV) value for T_F is reduced from 275 to 143 which is improvement of 48%. So, the main contribute of our paper is increasing number of faults which RTA considers during analysis. Now, for all that faults modify RTA can guarantees that RTS will be fault tolerant. Using modify RTA we get one more fault tolerant RTS. The modify RTA can be used for estimating the possibility of overcoming transient faults in one process control real-time system i.e. it can be concluded how much is one RTS fault tolerant.

ACKNOWLEDGEMENT

This paper is supported by Project Grant III44004 (2011-2014) financed by Ministry of Education and Science, Republic of Serbia

REFERENCES

[1] N. Nissanke, *Realtime Systems*, Prentice Hall, 1997.
[2] K. Juvva, "Real-Time Systems", Carnegie Mellon University 18-849b Dependable Embedded Systems ili http://www2.cs.cmu.edu/~koopman/des_s99/real_time/
[3] Nobuyasu Kanekawa, Eishi H. Ibe, Takashi Suga, Yutaka Uematsu, *Dependability in Electronic Systems: Mitigation of Hardware Failures, Soft Errors, and Electro-Magnetic Disturbances*, Springer, 2010.
[4] S. Đošić, M. Jevtić, "Planiranje zadataka u sistemu za rad u realnom vremenu sa redundansom u vremenu za prevazilaženje otkaza", Zbornik radova V simpozijuma industrijske elektronike, INDEL 2004, Banja Luka, pp. 146-149, novembar 2004.
[5] S. Đošić, M. Jevtić, "Analysis of transient fault tolerance in hard real-time systems with time redundancy", Facta Universitatis, Series: Automatic control and robotics, vol. 8, no 1, pp. 149-163, 2009.
[6] M. George de A. Lima and Alan Burns, "An Optimal Fixed-Priority Assignment Algorithm for Supporting Fault-Tolerant Hard Real-Time Systems", IEEE Trans. Computers, vol.52, no.10, pp. 1332-1346, Oct. 2003.
[7] F. Cottet, J. Delacroix, Z. Mammeri, "Scheduling in Real-Time Systems", John Wiley & Sons, 2002.

Interactive Evolutionary Algorithm for Multiple Objective Convex Integer Problems

Leoneed Kirilov[1] , Vassil Guliashki[2] and Krasimira Genova[3]

***Abstract* – An interactive evolutionary algorithm is proposed to solve multiple objective convex integer problems. The algorithm uses a heuristic for fast search, proposed to generate quickly a local approximate representative subset of the efficient frontier. Utility coefficients are calculated and used to support the Decision Maker (DM) to obtain a good reference point. A comparison with two other evolutionary algorithms for the same class optimization problems is done on an illustrative example.**

***Keywords* – Multiple objective integer optimization, Interactive evolutionary algorithms, Pareto-optimal front.**

I. INTRODUCTION

Multiple objective convex integer optimization problem is considered in this paper. It can be stated in the following general form:

$$\text{Maximize } \boldsymbol{f}(\boldsymbol{x}) = [f_1(\boldsymbol{x}), f_2(\boldsymbol{x}), \ldots, f_k(\boldsymbol{x})]^{\mathrm{T}} \quad \textbf{(1)}$$

$$\text{subject to: } \boldsymbol{g_j}(\boldsymbol{x}) \le 0, \quad j = 1,2,..., m; \quad \textbf{(2)}$$

$$\boldsymbol{x_i}^{(L)} \le \boldsymbol{x_i} \le \boldsymbol{x_i}^{(U)}, \ i = 1,2,\ldots, n; \quad \textbf{(3)}$$

$$\boldsymbol{x} \in \boldsymbol{Z^n}, \quad \textbf{(4)}$$

where $\boldsymbol{g_j}(\boldsymbol{x})$, $j = 1,2,\ldots, m$; are convex functions and $f_i(\boldsymbol{x})$, $i = 1,2,\ldots, k$; are concave nonlinear functions.

In the text of the paper is used the term "solution" as a vector of variables and the term "point" as a corresponding vector of objectives.

A solution $\boldsymbol{x} \in \boldsymbol{Z^n}$ is a vector of n integer decision variables: $\boldsymbol{x} = (x_1, x_2, \ldots, x_n)^T$. The value $x_i^{(L)}$ is the known lower bound and the value $x_i^{(U}$ is correspondingly the upper bound of variable x_i. The solutions satisfying the constraints (2)-(4) constitute a feasible decision variable space $\boldsymbol{V} \subset \boldsymbol{Z^n}$. The objective functions (1) constitute a k-dimensional space, called objective space $\boldsymbol{F} \subset \boldsymbol{R}^k$. For each solution $\boldsymbol{x}$ in the decision variable space, there exists a point $\boldsymbol{f} \in \mathbf{R}^k$ in the objective space, denoted by $\boldsymbol{f}(\boldsymbol{x}) = \boldsymbol{f} = (f_1, f_2, \ldots, f_k)^T$.

The problem (1-4) does not posses a unique optimal solution in the objective space. Instead that a conception of Pareto optimality or non-domination is used (see [2], [4], [13], [16]).

The domination between two solutions is defined as follows (see [2, 4, 13]):

[1]Leoneed Kirilov is with the Institute of Information and Communication Technologies – BAS, "Acad. G. Bonchev" str. Bl. 2, 1113 Sofia, Bulgaria, E-mail: leomk@abv.bg

[2]Vassil Guliashki is with the Institute of Information and Communication Technologies – BAS, "Acad. G. Bonchev" str. Bl. 2, 1113 Sofia, Bulgaria, E-mail: vggul@yahoo.com

[3]Krasimira Genova is with the Institute of Information and Communication Technologies – BAS, "Acad. G. Bonchev" str. Bl. 2, 1113 Sofia, Bulgaria, E-mail: kgenova@iinf.bas.bg

Definition 1. *A solution* $\mathbf{x}^{(1)}$ *is said to dominate the other solution* $\mathbf{x}^{(2)}$, *if both the following conditions are true*:

1. *The solution* $\boldsymbol{x}^{(1)}$ *is no worse(say the operator* $\prec$ *denotes worse and the operator* $\succ$ *denotes better) than* $\boldsymbol{x}^{(2)}$ *in all objectives*, or $f_j(\boldsymbol{x}^{(1)}) \not\prec f_j(\boldsymbol{x}^{(2)})$ for $j = 1,2,..., k$;.

2. *The solution* $\boldsymbol{x}^{(1)}$ *is strictly better than* $\boldsymbol{x}^{(2)}$ *in at least one objective*, or $f_j(\boldsymbol{x}^{(1)}) \succ f_j(\boldsymbol{x}^{(2)})$ for at least one $j \in \{1,2,..., k\}$.

All points which are not dominated by any other point $\boldsymbol{f} \in \boldsymbol{F}$ form the set of non-dominated points and the set of Pareto-optimal solutions in the variable space respectively.

There are two ideal goals in the multi-objective optimization:

1. Find a set of solutions which are diverse enough to represent the entire range of the Pareto-optimal front, and

2. Find a set of Pareto-optimal solutions, which satisfy in the best way the DM's preferences.

The interactive algorithms are the most popular in solving multi-objective optimization problems (see [14, 19]. They consist of two alternate phases: 1. Interaction (dialogue) with the DM and 2. Generating solutions. Usually an appropriate single objective convex integer optimization problem is solved during the second phase. Such problems belong to the class of NP-hard problems (see for example [6, 15]). There does not exist an exact algorithm, which can solve these problems in time depending polynomially on the problem input data length or on the problem size. For this reason many researchers investigate approximate algorithms with polynomial computational complexity, which solve such kind optimization problems. For the past 20 years evolutionary multiple objective optimization (EMOO) methodologies have demonstrated their usefulness in finding a set of near Pareto-optimal solutions [2, 3, 5]. As a sequence many source codes – both commercial and free have been created and the EMOO algorithms obtained wide application.

In principle the evolutionary optimization (EO) algorithms use a population-based approach, in which the iterations are performed on a set of solutions (called population) and more than one solution is generated at each iteration. The main positive features making popular the EO algorithms are the following: (i) They do not require any derivative information; (ii) EO algorithms are relatively simple to implement; (iii) EO algorithms are flexible and robust, i.e. they perform very well on a wide spectrum of problems (see [7]); The use of a population in EO algorithms has a number of advantages (see [2]): 1) it provides an EO procedure with a parallel processing power, 2) it allows EO procedures to find multiple optimal solutions, thereby facilitating the solution of multi-modal and multi-objective optimization problems, and 3) it provides an EO algorithm with the ability to normalize decision variables (as well as objective and constraint functions) within an evolving population using the best minimum and maximum values in the population.

Some important disadvantages of EMOO algorithms are: (i) their convergence to the Pareto-optimal front could be slow and may require large number of iterations; (ii) they face difficulty in solving problems with a large number of objectives, i.e. they could obtain difficult a well representative set of Pareto-Optimal Solutions (see [5]).

The number of objectives as a convergence factor is considered in [17]. Good approach in solving problems with large number of objectives is to use the EMOO methodologies to find a preferred and smaller set of Pareto-optimal solutions, instead of the entire front [5]. In this way the DM can concentrate to explore only the regions of Pareto-optimal front, which are of interest to her/him. An accelerating technique for population based algorithms is proposed in [8]. A technique for quickly moving the population to the Pareto-optimal front is proposed in [9, 12]. Some hybrid EMOO algorithms have been recently proposed to overcome the second mentioned disadvantage (see [5, 11]). They expand the use of classical multi-objective optimization procedures (see [13]) like reference point-, reference direction- and other type methods, proposing new approaches and hybrid techniques.

An interactive population-based (evolutionary) algorithm solving the problem (1)-(4) is proposed in this paper. To evaluate and arrange the solutions in the population is used the PROMETHEE method (see [1]). Utility coefficients like those proposed in [10] are calculated and used to support the DM in the choice of a reference point. The algorithm includes a heuristic procedure for quickly moving the whole population to the reference point, according the DM preferences. This procedure leads to better convergence of the search process to Pareto-optimal front.

II. UTILITY COEFFICIENTS AND CHOICE OF REFERENCE POINT

Let we have a population $\boldsymbol{P}$ of solutions in the variable space and let the size of $\boldsymbol{P}$ be p.

The idea here is the algorithm to support the DM in his/her orientation where to search the desired compromise solution. The application of a scalarization process such as weighted sums or root mean square is excluded in [18] by the assumption that the different dimensions of the objectives $\boldsymbol{f}_i(x)$ in (1) are not commensurable. To avoid this obstacle the algorithm uses utility coefficients $\eta_i(x)$ for each objective $\boldsymbol{f}_i(x)$, i=1,…,k; which are computed as follows:

$$\eta_i(x) = \frac{f_i - f_{i\min}}{f_{i\max} - f_{i\min}} \qquad \textbf{(5)}$$

where $f_{i\ max}$ and $f_{i\ min}$ are correspondingly the maximal known and the minimal value for i-th objective. In case $f_{i\ max} = f_{i\ min}$ the denominator of (5) is set to be 1.

On the base of 10% of best members of $\boldsymbol{P}$, arranged by means of special Gaussian generalized evaluation according the method PROMETHEE (see [1]), DM gives his preferences as utility coefficients for each objective $\boldsymbol{f}_i(x)$, i =1,…,k;. Let they be $\eta^r = (\eta_1, \eta_2, \ldots, \eta_k)^T$. Let the best and the worst solution among these 10% members of $\boldsymbol{P}$ are x^b and x^w. The direction $\mathbf{z}$ is calculated as follows:

$$\mathbf{z} = x^b - x^w \qquad \textbf{(6)}$$

Steps along $\mathbf{z}$ are done starting by x^b and corresponding solutions, candidate to be chosen as reference solutions are generated: $x^{(1)}, x^{(2)}, \ldots x^{(j)}$.

Then the vectors $\eta(x) = (\eta_1(x), \eta_2(x), \ldots, \eta_k(x))^T$ for each $x^{(1)}$, $x^{(2)}$, …, $x^{(j)}$ are calculated. The Euclidean distance between those vectors and the preferred utility vector η^r is calculated:

$$d^j = \sqrt{\sum_{i=1}^{k} \left(\eta^j{}_i - \eta^r{}_i\right)^2} \qquad \textbf{(7)}$$

The solution $x^{(j)}$, where d^j becomes minimal is chosen as current reference solution $\boldsymbol{x}^r$ and the corresponding point in the objective space becomes current reference point $\boldsymbol{f}^r$.

III. A FAST SEARCH HEURISTIC PROCEDURE.

The proposed algorithm uses a *heuristic procedure* to move quickly the whole population to the Pareto-optimal front. It consists of following steps:

The weight center $\boldsymbol{C}$ of the solutions $\boldsymbol{x}^i \in \boldsymbol{P}$, for i = 1,…,p; is calculated. The components $\boldsymbol{C}_i$ of $\boldsymbol{C}$ are:

$$\boldsymbol{C}_i = \frac{\sum_{j=1}^{p} x_i^j}{p}, \text{ for } i = 1,\ldots,n; \qquad \textbf{(8)}$$

A direction in the variable space for moving the whole population to the reference solution is calculated:

$$\boldsymbol{y} = \boldsymbol{x}^r - \boldsymbol{C} \qquad \textbf{(9)}$$

It is expected that the $\boldsymbol{y}$ vector is directed to the Pareto-optimal front, because the solutions x^b and x^w are evaluated by means of the Gaussian generalized criterion [1]. Then we move the whole population with step $\boldsymbol{y}$ to the reference solution $\boldsymbol{x}^r$. In case $\boldsymbol{x}^r$ is infeasible some members of the new population may become infeasible. In case x' violates some constraint in the system (2)-(3) the corresponding feasible solution is calculated by using Golden section method for line search along the segment xx' (where x is the corresponding starting solution) and by rounding the final x' to an integer solution.

IV. THE PROPOSED INTERACTIVE EVOLUTIONARY ALGORITHM

The considered problem has a closed feasible domain because there are given lower and upper bounds for each variable (see constraints **(3)**). The Tchebycheff center of the feasible domain can be calculated and it can be rounded off to the closest integer feasible solution $\boldsymbol{x}^{ch}$, called below rounded Tchebycheff center. There is also a possibility to use near Tchebycheff center $\boldsymbol{x}^{nch}$ for the domain determined by the constraint system **(3)**, but only if $\boldsymbol{x}^{nch}$ is feasible for the domain determined by **(2)-(3)**.

By means of the fast search heuristic procedure the whole population is translated fast and close to the Pareto-optimal front.

Below is presented the general scheme of the new algorithm:

Scheme of the algorithm

Step 1. Set iteration counter $h = 0$. **A**round the Tchebycheff center $\boldsymbol{x}^{ch}$ of the feasible domain generate a number of p uniform distributed solutions' vectors by using deviation of ±δ, where δ is a constant or % of corresponding component (for example δmax = ±5%). Use them to create the initial population P_h.

Step 2. Evaluate the members of P_h using the Gaussian generalized criterion:

$$F_l(x^{(i)}x^{(j)}) = 1 - e^{(-d^2/2s^2)},\ l = 1,\ldots,k; \qquad \textbf{(10)}$$

where $s = 2$ and $d = \boldsymbol{f}_l(x^{(i)}) - \boldsymbol{f}_l(x^{(j)})$.

$$\pi(x^{(i)}x^{(j)}) = \sum_{l=1}^{k} F_l(x^{(i)}x^{(j)}),\ \text{for } \forall i,j = 1,\ldots,p;\ \text{and } i \neq j; \qquad \textbf{(11)}$$

$$\boldsymbol{\Phi}^{+}(x^{(j)}) = \sum_{i \neq j,\ i=1}^{p} \pi(x^{(j)}x^{(i)}),\ j = 1,\ldots,p; \qquad \textbf{(12)}$$

Arrange the solutions in P_h in descending order according their $\boldsymbol{\Phi}^{+}$-values ($\boldsymbol{\Phi}^{+}(x^{(j)})$ for $j = 1,\ldots,p$;).

Step 3. Among the best 10% of members of P_h determine the best and the worst solution according their $\boldsymbol{\Phi}^{+}$-values. Let they are x^b and x^w. Then calculate direction **z** as shown in **(6).**

Step 4. Calculate the utility vectors $\eta(x) = (\eta_1(x), \eta_2(x), \ldots, \eta_k(x))^T$ for the best 10% of members of P_h.

Step 5. Show the calculated utility vectors to DM and ask he/she to put his/her preferences in form of utility coefficients for each objective $\boldsymbol{f}_i(x)$, $i = 1,\ldots,k$; Use these coefficients as components of the utility vector η^r.

Step 6. Starting by x^b make steps along **z** (calculated at Step 3.) and generate corresponding solutions, candidate to be chosen as reference solutions: $x^{(1)}, x^{(2)}, \ldots x^{(j)}$.

Step 7. Calculate the utility vectors $\eta(x) = (\eta_1(x), \eta_2(x), \ldots, \eta_k(x))^T$ for each $x^{(1)}, x^{(2)}, \ldots, x^{(j)}$.

Step 8. Calculate the Euclidean distance between those vectors and the preferred utility vector η^r. Choose the solution having minimal Euclidean distance to η^r as current reference solution $\boldsymbol{x}^r$ and the corresponding point in the objective space as current reference point $\boldsymbol{f}^r$.

Step 9. Perform the *heuristic procedure* to move P_h towards the Pareto-optimal front:

Calculate the weight center **C** of the solutions $\boldsymbol{x}^i \in P_h$, for $i = 1,\ldots,p$; (see **(8)**). Then calculate the vector $\boldsymbol{y}$ as shown in **(9)**.

Move the population with step size α along this direction: $\{Pnew\} = \{Ph\} + \alpha.\boldsymbol{y}$. The goal is the population *Pnew* to be located as close as possible to the Pareto-optimal front.

Step 10. Some solutions in the *Pnew* may be infeasible. For each infeasible solution in *Pnew* perform the Golden section method for line search to move it to the feasible region.

Step 11. The DM evaluates all points in *Pnew* and if he/she is satisfied by one of them go to **Step 12**, otherwise set $h = h+1$, $Ph = Pnew$, and go to **Step 2**.

Step 12. STOP. (End of the algorithm)

V. ILLUSTRATIVE EXAMPLE

The performance of presented algorithm is illustrated on the following test example:

$$\textbf{Max } \boldsymbol{f}(x) = [\boldsymbol{f}_1(x), \boldsymbol{f}_2(x)]^T,$$
$$\boldsymbol{f}_1(x) = x_1;\ \boldsymbol{f}_2(x) = x_2;$$

subject to:

$$x_1 + 3x_2 - 150 \le 0$$
$$0 \le x_1 \le 120,$$
$$0 \le x_2 \le 40,$$
$$x_1, x_2 \text{ – integer;}$$

The performance for this example for one iteration of the algorithm is presented on Fig. 1.

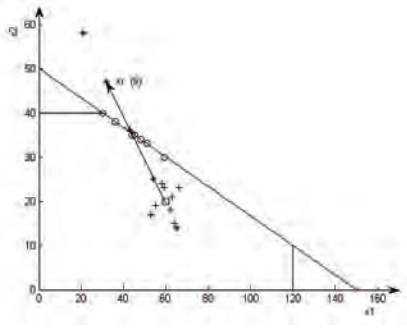

Legend:

\+ – initial population P_0
□ – weight center of P_0
* – solutions $x^{(j)}$ at **Step 6**
o – population *Pnew*

Fig.1. Result of algorithm after the first iteration

At Step 1. Here is used the near Tchebycheff center $\boldsymbol{x}^{nch}$ = (60, 20) because it is feasible solution. The following initial population P_0 is created: $x^{(1)}$ = (66,23), $x^{(2)}$ = (53,17), $x^{(3)}$ = (58,24), $x^{(4)}$ = (55,19), $x^{(5)}$ = (62,18), $x^{(6)}$ = (65,14), $x^{(7)}$ = (63,21), $x^{(8)}$ = (54,25), $x^{(9)}$ = (59,23), $x^{(10)}$ = (64,15);

At Step 2. The corresponding $\boldsymbol{\Phi}^{+}$-values are: 12,76215; 13,8756; 13,39125; 13,44787; 12,93763; 13,90183; 12,37131; 14,69332; 12,2522; 12,99491;

At Step 3. The best 10% of population are the solutions $x^{(8)}$ = (54,25) and $x^{(6)}$ = (65,14). The direction **z** = (-11, 11).

At Step 4. The minimal and maximal values for f_1 are (0, 120) and for f_2 are (0, 40). The utility vectors for $x^{(8)}$ and $x^{(6)}$ are: $\eta(x^{(8)})$ = (0.45; 0.625); $\eta(x^{(6)})$ = (0.54; 0.35);

At Step 5. The DM specifies as most preferable the utility vector η^r = (0.58; 0.75).

At Step 6. Starting by $x^{(8)}$ = (54,25) the following solutions are generated along z: (43, 36), (32, 47), (21, 58), (10, 69) and (0, 79).

At Step 8. The obtained reference solution $\boldsymbol{x}^r$ = (32, 47). It coincides with the corresponding reference point $\boldsymbol{f}^r$.

At Step 9. The weight center of P_0 is **C** = (60, 19.9). The vector $\boldsymbol{y}$ = (-28, 27.1).

At Step 10. The generated new population is *Pnew* = {(59, 30), (30, 40), (48, 34), (36, 38), (45, 35), (44, 35), (51, 33), (44, 35), (48, 34), (44,35)}.

At Step 11. The best obtained solutions are $x^{(2)}$ = (30,40) and $x^{(1)}$ = (59, 30). The corresponding $\boldsymbol{\Phi}^{+}$-values are: 17,22825 and 28,27333. The solution arranged on third position is: $x^{(4)}$ = (36, 38) with $\boldsymbol{\Phi}^{+}$-value 15,56581. The utility vectors are: $\eta(x^{(2)})$ = (0.25; 1); $\eta(x^{(1)})$ = (0.492; 0.75); $\eta(x^{(4)})$ = (0.3; 0.95); The DM chooses as compromise the solution $x^{(1)}$ = (59, 30) and terminates the calculations.

If DM wishes, she/he can perform a new iteration. In this case the algorithm continues by Step 2 and DM can specify new preferences in the form of utility coefficients. In this way DM could explore different parts of Pareto-optimal front.

The solution of the above example by the method SPEA (see [4], [20]) is as follows: Initial population P_0 is the same. External population is P_1^{ext} = {(65, 27), (67, 20)}. After the first iteration the current population is P_1= {(53, 17), (58, 24), (55, 19), (65, 27), (67, 20), (63, 21), (54, 25), (59, 23), (66, 23), (58, 23)}. The best obtained solutions are: $x^{(4)}$ = (65,27), $x^{(5)}$ = (67,20) and $x^{(8)}$ = (66, 23). The corresponding utility vectors are: $\eta(x^{(4)})$ = (0.542; 0.675); $\eta(x^{(5)})$ = (0.55; 0.575); $\eta(x^{(8)})$ = (0.558; 0.5);

It can be seen that SPEA generates dispersed sample along the whole Pareto-optimal front.

The same example is solved by means of algorithm MGA, proposed in [10], starting with the same initial population P_0. The following result is obtained: After the first iteration the current population is P_1= {(66, 25), (65, 25), (66, 24), (65, 24), (66, 23), (65, 23), (66, 21), (65, 21), (66, 19), (65, 19)}. The best obtained solutions are: $x^{(1)}$ = (66,25) and $x^{(2)}$ = (65, 25). The corresponding utility vectors are: $\eta(x^{(1)})$ = (0.55; 0.625); $\eta(x^{(2)})$ = (0.542; 0.625);

Obviously the algorithm proposed here has better convergence to the Pareto-optimal front than the algorithms SPEA and MGA.

VI. Conclusion

The proposed algorithm is suitable to solve real-life large size multiple objective integer optimization problems. It has the following basic characteristics:

- It is designed to find a preferred set of solutions instead of the entire Pareto-optimal set.
- It can quickly converge to the desired part of Pareto-optimal front.
- It is indifferent to the shape of Pareto-optimal front.
- It is applicable to problems with large number of objectives and large number of variables.
- It does not put great demands to the DM.
- It is an interactive evolutionary method and could generate a number of solutions in the region of interest, so that the DM would be able to find without great efforts the satisfactory non-dominated solution among them.

The algorithm is realized as module in a web-based interactive system for multiple objective optimization.

Acknowledgement

The authors gratefully acknowledge the support of Bulgarian National Science Fund, Grant No DTK02/71 "Web-Based Interactive System, Supporting the Building Models and Solving Optimization and Decision Making Problems" and IICT-BAS research project "Modeling, Optimization and Multiple Criteria Decision Making".

References

[1] Bana e Costa, C. A. ed., *Reading In Multiple Criteria Decision Aid*, Springer Verlag, Berlin-Heidelberg, 1990.

[2] Branke J., Deb K., Miettinen K., Słowiński R., „*Multiobjective Optimization. Interactive and Evolutionary Approaches*", Springer-Verlag Berlin Heidelberg, 2008

[3] Coello C. A. C., D. A. Van Veldhuizen, and G. Lamont *Evolutionary Algorithms for Solving Multi-Objective Problems*, Boston, MA: Kluwer Academic Publishers, 2002.

[4] Deb K., „*Multi-Objective Optimization Using Evolutionary Algorithms*", Wiley-Interscience Series in Systems and Optimization. John Wiley & Sons, Chichester, 2001

[5] Deb K., J. Sundar, U. B. Rao N., S. Chaudhuri, "Reference Point Based Multi-Objective Optimization Using Evolutionary Algorithms", *International Journal of Computational Intelligence Research*, Vol. 2, No. 3 (2006), pp. 273-286.

[6] Garey M. R. and Johnson D. S. *Computers Intractability: A Guide to the Theory of NP-Completeness*, W. H. Freeman, San Francisco 1979.

[7] Goldberg, D. E. *Genetic Algorithms in Search, Optimization and Machine Learning*, Reading Mass, Addison Wesley, 1989.

[8] Guliashki V., „An Accelerating Technique for Population Based Algorithms", Proceedings of Papers of IX Internatrional Conference CompSysTech'08, Gabrovo, Bulgaria, 12-13 June, 2008, pp. -IIIB.11-1- ÷ -IIIB.11-6-.

[9] Guliashki V., L. Kirilov, "SPEA-Based Method for MCDM Convex Integer Problems", *Cybernetics and Information Technologies*, Vol. 9, No. 4 (2009), pp. 93-101.

[10] Guliashki V. "A Modified Genetic Algorithm for Multiple Objective Convex Integer Optimization", Working paper No 43, Institute of Information Technologies, Section "Decision Support Systems", 1997.

[11] Ivanova J, "An Interactive Hybrid Algorithm of Integer Multiobjective Optimization", International Conf. Automatics and Informatics'08, Proc. "School for young Scientists Business Process management", (Ed. P. Ruskov), 2008, pp.45-48.

[12] Kirilov L., V. Guliashki, "Interactive Evolutionary Method FIEM for Solving Integer Multiple Objective Problems", *Comptes rendus de l'Academie bulgare des Sciences*, Tome 64, No2, (2011), pp. 203-212. (in the press).

[13] Miettinen K., P. Neittaanmäki, M. M. Mäkelä, J. Périaux, "*Evolutionary Algorithms in Engineering and Computer Science: Recent Advances in Genetic Algorithms, Evolution Strategies, Evolutionary Programming, Genetic Programming and Industrial Applications*", John Wiley & Sons, Chichester, 1999.

[14] Miettinen K., *Nonlinear multiobjective optimization*, Kluwer, Norwell. USA, 1999.

[15] Nemhauser G.L. and Wolsey L.A. *Integer and Combinatorial Optimization*, Wiley, New York 1988.

[16] Pareto V. "*Cours d'Economie Politique*", Rouge, Lausanne, Schwitzerland, 1896.

[17] Praditwong, K.; Xin Yao, „How well do multi-objective evolutionary algorithms scale to large problems", *Evolutionary Computation*, 2007. CEC 2007. *IEEE Congress on*, 25-28 Sept. (2007), pp. 3959 – 3966.

[18] Schaffer J. D. "Multiple Objective Optimization with Vector Evaluated Genetic Algorithms", Proceedings of I. International Conference on Genetic Algorithms and their Applications, (1985), Lawrence Erlbaum Associates, Publishers, pp. 160-168.

[19] Steuer R., *Multiple Criteria Optimization: Theory, Computation and Application*, John Wiley & Sons, New York, 1986.

[20] Zitzler E., L. Thiele. In: *IEEE Transactions on Evolutionary Computation*. **3**, 1999, No 4, 257-271.

One Domain Model for Software-Intensive Ingestion of Stereoscopic 3D Content

Aleksandar Spasic[1] and Dragan Jankovic[2]

***Abstract* – Three-dimensional television (3D TV) is expected by many to be the next step in the advancement of television. What is needed is a complete re-thinking of the way technology can be applied to the art and business of 3D program making and low-budget broadcasters should reconsider alternatives of partial in-house developments. Stereoscopic 3D TV content ingestion workflow is analysed in this paper. Modelling in problem space is used as a research method in this paper and behavioural description is modelled by the use case diagram. Class diagram is used to describe static representation of 3D content during ingestion phase of the stereoscopic content production.**

***Keywords* – Stereoscopic 3D TV production, Model of Problem Space (MOPS), Ingest system, 3D Content life cycle, Domain model**

I. INTRODUCTION

Primary aim of this paper is to propose one model-driven approach of ingestion system suitable for manipulation with stereoscopic (3D) multimedia content. The target of the project is to figure out one of possible future scenarios for implementing stereoscopic 3D technologies suitable for use in low-budget TV production.

The first step of the project is to describe the whole stereoscopic content ingestion chain, from planning and defining criteria for indexing, through acquisition, indexing and metadata manipulation, to final encoding and archiving.

The second step is to propose one 3D TV ingest workflow. This step is divided into two parts, the first one is to analyse the behavioural description of ingest processes, and the second one is to define the conceptual model in problem space which is suitable for low-budget 3D TV production.

Software-intensive ingesting is a part of 3D TV production system and can be considered as a part of multimedia information system and development practice applicable for that type of information systems should be applied [1], [2].

Modelling in problem space is used as a research method in this paper. A model, by its very nature, is an abstraction of the reality. Software projects use modelling throughout the entire life cycle. Successful modelling needs to consider the areas in which modelling needs to take place. These modelling spaces have been formally considered and discussed by Unhelkar in [3]. The three distinct yet related modelling spaces are defined: problem, solution and background. The modelling output in such software projects transcends both data and code and results in a suite of visual models or diagrams.

In Unified Model Language (UML) projects, model of problem space (MOPS) deals with creating an understanding of the problem, primarily the problem that the potential user of the system is facing. While usually it is the business problem that is being described, even a technical problem can be described at the user level in MOPS. In any case, the problem space deals with all the work that takes place in understanding the problem in the context of the software system, before any solution or development is attempted. Thus the problem space would focus entirely on what is happening with the business or the user [4].

Problem space will need the UML diagrams that help the modeller understand the problem without going into technological detail. The UML diagrams that help express what is expected of the system, rather than how the system will be implemented, are of interest here. These UML diagrams in the problem space are as follows: Use case diagrams, Sequence and state machine diagrams and Class diagrams.

Authors' previous experiences with modelling of problem spaces in television production are outlined in [5], [6].

II. 3D INGESTION WORKFLOW

The majority of 3D broadcast material available today has been produced using a twin-lens [7] or dual-camera configuration giving a stereo pair where the left-eye and the right-eye views are separately recorded from slightly different perspectives.

Model of life cycle of stereoscopic content shows the entire behaviour of the object, as it changes its state in response to the messages it receives. The state machine diagram representing the life cycle of the 3D TV content is shown in Figure 1.

The nature of the state machine diagram is considered dynamic-behavioural. The state machine diagram has the ability to represent time precisely and in a real-time fashion. "What happens at a certain point of time?" is a question that is answered by this diagram.

A fundamental way to capture a stereoscopic TV signal is to use two cameras mounted on the same axis and separated by the spacing of the average pair of human eyes (6.25cm). Camera spacing can be varied, and cameras can be 'toed in',

[1]Aleksandar Spasic is with College of Professional Studies for Pre-School Teachers, Cirila i Metodija 29, 18300 Pirot, Serbia E-mail: aspasic@hotmail.com

[2]Dragan Jankovic is with the Faculty of Electronic Engineering, Aleksandra Medvedeva 14, 18000 Nis, Serbia, E-mail: dragan.jankovic@elfak.ni.ac.rs.

to achieve different elements of picture composition. Filming parameters such as camera base distance (distance between the two cameras), convergence distance (distance from the cameras to the point where both optical axis intersect), and camera lens focal length can be used to scale the horizontal disparity and thus the degree of perceived depth.

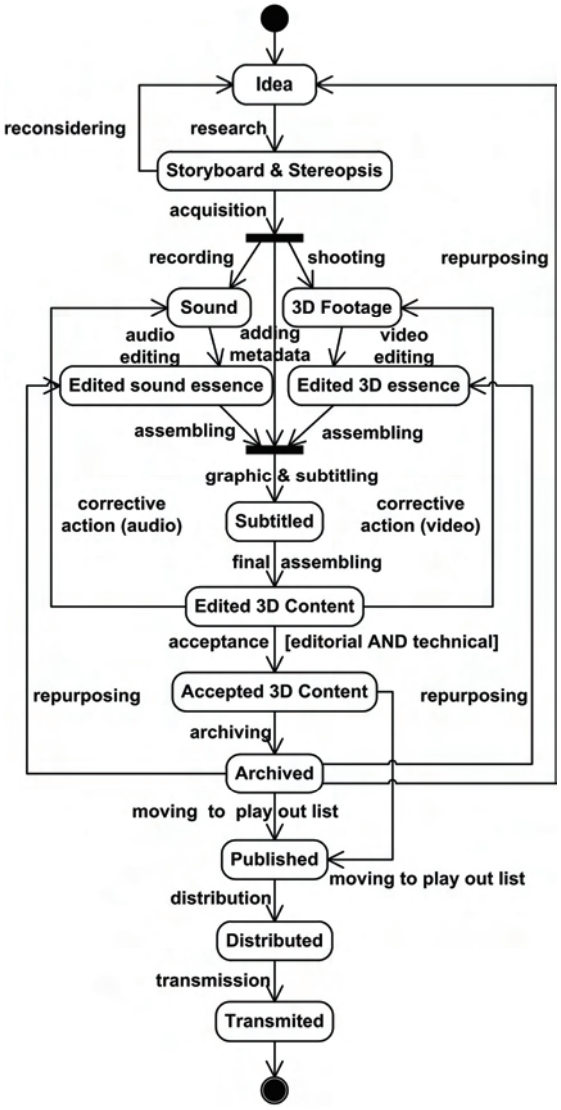

Fig.1. State Machine Diagram of 3D TV Content Life Cycle

At all points in capture there is an opportunity for metadata collection [8]. Devices that capture pictures or sound can automatically record much of the technical metadata from their own control systems—cameras that keep track of f-stop, filter wheel settings, and focal length are obvious examples. Likewise, it is becoming common for devices to capture the time of day and date and even the latitude, longitude, and altitude of their position when recording of the clip started. Those technical metadata can be very important during the postproduction phase, especially if dual camera adjustment and settings was not perfect and some minor imperfections and 3D image impairment can be corrected.

Ingest is the first stage to efficiently transfer captured 3D content to the television production infrastructure. During the ingest we take all the 3D content (both view) collected during a shoot, as well as new metadata, and transfer it into the production environment. More metadata can be generated at ingest and this can either be directly entered, for example by an operator marking technically poor sections, or regions for special processing, or it can be extracted automatically.

Simplified 3D content ingestion workflow is shown in Figure 2.

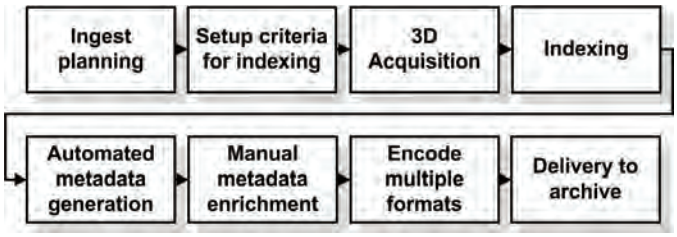

Fig. 1. 3D Ingest Workflow

Ingestion of multimedia content can be generally considered in terms of two processes, or fundamental tasks [9], [10]:

- Content acquisition and optimization, and
- Content description and referencing.

Content acquisition and optimization assume capturing the 3D audio-video essence and content compression.

Acquisition of stereoscopic content assumes transfer of two video streams, one captured for left eye and one captured for right eye. Low-budget ingesting and capturing based on two cameras usually assumes sequential transfer, i.e. ingest operator should start transfer for left and right view separately.

Typically, users of Content Management System will want to utilize high resolution master file which contains the content in professional broadcasting quality, as well as low resolution proxies (considered also as a meta-essence [8]) of same content for searching and previewing archived material or for web delivery. Ingest system should provide automatic generation of high and low resolution content representations.

Standardization of master format for 3D Home production is on-going [11] and details related to the quality of 3D video and audio as well as technical metadata important for ingest process will be suggested.

During the content optimization the key frames should be extracted and recorded. Key frames are valuable for providing asset management solutions with representative images for browsing video, as well as for making edit decisions. Key frames should be extracted and converted to JPEG images based on scene changes or predefined time intervals. Key frames can be extracted only for one eye or for both.

III. Modelling Behavioural Description of 3D Ingest Process

The main objective of a behavioural description is to visualize how the user (represented by the UML actor) will interact with and use the system. This is done by showing the actor associating with one or more use cases and, additionally, by drawing many use case diagrams.

Main actors in problem space of stereoscopic content ingest process are producer, ingest operator, 3D essence gathering crew (cameraman, sound recorder) and ingest automated system.

Use cases important for modelling in problem space of ingest process are as follows: Ingest planning, Setup criteria for indexing, Start acquisition, Automated metadata generation, Manual metadata enrichment, Indexing, Encoding multiple formats and Delivery to Archive. Use Case diagram of 3D ingest process is shown in Figure 3.

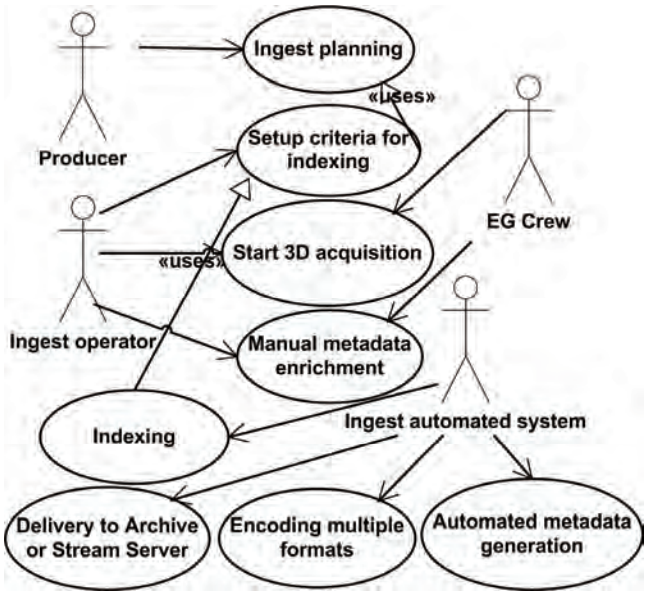

Fig. 2. Use Case Diagram of Stereoscopic Ingest Process

A. Use Case - Start Acquisition

Short Description: 3D video shoots, audio clips and other essence items, as well as attached metadata are extracted from the continuous acquisition bin, such as cameras, sound recorders, digital tape players, different editing workstations, servers etc.

Actors: Ingest operator and essence gathering crew members.

Pre-Conditions: 3D video essence is shoot for both views, audio essence is recorded, other program items are created and pre-selected.

Post-Conditions: All 3D essence materials, as well as related metadata, are ingested into production system.

Main Flow: (1) Ingest operator starts acquiring the 3D raw material or previously produced essence from cameras or other sources, separately for each view. (2) During ingest all the content collected during a shoot, recording and repurposing, as well as new metadata is taken and transferred into the production environment. (3) Ingest operator reviews what he/she has, and marks down its possible use. Use Case terminates.

B. Use Case - Indexing

Short Description: Ingest system extracts a number of key attributes from the source essence and converts them to metadata.

Actors: Ingest automated system.

Pre-Conditions: Criteria for indexing are defined and parameters are setup.

Post-Conditions: Key attributes are extracted and related metadata are produced.

Main Flow: (1) System analyses the acquired essence in accordance with parameters which are previously set-up. (2) Metadata generator module produces related metadata. Use Case terminates.

C. Use Case - Automated metadata generations

Short Description: System generates metadata from the acquired 3D essence files.

Actors: Ingest automated system.

Pre-Conditions: 3D essence material, both views, as well as files with related metadata, is ingested into production system.

Post-Conditions: Metadata are stored in database.

Main Flow: (1) System search for metadata files accompanying acquired essence. (2) System checks the metadata format and if metadata format is in accordance with systems metadata formats, metadata are stored in database. (3) If metadata format does not confirm, corrective actions must be undertaken [alternate flow A1]. (4) Steps (1) and (2) are repeated until all metadata is generated and Use Case terminates.

Alternate Flow (A1): No need for corrections. Metadata are approved and stored in database.

D. Use Case - Manual metadata enrichment

Short Description: Automatic extracted metadata can be validated. New metadata (descriptions, business information etc.) can be added.

Actors: Ingest operator, Essence gathering crew member.

Pre-Conditions: Essence material, as well as files with related metadata, including indexed and generated metadata are ingested into production system.

Post-Conditions: Stored essence, as well as related metadata.

Main Flow: (1) Ingest operator validates previously generated indexes and metadata. (2) Ingest operator add new descriptions of essence. Use Case terminates.

E. Use Case - Encoding multiple formats

Short Description: Create high-resolution master essence file and low-resolution proxy files.

Actors: Ingest automated system.

Pre-Conditions: 3D essence acquired, metadata generated and stored in database.

Post-Conditions: 3D essence encoded in hi-resolution version and stored in archive. 3D essence encoded in low-resolution version.

Main Flow: (1) In accordance with production format 3D essence is encoded in high quality broadcast format. (2) 3D essence is encoded in several different versions of low-res. files. Use Case terminates.

F. Use Case Delivery to Archive and Stream Server

Short Description: System stores 3D essence in deep archive and send low-resolution proxies to stream server.

Actors: Ingest automated system.

Pre-Conditions: 3D essence is encoded in hi-resolution version. 3D essence is encoded in low-resolution version.

Post-Conditions: 3D essence is stored in archive. 3D essence is delivered to stream server.

Main Flow: (1) System stores essence in deep archive. (2) System delivers low-resolution proxies to stream server which serves low-resolution proxies for searching, previewing, non-linear editing etc. Use Case terminates.

IV. Domain Model of 3D Ingest Process

The objective of modelling structural static representation is to represent, in one or more views, various business entities and their relationships in MOPS.

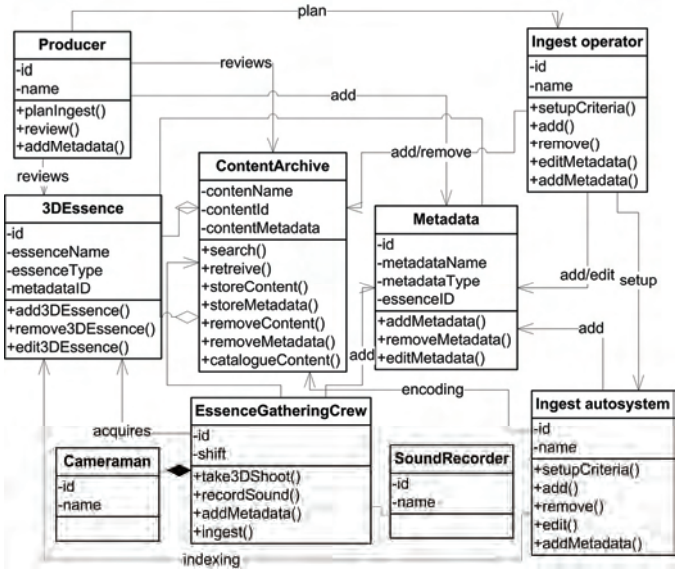

Fig. 3. Class Diagram of Stereoscopic Ingest Process

Class diagrams, by their very nature, are very strong, structural, static representations. Class diagrams show business-level classes as well as technical classes derived from the implementation language. In addition to showing the classes, class diagrams show the relationships between them. The entire description of the classes (or "entities," as they may be called in the problem space) and their relationships with each other is static. No dependency is shown in this diagram and no concept of time. Class diagram of the ingest process is shown in Figure 4.

V. Conclusions

The primary aim of this paper is to describe ingest system suitable for 3D content ingestion as one of the main areas in a 3D content production environment and to summarize the 3D essence, metadata and control flow, as well as the main processes involved in ingesting of 3D television content.

The first step in modelling of software intensive ingest system, modelling of problem space, is presented here. Use Case diagram is used as tool for behavioural description of the ingest system. Class diagram is used for description of Domain model.

The challenge for the future is to make complete business analysis of problem space using the use case, class, activity, state machine and sequence diagrams. Also, the model of solution space, as well as the model of background space should follow the current work presented in this paper.

References

[1] C. Barry, M. Lang, „A comparison of 'traditional' and multimedia information systems development practices", Information and Software Technology Vol. 45, pp 217–227, 2003.

[2] T. P. Rout, C. Sherwood, "Software Engineering Standards and the Development of Multimedia-Based Systems", Fourth IEEE International Symposium and Forum on Software Engineering Standards (ISESS '99), Curitiba, Brazil, pp.192-198, 1999.

[3] B. Unhelkar, *Verification and Validation for Quality of UML 2.0 Models.* Hoboken, New Jersey: John Wiley & Sons, Inc., 2005.

[4] M. O'Doherty, *Object-Oriented Analysis and Design: Understanding System Development with UML 2.0*., Chichester, West Sussex: John Wiley & Sons Ltd., 2005.

[5] A. Spasic, "Business Analysis of Software-Intensive Television Production: Modelling the Content Production Workflow", Serbian Journal of Management, vol. 1, no. 2, pp. 17-32, 2006.

[6] A. Spasic, M. Nesic and J. Bogdanovic, "Production of TV Multimedia Content: Modelling in Problem Space", Proceedings of the XLI International Scientific Conference on Information, Communication and Energy Systems and Technologies ICEST 2006, June 29- July 01, 2006, Sofia, Bulgaria pp.212-215, 2006.

[7] *Panasonic AG-3DA1 Integrated Twin-Lens 3D video recorder*, Panasonic Corporation, 2010, Available: http://panasonic.biz/sav/broch_bdf/AG-3DA1_e.pdf

[8] M. Cox, E. Mulder, L. Tadic,"*Descriptive metadata for television: an end-to-end introduction*", Elsevier, 2006.

[9] A. Spasic, D. Jankovic, "Framework for Software-Intensive Ingest System:One Behavioural Description", Proceedings of the ICT Innovations 2010 Conference, September 12-15, 2010, Ohrid, Macedonia, pp. 191-200, 2010.

[10] A. Spasic, D. Jankovic, "Modelling Software-Intensive Ingest System: Behavioural Description and Domain Model", Proceedings of 18th Telecommunications forum TELFOR 2010, Serbia, Belgrade, November 23-25, pp. 958-961, 2010.

[11] W. Zou, „Developing End-to-End Standards for 3D TV to the Home", SMTPE Motion Imaging Journal, October 2010, pp 32-38, 2010.

Calculation of Dyadic Convolution Using Graphics Processing Units and OpenCL

Dušan B. Gajić[1] and Radomir S. Stanković[1]

***Abstract* – Convolution is an important operation in many areas of science and engineering, including systems theory, signal processing, pattern recognition, switching theory, and logic design. In particular, when dealing with binary encoded signals and systems, the dyadic convolution is used, i.e., the convolution on finite dyadic groups consisting of binary *n*-tuples equipped with the addition modulo 2. Fast computation algorithms are essential for practical applicability of the dyadic convolution and algorithms based on it. These algorithms are defined by the application of the convolution theorem in the Walsh (Fourier) domain and then exploiting the Fast Fourier Transform (FFT).**

In this paper, we present a method for accelerating the computation of the dyadic convolution through a parallel implementation of the related algorithm on a Graphics Processing Unit (GPU). The architecture of the GPU is massively parallel, fully programmable, and it offers tremendous computational power and memory bandwidth. In order to be efficiently implemented, the fast algorithm for the dyadic convolution has to be suitably reformulated and adapted to the GPU resources. We present a solution to this problem using the Open Computing Language (OpenCL). Further, we consider several issues concerning the efficient mapping of the algorithm to the GPU architecture. Performance of the proposed implementation is compared with the referent C/C++ implementation processed on the Central Processing Unit (CPU). Experimental results show that significant speedups are achieved by the application of the proposed GPU calculation method.

***Keywords* – Dyadic convolution, Fast Walsh transform, GPU parallel programming, OpenCL.**

I. INTRODUCTION

Convolution is a mathematical operation that expresses relationships between values of two signals (modeled by functions f and g) in points at a fixed distance. The convolution $C = f * g$ of two functions f and g is a function that resembles any one of them, modified by the other one. The convolution operation has an important place in efficient solutions to many problems in engineering and mathematics which are of both practical and theoretical importance [8].

When the finite dyadic group is used as an underlying algebraic structure on which the convolution operation is defined, we use the term dyadic (or logical or XOR) convolution (see Section 3 and also [4, 8, 9, 12]). Dyadic convolution coefficients can, in principle, be calculated by the brute force application of the equation that defines the operation (see Eq. (1) in Section 3). However, this method has exponential complexity in the number of inputs and is unfeasible in practice for large signals. Therefore, algorithms for the fast computation of convolution are derived by using the convolution theorem [8] on the corresponding algebraic structure.

In this paper, we present a technique for an accelerated calculation of the dyadic convolution through a parallel implementation of the fast algorithm derived from the convolution theorem. Due to this theorem, computation of the dyadic convolution converts into performing two direct and an inverse Walsh transform, which can be done by the corresponding FFT-like algorithms, i.e., the Fast Walsh Transform – FWT [4, 5, 8].

The proposed implementation is developed using the Open Computing Language (OpenCL) and processed in a highly parallel manner on a GPU. Experimental results and comparisons with the classical implementation confirm that the proposed method leads to significant computational speedups.

The rest of this paper is organized as follows. After a discussion of the related work in Section 2, in Section 3 we give a short introduction to the dyadic convolution and the fast algorithm for its calculation. Section 4 is devoted to the mapping of the fast algorithm to the GPU architecture and the design of the corresponding OpenCL implementation. In Section 5, we describe the experimental environment that we used to evaluate the method, and present the experimental results that we recorded. Section 6 offers some conclusions drawn from the presented research.

II. RELATED WORK

The fast algorithm for the dyadic convolution is based on the application of the Walsh transform which is the Fourier transform on finite dyadic groups. The implementation of various Fast Fourier Transforms (FFTs) on different technological platforms is a widely considered topic, see for instance [4, 5, 6, 7] and references therein. The calculation of dyadic convolution on classical Central Processing Units (CPUs) through the application of the convolution theorem, both on vectors and decision diagrams, is presented in [9]. Reference [4] presents an application of the dyadic convolution for the fast multiplication of hyper-complex numbers.

In recent years, the technique of performing General Purpose computations on the GPU (GPGPU) has proven to be a suitable approach in solving many computationally-intensive tasks [2, 3, 6, 7, 10]. In particular, the GPU-accelerated calculation of FFT algorithms using CUDA is

[1]Dušan B. Gajić and Radomir S. Stanković are with the University of Niš, Faculty of Electronic Engineering, Aleksandra Medvedeva 14, 18000 Niš, Serbia, E-mails: dusan.gajic@elfak.ni.ac.rs, radomir.stankovic@gmail.com.

described in [7, 11]. Reference [6] presents an OpenCL implementation of the FWT that uses the GPU hardware and leads to significant speedups over traditional CPU processing.

However, in our best knowledge, there are no papers discussing neither CUDA nor OpenCL GPU implementations of the fast algorithm for the calculation of dyadic convolution based on the convolution theorem. This fact, together with the intended applications of the dyadic convolution for particular problems in logic design [8], was the motivation for the research on the dyadic convolution calculation that is presented in this paper.

III. DYADIC CONVOLUTION

A. Dyadic convolution

The finite dyadic group of order n is defined as $C_2^n = \underset{i-1}{\overset{n}{\times}} C_2$, where $C_2 = (\{0,1\}, \oplus)$, $\oplus$ stands for the addition modulo 2, and $\times$ is the direct (Cartesian) product.

For two functions f, $g : C_2^n \to \mathbb{R}$, where $\mathbb{R}$ is the field of rational numbers, the dyadic convolution, at a distance $\tau = 0,1,...,2^{n-1}$, is defined as:

$$\mathrm{C}_{f*g}(\tau) = f * g = \sum_{x=0}^{2^n-1} f(x) \cdot g(x \oplus \tau). \quad (1)$$

In binary notation, x is $x = (x_1, x_2, ..., x_n)$, and τ is $\tau = (\tau_1, \tau_2, ..., \tau_n)$, where $x_i, \tau_i \in \{0,1\}$.

B. Walsh transform and fast Walsh transform

The Walsh transform is defined by the Walsh matrix:

$$\mathbf{W}(n) = \overset{n}{\underset{i=1}{\otimes}} \mathbf{W}(1), \quad (2)$$

where $\otimes$ denotes the Kronecker product and

$$\mathbf{W}(1) = \begin{bmatrix} 1 & 1 \\ 1 & -1 \end{bmatrix} \quad (3)$$

is the basic Walsh matrix. Since $\mathbf{W}(n)$ is a self-inverse matrix up to the scalar 2^{-n}, the inverse Walsh transform is defined as:

$$\mathbf{W}^{-1}(n) = 2^{-n}\mathbf{W}(n). \quad (4)$$

It follows that both the direct and the inverse Walsh transforms can be computed using the same algorithm.

The Walsh spectrum $\mathbf{S}_{f,h} = [S_{f,h}(0), S_{f,h}(1), \ldots, S_{f,h}(2^n\text{-}1)]^T$ of a function $f : C_2^n \to \mathbb{R}$, specified by the function vector $\mathbf{F} = [f(0), f(1), \ldots, f(2^n\text{-}1)]^T$, is defined as:

$$\mathbf{S}_{f,h} = \mathbf{W}(n)\mathbf{F}. \quad (5)$$

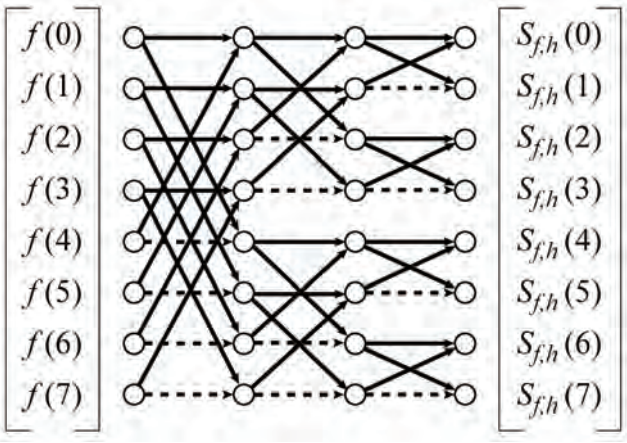

Fig. 1. Flow graph of the Cooley-Tukey FWT algorithm for $N = 8$ [6].

The spectral coefficients appear in natural (Hadamard) ordering, which is indicated by the index h in $\mathbf{S}_{f,h}$. The function f is reconstructed from the Walsh spectrum as:

$$\mathbf{F} = 2^{-n}\mathbf{W}^{-1}(n)\mathbf{S}_{f,h}, \quad (6)$$

and (5) and (6) form the Walsh transform pair.

The computation of the Walsh transform based on its definition (Eqs. (2) and (5)) is inefficient, since it expresses the $O(N^2)$ time complexity, where $N = 2^n$ is the size of the input vector. Fortunately, more efficient algorithms based on the FWT [4, 8], with the time complexity of $O(N\log N)$, exist.

The fast Walsh transform (FWT) can be defined using the following factorization:

$$\mathbf{W}(n) = \prod_{i=1}^{n} \mathbf{C}_{w_i}(n)_i \quad (7)$$

where

$$\mathbf{C}_{w_i}(n) = \overset{n}{\underset{j=1}{\otimes}} \mathbf{C}_{w_i}^j(1), \quad \mathbf{C}_{w_i}^j(1) = \begin{cases} \mathbf{W}(1), i = j, \\ \mathbf{I}(1), i \neq j. \end{cases} \quad (8)$$

The matrix $\mathbf{C}_{w_i}(n)$ defines the partial Walsh transform and corresponds to the i-th step of the FWT. The flow graph of the corresponding algorithm for $N = 8$ is given in Figure 1.

C. Convolution theorem

In the classical Fourier analysis, the convolution theorem states that the Fourier transform [4, 5, 8] of the convolution function $C = f * g$ is the componentwise product of Fourier transforms of f and g. In other words, a rather complex convolution operation in the original domain converts into a simple componentwise multiplication in the spectral domain.

In abstract harmonic analysis, the convolution theorem can be extended to the Fourier transform defined over locally compact Abelian groups [8]. For functions on the finite dyadic group C_2^n, the calculation of the dyadic convolution through the application of the convolution theorem is done as follows:

$$\mathbf{C}_{f*g} = 2^{-n}\mathbf{W}^{-1}(n)((\mathbf{W}(n)\mathbf{F})(\mathbf{W}(n)\mathbf{G})) \quad (9)$$

Algorithm 1 FAST CALCULATION OF DYADIC CONVOLUTION $C = f * g$

1 Allocate buffers *buffer1* and *buffer2* in the global memory of the GPU device.
2 Transfer input vectors *f* and *g* from the host CPU memory to GPU buffers *buffer1* and *buffer2*, respectively.
3 Perform the Walsh transform on vectors stored in *buffer1* and *buffer2* using the following in-place OpenCL implementation of the Cooley-Tukey algorithm for the FWT:
  a. For each step of the FWT, from $step \leftarrow 0$ to $step \leftarrow (\log_2 N) - 1$, call the OpenCL kernel for the FWT with input parameters being the appropriate buffer in the GPU's global memory and the value of the current step 2^{step}. The kernel is executed by *N/2* threads in parallel on the GPU. Each thread reads two elements, determined by (10) and (11), from the buffer, performs the operations defined by the Walsh matrix $\mathbf{W}(1)$ and stores back the results in the same locations.
4 After computing the FWT of both vectors, execute the OpenCL kernel for the componentwise multiplication of the two Walsh spectra with *N* threads executed in parallel. The resulting vector is stored in *buffer1*.
5 Perform the inverse FWT on *buffer1* using the same kernel as for the FWT.
6 Scale the contents of *buffer1* with the factor 2^{-n} using the OpenCL kernel with *N* threads executed in parallel.
7 Transfer the contents of the GPU buffer *buffer1*, which holds the resulting dyadic convolution coefficients, back to the host CPU memory.

Fig. 2. Algorithm for the fast calculation of dyadic convolution on the GPU.

where $\mathbf{W}$ is the Walsh transform, $\mathbf{W}^{-1}$ is the inverse Walsh transform, and $\mathbf{F}$ and $\mathbf{G}$ are function vectors for *f* and *g*, respectively.

Therefore, an efficient algorithm for the computation of the dyadic convolution can be developed in terms of the FWT.

IV. Mapping of the Algorithm and Implementation Details

The application of the convolution theorem, expressed in Eq. (9), leads to the following three-stage fast dyadic convolution calculation algorithm (shown in Figure 2):

Step 1. Perform the FWT on *f* and *g* and compute their Walsh spectra $\mathbf{S}_f$ and $\mathbf{S}_g$.
Step 2. Perform the componentwise multiplication of the two spectra $\mathbf{S}_f$ and $\mathbf{S}_g$.
Step 3. Perform the inverse FWT over $\mathbf{S}_f \cdot \mathbf{S}_g$ to obtain $\mathbf{C}_{f*g}$.

Since multiplication is done very fast on modern CPUs, the key issue in creating an efficient implementation of the above algorithm is the development of the fast implementation of the FWT. In order to perform the algorithm steps with the FWT and inverse FWT, we developed a kernel containing an OpenCL in-place implementation of the Cooley-Tukey algorithm for the FWT [6, 8]. As in all FFT-like algorithms, steps of the algorithm are executed sequentially and parallelism is used only within the steps. Within each of the steps, *N*/2 threads are executed in parallel. This large number of threads helps in hiding the data access latency to the GPU global memory [2, 3]. Each thread reads two elements from the GPU buffer with indices *op1* and *op2* calculated as:

$$op1 \leftarrow thread\_id \bmod step + 2 \times step \times (thread\_id / step), \quad (10)$$

$$op2 \leftarrow op1 + step. \quad (11)$$

Parameters *thread_id* and *step* are the global identifier of the thread and the identifier of the current step of the algorithm, respectively. All threads execute the elementary butterfly operation defined by the basic Walsh transform matrix $\mathbf{W}(1)$ and store the results back in the same locations in the GPU memory, as in other implementations of the in-place FWT algorithms.

The componentwise multiplication of vectors is also performed by the corresponding OpenCL kernel which is executed by *N* threads in parallel, with each thread multiplying the two corresponding elements of the input vectors.

After the multiplication, the inverse FWT is performed with the same kernel that is used for the direct transform, followed by scaling with 2^{-n}. The scaling is also performed in parallel through the execution of the corresponding OpenCL kernel.

Before executing any of the kernels, both input vectors are transferred from the main memory to the GPU global memory. After the calculations, the resulting convolution coefficients are transferred back to the host. These memory operations take a significant share of the total GPU running times as reported in Section 5.

V. Experimental Environment and Results

The test platform used to perform the experiments is an HP Pavilion dv7-4060us notebook computer (see Table I). The OpenCL kernels are developed using MS Visual Studio 2010 Ultimate and ATI APP SDK 2.3 [1]. ATI Stream Profiler 2.1 is used for GPU kernel performance analysis, in accordance with instructions provided in [2]. The referent C/C++ source code is compiled for the x64 platform with the maximum level of performance-oriented optimizations.

TABLE I TEST MACHINE SPECIFICATION

CPU	AMD Phenom II N830 triple-core (2.1GHz)
RAM	4GB DDR3
OS	Windows 7 (64-bit)
GPU	ATI Mobility Radeon 5650
- engine speed	650 MHz
- global memory	1 GB DDR3 800 MHz
- compute units	5
- processing elements	400
- price	~ 100$

TABLE II COMPUTATION TIMES FOR THE REFERENT CPU AND THE PROPOSED GPU IMPLEMENTATION

N	Time [ms]		
	CPU	GPU	
		Computation time	Memory time
16	0	0	0
256	0	0	1
1 024	0	1	1
65 536	15	3	2
262 144	53	6	3
1 048 576	108	24	9
8 388 608	1201	220	45
16 777 216	2512	469	86
33 554 432	5002	998	147

N – Number of elements in the input vector
CPU - C/C++ implementation, processed on the CPU
GPU - OpenCL C implementation, processed on the GPU

As in all FFT implementations over vectors, the resulting performance is independent of the function values. Therefore, we perform the experiments using randomly generated binary vectors. We present the results for the GPU calculation time and, also, the time for transfer of data to/from the GPU which offers a more complete perspective to the reader. In order to explore the performance of the proposed method, we performed a comparative analysis with respect to the classical C/C++ implementation of the same algorithm processed on the CPU.

The results of the experiments are presented in Table II and Figure 3. The OpenCL implementation processed on an inexpensive commodity GPU (see Table I) clearly outperforms the referent CPU implementation, by a factor of up to 5.5× when only calculation times are compared, and by a factor of up to 4.5× when total times, including memory transfers to/from GPU, are taken into account. The processing of the very same kernels on a more powerful GPU would directly lead to much larger speedups, which would not be the case if a more powerful CPU was used for processing the referent C/C++ implementation [3, 6].

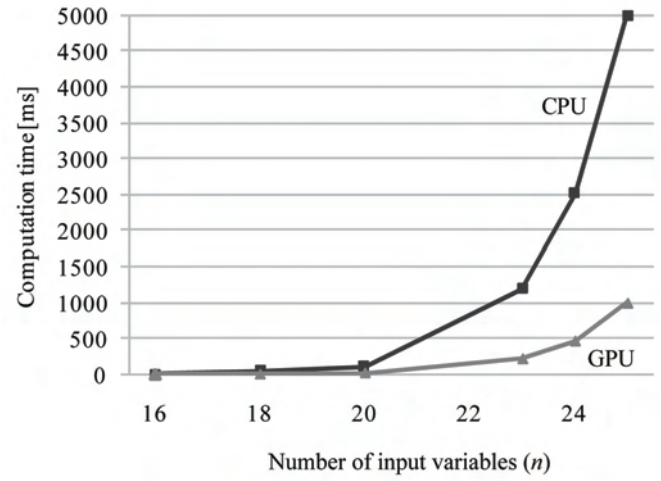

Fig. 3. Computation times for the referent (CPU) and the proposed (GPU) implementation.

VI. CONCLUSIONS

In this paper, we proposed a method for the fast calculation of dyadic convolution through an OpenCL parallel algorithm implementation which is processed on the GPU. We presented a comparative performance analysis of the proposed solution and the referent C/C++ implementation processed on a multicore CPU. A significant reduction of the calculation time is obtained due to an appropriate modification of the corresponding fast algorithm for the GPU implementation. Notice that, if $f(x) = g(x)$, then the dyadic convolution becomes the cross-correlation of a function with itself and produces coefficients which are referred to as the autocorrelation coefficients [8]. It follows that the same OpenCL implementation that is proposed in this paper can also be used for the fast calculation of both the dyadic convolution and the autocorrelation. The proposed method could, therefore, extend the area of applications of these operations to problems where algorithm running time is an essential and, often, limiting factor, since it allows time-efficient computations in systems theory, signal processing, pattern recognition, switching theory, and logic design.

REFERENCES

[1] *AMD Accelerated Parallel Processing SDK*, http://developer.amd.com/gpu/amdappsdk, AMD Inc., website last visited on 10/04/2011.

[2] *ATI OpenCL Programming Guide*, AMD Inc., 2010.

[3] T. M. Aamodt, "Architecting graphics processors for non-graphics compute acceleration," in *Proc. of the 2009 IEEE Pacific Rim Conf. on Communications, Computers and Signal Processing*, Victoria, BC, Canada, August 23-26, 2009.

[4] J. Arndt, *Matters Computational: Ideas, Algorithms, Source Code*, Springer, 2010.

[5] J. W. Cooley and J. W. Tukey, "An algorithm for the machine calculation of complex Fourier series", *Mathematics of Computation*, No. 90, 1965, 297-301.

[6] D. B. Gajić and R. S. Stanković, "Computing fast spectral transforms on graphics processing units using OpenCL," in *Proc. of the Reed-Muller 2011 Workshop*, Tuusula, Finland, May 25-26, 2011, 27-36.

[7] N. K. Govindaraju et al., "High performance discrete Fourier transforms on graphics processors," in *Proc. of the 2008 ACM/IEEE Conf. on Supercomputing*, IEEE Press, Austin, Texas, USA, November 15-21, 2008.

[8] M. G. Karpovsky, R. S. Stanković, and J. T. Astola, *Spectral Logic and Its Applications for the Design of Digital Devices*, Wiley-Interscience, 2008.

[9] M. M. Radmanović, "Calculation of dyadic convolution through binary decision diagrams," *Facta Universitatis: Series: Automatic Control and Robotics*, Vol. 8, No. 1, 2009, 89 – 97.

[10] *NVidia CUDA: Compute Unified Device Architecture*, http://developer.nvidia.com/object/gpucomputing.html, NVIDIA Corp., website last visited on 30/03/2011.

[11] *NVidia CUDA CUFFT Library*, NVIDIA Corp., 2007.

[12] R. S. Stanković, M. Bhattacharaya, and J. T. Astola, "Calculation of dyadic autocorrelation through decision diagrams," in *Proc. of the European Conference on Circuit Theory and Design*, August 2001, 337-340.

[13] *The OpenCL Specification 1.1*, Khronos OpenCL Working Group, 2010.

One Approach for Overlaying with Polygon Meshes

Emiliyan Petkov[1]

***Abstract* – Covering of three-dimensional objects is a part of the modeling process and building virtual three-dimensional scenes in the graphics systems. This research examines a case in which faces of a freely located 3D object must be overlaid with a 3D object as well. The last one should be duplicated and arranged over the faces.**

***Keywords* – Computer, Graphics, Systems, Modelling, Overlay, Polygon, Mesh.**

I. Introduction

From almost the very inception of computer graphics techniques for covering two-dimensional (2D) and three-dimensional (3D) objects in computer generated virtual spaces with bitmap images and textures are developed [1]. This is a good and relatively simple way to achieve greater realism in the output images. More over, covering with textures achieves the effect of three-dimensional relief on the otherwise flat faces of the objects (Fig. 1). This significantly reduces the number of vertices which leads to faster rendering [4]. So, when we look for fast rendering and a small volume of information in the representation of the models in the graphics systems the best approach is to cover with textures.

Fig. 1. A 2D texture that is placed over a 3D tore.

However, there are tasks and applications which seek maximum realism in computer synthesized images. This means that each object must be represented by three-dimensional model in the scene [2, 4]. Such a high level of realism is sought in fields such as architecture design, film industry, simulations, virtual reality, etc. When creating images comply with this requirement the rendering of the scenes is not needed to be in real time, i.e. rendering of one frame can be carried out within a few minutes and if necessary even hours [6]. The problem here is the volume of information that must be processed and stored. But when the applied field does not require this to be done in real time then this volume can be as much as the computer system allows. This research examines cases that require maximum realism – in which "just an effect" is not enough. These are the cases in which the time for rendering and the volume of information of the 3D objects in the scene are not critical.

There are several types of representation of 3D objects in computer graphics and graphics systems [1, 4, 6]. The most popular are: polygon mesh, patch, NURBS, Bezier, etc. And the most natural one is polygon mesh. Objects of all other types uniquely are converted to polygon mesh as well. Under polygon mesh or mesh we understand: collection of vertices, edges and faces that defines the shape of a polyhedral object in 3D computer graphics and solid modelling [4].

This report presents a solution of a problem which was given by a business company called Monblan Design Ltd., Bulgaria. This problem concerns overlaying faces of 3D objects with polygon meshes in graphics systems. For the last few years the problem stands before many architectures, designers, animators, etc. who work on computer graphics software.

The problem could be defined as follows: A mesh is given that is freely located in space (Fig. 2). We may call it *base*. A face or a group of faces that belong to the base have to be overlaid with another three-dimensional object. The last one must be polygon mesh as well and we may call it *target*. The target must be duplicated and arranged in two dimensions orthogonal each other over the face. We may call these new objects *instances*. If a set of faces are selected they must lie in one plane and we may call them *polygon*.

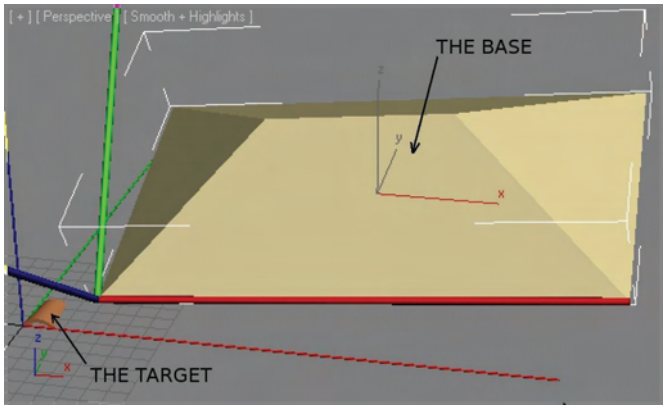

Fig. 2. A base and a target in 3D space.

If a face or a group of faces which belong to a base in 3D space and a coordinate system is fixed in it are collinear to one of the coordinate planes *Oxy*, *Oxz* or *Oyz*, then the overlaying can be accomplished only with translations along

[1]Emiliyan Petkov is with the Faculty of Mathematics and Informatics, St. Cyril and St. Methodius University, 2 Theodosii Turnovski Str., 5000 Veliko Turnovo, Bulgaria, e-mail: EPetkov@abv.bg.

the *X* axis, *Y* axis or *Z* axis. This could be easily realized in any graphics system. But these are only individual cases. There is a problem when the base is freely located in space. There are no tools in the graphics applications that can solve this problem.

II. THE SOLUTION

A. The main idea for solving the problem

Creation and setting up the base in a 3D space and creation of the target and applying transformations over it, as well as defining how the target will be positioned over the polygon, must be done in a fixed coordinate space. In computer graphics and graphics systems an orthonormal coordinate system is chosen generally [3, 5, 7].

Overlaying of the base (Fig. 2) with the target must be done in two directions. Let mark them with $\vec{u}$ and $\vec{v}$. In Fig. 2 $\vec{u}$ and $\vec{v}$ are drawn as red and green respectively. These directions could be determined as follows: one vertex from the polygon is determined as origin, an edge which comes from it determines $\vec{u}$ direction, and $\vec{v}$ is determined as an orthogonal vector to $\vec{u}$, where $\vec{u}$ and $\vec{v}$ belong to the plane that is defined by the faces (polygon). Then we could define the values of the distances between the duplicated instances of the target in both $\vec{u}$ and $\vec{v}$ directions.

There is one more question: How to define the position and orientation of the target over the polygon that we want to overlay? The most intuitive way (according to the author) is to locate and orientate the target in relation to the *Oxy* plane near to the origin. In Fig. 2 the target which is placed near the origin could be seen. In accordance to how the target is put to the origin in *Oxy* plane it will be located and arranged over the polygon. But this raises the following question: What is the transformation that can do this?

The idea is to find first the transformation that transforms every point from the polygon in *Oxy* plane where the target lies. After this we can take the reverse transformation which can transport the target over the polygon.

B. Mathematical formulation of the problem

Let an orthonormal coordinate system $K=\left\{O,\vec{e_1},\vec{e_2},\vec{e_3}\right\}$ be fixed in space (Fig. 3). The group of faces which have to be overlaid must lie in one plane. Let this plane be β. Let all vertexes that belong to the polygon be $A_i\left(x_i,y_i,z_i\right)$, $i=0,..,n$, $n\geq 2$ (every face is composed by three vertexes). Let mark $\sphericalangle\left(\left|\overrightarrow{A_0A_1}\right|\left|\overrightarrow{A_0A_n}\right|\right)$ with α. For β we have:

$$\beta: Ax+By+Cz+D=0 \tag{1}$$

$$\overrightarrow{A_0A_1}\times\overrightarrow{A_0A_n}=\vec{N}=\left(A,B,C\right) \tag{2}$$

$$\vec{n}=\frac{\vec{N}}{-sign(D).\left|\vec{N}\right|}=\left(n_1,n_2,n_3\right) \tag{3}$$

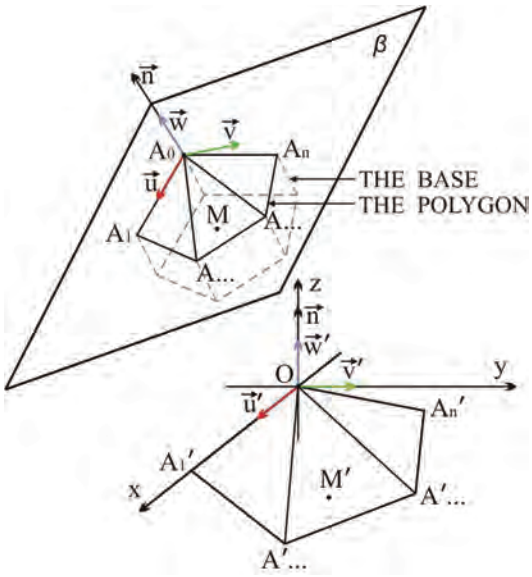

Fig. 3. The selected faces (polygon) that lie in β and their transformation by φ in *Oxy*.

We are seeking for a transformation of uniformity φ which is determined as follows:

$$\begin{aligned}
&\beta \xrightarrow{\varphi} Oxy\\
&A_0 \xrightarrow{\varphi} O\left(0,0,0\right)\\
&A_1 \xrightarrow{\varphi} A_1'\left(x_1',0,0\right)\\
&A_n \xrightarrow{\varphi} A_n'\left(x_n',y_n',0\right)\\
&N\left(n_1,n_2,n_3\right) \xrightarrow{\varphi} N'\left(0,0,1\right)
\end{aligned} \tag{4}$$

where:

$$x_1'=\left|\overrightarrow{A_0A_1}\right|=\sqrt{\left(x_1-x_0\right)^2+\left(y_1-y_0\right)^2+\left(z_1-z_0\right)^2}$$

$$\sphericalangle\left(\left|\overrightarrow{A_0A_1'}\right|\left|\overrightarrow{A_0A_n'}\right|\right)=\alpha$$

$$\left|\overrightarrow{OA_n'}\right|=\left|\overrightarrow{A_0A_n}\right| \tag{5}$$

To find φ, A_1' and A_n' have to be uniquely determined. But Eqs. (4) and (5) shows that x_1' and α are known. In the conditions that were set in Eqs. (4) two parameters are unknown. These are the coordinates of A_n': x_n' and y_n'. For α we have:

$$\cos\alpha=\frac{\overrightarrow{A_0A_1}.\overrightarrow{A_0A_n}}{\left|\overrightarrow{A_0A_1}\right|.\left|\overrightarrow{A_0A_n}\right|}=b \text{ – known,}$$

$$\alpha=\arccos\frac{\overrightarrow{A_0A_1}.\overrightarrow{A_0A_n}}{\left|\overrightarrow{A_0A_1}\right|.\left|\overrightarrow{A_0A_n}\right|}. \tag{6}$$

Considering the Eqs (6) and the conditions from Eqs (4) a system of equations is set:

$$\begin{cases} \cos\alpha = \dfrac{\overrightarrow{A_0A_1'}.\overrightarrow{A_0A_n'}}{\left|\overrightarrow{A_0A_1'}\right|.\left|\overrightarrow{A_0A_n'}\right|} = b \\ \sqrt{x_n'^2 + y_n'^2} = \left|\overrightarrow{A_0A_n}\right| \end{cases} \quad (7)$$

After elementary transformations over the Eqs. (7) the result is:

$$\begin{cases} x_n' = \left|\overrightarrow{A_0A_n}\right|.\cos\alpha \\ y_n' = \pm\left|A_0A_n\right|.\sin\alpha \end{cases} \quad (8)$$

C. Solution of the problem

Every transformation in space could be presented in matrix mode. Therefore, we are seeking of a transformation matrix A and a vector of translation $\vec{p}$ such that

$$\varphi: \begin{pmatrix} x' \\ y' \\ z' \end{pmatrix} = \underbrace{\begin{pmatrix} a_{11} & a_{12} & a_{13} \\ a_{21} & a_{22} & a_{23} \\ a_{31} & a_{32} & a_{33} \end{pmatrix}}_{A}.\begin{pmatrix} x \\ y \\ z \end{pmatrix} + \underbrace{\begin{pmatrix} p_1 \\ p_2 \\ p_3 \end{pmatrix}}_{\vec{p}} \quad (9)$$

and the conditions from Eqs. (4) to be performed. So, we are receiving the following system of four equations:

$$\begin{pmatrix} 0 \\ 0 \\ 0 \end{pmatrix} = A.\begin{pmatrix} x_0 \\ y_0 \\ z_0 \end{pmatrix} + \vec{p} \quad (10)$$

$$\begin{pmatrix} x_1' \\ 0 \\ 0 \end{pmatrix} = A.\begin{pmatrix} x_1 \\ y_1 \\ z_1 \end{pmatrix} + \vec{p} \quad (11)$$

$$\begin{pmatrix} x_n' \\ y_n' \\ 0 \end{pmatrix} = A.\begin{pmatrix} x_n \\ y_n \\ z_n \end{pmatrix} + \vec{p} \quad (12)$$

$$\begin{pmatrix} 0 \\ 0 \\ 1 \end{pmatrix} = A.\begin{pmatrix} n_1 \\ n_2 \\ n_3 \end{pmatrix} + \vec{p} \quad (13)$$

Considering Eqs. (10), (11), (12) and (13) as a system an elementary transformations are made and the result is:

$$\underbrace{\begin{pmatrix} x_1' & x_n' & 0 \\ 0 & y_n' & 0 \\ 0 & 0 & 1 \end{pmatrix}}_{C} = A.\underbrace{\begin{pmatrix} x_1 - x_0 & x_n - x_0 & n_1 - x_0 \\ y_1 - y_0 & y_n - y_0 & n_2 - y_0 \\ z_1 - z_0 & z_n - z_0 & n_3 - z_0 \end{pmatrix}}_{B} \quad (14)$$

Matrixes B and C are known. We are seeking for matrix A and a vector $\vec{p}$. The matrix is found as follows:

$$A.B = C \quad \Leftrightarrow \quad A = C.B^{-1} \quad (15)$$

The translation vector $\vec{p}$ is found by replacing A in Eqs. (10):

$$\vec{p} = -A.\begin{pmatrix} x_0 \\ y_0 \\ z_0 \end{pmatrix} \quad (16)$$

Therefore, the transformation of uniformity φ is already known. Now we are ready to find the reverse transformation of φ. This will be φ^{-1} that is determined as follows:

$$\varphi^{-1}: \begin{pmatrix} m_1 \\ m_2 \\ m_3 \end{pmatrix} = A^{-1}.\begin{pmatrix} m_1' \\ m_2' \\ m_3' \end{pmatrix} - A^{-1}.\begin{pmatrix} p_1 \\ p_2 \\ p_3 \end{pmatrix} \quad (17)$$

For every point $M'\left(m_1', m_2', 0\right)$ that belongs to *Oxy* we have a transformation φ^{-1} which transforms M' (Fig. 3) in point $M\left(m_1, m_2, m_3\right)$ which belongs to plane β and φ^{-1} satisfies the conditions in Eqs. (4). So, we have:

$$A_i \xrightarrow{\varphi} A_i'\left(x_i', y_i', 0\right), \quad i = 0,..,n, \quad n \geq 2 \quad (18)$$

Transformation φ is a transformation of uniformity, therefore, we have the polygon in Oxy (Fig. 4a). The polygon has dimensions along *x* and *y* axis that define a rectangular area. Le this area be determined by $x_{\min}$, $x_{\max}$, $y_{\min}$ and $y_{\max}$ that are determined as follows:

$$\begin{aligned} x_{\min} &= \min\left\{x_i, i = 0,..,n\right\} \\ x_{\max} &= \max\left\{x_i, i = 0,..,n\right\} \\ y_{\min} &= \min\left\{y_i, i = 0,..,n\right\} \\ y_{\max} &= \max\left\{y_i, i = 0,..,n\right\} \end{aligned} \quad (19)$$

a)

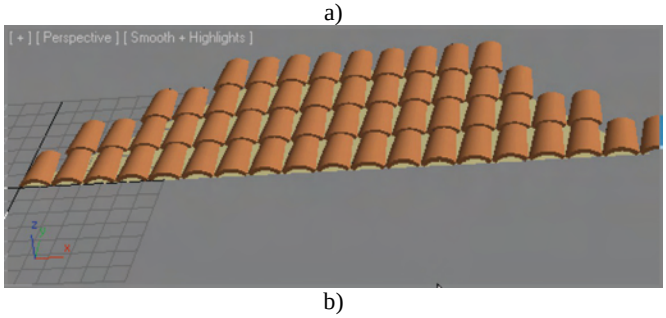

b)

Fig. 4 – a) the polygon is transformed by φ;
b) the polygon is overlaid with the instances.

Now the target could be duplicated and arranged in this rectangular area along both *x* and *y* axis. The instances that do

not belong to the polygon could be removed (Fig. 5b). Thus we have a overlaying of the polygon but it lies in Oxy. Using transformation φ^{-1} the polygon together with the instances is transformed to its primary position in space. The result could be seen in Fig. 5.

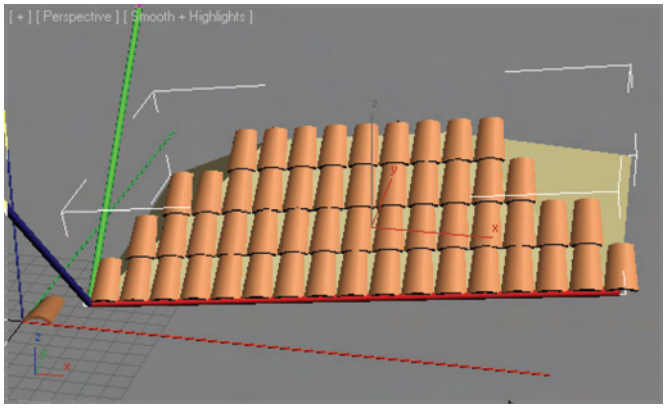

Fig. 5. The target has been duplicated and arranged over the polygon.

After we have the result a Boolean operation "cutting" could be applied over the instances. They may be cut with the outline of the polygon. This is shown in Fig. 6.

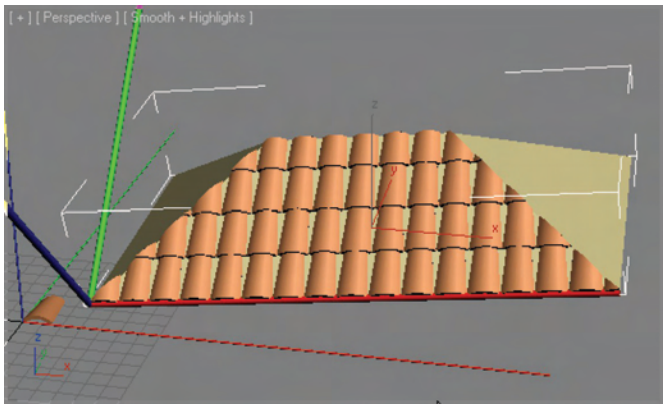

Fig. 6 – The instances of the target are cut.

III. Conclusion

In this paper an approach for overlaying faces of 3D objects with polygon meshes in computer graphics and graphics systems has been presented. It is well mathematical grounded and could be applied in any graphics system as additional software tool.

Figures 2, 4, 5 and 6 have been generated in Autodesk 3ds Max using Overlay software module (plug-in) which has been developed using the presented here solution. Overlay plug-in overview and trial version are available at http://www.creativecrash.com.

Acknowledgement

This paper is financed by project: Creative Development Support of Doctoral Students, Post-Doctoral and Young Researches in the Field of Computer Science, BG 051PO001-3.3.04/13, European Social Fund 2007–2013, Operational Program "Human Resources Development".

References

[1] Buss, S. R. 3-D Computer Graphics - A Mathematical Introduction with OpenGL. Cambridge University Press, UK, 2003.

[2] Gallier, J. Curves and Surfaces in Geometric modelling – theory and algorithms. Morgan Kaufmann Publishers, USA, 2000.

[3] Lowther, J. L., Ching-Kuang Shene. Computing with Geometry as an Undergraduate Course: A Three-Year Experience. ACM: SIGCSE 2001 2/01 Charlotte, NC, USA, 2001.

[4] Hill F. S., Stephen M. Kelley. Computer graphics using OpenGL. Pearson International edition, Prentice Hall, NJ 07458, USA, 2007.

[5] Rogers, D. F., J. A. Adams. Mathematical elements for computer graphics, second edition. McGraw-Hill, USA, 1990.

[6] Wang, H., J. Kearney, K. Atkinson. Curve and Surface Design. Saint-Malo 2002, Nashboro Press, Brentwood, TN, 2002, pp. 387–396.

[7] Weisstein, W. Eric. MathWorld – Web comprehensive and interactive mathematics encyclopedia. http://mathworld.wolfram.com.

AutoLISP Routines for 3D Modelling Of Railway

Luka Lazarević[1], Zdenka Popović[2], Dejan Gavran[3] and Leposava Puzavac[4]

***Abstract* – Computer aided design (CAD) is used in engineering, graphic, architectural and product design. CAD helps designers prepare drawings, specifications, parts lists and other design-related elements using special graphics and calculations intensive computer programs. AutoCAD® is leader in Serbia in 3D CAD design, drafting, modelling and drawing. It is also important that AutoCAD® has open architecture which can be customized and extended. AutoCAD® provides not only basic customization but also programming interfaces such as AutoLISP, ADS, ADS-RX and ObjectARX. In Serbia, civil engineers use GavranCivilModeller® (GCM®) for railways and roads designing, and this software is also in use in some countries of European Union. GCM® is developed with mentioned programming interfaces. This paper shows how to create AutoLISP routines which will be used along with GCM® in order to design model of railway with transition curve with nonlinear change of curvature.**

***Keywords* – AutoCAD®, AutoLISP, GavranCivilModeller®, railway, 3D model, transition curve.**

I. INTRODUCTION

Transition curve is an element of alignment that connects straight line and circular curve or two circular curves with same or different radius, which can have same or opposite direction of curvature.

Transition curve and cant transition form complex spatial geometric shape with simultaneous change of curvature of both track rails and change of cant of the outer rail [1]. Additionally, both track rails follow designed grade level in longitudinal profile.

In order to secure ride comfort, function of rail curvature change in the zone of the transition curve must coincide with function of cant change in the zone of the defined cant transition.

According to European standard EN 13803-1:2010 six forms of transition curves can be used: clothoid, cubic parabola, Bloss curve, cosine curve, Schramm curve and Klein curve (sine curve) [2].

From denominated transition curves only clothoid and cubic parabola have linear function of curvature and cant change (Fig. 1). Other transition curves require appropriate nonlinear function, namely [2]:

- third-order parabola for Bloss curve,
- second-order parabola for Schramm curve,
- cosine function for cosine curve and
- sine function for Klein curve.

Nonlinear cant transitions are designed in the way to reduce dynamic influences on a vehicle and vertical acceleration that affects the passengers. The main problem that occurs in these cant transitions during exploitation is deterioration of geometry of the track laid on ballast bed due to uneven bed settlement [3].

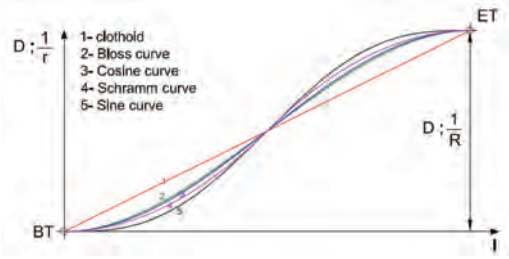

Fig. 1. Parallel review of different cant transition geometry [4]

In general, for curvature equation in random point of the transition curve applies:

$$\frac{1}{r} = f(l) \text{ boundary conditions: } \begin{cases} l = 0 \Rightarrow \dfrac{1}{r} = 0 \\ l = L \Rightarrow \dfrac{1}{r} = \dfrac{1}{R} \end{cases} \quad (1)$$

where:

l - distance from the random point to the beginning of transition curve,

L - length of transition curve,

R - radius of circular curve.

If θ represents an angle between tangent line and tangent in random point of transition curve, then it applies [3]:

$$\frac{d\theta}{dl} = \frac{1}{r} = f(l) \Rightarrow \theta = \int f(l) \cdot dl \quad (2)$$

boundary conditions: $\begin{cases} l = 0 \Rightarrow \theta = 0 \\ l = L \Rightarrow \theta = \tau \end{cases}$

Calculation of x and y coordinates is done relatively to local coordinate system whose origin is in the beginning of transition curve and with one axis parallel to tangent line and another perpendicular to it [3, 5, 6].

From observed, infinitely small element from Fig. 2, it follows:

[1]Luka Lazarević is with the University of Belgrade, Faculty of Civil Engineering, Bulevar kralja Aleksandra 73, 11000 Belgrade, Serbia, E-mail: llazarevic@grf.bg.ac.rs.

[2]Zdenka Popović is with the University of Belgrade, Faculty of Civil Engineering, Bulevar kralja Aleksandra 73, 11000 Belgrade, Serbia, E-mail: zdenka@grf.bg.ac.rs.

[3]Dejan Gavran is with the University of Belgrade, Faculty of Civil Engineering, Bulevar kralja Aleksandra 73, 11000 Belgrade, Serbia, E-mail: gavran@eunet.rs.

[4]Leposava Puzavac is with the University of Belgrade, Faculty of Civil Engineering, Bulevar kralja Aleksandra 73, 11000 Belgrade, Serbia, E-mail: leposava@grf.bg.ac.rs.

$$\cos\theta = \frac{dx}{dl} \qquad \sin\theta = \frac{dy}{dl}$$
$$dx = \cos\theta \cdot dl \qquad dy = \sin\theta \cdot dl \tag{3}$$
$$x = \int \cos\theta \cdot dl \qquad y = \int \sin\theta \cdot dl$$

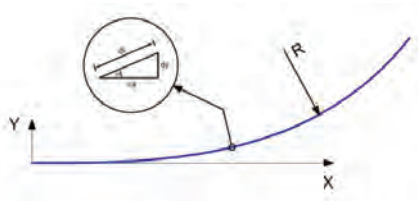

Fig. 2. Local coordinate system and transition curve

First of all, coordinates *x* and *y* are calculated relatively to local coordinate system, and then these coordinates should be defined in global coordinate system.

Cant is usually applied by raising the outer rail, while keeping the inner rail at the same level. It is also possible to simultaneously raise the outer and lower the inner rail for one half of cant value. But these types of track alignment are more difficult and more expensive to maintain, so they are rarely applied.

Railway centre line in the zone of transition curve is a complex trilinear curved line. From the aspect of mathematics, it represents smooth spatial curve defined with following parameter relation:

$$F(l) = (x(l), y(l), z(l)) \quad , \quad l \in [0, L] \tag{3}$$

By raising the outer rail for constant value *D* in the zone of circular curve, railway centre line will be raised for value *D/2* above the inner rail, so in general it follows:

$$z(l) = z_{ir} + \frac{D(l)}{2} \tag{4}$$

where z_{ir} is level of the inner rail.

II. MAIN PRINCIPLES OF 3D RAILWAY MODEL DESIGN IN GCM® ENVIRONMENT

Software products for road design, which are used in Republic of Serbia, support the use of clothoid as a transition curve, while software products for railway design support the use of cubic parabola. Most frequently used software GCM® supports the use of clothoid and offers big opportunities in railway and road design [7] (Fig. 3).

In order to create 3D model of the transition curve in GCM® environment, it is necessary that railway centre line in a horizontal plane and in a longitudinal profile was previously defined. This means creating *.hcl and *.vcl files, which contain necessary data about spatial centre line in both mentioned projections.

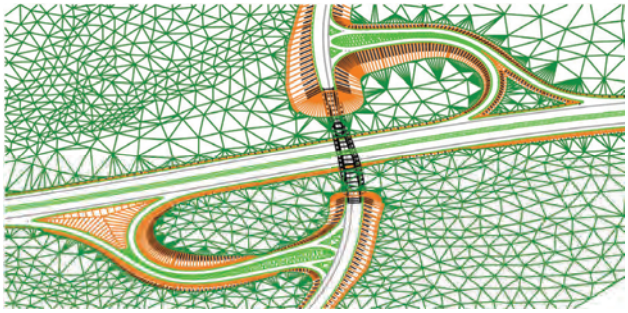

Fig. 3. Possible application of software GCM®

Next step is to define the so-called templates. Generally, template represents a set of lines that 3D model should have in its every cross section. For example, it can be only outer contour of ballast bed, or completely defined cross section with all the details. It is necessary to define templates for straight line and for every circular curve, and also for the specific places such as inflection points or for other characteristic places where cant is not applied in the usual manner.

When templates are completely defined, *.tmp files for each one of them are created. Then, these files are "attached" to the centre line on appropriate positions and command for 3D model generation is called. This command generates triangulated 3D model of railway (road or tunnel) by interpolation between the key points on previously chosen, constant distance. Key points are centre line points in which change of template occurs and these points can be stored in created *.tmc file, but also there is a command that can recognize these points by itself. Generation of 3D model between the beginning and the end of the transition curve is based on calculation of a cant value (cross grade) in every pair of consecutive points. Then, between those pair of points, according to created templates, triangulated model of surface that shall be represented in space is created.

In order to create a model of transition curve with nonlinear change of curvature in GCM®, it is necessary first to develop AutoLISP routines for their construction in horizontal plane.

Next step is final model generation using AutoLISP routine that will, by combining horizontal and vertical geometry, define the set of characteristic points in space on constant distance along the railway centre line. It is best that these points define outer contour of ballast bed, but they also can define upper edges of right and left rail, platform level, i.e. everything that would make completely defined model.

To invoke standard GCM® command for generation of triangulated model from chosen points, it is necessary to create *.pts file that will contain handles and coordinates of these points. This file can be created using the already existing GCM® command, or it can be one of the results of routine invoking. For the purpose of further adjustment of the railway model in the terrain model, it would be useful that routine also creates a couple of *.str files, above all two of them, which will define right and left edge of ballast bed, and if it is necessary those with the data about right and left rail and/or railway centre line. These files will enable further construction of railway cut and fill slopes, right and left rail, platform surface, drainage details etc. This is the way to create

fully defined and detail model, which will represent the stage after railway construction.

III. AUTOLISP ROUTINES FOR 3D MODEL DEVELOPMENT

Algorithm for construction of transition curves in horizontal plane is shown on Fig. 4.

First step is to adjust by need proper system variables and control variable *cv*. Selection of two tangent lines is done using two while loops. Both of these loops repeat until user selects line entity, and only then variable *cv* takes value nil, which terminates a loop. Selection point's coordinates and entity lists are read from both line entities and they are assigned to certain variables. Then user needs to input values of the circular curve radius and the transition curve length, and according to these values geometric elements for construction are calculated, as well as coordinates of all significant points.

Before invoking the command that draws polyline, variable *i* is assigned to a value 2. It means that points for transition curve construction are calculated in successive distances each of 2 m. After leaving the loop, it is checked if the last calculated point is also the end of the transition curve, and if not so the last segment of polyline is drawn and command is stopped. The same procedure is used for other transition curve. Next, command that draws arc using beginning point, ending point and radius is invoked. Hence, transition curve is actually polyline entity, whose vertices are calculated detail points.

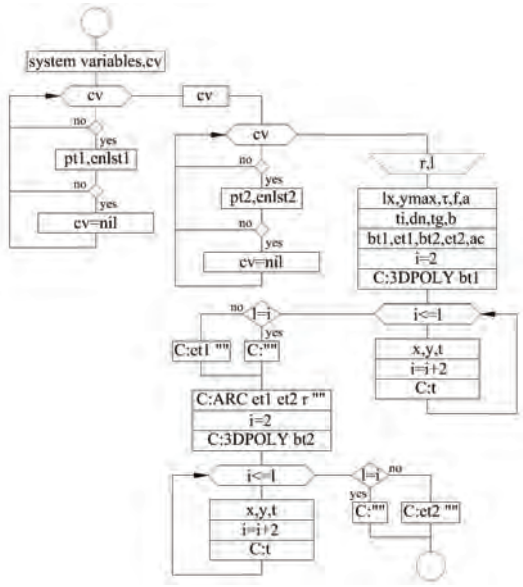

Fig. 4. Algorithm example for construction of transition curves in horizontal plane

In order to allow further work with model, every drawn transition curve has additional information that describes its geometry (extended data) attached with entity list. These pieces of information are: form of transition curve, its length, radius of the circular curve and direction angle along the tangent line gainst polygon vertex.

Algorithm for defining points for model generation is shown on Fig. 5.

First step in defining points for model generation is adjusting proper system variables. Then selection of *.hcl and *.vcl file is made, and also user should choose a distance d for calculation of previously mentioned points. Calculation begins at station *s*=0, but it would be more practical that user chooses this value. Loop repeats until current station becomes bigger than ending station *es*. In this loop it is first checked to what element of horizontal geometry current station belongs and this will dictate the way of calculation of all necessary points from cross section. After leaving the loop, it is checked if last calculated points belong to the ending cross section.

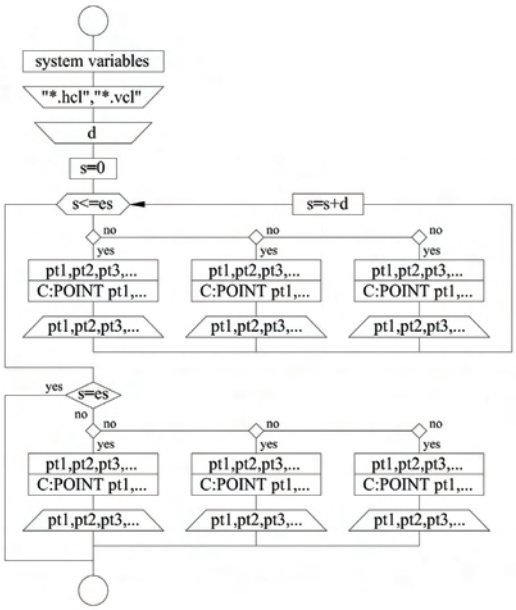

Fig. 5. Algorithm example for defining points for model generation

Since this algorithm makes *.pts file, as well as couple of certain *.str files [8], it is only left to invoke commands for calculation and drawing of triangulated model of railway. Now, it is possible to use all GCM® commands that work with strings in order to nest the railway model into the terrain model.

Complex 3D surfaces of transition curves with cant transitions are shown on Fig. 6.

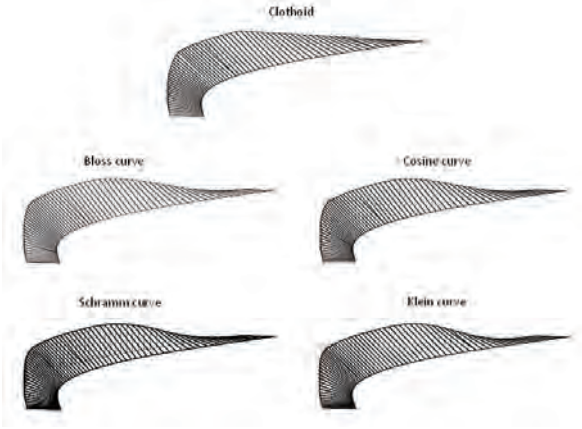

Fig. 6. Complex 3D surfaces of transition curves with cant transitions

Final result of 3D modelling is shown on Fig. 7.

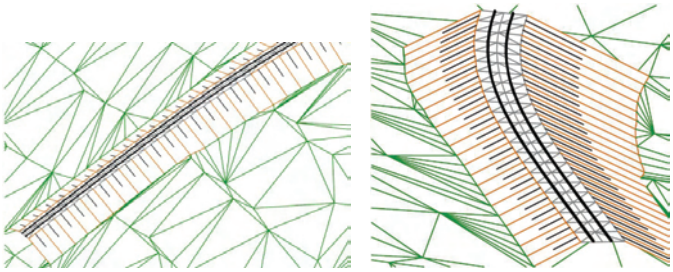

Fig. 7. 3D wireframe model

IV. Choosing the Distance for Model Generation

At the end, there is a question about the value of distance that should be used for model generation along the railway centre line in order to achieve its adequate precision. In fact, all needed values for model, first of all a value of cant, will be calculated in every cross section on chosen distance. It means that model will be made of linear segments between calculated cross sections, so it will cause a certain model fault. Diagrams on Fig. 8 show correlation between distance for model calculation and difference between calculated cant value and cant value on linear segments of model (V_R=80km/h).

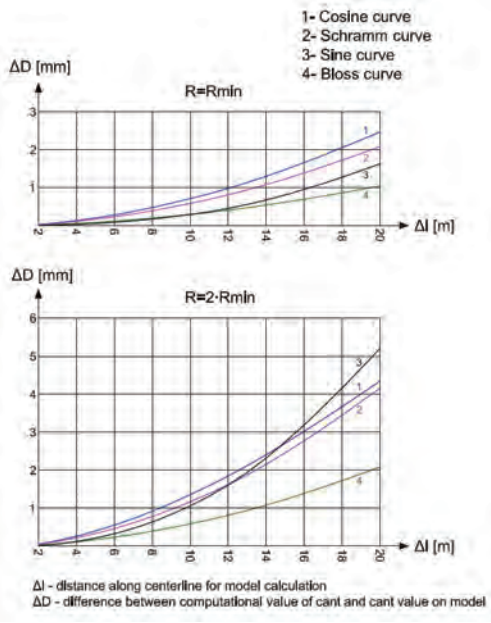

Fig. 8. Correlation between distance for model calculation and cant defect

From diagrams follow that in case of maximum length of transition curve, cant defect can be between 1-3 mm. By raising radius of the circular curve, i.e. by reducing length of the transition curve, cant defect raises. Also, from diagram follows that sine curve has fastest cant defect flow.

General recommendation is that distance for model generation should be at most 5-10 m, not only because of mentioned cant defect, but also because of length defect of nonlinear elements.

V. Conclusion

The European Union has enacted various legislative measures aimed at achieving the opening up, integration and harmonization of national railways to form a European railway network. Harmonization of the national railway legislation with the aquis communitare on safety and interoperability is of a special importance for integration of the Serbian railway systems [9].

Modern approach in railway design implies the selection of geometric form of transition curve and cant transition as a unique spatial element. Selection of spatial form of cant transition is required by type of superstructure or maintenance conditions of track geometry during exploitation.

In this paper 3D model of railway with transition curves with nonlinear change of curvature is represented, so that users can apply with ease complex spatial geometry.

Acknowledgement

This work was supported by the Ministry of Science and Technological Development of Republic of Serbia through the research project No. 36012: “Research of technical-technological, staff and organisational capacity of Serbian Railways, from the viewpoint of current and future European Union requirements”.

References

[1] M. Weigend, *Linienführung und Gleisplangestaltung*, Eurailpress, S. 120, Hamburg, 2004.

[2] CEN: EN 13803-1:2010 Railway applications - Track alignment design parameters –Track gauges 1435 mm and wider - Part 1: Plain line

[3] L. Lazarević, *Cant transition as spatial element of railway*, MSc Thesis, University of Belgrade, Faculty of Civil Engineering, Belgrade, Republic of Serbia, 2010.

[4] Z. Popović, L. Puzavac and L. Lazarević, "The Shape of Superelevation Ramps According to European Standards", XIV Scientific-Expert Conference on Railways with International Participation RAILCON '10, Conference Proceedings, pp. 151-154, Niš, Republic of Serbia, October 2006.

[5] L. Puzavac, Z. Popović and L. Lazarević, "Transition Curve Design According to European Standards", XIV Scientific-Expert Conference on Railways with International Participation RAILCON '10, Conference Proceedings, pp. 147-150, Niš, Republic of Serbia, October 2006.

[6] Z. Popović, L. Lazarević and L. Puzavac, "Superelevation Ramp Design", Izgradnja, No. 11-12, November-December, pp. 621-636, 2010.

[7] D. Gavran, GCM®2010 manual, 2010.

[8] AUTODESK, AutoCAD® R14, Visual LISP Guide, 1998.

[9] Z. Popović, "Interoperability and standardization of railway infrastructure of Serbian railways", Railway Technical Review, Hamburg, ISSUE 4/2007, Volume 47, pp. 6-9, 2007.

Session PDS I:

POWER TRANSMISSION AND DISTRIBUTION SYSTEMS I

Reconfiguration as a Measure for Reduction of Energy Losses in Distribution Networks

Dragan S. Tasić[1], Miodrag S. Stojanović[2] and Aleksa T. Ristić[3]

Abstract – **Reconfiguration as one of measures for energy loss reduction in distribution networks which do not requires investment is considered in this paper. A classification of reconfiguration methods is proposed. After this, detailed consideration of a heuristic method for reconfiguration of distribution networks is made. This method is based on the concept of optimal flow pattern. Results of analyzes made on real distribution networks show that reconfiguration should be performed in all cases where it is technically possible.**

Keywords – **Reconfiguration, Distribution network, Losses, Energy**

I. INTRODUCTION

Reduction of power losses in distribution networks should be considered as a part of general task which aims to enhance work efficiency of power systems. Since active and reactive power flows can be influenced in various ways and therefore the power losses, there is a wide range of measures for reduction of electric energy losses. These measures can be classified on different ways, but the most common is into: organizational and technical [1-3].

Organizational measures are those whose application leads to more economically exploitation of the network, and where is no need for additional investments. These measures include: optimization of load distribution, finding the optimal place of decoupling the distribution lines with two side feed, network reconfiguration, voltage regulation, disconnecting of transformers in periods with low load in substations with two or more transformers, balancing phase loads in low voltage networks etc. Besides they don't need additional investments, these measures can be accomplished in relative short period of time.

Technical measures for loss reduction include: network reconstruction, installation of compensation devices, conductor replacement at high loaded sections of distribution lines, replacement of overloaded or insufficiently loaded transformers, network automation etc. These measures require financial investments and they are usually fulfilled in relative long period of time.

Besides the already mentioned, it is necessary to bear in mind the measures taken for as much accurate measuring of consumed electric energy as possible. These measures contain: regular work conditions for instrument transformers and energy meters, replacement of older generation measuring devices with devices which have better characteristics, periodic checks of working accuracy of the measuring devices.

Reconfiguration of distribution networks is defined as altering the topological structure of distribution feeders, by changing the open/closed status of sectionalizing and tie switches in order to achieve optimal configuration [3-8]. From definition of reconfiguration, it can be seen that starting point in solving the reconfiguration task is defining the criterion (or more of them), which determine the optimal reconfiguration of distribution network. This criterion of optimality should be qualitative (or measurable).

There are lots of reasons for changing the configuration of distribution network and basically they can be divided into: a) improvement of network in normal conditions, b) supplying consumers in incidental conditions. Within the improvement of network in normal conditions, it can be distinguished two most important subgroups: reduction of power losses and eliminating of overloaded elements.

Reconfiguration can be considered as a planning task or real-time task. Reconfiguration task on daily, monthly or season planning level relies heavily on load estimation, which carries some uncertainty, therefore highly accurate calculations are not necessary here, and there is no need for particularly fast and reliable algorithms. On the other hand, real-time reconfiguration, which is possible only in fully automated system, demands high speed data acquisition as well as extremely fast reconfiguration algorithms. Considering the fact that every closing or opening of the switch reduces its operational life, it can be concluded that for small improvements of working conditions, reconfiguration has no sense.

In terms of loss reduction, reconfiguration task is reduced on determining the sectionalizing and tie switch whose opening and closing induces loss reduction. Since reconfiguration doesn't require additional investments, it should be always applied when technical capabilities allow its usage. Therefore, in this paper is made classification of the methods for reconfiguration and pointed to potential of their application, from aspect of electric energy losses. The effects of reconfiguration application are envisaged on a real distribution network.

II. METHODS FOR RECONFIGURATION OF DISTRIBUTION NETWORKS

Depending of mathematical model and applied solution technique, methods for reconfiguration of distribution

[1]Dragan S. Tasić is with the University of Nis, Faculty of Electronic Engineering, Aleksandra Medvedeva 14, 18000 Nis, Serbia, E-mail: dragan.tasic@elfak.ni.ac.rs.

[2]Miodrag S. Stojanović is with the University of Nis, Faculty of Electronic Engineering, Aleksandra Medvedeva 14, 18000 Nis, Serbia, E-mail: miodrag.stojanovic@elfak.ni.ac.rs.

[3]Aleksa T. Ristić is with the University of Nis, Faculty of Electronic Engineering, Aleksandra Medvedeva 14, 18000 Nis, Serbia, E-mail: aleksa.ristic@elfak.ni.ac.rs.

network, whose aim is to reduce power losses, can be globally divided into three groups [3, 8]:

- methods based on the application of optimization techniques,
- heuristic methods,
- methods based on the application of artificial intelligence techniques.

Methods based on the application of optimization techniques belong to category of nonlinear programming. As mentioned before, criterion of optimality should be qualitative (or measurable). Attaching technical constraints to the criterion of optimality (objective function), in general, leads to nonlinear dynamic task. As such, it can be solved with some of the well-known optimization techniques. Reconfiguration problem can be mathematically formulated in relation:

$$\min \sum_{i=1}^{n} \sum_{j=1}^{n} C_{ij} \Delta P_{ij} \tag{1}$$

Subject to:

$$\sum_{i=1}^{n} \underline{S}_{ij} = \underline{S}_{j} \tag{2}$$

$$S_{ij} \le S_{ij\max} \tag{3}$$

$$\Delta U_{ij} \le \Delta U_{ij\max} \tag{4}$$

$$\sum_{\forall ft} \underline{S}_{ft} \le \underline{S}_{ft\max} \tag{5}$$

$$\prod_{\forall ft} \lambda_{ft} = 1 \tag{6}$$

where:

C_{ij} - weight loss coefficient for the section with initial node *i* and end node *j*,

ΔP_{ij} - power losses in section *i,j*

S_{ij} - load of the section *ij*,

S_{j} - power consumption at node *j*,

ΔU_{ij} - voltage drop on section *ij*,

f_i - subset of the feeders supplied by transformer *t*,

λ_{ft} - coefficient with value of 1 if a feeder is radial, otherwise it is 0.

In general, problem of finding the optimal configuration of the network is problem of mixed integer programming. For real distribution networks, with very large sizes, finding the solution of this kind of optimization task can last a very long time. In some cases it may happen that some procedures do not converge at all. Besides, sometimes it's not possible to validate all relevant constraints.

Therefore, modern approaches to the reconfiguration of distribution networks are based on heuristic methods and techniques of artificial intelligence (expert systems, fuzzy logic and neural networks). The essence of heuristic algorithms, based on nature of the problem, is to find the optimal configuration. Within these methods, two main approaches are distinguished:

- methods with gradual opening of the contour ("minimum current" algorithms),
- methods with a single opening of the contour ("branch alteration" algorithms).

The essence of methods with gradual opening of the contour, or "minimum current" algorithms, is to initially close all switching devices, where radial network is transformed into meshed network (contour network). Then, switching devices in contour sections are opened one by one, until radial structure of the network emerges. Choice of opening switching device is performed with aim to minimize the power losses. Where, in every step the opening switching device is placed in section with the lowest current intensity, determined from optimal distribution requirement of power flow.

Methods with a single opening of the contour ("branch alteration" algorithms) are constrained on one executive operation with network where two switching devices change their open\close status, or shifting the load from overloaded feeder (or transformer) to relative lower loaded feeder (or transformer). These methods are very effective, because they don't require calculation of whole regime after changing the open\close status of switching devices. Their shortcoming is reflected in the fact that the final solution is a local optimum.

Artificial intelligence methods have a wide range of power applications. In expert system applications, task of finding the optimal configuration is treated as combinatorial and heuristic problem. When determining the solution, the list of the best network configurations is formed and supplemented (by the value of objective function) in every moment. This list is used to generate new possible network configurations. Generation is done by closing the normally opened switching devices and successively opening the switching devices is sections of formed contour. Thereby, every opening means creation of the new radial configuration with certain value of the objective function.

Application of genetic algorithms for solving the reconfiguration task of distribution network, gives very good results from aspect of time needed for finding the global optimum or solution which is near the global optimum. In these algorithms, every string (coded discrete information) contains information about possible radial structure of the network with calculated value of objective function which meets the certain constraints.

In solving the reconfiguration problem, neural networks can find significant application because they have the ability to perceive connection between nonlinear nature of power flows and its structure which corresponds to minimum of the losses. Although, application of neural networks allows abbreviation of time needed to obtain the solution, wider use is difficult because of:

- long time needed for their training,
- training must be made for every distribution network,
- accurate training file must be provided to neural network in order to give acceptable results.

It should be noted that the solution obtained by using neural networks is accurate as much as used data during the training are accurate.

Considering the fact that in reality the most common are heuristic methods, method with gradual opening of the contour ("minimum current" algorithms) will be more exposed.

In this approach, reconfiguration procedure starts with closing all switches in network, and thus the meshed distribution network is formed [3, 8]. Since distribution networks usually work radial, reconfiguration algorithm predicts one after another opening of the loops, on the way that allows achieving the optimal configuration with minimum of managing actions. The optimal configuration means states in which are had the optimal power flows, or power flows in branches which are producing minimal active losses in the network. These power flows are obtained from solving the Kirchhoff's laws written for the given network.

From the previous exposure follows that optimal power flows are found starting from the meshed network. That means that switch, which should be opened (to open the loop), is selected in the last step, because then only one loop exists in the network while the rest of network is radial. It is clear that in preceding steps can be several loops, which doesn't match with real conditions.

Procedure exposed previously can be simplified. This is achieved if only one switch is closed at a time instead of simultaneously closing all of the switches and forming the meshed network and then opening the switches one after another in order to obtain radial configuration. On that way a single loop is formed and radial configuration is obtained by opening the same or some other switch inside the loop, depending of optimal power flow results applied on the branches of a loop. As mentioned before, optimal power flows in branches of formed loop, are obtained by solving the Kirchhoff's laws for given loop.

Feeder reconfiguration algorithm begins with power flow calculation of radial network. Switch which is normally opened now is closing to form the loop. Normally opened switch can be selected depending of voltage on the switch or arbitrarily. There are three options:

- Normally opened switch on whose contacts the voltage has the highest value is closed (as effect of maximal voltage difference, there is expectation of gaining the maximal loss reduction).
- Switch on whose contacts the voltage has the lowest value is closed (because of minimal voltage value, expectation is very slow convergence of the solution).
- Switches are selected arbitrary.

It can be shown that gained final solution is the same regardless of the selection.

Closing the normally opened switch, changes the distribution of power flows and is needed to find the new solution. Here is assumed that consumption is replaced with constant current obtained by determining of power flows in radial network.

Previously exposed procedure that is radial network calculation start, forming of the loop by closing the normally opened switch, determining optimal power flows and forming of the radial network is repeated as long as it brings the loss reduction.

III. TEST EXAMPLE

In order to demonstrate the effects of reconfiguration as a measure for reduction of energy losses, in this chapter are displayed results for power loss calculation in distribution network with rated voltage of 10 kV, illustrated in Fig. 1. In this figure, circles marks the 10/0.4 kV/kV substations.

Insight into calculation results enables finding the critical spots in terms of power losses. Line sections which represent "critical spots" in terms of losses are circled in Fig. 2. Power losses are identified in 15 sections (of 158) and their value is 525.22 MWh, which represents 79.2 % of losses in all distribution lines of the observed 10 kV distribution network.

Applying these reconfiguration methods with minimal loss criterion, determines the optimal configuration of network. Translation of current stage to optimal requires 8 manipulations to be done (4 openings and 4 closing). In Fig. 2 there are market spots which represent made manipulations.

To perceive the effects of reconfiguration, in Table I are illustrated calculation results for the losses before and after reconfiguration. It can be seen that for considered period of time, reconfiguration leads to loss reduction of 154.8 MWh.

TABLE I
CALCULATION RESULTS FOR POWER LOSSES MEDIUM-VOLTAGE DISTRIBUTION NETWORK BEFORE AND AFTER THE RECONFIGURATION

	Before reconfig.	After reconfig.	Difference
Supplied energy (MWh)	52207.5	52052.7	154.8
Total power losses (MWh)	1252.34	1105.21	147.13
Power losses in percent (%)	2.4	2.123	0.277
Distribution line losses (MWh)	663.382	516.218	147.164
Transformer iron losses (MWh)	299.473	301.24	-1.767
Transformer copper losses (MWh)	289.485	287.75	1.735

IV. CONCLUSION

The paper points to the possibility of using reconfiguration to reduce energy losses in distribution networks. Classification of the methods is proposed, and after that the methods with gradual opening of the contour ("minimum current" algorithms) is discussed in details. This is heuristic method which proved to be very suitable for solving reconfiguration tasks, considering complexity and insufficient

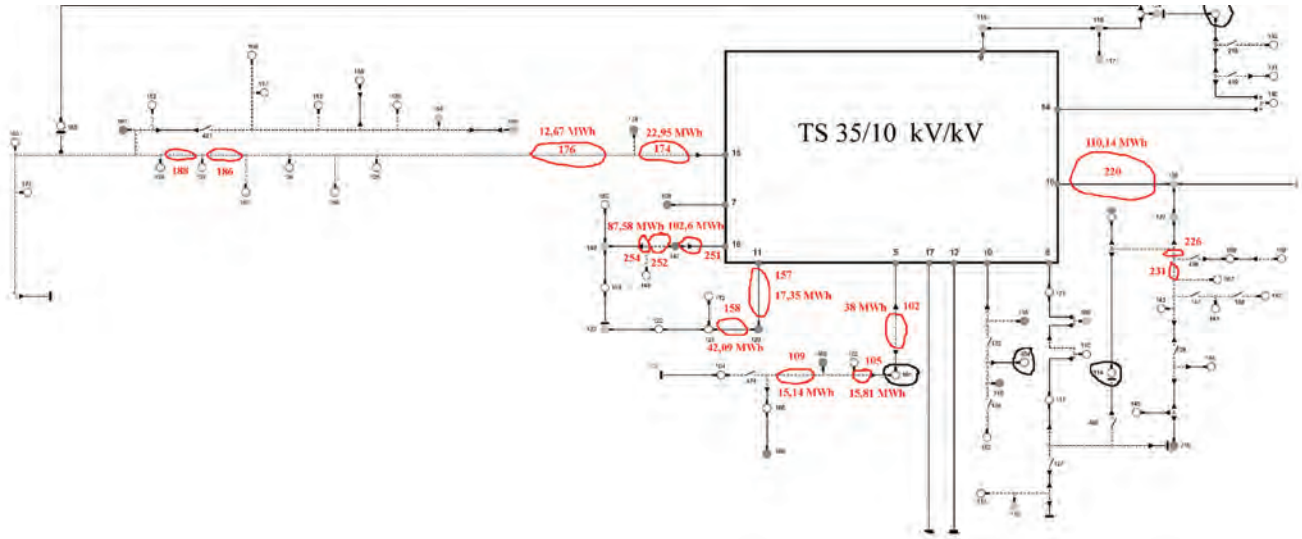

Fig. 1. Critical spots in 10 kV distribution network supplied from substation 35/10 kV/kV

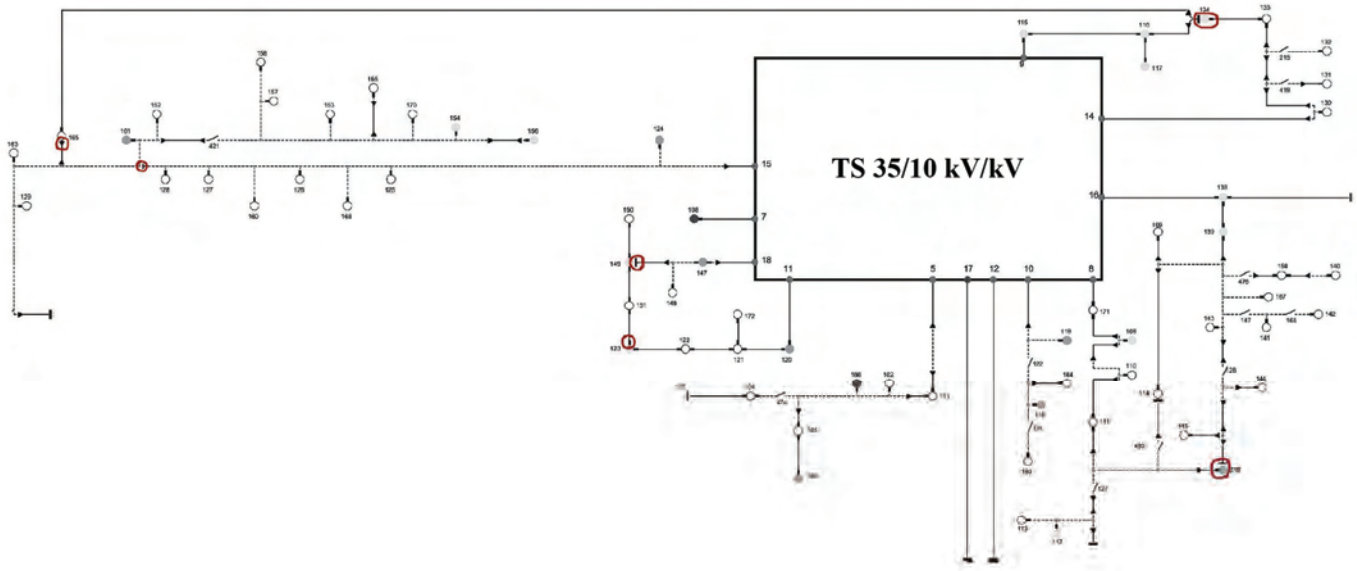

Fig. 2. Medium-voltage distribution network after the reconfiguration

reliability of data. Analyses that were undertaken by the authors on actual networks show that reconfiguration should be conducted always when technical capabilities allow that.

REFERENCES

[1] В. Э. Воротницкий, Ю. С. Железко, В. Н. Казанцев, В. Г. Пекелис, Д. Л. Файбисович, *Потери электроэнергии в электрических сетях энергосистем*, Энергоатомиздат, 1983.

[2] Ю. С. Железко, А. В. Артемьев, О. В. Савченко, *Расчет, анализ и нормирование потерь электроэнергии в электрических сетях*, НЦ ЭНАС, Москва, 2004.

[3] D. Tasić, M. Stojanović, *Gubici električne energije u distributivnim mrežama*, Edicija Monografije, Elektronski fakultet, Niš, 2006.

[4] M. E. Baran, F. F. Wu, “Loss Minimization”, IEEE Trans. on Power Delivery, Vol. 7, No. 3, July 1992, 1484-1491.

[5] S. K. Goswami, S. K. Basu, “A New Algorithm for the Reconfiguration of Distribution Feeders for Loss Minimization”, IEEE Trans. on Power Delivery, Vol. 7, No. 3, July 1992, 1484-1491.

[6] S. Cilanvar, J.J. Grainger, H. Yin, S. S. H. Lee, “Distribution Feeder Reconfiguration for Loss Reduction”, IEEE Trans. on Power Delivery, Vol. 3, No. 3, July 1988, pp. 1217-1223.

[7] D. Shirmohammadi, H. W. Hong, “Reconfiguration of Electric Distribution Networks for Resistive Line Losses Reduction”, IEEE Trans. on Power Delivery, Vol. 4, No. 2, April 1989, pp. 1492-1498.

[8] D. Popović, D. Bekut, V. Treskanica, *Specijalizovani DMS algoritmi*, DMS group, Novi Sad, 2004.

The Analysis of Load Type Influence on Loss Allocation in Radial Distribution Networks

Dobrivoje P. Stojanovic[1], Nebojsa R. Kreckovic[2]

Abstract – **The paper presents the results of power loss allocation in radial distribution networks for different load types. Three characteristic load types are considered: constant power, constant current and constant impedance load. Loss allocation is performed on the basis of current flows through network branches. The algorithm of the calculation regards all demands of fair allocation. Network topology is described by oriented graph. The folmulas for calculation and loss distribution in each branch of the network are given. It is shown that load type hardly influences on real power losses, and therefore it have to be regarded for loss allocation calculation.**

Keywords – **Loss allocation, Power losses, Distribution networks.**

I. INTRODUCTION

In conditions of power system deregulation, where electrical energy is treated as goods, it is necessary to determine the shares of all customers in total loss creation in distribution network. An intention is that every consumer could fulfill his obligation concerning paying of some part of loss expenses. To say by the other words, it is necessary to make loss allocation to the nodes or to the consumers supplied from these nodes. On that way, tariff system would take into account real influence of all consumers to expenses originating from energy losses. The problem of loss allocation is specially emphasized in transmission networks. In recent years, several papers have been appeared in literature offering special methods of loss allocation in distribution networks [1-5]. Main problems for loss allocation are: nonlinear connection between the losses and loads in the nodes and defining the way of common losses dividing.

Except aforementioned ones, additional problems appear due to unknown structure and load characteristic in some node. Namely, the calculations of active power losses always are carried out with load of constant power type, which is independent of voltage. In real conditions, load in some node depends on voltage and it reflects on power losses in distribution network [6]. This fact should be regarded if we want exact calculations of power and energy losses and after it allocation calculation on consumption nodes.

There are three characteristic load types: 1- constant power, 2-constant current and 3-constant impedance. In real situation no one of these three types suits to actual load which is changeable and unpredictable in time.

[1]Dobrivoje Stojanovic is with the Faculty of Electronic Engineering, Aleksandra Medvedeva 14, 18000 Nis, Serbia E-mail: dobrivoje.stojanovic@elfak.ni.ac.rs.

[2]Nebojsa Kreckovic is with Electrical distribution company „Elektrokosmet“, 28000 Kosovska Mitrovica, Serbia, E-mail: nkreckovic66@gmail.com

As authors of this paper know, there was no one attempt to solve this problem completely and to take into account load characteristics in every node of distribution network. Just therefore this work analyzes load type influence on calculation results of loss allocation. The calculations are carried out according the method proposed in [4]. Basic aim of this work was to research if, and in which extent, load type in some node of distribution network would impact on calculation results of loss allocation. In this sense, radial test network with 32 nodes is considered [7].

II. METHODOLOGY

Total active power losses, ΔP, in distribution network with n branches are obtained as a sum of losses in some branches ΔP_i,

$$\Delta P = \sum_{i=1}^{n} \Delta P_i \,. \tag{1}$$

Active power losses in *i*-th branch of network are:

$$\Delta P_i = 3R_i J_i^2 \tag{2}$$

where:

R_i – active resistance of *i*-th branch,

J_i – effective value of current of *i*-th branch.

Current of *i*-th branch is determined as a sum of the currents of these consumers (Z) supplied via this branch, $\underline{I}_j$,

$$\underline{J}_i = \sum_{j \in Z} \underline{I}_j \,, \tag{3}$$

which is illustrated on Fig. 1.

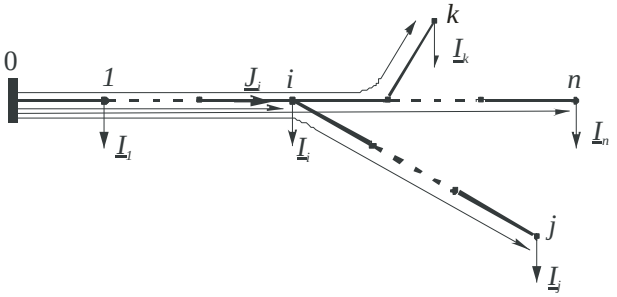

Fig. 1. Forming of radial network paths

When one express each load through their components $\underline{I}_j = I_{pj} + jI_{qj}$, it is easy to find the contributions of all loads/consumers to real and imaginary part of *i*-th branch current.

$$\underline{J}_i = \sum_{j\in Z} \underline{I}_j = \sum_{j\in Z} I_{pj} + j\sum_{j\in Z} I_{qj} \ . \qquad (4)$$

If Eq. (4) is put into Eq. (2), for active power losses in *i*-th branch we obtain:

$$\Delta P_i = 3R_i\left[\left(\sum_{j\in Z} I_{pj}\right)^2 + \left(\sum_{j\in Z} I_{qj}\right)^2\right]. \qquad (5)$$

Developing Eq. (5) gives:

$$\Delta P_i = 3R_i\left[\sum_{j\in Z} I_{pj}^2 + 2\sum_{\substack{j\in Z\\ k\in Z\\ j\neq k}} I_{pj}I_{pk} + \sum_{j\in Z} I_{qj}^2 + 2\sum_{\substack{j\in Z\\ k\in Z\\ j\neq k}} I_{qj}I_{qk}\right], \qquad (6)$$
$$= \sum_{j\in Z} \Delta P_{ij}$$

From Eq. (6) we can calculate impact of *j*-th load to *i*-th branch losses, designated here as ΔP_{ij}.

It means that *j*-th load has impact to *i*-th branch losses through items I^2_{pj} and I^2_{qj}, corresponding exclusively to *j*-th consumer and via items $2\sum_{\substack{j\in Z\\ k\in Z\\ j\neq k}} I_{pj}I_{pk}$ and $2\sum_{\substack{j\in Z\\ k\in Z\\ j\neq k}} I_{qj}I_{qk}$ showing simultaneous impact of *j*-th and *k*-th loads to the losses in *i*-th branch.

If *j*-th currents does not pass through *i*-th branch ($j \notin Z$) then would be $\Delta P_{ij}=0$.

Question arises how to divide power losses in some branch to individual consumers (ΔP_{ij}). This problem is not unique due to nonlinearity of products appearing in [4]. Two easy feasible principles are possible: linear and square. Here the first principle is used. The losses should be divided proportionally to loads current components. So it is obtained:

$$\Delta P_{ij} = 3R_i[I_{pj}^2 + 2\sum_{\substack{j\in Z\\ k\in Z\\ j\neq k}} I_{pj}I_{pk}\frac{I_{pj}}{I_{pj}+I_{pk}}$$
$$+ I_{qj}^2 + 2\sum_{\substack{j\in Z\\ k\in Z\\ j\neq k}} I_{qj}I_{qk}\frac{I_{qj}}{I_{qj}+I_{qk}}]. \qquad (7)$$

Beginning from adopted distribution principle (Eq. (7)), network losses belonging to *j*-th load/node are obtained as a sum of the losses in network branches on the way from considered node to source one (Fig. 1)

$$\Delta P_j = \sum_{i=1}^{n} \Delta P_{ij} \ , \qquad (9)$$

where n shows number of branches.

III. NUMERICAL EXAMPLE AND CALCULATION ANALYSIS

Test network of rated voltage U_n=12.66kV with 32 nodes, shown in Fig. 2 is considered [7]. Loads and network elements are balanced. Loads are presented according their static characteristics:

$$P_i = P_{ni}\left(\frac{U_i}{U_n}\right)^{k_{pi}}$$
$$Q_i = Q_{ni}\left(\frac{U_i}{U_n}\right)^{k_{qi}} \qquad (10)$$

Different load types can be simulated by choosing the values of coefficients k_{pi} and k_{qi}. Load of constant power ($k_{pi} = k_{qi}=0$), constant current ($k_{pi} = k_{qi}=1$) and constant impedance ($k_{pi} = k_{qi}=2$ are considered here.

Voltage and load flow calculation is done by power summation method [8]. After iterative procedure finishing, load and current flows are obtained and current components in network branches so. On the basis of these currents, power losses in each branch and total network losses are calculated.

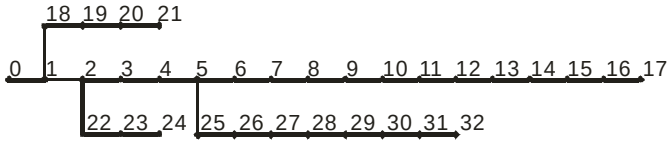

Fig. 2. Test network

Active power losses in the network of given configuration depend on individual loads, their locations, type of load and voltage of source node [6]. As the theme of this work is load type influence on loss allocation, furthermore the losses will be considered only when source node voltage is U_0=12.66kV.

For source node voltage $U_0 = 12.66\text{kV}$ and basic loads, total active power losses in considered network are: $\Delta P = 202{,}677\,\text{kW}$, if all loads are of constant power type, $\Delta P = 176{,}628\,\text{kW}$, if all loads are of constant current type and $\Delta P = 156{,}872\,\text{kW}$, if all loads are of constant impedance type. Calculation results of loss allocation according exposed method, for linear principle of common loss distribution (Eq. 7) in some branch, are shown in Table 1. Percentage shares of active power of individual consumers in total network load (columns 4, 7 and 10) are given in the same table. Graphical presentation of the results from table 1 is given in two figures due to clearness. Fig. 3 shows absolute values of allocated losses in the nodes. Fig. 4 presents percentage values of allocated losses in relation to total losses.

TABLE I
LOSS ALLOCATION FOR DIFERENT LOAD TYPES

Node	P	Q	Constant power			Constant current			Constant impedance		
			$\frac{P_i}{\sum P_i}\cdot 100$	ΔP_i	$\frac{\Delta P_i}{\Delta P}\cdot 100$	$\frac{P_i}{\sum P_i}\cdot 100$	ΔP_i	$\frac{\Delta P_i}{\Delta P}\cdot 100$	$\frac{P_i}{\sum P_i}\cdot 100$	ΔP_i	$\frac{\Delta P_i}{\Delta P}\cdot 100$
	[kW]	[kVAr]	[%]	[kW]	[%]	[%]	[kW]	[%]	[%]	[kW]	[%]
1	100	60	2.692	0.244	0.120	2.814	0.236	0.134	2.925	0.230	0.147
2	90	40	2.423	1.066	0.526	2.499	1.010	0.572	2.566	0.962	0.613
3	120	80	3.230	2.854	1.408	3.309	2.659	1.505	3.377	2.497	1.592
4	60	30	1.615	1.177	0.581	1.643	1.089	0.616	1.666	1.016	0.648
5	60	20	1.615	1.661	0.819	1.614	1.487	0.842	1.612	1.350	0.861
6	200	100	5.384	11.604	5.725	5.361	10.292	5.827	5.339	9.268	5.908
7	200	100	5.384	13.176	6.501	5.336	11.594	6.564	5.292	10.372	6.611
8	60	20	1.615	2.332	1.151	1.591	2.034	1.152	1.570	1.806	1.151
9	60	20	1.615	2.643	1.304	1.582	2.281	1.292	1.553	2.007	1.279
10	45	30	1.211	2.077	1.025	1.185	1.790	1.014	1.163	1.573	1.003
11	60	35	1.615	3.229	1.593	1.578	2.775	1.571	1.546	2.433	1.551
12	60	35	1.615	3.589	1.771	1.569	3.051	1.727	1.529	2.650	1.689
13	120	80	3.230	10.955	5.405	3.130	9.289	5.259	3.046	8.053	5.133
14	60	10	1.615	3.035	1.497	1.563	2.562	1.451	1.519	2.213	1.411
15	60	20	1.615	3.361	1.658	1.561	2.831	1.603	1.515	2.440	1.555
16	60	20	1.615	3.458	1.706	1.558	2.902	1.643	1.510	2.494	1.590
17	90	40	2.423	6.914	3.411	2.335	5.804	3.286	2.262	4.988	3.180
18	90	40	2.423	0.229	0.113	2.532	0.223	0.126	2.630	0.218	0.139
19	90	40	2.423	0.507	0.250	2.523	0.496	0.281	2.611	0.486	0.310
20	90	40	2.423	0.558	0.275	2.521	0.545	0.309	2.608	0.534	0.340
21	90	40	2.423	0.602	0.297	2.519	0.588	0.333	2.604	0.576	0.367
22	90	50	2.423	1.281	0.632	2.490	1.208	0.684	2.549	1.147	0.731
23	420	200	11.306	13.842	6.830	11.545	12.876	7.290	11.742	12.070	7.694
24	420	200	11.306	15.193	7.496	11.506	14.086	7.975	11.666	13.161	8.390
25	60	25	1.615	1.809	0.892	1.611	1.614	0.914	1.606	1.461	0.932
26	60	25	1.615	1.892	0.934	1.607	1.681	0.952	1.599	1.517	0.967
27	60	20	1.615	2.081	1.027	1.589	1.812	1.026	1.566	1.607	1.024
28	120	70	3.230	7.828	3.862	3.152	6.722	3.806	3.085	5.890	3.754
29	200	600	5.384	50.447	24.890	5.235	43.117	24.411	5.109	37.634	23.990
30	150	70	4.038	11.193	5.522	3.910	9.491	5.374	3.803	8.228	5.245
31	210	100	5.653	18.347	9.052	5.470	15.547	8.802	5.315	13.471	8.587
32	60	40	1.615	3.160	1.559	1.562	2.668	1.511	1.518	2.305	1.469
	3715	2300	100.00%	202.677	100.00%	100.00%	176.362	100.00%	100.00%	156.655	100.00%

Exposed allocation method is taking into account location and power factor by summing belonging parts of losses in all network branches through which some consumer is supplied. It is the best to see comparing of calculation results of loss allocation concerning the nodes 5, 8, 9, and 16 and the nodes 17, 18, 19, 20 and 21 in which loads of the same powers exist. So, for example, loads in the nodes 17 and 18 are of the same powers, but due to unequal distances from source node significantly bigger losses are allocated to the consumer in node 17. In dependence of load type the losses in node 17 are 3.4112%, 3.2858% and 3.1799% for load of constant power type, constant current type and constant impedance type, respectively. For the same power and load type, the losses of 0.1127%, 0.1260% and 0.1386% are allocated to node 18.

Loss allocation method cares about power factor and reactive load flows. It is important because of the fact that reactive powers impact on amount of active power losses in great extent. So, the consumer in node 31 has greater active power and it is situated on bigger distance, but it shares in the losses less than consumer in node 29, which have distinctly bad power factor.

This example shows there is no proportion between the shares of active powers of individual consumptions in total power toward the shares of individual consumptions in network losses. In concrete example, the biggest losses in accounts of 24.8902%, 22.853% or 21.0217% depending on load type, are allocated to node 29, although it shares with 5.383%, 5.236% and 5.109% in network active power. The least losses are allocated to node 18.

The results from Table 1 show that load type impact in great extent as on total losses value as on allocated losses in the nodes (Fig. 3). However, comparing allocated losses in the nodes, for different load types, expressed in percentage of total losses, shows then the difference is much less (Fig. 4). With load type changes it comes to insignificant reallocation of percentage losses. The consumers located close to source node accept proportionally bigger allocated losses if they are

of constant impedance than if they are of constant power. For distant ones it is opposite, what can be seen on Fig. 4.

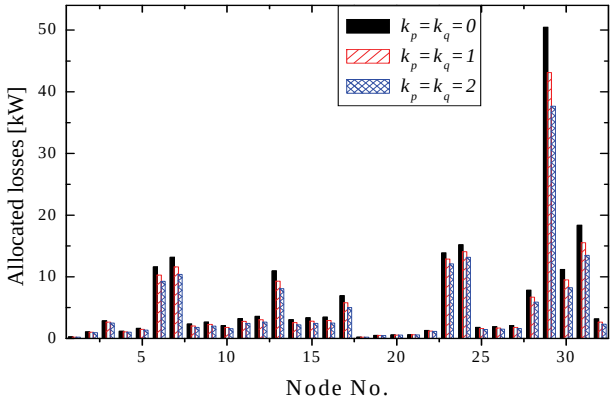

Fig. 3. Allocated losses in the nodes for different load types

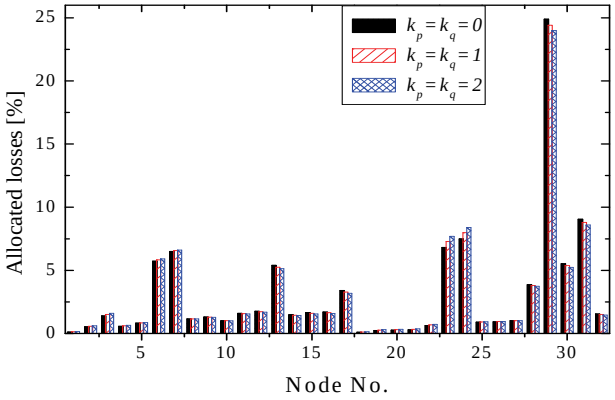

Fig. 4. Percentage values of allocated losses for different load types

TABLE II
ALLOCATED LOSSES TO NODE 29 FOR INDIVIDUAL LOAD TYPES IN DISTRIBUTION NETWORK

Load type	Allocated losses to node 29					
	$k_p = k_q = 0$		$k_p = k_q = 1$		$k_p = k_q = 2$	
	[kW]	[%]	[kW]	[%]	[kW]	[%]
Constant ppower	50.44	24.89	44.91	22.85	40.20	21.02
Constant current	48.11	26.45	43.12	24.41	38.83	22.56
Constant imped.	46.16	27.88	41.58	25.84	37.63	23.99

In some distribution network all loads are not of the same type. As a rule, they are different with unequal self-regulation coefficients for active and reactive power. With load type changing the total losses are changing also and certainly allocated losses in the nodes. From many possible combinations, three hypothetic cases are considered here. Load type is changed only in one node and all others are of the same type: a) constant power, b) constant current, c) constant impedance. A node number 29 is chosen for load type variations as the node with greatest allocated losses. Calculation results are shown in Table 2. In nine analyzed combinations, the losses allocated to node 29 are varying in the range from 37,643kW to 50,477kW in dependence on load type or in percentage from 21,022% to 27,884%. This example shows it is necessary to regard load type in every node to make fair loss allocation.

Due to the fact that load level in the nodes varies during the day, allocated losses of active power will be varying also. Therefore it is necessary to repeat the procedure of power loss allocation for every hour or another time interval. On that way allocated losses per nodes can be obtained. By implementation of complete procedure of loss allocation for longer period, for example a season or a year, loss factor could be established for distribution network and for the part of network supplied from some node.

IV. CONCLUSION

This work gives presentation and comparative analysis of calculation results of loss allocation in distribution networks for different load types. It is shown that load type in great extent impact on the level of allocated losses. Calculation results could be used as the basis for criterion choice for power and energy account and for forming one more impartial tariff system.

ACKNOWLEDGEMENT

This paper is the result of the project “Development, realization, optimization and monitoring of a 5kW grid-connected modular sun-tracking photovoltaic system” financially supported by Ministry of Science and Technological Development, Republic of Serbia.

REFERENCES

[1] C. N. Macqueen, M.R Irving “Algorithm for the allocation of distribution system demand and energy losses“, IEEE Trans. on Power Systems, Vol.11, pp 338-343, 1996.

[2] J. Mutale, G. Strbac, S. Curcic, N. Jenkins, “Allocation of losses in distribution systems with embedded generation,” *Proc. IEE Gen. Trans. Dist.*, vol. 147, no. 1, pp. 7-14, 2000.

[3] D. Stojanović, I. Mladenović, L. Korunović, “Loss Allocation in Distribution Networks” (in Serbian), Elektroprivreda, No. 1, pp. 36-43, 2007.

[4] P. Costa, M. Matos, “Loss Allocation in Distribution Networks With Embedded Generation“, IEEE Trans. on Power Systems, Vol.19, No. 1, pp 384-389, 2004.

[5] R. Ćirić, “Loss Allocation in Distribution Systems with Small Generators” (in Serbian), Elektrodistribucija, Vol. 31, No. 1, pp. 24-30, 2003.

[6] D. Stojanović, L. Korunović, “The Analysis of Load Types Influence on Distribution Network Calculation Results” (in Serbian), Elektroprivreda, No. 1, pp. 76-81, 2000.

[7] M. E. Baran and F. F. Wu, “Network Reconfiguration in Distribution Systems for Loss Reduction and Load Balancing“, IEEE Trans. on PWRD, Vol. 4. No 2. pp. 1401-1407, 1989.

[8] R. Cespedes G., “New Method for the Analysis of Distribution Networks“, IEEE Trans. on PWRD, vol. 5, No. 1, pp. 391-396, 1990.

Selection of DG Units and Location in Radial Distribution Networks

Milena Ciric[1], Nebojsa R. Kreckovic[2], Miroslav O. Veselinovic[3], Dobrivoje P. Stojanovic[4]

Abstract – **This paper presents a methodology of optimal power selection and procedure for finding convenient location of distributed generations (DG) in the aim of total real power loss reduction in the radial distribution networks. This methodology is based on exact formula for real power losses in distribution network. Impact of DG size and location to real power losses has been investigated. Calculation results are illustrated on standard IEEE 32 node MV distribution test network.**

Keywords – **Distributed generation, Radial distribution network, Power losses**

I. INTRODUCTION

The share of distribution generation in power systems has been slowly increasing in recent years. There is an initiative to promote DG and it means that number of the generators will be quickly increasing, especially in distribution systems. Definition of distribution production assumes different shapes on the markets in different countries. Usually it is defined as production plant serving consumer on the spot or support distribution network. Distribution generator is electric energy source connected directly to distribution network. DG can be considered as one option for energetic problem mitigation with who power system is confronted and to cope with continually increasing of electric energy demand.

The biggest interest is to arrange DG locations in optimal way to diminish power losses of distribution systems and in the same way to improve voltage profile. So, DG must be placed on convenient locations and have suitable size. Unadequate selection of DG location and size can lead to bigger losses than in a case without DG. Due to it, it is necessary to develop the tools for investigation location and size of DGs. There are many accesses for determination of DG location and size in intention of loss minimisation as: classical method [1], genetic algorithm [2], fuzzy genetic algorithm [3], tabu search [4] and analytic accesses [5-9].

There are two accesses. The first one determinates optimal DG location and size supposing that DG can be installed in every node without any constraints. According the second, analytic principle, one optimal size and location is searched on the base of current flows for supposed load distribution along the line. Often so called "Golden Rule" or "2/3 rule" is used when DG is installed with size equal to 2/3 of total consumption power at the distance of approximately 2/3 of line length. This rule is simple but can be applied only at radial lines with equal distributed load alongside the line. Paper (9) gives analytical expressions for optimal size and location for different load distributions alongside the line.

In [6], DG location and size is determined on the base of sensitivity factors. Although, it is shown that sensitivity factors are not reliable indices of DG location, especially at radial distribution networks with bigger DG units.

This paper shows the methodology where optimal DG size is determined on the base of simple analytical expressions, and then optimal DG location is selected by loss diminishing search. Section II gives survey of the methodology of optimal DG size calculation. Section III shows numerical results on IEEE the 33-node test distribution network, remarks and discussion also. At the end, the conclusions are summarized in section IV.

II. METHODOLOGY

Total active power losses, ΔP, in distribution network with n branches are obtained as a sum of losses in some branches,

$$\Delta P = 3\sum_{i=1}^{n} R_i J_i^2 , \tag{1}$$

where R_i is resistance of branch i and J_i is the magnitude current flow in branch i.

The branch current can be obtained from the load flow solution. The branch current (J_i) has two components, active component (J_{ai}) and reactive component (J_{ri}). The losses associated with the active and reactive components of branch currents can be written as

$$\Delta P = \Delta P_a + \Delta P_r . \tag{2}$$

$$\Delta P = 3\sum_{i=1}^{n} R_i J_{ai}^2 + 3\sum_{i=1}^{n} R_i J_{ri}^2 . \tag{3}$$

For a given configuration of a single source radial distribution network, the losses ΔP_a associated with the active component of branch current can not be minimized because all the active power must be supplied by the source at the root bus. However by placing DGs, the active components of branch currents are compensated and losses due to active

[1]Milena Ciric is with the High School "17. Septembar", Vuka Karadica 19, 14224 Lajkovac, Serbia E-mail: milena.ciric@hotmail.com.

[2]Nebojsa Kreckovic is with Electrical distribution company „Elektrokosmet", 28000 Kosovska Mitrovica, Serbia, E-mail: nkreckovic66@gmail.com.

[3]Miroslav Veselinovic is with the Faculty of Electronic Engineering, Aleksandra Medvedeva 14, 18000 Nis, Serbia E-mail: miroslav.veselinovic@elfak.ni.ac.rs.

[4]Dobrivoje Stojanovic is with the Faculty of Electronic Engineering, Aleksandra Medvedeva 14, 18000 Nis, Serbia E-mail: dobrivoje.stojanovic@elfak.ni.ac.rs.

components of branch currents are reduced. Simultaneously, there is significant change of reactive power losses.

In this work, main interest is active power losses ΔP_a in distribution network. DG influence to reactive power losses and voltages is neglected. It should find optimal DG size and location to obtain biggest decreasing of losses.

The methodology of selection of DG size and location can be explained on the feeder sample with n branches, shown on Fig. 1. Let DG is connected at bus k with current I_{DG} injected in the network.

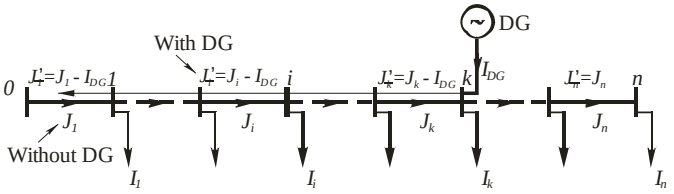

Fig. 1. Radial feeder with DG connected at bus k

As it is shown on Fig. 1, DG connection to system results with current reduction flowing from root substation to the node of DG connection, but there is no influence to branch currents from node k to terminal one n.

The currents of some feeder branches are

$$J_i^{'} = \begin{cases} J_i - I_{DG} & i \le k \\ J_i & i > k \end{cases}. \quad (4)$$

Let DG inject active power and active component of current only I_{DG}. Then, active power losses, $\Delta P_a^{'}$, depending on active components flows of branch currents become

$$\Delta P_a^{'} = 3\sum_{i=1}^{k} R_i (J_{ai} - I_{DG})^2 + 3 \sum_{i=k+1}^{n} R_i J_{ai}^2 . \quad (5)$$

Diminishing (saving) of active power losses is

$$S = \Delta P_a - \Delta P_a^{'} = 3\sum_{i=1}^{k} R_i J_{ai}^2 - 3\sum_{i=1}^{k} R_i (J_{ai} - I_{DG})^2 . \quad (6)$$

Maximal saving is obtained when derivation of (6) by I_{DG} is equal to zero,

$$\frac{dS}{dI_{DG}} = \Delta P_a - \Delta P_a^{'} = 2 \cdot 3\sum_{i=1}^{k} R_i (J_{ai} - I_{DG}) = 0 . \quad (7)$$

From Eq. (7) follows that maximal saving is obtained when DG current is

$$I_{DG} = \frac{\sum_{i=1}^{k} R_i J_{ai}}{\sum_{i=1}^{k} R_i} . \quad (8)$$

Corresponding active power of three-phase DG will be

$$P_{DG} = \sqrt{3} V_k I_{DG} , \quad (9)$$

where V_k is voltage in the node k. Optimal DG power in each node is determined on the base of Eq. (9). The change of DG active power losses in any node is calculated by Eq. (6). DG with biggest loss changing is "candidate" for a location for one DG placement.

Calculation procedure for determination of DG size and location is carrying out according following algorithm.

1. Load flow calculation for basic case (without DG).
2. Optimal current I_{DG} and power P_{DG} calculation of DG by using Eqs. (8) and (9).
3. Calculation of total active power losses by means Eq. (5) for every node by putting DG of optimal power at this node.
4. Node selection for which we have minimal active power losses (maximal saving) after DG connection at optimal location.
5. To change total active power of the node selected for DG placement for the amount of DG optimal power in that node.
6. To carry out analysis of power/current flows of distribution network with switched on DG.
7. To check is the voltage values are inside allowed borders.
8. If node voltage values ware not inside allowed borders then DG should be omitted from given node and procedure would return to the step 4.

If there was more DGs, next "node candidate" for DG placement, would be determined so that process would be repeated assuming that the first DG is put at optimal place and operate with optimal power. Placement of next DG would be justified if significant further loss diminishing achieved. On that way, all locations candidates for DG placement are established.

As DGs are added one by one, the powers obtained by each DG placement are optimal locally, so they are not global optimal solution. Global optimal solution was obtained if more DGs would be put in the system simultaneously [4].

III. Simulation Results and Analysis

The methodology of DG optimal size and location calculation is applied on test network of rated voltage U_n=12.66kV containing 33 nodes and 32 branches, shown on Fig. 2 [9]. This is radial distribution network with total consumption power of 3715 kW and 2300 kVAr. Load flow and voltage calculation is made according power summation method. After iterative procedure finishing, power and current flows are obtained, and current components along network branches also. On the base of them power losses in each branch and total network losses are calculated.

At root node voltage $U_0 = 12.66$kV and at basis loads, total active power losses are $\Delta P = 202.677$ kW, power losses depending on active component of current are $\Delta P_a = 135.527$ kW and power losses depending on reactive component of current are $\Delta P_r = 67.150$ kW.

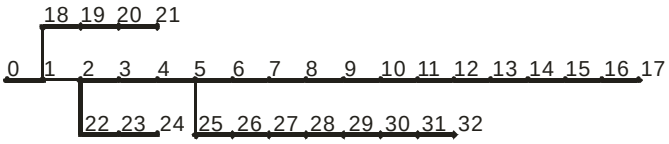

Fig. 2. Single-line diagram of the test network

On the base of established currents along network branches, optimal DG currents and powers are calculated according Eqs. (8) and (9), respectively. Optimal DG powers are shown on Fig. 3.

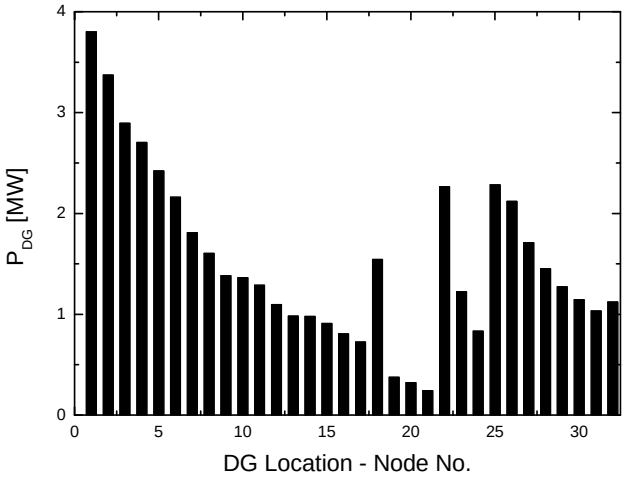

Fig. 3. Optimal DG powers for every nodes

Maximal loss diminishing appears when DG of power $P_{DG} = 2.4218\,\text{MW}$ is installed at the node 5. By DG integration in distribution network all branch currents are reduced from root node to the node number 5. Fig. 4 shows active current components along the branches before and after DG installing. Active current component of supply (the first) branch is diminishing from 178.6348A to 63.6279A. Simultaneously, total current is decreasing from 210.3644A to 125.6622A (reduction is 59.97%).

By current reduction, active power losses along branches are reduced, what is shown on Fig. 5. By installing DG total active power losses fall to $\Delta P' = 104.2926\,\text{kW}$.

DG installing results better voltage conditions. Voltage profile at network nodes with and without DG is shown on Fig. 6. Voltages of outskirts nodes 17 and 32 are increasing for 3.922% and 3.896%, respectively.

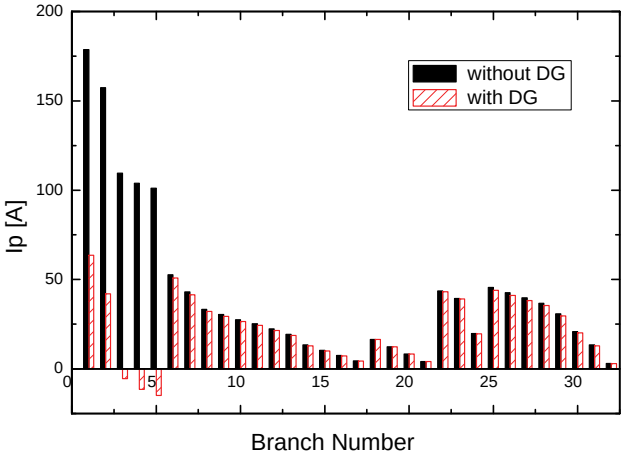

Fig. 4. Active components of branch currents with and without DG

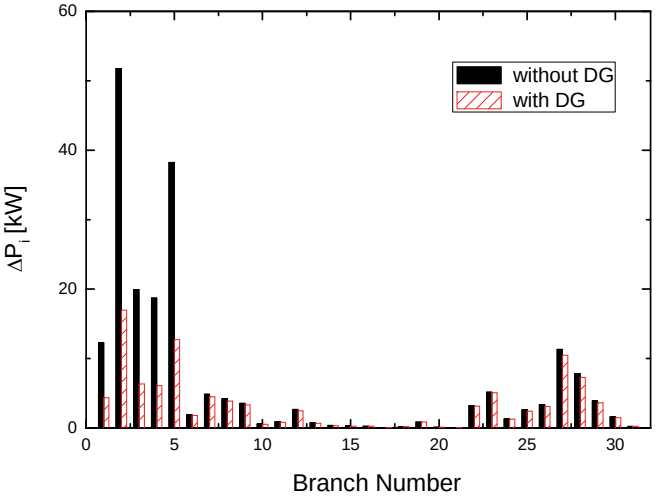

Fig. 5. Active power losses of each branch with and without DG

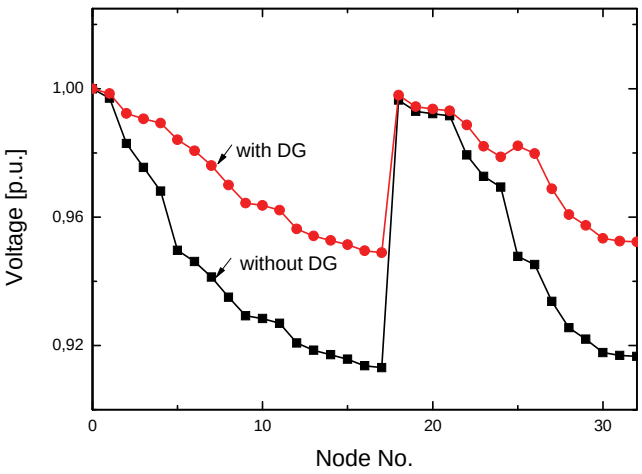

Fig. 6. Voltage profile of the test network with and without DG at the node number 5

Often the size of DG is limited. If DG is mobile one, logic question arises where to connect DG to achieve minimal network losses. Investigations are carried out for four different powers of DGs (0,5MW, 1MW, 2MW and 3MW). Active power losses of the test network for four different sizes of DG are shown on Fig. 7.

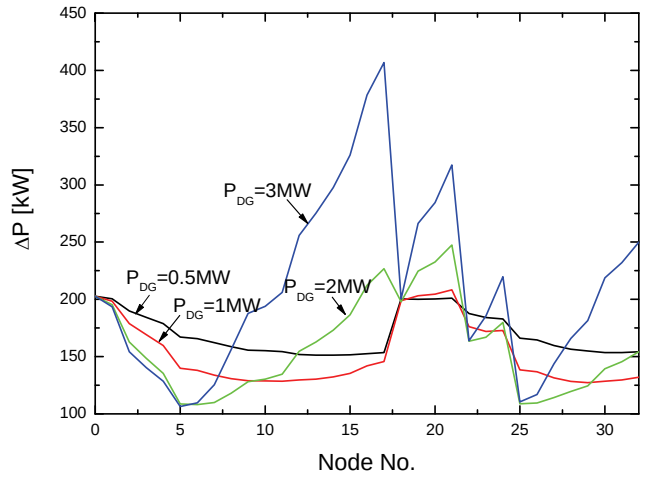

Fig. 7. Active power losses for different sizes of DG at single nodes

Obviously, contribution of DG to losses diminishing depends very much on the place of connection (DG location). So, efficiency of DG of the least power grows if it is connected further from root node.

DG of small power is the best to connect to the nodes 17 or 32, to most far nodes. DGs of powers 2MW and 3MW should be connected to the node 5 or 6. DG connection of power 3MW at the nodes 11, 12, 13, 14, 15, 16, 17, 19, 20, 21, 24, 30, 31 and 32 is increasing losses. Negative effect is bigger if DG is closer to terminal node. From this we can conclude that loss sensitivity to active consumption power at the node is not reliable index for selection of DG optimal location.

IV. Conclusion

This work shows the methodology of finding optimal DG size and location for maximal reduction of active power losses in radial distribution networks. The method is simple, fast and gives results of sufficient exactness. DG location is established by search of results of loss diminishing for calculated optimal powers for every node. Although this paper analysis the case of single DG putting, this procedure can be used for calculation DG location and size in more nodes. By installation of DG at optimal location, total power losses in the system are reduced drastically, and voltage profile is improved also.

Acknowledgement

This paper is the result of the project “Development, realization, optimization and monitoring of a 5kW grid-connected modular sun-tracking photovoltaic system” financially supported by Ministry of Science and Technological Development, Republic of Serbia.

References

[1] S. Rau, Y.H. Wan, „Optimum location of resources in distributed planning“, IEEE Trans. Power Syst. vol. 9, 2014–2020, 1994.

[2] M. Mardaneh and G. B. Gharehpetian, “Siting and sizing of DG units using GA and OPF based technique,” Proc. TENCON 2004, IEEE Region 10 Conference, vol. 3, pp. 331-334, 2004.

[3] K. H. Kim, Y. J. Lee, S. B. Rhee, S. K. Lee, and S. K. You, “Dispersed generator placement using fuzzy-GA in distribution systems,” Proc. IEEE Power Eng. Soc. Summer Meet., vol. 3, pp. 1148–1153, 2002

[4] K. Nara, Y. Hayashi, K. Ikeda, T. Ashizawa, „Application of tabu search to optimal placement of distributed generators“, Proc. IEEE PES Winter Meeting, Vol. 2, pp. 918–923, 2001,

[5] C. Wang, M.H. Nehrir, „Analytical approaches for optimal placement of DG sources in power systems“, IEEE Trans. Power Syst. Vol. 19, no. 4, pp. 2068–2076, 2004.

[6] N. Acharya, P. Mahat, N. Mithulananthan, „An analytical approach for DG allocation in primary distribution network“, Int. J. Electr. Power Energy Syst. Vol. 28, no. 4, pp. 669–678, 2006.

[7] W. Caisheng and M. H. Nehrir, “Analytical Approaches for Optimal Placement of Distributed Generation Sources in Power Systems“, IEEE Transactions on Power Systems, vol. 19, no. 4, pp. 2068 – 2076, 2004.

[8] T. Gözel, M.H. Hocaoglu, „An analytical method for the sizing and siting of distributed generators in radial systems“, Electric Power Systems Research, vol. 79, no. 6, pp. 912–918, 2009.

[9] M. E. Baran and F. F. Wu, “Network Reconfiguration in Distribution Systems for Loss Reduction and Load Balancing“, IEEE Trans. on PWRD, vol. 4, no. 2, pp. 1401-1407, 1989.

Study of Power Quality Indexes and Consumption Regimes in Electrical Distribution System of "Albena" Resort

Rumen Kirov[1], Valentin Gyurov[2], Vladimir Chikov[3]

Abstract – **In this paper are shown methods and technical solutions for determining of power quality indexes and consumption regimes in electrical distribution system of Albena Resort. The research proposes technical solutions for improving energy efficiency of electrical distribution system. Study gives assessment of effectiveness by application and installation of reactive power compensation systems in electrical distribution system of Albena Resort.**

Keywords – **Energy Efficiency, Power Quality, Electrical Distribution Systems.**

I. Introduction

To achieve the task of research, studying of electrical quantitative and quality indexes is made. Measurement system is used, based on network analyzers, which identify the values, ranges and deviation of different electrical parameters. On their base are evaluated some technical-economic indicators, such as relative increasing of active power loss caused by reactive, unbalance power and harmonic power. Based on the results some technical decisions are obtained for application of reactive power compensating systems. The research shows particular example, but the approach is applicable for similar objects and distribution systems.

II. Object Description

Last years, due to tourism sectors growth, in Republic of Bulgaria many new and reconstructed existing hotel resorts were built. They are very specific object as regards to electrical consumption, because they are directly related to annual loading and they use specific electrical equipment. The installed load of the largest, like Albena Resort is about 20÷50 MVA, which makes researches for improving power quality and energy efficiency reasonable. In the large hotel complexes, electrical equipment, determining the consumption regimes, can be divided into the following main groups, each of which has its specific characteristics:

- Main electrical installations – interior lighting and household equipment;
- Ventilation and Air Conditioning Systems (HVAC) in hotel rooms and public premises (restaurants, bars, fitness and spa centers, etc.);
- Technological equipment – hot and cold cooking, heaters, ovens, cold-storage rooms;
- Water supply and sewerage equipment - pumps, pressure boosting equipment, etc.;
- Exterior lighting – facade, street, park and security lighting, etc.
- Transport equipment – escalators, elevators, etc.

For each group, electrical equipment determines the performance of electric consumption and quantitative and quality indexes of power quality. Characteristics can be classified in the most general form as:

- Low power factor - a big part of interior lighting is made up of gas discharge lamps without compensation. The majority of HVAC facilities and water supply equipment using asynchronous motors without local compensation;
- Asymmetry of electrical power - caused by the random nature of the switching of single phase loads and single phase installations to three-phase network;
- Presence of harmonic currents - main source is HVAC systems, high power frequency inverters, lighting equipment, household appliances and motor drive equipment.

This shows the necessity of performing a research aimed defining of conventional power loss and reducing power loss in condition of non-linear and non-symmetrical regimes in resorts electrical distribution systems.

III. Practical Research

For 3 months, during the summer period (touristic season) in 2010, 22 electric power substations in the Albena Resort electrical distribution system registered various regimes of electrical consumptions and power quality.

Albena Resort Electrical Distribution System Topology

Electrical distribution system has triple "closed-loop" scheme on medium voltage 20 kV including 22 power transformer substations. The "closed-loop" scheme (three medium voltage feeders 'A", "B" and "C") are shown in Fig. 1, Fig.2 and Fig.3

[1]Valentin Gyurov is with the Faculty of Electric Power Engineering, Studentska 1, 9010, Varna Town, Republic of Bulgaria E-mail: vgiurov@yahoo.com.

[2] Rumen Kirov is with the Faculty of Electric Power Engineering, Studentska 1, 9010, Varna Town, Republic of Bulgaria E-mail: kvc_electroinvest@yahoo.com.

[3] Vladimir Chikov is with the Faculty of Electric Power Engineering, Studentska 1, 9010, Varna Town, Republic of Bulgaria E-mail: vladimir_128@abv.bg.

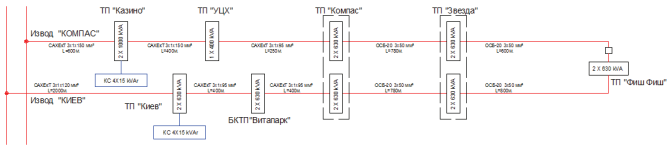

Fig. 1. Albena Resort Feeder "A" 20 kV

Fig. 2. Albena Resort Feeder "B" 20 kV

Fig. 3. Albena Resort Feeder "C" 20 kV

In order to achieve the task of studying is used specialized power meter production of ABB USA composed of the following components:

- ABB Power Plus type A1RL+ with accuracy class 0.2 with additional secured current and voltage circuits;
- IRDA to RS232 converter;
- portable PC;
- Power Plus Diagnostic Software (PPDS) v.1.08 developed by ABB Power T&D;

For the study purposes a specialized algorithm in MathCAD is used. System allows collaboration between other digital power meters after consultation of the source data format with the developed algorithm in MathCAD. In the case the starting file is DAT format with certain size. The whole file, containing the measured value is assigned as a matrix named "data" and after that values for analysis are derived from it. Therefore, only by a change in the matrix name, MathCAD automatically makes the analysis of a new study object. Defining variable *point*s that show the *number* of measurement points for each file: *points = rows (data)*, but also counters j and v : *j=0…points-1 v=2.5 points-1*. Counter i is set from the second row of the matrix (the first is text showing the measured value) till the last one *(points -)* in tree values because the phase values for each measurement alternate by rows. Matrix contains values for the first harmonics of currents and voltages (Ia, Ib, Ic ; Va, Vb, Vc) and values to the fifteenth harmonic in percents of the first one. Moreover, the matrix contains the phasing angles PhAngB and PhAngC of the voltages Ub and Uc refer to Ua, phasing angles of the currents to appropriate voltages PFA, PFB and PFC reported from the first harmonic.

Calculating of the active power (P), non-symmetry power (mod N) and harmonic power (D) is possible by using of the primary indexes. Total power can be defined by Eq. 1 [1]:

$$S_j = \sqrt{(P_j)^2 + (Q_j)^2 + (N_j)^2 + (D_j)^2} \quad (1)$$

Real power factor can be calculated by Eq. 2:

$$Km_j = \frac{P_j}{S_j} \quad (2)$$

Then increase of partial power losses is given by Eq.2, Eq. 3 and Eq. 4 [1]

$$\Delta Pq_j = \frac{Q^2{}_j}{P^2{}_j} \cdot 100,\% \quad (3) \qquad \Delta Pn_j = \frac{\mathrm{mod}\, N^2{}_j}{P^2{}_j} \cdot 100,\% \quad (4)$$

$$\Delta Pd_j = \frac{D^2{}_j}{P^2{}_j} \cdot 100,\% \quad (5)$$

$$Sum\Delta P_j = \Delta Pq_j + \Delta Pn_j + \Delta Pd_j \quad (6)$$

$$DP_j = \left(\left(\frac{S_j}{\mathrm{mod}\, Sa_j} \right)^2 - 1 \right) \cdot 100 \quad (7)$$

The index DP shows increasing of active power loss in conditions of non-symmetry and harmonics, compared to power loss in ideal regime.

Examples for these indexes and characteristics for a substation 1000 kVA are shown in Fig. 4, Fig. 5 and Fig 6.

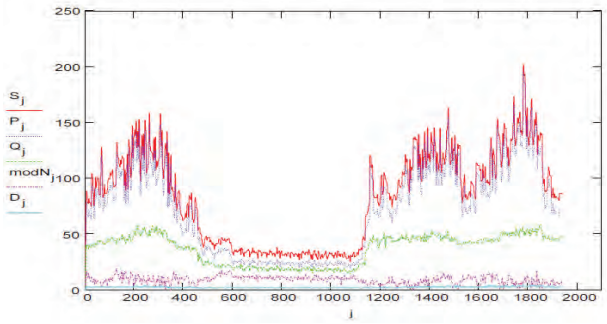

Fig. 4. LV/MV Substation – P, Q, modN, D and S for one day

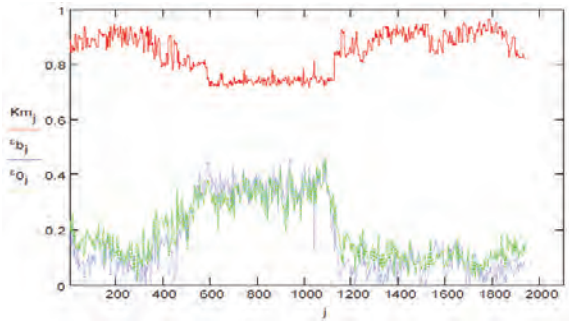

Fig. 5. LV/MV Substation – Km, εb and ε for one day

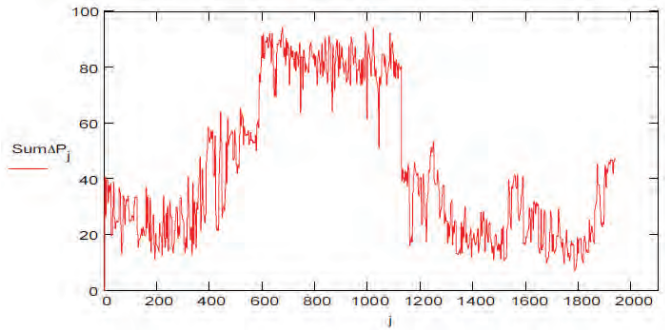

Fig. 6. LV/MV Substation SumΔP

Use of cosφ-P plan

The cosφ-P plan [2] is applicable for defining power loss in substation transformers in conditions of non-liner load and non-symmetry. Basic cosφ-P plan is given by Eq. 8

$$\delta(P,\cos\varphi)=\left[\frac{Po+\left(\frac{Pk}{S_H{}^2}\right)\cdot\left(\frac{P^2}{\cos\varphi^2}\right)}{P+Po+\left(\frac{Pk}{S_H{}^2}\right)\cdot\left(\frac{P^2}{\cos\varphi^2}\right)}\right]\cdot 100,\% \qquad (8)$$

In conditions of non-symmetry and harmonics, cosφ-P plan changes to Eq.9 [3]

$$\cos\phi_{ND}(P,\delta_{ND})=\sqrt{\frac{P^2\cdot k\cdot\left(1-\frac{\delta_{ND}}{100}\right)}{\frac{\delta_{ND}}{100}\cdot P+\left(\frac{\delta_{ND}}{100}-1\right)\cdot(Po+k\cdot N^2+kD^2)}} \qquad (9)$$

Where k is: $k=\frac{Pk}{S_H{}^2}=const$

Thus, in presence of D and N power, function will be a surface family with two variables (P,δ_{ND}) and two parameters (N, D). The horizontal section of surface family is curves family (Fig. 7).

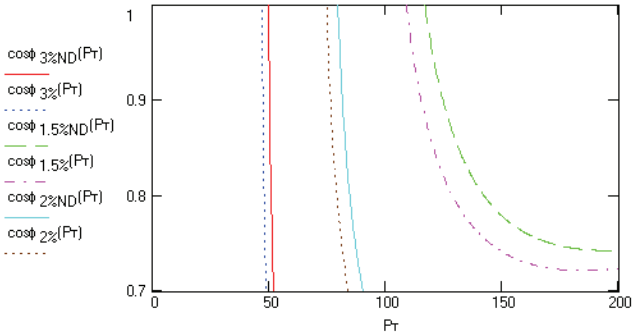

Fig. 7. Zones of δ for 1000 kVA transformer

The regime will be as more effective as the operation point is closer to the right top edge of diagram.

IV. Results

For the following research, an example for power ratio of a substation transformer is given in Fig 8.

Active power loss increase from low quality has three components ΔPq, ΔPn and Δ Pd respectively provoked by

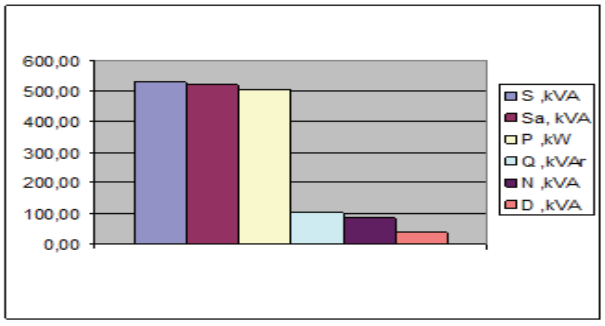

Fig. 8. Power ratio of one transformer in Albena Resort

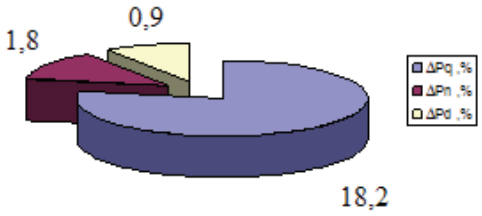

Fig. 9. Ratio of active power loss increasing in condition of non-symmetry and non-linear load

reactive power, non-symmetry and current and voltage harmonics in electrical grids. Total increase of conventional power loss SumΔP in Albena Resort electrical distribution system is about 21%. Fig. 9 shows that the major effect has ΔPq = 18,2% and the lowest one ΔPd = 0.9%

Conventional Δ P% losses represent active power losses in all units and elements associated with the transmission of electricity from power substation to consumer. They can be defined by deterministic methods and the average value is within ΔP% = (6.56÷10.31) % from total active power consumption.

V. Conclusion

Conventional losses depend on electrical distribution systems characteristics and reductions, are associated with changes in these features or system upgrades as a whole. This process is associated with serious capital investment, which recently made a very good efficiency in the Albena Resort.

As mentioned, the purpose of this study is to demonstrate the ability to achieve energy efficiency through influence on the regime parameters of the system.

Maximum economic effect can be achieved by minimizing the ΔSumP. The resultant reduction of active power losses is determined by the expression:

$$\Delta P_{TOTAL} = \Delta P \cdot \left(1 - \frac{Sum\Delta P_{AVERAGE}}{100}\right),\% \qquad (10)$$

The average economic effect of minimizing the negative components Q, N, D and reducing ΔPn, ΔPq, and ΔPd to achieve is saving of active power in the range of (1.32÷1.6)%.

Technical solution for minimizing the losses can be achieved through the implementation of universal compensators. In this case, due to the limited availability of harmonic power and ΔPd, compensation system in scheme “Soldatkina” can be used.

Total investment for application of compensation systems Soldatkina in 22 transformer substations in Albena Resort, low voltage distribution system, is about 150 000 euro. Nominal lifetime of these facilities is about 15 years. The return period for this type technical solution is about 5 years.

REFERENCES

[1] Дрехслер, Р., Измерение и оценка качества электроэнергии при несиметричной и нелинейной нагрузке, Москва, Энергиатомиздат, 1985 г.

[2] Yang M., Yajun Shi, Zhang Jing, “Efficient Operation Regions of Power Distribution Transformers”, IEEE Power Delivery vol.19 No4 2004

[3] Киров, Р.М., В.Н. Гюров, Ц.К. Цонев, Р.Н. Василев, Подобряване ефективността на работа на електрическите мрежи чрез изследване на коефициента на загубите δ в реални експлоата-ционни условия., Енергиен Форум 2005, Сборник доклади том II., стр.343-346.

Exported Potentials in the Grouding System of the Mine „Brod – Gneotino ”

Nikolce Acevski[1] and Alekandar Jurukovski[2]

Abstract - **This paper is presenting the problem of exported potentials in the grounding system of the mines with surface exploitation of minerals. An example is taken from mine Brod - Gneotino near Bitola which is a complex technological technical unit which consists of multiple items such as bulldozers, power stations, belt conveyors, transformers and other consumers. Using the software package MATLAB - Simulink estimated voltage of touch-up and step grounding of all places, and then exceeds to the assessment of conditions of safety of too high touch voltages and steps around various types of grounding.**

Keywords - **grounding system, touch voltages and step.**

I. INTRODUCTION

Export of electricity potentials in buildings in case of fault to ground in HV transmission network is a problem that is given attention because the dangerous consequences that it may cause. This paper was reviewed mine "Brod - Gneotino" which is a complex technological and technical unity and it 6kV cable distribution network is connected to the power transformers T1 and T2 of TS 110/6kV and whose role is to supply powered surface mine in mine. The mine is given special consideration to meet the requirements for safety in 6kV cable network in the 0.4 kV network. The specificity of the elements of the grounding system Mine (earthing Plant 6 / x kV, operating machinery, excavators, transporters, etc.). Despite the complete earthing galvanic connection of the entire system through the protective conductors of cables EpN 78, are also required to ensure conditions of safety regulations defined by the potential of 6kV neutral grounding point, because the mine where about mining systems is always present working staff who serve their level maintenance and occasionally moving (along with their earthing).

When a single-phase short circuit in the plant 110 / 6 kV / kV at the mine or the 110 kV network in the vicinity of the mine that power is distributed to all the earthing system (earthing of the poles of 110 kV transmission lines, earthing of substation110/6 kV and medium earthing the individual consumers). Because mutual galvanic connection of the earthing powered facilities in 6 kV input power network in case of any fault to ground 110 kV network, the metal parts of equipment in the mine could occur potentials considerably higher than the potential of the surrounding soil.

[1]Nikolce Acevski is with the Faculty of Technical Sciences, Bitola, R. Macedonia, nikola.acevski@uklo.edu.mk.

[2]Aleksandar Jurukovski is with the Faculty of Technical Sciences, Bitola, R.Macedonia, acejuruk@yahoo.com.

II. MODELLING GROUNDING SYSTEM

2.1 Modelling mesh grounding and calculation of its grounding resistance.

The TS 110 / 6 kV Brod - Gneotino is set earthing mesh that connects all electrical equipment in the plant. Mesh grounding affecting the entire area inside the fence, beyond which the plants are located 110 and 6 kV, with ancillary facilities. About grounding is placed outside a fence that is separated from the plated mesh grounding.

In this paper calculations are made, more grounding resistance and the corresponding values are shown in Table 1, depending on the applied method.

TABLE 1. GROUNDING RESISTANCE WHICH WAS OBTAINED IN SEVERAL WAYS

Applied methods	Resistance $R_{TS}[\Omega]$
Software - Mrez.zaz	0,783
Model of a circular plate	0,657
Formula Laurent	0,787
Formula Sverak	0,777
Formula Thapar	0,908
Formula Nahman	0,796

From Table 1 we can conclude that the formula of Nahman and Laurent are gained about the closest value to the value of resistance circulation which was obtained by using the software Mrez. zaz.

In this paper calculations are made for the percentage values of touch voltage and step Ed% and Ec% and the TS 110 / 6 kV by using the software package (Zazem), and is: Ed = 30.2% and Ec = 5,8%.

2.2 Modeling of overhead lines with protective rope

Overhead lines also participate in exports of currents and potentials in case of short links in the 110kV system, and because any such line should be represented in an appropriate manner so-called "π- replacement scheme". Protective rope is of the type OPGWAA / St 77/43 - 10,3 Fe from 50 mm^2, and a range of power lines lj = 320m.

Impedance of the protective conductor (cable) for a span is calculated according to the formula:

$$\overline{Z_{r1}} = (r_j + jx_j)\cdot l_j = (1{,}322 + j0{,}31)\Omega \quad (1)$$

r_j, x_j - active and inductive resistance of the rope per km length

$$r_j = \rho_j \frac{10^3}{S_j} = 4{,}13\Omega / km \quad (2)$$

$$x_j = 0{,}1445 \cdot \log \frac{2 \cdot De}{d_j} + 0{,}016 \cdot \mu_r = 0{,}97\Omega / km \quad (3)$$

dj - diameter of the rope for which Sj = 50mm^2 is: dj = 0,009 m.

De - equivalent distance between the protective conductor and Phase conductors of power lines (m).

Rs - grounding resistance of each of the columns, which for 110 kV is the average power lines: Rs=10Ω.

The equivalent impedance of the grounding of power lines is:

$$\overline{Zek.v} = \sqrt{\overline{Zr_1 \cdot Rs}} - \frac{\overline{Zr_1}}{2} = (2{,}97 + j1{,}61)\Omega \quad (4)$$

2.3 Modelling 6kV cables and characteristics of their models

6 kV cables used for distribution of electricity in 6 kV input power network in the area of the mine, despite the power conductors (three phase conductors), have more and signal conductors or a conductive sheath. Signal conductors (ie conducting sheath) are isolated in terms of land and phase conductors, and the emergence of single-phase short links in 110 kV network through them the export potentials in the grounding system of the mine.

Thus, each cable, watched with its return route across the ground, may be presented with a I-replacement scheme, ie an ordinal impedance Z = z·l. Thus, ie longitudinal impedance impedance per unit length in this case i will be calculated using known formulas Carson-'s:

$$\underline{z} = r + jx = \left(\frac{1000}{k \cdot s} + 0{,}05 \right) + j \log \frac{D_e}{D_S} \quad (6)$$

k [Skm/mm^2] - conductivity specific material from which is made cable signals;

S [mm^2] - total cross section of signal cables;

De [m] - the equivalent depth of return current path across the ground (soil);

ρ [Ω · μ] - average value of the specific resistance of the terrain through which the cable passes;

Ds [m] - own middling geometric distance band signal conductors of the cable.

$D_S = \sqrt[3]{r_p \cdot (D/2)^2}$ - when the signal cable has three conductors, placed in the vertices of an equilateral triangle with side D / 2.

r_p is the radius which is indicated by the conductor signal cable, and D is the outside diameter of the conducting sheath.

2.4 Modelling of grounding of TS 6 / x kV / kV

Each TS 6 / x kV will be modeled with transverse mounted active resistance R. The calculation of resistances is done using the well-known model of high potentials, and to this end it is necessary to know the specific resistance to ground and geometry of each grounding.

2.5 Modelling of auxiliary groundings

Auxiliary groundings of the various types of mining facilities and machines are modeled in an identical manner as the town's transformer stations grounding TS 6 /x kV / kV. It should be noted that cases are possible when more diverse plated grounding are connected to the same grounding spot. In that case, the replacement scheme grounding system will emerge as active resistors connected in parallel as there are various grounding, cadmium connected observed grounding places.

2.6 Modelling the surface grounding

2.6.1 Rails and strips placed on the surface of the earth

Resistance to ground of the sliding bar or a length l and an equivalent diameter d, placed on the surface of the earth, with the average specific resistance of soil is ρ, will be:

$$R = \frac{\rho}{\pi \cdot l} \ln \frac{2l}{d} \quad (7)$$

If the bar is on one end tied to the grounding system and thus is free of its other end, then it will be presented with a transversely mounted active resistance R.

The picture we are given is a replacement scheme of the track when the two ends are connected to different plated grounding.

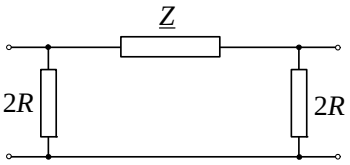

Fig. 1 π- replacement scheme

The value of the parameter Z is calculated by the relation:

$$Z = \left[\frac{\rho_{Fe} \cdot l}{S} + 0{,}05 \right] + j \left[0{,}1445 \log \left(\frac{2D_e}{d} \right) + 0{,}0157 \mu_r \right] \quad (8)$$

ρ_{Fe} [Ω·mm^2/km] - specific resistance of iron

l [km] - the length of rail / bar;

S [mm^2] - cross section of rail / bar;

μ_r - relative magnetic permeability of the material;

De [m] - the equivalent depth of return current path across the country, calculated according to Carson - 's model, using the following relation:

$$D_e = 658\sqrt{\rho / f} \quad (9)$$

d [mm] - equivalent diameter of the bar / rail, with approximately valid $d = 1{,}128 \cdot \sqrt{S}$.

If there is cessation of bar / rail, at least of one place, then the replacement scheme of the picture would have to go to the next branch Z.

2.6.2 Modeling of excavators and other machines with a large land area

Excavators and other mining machinery and buildings that have large land area, with its caterpillars achieve good electrical contact with the ground. Thus, in case of short circuit in a 110 kV network, where they will get some potential, through the said contact lead the current in the ground and in their current environment creates a field that can be dangerous for people who are in their immediate nearby.

For the purposes of modeling the equivalent scheme grounding system, they can be treated as concentrated earthed grounding that the appropriate place of the equivalent scheme would introduce an active resistance Rp. Analyses show that the land surfaces of the excavators, machine with caterpillars and other devices that have contact with the ground surface, can be satisfactorily modeled by a suitable mesh grounding system, mounted horizontally on the ground of a certain small depth h. Moreover reticulated grounding system should have the same geometry as the geometry of land area of the dredge / device, and modeling can only be successfully performed if land surface is replaced by a dense network of horizontal strips, placed on a small distance between (the example D = 50 cm), buried in shallow (eg h = 5 cm).

III. Currents in the Grounding System in Case of Short Connections

The emergence of single-phase short and double, phased ties with a country in 110 kV distribution facilities of the mine "Brod – Gneotino" or at any place of manifolds 110 kV TS 110 / 6 "Brod - Gneotino " - TS 400/110 "Bitola 2 ", comes to leak currents through the earthing of the plant.

Analyses show that the most unfavorable case, in terms of the potential size of earthing, is when it comes to single - phase short circuit occurs in the distribution plant, ie the first pillar of the manifolds 110 kV, as is shown in Fig. 2.

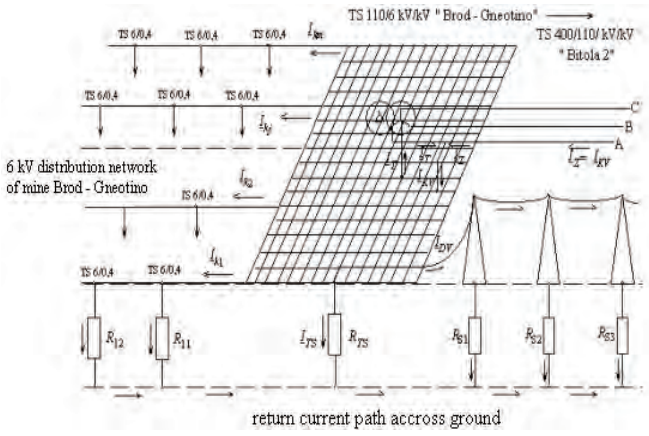

Fig.2 Grounding system in the mine " Brod - Gneotino"

Single - phase current short circuit at 110 kV by the TS "Brod-Gneotino" is calculated using the software package NEPLAN 5.2.2 13610 A and refers to the maximum mode when all units of TEC REK Bitola is in motion.

IV. Results of the Calculations

Resolving GS with a larger number of nodes in a classical way without using a computer is practically unfeasible. This paper will be considered one way of resolving the GS using MATLAB - Simulink, which is basically a simulation program, but can be successfully applied to solve the grounding systems. Simulink (simulation and connection) is an addition to MATLAB working with its support and allows modeling, simulation and analysis of dynamic systems. This program includes a wide range of tools from the library for linear and nonlinear analysis.

For purposes in this paper that current is injected into the system before grounding TS HV/MV in the replacement scheme the grounding system will be modeled with an ideal current generator, with power equal to the injected grounding system set in place of short circuit or in the case, the node that marks TS HV/MV. Assuming current fault anywhere from MV replacement grid pattern remains the same except that the ideal electric generator sets in place of an fault. In this case the site of short circuit is at 110 kV on the TS 110 / 6 kV.

Belt conveyors together with power stations are considered as distributed earthing introducing three nodes in the network (beginning, middle and end).

Using the software package MATLAB - Simulink, estimated distribution of current in short circuit single - phase in GS, the fault of HV side of the TS 110 / 6 kV / kV, and voltage is calculated to touch and move. Grounding system in the mine Brod - Gneotino "consists of 75 grounding posts. In Table 2 there are given grounding places with the touch voltages higher than 200V, ie the highest voltages are obtained. Voltage step is always smaller than the touch voltage.

Table 2. Results of the calculations of voltage and current circumstances of the grounding points in the mine "Brod – Gneotino"

Name	U(V)	Uc(V)	Ud(V)	Iz(A)
TS110/6	1020	36,99	284,1	1303
RP1	700,9	98,13	228,5	182,1
RP4	720,2	100,8	234,8	187,1
TS6/0,4	971,1	174,8	253,4	117,1
RP10	618,2	86,55	201,5	160,6

1. Name of grounding place;
2. Voltage of grounding place;
3. Voltage step of grounding place;
4. Touch voltage of grounding place;
5. Current which is injected in the grounding site.

V. INTERPRETATION OF THE RESULTS OF CALCULATIONS

In assessing whether the calculated touch voltages and step up in limits, should be acceptable:

1. time off of the single - phase short circuit, ie total duration of short circuit, counting from the moment of occurrence of single - phase short circuit until its termination;

2) allowable touch voltages and steps, depending on the time of exclusion, defined by appropriate technical regulation.

The technical regulation in the former Yugoslavia, the allowable touch voltages and steps are given depending on the time of disconnection. Thus, according to the diagram in the article. 111 of the Regulation on technical norms for electricity plants with a rated voltage above 1000 V (Official Gazette of SFRY no. 4 / 74 and no. 13/78), if time off is t = 0,1 s, the allowed voltage step outside the plant is estimated at 320 V, but in the case when it comes to public roads with traffic, the voltage is at 180 V. The question about the amount of allowable touch voltage is processed in the Regulation on technical standards for electrical installations and equipment in mines with surface mining of mineral raw materials (quarries) [5]. Under article 29 of the Rules, if the time off of the short circuit was 0,1 seconds, the allowable touch voltage is 300 V. According to U.S. standards (ANSI / IEEE Std80-1986), the lowest values touch voltages and step for a man whose weight is 50kg is calculated by the formula:

$$\Delta U_{d.doz} = \Delta U_{c.doz} = \frac{116}{\sqrt{t}} \tag{10}$$

for a man weighing 70 kg, with the formula:

$$\Delta U_{d.doz} = \Delta U_{c.doz} = \frac{157}{\sqrt{t}} \tag{11}$$

We can conclude that the value here is higher and is 367V for a man who is 50kg.

From here you can draw the conclusion that if the time off of the single - phase short circuit occurred in the 110 kV network is 0,1 seconds, allowed to touch voltage or voltage step, in accordance with Rule [5] is:

$$\Delta U_{d.doz} = \Delta U_{c.doz} = 300 \text{ V} \tag{12}$$

The values of specific resistances to ground in the area of the mine ranges from $25 < \rho < 100$ Ωm, Sd correction factor for the touch voltage ranges from 1,04 to 1,16, while correction factor Sc for the touch voltage ranges within the limits of 1,31 to 1,63.

From the above we can conclude that these values are too high and it illustrates the severity of the cited regulations. The presence of adequate equipment (rubber boots, gloves, etc.) in an even greater extent to increase these differences, and consequently the calculated results will always give a pessimistic picture regarding the actual risks and hazards of electric shock.

VI. CONCLUSION

Problem analyzed in this paper belongs to the rare events but its importance is undeniable in terms of security of the people who serve. During the studies carried out in preparation of this paper is developed in detail at the GS mine Brod - Gneotino, developed detailed models of power cables with insulated metal sheathed type EpN 78, and models of overhead lines with protective rope with a nominal voltage 110 kV and analyzed in details reticulated earthing, also is calculated its resistance circulation and calculated the percentage of touch voltages and step through computer programs Mrez.zaz and Zazem and using a developed software package NEPLAN 5.2.2 is prepared part of the power system around TE REK Bitola, which is calculated single – phase short circuit current of the HV side of the TS 110/6kV/kV of "Brod - Gneotino" and with the maximum mode generator when all are in operation. Using the MATLAB software package it is calculated the distribution of current in short circuit in single-phase GS fault on HV side of the TS 110/6kV/kV Brod - Gneotino and it is calculated touch voltages and step grounding of all places.

From the results we can observe that there is no danger of too high touch voltages and steps along the shipping lanes through the mine. Possible occurrence of a critical voltage is only in the vicinity of their home so they can be modeled by a concentrated active resistor placed in their home whether both their ends are connected to different plated grounding stations.

After determining the distribution of the currents and potentials of the grounding system, is applied to evaluate the safety conditions of excessive stress on the touch and move around the various types of earthing in accordance with existing regulations listed above, which are largely related to unjustifiably increasing costs for construction of earthing. In this context it is necessary to emphasize the need of revision sooner or mitigation of these regulations.

REFERENCES

[1] R. Ackovski: " Visokonaponski mrezi i sistemi", ETF – Skopje, 1995 god.

[2] R. Ackovski: "Zazemjuvaci i zazemjuvacki sistemi vo elektroenergetskite mrezi", septemvri 2006 god.

[3] D.Vidanovski, M.Stojanovski, B.Dungovski i N.Stojanovski "Analiza za sprecuvanje na izvos na opasni potencijali po transporterite na Rudnik Suvodol". Elaborat izraboten za potrebite na REK- Bitola, 1993 god.

[4] N.Acevski, "Prilog kon modelite za resavanje i analiza na zazemjuvaci i zazemjuvacki sistemi", doktorska desertacija, ETF–Skopje, 2003 god.

[5] Pravilnik za tehnickite normative na elektricni postrojki i uredi vo rudnicite so povrsinska ekspoloatacija na mineralni surovini. "Sl. List na SFRJ br. 66/87".

[6] D.Rajicik, "Analiza na elektro energetski sistemi", ETF – Skopje 1996 god.

[7] N.Acevski, R.Ackovski, "Prilog kon postapkata za dimenzioniranje na mrezest zazemjuvac na TS VN/SN", Referat na MAKRO – SIGRE, Ohrid 2004 god.

[8] R.Ackovski, R.Talevski, Programski paket ZAZEM, Elektrotehnicki fakultet – Skopje 1991 god.

[9] Katalog za stolbovi so nadzemni vodovi so nominalen napon 110 kV (EMO – Ohrid), Skopje 2003god.

[10] D. Tasic, "Osnovi elektroenergetske kablovske tehnike" maj 2001 god.

[11] J.Nahman, V.Mijailovic, “Odbrana poglavja iz visokonaponskih postroenja”,Akademska misao, Beograd 2002 god.

Comparative Analysis of Power Losses in Overhead Power Lines for High Voltage, for Different Parameters of the Aluminum Wires

Yulian Rangelov[1]

Abstract – **With regard to the widening use of renewable energy sources, it becomes necessary to increase the transmission capacity of the existing lines, exporting the produced electric energy to the power distribution system. This paper discusses an exemplary closed electric network for high voltage (110 kV). In view of the need to increase the transmission capacity two options are considered: increasing the cross-section of wires and replacement of traditional steel-aluminum wires with super heat resistant ones. A comparative analysis is made of power losses in both cases.**

Keywords – **Renewable energy sources, Transmission capacity, high voltage overhead powerlines.**

I. INTRODUCTION

The rapid development of electricity production from renewable sources and the requirements of the European Union in this area led to the need for a change in the strategies of the power system of Bulgaria. A typical example is the construction of wind farms in Northeastern Bulgaria. This region has a well-established power grid, whose capacity cannot meet the increasingly growing number of wind farms. The rapid construction of new lines or replacing the old lines with new ones of larger capacity could solve the problem, but the procedures on land expropriation and negotiations with local authorities would take a long time. A possible solution would be to increase the cross-section of the wires of the available high-voltage power lines (entailing a new mechanical sizing and replacement of poles, insulators and supporting fixtures) or to replace only the wires with so-called superheat resistant wires of the same cross-section (no need for replacement of poles here). The purpose of this paper is to assess the advisability of either option: fitting the power lines with superheat resistant wires or increasing the cross-sections.

II. ARRANGEMENT OF THE TASK

Fig. 1 shows the structural design of a looped power network for high voltage. It connects to the power grid through nodes 1 and 13. It is designed to supply 10 local sub-stations (nodes 2, 3, 6 ÷ 13). Two large wind farms are connected to it, their installed capacity being 156MW and 35MW in nodes 4 and 5. A multitude of small wind farms (with total installed capacity of approximately 200MW) are connected to the distribution network of medium voltage; on the diagram, they are presented as equivalent sources while accounting for the circumstance that part of the power produced by them is utilized by consumers and thus it is not transmitted to the discussed network. All wind farms are presented as equivalent generators using PQ model, i.e. with assigned active and reactive power.

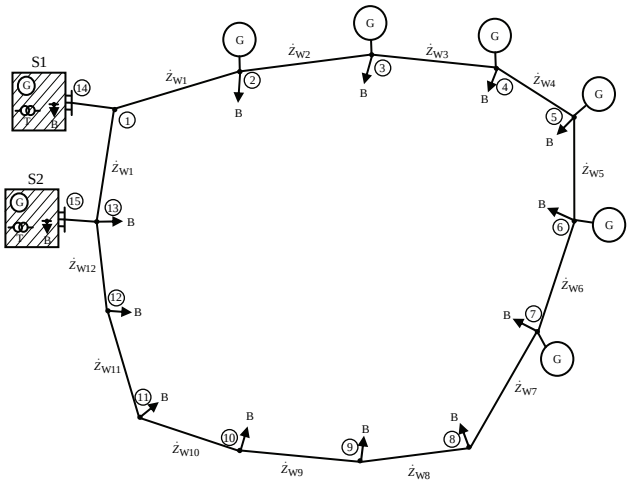

Fig. 1. Structural design of the discussed power network

All power lines are overhead and are presented by Π-shape equivalent circuits, taking into account their longitudinal and transverse parameters (Table I) without the active conductivities to the earth, and taking into account the crown effect and leakages. The active resistance of the wires is calculated at maximum permissible temperature, which is 70°C for conventional steel-aluminum wires, whereas for superheat resistant ones it is 210°C. Their total length is 267 km.

All three kinds of wires are combined alloys of aluminum and steel. The designations AC/ACO show the ratio of aluminum/steel: - AC (normal) - s_A/s_C = 5:1÷6:1;-ACO (reduced) - s_A/s_C = 8:1. The third type (ZTACIR) is s superheat resistant wire of aluminum alloy with zirconium, reinforced with iron-nickel alloy (invar) [1,2,3,4]. The wire is so designed that it would not sag down at temperatures of the order of 200°C. The maximum operative temperature is determined based on reduction of the physical and mechanical properties by 10% during the whole period of operation. Because the amount of zirconium in the alloy is small, the characteristics of the wires based on these alloys do not differ much from AC with the exception of their increased specific resistance.

[1]Yulian Rangelov, Faculty of Electrical Engineering, Electric Power Engineering department, Technical University of Varna, Bulgaria, E-mail: j.rangelov@tu-varna.bg

Table II shows the values of maximum permissible currents of the different wires [4.6]. A simulation has been made of a mode of maximum consumption in the presence of wind allowing maximum generation of all wind farms. The aim is to achieve as high generation as possible, while not exceeding the permissible currents for the cross-sections under consideration here and keeping the voltage at the nodes of the network within 98 ÷ 123 kV [5]. Three options are discussed, and the entire network is built with one of the wires indicated in Table. I. Calculations are made with Prof. Federico Milano's [7] program PSAT (Power System Analysis Toolbox).

TABLE I
PARAMETERS OF THE POWER LINES

Conductor type	r_o	x_o	C_o
	Ω/km	Ω/km	F/km
AC-185	0.1920	0.4043	$9.00931 \cdot 10^{-9}$
ACO-400	0.0888	0.3816	$9.57003 \cdot 10^{-9}$
ZTACIR-185	0.2783	0.4043	$9.00931 \cdot 10^{-9}$

TABLE II
MAXIMUM PERMISSIBLE CURRENTS AND OPERATIVE TEMPERATURE

Conductor type	$I_{доп}$	$\theta_{раб}$
	A	°C
AC-185	500	70
ACO-400	815	70
ZTACIR-185	906	210

III. RESULTS FROM CALCULATIONS

Calculations have been made at three stages:

1. Modeling of the design with wires AC-185, connecting consumers and adding power generated by the wind farms, so that none of the above limitations of current and voltage are violated;

2. Modeling of the design with wires ACO-400 with the same loads and generation and gradual increase of the power of wind farms until close maximum permissible currents are achieved through the power lines and non-permission of any increase or decrease of voltage outside the assigned limits.

3. Modeling of the design with wires ZTACIR-185 and the established mode achieved in item 2. Adjusting the generating powers until getting a permissible mode of maximum generation.

Part of the results from the calculations for the three stages are shown in Tables III ÷ V

TABLE III
RESULTS FOR VOLTAGES AND POWERS AT THE NODES AT STAGE 1
(AC-185)

Bus	U	phase	P_{gen}	Q_{gen}	P_{load}	Q_{load}
	kV	rad	MW	MVar	MW	MVar
Bus01	109.69	0.004	0.00	0.00	0.00	0.00
Bus02	116.15	0.124	10.00	-2.00	0.00	0.00
Bus03	121.27	0.194	34.18	6.00	0.00	0.00
Bus04	122.09	0.207	85.00	17.00	0.00	0.00
Bus05	118.57	0.171	16.00	3.20	0.00	0.00
Bus06	114.34	0.123	20.00	3.00	0.00	0.00
Bus07	110.92	0.079	0.40	-2.73	0.00	0.00
Bus08	108.57	0.042	0.00	0.00	9.20	4.50
Bus09	106.46	0.002	0.00	0.00	6.10	3.00
Bus10	105.72	-0.014	0.00	0.00	8.00	4.00
Bus11	105.18	-0.030	0.00	0.00	52.00	25.00
Bus12	105.59	-0.034	0.00	0.00	100.00	48.00
Bus13	106.48	-0.029	0.00	0.00	32.00	15.00
Bus14	110.00	0.000	-21.21	14.32	0.00	0.00
Bus15	110.00	0.000	79.43	91.69	0.00	0.00
Summary			223.8	130.48	207.3	99.5

The power generated by the wind farms at the first stage is limited by the size of the cross-section, i.e. by the permissible current in the wires. The wind farms exporting directly to the discussed network operate at cos φ=0.98 and produce 165.58 MW active power. The active power exported to the system is 21.21 MW.

TABLE IV
RESULTS FOR VOLTAGES AND POWERS AT THE NODES AT STAGE 2
(ACO-400)

Bus	U	phase	P_{gen}	Q_{gen}	P_{load}	Q_{load}
	kV	rad	MW	MVar	MW	MVar
Bus01	109.23	0.012	0.00	0.00	0.00	0.00
Bus02	112.21	0.188	10.00	-2.00	0.00	0.00
Bus03	116.20	0.302	34.18	6	0.00	0.00
Bus04	117.39	0.334	105.00	21.52	0.00	0.00
Bus05	115.24	0.303	35.00	7.2	0.00	0.00
Bus06	112.09	0.248	70.00	8.6	0.00	0.00
Bus07	108.98	0.176	0.40	-2.73	0.00	0.00
Bus08	107.11	0.119	0.00	0.00	9.20	4.50
Bus09	105.67	0.053	0.00	0.00	6.10	3.00
Bus10	105.27	0.026	0.00	0.00	8.00	4.00
Bus11	105.08	-0.001	0.00	0.00	52.00	25.00
Bus12	105.50	-0.012	0.00	0.00	100.00	48.00
Bus13	106.39	-0.011	0.00	0.00	32.00	15.00
Bus14	110.00	0.000	-60.46	36.66	0.00	0.00
Bus15	110.00	0.000	30.77	93.16	0.00	0.00
Summary			224.89	168.40	207.30	99.50

With the increase of the transmission capacity in the second model, the generation is increased to the upper limit of the transmission grid, whereby cosφ remains close to unity. 60.46 MW are delivered to the system, and the total active power, generated by wind power is 254.8 MW.

TABLE V
RESULTS FOR VOLTAGES AND POWERS AT THE NODES AT STAGE 3 (ZTACIR-185)

Bus	U	phase	P_{gen}	Q_{gen}	P_{load}	Q_{load}
	kV	rad	MW	MVar	MW	MVar
Bus01	108.27	0.011	0.00	0.00	0.00	0.00
Bus02	113.17	0.256	10.00	-2.00	0.00	0.00
Bus03	119.77	0.412	37.18	-7.00	0.00	0.00
Bus04	122.18	0.455	117.00	-15.00	0.00	0.00
Bus05	119.82	0.418	35.00	-5.00	0.00	0.00
Bus06	116.23	0.354	91.00	8.59	0.00	0.00
Bus07	110.45	0.264	5.40	-2.73	0.00	0.00
Bus08	106.69	0.187	0.00	0.00	9.20	4.50
Bus09	103.68	0.095	0.00	0.00	6.10	3.00
Bus10	102.82	0.055	0.00	0.00	8.00	4.00
Bus11	102.34	0.015	0.00	0.00	52.00	25.00
Bus12	103.05	-0.006	0.00	0.00	100.00	48.00
Bus13	104.63	-0.012	0.00	0.00	32.00	15.00
Bus14	110.00	0.000	-54.43	81.36	0.00	0.00
Bus15	110.00	0.000	32.21	138.49	0.00	0.00
Summary			273.36	196.70	207.30	99.50

The third model is characterized by theoretically greater transmission capacity of the power lines in comparison with the second model at the same cross-section as the one in the first model, but with three times higher active resistances of wires, compared to the ones in ACO-400. The impact of this is clear from the calculated established mode. To generate the same or greater power as in the second model and keep voltages within permissible limits, the generators in the wind farms must operate in a mode of suppressed excitation, i.e. consume reactive power from the discussed network. However, this has a negative effect for it leads to depletion of the capacity of the power lines and limitation of the effective transmission. The produced active power is 295.58 MW.

Losses of active power increase more than three times with respect to a unit of transmitted active power.

In order to check the opportunities for maximum generation in the three models, we explore a minimal mode, designed in a simple way by means of decreasing the consumers' powers by 40% relative to the previous one. The calculations are repeated and again care is taken that the power lines are not overload and at the same time that the voltages at the nodes do not exceed the permissible ones.

TABLE VI
RESULTS FOR VOLTAGES AND POWERS AT THE NODES AT STAGE 4 (MIN. LOAD, AC-185)

Bus	U	phase	P_{gen}	Q_{gen}	P_{load}	Q_{load}
	kV	rad	MW	MVar	MW	MVar
Bus01	109.47	0.012	0.00	0.00	0.00	0.00
Bus02	114.42	0.170	17.20	2.14	0.00	0.00
Bus03	117.74	0.261	35.98	-6.97	0.00	0.00
Bus04	118.70	0.278	80.00	-1.00	0.00	0.00
Bus05	116.81	0.241	20.00	1.00	0.00	0.00
Bus06	114.25	0.189	23.00	2.40	0.00	0.00
Bus07	111.95	0.142	4.00	-0.30	0.00	0.00
Bus08	110.31	0.103	0.00	0.00	3.68	1.80
Bus09	108.76	0.058	0.00	0.00	2.44	1.20
Bus10	108.20	0.038	0.00	0.00	3.20	1.60
Bus11	107.75	0.019	0.00	0.00	20.80	10.00
Bus12	107.77	0.009	0.00	0.00	40.00	19.30
Bus13	108.15	0.006	0.00	0.00	12.80	6.00
Bus14	110.00	0.000	-61.68	25.17	0.00	0.00
Bus15	110.00	0.000	-17.55	47.83	0.00	0.00
Summary			100.95	70.27	82.92	39.90

The wind farms exporting directly into the discussed network operate at cos φ=0.98 and produce 180.18 MW active power. The active power exported to the system is 79.29 MW. For this purpose, 73 MVAr of reactive power must enter the system. To maintain the voltage, the wind farms in nodes 3 and 4 must consume reactive power.

TABLE VII
RESULTS FOR VOLTAGES AND POWERS AT THE NODES AT STAGE 5 (MIN. LOAD, ACO-400)

Bus	U	phase	P_{gen}	Q_{gen}	P_{load}	Q_{load}
	kV	rad	MW	MVar	MW	MVar
Bus01	109.53	0.020	0.00	0.00	0.00	0.00
Bus02	114.37	0.215	17.20	2.10	0.00	0.00
Bus03	119.25	0.331	35.98	6.90	0.00	0.00
Bus04	120.82	0.364	105.00	21.52	0.00	0.00
Bus05	119.16	0.338	35.00	7.20	0.00	0.00
Bus06	116.48	0.290	75.00	12.90	0.00	0.00
Bus07	113.40	0.223	6.00	0.09	0.00	0.00
Bus08	111.35	0.168	0.00	0.00	3.68	1.80
Bus09	109.50	0.104	0.00	0.00	2.44	1.20
Bus10	108.87	0.075	0.00	0.00	3.20	1.60
Bus11	108.37	0.047	0.00	0.00	20.80	10.00
Bus12	108.28	0.031	0.00	0.00	40.00	19.20
Bus13	108.49	0.024	0.00	0.00	12.80	6.00
Bus14	110.00	0.000	-104.93	23.07	0.00	0.00
Bus15	110.00	0.000	-67.47	39.83	0.00	0.00
Summary			101.77	113.61	82.92	39.80

When the network design is made with ACO-400, the possible generated power of the wind farms naturally increases to 274.18 MW. There is no need to alter the operative mode to maintain the voltages at the nodes. 172.41 MW are exported to the system, and 62.9 MVAr are imported.

TABLE VIII
RESULTS FOR VOLTAGES AND POWERS AT THE NODES AT STAGE 6 (MIN. LOAD, ZTACIR-185)

Bus	U	phase	P_{gen}	Q_{gen}	P_{load}	Q_{load}
	kV	rad	MW	MVar	MW	MVar
Bus01	108.22	0.018	0.00	0.00	0.00	0.00
Bus02	113.02	0.289	17.20	2.10	0.00	0.00
Bus03	118.83	0.458	35.98	6.90	0.00	0.00
Bus04	120.04	0.515	117.00	-30.00	0.00	0.00
Bus05	117.58	0.482	35.00	-10.00	0.00	0.00
Bus06	114.24	0.419	90.00	-16.00	0.00	0.00
Bus07	110.05	0.322	6.40	-0.18	0.00	0.00
Bus08	107.43	0.241	0.00	0.00	3.68	1.80
Bus09	105.51	0.144	0.00	0.00	2.44	1.20
Bus10	105.04	0.102	0.00	0.00	3.20	1.60
Bus11	104.85	0.060	0.00	0.00	20.80	10.00
Bus12	105.19	0.034	0.00	0.00	40.00	19.20
Bus13	105.87	0.021	0.00	0.00	12.80	6.00
Bus14	110.00	0.000	-89.86	84.33	0.00	0.00
Bus15	110.00	0.000	-56.78	107.02	0.00	0.00
Summary			154.94	144.18	82.92	39.80

The opportunities to produce electric power from wind have increased to 301.18 MW, but to maintain the voltage, wind farms need to consume about 56 MVAr reactive power, whereby the entering one increases to 191.35 MVAr. The active power exported to the system is 146.64 MW.

It should be noted that the presented results do not cover all possible modes and situations. It is not taken into consideration that during normal mode of operation, the power transmission grid should meet at least the „n-1“ [5] criterion of safety. Also, the temperature of the wires will not always be equal to the permissible one, which implies that the active resistances will also vary within certain limits. The most realistic idea about whether it is advisable to use superheat resistant wires, from the point of view of the grid operation, would be obtained by calculating the losses of energy based on real load schedules, with accounting for a possible heating of the wires.

Table IX shows a comparison between the losses of active and reactive power and what part they are of the total power generated by wind farms.

IV. CONCLUSION

Based on the results presented in this paper, the following conclusions can be made:

1. A replacement of wires would lead to increased opportunities for production of electric power from renewable sources, i.e. owners of wind farms could benefit from this;
2. A utilization of superheat resistant wires could significantly increase the losses of power and energy, which would increase the grid owners' expenses;
3. To retain the voltages at the nodes within permissible limits, wind farms might need to use modes of consumption of reactive power.

TABLE IX
RESULTS FOR TOTAL LOSSES OF POWER IN THE THREE MODELS

Conductor type	ΔP_{sum}	ΔQ_{sum}	ΣP_{gen}	ΣQ_{gen}	$\frac{\Delta P_{sum}}{\Sigma P_{gen}} \cdot 100$
	MW	MVar	MW	MVar	%
Maximal load					
AC-185	16.50	30.98	165.58	24.47	9.96
ACO-400	17.59	68.90	254.80	38.59	6.90
ZTACIR-185	66.06	97.20	295.58	-23.14	22.35
Minimal load					
AC-185	18.02	30.37	180.18	-2.73	10.00
ACO-400	18.85	73.80	295.58	50.71	6.38
ZTACIR-185	72.02	104.37	301.18	-47.18	23.91

REFERENCES

[1] Edris, A. High-Temperature, Low-Sag Transmission Conductors. Technical report. EPRI, 2002

[2] Hirsch, J., B. Skrotzki. G. Gottstein. Aluminium Alloys Their Physical and Mechanical Properties. Proceedings of the 11th International Conference on Aluminum Alloys. 22-26 Sept. 2008. Aachen, Germany

[3] Wetzer J., M. Upgrading overhead lines With high temperature, low sag conductors. Tethnisthe universiteit Eindhoven. Jan. 2007

[4] Compact Conductors in Aluminum-Zirconium alloy resistant to high temperatures for aerial lines with high thermal limit. Deangeli prodotti

[5] Правила за управление на електроенергийната система. Приложение към т. 1 на Решение № П-5 от 18.06.2007 г., обн., ДВ, бр. 68 от 21.08.2007 г.
(Rules for management of the electric power system. Appendix 1, 18.06.2007, Bulgaria)

[6] Тенденции при изграждането и реконструкцията на електропроводи за високо напрежение. Годишник на ТУ-Варна. 2010, Варна, България
(Tends in construction and reconstruction of a high voltage overhead power line. Annual of Technical University – Varna, 2010, Bulgaria)

[7] Рангелов, Ю. Изследване на установени режими и преходни процеси в електроенергийни системи (ЕЕС) чрез софтуерния пакет Power system analysis toolbox (PSAT). Годишник на ТУ-Варна. 2009, Варна, България
(Y. Rangelov, Steady state and transient analysis in power systems using Power System Analysis Toolbox (PSAT), 2009, Varna, Bulgaria)

Session PDS II:

POWER TRANSMISSION AND DISTRIBUTION SYSTEMS II

The Analysis of Typical Seasonal Load Duration Curves of Low Voltage Consumers

Lidija Korunovic[1], Marko Vuckovic[2], Miodrag Stojanovic[3] and Dragan Tasic[4]

Abstract – **The paper presents typical load duration curves of months belonging to winter and summer season. Typical load duration curves of different load classes at low voltage are mutually compared. The influence of different number of working days, Saturdays and Sundays on monthly load duration curves is discussed and corresponding load factors and loss factors for winter and summer months are statistically analysed.**

Keywords – **Load Duration Curve, Low Voltage Consumer, Load factor, Loss factor.**

I. INTRODUCTION

Load data are necessary for exploitation and planning of electric power system. Thus, load curves are very important for power plant operation, electric power system control, the analysis of operation conditions in the future, calculation of electric power and energy losses in distribution networks etc.

Many factors such are: load composition, influence of seasons, life habits, economic standard of living, usage of central heating, tariffs and other factors, influence on load curves. Therefore, load curve determining is pretty difficult job and the subject of many research papers. For example, one of the very first researches regarding load curves in electric power system of this region is published in [1]. The results of one comprehensive study that regard determining of loss factor in distribution network of PD "Jugoistok" Nis are presented in [2]. The necessary data for this study are obtained from load curves recorded during ten years at the buses where utility buys electric energy.

However, small number of papers deals with analysis of load curves on low voltage level. The reasons are the larger influence of stochastic load variation on the shape of load curves and the lack of measurements at large number of low voltage consumers. One of the papers presents the load curves obtained on the basis of questionnaires completed by low voltage consumers [3]. More recent research [4] presents typical curves of real and reactive power in four seasons. These are obtained by measurements at low voltage in town Novi Sad during three years. These curves are used for reactive power and energy compensation in distribution network. Typical daily load curves in low voltage distribution network in the area of town Nis are presented in [5]. These curves are the result of procession of data collected by the system for remote energy meter reading in time period longer than two years. Since data regarding nearly 7000 consumers are processed, statistically reliable daily load curves of seven load classes are obtained and implemented in the software for energy loss calculation in low voltage distribution network. In [6] the results of another comprehensive research of load curves on the basis of measurements during two years at low voltage consumers that belong to residential, commercial and industrial load class are presented.

As mentioned before, the shape of load curves depends of lot of factors that can be climate, social and economic. This factors are so important that the load curves of the same load class and the same season can be significantly different in different countries, as can be noticed by comparison of load curves presented in [5] and [6]. Also, load curves in two regions of one country can be pretty different that is the case of load curves published in [4] and [5].

This paper presents typical seasonal load duration curves of different load classes in the area of town Nis on the basis of typical winter and summer daily load curves for working day, Saturday and Sunday taken from [5]. Seasonal load duration curves are actually load duration curves of winter and summer month. These load duration curves are devoted on those that relate to load classes of households and other load classes, analysed and mutually compared. Afterwards, the influence of number of days in winter and summer month and the number of working days, Saturdays and Sundays in the month on monthly load duration curves is investigated. This influence has not been treated by now, but in the paper it is quantified as well as the influence on corresponding load factor and loss factor values. The values of load factor and loss factor of individual load classes are statistically analysed.

II. LOAD FACTOR AND LOSS FACTOR CALCULATION

Variable losses of energy in the line can be calculated [2, 7] as

$$\Delta W = R\frac{P_m^2}{U_n^2\cos^2\varphi}T\vartheta, \qquad (1)$$

where: R - line resistance, P_m - maximum (peak) power known in most cases, U_n - nominal voltage, $\cos\varphi$ - power factor of the load that regard to be constant since varies in narrow ranges, T - time period in which the losses of energy are calculated (mainly year or month) and ϑ - loss factor. Loss factor depend on the shape of load curve and it is calculated on the basis of normalized load duration curve

$$\vartheta = \int_0^1 \left(y(x)\right)^2 \cdot dx\,. \qquad (2)$$

[1]Lidija Korunovic, [2]Marko Vuckovic, [3]Miodag Stojanovic and [4]Dragan Tasic are with the Faculty of Electronic Engineering, University of Nis, Aleksandra Medvedeva 14, 18000 Nis, Serbia, E-mail: lidija.korunovic@elfak.ni.ac.rs.

In this equation x and $y(x)$ denote normalized time and normalized load power, respectively. Also, loss factor can be calculated from load factor using one the formulae from the literature [7]. The selection of the formula depends on the load curve of considered load. Load factor is calculated on the basis of normalized load duration curve using formula

$$m = \int_0^1 y(x) \cdot dx \,. \tag{3}$$

In concrete cases when discrete measurements of real power are performed and the values are memorized, formulae (2) and (3) are in the form

$$\vartheta = \frac{1}{N} \sum_{i=1}^{N} p_i^2 \,, \tag{4}$$

$$m = \frac{1}{N} \sum_{i=1}^{N} p_i \,, \tag{5}$$

where N and p_i denote number of measurements and normalized real power value from i^{th} measurement, respectively. If load and loss factors are calculated for the month which has 30 days and the measurements are performed every 15 minutes, N is calculated as $N = 4 \times 24 \times 30 = 2\,880$.

III. Seasonal Load Duration Curves

Typical seasonal load duration curves are formed on the basis of averaged (typical) daily load curves for winter and summer season and working day, Saturday and Sunday that are presented in [5]. Table I summarizes maximum power of different load classes obtained from these typical daily load curves in winter and summers season. For all investigated load classes at low voltage, the maximum power in winter is larger than corresponding power in summer season. The ratio of maximum power in winter and maximum power in summer season belongs to the range from 0.473 for load class 2 - households in buildings without central heating to 0.884 for class 3 - households in buildings with central heating.

Typical seasonal load duration curves presented in this section are actually monthly load duration curves for winter and summer season. It is taken that the month in both seasons has 30 days and starts with Monday, Tuesday, Wednesday or Thursday, i.e. each has 22 working days, four Saturdays and four Sundays. Normalization of the curves is performed by maximum load of the load class in considered season given in Table I.

The curves from Fig. 1 regard to winter month for three load classes of households. These are clearly different. The curve corresponding to class 1 - individually built households without central heating, is the one with highest normalized power values along whole length. This curve has the values larger than 0.8p.u. even 21.6% of time during typical winter month.

TABLE I
MAXIMUM POWER OF DIFFERENT LOAD CLASSES

Load Class	Season	P_{max} [kW]
Class 1 - individually built households without central heating	Winter	1.477
	Summer	0.973
Class 2 - households in buildings without central heating	Winter	1.723
	Summer	0.814
Class 3 - households in buildings with central heating	Winter	1.054
	Summer	0.932
Class 4 - commercial load excluding craft stores and shops	Winter	2.049
	Summer	1.469
Class 5 - common equipment and installations in residential buildings	Winter	0.832
	Summer	0.429
Class 6 - craft stores	Winter	1.970
	Summer	1.289
Class 7 - shops	Winter	1.721
	Summer	1.432

The smallest power values for load class 1 in winter season is 0.5568 indicating that the ratio maximum to minimum power is pretty small for this load class. It is 1.796, while other load classes of households have larger ratios, close to 3 since their minimum power values are around 0.34. The curve corresponding to class 2 - households in buildings without central heating has larger slope in the first part of the curve and after 0.2p.u. of time reaches 0.59p.u. power value.

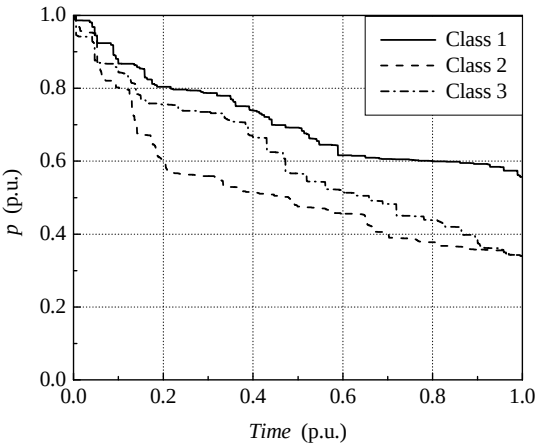

Fig. 1. Typical load duration curves of winter month for three load classes of households

Characteristic of all typical load curves of winter month, for load classes 4-7 which are not households (Fig. 2), is that duration of high power values, greater than 0.8, is longer than the duration in the case of load classes of households. It belongs to the range from 0.3p.u. for class 6 - craft stores, to 0.517p.u. for class 4 - commercial load excluding craft stores and shops.

Typical load duration curve for class 4 in winter season has almost constant slope and its smallest value is 0.6232. Load curve of class 6 also has approximately constant slope, but it is lower and its smallest power value is 0.256. The curve of class 5 (common equipment and installations in residential buildings) has even smaller minimum power value, 0.241. Thus, maximum to minimum power ratio of four investigated

load classes that are not households, belongs to the range from 1.605 for class 4 to 4.149 for class 5.

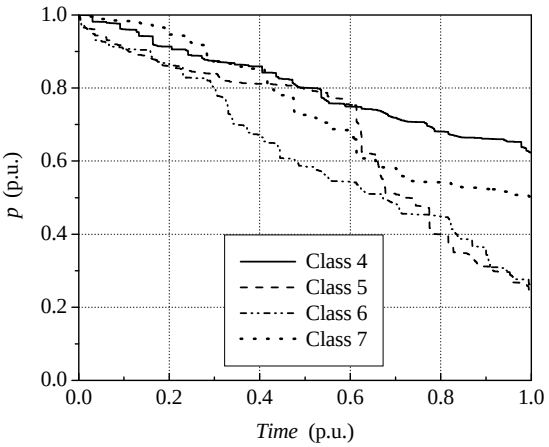

Fig. 2. Typical load duration curves of winter month for load classes other than households

Fig. 3 presents typical load duration curves of summer month for load classes of households. The curve of class 1 can be roughly separated into three parts: almost linear drop with the increase of normalized time up to 0.386p.u., region of approximately constant power from 0.386p.u. to 0.478p.u. of normalized time and after that drop up to 0.4354p.u. power value. The curves of class 2 and 3 decrease continuously with time, have similar shape and finish at 0.2601p.u. and 0.3545p.u. power value, respectively. Maximum to minimum power ratios vary in relatively narrow range in comparison with ratios obtained in winter season. They change from 2.297 for class 1 (individually built households without central heating) to 3.845 for class 2 (households in buildings without central heating).

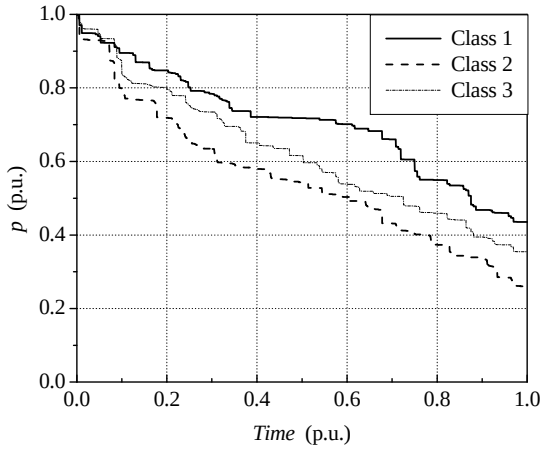

Fig. 3. Typical load duration curves of summer month for three load classes of households

Narrower range of maximum to minimum power ratios in summer in comparison with corresponding range in winter season is also obtained for load classes other than households. The smallest ratio is 1.816 in the case of class 4 (commercial load excluding craft stores and shops) and the largest is 2.867 for class 5 (common equipment and installations in residential buildings). For load classes 4-7 the time periods when the power values are larger than 0.8p.u., are quite long, similarly to those found in winter season. In summer season these periods belong to the range from 0.191p.u. for class 5 to 0.478p.u. for class 4.

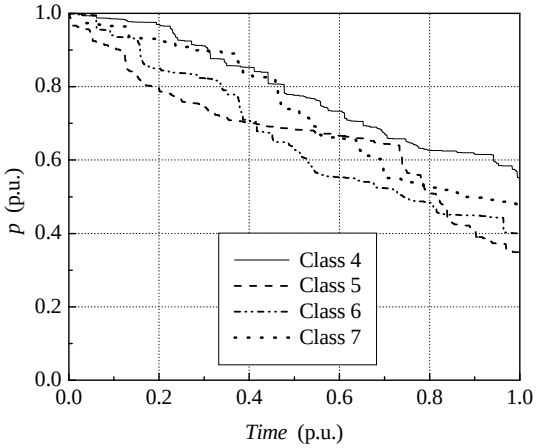

Fig. 4. Typical load duration curves of summer month for load classes other than households

IV. The Effect of Number of Days

Since seasonal load duration curves are obtained by using typical daily load curves of working day, Saturday and Sunday in winter or summer season, their shape depends on the number of days in winter or summer month. As mentioned in previous section, the curves from Figs. 1-4 correspond to winter and summer months that have 30 days - 22 working days, four Saturdays and four Sundays.

However, the month in winter season can also have 31 days, 28 days or 29 days in leap year. The month in summer season can have 30 or 31 days. Furthermore, the number of working days, Saturdays and Sundays in particular month can be different. For example, the month that has 30 days can consist of:

- 22 working days, 4 Saturdays and 4 Sundays (if the month begins with Monday, Tuesday, Wednesday or Thursday),
- 21 working days, 5 Saturdays and 4 Sundays (if the month begins with Friday),
- 20 working days, 5 Saturdays and 5 Sundays (if the month begins with Saturday) and
- 21 working days, 4 Saturdays and 5 Sundays (if the month begins with Sunday.

For every load class and winter and summer season, monthly load duration curves are created for all possible number of days in the month and all possible combinations of number of working days, Saturdays and Sundays. Thus, for winter season even 12 curves are plotted on the same figure for every load class. Similarly, 8 load duration curves are plotted for summer season.

It is found that these individual curves belonging to the same season and the same load class are very close to each other. For example, in the case of class 5 the curves are almost identical. Maximum difference between individual curves is obtained for the curves of class 7 in summer season (Fig. 5),

and the difference is 0.0825p.u. For the same load class, but winter season, maximum difference between individual load curves is 0.06p.u., while for other load classes the difference is smaller, up to 0.05p.u.

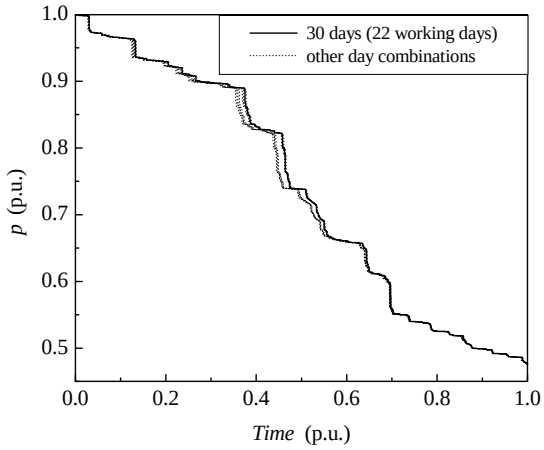

Fig. 5. Individual load duration curves of summer month for class 7

V. Load Factor and Loss Factor Analysis

Regarding the fact that load duration curves slightly differ with number of days in the month and the number of working days, Saturdays and Sundays, load factor and loss factor are calculated for all 12 and 8 possible combinations of days in winter and summer month, respectively. Table II presents only extreme values of these factors for every load class. It can be noticed that minimum and maximum values of corresponding factor differ from each other at third decimal place. The analysis of the ranges the factors belong to, showed that these are less than 1% of the mean value of corresponding factor.

Therefore, mean values of load factor and loss factor should be used. Mean values of load factor in winter season are: 0.7128, 0.5230, 0.6057, 0.8019, 0.6798, 0.6200 and 0.7416 for classes 1-7, respectively. In summer season mean values of this factor in the same order are: 0.7051, 0.5532, 0.6233, 0.7889, 0.6705, 0.6640 and 0.7352.

TABLE II
EXTREME VALUES OF LOAD FACTOR AND LOSS FACTOR

Season	Load class	m_{min}	m_{max}	ϑ_{min}	ϑ_{max}
Winter	Class 1	0.7108	0.7149	0.5194	0.5253
	Class 2	0.5201	0.5260	0.2974	0.3039
	Class 3	0.6030	0.6086	0.3932	0.4010
	Class 4	0.7990	0.8047	0.6504	0.6597
	Class 5	0.6792	0.6804	0.5120	0.5147
	Class 6	0.6164	0.6233	0.4227	0.4320
	Class 7	0.7387	0.7442	0.5772	0.5861
Summer	Class 1	0.7037	0.7065	0.5162	0.5205
	Class 2	0.5515	0.5549	0.3371	0.3412
	Class 3	0.6207	0.6259	0.4150	0.4222
	Class 4	0.7853	0.7923	0.6366	0.6480
	Class 5	0.6693	0.6716	0.4745	0.4778
	Class 6	0.6601	0.6678	0.4697	0.4814
	Class 7	0.7320	0.7382	0.5675	0.5772

Statistical analysis of loss factor values yields that mean values in winter season are: 0.5223, 0.3006, 0.3971, 0.6551, 0.5133, 0.4274 and 0.5817, while in summer season these are: 0.5183, 0.3391, 0.4186, 0.6424, 0.4761, 0.4756 and 0.5724 for load classes 1-7, respectively.

VI. Conclusion

Typical load duration curves of months belonging to winter and summer season for seven load classes at low voltage are presented in the paper. The curves that correspond to three load classes of households are clearly different from each other in both winter and summer season. There is increase of maximum to minimum power ratio in summer season for all three load classes. Load duration curves for investigated load classes other than households have pretty long period of the load greater than 0.8p.u. This period for commercial load excluding craft stores and shops reaches approximately 0.5p.u. of normalized time in both winter and summer season.

It is shown that different number of days in winter or summer month, as well as different number of working days, Saturdays and Sundays does not influence on significantly the shape of seasonal load duration curves. Consequently, load factor and loss factor calculated from these curves differ from each other at third decimal place.

Acknowledgement

The work presented here was supported by the Serbian Ministry of Education and Science (project III44006).

References

[1] H. Pozar, *Power and Energy in Electric Power Systems*, Zagreb, Informator, 1983. (in Serbo-Croatian)

[2] D. Stojanovic, L. Korunovic, S. Jovanovic, A. Vukasinovic, M. Docic, "Loss Factor in Distributive Area of Utility "Elektrodistribucija Nis", Elektroprivreda, vol. 57, no. 4, pp. 51-61, 2005. (in Serbian)

[3] Lj. Geric, P. Konjovic, P. Djapic, M. Sindjelic, "Modeling of Residential Load Shapes Using Method of Questionnaire", XXXVIII konferencija ETRAN-a, Conference Proceedings, Vol. I, pp. 251-252, Nis, Yugoslavia, 1994. (in Serbian)

[4] D. Comić, Lj. Geric, S. Gusavac, "Characteristic Diagrams of Active and Reactive Power of Typical Consumers' Groups in Elektrodistribution "Novi Sad", Second Regional Conference & Exibition on Electricity Distribution, Conference Proceedings, R6.3, Zlatibor, Serbia, 2006.

[5] L. Korunovic, M. Stojanovic, D. Tasic, L. Stoimenov, A. Krstic, "Analysis of load diagrams at low voltage of distribution network of Nis", VII Conference on Electricity Distribution in Serbia and Montenegro, R-6.02, Vrnjacka Banja, Serbia, 2010. (in Serbian)

[6] J. A. Jardini, C. M. V. Tahan, M. R. Gouvea, S. U. Ahn, F. M. Figueiredo, "Daily Load Profiles for Residential, Commercial and Industrial Low Voltage Consumers", IEEE Trans. on Power Delivery, vol. 15, no. 1, pp. 375-380, 2000.

[7] D. Tasic, M. Stojanovic, *Losses of electric energy in distribution networks*, Nis, Faculty of Electronic Engineering, 2006. (in Serbian)

Load Modelling by using Normal Operation Data

Lidija Korunovic[1], Bratislav Nikolic[2], Dalibor Nikolic[3] and Milutin Petronijevic[4]

Abstract – **This paper presents the results of load modelling obtained by using the data from normal operation of electric power system. Necessary data are stored by the computer which is the part of the equipment of transformer station TS 35/10kV. Voltage and real and reactive power data at the higher side of the station are analysed. The parameters of exponential load model are identified and grouped according to day periods and days of the week.**

Keywords – **Load modelling, Normal operation, Exponential load model.**

I. INTRODUCTION

The adequate load modeling is the base for electric power systems analysis of both steady-state operating conditions and transients. Therefore, load modelling is a very actual scientific theme and many papers concerning this matter have been published by now.

The parameters of low voltage devices can be determined on the basis of laboratory tests as explained in [1]. Much complicated task is determining of total load on medium voltage level. If the parameters of individual load components are known as well as its participation in total load, the task will be accomplished by the method of aggregation, i.e. by component based approach to load modelling [2]. Otherwise, measurement based approach to load modelling should be used [3]. The participation of load components in total load is very difficult to determine, since it varies during the day, changes depend on the day of the week and the season. Therefore, the second mentioned approach is the better one. It comprehends field measurements at selected buses of the network. Afterwards, the obtained load model parameters can be applied at the buses with similar load structure. However, measurement based approach is more complicated, since it implies permission of electrical distribution company, relatively expensive measuring equipment and participation of a group of people during the measurements.

The investigations regarding load modelling can be developed on those that are based on field tests and on the investigations based on continuous measurements. The field tests are allowed to be performed in time periods when they can not endanger electric power system operation. Furthermore, during the field tests, the changes of operating conditions are performed in a way that safety and the quality of a supply are bellow the limits [4]. Therefore, the ranges of the voltage changes during the tests are rather narrow [5]. Additionally, it becomes to be very difficult to get the permission for the field test in electric power system in the environment of electric energy deregulated market and generally in the market economy.

In the case of continuous measurements for load modelling, it is important to record the data in the time intervals when the disturbances in electric power system occur. For example, these are short-circuits or switching on/off large consumers [6]. Therefore, it is necessary to measure for a very long time to get relevant data, but despite that, this kind of investigations are usually based on the relativelly small number of valid data sets. Recording equipment used for continuous measurements should have much larger memory for data storage than the equipment used during field tests. Also, the recording equipment for continuous measurements very often have the possibility to proceed the data and sometimes even process the data by themselves [5], and by rule, it is very expensive.

This paper is the continuation of the research in the area of load modelling which results are collected in [4]. For this dissertation field tests were performed to obtain the load model parameters in distribution network of Nis. Due to the listed shortcomings of data gathering using field test, the paper deals with load modelling using continuous measurements. For this measurements microprocessor relays and the computer (so called station unit) which are the part of the remote control equipment in transformer station, are used instead of other expensive recording equipment.

The aim of the paper is to demonstrate the possibilities that the data stored by station unit enable in the domain of load modelling. Therefore, the results that relate to three week period during normal operation of the system are presented.

II. NORMAL OPERATION DATA

Simplified principal schema of the equipment used for data storage, data transmission within the transformer station TS "Centar 1" and the transmission to other networking computers is presented on Fig. 1. The transformer station is equipped with microprocessor relays Siemens 7SJ63 that can send large number of variables. Near by relays are mutually connected with double optical cable and the first and the last one are also connected with the switch.

The computer in transformer station store the data from the relays, while remote terminal unit (RTU) communicate with the Control centre, that is equipped with supervisory control and data acquisition system (SCADA), over WAN (Wide Area Network) using Telekom router. In the case of

[1]Lidija Korunovic and [4]Milutin Petronijevic are with the Faculty of Electronic Engineering, University of Nis, Aleksandra Medvedeva 14, 18000 Nis, Serbia, E-mail: lidija.korunovic@elfak.ni.ac.rs.

[2]Bratislav Nikolic and [3]Dalibor Nikolic are with electric power distribution company „Jugoistok" Nis, 46a Bul. Z. Djindjica, Nis 18000, Republic of Serbia.

interruption of this communication, alternative communication path is performed by the radio link.

The necessary data for load modelling are obtained from station unit in transformer station which is controlled by electric power distribution company „Jugoistok“ Nis.

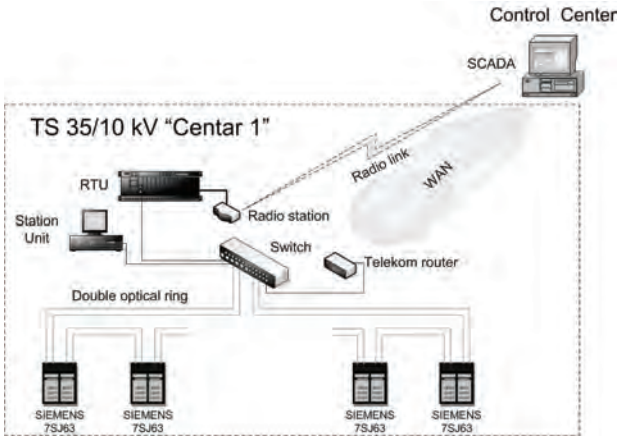

Fig. 1. Principal schema of the equipment for storage and transmission of data

Electrical simplified single-phase schema of TS “Centar 1” during the measurements is presented on Fig. 2. Two lines that are fed from TS “Nis 3” supply the transformer station which consists of two transformers 35/10kV. The station delivers the electric energy to the center of Nis trough 12 feeders. Since the aim of load modelling was to determine the parameters of the total load at 35kV voltage level, some of variables were selected to be stored in station unit every second. These are: three line voltages at 35kV bus, three-phase real and three-phase reactive power of both transformer T_1 and transformer T_2.

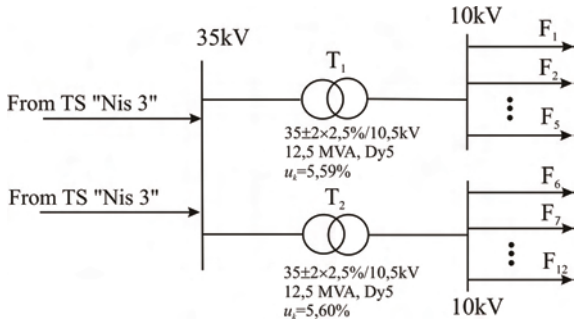

Fig. 2. Simplified single-phase schema of TS “Centar 1”

The data were recorded during three weeks every second, from Thursday 21st October to Wednesday 10th November in 2010. During this period the abrupt voltage changes that are characteristic of normal operation of the system were tracked. These changes are caused by electric power system regulation and/or disturbances and they are used for modelling of real and reactive power.

During 21 day period there were two days without any abrupt voltage change - Sunday and Monday, 24th and 25th October. Also, there were the days with several abrupt voltage changes. For example, Fig. 3 presents the voltage vs. time diagram recorded on Saturday 30th October when three abrupt voltage changes occurred.

The first voltage change is typical for most of the concerned days. It is the voltage decrease after the midnight when the voltage reaches pretty high value due to load decrease in electric power system and the decrease is the result of power system regulation that tend to keep the voltage under acceptable limits. This voltage decrease is for 1.268% of rated voltage value (U_n) and in other days it has similar amount.

The second abrupt voltage change from the figure is the voltage increase for 2.612% of U_n. It occurred at 20:25. In most of examined days, the voltage increase of approximately 1.3% of rated voltage happened earlier, from 16:30 to 18:30. This increase was the results of power system regulation, since in this time interval the voltage reached the lowest values.

The third abrupt voltage change from Fig. 3 is the voltage decrease for 1.345% of U_n at 23:20 also caused by the voltage regulation. Such kind of the voltage change before the midnight happened only five times during three week period. It is more usual that the voltage decrease appear after the midnight.

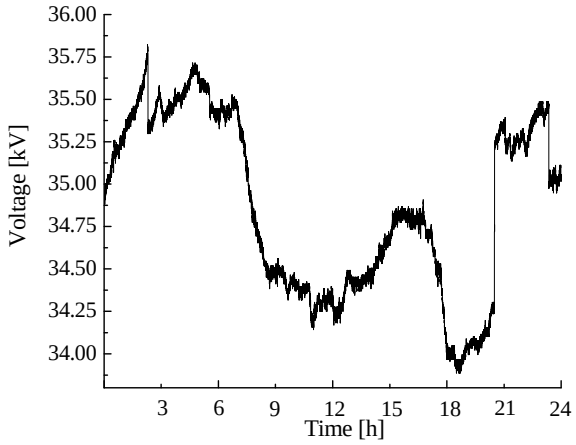

Fig. 3. The voltage diagram on Saturday 30th October

In concerned three week period 41 abrupt voltage changes occurred and all of them are considered in load modelling process. These changes are grouped according to time intervals of a day and days of the week and their number in considered intervals and days is presented in Table I. Most of the voltage changes occurred in the periods from 0 to 6h and from 12 to 18h - totally number 25, while per 8 changes happened from 6 to 12h and from 18 to 24h.

The voltage changes are also grouped according to days of the week. It is found that 30 changes appeared during working days (Table I), i.e. averagely 6 changes per one day - Monday to Friday. During three Saturdays and three Sundays in the period of 21 days, only 6 and 5 changes occurred, respectively. It shows the necessity of the further research in the longer time periods in order to capture much more abrupt voltage changes during weekends.

TABLE I
THE NUMBER OF ABRUPT VOLTAGE CHANGES

Time interval [h]	Number of changes	Day of the week	Number of changes
0-6	16	Monday - Friday	30
6-12	8		
12-18	9	Saturday	6
18-24	8	Sunday	5

III. ADOPTED LOAD MODEL

Exponential load model is one of the most frequently used static load models:

$$P = P_n\left(\frac{U}{U_n}\right)^{k_{pu}}, \quad (1)$$

$$Q = Q_n\left(\frac{U}{U_n}\right)^{k_{qu}}. \quad (2)$$

In this model P and Q denote real and reactive load power at voltage U, P_n and Q_n are real and reactive load power at rated voltage, respectively, k_{pu} and k_{qu} denote voltage exponent of real and reactive power.

In the vicinity of rated voltage, the parameters k_{pu} and k_{qu} represent partial derivatives of real and reactive power with respect to voltage [7]

$$k_{pu} = \frac{\partial P}{\partial U}, \quad (3)$$

$$k_{qu} = \frac{\partial Q}{\partial U}, \quad (4)$$

or real and reactive power sensitivities on voltage [8]. These parameters practically show the value of real and reactive power change in percents for one percent of voltage change in the vicinity of rated voltage [9]. If both voltage exponents in model (1) and (2) are 0, 1 or 2, the load is of constant power, current or impedance type, respectively.

The model (1)-(2) describes the changes of real and reactive power for voltage variations around the rated voltage. The analysis of all abrupt voltage changes during concerned three week period shows that almost all voltage changes are pretty small. Even 38 changes were smaller than 1.5% of U_n, two were around 2.6% of U_n and only one was 5.46% of rated voltage. Previous researches [8, 10] showed that exponential load model can be applied in relatively wide voltage range, somewhat smaller than the range 0.95-1.1pu with acceptable mistakes - up to 5%. Therefore, exponential load model is used for modelling of examined load.

However, most of the abrupt voltage changes during power system normal operation are not so close to rated voltage value. Therefore, another variant of exponential load model is applied. It uses initial real and reactive power values, P_0 and Q_0, at initial voltage U_0, instead of P_n and Q_n at U_n [11]. Thus, the parameters of exponential load model for small voltage deviations and therefore small power deviations are calculated as:

$$k_{pu} = \ln\left(\frac{P}{P_0}\right)\Big/\ln\left(\frac{U}{U_0}\right) \approx \frac{(P-P_0)/P_0}{(U-U_0)/U_0}, \quad (5)$$

$$k_{qu} = \ln\left(\frac{Q}{Q_0}\right)\Big/\ln\left(\frac{U}{U_0}\right) \approx \frac{(Q-Q_0)/Q_0}{(U-U_0)/U_0}. \quad (6)$$

IV. ANALYSIS OF THE RESULTS

The station unit stored the data averaged every second. According to these data, the power changes "momentary" with the voltage to its new value. One of these power responses to voltage change recorded on 23rd October at 3:30 is depicted in Fig. 4 through *P-U* and *Q-U* characteristics. These characteristics demonstrate the power changes for small voltage change (only 0.884% of U_n in examined case) that finish within 1 second. The data from these characteristics are enough for determining of the exponential load model parameters according to formulae (5) and (6). Thus, identified parameters from the voltage change from Fig. 4 are: k_{pu}=1.383 and k_{qu}=4.081.

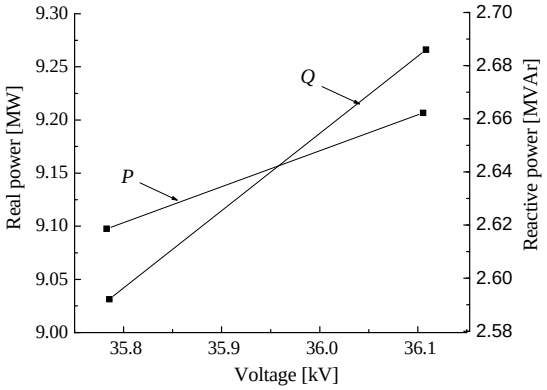

Fig. 4. *P-U* and *Q-U* characteristic

Table II presents exponential load model parameters grouped according to time intervals. Mean values and standard deviations of the parameters are given in this table. The value of k_{pu} slightly increases from the first time interval to the third one, but is close to 1. In the last analysed time interval of the day, 18-24h, k_{pu} increases significantly that indicates that the usage of resistive load devices increases. These load devices have parameter k_{pu} that is approximately 2 [12].

Variation of parameter k_{qu} is most likely the consequence of the change of the voltage values in the investigated time intervals. Mean value of k_{qu} varies in the range from 2.281 in time interval 12-18h when the voltage values are the lowest, to the value 3.993 in the interval 0-6h when the voltage reaches its maximum. That is because higher network voltages affect the saturation of 35/10kV transformer and 10/0.4kV distribution transformers known to have highly nonlinear reactive power–voltage characteristics.

Load model parameters are also grouped according to days of the week: working day, Saturday and Sunday. Mean values and standard deviations of identified parameters are given in Table III. Both parameters vary in relatively narrow range: mean value of k_{pu} changes from 1.070 on working days to 1.338 on Saturday, while mean value of k_{qu} varies from 3.150 during working days to 3.635 on Sunday. It approves that the load parameters, i.e. load composition, vary rather with day periods than with the days of the week.

TABLE II
MEAN VALUES AND STANDARD DEVIATIONS OF THE PARAMETERS GROUPED ACCORDING TO TIME INTERVALS

Parameter	Time interval [h]	Mean	Standard deviation
k_{pu}	0-6	0.970	0.278
	6-12	0.966	0.313
	12-18	1.177	0.376
	18-24	1.511	0.353
k_{qu}	0-6	3.993	1.409
	6-12	3.112	0.986
	12-18	2.281	1.426
	18-24	2.787	0.972

TABLE III
MEAN VALUES AND STANDARD DEVIATIONS OF THE PARAMETERS GROUPED ACCORDING TO DAYS OF THE WEEK

Parameter	Day of the week	Mean	Standard deviation
k_{pu}	Monday - Friday	1.070	0.361
	Saturday	1.338	0.447
	Sunday	1.160	0.357
k_{qu}	Monday - Friday	3.150	1.236
	Saturday	3.334	1.851
	Sunday	3.635	1.816

At the end it should be emphasized that the paper demonstrates what a powerful tool for load modelling electric power distribution company has got. It is the station unit that stores the huge amount of data from microprocessor relays. The results of load modelling on the bases of data from normal operation during three weeks show the applicability of presented procedure for parameter identification. The small number of abrupt voltage changes in some day intervals and during weekend, and consequently significant values of standard deviations approve the necessity of further data processing in order to obtain even more reliable results as well as the parameters in other seasons.

V. CONCLUSION

The paper presents the procedure of load modelling using the station unit - computer which is the part of the remote control equipment in transformer station. Exponential load model parameters are obtained from normal operation data during three weeks in autumn. The parameter k_{pu} shows the significant increase from nearly 1 to the value 1.511 that is reached in the period from 18 to 24h as the result of the increase of the usage of resistive load devices. The values of k_{qu} vary predominantly as the consequence of transformer saturation, from 2.281 in the afternoon to 3.993 after the midnight. The investigation can be continued in order to obtain the parameters in other seasons.

ACKNOWLEDGEMENT

The work presented here was supported by the Serbian Ministry of Education and Science (project III44004).

REFERENCES

[1] L. M. Korunović, D. P. Stojanović, "Dynamic Load Modelling of Some Low Voltage Devices", Facta Universitatis (Niš), Series: Electronics and Energetics, vol. 22, no. 1, pp. 61-70, 2009.

[2] K.-W. Louie, "A New Approach to Compose Load Devices in Electric Power Systems", International Journal of Applied Science and Engineering, vol. 2, 2004, pp. 197-210.

[3] K. Tomiyama, S. Ueoka, T. Takano, I. Iyoda, K. Matsuno, K. Temma, J. J. Paserba, "Modeling of Load During and After System Faults Based on Actual Field Data", IEEE Power Engineering Society General Meeting, Conference Proceedings, pp. 1385-1391, pp. 1385-1391.

[4] L. M. Korunović, *Modelling of Medium Voltage Distribution Network on the Basis of Experiments*, PhD thesis, Faculty of Electronic Engineering, University of Niš, Niš, 2008. (in Serbian)

[5] Y. Baghzouz, C. Quist, "Determination of Static Load Models from LTC and Capacitor Switching Tests", Proc. IEEE Power Engineering Society Summer Meeting, 16-20 July 2000, Vol. 1, pp. 389–394.

[6] B.-K. Choi, H.-D. Chiang, Y. Li, H. Li, Y.-T. Chen, D.-H. Huang, M. G. Lauby, "Measurement-Based Dynamic Load Models: Derivation, Comparison, and Validation", IEEE Trans., Power Systems, vol. 21, no. 3, pp. 1276-1283, 2006.

[7] J. Ribeiro, F. Lange, "A New Aggregation Method for Determining Composite Load Characteristics", IEEE Trans., Power Apparatus and Systems, vol. PAS-101, no. 8, pp. 2869-2875, 1982.

[8] L. Korunović, D. Stojanović, "Load Modeling in Distribution Networks", Facta Universitatis (Niš), Series: Electronics and Energetics, vol. 15, no. 3, pp. 419-427, 2002.

[9] C. Taylor, *Power System Voltage Stability*, Mc Graw-Hill, New York, 1994.

[10] L. M. Korunović, D. P. Stojanović, J. V. Milanović, "Identification of Static Load Characteristics Based on Measurements in Medium-Voltage Distribution Network", IET Generation, Transmission & Distribution, vol. 2, no. 2, pp. 227-234, 2008.

[11] P. Kundur, *Power System Stability and Control*, Mc Graw-Hill, New York, 1994.

[12] L. Korunović, D. Stojanović, "Load Model Parameters on Low and Middle Voltage in Distribution Networks", Elektroprivreda, vol. 55, no. 2, pp. 46-56, 2002. (in Serbian)

Selection of Weight Functions for Unstructured Uncertainty in the Synchronous Generator Model

Konstantin Gerasimov[1]

Abstract – **An output multiplicative representation of uncertainties in the synchronous generator unit model is discussed for the purposes of the stability analysis of the electromechanical modes under small disturbances. A study is carried out analyzing the influence of the choice of nominal model and calculation algorithms over the weight functions.**

Keywords – **weight functions, unstructured uncertainty, synchronous generator.**

I. INTRODUCTION

The electric power system (EPS) analysis under small disturbances is based on a mathematical description linearized around a certain operating point. In fact the operating point depends on a number of factors and is dynamic in time. This is why the linearized model should be treated as uncertain model. Another source of uncertainties is the inaccurate information about the schematic parameters of the elements of EPS. When the source of uncertainties is known, a common practice is to use structured representation of the uncertainties [1-3]. This approach was used in [4] and was shown that it is not applicable for modeling EPS because of the very high order of the obtained model. This is why it is appropriate to represent the uncertainty of the system as unstructured. Main problem with this method is the determination of adequate weight functions that properly describe the uncertainty effect in the model. In most books this problem is not treated thoroughly for MIMO systems and even less for the case of EPS.

When the sources of uncertainty are known, usually the unstructured uncertainty weight functions are determined from the bounds of the frequency responses of the family of models built under the conditions of different combinations of values of the uncertain quantities amongst their range of variation. The ranges of the schematic parameters are relatively small in comparison with the variation of the regime parameters (caused by the change of the operating point) and this is why the latter have bigger influence. The purpose of this paper is to share the experience with calculation of appropriate unstructured uncertainty weight functions for representation of the operation point changes.

[1]Konstantin Gerasimov is PhD student at Department "Power Engineering", Technical University of Varna, Studentska Str. 1, Varna, 9010, Bulgaria, E-mail: kosio_gerasimov@abv.bg

II. TEST MODEL

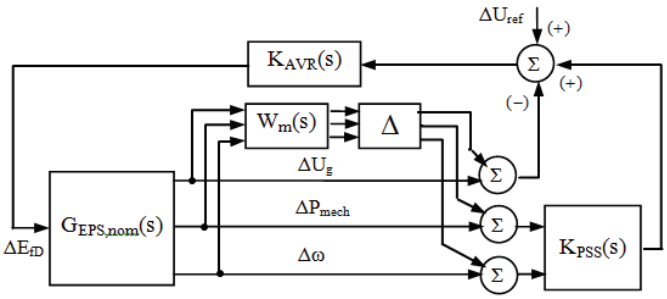

Fig. 1. Structural scheme of the model of single machine infinite bus system with multiplicative output uncertainty and AVR and PSS

In Fig. 1 is shown the structural scheme of the model of single machine infinite bus (SMIB) system ($G_{EPS,nom}(s)$). The generator is equipped with AVR ($K_{AVR}(s)$) and PSS ($K_{PSS}(s)$). The uncertainty is presented as output multiplicative unstructured, having matrix transfer weight function $W_m(s)$. The generator parameters are X_d=1.6 p.u., X_q=1.6 p.u.; X_σ=0.15 p.u., X_d'=0.266 p.u., X_d"=0.205 p.u., Xq"= 0.205 p.u., T_{d0}=5.8 s, T_{d0}"=0.13, T_{q0}"=0.13 s, T_J=6.3 s. The connecting power line has resistance X_{TW}=0.5 p.u. The AVR is type UNITROL F and the PSS is type PSS2A.

In the studied SMIB system, the independently changing regime parameters (i.e. changed by external for the system signals) are: the AVR reference ΔU_{ref}, voltage of the generalized system ΔU_s, and turbine power ΔP_{mech}. Their allowable ranges of change are approximately ΔU_{ref}=1÷1.05 p.u., ΔU_s=0.95÷1.05 p.u. and ΔP_{mech}= 0.2÷0.85 p.u. (for steam turbine, with $P_{base} = S_{G.nom}$).

The analysis in the paper is done based on the condition that the weight functions are calculated in respect to the family of models, generated by the change only of the turbine power in a certain range (0.4÷0.8 p.u.). The step of change of ΔP_{mech} is 0.025 p.u. and is small enough so that there is the confidence that no specific situations are missed. In Fig. 2 are shown the frequency responses of the family open systems G_{EPS}, and in Fig. 3 – the frequency responses of the family of systems closed with AVR and PSS (see Fig. 1). It is interesting to notice how the introduction of AVR and PSS completely changed the behavior of the generator unit.

One should always keep in mind what will be the purpose of the uncertain model he is constructing. In this paper the purpose of the model is to validate that the introduction of unstructured uncertainty represents adequately the real family of models for a range of possible operating point and to check if it gives proper assessment of the robust stability of the system. Also, the other purpose is to check the robust stability when certain AVR and PSS are introduced into the model and to be able to compare the robustness of the system for other

AVR and/or PSS. Having this in mind, the weight functions are calculated in respect to the outputs of the generator itself.

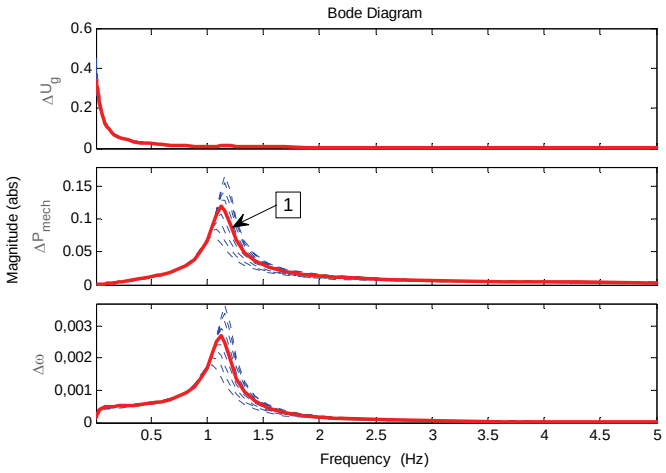

Fig. 2. Frequency response of family open systems G_{EPS} for P_{mech} in the range 0.4÷0.8 p.u. (1 – nominal model for P_{mech} = 0.6 p.u.)

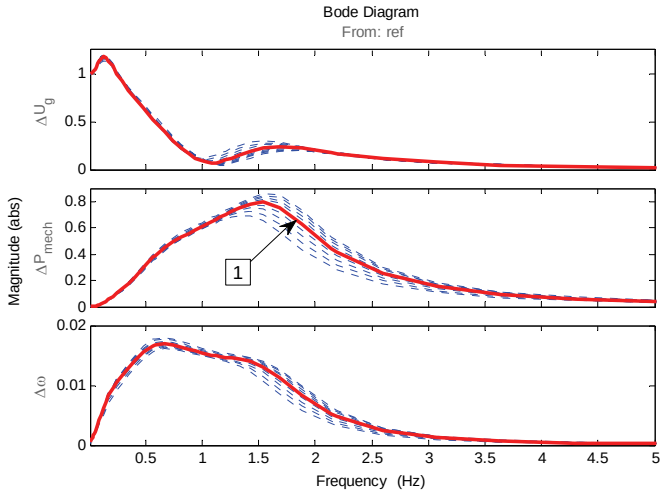

Fig. 3. Frequency response of family closed with AVR and PSS systems, for P_{mech} in the range 0.4÷0.8 p.u. (1 – nominal model for P_{mech} = 0.6 p.u.)

But if one wants for example to synthesize a PSS, the approach to constructing the model should be different. First uncertainty should be introduced only in the channel of the AVR. Its weight function should be calculated, of course, in respect to that channel of the open system (because after all the AVR is fixed and its purpose is to cope with the uncertainties). Only then the AVR is introduced and this way the uncertainty of this channel is "trapped" in the AVR feedback channel. As seen in Fig. 3, the other channels, which the PSS is going to use, change their behavior significantly and this is the uncertainty that the synthesized PSS should deal with. This is why the weight functions of the uncertainties in the channel, which the PSS is going to use, should be calculated in respect to the system closed with the AVR. Only then the uncertainties will be presented correctly for the purpose of synthesis of robust PSS.

An illustration of the above said are the step responses of the family open systems G_{EPS} (Fig. 4) and of the family closed with AVR and PSS systems (Fig. 5). It is interesting how despite the wide range of deviation of P_{mech}, the outputs closed system vary very little.

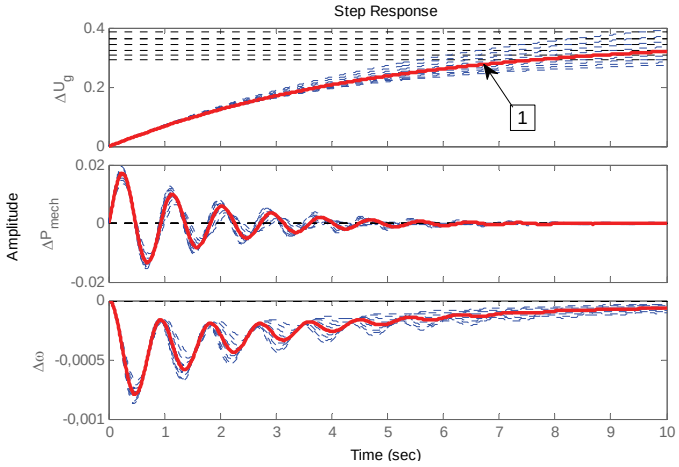

Fig. 4. Step response of family open systems G_{EPS} for P_{mech} in the range 0.4÷0.8 p.u. (1 – nominal model for P_{mech} = 0.6 p.u.)

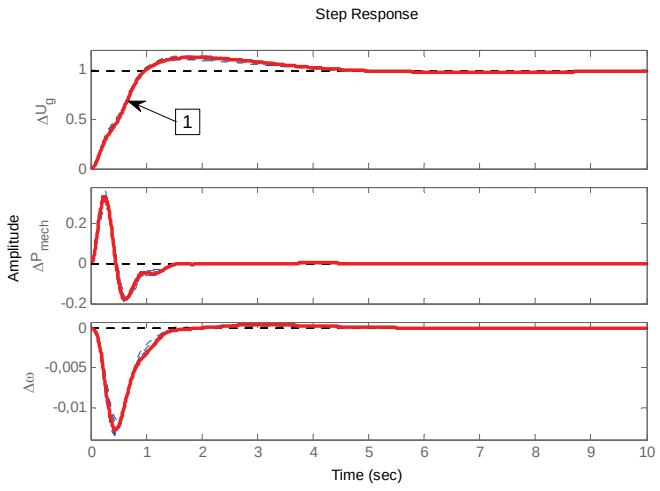

Fig. 5. Step response of family closed with AVR and PSS systems, for P_{mech} in the range 0.4÷0.8 p.u. (1 – nominal model for P_{mech} = 0.6 p.u.)

III. Case Study

A. Choice of nominal model

In this paper is analyzed the influence of different preconditions on the selection of appropriate weight functions. First the effect of the choice of nominal model is studied. Three distinct cases were considered – for nominal was chosen the model corresponding to an operating point, determined by P_{mech} at the upper limit of its supposed deviation range ($P_{mech,1}$ = 0.8 p.u.), at the middle of the range

($P_{mech,2}$ = 0.6 p.u.) and at the lower limit ($P_{mech,3}$ = 0.4 p.u.). The weight functions were calculated according to the well-known expression [1,2] separately for each input-output channel, based on the boundaries of the frequency responses of the family generated models, i.e.

$$\left|W_{m_{P,K}}(j\omega)\right| \geq \frac{\left|G_{P,K}(j\omega) - G_{EPS,nom_{P,K}}(j\omega)\right|}{\left|G_{EPS,nom_{P,K}}(j\omega)\right|} \qquad (1)$$

where indexes *p* and *k* represent the outputs and the inputs of the system, *G* represents the family of generator's models, obtained by the change of P_{mech} in the range 0.4÷0.8 p.u. An interpretation of that expression is that $W_{m_{P,K}}$ holds the biggest relative (to the particular nominal model) variations of *G* over the frequencies. In Fig. 6 are shown the weight functions for the three different cases of choice of nominal model.

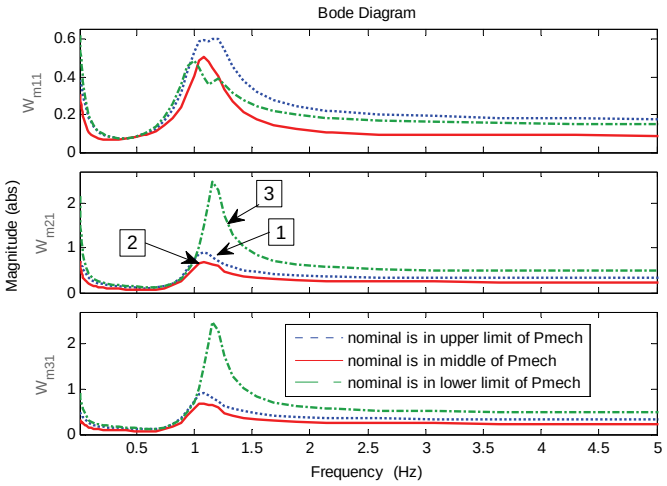

Fig. 6. Weight functions (for each input/output channel) in respect to nominal model for:
1 – $P_{mech,1}$ = 0.8 p.u.; 2 – $P_{mech,2}$ = 0.6 p.u.; 3 – $P_{mech,3}$ = 0.4 p.u.

In the course of generation of the family of models was validated that all open systems G_{EPS} , together with the closed with AVR and PSS systems are stable. It should be mentioned here that G_{EPS} has the particularity that its output do not change independently. In order to account this feature, when building the uncertainty matrix $\mathbf{\Delta}$, one and the same uncertainty block was placed in the main diagonal of the matrix, instead of using different and independently varying uncertainty blocks for each output.

After the formation of the uncertainty models for the different cases of choice of nominal model, the system was closed with the AVR and PSS and its robust stability was checked with MATLAB function robuststab.

The results in Table I clearly show that choice of the nominal model on the limit values of the independently varying parameter leads to more pessimistic assessments of the structured singular value μ and respectively of the robust stability. Even more – in the case of nominal model corresponding to the lower limit of P_{mech} , the uncertain system was assessed as robustly unstable and this is misleading.

TABLE I. ROBUST STABILITY FOR DIFFERENT CHOICES OF NOMINAL MODEL

Nominal mode of the uncertain system for the case of:	Robustly stable uncertain system?	Maximal value of upper limit of μ
$P_{mech,1}$ = 0.8 p.u.	Yes	0.7524
$P_{mech,2}$ = 0.6 p.u.	Yes	0.6674
$P_{mech,3}$ = 0.4 p.u.	**NO**	1.973

These results are basis to recommend the choice of the nominal model for the uncertain system to correspond to value of the varying parameter in the middle of their range instead of the actual nominal operating point of the generator. This is why the rest of the study is carried with nominal model corresponding to P_{mech}=0.6 p.u.

B. Shape of the weight function

The second aspect of the study is the comparison the possibility to represent the uncertainty with different weight functions for each input-output channel or with one and the same for all input-output channels. Two cases for formulation of single weight function are considered. The first one is based on the maximal relative deviation of the maximal singular value of the family of generated models in respect to the maximal singular value of the nominal model, i.e.

$$\left|W_m(j\omega)\right| \geq \bar{\sigma}\left(G(j\omega) - G_{EPS,nom}(j\omega)\right) ./ \bar{\sigma}\left(G_{EPS,nom}(j\omega)\right) \qquad (2)$$

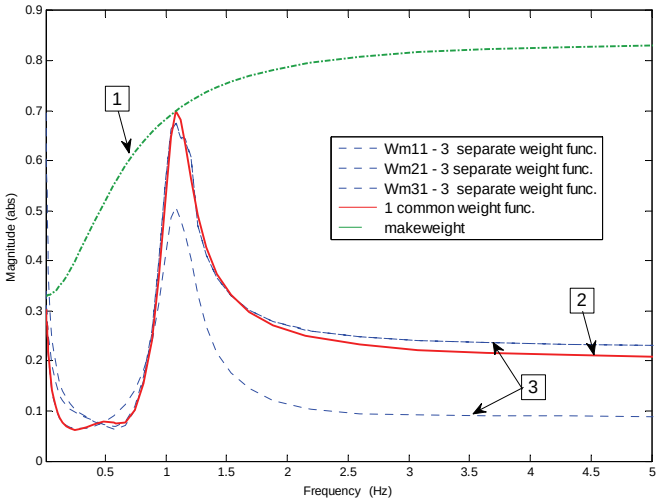

Fig. 7. Calculated weight functions:
1 – single function, common for all input/output channel, calculated by makeweight; 2 – single function, common for all input/output channel, calculated by maximal sigma of the system; 3 – three separate functions (by one for each input/output channel)

The second case is based on the MATLAB function makeweight, often used in the literature. It has the following syntax G = makeweight(dc, crossw, hf) and creates a stable, 1st-order continuous time state-space system G such that the frequency response of G satisfies G(j*0) = dc,

|G(j*crossw)| = 1, and G(j*∞) = hf. It must be that |DC| < 1 < |HF|, or |HF| < 1 < |DC|.

It is calculated in such a way that it encloses the weight function calculated by the maximal singular values. All different weight functions are shown in Fig. 7.

Table II shows the robust stability analysis for the different choices of weight functions. It is obvious that makeweight generates a weight function which with its shape is inappropriate for the problem of uncertainties in an EPS.

TABLE II. ROBUST STABILITY FOR DIFFERENT CHOICES OF WEIGHT FUNCTIONS

Case of choice of weight function:	Robustly stable uncertain system?	Maximal value of upper limit of μ
3 separate weight functions	Yes	0.6674
1 weight function for all input/output channels, calculated by maximal sigma of the system	Yes	0.5915
1 weight function for all input/output channels, calculated by makeweight	**NO**	1.021

The MATLAB function wcgain was used to calculate (for each frequency point) the worst gains on the input-output channels for the 3 separate and 1 common weight functions and was compared with the worst gains of the family of models corresponding to real systems with operating points of P_{mech} in the range 0.4÷0.8 p.u. The results are shown in Figs. 8 and 9. It is clearly seen that both cases enclose the reactions of the real systems meaning the they are both good representation of the family of real models.

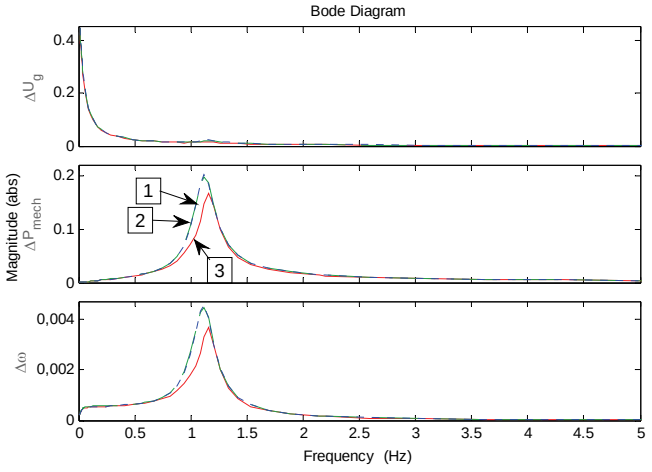

Fig. 8. Worst case gains by frequency points of the open system G_{EPS}:
1 – with single weight function, common for all input/output channel; 2 – with three separate weight functions (by one for each input/output channel); 3 – the limits of the family of real models;

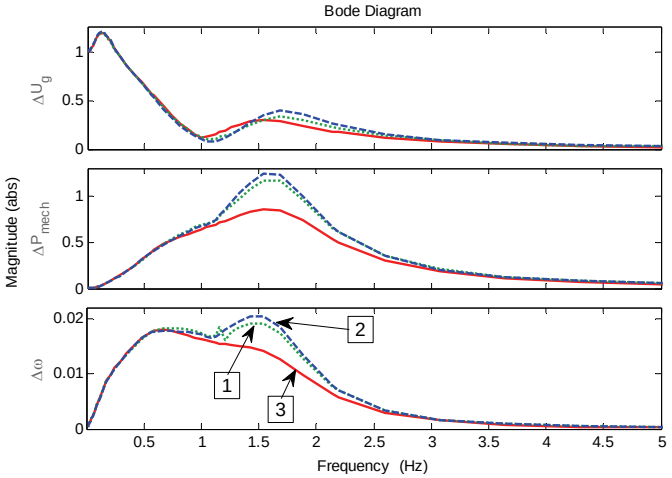

Fig. 9. Worst case gains by frequency points of the closed with AVR and PSS system:
1 – with single weight function, common for all input/output channel; 2 – with three separate weight functions (by one for each input/output channel); 3 – the limits of the family of real models;

IV. CONCLUSION

Having specified a range of change of the independent regime parameters of EPS, it is appropriate to choose the nominal system to correspond to an operating point in the middle of the variation ranges.

The weight functions for modeling unstructured output multiplicative uncertainty should represent the character of the frequency responses of the channels because in the general case there is more than one resonant frequency caused by the interaction of electrical and mechanical processes in EPS. In this sense the use of the MATLAB function makeweight for generation of weight function is not appropriate for modeling uncertainties in EPS.

REFERENCES

[1] Петков П., М. Константинов, Робастни системи за управление, АВС Техника, С. 2002
(Petkov P., M. Konstantinov, Robust control systems, ABC Tehnika, 2002)

[2] Петков П., Г. Лехов, А. Марковски, Ръководство по робастни системи за управление, АВС Техника, С. 2006
(Petkov P., G. Lehov, A. Markovski, Handbook on robust control systems, ABC Tehnika, 2006)

[3] Zhou K., Essentials of Robust Control, Prentice Hall, 1999

[4] Герасимов К., Й. Каменов, Приложимост на структурираното представяне на неопределености в модела на синхронен агрегат, Сборник с доклади на международна научно-техническа конференция “Електроенергетика”, стр.224-232, март 2010
(Gerasimov K., Y. Kamenov, Applicability of structured uncertainty in the synchronous generator model, Collection of reports from the international scientific conference “Elelktroenergetkia”, p.224-232, March 2010)

Structuring the Nominal Mathematical Model of the Electric Power System for the Aims of Robust Analysis

Yoncho Kamenov[1], Konstantin Gerasimov[2] and Yulian Rangelov[3]

Abstract – **A structured representation of the mathematical description of the electric power system (EPS) is proposed. It allows flexible introduction of uncertainties in the separate constituent elements of EPS. An algorithm is discussed for reduction of the order of the analyzed model by frequency equivalentation in respect to a certain generator bus.**

Keywords – **structuring the nominal mathematical model, robust analysis.**

I. INTRODUCTION

The most widely used tool for damping electro-mechanical oscillations in the modern electric power systems (EPS) is the device power system stabilizer (PSS). The PSS task is to create additional damping momentum which is in phase with the rotor mechanical speed deviation. Only then the device can successfully damp the mechanical oscillations. A common practice is to calculate the PSS settings from a determinate mathematical model of EPS, linearized around a certain operating point [1-3]. It is obvious that change of the EPS operating point (i.e. the regime) can result in inappropriate PSS settings. The authors of this article have the purpose to create an algorithm for calculation of robust PSS settings. This means that the EPS mathematical model has to include uncertainties which represent the constantly changing operating point and the inaccuracies in the EPS scheme parameters. In order to be able to model them easily, the paper proposes an appropriate structuring of the EPS mathematical description of the mechanical oscillations under small disturbances.

II. MATHEMATICAL MODEL

The structural scheme from Fig. 1 represents the proposed EPS electro-mechanical oscillations mathematical model which will be used for calculation of robust PSS settings of a certain generator.

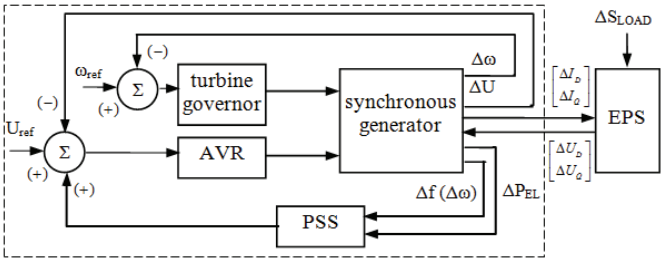

Fig. 1. Structure of the proposed EPS mathematical model

The generator linearized mathematical description, written in per unit system for nominal base conditions in *dq*-coordinates is:

$$
\begin{aligned}
&\Delta U_d = \Delta E''_d - x''_q \cdot \Delta I_q - r \cdot \Delta I_d;\\
&\Delta U_q = \Delta E''_q + x''_d \cdot \Delta I_d - r \cdot \Delta I_q;\\
&\frac{d\Delta E''_d}{dt} = \frac{-1}{T''_{q0}} \cdot \Delta E''_d + \frac{-(x_q - x''_q)}{T''_{q0}} \cdot \Delta I_q;\\
&\frac{d\Delta E''_q}{dt} = \frac{k_1}{T''_{d0}} \cdot \Delta E_{fD} + \frac{k_3 - k_1}{T''_{d0}} \cdot \Delta E'_q + \frac{-k_3}{T''_{d0}} \cdot \Delta E''_q + \\
&\qquad \frac{(x_d - x'_d)\cdot k_1 + (x'_d - x''_d)\cdot k_3}{T''_{d0}} \cdot \Delta I_d;\\
&\frac{d\Delta E'_q}{dt} = \frac{1}{T_{d0}} \cdot \Delta E_{fD} + \frac{-(1+k_2)}{T_{d0}} \cdot \Delta E'_q + \\
&\qquad \frac{x_d - x'_d - (x'_d - x''_d)\cdot k_2}{T_{d0}} \cdot \Delta I_d + \frac{k_2}{T_{d0}} \cdot \Delta E''_q;\\
&\frac{d\Delta\omega}{dt} = \frac{-P_0}{T_J} \cdot \Delta\omega + \frac{1}{T_J} \cdot \Delta P_{мех} - \frac{\left(E''_{q0} - I_{d0}\cdot\left(x''_q - x''_d\right)\right)}{T_J} \cdot \Delta I_q - \\
&\qquad \frac{\left(E''_{d0} - I_{q0}\cdot\left(x''_q - x''_d\right)\right)}{T_J} \cdot \Delta I_d - \frac{I_{d0}}{T_J} \cdot \Delta E''_d - \frac{I_{q0}}{T_J} \cdot \Delta E''_q;\\
&\frac{d\Delta\theta}{dt} = 2\pi f_{nom} \cdot \Delta\omega + \left(-2\pi f_{nom}\right) \cdot \Delta\omega_R
\end{aligned}
\tag{1}
$$

where

$$
\begin{aligned}
k_1 &= \frac{T''_{d0}}{T_{d0}} \cdot \frac{x_{ad} - (x_d - x''_d)}{x_{ad} - (x_d - x'_d)};\\
k_2 &= \frac{x_d - x'_d}{x_{ad} - x_d + x'_d};\\
k_3 &= 1 - k_1 \cdot k_2;
\end{aligned}
\tag{2}
$$

U_d, U_q, I_d, I_q are the stator winding voltage and current, respectively for *d* and *q* axis, in p.u.;

[1]Yoncho Kamenov is assoc. prof. at Department "Power Engineering", Technical University of Varna, Studentska Str. 1, Varna, 9010, Bulgaria, E-mail: j.kamenov@tu-varna.bg

[2]Konstantin Gerasimov is PhD student at Department "Power Engineering", Technical University of Varna, Studentska Str. 1, Varna, 9010, Bulgaria, E-mail: kosio_gerasimov@abv.bg

[3]Yulian Rangelov is chief assist. prof. at Department "Power Engineering", Technical University of Varna, Studentska Str. 1, Varna, 9010, Bulgaria, E-mail: j.rangelov@tu-varna.bg

E''_d, E''_q – subtransient voltages, respectively for *d* and *q* axis, in p.u.;

E_{fD} – the rotor voltage, proportional to the excitation voltage in p.u.;

x_{ad}, x_d, x'_d, x''_d – mutual, synchronous, transient and subtransient generator reactances in *d*-axis, in. p.u.;

x_q, x''_q – synchronous and subtransient reactances in *q*-axis, in p.u.;

r – stator winding active resistance, in p.u.;

T_{d0}, T''_{d0} – the catalogue time constants in d-axis for open stator winding, in s;

T''_{q0} – the catalogue time constant in *q*-axis for open stator circuit, in s;

T_J – mechanical time constant of the synchronous generator rotor, in s;

t – time, in s;

ω – electrical angular velocity of the generator's rotor, in p.u.;

ω_R – electrical angular velocity of the EPS referent coordinate system, in p.u.;

θ – the mutual angle between generator's *q*-axis and *Q*-axis of the referent EPS coordinate system, in rad;

P_{mech} – turbine mechanical power, in p.u.

The mathematical descriptions of PSS, AVR and the turbine governor most often are represented by structural schemes of directional blocks. For example, Fig. 2 shows the structural scheme of the widely used in the EPS of Bulgaria PSS-2A.

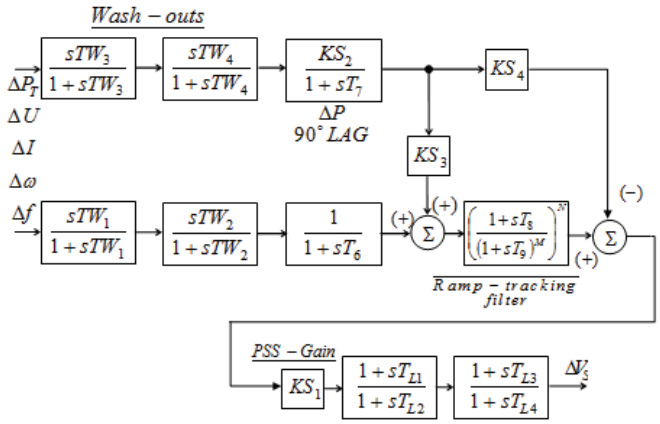

Fig. 2. PSS-2A block diagram

The synchronous generator model, whose PSS is being tuned, is represented by the mathematical descriptions of its constituent elements: synchronous generator, turbine and turbine governor, excitation system and automatic voltage regulator (AVR), power system stabilizer (PSS). The connection between the model of the synchronous unit and the model of the EPS is made by the variations of the current and voltage, defined in Cartesian coordinate system (DQ) which rotates with the referent generator speed ω_R.

These are transformed into transfer matrix connecting the input and output quantities, as shown on Fig. 1. In same details is described and each other generator in the EPS. Their descriptions are joined by the network description into a single transfer matrix connecting the variations of current in the generator with the PSS to be tuned (ΔI_D, ΔI_Q) with variations of the voltage in the same generator (ΔU_D, ΔU_Q) and the referent generator speed ($\Delta\omega_R$).

The realizations of these transfer matrixes in the state space have too big dimensions. Due to the big number of generators in the detailed model of a real EPS these dimensions can reach order of a few thousand. This is a significant problem for the optimization procedure for calculation of optimal PSS settings. To overcome this difficulty it is necessary to reduce the order of the system in respect to the bus of the generator whose PSS is going to be tuned.

III. Model Order Reduction

For this purpose the calculated frequency responses of the whole transfer matrix

$$G_{EPS}(j\omega)=\begin{bmatrix} \frac{\Delta\omega_R}{\Delta I_D} & \frac{\Delta\omega_R}{\Delta I_Q} \\ \frac{\Delta U_D}{\Delta I_D} & \frac{\Delta U_D}{\Delta I_Q} \\ \frac{\Delta U_Q}{\Delta I_D} & \frac{\Delta U_Q}{\Delta I_Q} \end{bmatrix} \quad (3)$$

for the frequency range significant for the EPS electromechanical oscillations ($\omega = 0 \div 30$ rad/s) are approximated and this way a reduction of the order of the mathematical description is achieved without loss of the real EPS influence over the PSS which is going to be tuned.

The approximation gives the following transfer matrix (in Laplace space):

$$\mathbf{G}(s)=\begin{bmatrix} Y_{RD}(s) & Y_{RQ}(s) \\ Y_{DD}(s) & Y_{DQ}(s) \\ Y_{QD}(s) & Y_{QQ}(s) \end{bmatrix} \quad (4)$$

The elements of the transfer matrix $\mathbf{G}(s)$ are transformed into state space and have the following realizations

$$Y_i(s)=\left[\begin{array}{c|c} \mathbf{A}_i & \mathbf{B}_i \\ \hline \mathbf{C}_i & \mathbf{D}_i \end{array}\right] \quad (5)$$

where $i = RD, RQ, DD, DQ, QD, QQ$. Then the realization in state space of the whole transfer matrix $\mathbf{G}(s)$ is [4]:

$$\mathbf{G}(s)=\left[\begin{array}{cccccc|cc}
\mathbf{A}_{RD} & 0 & 0 & 0 & 0 & 0 & \mathbf{B}_{RD} & 0 \\
0 & \mathbf{A}_{RQ} & 0 & 0 & 0 & 0 & 0 & \mathbf{B}_{DQ} \\
0 & 0 & \mathbf{A}_{DD} & 0 & 0 & 0 & \mathbf{B}_{DD} & 0 \\
0 & 0 & 0 & \mathbf{A}_{DQ} & 0 & 0 & 0 & \mathbf{B}_{DQ} \\
0 & 0 & 0 & 0 & \mathbf{A}_{QD} & 0 & \mathbf{B}_{QD} & 0 \\
0 & 0 & 0 & 0 & 0 & \mathbf{A}_{QQ} & 0 & \mathbf{B}_{QQ} \\
\hline
\mathbf{C}_{RD} & \mathbf{C}_{DQ} & 0 & 0 & 0 & 0 & \mathbf{D}_{RD} & \mathbf{D}_{DQ} \\
0 & 0 & \mathbf{C}_{DD} & \mathbf{C}_{DQ} & 0 & 0 & \mathbf{D}_{DD} & \mathbf{D}_{DQ} \\
0 & 0 & 0 & 0 & \mathbf{C}_{QD} & \mathbf{C}_{QQ} & \mathbf{D}_{QD} & \mathbf{D}_{QQ}
\end{array}\right] \quad (6)$$

It is worth noticing that the obtained state space realization $\mathbf{G}(s)$ is not always the minimal realization. To get the minimal realization, decomposition in respect to controllability and observability has to be made, which will eliminate the uncontrollable and/or unobservable states. This can be done with the MATLAB function mineral. Then additional model order reduction can be done by means of the the hankel norm.

It is well known [5] that Hankel norm of a system with transfer matrix **G** is equal to:

$$\left\|\mathbf{G}\right\|_H = \sqrt{\rho\cdot(\mathbf{P}\cdot\mathbf{Q})} \quad (7)$$

where ρ is the spectral radius of the product of **P**.**Q**; **P** – controllability Gramian of **G**; **Q** – observability Gramian of **G**. Because ρ is the maximal eigenvalue of the **P**.**Q**, they are often called Hankel singular values, i.e.

$$\sigma_{Hi} = \sqrt{\lambda_i(\mathbf{P}\cdot\mathbf{Q})} \quad (8)$$

From all this follows that the Hankel norm of a **G** is equal to the maximal Hankel singular value, i.e.

$$\left\|\mathbf{G}\right\|_H = \max\sigma_{\mathrm{H},i} = \sigma_{\mathrm{H},1} \quad (9)$$

The ratio of the Hankel singular values to the Hankel norm

$$O_{\mathrm{H},i} = \frac{\sigma_{\mathrm{H},i}}{\left\|\mathbf{G}\right\|_H} = \frac{\sigma_{\mathrm{H},i}}{\sigma_{\mathrm{H},1}},\ i=\overline{2,n} \quad (10)$$

is indicator for the possibilities for **G** order reduction**.**

IV. Results

In the study, for test model was used the detailed mathematical model of real EPS consisted of: 787 generators, 124 PSS, 5749 power lines, 1495 transformers, 5176 buses and 3255 loads and shunts.

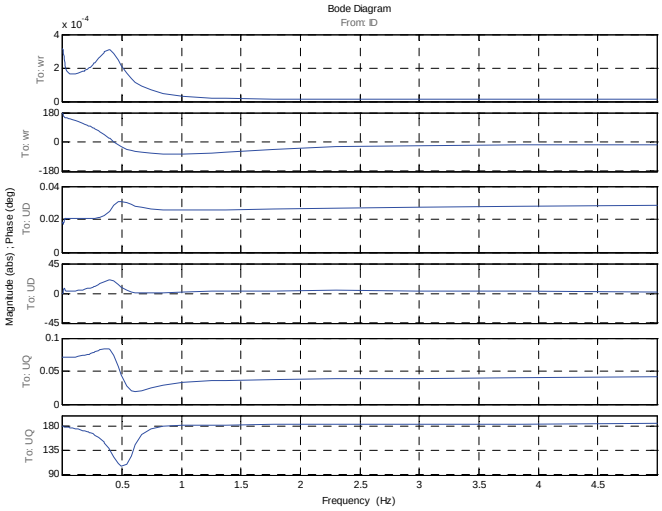

Fig. 3. Frequency response of the analyzed EPS in respect to the bus of a certain 300MW generator in the system for input I_D

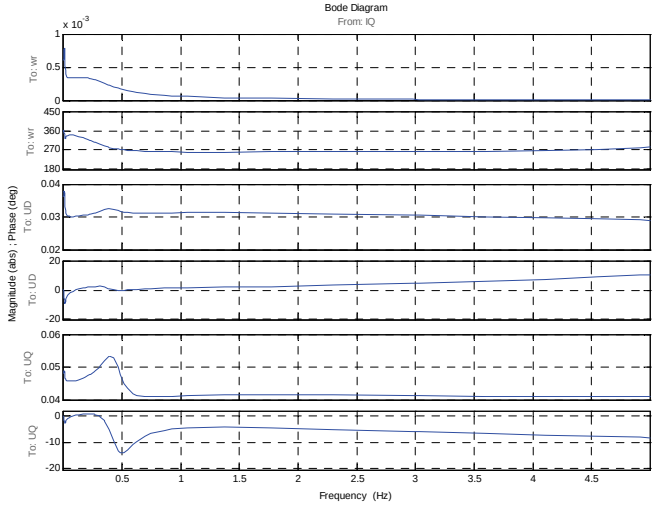

Fig. 4. Frequency response of the analyzed EPS in respect to the bus of a certain 300MW generator in the system for input I_Q

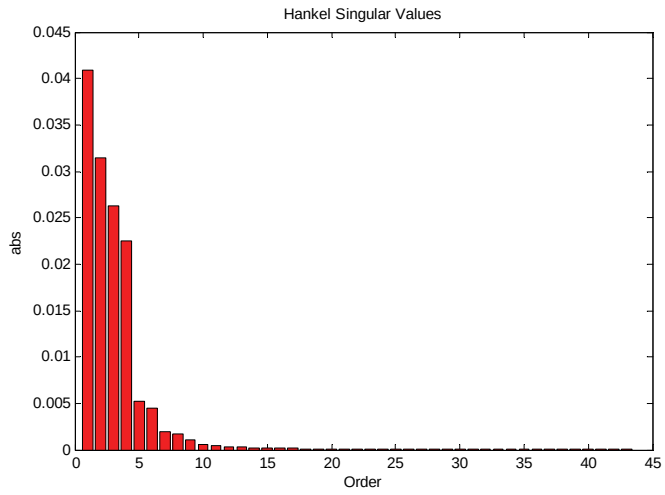

Fig. 5. Hankel singular values of the approximated EPS

Figs. 3 and 4 shows the calculated frequency responses of the EPS model in respect to the bus of a certain 300MW generator in the system.

The full EPS model matrix in state space is of order 7139x7139. After the approximated the system is reduced to order 43x43. The Hankel singular values of the approximated model are shown in Fig. 5. They are calculated with the MATLAB function hankelmr.

It is clearly seen that the order of the obtained equivalent system description can further be reduced to 17x17. A confirmation of this is seen from the closeness of the step responses of the two systems (Figs. 6 and 7).

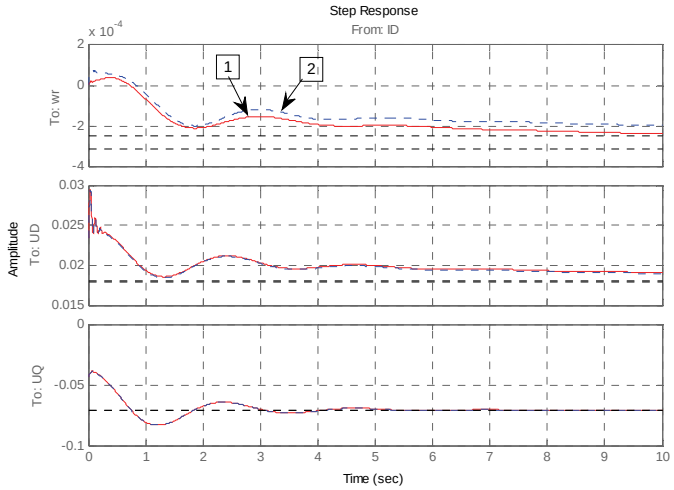

Fig. 6. Comparison of step responses for input I_D of:
1 – approximated to 43x43 EPS model;
2 – reduced to 17x17 approximated EPS model

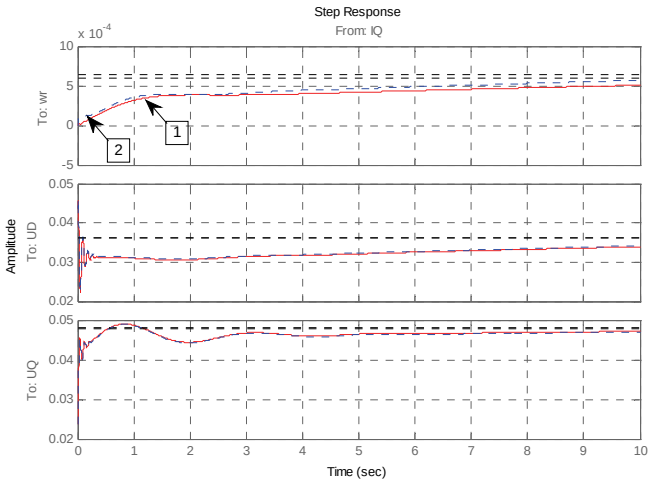

Fig. 7. Comparison of step responses for input I_Q of:
1 – approximated to 43x43 EPS model;
2 – reduced to 17x17 approximated EPS model

V. Conclusion

The proposed structuring of the mathematical model of EPS and the method for reduction of the order of the system allow easy introduction of variations of the EPS constituent elements due to the variations of the operating point parameters and inaccuracies in the knowledge about the scheme parameters. As a result a family of transfer matrixes of the corresponding elements can be calculated and thus easily appropriate weight functions for unstructured representation of the uncertainties in the EPS elements can be constructed.

References

[1] Farmer R. G., B. L. Agrawal, State-of-the-art technique for power system stabilizer tuning, IEEE Trans. on Power Apparatus and Systems, Vol.PAS-102, No.3, March 1983.

[2] Kundur P., D. C. Lee, H. M. Zein El-din, Power system stabilizers for thermal units: Analytical techniques and on-site validation, IEEE Trans. on Power Apparatus and Systems, Vol.PAS-100, No.1, January 1981.

[3] Maslennikov V.A., S.M.Ustinov. Method and software for coordinated tuning of power system regulators. - IEEE Trans. on Power Systems, Vol.12, No.4, pp. 1419-1424, November 1997.

[4] Герасимов К., Математическо описание на електро-механичните движения в електроенергийната система и алгоритми за изследване на устойчивостта им при малки смущения. Дисертационен труд за придобиване на научна степен доктор на науките. ТУ-Варна, 2006
(Gerasimov K., Mathematical description of the electric power system electro-mechanical oscillations and algorithms for analysis of small signal stability, Dissertation, TU-Varna, 2006)

[5] Петков П., М. Константинов, Робастни системи за управление, АВС Техника, С. 2002
(Petkov P., M. Konstantinov, Robust control systems, ABC Tehника, 2002)

Heating of Contacts and Terminals of Power Cables

Radisa Dimitrijevic[1], Dragan Tasic[2], Slavoljub Aleksic[3] and Nebojsa Raicevic[4]

Abstract – **Temperature rise, encountered along the power cable line due to the losses in the conductor, dielectric and contacts is of great importance in the service. Concerning the cable joints and terminations, jointing two cables by means of connector or terminating the cable by means of terminal lug represent significant phases during their installation. The nature of contacts was considered, such as their ageing in the exploitation. Calculation of temperature rise was analyzed and based on it, two numerical samples were performed. For one general case, temperature distribution in the vicinity of terminal lug was shown by means of commerically available program.**

Keywords – **Temperature rise, cable terminal lug, cable connector, temperature distribution.**

I. INTRODUCTION

Well done jointing and terminating the power cables play great role for the reliable service of cable lines in the power cable network. In these procedures, at the same places, electric and thermal fields get worse, due to interrupting the semi conducting screen of the cable and presence cable conductor or terminal lug. While the ends of semi conducting screen of the cable insulation are weak spots from point of the electric field, connectors and terminal lugs are critical from point of the thermal field.

Generally, when two metals are in touch, the contact is not made over the whole apparent surface, but only over certain number of points. These are elementary contacts [1]. Let's assume that there are *n* elementary contacts of the same radius *a*, uniformly distributed over the whole apparent surface. Then effective contact surface is:

$$S_a = n \pi a^2 \tag{1}$$

The contact surface depends on the applied contact force, surface state and hardness of the contact metals. Electric resistivity of elementary contact consists of two components:

- Constriction resistance R_e, due to passing the current through the elementary contact and
- Film resistance R_i, relating to thin oxide layer or absorbed molecules at the interface.

The total contact resistance is the sum of metioned components, i.e:

$$R_c = R_e + R_i = \frac{\rho}{2na} + \frac{\sigma_0}{n\pi a^2} \tag{2}$$

where ρ - specific electric resistivity of the metals and

σ_0 – surface ("tunnel") resistivity of oxide layer (depends on the nature of oxide and its thickness).

If electric conductor is very long compared to elementary contact of radius *a*, the lines of current are hyperbola and equipotential surfaces are flattened ellipsoids (Fig.1). Both hyperbola and ellipsoid are focused around the end of contact.

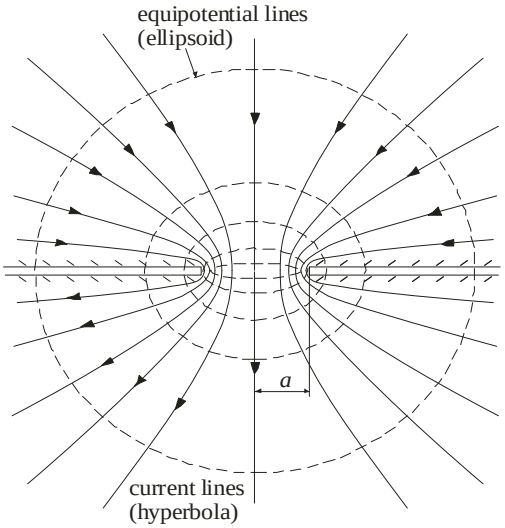

Fig. 1. Elementary contact

II. AGEING OF CONTACTS

The ageing of closed electric contacts, which are not subjected to arc effect, occurs due to reaction of the metals with the surrounding environment at contact interface [2]. This is very slow pending process, which could brings to the failure of contact under the certain undesirable circumstances. This reaction could be:

- Oxidation, due to presence of oxigen, sulphurous vapor,
- Corrosion, at bimetallic contacts, due to different electrochemical potential in the presence of higher humidity (more than 50% r.h.). Acceptable combination of metals to avoid corrosion shall have potential differences less than 350 mV.

Two simultaneous process can appear at the elementary contacts due to oxidation:

- Reduction of cross section of conducting zone,
- Increasing the thickness of oxide layer of surface resistivity σ_0.

There are other mechanisms of degradation, affecting the ageing level, but they can not be easily described by mathematical laws and therefore can not be easily analyzed. The only way to find out something about their influence is testing in laboratory.

[1]Radisa Dimitrijevic is with the Institute FKS, Marka Kraljevica bb, 35000 Nis, Serbia, E-mail: radisa.dimitrijevic@fks.co.rs

[2]Dragan Tasic, [3]Slavoljub Aleksic and [4]Nebojsa Raicevic are with the Faculty of Electronic Engineering, Aleksandra Medvedeva 14, 18000 Nis, Serbia, E-mail: dragan.tasic@elfak.ni.ac.rs; slavoljub.aleksic@elfak.ni.ac.rs; nebojsa.raicevic@elfak.ni.ac.rs

III. INFLUENCE OF TEMPERATURE RISE

Generally, when the contact is exposed to oxidation in the air and the temperature rise overcomes permissible value, accelerated ageing of contact occurs. Its shelf life shall be multiplied by ageing factor K_{th}.

In more general case, when both temperature rise of ambient and temperature rise of inner contacts act simultaneously, the following assumptions are adopted:

- Temperature rise is proportional to current by exponent between 1,5 and 2, depending on emissivity of the surface (for cooling by radiation and natural convection, average value of 1,67 can be used, but for radiation and forced convection, average value 2);
- Shelf life of contact is reduced by half, if ambient temperature rise ΔT_i is increased by 6,5 K;
- Shelf life of contact is reduced by half, if average temperature θ_e of medium, surrounding the contact, is increased by 8,5 K.

The ageing factor K_{th} can be expressed by:

$$K_{th} = 2^{\left(\frac{\theta_e - \theta_{an}}{8.5} + \frac{\Delta T_i - \Delta T_n}{6.5}\right)} \qquad (3)$$

where

θ_{an} (T_{an}) – standard temperature of surrounding air (^{0}C) or (K);

ΔT_n – contact temperature rise, relating to surrounding medium (average values in K).

Analysis indicates, that effect of ageing in short term can not be compensated, if the contacts are subjected to reduced load and lower temperature under the similar terms.

IV. CALCULATION OF TEMPERATURE RISE OF CONDUCTORS AND CONTACTS

The changing of temperature along two conductors, connected in point O is shown in the Fig.2.

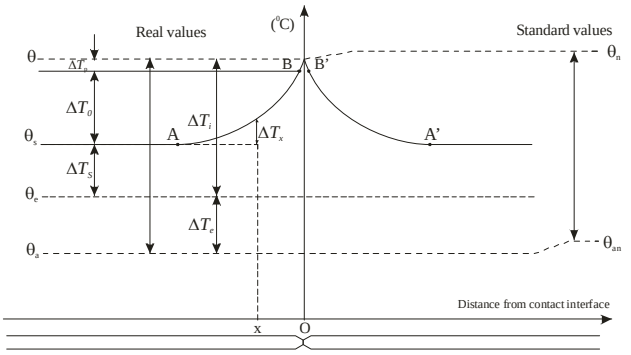

Fig. 2. The changing of temperature along two conductors

Maximum temperature θ represents the following addition:

$$\theta = \theta_a + \Delta T_e + \Delta T_s + \Delta T_0 + \Delta T_p \qquad (4)$$

where : θ_a – the temperature of outside ambient (accepted 40^0C). If termination is inside an enclosure, θ_a is the temperature of the air outside enclosure;

ΔT_e – the temperature rise of the air surrounding contact or terminal, in relation to ambient temperature;

ΔT_s – real temperature rise without contact. Contacts and conductors are usually cooled by radiation or natural convection [2];

ΔT_0 – temperature rise in the vicinity of contact, caused by Joule effect at resistance of contact;

ΔT_p – additional temperature rise at elementary contacts.

A. Temperature rise ΔT_s relating to ambient temperature T_e

It is calculated by expression:

$$\Delta T_s = \frac{\left[\left(T_e + \Delta T_s - 273.15\right)\alpha + 1\right] R_0 I^2 + r\,\varphi_s S_r}{Bl\left[\sigma\varepsilon\dfrac{\left(T_e + \Delta T_s\right)^4 - T_e^4}{\Delta T_s} + \dfrac{\lambda}{D_h} N_u\right]} \qquad (5)$$

where: α – temperature coefficient of conductor;

R_0 – longitudinal resistance of conductor at 0^0C;

I – current;

r –coefficient of receiption of sun radiation $0 \le r \le 1$;

φ_s – thermal flux;

S_r – surface of conductor, receiving thermal flux φ_s;

B – external periphery of conductor, emitting heat;

l – length of conductor; average distance between elementary contacts;

σ – Stefan-Boltzman constant $5.67 \cdot 10^{-8}$ ($Wm^{-2}K^{-4}$);

ε – total emissivity of conductor;

λ – thermal conductivity of surrounding medium;

D_h – diameter of conductor, leading to contact or total height of section conductor (m);

N_u , G_r , P_r , R_E – Nusselt number;

B. Temperature rise ΔT_0 of conductor in the vicinity of contact or terminal, cooled by radiation and natural convection

Additional temperature rise of contact or terminal, which is cooled by radiation and natural convection, is expressed by:

$$\Delta T_0 = \left(W\sqrt{\frac{\delta + 1}{2\lambda_c S \gamma B}}\right)^{\frac{2}{\delta+1}} \qquad (6)$$

where: W – dissipation at the contacts;

δ – exponent of ΔT in expression $\varphi = \gamma \Delta T^{\delta}$;

λ_c – thermal conductivity of conductor;

S – cross section of conductor;

γ – constant relating to emission.

C. Temperature rise T_p of elementary contacts

Finally, there is additional temperature rise at the elementary contacts due to opening the thermal flux lines from their boundary surface. This rise is small and can be expressed by:

$$\Delta T_p = \frac{I^2}{2\pi^2 n^2 \lambda_c}\left(\frac{\rho}{4a^2} + \frac{\sigma_0}{a^3}\right) \qquad (7)$$

where a, n are radius and number of elementary contacts and coefficient $n_k = 2{,}5 \cdot 10^{-5}$ [1].

V. NUMERICAL EXAMPLES

A. Example

Indoor cable termination is installed in bay of power plant. Temperature rise of contacts during the short term overload is $\Delta T_i = 65^0$C, while ambient (enclosure) temperature $\theta_e = 40^0$C. Calculate the effect of ageing contacts, if standard temperature of surrounding air $\theta_a = 20^0$C, and maximum permissible standard temperature rise of contact $\Delta T_n = 50^0$C.

Solution. From Eq.3 ageing factor will be:

$$K_{th} = 25.3 \text{ h}$$

It means, that 1 hour service in the new worse condition during the short term overload at higher ambient temperature will shorten shelf life of cable termination by 25,3 hours. If ambient temperature increases by $8,5^0$C above standard 20^0C, and temperature rise of contact by $6,5^0$C above maximum permissible 50^0C relating to ambient temperature, then ageing of contacts will occur.

B. Example

Cable line of three cables A2XSY 1×150/25 mm^2 12/20 kV in trefoil formation is laid in air and terminated with outdoor terminations. Fitting is performed by bimetallic terminal lugs. Calculate maximum temperature of contact, if the cable terminal is cooled by radiation an natural convection.

Cable data:

- Nominal current carrying capacity for trefoil formation and laying in the air I=322 A (calculated value);
- Thermal coefficient of resistivity at 0^0C $\alpha_{0\,Cu}=4{,}265\cdot10^{-3}$ K^{-1} and $\alpha_{0\,Al}=4{,}383\cdot10^{-3}$ K^{-1} [1];
- Specific resistance at 0^0C for copper $\rho_{0\,Cu}=1{,}5881\cdot10^{-8}$ Ωm and for aluminium $\rho_{0\,Al}=2{,}6\cdot10^{-8}$ Ωm [1];
- Thermal conductivity at 20^0C $\lambda_{c\,Cu}=387$ W/mK i $\lambda_{c\,Al}=203$ W/mK [1];
- Physical properties of air at 20^0C – density $M=1{,}205$ kg/m^3; compressibility $\beta=3{,}4\cdot10^{-3}$ K^{-1}; specific heat $C_p=1006{,}3$ J/kg K; thermal conductivity $\lambda=0{,}02585$ W/mK; dynamic viscosity $\mu_d=1{,}822\cdot10^{-5}$ Pa s [1];
- The remaining physical properties and constants – emissivity of outer cable sheath $\varepsilon=0.95$ [3]; $g=9{,}81$ m/s^2; cross section $S=150\cdot10^{-6}$ m^2; periphery $B=0{,}11$ m; cable diameter $D_h=0{,}035$ m; specific surface of cable cooling $S_c=\pi D_h\ l$ m^2; average temperature of surrounding air $T_e=293{,}15$ K; coefficient of receiption of sun radiation $0<r<1$ accepted $r=0{,}5$; thermal flux $\varphi_s = \gamma\Delta T^{\delta}$ W/m^2, where $\gamma=5.9$ and $\delta=1{,}2$; resistance of aluminium conductor $R_0 = \rho_{0\,Al}\cdot l/S = 2{,}6\cdot10^{-8}\cdot1/150\cdot10^{-6}\ \Omega$ na 0^0 C [1];
- Specific resistivity at 20^0C $\rho_{Cu}=1{,}8\cdot10^{-8}$ Ωm and $\rho_{Al}=3{,}06\cdot10^{-8}$ Ωm; tunnel resistivity of contact surface $\sigma_{0Cu}=5\cdot10^{-12}$ Ωm^2 and $\sigma_{0\,Al}=10^{-11}$ Ωm^2; $n_k=2{,}5\cdot10^{-5}$; hardness $H_{Cu}=5{,}5\cdot10^8$ Pa and $H_{Al}=3\cdot10^8$ Pa; $N_{u\,Cu}=0{,}05$ and $N_{u\,Al}=0{,}07$; evenness coefficient $\xi=0.15$ and $F=50$ N [1].

Maximum contact temperature θ according to Eq.4 is:

$$\theta = \theta_a + \Delta T_e + \Delta T_s + \Delta T_0 + \Delta T_p$$

It is adopted $\theta_a = 40^0$C and $\Delta T_e = 5^0$C. Temperature rise of air ΔT_e, surrounding the contact (terminal), compared to ambient temperature is estimated to be 5^0C. Higher values should not be expected, because the contact is in the open space and is cooled by radiation and natural convection, so that these temperatures are very close.

In the case of natural convection, a value of temperature rise of horizontal "infinite" long single core cable, related to ambient temperature can be obtained from Eq. 5, after several iterations:

$$\Delta T_s = 23{,}2 \text{ K}$$

Contact resistance at the point of compression of aluminium conductor and aluminium part of bimetallic terminal lug (Eq.2) will be as follows:

$$R_c = 9{,}01\cdot10^{-6}\ \Omega$$

and at the point of tightening its copper part:

$$R_c = 8{,}26\cdot10^{-6}\ \Omega$$

Total power dissipation towards the conductor, taking into account both transient contact resistances amounts:

$$W = \frac{1}{2}R_{c\,Cu}I^2 + \frac{1}{2}R_{c\,Al}I^2 = 0{,}9 \text{ W}$$

Additional temperature rise of contact, cooling by radiation and natural convection will be (Eq.6):

$$\Delta T_0 = 24 \text{ K}$$

Finally, additional temperature rise at the elementary contacts due to openning the thermal flux lines from their boundary surface will be (Eq.7):

$$\Delta T_p = \frac{I^2}{2\pi^2 n^2 \lambda_c}\left(\frac{\rho}{4a^2} + \frac{\sigma_0}{a^3}\right) = 0{,}4 \text{ K}$$

Now, total maximum temperature of contact θ amounts:

$$\theta = \theta_a + \Delta T_e + \Delta T_s + \Delta T_0 + \Delta T_p = 92{,}6^0\text{C}$$

Taking into account that maximum permissible temperature of contact is 90^0C (because of XLPE insulation and other similar materials, overlapping the conductor, close to contact), the temperature rise $2{,}6^0$C, obtained in calculation, will not cause its ageing, because this overheating is not continuous. As noted in Example 1, ageing of contact will occur, if average annual ambient temperature will be increased by $8,5^0$C above standard one (20^0C) or if temperature rise of contact would be by $6,5^0$C above maximum permissible temperature rise related to ambient temperature (50^0C).

VI. TEMPERATURE DISTRIBUTION IN THE VICINITY OF CONTACT OF CABLE TERMINATION

Generally, in the case of indoor mounting, cable termination is connected through terminal lug or connector to the copper bus bar. The terminal lug or connector is fixed with the screws by the force, which is prescribed.

The warmest place is contact between terminal connector and bus bar, which is usually cooled by radiation and natural convection. Approximate temperature distribution is shown in Fig.3. Some simplifications were applied. The influence of

other terminations in the same enclosure is neglected and only one section of the metal enclosure around the fitting the cable termination is analyzed. Fig.3 is not scaled.

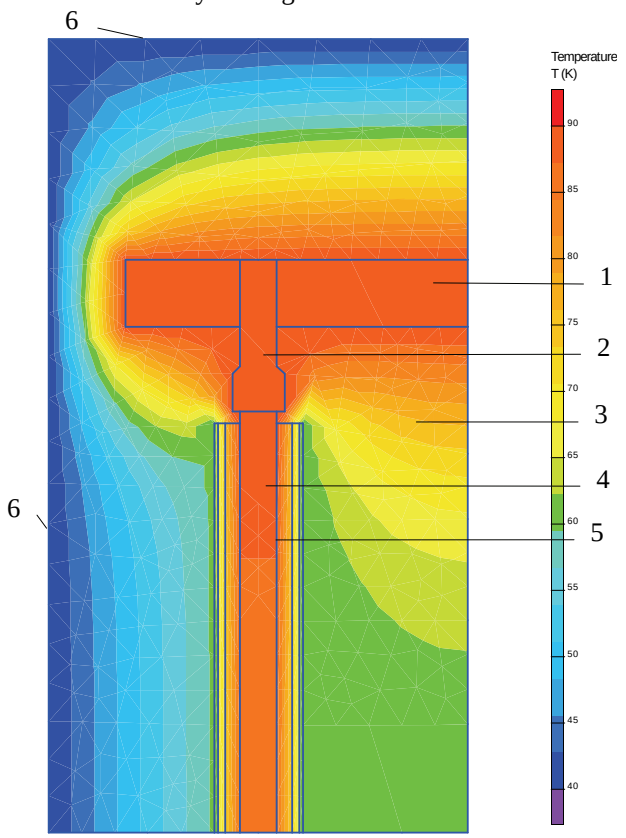

Fig. 3. Temperature distribution in the vicinity of contact of cable termination in the metal enclosure.

Legend: 1 – copper bus bar; 2 – terminal connector; 3 – surrounding air; 4 – aluminium conductor; 5 – XLPE insulation; 6 – enclosure.

The values of thermal conductivity, used in calculation, are shown in the Table I [4]. Finite temperatures, which were adopted in calculation, are 90^0C for the contact surface and 40^0C for surface of metal enclosure. Applied method was based on finite element method.

TABLE I
VALUES OF THERMAL CONDUCTIVITY

Block	Copper contact and bus bar	Aluminium conductor	XLPE insulation	Air
Thermal conductivity λ (W/mK)	387	210	0.25	0.0258

VII. CONCLUSION

Temporary monitoring of contact temperature at the place of fitting the cable indoor termination in the metal enclosure is important for safe service of the cable line. Each overheating the contact in some period can cause its ageing and cannot be compensated by subsequent cooling (decreasing the load current). As seen in numerical examples, analytical calculation of temperature is very complex and obtained results are not reliable. Therefore, some numerical method can be applied in the case of more complex configuration. Knowing the thermal conductivity of applied materials and geometry of analyzed domain, the temperature distribution can easily be obtained.

For the best reliable results, infra red camera shall be applied

REFERENCES

[1] IEC 60943 Guidance concerning the permissible temperature rise for the part of electrical equipment, in particular for terminals

[2] D.Tasić, Termički aspekti strujne opteretljivosti provodnika nadzemnih elektroenergetskih vodova, Edicija Monografije, Elektronski fakultet, Niš, 2002.

[3] L.Heinhold: Kabel und Leitungen für Starkstrom, Siemens Aktiengesellschaft, 4. überarbeitete Aufulage 1987.

[4] R.Dimitrijević, G.Jovović: Thermal field in premoulded 110 kV cable joint, R 2.04 JUKO CIGRE XVI Conference about power cables, Commitee 21, Soko Banja 27.-31.5. 2000.

Calculation of the Attraction Force between Permanent Magnet and Infinite Linear Magnetic Plane Using Ampere's Currents

Ana N. Vučković[1], Saša S. Ilić[2] and Slavoljub R. Aleksić[3]

Abstract – **The paper presents calculation of the attraction force between ring permanent magnet of trapezoidal cross section and infinite linear magnetic plane using distribution of Ampere's currents and discretization. The results obtained using the analytical method and discretization are compared with ones calculated numerically using FEMM software.**

Keywords – **Permanent magnet, Attraction force, Ampere's current.**

I. Introduction

Permanent magnets of various shapes are often utilized in magnetic actuators, sensors or releasable magnetic fasteners. Knowledge of the magnetic force, either levitation or attraction, is required to control devices reliably. The attraction force between ring permanent magnet and infinite linear magnetic plane of permeability μ_r, presented in Fig. 1, is derived using the analytical method based on surface Ampere's current distribution and discretization. Attraction force depends on the magnetic properties of permanent magnet (permanent magnetization *M*), permeability μ, on the distance between magnet and plane *h*, and on the geometrical design of the magnet [5].

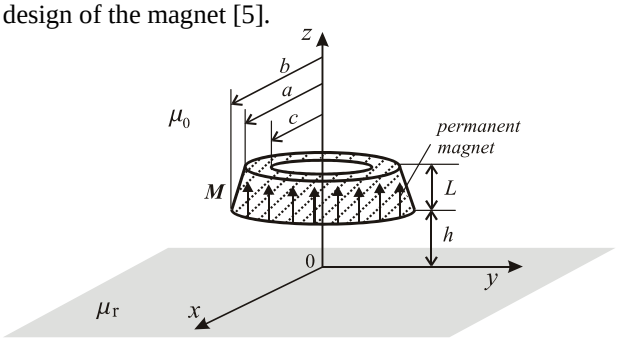

Fig. 1. Permanent magnet and infinite linear magnetic plane.

There are numerous techniques for analyzing permanent magnet devices and different approaches for determining attraction or levitation forces between magnets [1]-[4]. Many authors proposed simplified and robust formulations of the magnetic field components created by ring permanent magnets. Moreover, the evaluation of the magnetic field created by ring magnets is the step that can help calculating the force. Indeed, the force is the value of importance for the design and optimization of a bearing. In [2] permanent magnets are modeled as distributions of equivalent magnetic charge and the levitation forces are determined by computing the force between the two charge distributions. Attraction force between permanent magnets in [1] is established by magnetostatic interaction. In this paper the attraction force is derived using the analytical method based on surface Ampere's current distribution and discretization.

II. Procedure for Attraction Force Calculation

For solving this problem the image theorem in the plane mirror is used. The treated system can be replaced with system presented in the Fig 2. where

$$\alpha = \frac{\mu_r - 1}{\mu_r + 1}. \tag{1}$$

It is assumed that the magnetization is uniform throughout the magnet and it is

$$\boldsymbol{M}_1 = \boldsymbol{M} = M\hat{z}, \tag{2}$$

and for the image $\boldsymbol{M}_2 = \alpha \boldsymbol{M} = \alpha M\hat{z}$. (3)

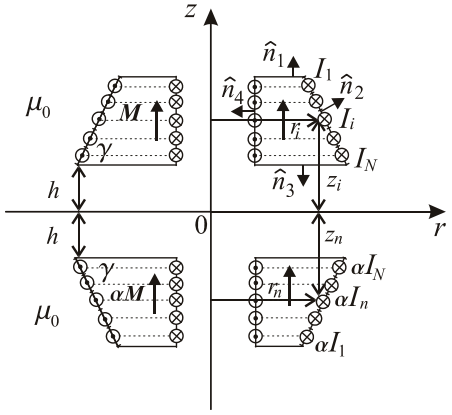

Fig. 2. Discretizing model.

Due to uniform axial magnetization of the magnet and image, the volume density of the Ampere's currents is

$$\boldsymbol{J}_a = \operatorname{curl} \boldsymbol{M} = 0. \tag{4}$$

Only the surface Ampere's current, with density

$$\boldsymbol{J}_{sa} = \boldsymbol{M} \times \hat{n}, \tag{5}$$

[1]Ana Vučković is with the University of Niš, Faculty of Electronic Engineering, Aleksandra Medvedeva 14, 18000 Nis, Serbia, E-mail: ana.vuckovic@elfak.ni.ac.rs.

[2]Saša Ilić is with the University of Niš, Faculty of Electronic Engineering, Aleksandra Medvedeva 14, 18000 Nis, Serbia, E-mail: sasa.ilic@elfak.ni.ac.rs.

[3]Slavoljub Aleksić is with the University of Niš, Faculty of Electronic Engineering, Aleksandra Medvedeva 14, 18000 Nis, Serbia, E-mail: slavoljub.aleksic@elfak.ni.ac.rs.

(where $\hat{n}$ is unite vector of outgoing normal), exists on the inner and outer torus covers, in angular direction and the permanent magnet and its image behave as a thin, single layer, uniformly winded solenoid coils.

The goal of this approach is to determine analytically the magnetic flux density generated by the image in any point and then to calculate the force on the magnet. In order to determine the magnetic flux density produced by the lower permanent magnet, the circular current loop *C* is considered (Fig.3).

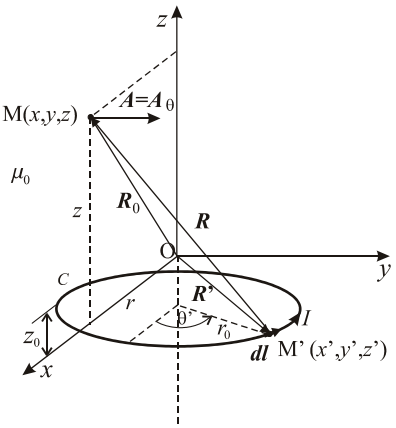

Fig. 3. The circular current loop.

In [3] the final form of the magnetic flux density components generated by circular current loop are obtained as:

$$B_r = \frac{\mu I}{2\pi}\frac{z-z_0}{r\sqrt{(r+r_0)^2+(z-z_0)^2}}\left(-K\left(\frac{\pi}{2},k\right)+\right.$$
$$\left.+\frac{r^2+r_0{}^2+(z-z_0)^2}{(r-r_0)^2+(z-z_0)^2}E\left(\frac{\pi}{2},k\right)\right), \quad (6)$$

$$B_z = \frac{\mu I}{2\pi}\frac{1}{\sqrt{(r+r_0)^2+(z-z_0)^2}}\left(K\left(\frac{\pi}{2},k\right)+\right.$$
$$\left.+\frac{r_0{}^2-r^2-(z-z_0)^2}{(r-r_0)^2+(z-z_0)^2}E\left(\frac{\pi}{2},k\right)\right). \quad (7)$$

Using the results that are obtained for the circular loop the magnetic flux density generated by the image could be determined in any point. The idea is to discretize each magnet cover into system of segments (circular loops) where *N* is the number of segments. Considering Fig. 2 it is obvious that the following formulas are satisfied:

$$\boldsymbol{M}\times\hat{n}_1=0\,,\ \boldsymbol{M}\times\hat{n}_2=\boldsymbol{J}_{\mathrm{sa}}\,,\ \boldsymbol{M}\times\hat{n}_3=0\,,\ \boldsymbol{M}\times\hat{n}_4=\boldsymbol{J}_{\mathrm{sa}}\,. \quad (8)$$

Since only the surface Ampere's currents, with density $J_{\mathrm{sa}}=M$, exists on the inner and outer magnet covers, the total magnetic flux density produced by the lower magnet can be determined by summing the contribution of both magnet covers.

By taking into account the magnet geometry, from Fig. 2, the following parameters can be defined

$$z_n = h+\frac{2n-1}{2N}L\,; \quad (9)$$

$$r_n = b+\frac{a-b}{L}(z_n-h)\,; \quad (10)$$

$$\sin(\gamma)=\frac{L}{\sqrt{(b-a)^2+L^2}}\,; \quad (11)$$

$$\Delta l=\frac{\sqrt{(b-a)^2+L^2}}{N}\,; \quad (12)$$

and the current of each circular loop of radius r_n is

$$I_n=\alpha M\Delta l\sin(\gamma)\,,\qquad n=1,\ldots,N\,. \quad (13)$$

The magnetic force that acts on the one segment of upper magnet, that is circular loop of radius r_i or radius c, due to the magnetic field generated by lower magnet, can be expressed as

$$\mathrm{d}\boldsymbol{F}=I_i\,\mathrm{d}\boldsymbol{l}\times\boldsymbol{B}\,, \quad (14)$$

where current of the circular loop is

$$I_i=M\Delta l\sin(\gamma) \quad (15)$$

and

$$r_i=r_n=b+\frac{a-b}{L}(z_n-h)\,. \quad (16)$$

Since $\mathrm{d}\boldsymbol{l}=-r_i\,\mathrm{d}\theta\,\hat{\theta}$, using following relations

$$\hat{\theta}=-\sin(\theta)\,\hat{x}+\cos(\theta)\,\hat{y}\,,$$
$$\hat{r}=\cos(\theta)\,\hat{x}+\sin(\theta)\,\hat{y}\ \text{ and}$$
$$\hat{z}=\hat{z}\,, \quad (17)$$

from Eq. (14) the magnetic force is finally obtained as

$$\mathrm{d}\boldsymbol{F}=I_i\,r_i\,B_z\cos(\theta)\,\mathrm{d}\theta\,(-\hat{x})+I_i\,r_i\,B_z\sin(\theta)\,\mathrm{d}\theta\,(-\hat{y})$$
$$+I_i\,r_i\,B_r\,\mathrm{d}\theta\,\hat{z}. \quad (18)$$

The z component of this force represents the attraction force that acts on the one magnet's segment

$$\mathrm{d}F_z=I_i r_i B_r\,\mathrm{d}\theta\ . \quad (19)$$

The *x* and *y* components of the force are equal to zero. Therefore, the attraction force of the one magnet's segment, can be obtained using Eqs. (19) and (15) as

$$F_{zi}=2\pi r_i B_r M\Delta l\sin(\gamma)\,. \quad (20)$$

Contributions of inner and outer cover of both magnets must be included:

$$F_{z1}=\frac{\mu_0\alpha M^2L^2}{N^2}\sum_{i=1}^{N}\sum_{n=1}^{N}\frac{z_i+z_n}{\sqrt{(r_i+r_n)^2+(z_i+z_n)^2}}\times$$
$$\times\left(-K\left(\frac{\pi}{2},k_1\right)+\frac{r_i{}^2+r_n{}^2+(z_i+z_n)^2}{(r_i-r_n)^2+(z_i+z_n)^2}E\left(\frac{\pi}{2},k_1\right)\right), \quad (21)$$

$$k_1^2=\frac{4r_ir_n}{(r_i+r_n)^2+(z_i+z_n)^2}\,, \quad (22)$$

$$F_{z2}=\frac{\mu_0\alpha M^2L^2}{N^2}\sum_{i=1}^{N}\sum_{n=1}^{N}\frac{z_i+z_n}{\sqrt{(r_i+c)^2+(z_i+z_n)^2}}\times$$
$$\times\left(-K\left(\frac{\pi}{2},k_2\right)+\frac{r_i^2+c^2+(z_i+z_n)^2}{(r_i-c)^2+(z_i+z_n)^2}E\left(\frac{\pi}{2},k_2\right)\right), \quad (23)$$

$$k_2^2=\frac{4r_ic}{(r_i+c)^2+(z_i+z_n)^2}, \quad (24)$$

$$F_{z3}=\frac{\mu_0\alpha M^2L^2}{N^2}\sum_{i=1}^{N}\sum_{n=1}^{N}\frac{z_i+z_n}{\sqrt{(c+r_n)^2+(z_i+z_n)^2}}\times$$
$$\times\left(-K\left(\frac{\pi}{2},k_3\right)+\frac{c^2+r_n^2+(z_i+z_n)^2}{(c-r_n)^2+(z_i+z_n)^2}E\left(\frac{\pi}{2},k_3\right)\right), \quad (25)$$

$$k_3^2=\frac{4cr_n}{(c+r_n)^2+(z_i+z_n)^2}, \quad (26)$$

$$F_{z4}=\frac{\mu_0\alpha M^2L^2}{N^2}\sum_{i=1}^{N}\sum_{n=1}^{N}\frac{z_i+z_n}{\sqrt{4c^2+(z_i+z_n)^2}}\times$$
$$\times\left(-K\left(\frac{\pi}{2},k_4\right)+\frac{2c^2+(z_i+z_n)^2}{(z_i+z_n)^2}E\left(\frac{\pi}{2},k_4\right)\right), \quad (27)$$

$$k_4^2=\frac{4c^2}{4c^2+(z_i+z_n)^2}. \quad (28)$$

Finally the total attraction force between ring permanent magnet and plane can be calculated easily and it is valid for any distance between magnet and plane

$$F_z=F_{z1}-F_{z2}-F_{z3}+F_{z4}. \quad (29)$$

III. Numerical Results

The results of the presented approach are given in the graphical form and they are compared with ones calculated numerically using FEMM software.

Table I presents the attraction force calculated when dimensions of the magnet are: $a=3\,\text{mm}$, $b=4\,\text{mm}$, $c=2\,\text{mm}$, $L=1\,\text{mm}$, magnetization $M=900\,\text{kA/m}$ and relative permeability of the plane $\mu_r=3$ when the number of segments of each magnet's cover is $N=100$. Results of FEMM 4.2 software are obtained for 1.7 million elements. Difference between presented approach and FEMM is greater as the distance is smaller. That difference lowers when the separation distance, *h*, increases. Fig. 4 shows normalized attraction force dependency versus outer radius of the circular bottom of the magnet for various separation distance, when $\mu_r=3$.

TABLE I
ATTRACTION FORCE FOR DIFFERENT SEPARATION DISTANCE.

h [mm]	F_z^{femm} [N]	F_z [N]
0.5	-0.550230	-0.549755
0.6	-0.438152	-0.437758
0.7	-0.353875	-0.353520
0.8	-0.289550	-0.289242
0.9	-0.239870	-0.239567
1.0	-0.201039	-0.200721
1.1	-0.170331	-0.170000
1.2	-0.145767	-0.145441
1.3	-0.125960	-0.125599
1.4	-0.109783	-0.109402
1.5	-0.096491	-0.096049

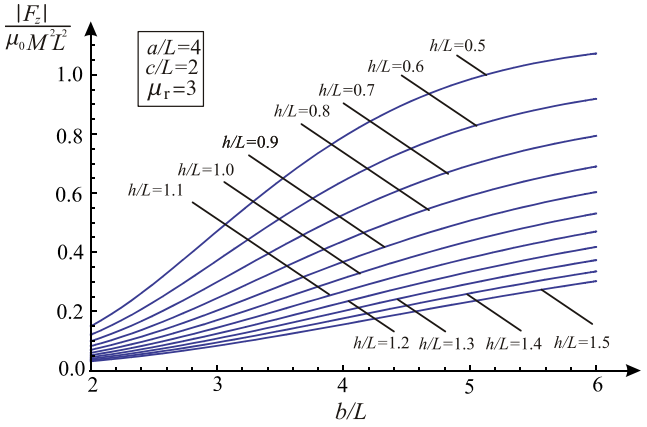

Fig. 4. Attraction force versus outer radius of a circular bottom of the magnet.

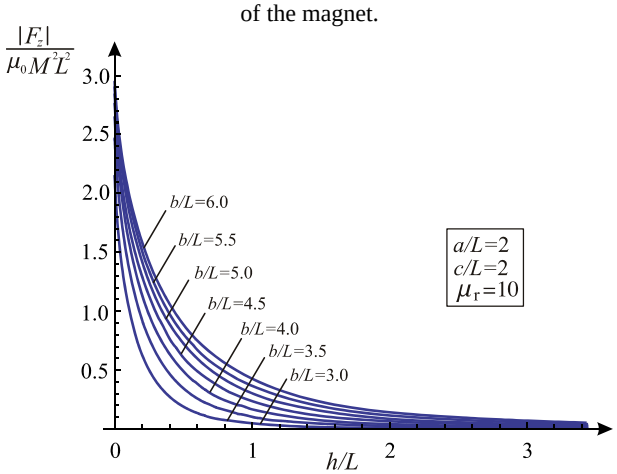

Fig.5. Attraction force versus separation distance.

In Fig.5 normalized attraction force versus separation distance is presented when relative permeability of plane is $\mu_r=10$. Figs. 6 and 7 present distribution of magnetic flux density and distribution of magnetic field, respectively. They are obtained using semi-analytical method when the radii of circular top and circular bottom are equal $a=b=3\,\text{mm}$, $c=1\,\text{mm}$, $L=1\,\text{mm}$ and separation distance $h=1\,\text{mm}$.

When the inner radius of magnet is equal to zero, $c=0$, the system is composed of truncated cone shaped permanent magnet and infinity plane. Fig.9 presents attraction force

versus separation distance when $\mu_r = 50$ while Fig.8 shows attraction force dependency versus relative permeability.

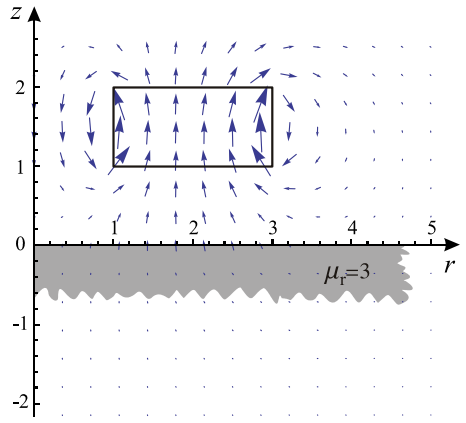

Fig. 6. Distribution of magnetic flux density.

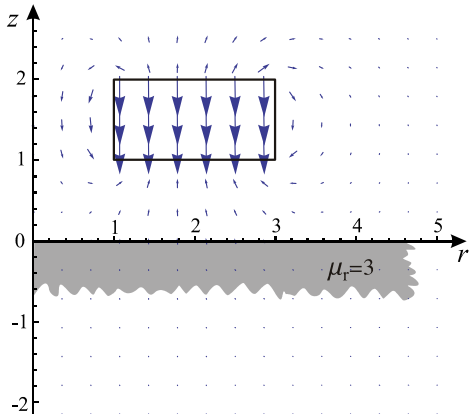

Fig. 7. Distribution of magnetic field.

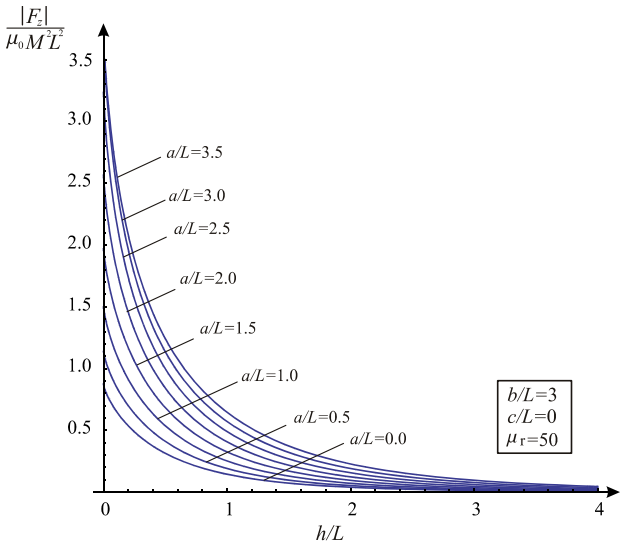

Fig.8. Attraction force versus separation distance.

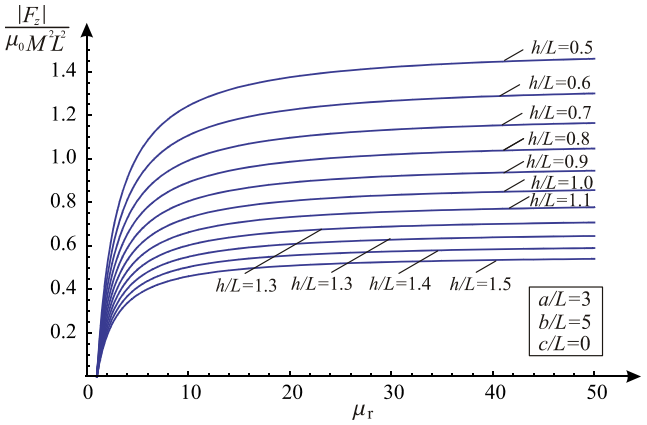

Fig.9. Attraction force versus relative permeability.

IV. Conclusion

The derived algorithm for attraction force calculation between ring permanent magnet and infinite magnetic plane is easily implemented in any standard computer environment and it enables rapid parametric studies of the force. The resulting expression is given in terms of elementary functions that are available in all programming languages. The results of the presented approach are successfully confirmed using FEMM 4.2 software. Attraction force calculation using presented approach for mentioned parameters and $N = 100$ is performed with Intel Core 2 Duo CPU at 2.4GHz and 2GB RAM memory and it took ten seconds of run time. The force is also determined on the same computer using FEMM 4.2 software and the computation time was 14 minutes. Therefore the advantage of presented approach is its simplicity and time efficiency.

Acknowledgement

The authors would like to acknowledge the support of the Ministry of Science and Technological Development, Serbia (Project No. 33008).

References

[1] D. Vokoun, M. Beleggia, L. Heller, P. Sittner, “Magnetostatic Interactions and Forces Between Cylindrical Permanent Magnets”, Journal of Magnetism and Magnetic Materials, Vol. 321, Issue 22, November 2009, pp. 3758-3763.

[2] E. P. Furlani, “A formula for the Levitation Force Between Magnetic Disks”, IEEE Transactions on Magnetics, Vol. 29, No.6, November 1993, pp. 4165-4169.

[3] S. I. Babic, C. Akyel, “Magnetic Force Calculation Between Thin Coaxial Circular Coils in Air”, IEEE Transactions on Magnetics, Vol. 44, No.4, April 2008, pp. 445-452.

[4] V. Lemarquand, G. Lemarquand, “Passive Permanent Magnet Bearings for Rotating Shaft: Analytical calculation”, in Magnetic Bearings, Theory and Applications, Sciyo Published, October 2010, pp. 85-116.

[5] A. Mladenović, S. Aleksić, S. Ilić, Levitation Force Calculation for Permanent Magnet Bearings Using Ampere’s Currents, The 14th International IGTE Symposium on Numerical Field Calculation in Electrical Engineering, Graz, 20-22 September 2010, pp. 149-153.

STUDENT SESSIONS

Session SS I:

STUDENT SESSION I

A Software Solution for Data Compression Using the Prefix Encoding

Student authors: Ilija J. Urošević[1] and Dejan Ž. Jevtić[1]
Mentors: Radomir S. Stanković[2] and Dušan B. Gajić[2]

Abstract – **Prefix encoding is one of the basic coding systems that use the prefix property. Various applications of the prefix encoding are in use today, e.g. country calling codes, UTF-8 system for encoding Unicode characters, the Secondary Synchronization codes used in the UMTS W-CDMA 3G Wireless standard. In this paper, we first present theoretical bases of prefix encoding and some of the elementary types of prefix coding techniques. Afterwards, we discuss the software implementation of these coding algorithms realized in C# programming language. Experimental results considering data compression ratio and time needed for the compression are also included. The application is primarily developed with educational purposes in mind.**

Keywords – **Data compression, C# application, prefix encoding.**

I. Introduction

Data compression methods are very important in computer science for many reasons, including faster time for data transmission that they allow, and more free space on storage disks. There are many compression methods developed for this purposes.

This paper first describes prefix encoding as one of the basic coding systems and presents the theoretical bases of the prefix coding and some types of prefix codes, described in Sections 2 and 3, respectively. Next, in Section 4 we present a software solution for data compression using the prefix encoding, realized in C# programming language, along with the experimental results representing data compression ratio and time of compression. This application is mainly developed for educational purposes.

II. Prefix Codes

In this Section, we use references [1] and [4]. Prefix encoding is one of the basic and most common coding systems. Prefix code is a variable-type code which satisfies the prefix property. The prefix property requires that once a certain bit pattern has been assigned as the code of a symbol, no other valid code words should start with that pattern (the pattern cannot be prefix of any other code word). For instance, we will define two codes: code-1 with following code words: {1, 01, 010, 001}, and code-2 with code words: {1, 01, 000, 001}. In this case, code-1 does not satisfy the prefix property because code word 010 begins with 01, which is also valid code word in code-1. On the other hand, code-2 does not have an issue with this property, and therefore it satisfies the prefix property. Coding systems with the prefix property can be transmitted with a sequence of code words without any symbol for dividing individual words. If a code does not satisfy the prefix property, situation mentioned above can lead to ambiguous codes. We will demonstrate this with one simple example. Let us define symbols a1, a2, a3 and a4 which we will assign to code-1 and code-2, as shown in Table I:

TABLE I
EXAMPLE OF CODES WITH PREFIX PROPERTY

Symbol	Code-1	Code-2
a1	1	1
a2	01	01
a3	010	000
a4	001	001

We will now code the following sequence of symbols: a1, a3, a2, a1, a4. Code-1 will decode this sequence as 1|010|01|1|001 (without vertical bars). However, this code can be decoded wrongly because of the lack of the prefix property. The decoder doesn't know whether to decode the sequence as 1|010|01… (which is a1, a3, a2,…) or as 1|01|001… (which is a1, a2, a4,…). From this example we can conclude that code-1 is ambiguous. Code-2 has the prefix property and it can be decoded unambiguously.

There are many algorithms which are based on the prefix encoding. Two most well known are the Shannon-Fano method and the Huffman method. Prefix encoding is good solution in situations when we want to code integers because the binary representation of integers does not satisfy the prefix property and size of the set of integers must be known in advance. With prefix encoding we don't have to know size of the set of integers in advance which is required in some applications. There are lot of variations of the prefix codes, and we will describe some of them in the next Section.

Student authors:
[1]Ilija J. Urošević and Dejan Ž. Jevtić are with the Faculty of Electronic Engineering, Aleksandra Medvedeva 14, 18000 Niš, Serbia, E-mails: kieknai@elfak.rs and dejanjevtic@elfak.rs.

Mentors:
[1]Radomir S. Stanković and Dušan B. Gajić are with the Computational Intelligence and Information Technology Laboratory, Department of Computer Science, Faculty of Electronic Engineering, Aleksandra Medvedeva 14, 18000 Niš, Serbia, E-mails: radomir.stankovic@elfak.ni.ac.rs and dusan.gajic@elfak.ni.ac.rs.

III. Types of Prefix Codes

We based this section mostly on reference [1]. First, we will present the Unary Code. The Unary Code is operating with non-negative integers, and the code of the integer *n* is defined as *n* - 1 ones, followed by one zero. There is also an alternative version of this code. With the alternative version, integer *n* is defined as *n* - 1 zeros, followed by single one. Unary codes are very easy to work with, but disadvantage of these codes is very large size for large numbers, which is not the good solution for compression of integers. Some Unary Codes are represented in Table II.

TABLE II
UNARY CODES

n	Code	Alt. Code
1	0	1
2	10	01
3	110	001
4	1110	0001
5	11110	00001

It is also possible to define general unary codes, also known as start-step-stop codes. This code consists of a triplet (start, step, stop) of integer parameters, and code words are created with the following procedure: *n*th code word consists of *n* ones, followed by one zero, followed by all the combinations of *a* bits where *a* = start + n*step. If *a* = stop, then the single zero preceding *a* bits is left out. The number of codes for the given triplet is finite and depends on the selection of parameters. The example for triplet (3, 1, 7) is shown in Table III. This triplet generates 248 code words.

TABLE III
GENERAL UNARY CODE FOR TRIPLET (3, 1, 7)

n	*a*=3+n*1	*n*th code word	number of code words	range of integers
0	3	0xxx	$2^3 = 8$	0-7
1	4	10xxxx	$2^4 = 16$	8-23
2	5	110xxxxx	$2^5 = 32$	24-55
3	6	1110xxxxxx	$2^6 = 64$	56-119
4	7	1111xxxxxxx	$2^7 = 128$	120-247

As we can see from the table, the number of code words depends on the value of the *a* parameter. With smaller value of *a*, we can present smaller range of integers. As the value of *a* changes, for each group of code words we have a certain prefix. Of course, the prefix property is satisfied.

The number of different general unary codes is given in the Eq. (1).

$$\frac{2^{\text{stop}+\text{step}} - 2^{\text{start}}}{2^{\text{step}} - 1}. \qquad (1)$$

This expression increases exponentially with parameter "stop", so large sets of these codes can be generated with small values of (start, stop, step) parameters. For example:

1) The triplet (*n*, 1, *n*) defines the standard *n*-bit binary codes, whose number is given in the Eq. (2).

$$\frac{2^{n+1} - 2^n}{2^1 - 1} = 2^n \qquad (2)$$

2) The triplet (0, 0, ∞) defines the codes 0, 10, 110, 1110,... which are the unary codes but assigned to integers 0, 1, 2, ... instead of 1, 2, 3, ...

3) The triplet (1, 1, 30) produces $(2^{30} - 2^1) / (2^1 - 1)$ codes, which is approximately a billion codes.

Besides the unary codes, there are often prefix codes which are built in a different way. We will explain four of them. Symbol $B(n)$ is used to denote the binary representation of integer *n*, $|B(n)|$ is the length, in bits, of this implementation, and $\overline{B}(n)$ is used to denote $B(n)$ without its most significant bit, which is always 1.

Code C_1 is made of two parts. To code the positive integer *n*, we first generate the unary code of $|B(n)|$ which is the size of the binary representation of *n*, then we append $\overline{B}(n)$ to it. Let us demonstrate this in one example, for $n = 19 = 10011_2$. The size of $B(19)$ is 5, so we start with the unary code 11110 and append $\overline{B}(n)$=0011. The complete code is 11110|0011. Length of code $C_1(n)$ is $2\lfloor \log_2 n \rfloor + 1$ bits.

Code C_2 is a rearrangement of code C_1 where each of the $1+\lfloor \log_2 n \rfloor$ bits of the first part (the unary code) of C_1 is followed by one of the bits of the second part (the $\overline{B}(n)$ part). For $n = 19 = 10011_2$, $C_1(19)$=111100011, after every of first 5 bits we insert one bit from the second part. As a result we have $C_2(19)$=101011110.

Code C_3 is constructed with the following procedure: We start with $|B(n)|$ coded in C_2, and then append $\overline{B}(n)$. For n = $19 = 10011_2$, $|B(19)|$ is 5 bits, then we code this value in C_2, $C_2(5)$=11101 and append $\overline{B}(19)$=0011, and finally we have $C_3(19)$=111010011. The size of $C_3(n)$ is $1+\lfloor \log_2 n \rfloor + 2\lfloor \log_2 (1+\log_2 n) \rfloor$ bits.

Code C_4 consists of several parts. We start with $B(n)$. To the left of this value we write the binary representation of $|B(n)|-1$ (the length of *n*, minus 1). This procedure continues recursively, until a 2-bit number is written. A zero is then added to the right of the entire number to make it decodable. For n = $19 = 10011_2$, we start $B(19)$=10011, then add the binary representation of $|B(19)-1|=4$ which is 100_2, and we have 100|10011. In the next step, we add the binary representation of $|B(4)-1|=2$ which is 10_2, add it to right of the current result, and we get 10|100|10011. Finally, we add a zero to the right of current result, and as the final result we have $C_4(19)$=10|100|10011|0.

The length of these four codes increases as $\log_2 n$ while the length of unary code increases as *n*. These codes are therefore good choices in cases where the data consists of integers *n* with probabilities that satisfy certain conditions.

IV. Software Implementation and Experimental Results

For software implementation, we used references [2], [3] and [5]. The software solution for prefix encoding that we implemented is "Prefix Coder". This application can encode data using unary code and codes C_1 and C_2. "Prefix Coder" is developed in C# programming language and .NET Framework 3.5. The architecture of the application is shown in Fig. 1.

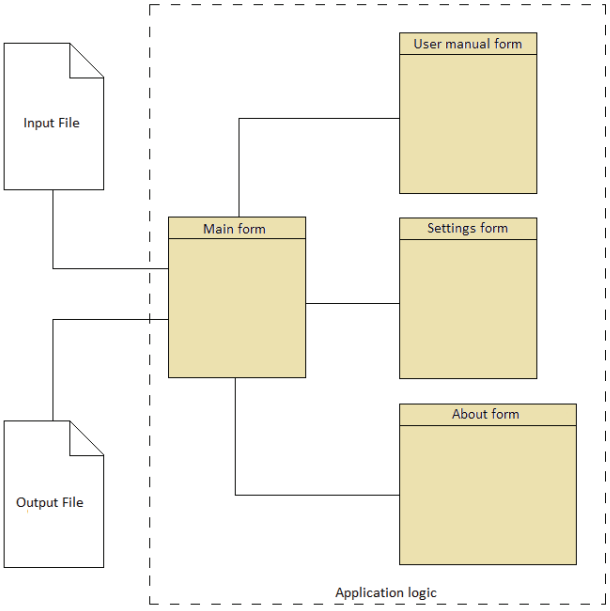

Fig. 1. "Prefix Coder" architecture.

Prefix coder consists of Main form, Settings form, About form and User manual form. Main form represents the starting window of the application and it's linked with 3 other forms. Settings form is used for simple settings of the application, like separators that are used or default input name etc. User manual form contains instructions for using the "Prefix Coder", and the About form has a description of the application and authors. These four forms together make the application logic. Main form is also connected with input and output files.

Input data of the application can be inserted via text field or a text file. Possible outputs are a text field, a text file or a binary file. Text field and text file as outputs are used for representation of the coding results. If the selected output method is binary file, after the encoding process is finished the compression rate is shown.

When the encoding process starts, first the input data is read from the selected input and stored in array of strings, where each string is a number that needs to be encoded. Next, that data is forwarded to one of the functions which implements a coding algorithm for the selected coding method. All of these functions generate an array of BitArrays. In this array is the sequence of ones and zeros that is the result of the coding. All of the functions call SaveCode function which saves the data in the way that is selected as output method. Since the C# language doesn't have an interface that allows for single bits to be written into a file, all the coded data is first transferred into bytes and written into files in that form. This also means that neutral characters (zeros) will be added to last chunks of data until the chunk is 8-bit long.

Interface of the "Prefix Coder" is designed to be intuitive and easy to use and it is shown in Fig. 2.

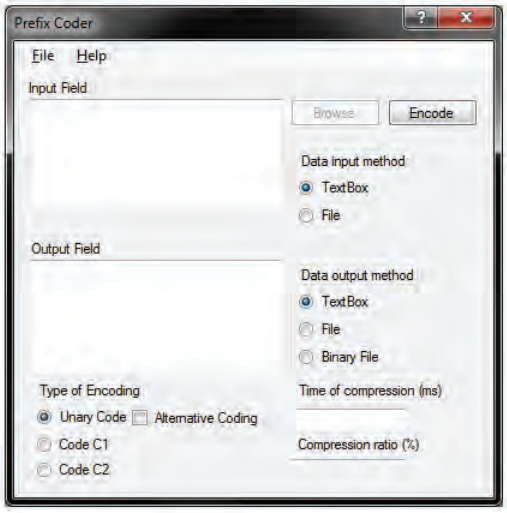

Fig. 2. Interface of the "Prefix Coder".

The Settings form of the "Prefix Coder" is shown in Fig. 3. In this form we can adjust properties of the "Prefix Coder". These properties are Tooltip time (display time of tooltip), Separators, Default path for the output file and Default name for the output file. These properties are initially set to optimal values. These properties are kept in a separate file. Separators are used to separate numbers in the Input Field when "Textbox" is selected as Data input method. User can define his own separator. In order to do this, he must follow certain rules. The default separator is white space. If user wants to add a separator, after entering desired symbol he must add character "s" without making any spaces. If user does not want to use white space as a separator, he must first clear Separators field and then add his separators in a procedure described above.

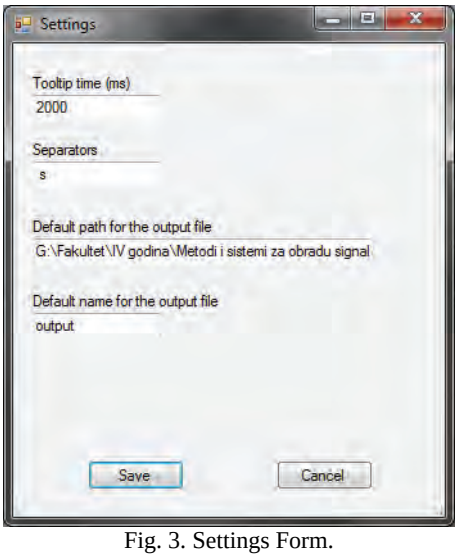

Fig. 3. Settings Form.

The experimental results considering time needed for compression are shown in Table IV. For all the data in Table IV tests were performed several times and calculated average values of the results are taken as final results. It should also be noted that the duration of the compression depends on the computer hardware and current utilization of computer resources. These tests were performed on the AMD Phenom(tm) 8450 with 2 GB of DDR2 RAM and on Windows 7 64-bit OS.

TABLE IV
TESTS FOR TIME OF COMPRESSION

	Time of compression (ms)		
Input data	Unary code	Code C_1	Code C_2
0-100	~1	~1	~1
500	~5	~1	~1
10000	~400	~1	~1
10 two-digit integers	9	3	3
10 four-digit integers	22500	8	8
10 five-digit integers	350000	10	10

From the Table IV it can be seen that the compression with the unary coding needs much more time than with the codes C_1 and C_2, since the length of the unary code increases linearly, and the compression time is longer for one larger integer number than for several smaller ones.

In Table V experimental results for compression ratio are shown. As mentioned before, C# language doesn't have the interface for writing single bits in a file, all the output data have several bits more than it would have if this restriction doesn't exist.

TABLE V
TESTS FOR COMPRESSION RATIO

		Size of the output file (Byte) / compression ratio		
Size of input file (Byte)	Input Data	Unary code	Code C_1	Code C_2
5	500	63 /0%	3 /40%	3 /40 %
5	5,5,5	2 /60%	2 /60%	2 /60%
1	5	1 /0%	1 /0%	1 /0%
20	5,5,5,5,5,5,5,5,5,5	6 /70%	6 /70%	6 /70%
11	500,500,500	187 /0%	7 /36%	7 /36%

Table V shows that compression ratio increases as the number of the parameters increase, and decreases with larger value of numbers in input data.

V. CONCLUSION

In real-world circumstances, the unary code does not give satisfying results, but it is very important because of the idea of prefix encoding. For specific values of input data, it takes a very long time for program execution, and no compression is achieved.

Codes C_1 and C_2 give results which are mostly satisfying and similar. For specific values of input data a very high compression ratio can be achieved. The time of compression is very short in most of the cases. Our application implements the unary code, and both codes C_1 and C_2, and it is developed mainly for educational purposes.

REFERENCES

[1] D. Salomon, *Data Compression – The Complete Reference*, Springer, 2007.

[2] *Form Class*, http://msdn.microsoft.com/en-us/library/system.windows.forms.form%28VS.71%29.aspx, website last visited on 4/4/2011.

[3] *Measuring Execution Time in C#*, http://www.codersource.net/microsoft-net/c-miscellaneous/measuring-execution-time-in-c.aspx, website last visited on 4/4/2011.

[4] *Prefix code - Wikipedia, the free encyclopedia*, http://en.wikipedia.org/wiki/Prefix_code, website last visited on 4/4/2011.

[5] *BitArray Class (System.Collections)*, http://msdn.microsoft.com/en-us/library/system.collections.bitarray.aspx, website last visited on 4/4/2011.

A C# Software Implementation of the Golomb Encoding Method for Text Compression

Student authors: Danijel M. Pavlović[1] and Marko B. Mitić[1]

Mentors: Radomir S. Stanković[2] and Dušan B. Gajić[2]

Abstract – **Lossless data compression is a very important class of data compression algorithms. Golomb encoding is a type of prefix encoding which is often used as part of complex lossless data compression algorithms. In this paper, we present a C# software implementation of Golomb encoding with an intuitive graphical user interface. Experimental results, showing compression values and algorithm running times, are also presented and discussed. The main motivation for developing this software solution was to create an educational tool that can help in better understanding and presentation of algorithms for data compression.**

Keywords – **C# programming solution, data compression, Golomb code, text compression.**

I. INTRODUCTION

The large amount of data which people use in every day work is forcing the data compression methods to develop fast and give better and better results in lossless data compression. Golomb encoding [1] is a type of a prefix code often used for such purposes. A prefix code is a variable size code that satisfies the prefix property. Golomb encoding is based on run-length encoding (RLE). For example, if there is a binary string where zero appears with probability p and a one appears with probability 1-p, and with the growth of p it is more likely that longer sequences of one and the same values will appear. But, whether this is true for a particular data set to be coded highly depends on the volume of the data itself and the preliminary chosen code type.

The probability of a run of n zeros is p^n and the probability of a run of n zeros followed by a 1 is $p^n(1-p)$, indicating that run lengths are distributed geometrically [2].

Golomb code for nonnegative integers n depends on the choice of parameter m, which is median and its value is such that about half the run lengths are shorter than m and about half are equal to or greater than m, which make this code parameterized prefix code. In computing the Golomb code [4] we need three other quantities q (quotient), r (remainder), and c. These three quantities are based on the following equations:

$$q = \left\lfloor \frac{n}{m} \right\rfloor, \tag{1}$$

$$r = n - qm, \tag{2}$$

$$c = \lceil \log_2 m \rceil. \tag{3}$$

The code is constructed in two parts; the first is the value of q, coded in unary, and the second is the binary value of r coded in a special way. The first $2^c - m$ values of r are coded, as unsigned integers, in c-1 bits each and the rest are coded in c each (ending with the biggest c-bit number, which consists of c 1`s). Example of calculating necessary quantities and creating family of Golomb codes for m = 2 through 7 are shown in Table I.

TABLE I
FAMILY OF GOLOMB CODES FOR M = 2 THROUGH 7.

m	2	3	4	5	6	7
c	1	2	2	3	3	3
-m	0	1	0	3	2	1

m/n	0	1	2	3	4	5	6
2	0|0	0|1	10|0	10|1	110|0	110|1	1110|0
3	0|0	0|10	0|11	10|0	10|10	10|11	110|0
4	0|00	0|01	0|10	0|11	10|00	10|01	10|10
5	0|00	0|01	0|10	0|110	0|111	10|00	10|01
6	0|00	0|01	0|100	0|101	0|110	0|111	10|00
7	0|00	0|010	0|011	0|100	0|101	0|110	0|111

Software implementation, which we will discuss in this paper, implements the algorithm for lossless data compression [5] using the Golomb code. We will also say a few words about experimental results which we collected from the application. In the end, we will also offer some conclusions.

II. SOFTWARE IMPLEMENTATION DETAILS

A. Implementation details

Application which is presented in this work is developed in C# programming language and .NET 3.5 framework. Designed graphical user interface is very simple because focus is not on interface, it is on implemented algorithm. Also application is very easy for usage. Simply choose an input text

Student authors:
[1]Danijel Pavlović and Marko Mitić are with the Faculty of Electronic Engineering, Aleksandra Medvedeva 14, 18000 Nis, Serbia, E-mails: daki88@elfak.rs, zmicezmaj@elfak.rs

Mentors:
[2]Radomir Stanković and Dušan Gajić are with the Faculty of Electronic Engineering, Aleksandra Medvedeva 14, 18000 Nis, Serbia, E-mails: radomir.stankovic@elfak.ni.ac.rs, dusan.gajic@elfak.ni.ac.rs.

file for compressing, and choose output text file if it exist, if not just type name for that output file and application will create it for you, then start compression on one single button.

Architecture of application composed from two forms, first of them is main form which contains all functionality for making compression complete, and the second form which is just user manual. Input in application is text file for compression, and the output is compressed text file. Graphical view of application architecture is shown in Figure 1.

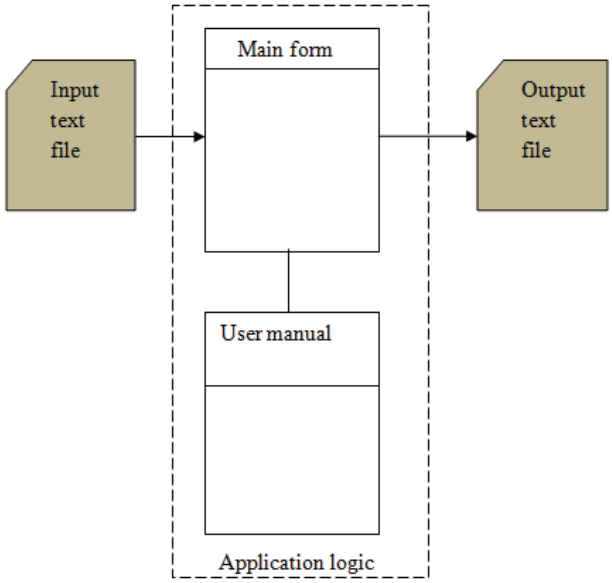

Figure 1. Architecture of the application.

Main problem during developing this application was that bit-level operations are not a natural way of thinking in C# [3]. As it is explained before Golomb code uses run lengths of zeros and ones for creation families of codes for coding those values. Therefore in the application work with bits is simulated on special way.

As we implemented algorithm for text compression, and as we knew that characters inside the text are coded with values from ASCII table which consist of zeros and ones, we read one character from text, convert it to its ASCII value, and we saved it in one string variable. Every other character is also converted to ASCII value and concatenated to the string variable that is used in the beginning. This process practically converts whole text document into string variable that represents bit representation of text. Example of this conversion is shown in Example 1.

Text = “abc”

Characters	a	b	c
ASCII values	1100001	1100010	1100011

Result string = “a”+”b”+”c”=
=”1100001”+”1100010”+”1100011”=
=“110000111001011000011”

Example 1. Conversion from text to a binary string value.

Based on that string value, we calculated all necessary parameters that are explained in introduction. Using that parameters we created family of Golomb code. Family of code is used for coding run lengths of zeros in primary string value. On that way whole text from document is encoded with Golomb code. Example of encoding is shown in Example 2.

StringForCoding =“110000111001011000011”

Run length of zeros	Code
0	0
1	10
2	110
3	1110
4	11110

Encoded String = “10111110101011101101011110101”

Example 2. Encoding of a binary string.

When we have encoded binary string we convert that string into ASCII values, practically we do reverse process compared to the previous. We read from this encoded binary string values of zeros and ones for one ASCII character, and convert that zeros and ones into ASCII character. That character is written into output text file. This process is repeating while there are still not processed zeros and ones in encoded binary string. When this process is finished also is finished whole process of text compression.

Because of using the C# development environment and .NET 3.5 framework during implementation of this solution, it is necessary for proper functioning of application to use application on Microsoft Windows platforms with installed .NET framework 3.5. In any other case application will not work properly.

B. Graphical user interface details

Graphical user interface is shown in Figure 2. The user interface is designed to be as simple as possible. There are text fields where is shown path to the input and output file respective, when they are chosen by the user of application by clicking on the browse buttons. Below browse section of the main form, is statistical section where user can see details from compression, like size of input and output file, output/input ratio, which is calculated using equation 4, and run time for compression.

$$\frac{Output}{InputRatio} = \frac{sizeOfOutputFile}{sizeOfInputFile} \times 100\% \qquad (4)$$

There is also one list box on the form which is used to show how run lengths of zeros are encoded with created family of Golomb code. In the top right corner of main form is a button which starts user manual form. In the top left corner there is a button which starts info form about developers.

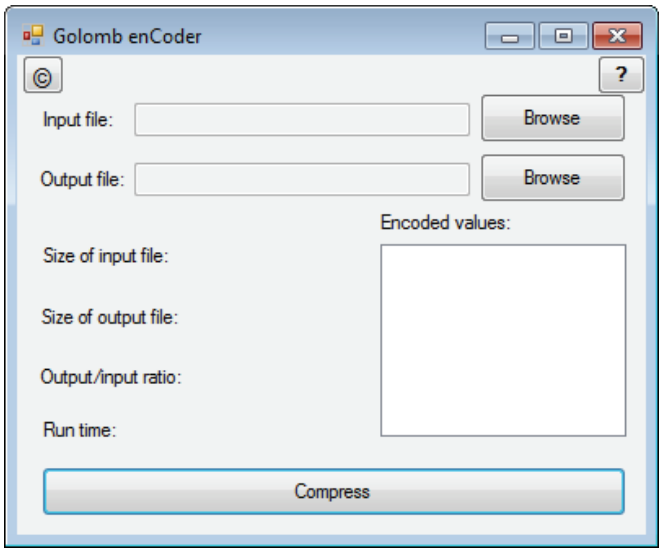

Figure 2. Graphical user interface of the application.

III. Experimental Results and Discussion

During the testing of the application for different sizes of input files we collected different results. The application is tested on a desktop PC with the specification given in Table II. Results and values of input, output files and run times are shown in the Table III.

As we can see from the Table III results are not so good. The main reason why the ratio is not so good is in characteristics of the Golomb code. Golomb code as it said before, is a parameterized prefix code. It depends on median *m* of run lengths of zeros, and *m* depends on probability *p* of appearance of zero lengths. The nature of ASCII code for characters is that there are no long runs of zeros, which are necessary for creating a good family of Golomb codes. A good family of the Golomb code provides us with better output/input ratio.

Because of this fact we tried to improvise long runs of zeros. If we look at ASCII table we can see that long run of zeros is in character "*space*". We tested our application with text file in which we have table of integer values, in that table columns are separated with space character. As we can see from the Table III results for input/output ratio showing us minimal compression of the input files. In this kind of the input files the runs of zeros are more frequently than in input files with text content, therefore and parameters for Golomb code are better as well as family of codes.

Table II
Test PC specification

CPU	Pentium® Dual-Core CPU E5200 @2.5 GHz
RAM	2 GB DDR2
OS	Windows 7 (64-bit)
GPU	NVIDIA GeForce 9400 GT
Motherboard	MSI Intel P31 Neo-F

Table III
Experimental results for input text files with table of integer content

Size of input file (KB)	Size of output file (KB)	Output/Input ratio (%)	Run time (ms)
0.53	0.49	92.45	13
1.05	0.99	94.29	32
2.00	1.88	94.00	56
5.96	5.58	93.62	820
10.03	9.39	93.60	3570
20.04	18.78	93.71	10356
50.26	47.1	93.71	140917
100.3	93.99	93.72	506916

Beside the bad output/input ratio from the Table III, we can also see that run time for compression is unsatisfactorily. The cause for long compression time is in chosen development environment. Like it is said before the main problem in implementation was because C# is not created with focus on bit-level operations. Because of this constraint we had to do conversions between data types into two directions, as we explained in implementation details, and this significantly slows the process of compression. If we had chosen some other development environment in which working with bits is faster and easier, for example C or C++, the run time for compression will have been undoubtedly shorter, but good compression ratio will be probably the same like in this example.

IV. Conclusions

In this paper we presented the software solution which implements the algorithm for text compression using the Golomb code. Considering what has been said above we can conclude that: the Golomb code is not the best choice, for algorithms which are used for text compression. This is because of the fact that the probability of run lengths of zeros in binary text representation is too small. The other reason is when we want to implement this algorithm for compression which uses the Golomb code, it is better to use it in a development environment which has ability and good interface for working with bits.

The Golomb code would show better results in compression for a different type of data. The data where probability, of run lengths of zeros, is big are suitable for encoding with this code, for example monochromatic pictures.

The application which is presented in this paper is developed for educational purposes. It can be a good educational tool for presentation and understanding the compression algorithm which uses the Golomb code for text compression.

REFERENCES

[1] David Salomon, *Data Compression – The Complete Reference*, Springer, 2007.

[2] *Golomb coding*, http://en.wikipedia.org/wiki/Golomb_coding, website last visited on 12/04/2011.

[3] *C# Tutorials*, http://msdn.microsoft.com/en-us/library/aa288436(v=vs.71).aspx, website lat visited on 12/12/2010.

[4] *Compression Algorithms*, http://www.inference.phy.cam.ac.uk/itprnn/code/c/compress/, website last visited 12/04/2011.

[5] *Lossless data compression*, http://en.wikipedia.org/wiki/Lossless_data_compression, website last visited on 05/04/2011.

A Software Implementation of the Shannon-Fano Coding Algorithm

Student authors: Đorđe K. Manoilov[1] and Daniel S. Dimitrov[1]
Mentors: Radomir Stanković[2] and Dušan Gajić[2]

Abstract – **The Shannon-Fano coding technique is one of the earliest algorithms which produce code words with minimum redundancy and it serves as a basis for some more recent methods. In this paper, we present a C# implementation of the Shannon-Fano encoding method for data compression. We conducted various experiments with different inputs provided to the application and recorded compression rates and algorithm running times. The presented solution features a graphical user interface and has solid real-world performance, but it was developed primarily as an education tool that can help students to better understand this encoding technique.**

Keywords – **Shannon-Fano encoding, C# programming solution, text compression.**

I. INTRODUCTION

Data compression is a mathematical method - an algorithm used to decrease the number of the bits in a file that are necessary for storage, sending or transferring of electronic information. In other words, by using compression the size of a file or group of files is decreased and space needed for storing the information becomes smaller.

There are some compression methods that loose data, but we will discuss only compression that occurs without loss. The "good" part is that the compressed data will be decompressed in the same form (recovering the data into its initial state), but an error producing even a bit less would be fatal. Compression with no loss can be realized with different algorithms like: RLE (Run Length Encoding) algorithm, algorithm for removing all zeros, Shannon-Fano algorithm, Huffman algorithm [1].

We will discuss the Shannon-Fano compression. For Shannon-Fano compression there is an algorithm which uses prefix coding [1].

In this paper, we will present its implementation and include test results for different textual files [7]. In Section II we describe the theoretical basis of the Shannon-Fano coding. Next, in Section III we present a software solution for data compression using the Shannon-Fano algorithm realized in C# programming language. This application is mainly developed for educational purposes. In the following Section IV we give experimental results for data compression ratio, time and number of different characters. We close the paper with some conclusions in the final section.

Student authors:
[1]Đorđe Manoilov and Daniel Dimitrov are with the Faculty of Electronic Engineering, Aleksandra Medvedeva 14, 18000 Niš, Serbia, E-mails: djordje.manoilov@elfak.rs, ddaniel@elfak.rs.

Mentors:
[2]Radomir Stanković and Dušan Gajić are with the University of Niš, Faculty of Electronic Engineering, Aleksandra Medvedeva 14, 18000 Niš, Serbia, E-mails: radomir.stankovic@gmail.com, dusan.gajic@elfak.ni.ac.rs.

II. SHANNON - FANO ALGORITHM

A. Theoretical basis and the algorithm

Shannon-Fano coding was developed by Claude Elwood Shannon and Robert Fano [1]. This is a technique which uses prefix encoding. It is based on a set of symbols and their probabilities.

A prefix code is a type of a code system which is characterized by a prefix property. This property states that there is no valid code word in the system that is a prefix (start) of any other valid code word in the set. Message can be transmitted as a sequence of concatenated code words, without any extra markers to frame the words in the message using prefix code. The recipient decodes the message by repeating the process searching for prefixes that form valid code words. This is not possible with codes that lack the prefix property. Shannon–Fano coding starts with the set of symbols, with elements arranged in order from most probable to least probable. After that, the set is divided into two sets whose total probabilities are as close as possible to being equal. All symbols then have the first digits of their codes assigned. Symbols in the first set receive "0" and symbols in the second set receive "1". Shannon–Fano coding uses a binary tree structure. As long as any set with more than one member remains, the same process is repeated. When a set has been reduced to one symbol this means that the symbol's code is complete and will not form the prefix of any other symbol's code.

The algorithm produces codes with variable and fairly efficient length. When the two smaller sets produced by partitioning are of exactly equal probabilities, one bit of information used to distinguish them is used most efficiently. It can be seen from the examples that the Shannon – Fano algorithm does not always produce the optimum length codes. For a set of probabilities {0.35, 0.17, 0.17, 0.16, 0:15} Shannon - Fano coding does not give the optimal length code. The Shannon – Fano compression uses binary tree as data structure where the encoded symbols are placed in the leaves of this tree.

The tree is constructed in the specific way in order to define the effective code table. The actual algorithm is simple:

– For a given list of symbols, develop a corresponding list of probabilities or frequency counts, so that each symbol's relative frequency of occurrence is known.

– Sort the lists of symbols according to frequency, with the most frequently occurring symbols at the left and the least common at the right.
– Divide the list into two parts, with the total frequency counts of the left half being as close to the total of the right as possible.
– The left half of the list is assigned the binary digit 0, and the right half is assigned the digit 1. This means that the codes for the symbols in the first half will all start with 0, and the codes in the second half will all start with 1.
– Recursively apply the steps 3 and 4 to each of the two halves, subdividing groups and adding bits to the codes until each symbol has become a corresponding code leaf on the tree.

B. The field of use

Shannon–Fano coding is used in the `IMPLODE` [2] compression method, which is part of the `ZIP` file format. Huffman algorithm [1] is an improved version of the Shannon – Fano algorithm used to compress music files in MP3 format and for JPEG picture compression [8].

III. Architecture of the Application and the Programming Implementation

The application is developed in Visual C# .NET 3.5 and it can be only used within Microsoft Windows operating system.

The application consists of four forms (Fig. 2.). "Main form" is used for selection of file (for coding) or for manual input of text for coding. Also, on the form "Main form" (Fig. 1.) the symbols and their respectable codes are displayed. It is possible to save coded text on desired location on disk or other medium. "Manual form" offers a brief user manual. In "Statistics form" (Fig. 3.) we can see degree of compression for selected text. "Information form" includes information about authors of the application.

Text that is necessary to compress is placed into a string variable. In the application there is a function for the separation of the different nodes, and also for calculating their probabilities of occurrence. Probability of occurrence of symbols is calculated as the ratio of the number of occurrences of this symbol and the number of symbols in the file. For the purposes of the algorithm, it is necessary to arrange these symbols in ascending or descending order. After sorting, coding of symbols is done by calling the Shannon-Fano algorithm implementation. All symbols in the text change in to their code and all of that put into the new string. Code is replaced with its symbols via library function StringReplace.

C# does not support work on the level of bits. Therefore, before entering into a binary file, the sequence of 8 characters is stored in the buffer, which is the size of a byte. 0 is entered into the buffer by moving the contents of the buffer to the left (shift - left), 1 is entered into the buffer using the shift - left and logical OR operation with 0x01h. This method is possible if the length of the coded text is divisible with 8. It is therefore

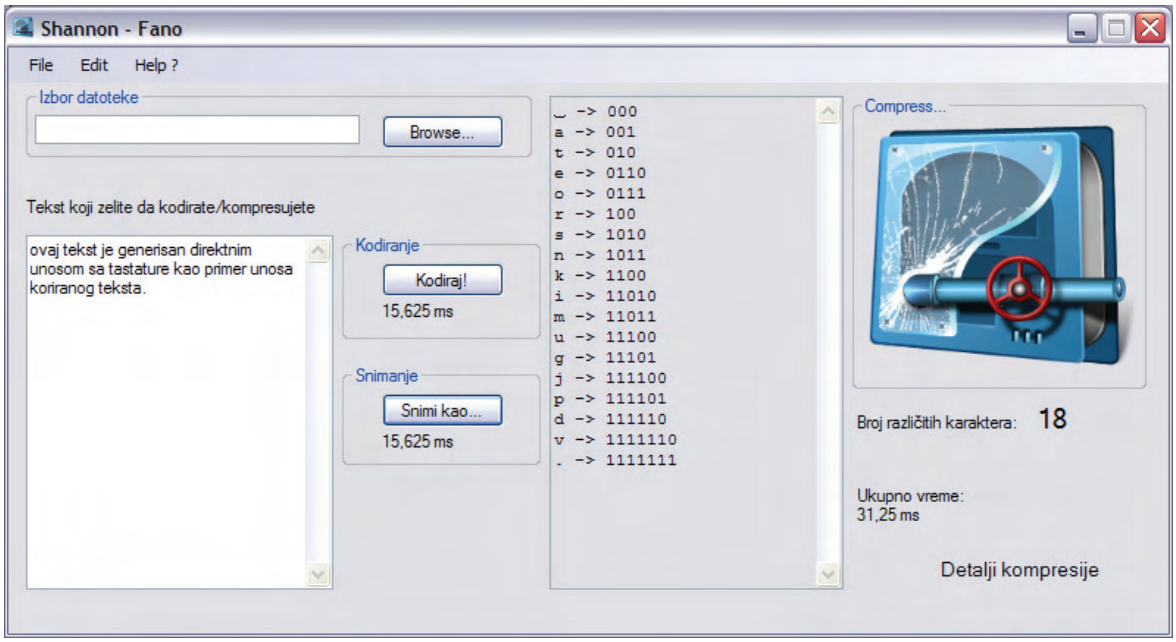

Fig. 1. Main form of the application.

necessary to add additional 0 in buffer with last entry in the file. This way leads to an increase in encoded file, for up to 7 bits, but it allows the simulation of work on the level of bits in C#.

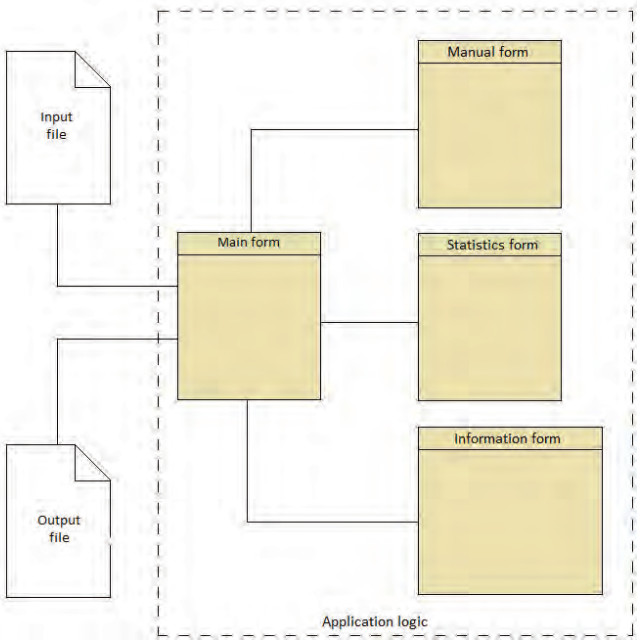

Fig. 2. The architecture of the application.

IV. Experimental Results

The application was tested for various input files in order to get time and percentage of compression. Input file is a text. The all of the experiments were done using a Laptop PC with Intel Core 2 Duo T5450 processor and 3 GBs of RAM, running a Windows XP Service Pack 2 operating. The duration of compression depends on the computer's hardware and current utilization of computer resources. The test results for normal text are shown in Table I, and test results for source code are shown in Table II. Tables I and II also show that the compression speed and compression ratio also depend on the number of different characters and file size. For a small number of different character(s) encoding goes fast regardless of the size of the file. This is because each character encodes a small number of bits and operations with strings quickly completed. For very large files (about 60 MB) the application reports “Memory error”. The problem is caused because of the usage of strings and can be solved by using a StringBuilder. Time coding for a normal text file as source code or a book is at most a few seconds. Compression ratio is about 50% but if there are lots of similar character goes up to 80%. From the presented results we can also conclude that the compression ratio of source codes is less than for the plain text.

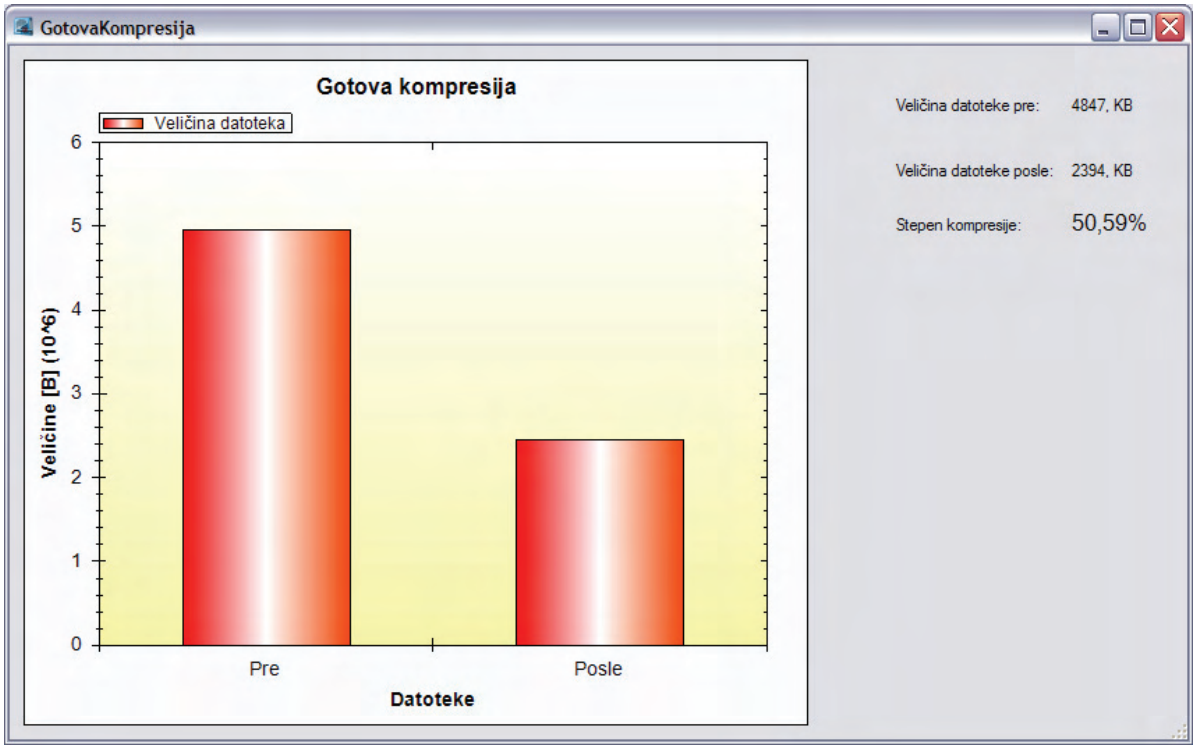

Fig. 3. Statistics form.

TABLE I

DIFFERENT TEXT FILES, *n* – NUMBER OF DIFFERENT CHARACTERS, t_1 – TIME CODING, t_2 – RECORDING TIME, *fs* – FILES SIZE, *cr* – COMPRESSION RATIO

n	t_1	t_2	fs	cr
4	0 ms	15.625	10B -> 3B	70 %
10	0 ms	0 ms	10B -> 5B	50 %
15	0 ms	15.625 ms	21B -> 11B	47.6 %
5	0 ms	15.625 ms	39B -> 12B	69.2 %
47	0 ms	15.625 ms	1,88K -> 1006B	47.7 %
116	656.2 ms	703.12 ms	100,9K -> 49,8K	50.6 %
116	31.9 s	29 s	4847K -> 2394K	50.6 %
3	10.01 s	3.625 s	23523K->4324K	81.8 %
3	27 s	Mem error	61.2M -> ?	?
79	5.112 s	3.718 s	889K -> 501,B	43.26%

TABLE II

SOURCE CODES, *n* – NUMBER OF DIFFERENT CHARACTERS, t_1 – TIME CODING, t_2 – RECORDING TIME, *fs* – FILES SIZE, *cr* – COMPRESSION RATIO

n	t_1	t_2	fs	cr
92	807 ms	620ms	126K -> 55,1K	56.2%
95	186 ms	144ms	29,2K -> 14,2K	51.13%
71	44 ms	36ms	8,56K -> 4,55K	46.88%
90	187 ms	118ms	29,7K -> 12,8K	56.99%
90	153 ms	116 ms	21,3K -> 13,2K	38.14%
71	19 ms	17 ms	3,1K -> 1,9K	38,71%
58	5 ms	7 ms	1K -> 647B	41.5%
65	28 ms	22 ms	5,4K -> 3,15K	41.9%
63	13 ms	12 ms	2,3K -> 1,35K	41.61%

V. CONCLUSION

Through performing the experiments with our implementation of the Shannon-Fano algorithm we reached the following conclusions:

- The most common characters have shorter code words and opposite.
- For the same number of different characters, the algorithm has the same compression ratio.
- For two files with the same size, but with different number of unique characters, a file with a smaller number of different characters has a higher compression ratio.
- Time required for recording and encoding increases with the size of the input file.

Application that we have developed cannot actually compete with existing commercial applications that compress data. It was developed primarily as an education tool that can help students to better understand this encoding technique that serves as basis of more recent compression methods.

REFERENCES

[1] David Salomon, *Data Compression: The Complete Reference*, 3rd Edition, Springer, 2004. (ISBN 0-387-40697-2)

[2] *http://en.wikipedia.org/wiki/Shannon%E2%80%93Fano_coding* website last visited on 14/04/2011.

[3] *http://www.ustudy.in/node/6409,* website last visited on 15/12/2010.

[4] *http://www.binaryessence.com/dct/en000041.htm,* website last visited on 14/04/2011.

[5] *http://cppgm.blogspot.com/2008/01/shano-fano-code.html,* website last visited on 14/04/2011.

[6] *http://www.dotnetspark.com/Forum/169-how-to-open-one-chm-help-file-c-sharp-windows.aspx,* website last visited on 14/04/2011.

[7] *http://www.onlinehowto.net/Why-compress-/2,* website last visited on 14/04/2011.

[8] *http://en.wikipedia.org/wiki/Huffman_coding,* website last visited on 14/04/2011.

A Software Tool for Data Compression Using the LZ77 ("Sliding Window") Algorithm

Student authors: Vladan R. Djokić[1], Miodrag G. Vidojković[1]
Mentors: Radomir S. Stanković[2], Dušan B. Gajić[2]

Abstract – **Data compression is a field of computer science that is always in need of fast algorithms and their efficient implementations. Lempel-Ziv algorithm is the first which used a dictionary method for data compression. In this paper, we present the software implementation of this so-called "sliding window" method for compression and decompression. We also include experimental results considering data compression rate and running time. This software tool includes a graphical user interface and is meant for use in educational purposes.**

Keywords – **Lempel-Ziv algorithm, C# programming solution, text compression.**

I. Introduction

While reading a book it is noticeable that some words are repeating very often. In computer world, textual files represent those books and same logic may be applied there. On the other hand, we can be reasonably sure that some words occur in a very small fraction of the text sources in existence.

Following an idea of repeating words, it is logical to keep a list, or dictionary, of frequently occurring patterns. When any of those patterns appear in the source output, they are encoded with appropriate reference to the dictionary. If the pattern does not occur in the dictionary, encoding should look for some other, less efficient, method for encoding. In effect, we are splitting the input into two classes - the frequently occurring patterns and the infrequently occurring patterns. In order to name this technique as successful, occurring patterns must appear often and also the size of the dictionary must be much smaller than the number of all possible patterns.

This paper describes an implementation of the LZ77 encoding which is one of the dictionary method techniques. In Sections II and III, we describe the theoretical bases of the LZ77 coding and some other types of dictionary coding, respectively. Next, in Section IV we present a software solution for data compression using the LZ77 algorithm realized in C# programming language, along with the experimental results for data compression ratio. This application is mainly developed for educational purposes. We close the paper with some conclusions in the final section.

Student authors:
[1]Vladan R. Djokić and Miodrag G. Vidojković are with the Faculty of Electronic Engineering, Aleksandra Medvedeva 14, 18000 Nis, Serbia, E-mail: djolecorp@elfak.rs, miske87@gmail.com.

Mentors:
[2]Radomir S. Stanković and Dušan B. Gajić are with the University of Niš, Faculty of Electronic Engineering, Aleksandra Medvedeva 14, 18000 Niš, Serbia, E-mails: radomir.stankovic@gmail.com, dusan.gajic@elfak.ni.ac.rs.

II. Lempel-Ziv Algorithm

A. Theoretical basis

The Lempel-Ziv algorithm [1] is an algorithm for lossless data compression. It is actually a whole family of algorithms, (see Figure 1) stemming from the two original algorithms that were first proposed by Jacob Ziv and Abraham Lempel in their landmark papers in 1977. [1] and 1978. [2]. LZ77 and LZ78 got their name by year of publishing.

The Lempel-Ziv algorithms belong to adaptive dictionary coders [1]. On start of encoding process, dictionary does not exist. The dictionary is created during encoding. There is no final state of dictionary and it does not have fixed size.

B. The field of use

Some of modern algorithms for compression and decompression are variations of LZ77. Known compression methods like *arj*, *lha*, *zip*, *zoo*, *stac*, *auto-doubler*, *7-zip*, *DEFLATE* have roots in this algorithm. Also GIF image compression [4] and the V.42 modem standard [4] are based on the LZ algorithm.

III. LZ77 Algorithm

A. Terms used in algorithm description

In order to explain how algorithm works some terms should be explained. Sequence of characters that needs to be compressed is an input stream. One element in input stream is a character. Coding position is position of the character that is currently coded and in same time it is beginning of look-ahead buffer which size is predefined and consists of another sequence of characters. A pointer has task to point to the match in the window. It also declares length of match.

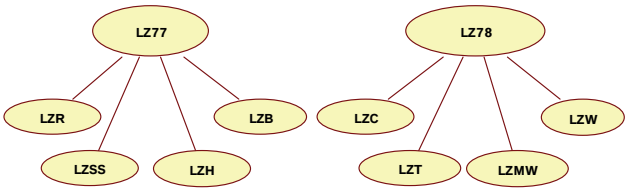

Figure 1. LZ family of algorithms.

Figure 2. LZ77 application architecture.

B. The encoding method

Idea of algorithm is to search the window for the longest match. If window reached end, it also should check beginning of the look-ahead buffer. Finally, it should output a pointer to appropriate match. Output may not contain only pointers since it may occur that there is not a single match. In that case, output is pair of zeros plus character which could not be found in dictionary. If there is a match, pair has number of repetitions, position where match is found and following character (see Table II, column Output).

C. The decoding method

Generally, decoder is much simpler than the encoder. It has to know some parameters which are used during compression and those are size of a dictionary and length of a look-ahead buffer. Then decoder should reconstruct dictionary and look-ahead buffer from original. Finally, it may start decoding process. First should get following token, if there exists any, then to find the match in its buffer. Output is complete match and character which comes after pair of numbers. Next action is to shift the matched string and the third field into the buffer. That process is repeated as long as there are tokens available.

D. Practical example

The encoding process is presented in Table II. The column Step is used only for numeric purposes so that can be seen when one turn of encoding is completed. The column Pos is current position that is coded. In first place, first character has position 1. The column Match represents the longest match found in the window. The column Char shows the first character in the look-ahead buffer after the match. Finally, the column Output, as already mentioned in section B, presents the output in the format (number, number) character. One example of encoding process may be seen in Table II. Notice how in step 3 match is longer than current dictionary and it goes through look-ahead buffer so output sequence is (3,1) S.

TABLE I
INPUT STREAM FOR ENCODING

Pos	1	2	3	4	5	6	7	8	9
Char	A	N	A	N	A	S	S	A	A

TABLE II
THE ENCODING PROCESS

Step	Pos	Match	Char	Output
1.	1	--	A	(0,0) A
2.	2	--	N	(0,0) N
3.	3	A N	S	(3,1) S
4.	7	--	S	(0,0) S
5.	8	A	A	(5,1) A

IV. SOFTWARE IMPLEMENTATION AND EXPERIMENTAL RESULTS

The software solution for LZ77 encoding and decoding that is implemented is named LZ77, and this application can encode and decode ASCII text. LZ77 is developed in C# programming language and .NET Framework 3.5. The architecture of the application is created using Visual Studio 2010 and is shown in Figure 2. Main window of application is shown in Figure 3.

The application consists of three buttons and two combo boxes. First one on the far left is “Load” which is used to load a file. It is possible to load files with any extension, textual files and special archives which are created with this programme using .lz77 extension.

After successful load, all text from input file is transferred into string and ready for compression or decompression. If we have loaded textual file, we can choose dictionary size in bits and look-ahead buffer size. Application offers several values as choice for dictionary size – from 8 to 16, 20, 24 and 28. Theoretically, dictionary size of 32 bits is possible but due to integer constraint it is not applicable. Also, length of look-ahead buffer can be changed with one of values 2, 4, 8, 16, 32, 64 and 128 characters or translated in bits, from 1 to 7 bits can be used for look-ahead buffer. Statistically is proven that optimal results are achieved with dictionary size between 10 and 12 bits and size of look-ahead buffer should be from 5 to 7 bits [7]. If user doesn’t choose any of these values, default values are used and they are 10 bits for dictionary and 5 bits for look-ahead buffer.

By clicking on “Compress” button, text is compressed using LZ77 algorithm and new window opens where output location of archive may be chosen with .lz77 extension. Besides regular LZ77 compression algorithm, already described in this paper, we have added file header which is useful for decoding. First byte is reserved for this file header. First five bits contain value of dictionary size and following three contain look-ahead buffer size. Even those bits have mini dictionary and for example, combination of 01010|101 means that dictionary size is 10 bits and look-ahead size is 5 bits. Binary value is decoded into decimal value. Now, dictionary size in characters is 2^d and size of look-ahead buffer is 2^l where d and l are values received from first bit.

If compression is successful to user is shown message box with speed of compression, measured in milliseconds. For small input files speed is usually around 0. Ratio and speed of compression may be seen in Table III.

To decompress file, first, file should be loaded using “Load” button and then by clicking on “Decompress”, it is decompressed. Note that only files created with this programme have extension .lz77 and therefore only those files may be successfully decompressed. If decompressing is successful to user is shown speed of decompression in message box, similar like compression. Speed of decompression may be seen in Table IV.

Decompress works as follows, first byte is read and values of dictionary and look-ahead are stored in variables, on way

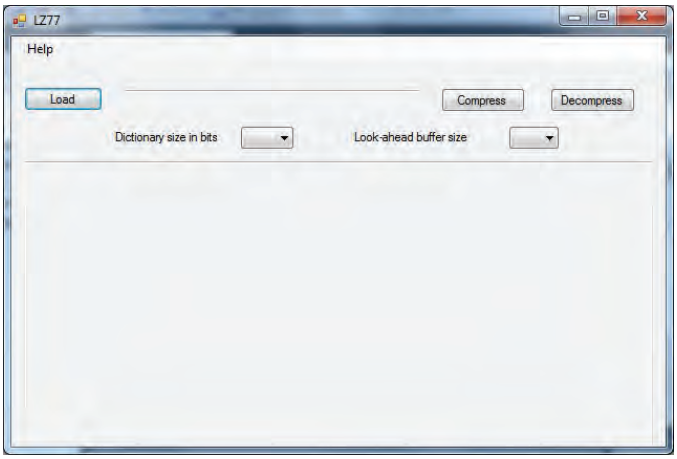

Figure 3. LZ77 application main window.

that is already explained in this paper. Then each pair is read, and returned their original value. Note that compression/decompression only works with ASCII characters since ASCII requires 7-bits for each character. Unicode coding/decoding is harder to achieve since Unicode coded character doesn’t have constant size in bits.

All tests are performed using optimal compression values for dictionary and look-ahead buffer. Also, all tests are performed on same machine HP Pavilion dv6 Notebook PC using Intel(R) Core(TM)2 Duo CPU T6600 @ 2.20GHz, 2.20GHz, 3GB Ram memory on 64-bit Operating System Win7. All values (unless there are written actual measurements) of files are measured in bytes, speed in milliseconds and ratio in percents.

TABLE III
RATIO AND SPEED OF ENCODING PROCESS

Input type	File size	Compressed	Speed	Ratio
Text- normal	5	16	0	320%
Text- repetitive	179	47	0	26%
Text- normal	640	709	0	111%
C++ code text	1528	384	16	25%
Book	12534	9853	63	79%
Book	69369	49518	281	71%
Book	544792	385953	2512	71%
Text- repetitive	760320	68361	172	9%
Text- repetitive	12MB	1MB	4200	8%
Text	100 MB	62.5MB	330 s	63%

TABLE IV
SPEED OF DECODING PROCESS

Input type	File size	Speed
Text- normal	16	0
Text- repetitive	47	0
Text- normal	709	0
C++ code text	384	0
Book	9853	56
Book	49518	405
Book	385953	2215
Text- repetitive	68361	180
Text- repetitive	1MB	7400
Text	62.5MB	350 s

V. CONCLUSION

In this paper, we have presented a software implementation of LZ77 algorithm. We have performed various tests on different file sizes and file types, and gathered experimental results which may be used in educational purposes. The application may be used in better understanding of LZ77 algorithm.

Implementation of LZ77 algorithm is giving the best results when the input file has repetitive text. Also, good compression is achieved on C++ source files and on book text. Compression is not satisfactory when the input file is too small. Normally, in real-world applications, the compression is performed on books and results in compression rates around 70-80% of the original file size.

REFERENCES

[1] Jacob Ziv, Abraham Lempel, “A universal algorithm for sequential data compression”, *IEEE Transactions On Information Theory*, Vol. It-23, No. 3, May 1977.

[2] Jacob Ziv, Abraham Lempel, "Compression of Individual Sequences via Variable Rate Coding", *IEEE Transactions on Information Theory*, Vol. 24, No. 5, pp. 530-536, Sep. 1978.

[3] Khalid Sayood, *Introduction to Data Compression*, Morgan Kaufmann Publishers, Published 1996, Second Edition 2000.
[4] Christina Zeeh, *The Lempel Ziv Algorithm*, Seminar ”Famous Algorithms”, January 16, 2003.
[5] *http://oldwww.rasip.fer.hr/research/compress/algorithms/fund/lz/lz77.html*, last visited on 8/12/2010-10:00.
[6] David Salomon, *Data Compression*, Fourth Edition, Springer 2007.
[7] Terry Welch, A Technique for High-Performance Data Compression, IEEE Computer, 17(6):8-19, June 1984.
[8] M. Salson, T. Lecroq, M. L´eonard, and L. Mouchard. Dynamic extended suffix arrays. Journal of Discrete Algorithms, In Press, Corrected Proof, 2009.
[9] M. Crochemore, L. Ilie, and W. Smyth. A simple algorithm for computing the Lempel-Ziv factorization. In DCC ’08: Proc. of the IEEE Conference on Data Compression, pages 482–488, 2008.

HED (Huffman Encoder - Decoder) - An Application for Text Encoding and Decoding

Students: Miroslav Z. Manić[1] and Ivan S. Nikolić[1]

Mentors: Radomir Stanković[1] and Dušan Gajić[1]

Abstract – **Huffman encoding is a lossless data compression method often used in practical applications like MP3 audio encoding, JPEG image encoding or ZIP's DEFLATE algorithm. In this paper we present the application we named HED (Huffman Encoder - Decoder) which we developed using C#. This software tool can be used for both text compression and decompression and includes the compression statistics (compression ratio, compression time etc.). Results of the practical experiments conducted with the HED application are also presented and analyzed.**

Keywords - **Huffman encoding and decoding, algorithm implementation in C#.**

I. INTRODUCTION

Lossless data compression is a class of data compression algorithms. Those algorithms allows the exact original data to be reconstructed from the compressed data.

In computer science, data compression is the process of encoding information using fewer bits than a more obvious representation would use, through use of specific encoding schemes. For example, this article could be encoded with fewer bits if we accept the convention that the word "Huffman" be encoded as "Huf". One popular instance of compression that many computer users are familiar with is the ZIP file format, which storing many files in a single output file.

Compressed data communication only works when both the sender and receiver of the information understand the encoding scheme. It means that compressed data can only be understood if we know which decoding method is used by the sender. This is possible because most data that we use have statistical redundancy. Detailed explanation of this is given in [2]. For example, the letter 'e' is much more common in English text than the letter 'z' [3]. Lossless compression algorithms exploit statistical redundancy in such a way as to represented the sender's data more concisely, but nevertheless perfectly. Compression is important because it helps reduce the consumption of expensive resources, such as disk space. On the other side, compression requires information processing power, which can also be expensive. Some schemes are reversible so that the original data can be reconstructed (lossless data compression), while others accept some loss of data in order to achieve higher compression (lossy data compression).

Huffman coding is a statistical technique which attempts to reduce the amount of bits required to represent a string of symbols. The algorithm allows symbols to vary in length. Shorter codes are assigned to the most frequently used symbols, and longer codes to the symbols which appear less frequently in the string. Applications which uses Huffman code are very frequent in computer science. This code is not only for text coding, it is used for picture compression, audio and video compression etc. Huffman coding is useful for compression data where there are bits which are most frequently used.

In this paper we present the application we named HED (Huffman Encoder - Decoder) which is developed using C#. This software tool can be used for both text compression and decompression and under the hood there is Huffman algorithm for data compression.

The paper is organized as follows. In section 2 we will see Huffman coding procedure. The architecture and implementation of Huffman algorithm in our application is given in Section 3. Section 4 is reserved for practical experiments and results which are presented and analyzed. Section 5 summarizes the results.

II. HUFFMAN ENCODING AND DECODING PROCEDURE

Arithmetic coding can be viewed as a generalization of Huffman coding. Although arithmetic coding offers better compression performance than Huffman coding, Huffman coding is still in wide use because of its simplicity.

Encoding

Huffman encoding today is often used as a "back-end" to some other compression method. DEFLATE (PKZIP's algorithm) and multimedia codecs such as JPEG and MP3 have a front-end model and quantization followed by Huffman coding [1].

Huffman coding uses a specific method for choosing the representation for each symbol. It results in a prefix code that expresses the most common source characters using shorter strings of bits.

Students: [1]Miroslav Z. Manić and Ivan S. Nikolić are with the Faculty of Electronic Engineering, Aleksandra Medvedeva 14, 18000 Nis, Serbia, E-mails: mmanic@elfak.ni.ac.rs, slashdance007@gmail.com.

Mentors: [1]Radomir Stanković and Dušan Gajić are with the University of Niš, Faculty of Electronic Engineering, Aleksandra Medvedeva 14, 18000 Niš, Serbia, E-mails: dusan.gajic@elfak.ni.ac.rs, radomir.stankovic@gmail.com.

First that we need to resolve before we start is "What is a character?". For our implementation a character is any 8-bit combination. In general, a Huffman code for an N characters alphabet, may yield symbols with a maximum code length of N - 1.

The Huffman algorithm works by creating a binary tree of nodes. These can be stored in a regular array. The size of which depends on the number of symbols. A node can be either a leaf node or an internal node. All nodes are leaf nodes, which contain the symbol itself, the link to a parent node which makes it easy to read the code (in reverse) starting from a leaf node. Internal nodes contain symbol weight, links to two child nodes and the link to a parent node. As a common convention, bit '0' represents following the left child and bit '1' represents following the right child. A Huffman tree that omits unused symbols produces the most optimal code lengths.

The process essentially begins with the leaf nodes containing the probabilities of the symbol they represent, then a new node whose children are the 2 nodes with smallest probability is created, such that the new node's probability is equal to the sum of the children's probability. With the previous 2 nodes merged into one node and with the new node being now considered, the procedure is repeated until only one node remains, the Huffman tree. Detailed explanation of this is given in [1]. Here is one example which shows how to create Huffman tree. Given a 6 symbol alphabet with the following symbol probabilities: A = 1, B = 2, C = 4, D = 8, E = 16, F = 32. Step 1. Combine A and B into AB with a probability of 3. Step 2. Combine AB and C into ABC with a probability of 7. Step 3. Combine ABC and D into ABCD with a probability of 15. Step 4. Combine ABCD and E into ABCDE with a probability of 31. Step 5. Combine ABCDE and F into ABCDEF with a probability of 63. Result is shown on Fugure 1.

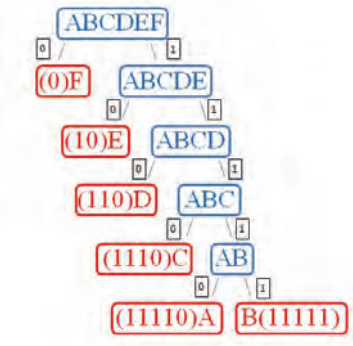

Fig.1 Tree results

Decoding

Generally, the process of decoding is simply a matter of translating the stream of prefix codes to individual byte values, usually by traversing the Huffman tree node by node as each bit is read from the input stream. The Huffman tree must be somehow reconstructed if we want to decode aor file. In the simplest case, where character frequencies are fairly predictable, the tree can be preconstructed. A naive approach might be to prepend the frequency count of each character to the compression stream. Another method is to simply prepend the Huffman tree, bit by bit, to the output stream. For example, assuming that the value of 0 represents a parent node and 1 a leaf node, whenever the latter is encountered the tree building routine simply reads the next 8 bits to determine the character value of that particular leaf. The process continues recursively until the last leaf node is reached; at that point, the Huffman tree will thus be faithfully reconstructed. The overhead using such a method ranges from roughly 2 to 320 bytes. For details see article given in [1]. On the end, the decoding must be able to determine when to stop producing output. In section 3 we presented technic that we used for decompression in our application [5]. Before we see the experimental results for our application, we should be first introduced to the architecture of application and how it works under the hood.

III. Architecture and Implementation of HED

HED application is developed in C#. We used Visual Studio 2010 and .NET Framework 3.5. This is powerfull tool for making applications which have really good design and which works in real time with low lag.

The main task of Huffman Encoder – Decoder (that we named HED application) is compression of text files. Our version of application has decoder, so you can decode file which is encoded with HED and which has no losses.

Design for application was made using Adobe Photoshop. Specifically, we used Microsoft Visual Studio 2010 professional, with .net framevork3.5. Adobe Photoshop was used to design the program and the algorithm is implemented in C#. Application is designed to simulate the Windows Aero interface. Following the example of Microsoft Office wizard to help, we created a robot that appears during the operation of the application and asks the user to simply click it toget help for HED application.

Fig.2 Help Wizard

HED applications can be divided into several units. Based on the Huffman algorithm and its modes, the first thing the program has to do is to count the characters which appear in the entered text. This counter is the first important unit in the HED application. In addition, it makes a Huffman tree. It also

makes code for all the different characters that appear in the entered text. When the application has the code it may start coding.

HED application is made to do compression, called encoding, and also the decompression or decoding of already compressed text. Decoding is implemented with two functions. The first function reads file header which contains data required for decompression and then makes Huffman tree. It's Based on the tree. Compressed data is stored in the rest of the file. The second group of functions perform decompression.

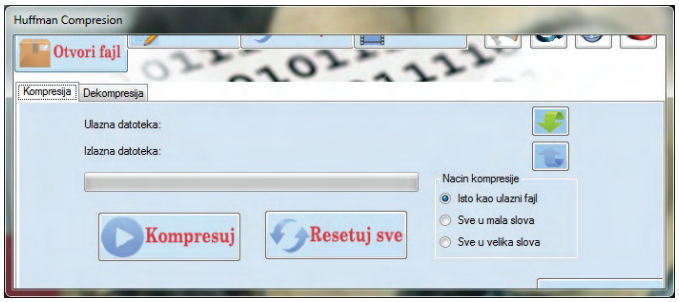

Fig.3 Application interface

First function of the HED application performs counting of different characters which appear in the input text. It consists of "for loops" which do counting in just one pass.This is one of reasons why this program is so fast. The number of character occurrences is remembered in a row, and the characters that appear in the input text of this function are remembered in the second row. Application uses this rows during labor. Building of the Huffman tree is performed by several functions related to the entity. This tree is used for creating the character codes. Each tree node represents a data structure and contains the character and number of its occurrences. One of these functions is used to insert the node to the right place, the second is used to create a new node based on two adjacent nodes.Making accurate Haffman tree is very important because function read character codes used for encoding from it.

Creating codes is perform by special functions. She moves through Haffman tree recursively calls itself and remember in a series of codes based on Haffman algorithm. Codes are stored as a string, but only temporarily. During encoding, these codes are converted to a sequence of bits. This conversion is done with a special function.

This works on the principle of logical shifting buffer to the left. If the input string (a sequence of 0 or 1) logic 1, the functions other than shift to the left adds a 1 at the endof the buffer, if the input string 0 then just shift the contents of the buffer left. Enteringinto the buffer is complete when the buffer is full rapport, when write 8 bits. This function is used for coding the input text. Coding performs a function that reads character by character from text input, read itscode, converts it into a series of bits and stored in the output file.Switch code that is remembered as a string into a sequence of bits perform functions which we write because C # programming language does not support working with bits. This function returns one byte witch is through the buffer stored in the output file.Compression is also performed one-pass through to enter text.

Decompression performed reverse work than the work which is performed by compression. Since some data that are used in the compression is also required for decompression, we must remember them in the outputfile.This part of the file is called a header. It remembers all the characters that appear in the coded text and the number of occurrences (frequency) of these characters. So that all characters were included they must be remembered in UNICODE code system, so each character in the header occupies 2 bytes.The number of occurrences of character is an integer and takes a byte in header file.These data are important because we need to have the decoding Huffman tree from which we read the character of the input code.Creating a Huffman tree performs a function that is very similar to that as incompression, because their input data practically are the same.The very process of decoding performs a function on the basis of already made huffnan trees and coded data, reading the characters and remember them in the output text file.Here we have a function which for easy work turning sequence of bits in the string.

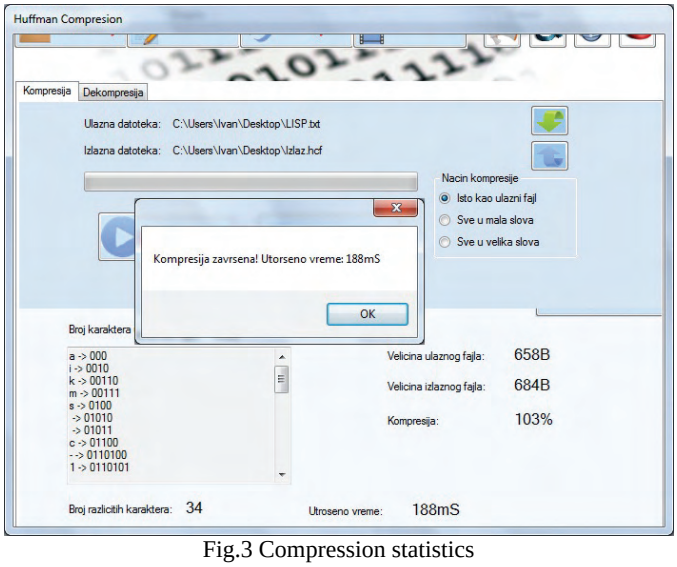

Fig.3 Compression statistics

IV. PRACTICAL EXPERIMENTS AND RESULTS

For testing our application we have used different types of textual files. We used txt, .h, .cpp, HTML, XML, etc. Results shows that there is no matter which format of text document is, it works with all of file formats we mention above, and size of output file does not depend on type of text file. Size of output file directly depends on size of input file. On the other side, characteristics if letters in text have higher frequency is one of the most important reasons why output file is smaller or bigger. So, we have made some txt files and tested our application using them. Some of them have few characters, other have different characters. In the following table we can see some results how output file depends on number of characters and frequency of its occurence.

TABLE I
VALUES IN BYTES AND NUMBER OF CHARACTERS FOR INPUT AND OUTPUT FILES AND COMPRESSION RATE AND TIME ELAPSED FOR OUTPUT FILES

File No.	Input file/Output file [B]	Input No.diferent char./All characters	Compression ratio [%]	Time
1.	5/14	2/2	280	11 ms
2.	10/28	4/10	280	12 ms
3.	10/74	10/10	740	21 ms
4.	21/124	15/21	590	27 ms
5.	39/44	5/39	112	12 ms
6.	1.926/1.617	49/1.926	83	140 ms
7.	11.529/9.062	86/11.529	78	334 ms
8.	103.555/52.709	116/103.408	50	839 ms
9.	3.362.038/963.113	90/1.681.018	28	5.061 ms
10.	4.963.584/2.453.939	116/4.963.584	49	17.713 ms
11.	65.078.895/37.621.271	116/64.851.952	57	3 min 48 s
12.	193.547.880/96.253.836	22/193.547.880	49	3 min 11 s

Now we will discuss results that we got. This is tasted on Intel Dual core processor and it's important for following discussion about duration of this operations. First off all, we can notice that size of output file depends of number of different characters. In file 1 we have only 2 different characters and whole file have only 2 characters. So we can see that result for this is not so good, because output file is bigger than input file. Compression ratio here is 280% (Table 1).

When we have same number of different characters and all characters like in file 3, results are worst and output file is much bigger then input. In file in which number of all characters is more bigger then number of different characters, compression ratio is better (112 %). This is because codes for characters are shorter then ASCII code, and they occurs frequently. We must mention again that output files should be smaller if we didn't used header. Better results are in file 6 (112% compression ratio) because we have larger number of characters then number of different characters. You can see this in other files (7 - 12). Compression ratio is greater and when number of all characters increases. We tasted application with maximum 116 different characters, and best result is in file 10 (49% compression ratio) which has 4.963.584 different characters. In table 2 we can see duration of each compression process. We can notice that the best time is for file 1, and the worst for file 12.

V. CONCLUSION

In this paper An Application for Text Encoding and Decoding is proposed. It uses Huffman algorithm. Experimental results shows that compression ratio depends on ratio of number of different characters and number of all characters in file; when number of different characters is lower, and number of all characters is higher, results are better. Time for compression is lower when we have less number of all characters.

This application can not be compared with other commercial programs that doing encoding and decoding data. It can be used in educational purposes to show students how Huffman algorithm works.

REFERENCES

[1] The Data Compression Book 2nd edition by Mark Nelson and Jean-loup Gailly, M&T Books, New York, NY 1995

[2] Text Compression by Timothy C. Bell, John G. Clearly and Ian H. Witten 1990

[3] Data Compression: The Complete Reference by David Salomon 2nd edition, 2000

[4] http://www.cs.cf.ac.uk/Dave/Multimedia/node210.html, website last visited on 13/04/2011.

[5] http://www.cs.auckland.ac.nz/~jmor159/PLDS210/huffman.html, website last visited on 14/04/2011.

[6] http://www.huffmancoding.com/my-family/my-uncle/huffman-algorithm, website last visited on 12/04/2011.

Implementation of the Generalized FFT on Finite Groups

Student authors: Igor Mihajlović[1], Milan Marković[1], Nenad Andrejević[1], and Milan Djokić[1]
Mentors: Radomir Stanković[2] and Dušan Gajić[2]

Abstract - **FFT is one of the most important algorithms in signal processing and computing. The group theoretical approach to Fourier analysis is useful in solving several optimization problems in these areas. For practical application of this approach, the corresponding FFT algorithms on finite groups are required. It is interesting to explore how different group choice at various steps of FFT affects computational efficiency and function spectra. This paper presents a C/C++ implementation of FFT over finite not necessarily Abelian groups allowing to freely choose the underlying group structure at each step of the FFT. We also provide results and conclusions drawn from experiments over a set of benchmark functions viewed as functions on different groups with group representations selected in different fields, including the field of complex numbers and few preselected finite fields. These results could be helpful in tracing directions for further research in this area.**

Keywords – **FFT, C/C++ implementation, finite non-Abelian groups, experimental results.**

I. Introduction

Fourier analysis is the cornerstone of signal processing and system analysis and, hence, has many applications in modern computational problems. Classical Fourier analysis is defined on the unit circle, on the integers and on the real line. A vast number of different fast algorithms have been developed for such theoretical settings [1].

Group theoretical approach to Fourier analysis has been implicit in many of the classical works and its implicit introduction into the field produced many important theoretical conclusions. This approach creates a powerful platform for the unified approach when applying Fourier transform on signals defined on different algebraic structures that reflect the properties of the modelled phenomenon.

Methods based only on finite Abelian groups has provided many successful applications in signal processing, however, recent studies have shown that this approach does not always yield best performance of related algorithms.[2] Hence, non-Abelian groups have been introduced in order to supplement for disadvantages of the former approach.

In this work we investigate how choice of algebraic structures influences performance of the FFT and sparsity of the Fourier spectra.

Student authors:
[1]Igor Mihajlović, Milan Marković, Nenad Andrejević, and Milan Djokić are with the Faculty of Electronic Engineering, Aleksandra Medvedeva 14, 18000 Niš, Serbia, E-mails: igor.mihajlovic1987@gmail.com, milan@elfak.rs, neca.87@gmail.com, Milan.djokic.87@gmail.com .

Mentors:
[2]Radomir Stanković and Dušan Gajić are with the Faculty of Electronic Engineering, Aleksandra Medvedeva 14, 18000 Niš, Serbia, E-mails: radomir.stankovic@gmail.com, dusan.gajic@elfak.ni.ac.rs.

II. Fourier Transform on Finite Groups

The Fourier transform on finite Abelian and non-Abelian groups can be studied in a unique setting with a classical Fourier transform in the frame of abstract harmonic analysis [2].

From the mathematical topology point of view, the real line R is a locally compact Abelian group and the theory of Fourier analysis can been extended to such groups if the exponential functions used in Fourier analysis on R are replaced by the group representations [2].

Def. 1. Finite-dimensional representation of a finite group G over a field P is a homomorphism

$$R : G \rightarrow GL(n, P)$$

where $GL(n,P)$ is the general linear group, i.e., the group of ($n \times n$) invertible matrices (n is a natural number) with respect to matrix multiplication, with entries in a field P.

It can be proven, see for instance [2], that if representations are unitary and irreducible that they form a complete orthogonal system and, hence, the Fourier transform for a function f on a group G of order g can be defined as follows:

$$\mathbf{S}_f(w) = r_w g^{-1} \sum_{u=0}^{g-1} f(u) R_w(u^{-1}), \quad (1)$$

$$f(x) = \sum_{w=0}^{K-1} Tr(\mathbf{S}_f(w)\mathbf{R}_w(x)), \quad (2)$$

where $\mathbf{S}_f(w)$ is the Fourier spectrum for f, R_w are the group representations of orders r_w, K is the dimension of the dual object $\Gamma$for G, and $Tr(\mathbf{X})$ denotes the trace of a matrix $\mathbf{X}$.

In matrix notation, the Fourier transform pair defined by (1) and (2) can be **Error! Bookmark not defined.**expressed as follows [2]:

Given a function f on a group G of order g by the function vector $\mathbf{f}=[f(0),\ldots,f(g\text{-}1)]^T$. The Fourier spectrum for f , represented as a matrix-valued vector $[\mathbf{S}_f]=[\mathbf{S}_f(0),\ldots,\mathbf{S}_f(K\text{-}1)]^T$ is defined as

$$[\mathbf{S}_f] = g^{-1}[\mathbf{R}]^{-1} \bullet f, \quad (3)$$

where $[\mathbf{R}]^{-1} = [\mathbf{b}_{sq}]$, with $\mathbf{b}_{sq} = r_w \mathbf{R}_s^{-1}(q)$, $s=\{0,1,\ldots,K\text{-}1\}$, $q=\{0,1,\ldots,g\text{-}1\}$. The inverse transform is defined as

$$\mathbf{f} = [\mathbf{R}] \circ [\mathbf{S}_f] \quad (4)$$

where $\bullet$ and $\circ$ denote the generalized multiplications permitting dealing with vectors and matrices whose entries are matrices defined in [2], and $[\mathbf{R}]=[\mathbf{a}_{ij}]$, with $\mathbf{a}_{ij} = \mathbf{R}_j(i)$, $i=\{0,1,\ldots,g\text{-}1\}$, $j=\{0,1,\ldots,K\text{-}1\}$.

The matrix expression of the Fourier transform is important, since permits an elegant way towards devising the fast computing methods discussed in this paper.

III. Fast Algorithms for Computing the Fourier Transform

The fast Fourier transform (FFT) is a method for computing the Discrete Fourier transform (DFT) efficiently in terms of space and time [3].

This algorithm is based upon the factorization of the DFT transform matrix into the product of sparse matrices, each matrix describing a step in the FFT. The same approach can be used to devise fast algorithms for the Fourier transforms on finite groups, see for instance [2] and references therein. It is assume that the domain group G can be written as the direct product of groups $\mathbf{G}_i$, $i=\{0,1,\ldots,n\text{-}1\}$ of smaller orders. Then, the Fourier transform on G can be performed as n Fourier transforms on the constituent groups G_i. This could be considered as a restriction of the FFT from the whole group G to the FFT of its subgroups G_i. It follows that the i-th factor matrix can be represented as the Kronecker product of the Fourier transformation matrix on Gi of order gi at the i-th position and the identity matrices of orders gj, j $\in\{1,...,n\}\backslash\{i\}$,at all other positions into the Kronecker product. The same approach can be extended to non-Abelian groups using generalized matrix multiplications as described in [2].

The matrix [**R**] in the definition of the Fourier transform on finite non-Abelian groups is the matrix of unitary irreducible representations of G over P [2]. Matrix [**R**] and also its inverse $[\mathbf{R}]^{-1}$ can be generated as Kronecker products of ($\boldsymbol{K}_i \times g_i$) unitary irreducible representations of subgroups.

$$[\mathbf{R}] = \overset{n}{\underset{i=1}{\otimes}}[\mathbf{R}_i] \tag{6}$$

This matrix can be can be further factorized into elementwise Kronecker product of n sparse factors [Ci], i $\in$ {1,…,n} as

$$[\mathbf{C}^i] = \overset{n}{\underset{j=1}{\otimes}}[\mathbf{S}^i_j], i = 1,....,n \tag{7}$$

where

$$[\mathbf{S}^i_j] = \begin{cases} \mathbf{I}_{(g_j \times g_j)}, j < i \\ [\mathbf{R}_j]^{-1}, j = i \\ \mathbf{I}_{(K_j \times K_j)}, j > i \end{cases} \tag{8}$$

and $\mathbf{I}_{a\times a}$ is an $(a\times a)$ identity matrix.

Although the (a) classical FFT algorithm can be derived in a similar fashion, there are some important differences with respect to dealing with finite non-Abelian group. Elements of vectors are not just scalars but could also be square matrices depending on (of) the representation of the corresponding non-Abelian group. Therefore, the number of representations of a non-Abelian group is always smaller than the order of that group. This implies that the vector size in different steps of FFT varies.

Fast algorithm is performed in n steps where n is (represents) the number of subgroups of G. The time complexity of each step is linear with the vector size.

IV. Implementation

We implemented the algorithm for computing the Fourier spectrum on finite non-necessarily Abelian groups using the C++ programming language. Since vector elements can be either scalars or matrices, we resorted to usage of OO techniques by abstracting the vector element as a class *Element [Complex]* on which we define the generalized multiplication operator as stated in the previous section.

Numbers of subgroups as well as the subgroups themselves for the each step could be chosen by the user, giving the chance to find the best suited decomposition for the problem at hand. Some of the subgroups implemented include: the additive groups of integers Z2, Z4, Z8, the symmetric group of permutations of order three S3, and the quaternion group Q8 [4]. This is implemented as a quad pointer to the object of the class element which represents the n-element vector of the subgroup transformation matrices with entries in the class *Element*. Since the size of vector during the different steps varies, we need to maintain the current vector size. In order to achieve the optimal space complexity in each step, memory is dynamically allocated and later de-allocated. The products of sizes of the left and the right identity matrices $\mathbf{S}^i_j$ defined by (8) are also maintained for fast multiplication of sparse matrices.

The algorithm for computing the Fourier spectrum can be specified in the pseudo code as:

```
FFT(N,g,K,V,NV)
1.  l ← 1
2.  for i ← 1 to N-1
3.    l ← l*g[i]
4.  d ← 1
5.  NX ← NV
6.  X ← V
7.  for i1 ← 0 to N-1
8.    mat ← mats[i1]
9.    NY ← NX*K[i1]/g[i1]
10.   KX=NX/l
11.   KY=NY/l
12.   for i2 ← 0 to l-1
13.     for i3 ← 0 to d-1
14.       for I ← 0 to K[i1]-1
15.         Y[i2*KY+i*d+i3] ← 0
16.         for j ← 0 to g[i1]-1
17.           Y[i2*KY+i*d+i3]←mat[i][j]* X[i2*KX+j*d+i3]
        +  Y[i2*KY+i*d+i3]
18.     l←l/g[i1+1]
19.     d←d*K[1i]
20.     X ← Y
```

21. NX ← NY

In the algorithm above *N* represent the number of steps i.e. the number of subgroups G is factored into, g and K represent arrays of sizes of those subgroups and their dual objects [2] respectively, while V is the input vector and NV its size. As mentioned above, sizes of left and right identity matrices are represented with *l* and *d* which are set to $\prod_{i=1}^{n-1} g[i]$ and 1 respectively in lines 1-4. A temporary vector X of size NX is used for containment at various steps and is initially set to V and NV at lines 5-6. In lines 7-21, the Fourier spectrum is computed in *n* steps. In lines 8-9 the i^{th} transformation matrix is loaded and the corresponding size of the vector Y is set. Each step could be performed by dividing the input vector into *l* parts each consisting of d interlacing g[i1] × K[i1] butterflies.

In lines 12-17, the algorithm iterates through the parts and then trough butterflies performing the i^{th} transformation on the appropriate vector elements. In lines 18-19, new values for *l* and *d* are calculated.

V. Experimental Results

Asymptotic time complexity of FFT is $O(n\log n)$ where *n* is the size of the input vector. Since the complexity of FFT over vectors does not depend on the values f vector entries, the computations are performed over randomly generated integer vectors of different sizes.

In the following table we present the running time of algorithm depending on the input size when the domain group *G* is factored in the product of subgroups Z_2.

TABLE I
Running time comparison with same factoring and different vector sizes.

Input vector size	Running time [ms]
32	2
128	15
256	16
512	31
1024	31
2048	93
4096	203
8192	468
16384	1061

Next we present the running time of algorithm depending on the input size when factoring the froup to the subgroups Q8

TABLE II
Running time comparison with same factoring and different vector sizes.

Input vector size	Running time [ms]
8	0
64	1
512	31
4096	156
32768	1314
262144	12324

The same results will be shown graphically it the figures 1 and 2 for better running time comparison of factoring same vectors over different subgroups.

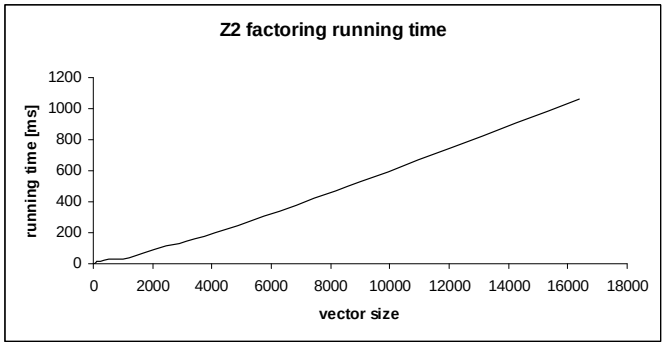

Fig.1. Z2 factoring running time.

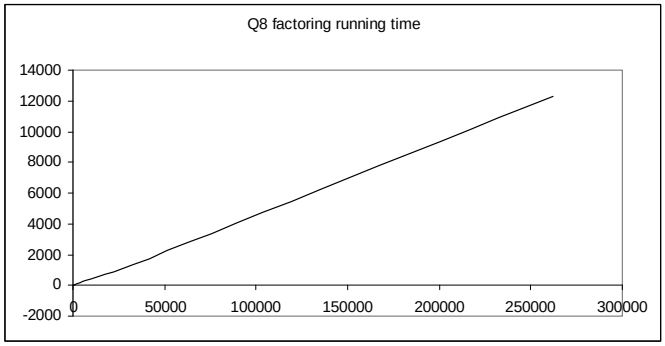

Fig.2. Q8 factoring running time.

As shown in the Figures 1 and 2, with our non-Abelian algorithm the asymptotic complexity remains the same, but with proper group choice, number of operations can be dramatically reduced.

We present the obtained results of running time over the same vector of size 214 while using different factoring.

TABLE III
Running time comparison with different factoring and same vector sizes.

Factoring	Running time [ms]
Z_2^{14}	1061
$Z_8^4 \times Z_2^2$	1029
Z_4^7	780
$Q_8^2 \times Z_8^2 \times Z_4$	718
$Q_8^4 \times Z_2^2$	624

Apart from the running time, different factoring also affects the sparseness of the function spectra.

We present the obtained results of non-zero elements over the same vector of size 2^5 while using different factoring.

TABLE IV
COMPARISON OF NON-ZERO ELEMENTS OVER DIFFERENT FACTORING AND SAME VECTOR.

Factoring	Percentage of non-zero elements
$Q_8 \times Z_2^2$	90%
$Z_2 \times Z_8$	53.13%
$Z_8 \times Z_4$	31.20%
$Z_2 \times Z_4^2$	15.62%
$Z_4 \times Z_2^3$	9.37%
Z_2^5	6.25%

VI. CONCLUSION

Group theoretical approach provides us with uniform treatment of signals defined over different algebraic structures. The first part of our work was to implement FFT when the user can arbitrary select factorization into subgroups. The second part was devoted to experimentally analyze how different factoring affects output data and time complexity of the algorithm.

As shown above, by a careful choice of subgroups we can obtain better running time and spectra sparseness. Apart of that different group choices can provide us with various perspectives of function properties.

The implementation can be further improved by adding more group choices and by code optimization of calculations at each step.

REFERENCES

[1] W. Rudin, *Fourier Analysis on Groups*, New York, Interscience Publishers, 1962.

[2] R. S. Stankovic, C. Moraga, J.T. Astola, *Applications of Fourier Analysis on Finite non-Abelian Groups in Signal Processing and System Design*, New York, John Wiley & Sons, 2005.

[3] C. V. Loan, *Computational Frameworks for the Fast Fourier Transform*, Society for Industrial Mathematics, 1992.

[4] Rober B. Ash, *Basic Abstract Algebra: For Graduate Students and Advanced Undergraduates*, Dover books on Mathematics, 2000.

Comparative Analysis of C/C++, Java, Python, and LISP Implementations of Greedy Algorithms for the Graph Coloring Problem

Student authors: Nenad Mančević[1], Igor Mihajlović[1], Nenad Andrejević[1], and Milan Đokić[1]
Mentors: Radomir Stanković[2] and Dušan Gajić[2]

Abstract – **Graph coloring is a very interesting NP-complete problem. Coloring of a simple graph is the assignment of a color to each vertex of the graph so that no two adjacent vertices are assigned the same color. It is interesting to compare performances of different variations of the greedy algorithm for graph coloring depending on parameters and vertex order. Also, it is interesting to determine how much the implementation in different programming languages affects performances of the algorithm. In this paper, we present implementations of three variations of greedy algorithm for graph coloring in several programming languages including C/C++, Java, Lisp, and Python, as well as results and conclusions drawn from experiments. These results could be helpful in tracing directions for further research towards efficient implementation of various algorithms for NP-complete problems.**

Keywords – **greedy algorithm, graph coloring problem, NP-complete problems, programming languages.**

I. Introduction

Graph theory, as one the most important fields in discrete mathematics, has many applications in modern computer science. During its rich evolution, graph theory has produced great deal of many interesting problems. Many of those problems are NP-complete, including one of the most popular problems – graph coloring.

In graph theory, we can define a vertex coloring of a graph G = (V,E) as a map c: V → S such that $c(v) \neq c(w)$ whenever *v* and *w* are adjacent. The elements of the set S are called the available *colors* [1]. The minimum number of unique colors that we could use to paint graph vertices is called a *Chromatic number* χ(G). Similarly, the minimum number of unique colors used in coloring the edges so that two adjacent edges don't share the same color gives a *Chromatic index*.

In this paper, we will focus on vertex coloring problem which belongs to a class of NP-complete problems.

Since this problem is NP-complete, many algorithms have been proposed to obtain approximate colorings in reasonable time. Those algorithms can be categorized in the following classes: greedy, partition, clique, Zykov and others [2].

In the following sections we will further present three variations from a class of Greedy algorithms. We will later discuss their software implementations in four different programming languages including C/C++, Java, Python and LISP. Finally we will show experimental results, obtained by running these implementations on random generated graphs, presenting time efficiency over different programming languages and computed chromatic number using different algorithms.

Student authors:
[1]Nenad Mančević, Igor Mihajlović, Nenad Andrejević, and Milan Đokić are with the Faculty of Electronic Engineering, Aleksandra Medvedeva 14, 18000 Nis, Serbia, E-mails: manca@elfak.rs, igor.mihajlovic1987@gmail.com, neca.87@gmail.com, Milan.djokic.87@gmail.com .
Mentors:
[2]Radomir Stanković and Dušan Gajić are with the Faculty of Electronic Engineering, Aleksandra Medvedeva 14, 18000 Nis, Serbia, E-mails: radomir.stankovic@gmail.com, dusan.gajic@elfak.ni.ac.rs.

II. Greedy Algorithms

One of the simplest methods for coloring a graph is by using a greedy approach. This approach consists of the following:

Given a graph G = (V,E) and a fixed vertex enumeration $a_0, a_1, \ldots, a_n$:

$c(a_0) = 1$

If $a_1, \ldots, a_{i-1}$ ($i \geq 1$) have already received colors, let $c(a_i)$ be the smallest color not yet used in the neighborhood of a_i.

It could be shown that the number of colors used hugely depends on the order of vertices. There are many heuristic techniques for Greedy coloring. We will now present two different methods for vertex ordering that could yield good results in terms of chromatic number.

A. Largest degree ordering

Degree based ordering is one of the easiest methods for coloring a graph. It provides a slightly better strategy than the algorithm provided above which simply picks a vertex from an arbitrary order [3].

Largest degree based ordering chooses a vertex with the highest number of neighbors. Initially graph vertices are sorted in a non-increasing order according to their degree after which former algorithm is applied. This approach produces better chromatic number but it's time consumable.

B. Saturation degree ordering

The algorithm DSATUR (Degree of Saturation) of Brelez [3] is a sequential coloring algorithm with a dynamically

established order of the vertices. The degree of saturation of a vertex *u*, $deg_c(u)$, is the number of different colors at the vertices adjacent to *u*. This algorithm at *i*-th step chooses the not yet colored vertex with the largest degree of saturation. Since degrees change dynamically through algorithm iterations, we can conclude that it is even more time consumable than the previous one.

III. Software Implementations

We implemented above discussed algorithms using four different programming languages. We will now present a short pseudo-code [4] that is the basis for each of them and then show particular implementation techniques in each of the programming languages.

```
Color(V,E):
1. color[v[0]] = 1
2. for i ← 1 to |V|
3.    do  ColorsTaken [] ← 0
4.    for each u ∈ V
5.        do if (u,V[i]) ∈ E
6.             ColorsTaken[color[u]] ←1
7.    k ← 1
8.   while ColorsTaken[k]=1
9.        do k ←k+1
10   color[v[i]] = k
```

In line one first color is assigned to the first vertex. Lines 2-10 algorithm iterates through the rest of the vertices. In line 3 ColorsTaken for current vertex is reseted to zero. In lines 4-6 neighbors list of current vertex is explored and colors assigned to each of them are marked as taken. In lines 7 - 9 first non-used color is chosen and assigned to current vertex in line 10.

Depending on the variation of the algorithm used input set of vertices V is sorted accordingly.

A. C++ and Java implementations

An array of adjacency lists is used to represent graph G.[5]The i^{th} adjacency list is integer array of size *d(i)*,which is degree of vertex *i*, where each entry represents vertex adjacent to *i*. Above given algorithm is used to color vertices. Merge-sort [5] is used for sorting vertices in a non-increasing order according to their degree. In DSATUR algorithm [3] ColorsTaken matrix is used instead of array in former algorithm where ColorsTaken(*i*,*j*) is equal to 1 if and only if node *i* has neighbor colored with color *j*. In this way both the smallest available color for vertex *i*, and its degree of saturation could be easily calculated. For purpose of testing random number generator is created which generates random graphs with given number of vertices and edges.

Same logic was used for implementation of the above algorithm in Java. To use all the benefits that Java offer, adjacency list is represented using built-in data structure ArrayList, encapsulated in class AdjacentList, which has easy methods for adding and removing element from the list. For vertices sorting Heap-sort was used [5]. Tests were performed on same random generated graph parsed to fit input format of given implementation.

B. LISP implementation

List of vertices is used to represent graph G. Vertices are represented as a list, each containing vertex ID, its color and list of adjacent vertices IDs. Algorithm given above is used to color vertices. To sort vertices according to their degree Merge-sort [5] is used. In its modified version, it sorts vertices by their degree of saturation to determinate a vertex that will be colored next in DSATUR algorithm [3].

C. Python implementation

For this implementation we used already existing library for graph manipulation – *networkx* [6]. Adding set of edges to the Graph structure creates graph. We use built-in methods for manipulation with set of vertices. The aforementioned algorithm in its adapted version is used to color vertices. To sort the vertices, built-in quick-sort algorithm is used.

IV. Experimental Results

We will now show obtained results from above mentioned implementations. For purpose of testing random graph generator was created which generates random graphs for a given number of vertices and edges.

It is worth mentioning that the performance in terms of chromatic number of the implemented algorithms will vary due to different sorting algorithms used in different programming languages.

In the next four tables we will show running times for C++, Java, Python and LISP implementations considering different algorithms and graph sizes, respectively. Finally the comparison between the average chromatic numbers will be shown, as well as the best performed implementation.

TABLE I
Running time [ms] of different algorithms on various graph size using C++ implementation

Number of Vertices	Number of Edges	Naïve Greedy	LDO	DSATUR
1000	10000	0	0	16
1000	50000	0	4	16
1000	100000	0	8	18
5000	50000	0	8	162
5000	100000	0	16	172
5000	500000	31	32	193
5000	10^6	62	78	246
10000	10^5	15	31	671
10000	$5*10^5$	78	83	718
10000	10^6	125	140	796
10000	10^7	1373	1382	2718
20000	$2*10^5$	47	78	2527
20000	10^6	219	254	2543
20000	$2*10^6$	421	468	2730
20000	10^7	2122	2169	4633
20000	$2*10^7$	4228	4290	6254

As it could be seen from the results running time of Naïve Greedy varies a little from LDO while DSATUR has far worse performance. On the other hand Naïve and LDO much more depend on the number of edges than the DSATUR.

In Table II the running time results are given considering the same test input on the same graphs as for the previous implementation, but in Java.

TABLE II
RUNNING TIME [MS] OF DIFFERENT ALGORITHMS ON VARIOUS GRAPH SIZE USING JAVA IMPLEMENTATION

Number of Vertices	Number of Edges	Naïve Greedy	LDO	DSATUR
1000	10000	52	53	75
1000	50000	30	39	41
1000	100000	31	38	42
5000	50000	33	47	325
5000	100000	34	58	320
5000	500000	48	69	391
5000	10^6	59	76	436
10000	10^5	71	91	1203
10000	$5*10^5$	86	106	1301
10000	10^6	88	112	1430
10000	10^7	213	245	NA
20000	$2*10^5$	221	248	NA
20000	10^6	255	285	NA
20000	$2*10^6$	257	278	NA
20000	10^7	369	417	NA

TABLE III
RUNNING TIME [MS] OF DIFFERENT ALGORITHMS ON VARIOUS GRAPH SIZE USING PYTHON IMPLEMENTATION

Number of Vertices	Number of Edges	Naïve Greedy	LDO	DSATUR
500	5000	6	15	113
500	10000	12	12	120
500	25000	26	27	128
1000	50000	57	59	480
1000	100000	119	122	521
5000	50000	173	176	11169
5000	10^5	223	229	11572
5000	$5*10^5$	710	731	11613
5000	10^6	1520	1580	12077
10000	10^5	590	588	45161
10000	$5*10^5$	1156	1056	45480
10000	10^6	1794	1699	45766
20000	10^6	4011	4034	NA
20000	$2*10^6$	5415	7012	NA

From the experimental results in Java implementation we can notice that the running time is not that much worse than in C++. For example, for 20000 vertices and 10^7 edges give much better running time in Java than in C++. However, Java cannot compute chromatic number using DSATUR algorithm for more than 10000 vertices and 10^6 edges due to memory limitations.

TABLE IV
RUNNING TIME [MS] OF DIFFERENT ALGORITHMS ON VARIOUS GRAPH SIZE USING LISP IMPLEMENTATION

Number of Vertices	Number of Edges	Naïve Greedy	LDO	DSATUR
500	20000	244	295	400
500	28000	442	493	672
1000	30000	623	661	1029
2000	11000	420	428	537
2000	25000	1101	932	1588
5000	33000	3342	3504	4760
10000	25000	7492	9250	10656

On the other hand Python's implementation using already built-in library performs considerable worse than Java and C++. Maximum number of vertices and edges that this implementation could handle on our test system was 20000 and 10^6, respectively. Also, the same rule applies as for C++ and Java implementations that the first two algorithms perform much faster than the DSATUR algorithm.

Finally, LISP implementation gives the worst results. Although it has dynamic typing as Python, it performed much worse due to its recursive structure. That implies vertex number limitation for our tests.

In Table V we show the average chromatic number obtained from all three implementations for given test results, performed on all three algorithms used.

TABLE V
AVERAGE CHROMATIC NUMBER FOR DIFFERENT IMPLEMENTATIONS ON THREE ALGORITHMS

Number of Vertices	Number of Edges	Naïve Greedy	LDO	DSATUR
500	5000	11	7.6	7.6
500	10000	17	11.5	11.5
500	25000	31.5	21.8	22.5
1000	50000	31.6	30.3	29.1
1000	100000	54	51.3	51
5000	50000	11.33	10.8	9.8
5000	10^5	17	15.6	15.5
5000	$5*10^5$	51	49.3	47.8
5000	10^6	87.6	85	83.3
10000	10^5	11.8	10.5	10
10000	$5*10^5$	33	29.6	28.6
10000	10^6	51.3	48.3	47.6
20000	10^6	32	30	NA
20000	$2*10^6$	52	48.6	NA

From the Table V we observe that the LDO algorithm performs the best comparing the runing time seen in Tables I, II, III and IV. DSATUR algorithm is more time consuming and does not provide the expected results. Hence, we can state that from our tests LDO is recommended algorithm for greedy graph coloring.

V. Conclusion

In this paper we presented a comparative analysis of four different programming language implementations of three variations of a greedy algorithm applied on the graph coloring problem.

First we introduced graph coloring as an important field in modern computer science and discussed different approaches in solving this NP-complete problem. We presented greedy coloring as one of the popular methods that gives good results for most graphs. This paper shows three different variations of basic greedy algorithm: Naïve greedy, largest degree ordering and DSATUR.

Comparing the results obtained from all four implementations, we can notice that C++ and Java gave the best running times for most of our tested graphs, whereas Python and LISP were considerably slower due to their dynamic typing and interpreting nature of program execution. We can conclude that the second algorithm produces the best chromatic number in terms of time consumption for most randomly generated graphs. LDO algorithm is not much slower than the Naïve algorithm because it uses sorting algorithms of $O(n\log n)$ complexity.

References

[1] Reinhard Diestel, *Graph Theory*, 2000.

[2] Joseph C. Culberson, "Iterated Greedy Graph Coloring and the Difficulty Landscape", Technical Report TR 92-07, June 1992.

[3] Walter Klotz, *Graph Coloring Algorithms*, 2002.

[4] James A. Anderson, *Discrete Mathematics with Combinatorics*, 2nd Edition, 2003.

[5] Thomas H. Cormen, Charles E. Leiserson, Ronald L. Rivest, Clifford Stein, *Introduction to algorithms*, 2nd Edition, 2001.

[6] Networkx 1.4 Library (http://networkx.lanl.gov/), 10.04.2011.

Semi-virtual Laboratory Exercise in SMT

Student author: Aleksey Stratev
Mentors: Valentin Videkov[1], Rosen Radonov[2]

Abstract – **This paper examines the methodology and results of laboratory exercise in Surface Mounting Technique using different techniques to conduct it. The exercise is conducted in the presence of students, but with application of distant and multimedia resources. Combining these tools allows detailed examination of the elements of both products and processes by several students. The methodology does not limit the direct participation of students in various tasks. The results from the application of the e-management environment are presented.**

Keywords – **multimedia, SMD, education**

I. INTRODUCTION

Surface mounting is dominant in modern electronic production. The main part of the electronic components are mounted using this technology. The mounting as a technology is described in numerous publications and monographs [1] [2] [3]. Due to the massive expansion at production, they need to adequately represent it in training and electronic fields. At the Technical University of Sofia, it is covered by a discipline named Surface Mounting Technique [4].

The use of increasingly smaller elements [5], and high density mounting is typical of today's level of development of surface mounting. This makes requirements for the systems for monitoring and control, and the operators themselves. The latter is strongly linked to the operators training approaches in dealing with different elements. They must be able to identify and classify the various defects in the assembly of the elements and the type of individual elements mounted. Miniature sizes make prerequisites for the learning approach.

II. THE PLAN OF THE EXERCISE

In SMT, there are three main groups of processes. The first is the application of a soldering paste, the second is the placement of the elements and the third is the soldering itself. However, students should know the auxiliary activities related to the choice of material, components, substrate, optimal topological design, programming of the machines, etc. In this respect the study of SMT should cover several topics including relevant laboratory exercises.

Laboratory exercises in the classical case are associated with measuring parameters, running calculations and in some cases carrying out experimental processes. The latter are combined with the provision of adequate work places and resources. The resource is the availability of the technological environment, equipment and supplies (parts, materials, energy).

In connection with the above a planning of the exercise is carried out. It should cover topics and tasks for implementation, preparation of relevant work places, number of students working on a task. The situation gets complicated when the topic of an exercise is associated with a specific lecture and the aim is to have the same exercise topic for everyone.

One possible approach to solve the problem of work places for all students on the same topic is the creation of virtual workbenches by means of multimedia. But in that case one loses the connection between the real object and the student.

Given the above the following structure for conducting the exercise as combining work with real objects and processes and use of virtual environments and multimedia resources was proposed. The exercise covers:

- Understanding the basic elements of the topic by means of animation and multimedia. Such a solution allows to demonstrate objects with tiny (micron) sizes, which cannot be observed directly;
- Individual examination of the objects through animation;
- Observation of a specific object by using electronic means, and multiplexing of the image. The work is carried out in real time with real objects;
- Processing the results of object's observation;
- Doing a research on the topic using the Internet. Archiving the results of the general research.
- Submission of an electronic report in the e-management environment.

• III. A SAMPLE PERFORMANCE

A stage of the first phase of the exercise, namely the use of multimedia and animation is shown in Fig.1. In this example the presentation of surface mount resistors is shown.

Student author:
Aleksey Stratev is with the Faculty of Electronic Technologies, Technical University of Sofia, 8 St. Kl. Ohridsky blvd., 1797, Sofia, Bulgaria, E-mail: astratev@ivastech.com

Mentors:
[1] Valentin Videkov is with the Faculty of Electronic Technologies, Technical University of Sofia, 8 St. Kl. Ohridsky blvd., 1797, Sofia, Bulgaria, E-mail: videkov@ecad.tu-sofia.bg
[2]Rossen Radonov is with the Faculty of Electronic Technologies, Technical University of Sofia, 8 St. Kl. Ohridsky blvd., 1797, Sofia, Bulgaria, E-mail: rossen.radonov@ecad.tu-sofia.bg

Fig. 1. Animation module for the demonstration of surface mount components: Part I - resistors.

Upon completion of this stage, each student gets access to the animation related to the topic of the exercise and opportunity for individual observation. The work places for animation observation - in this case the animation is related to soldering defects - are shown in Fig. 2.

Fig. 2. Getting acquainted with the exercise.

The third part of the laboratory exercise is related to the usage of a digital camera for monitoring a process or an object. The images are multiplied on each monitor. For example an image may be from a camera mounted on the machine for placement of elements, or the process control camera.

Fig. 3 presents the results of implementing the next phase - image processing. This stage may involve different tasks depending on the specifics of the topic. In this case, determining the sizes of objects, their repeatability and matching with catalogue data.

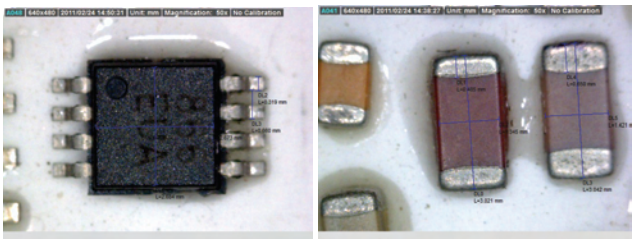

Fig. 3. Measuring the parameters of SM devices.

Then students perform research on the topic using the Internet and record the data in the e-management environment. There they prepared their electronic reports. A screenshot of such electronic report is shown in Fig. 4.

Fig. 4. Review of an electronic report in the e-management environment.

IV. Conclusion

The plan and results of conducting a laboratory exercise in Surface Mounting Technique at the Faculty of Electronic Technologies, the Technical University of Sofia had been reviewed in this paper. Multimedia and animation were implemented during the carrying out of the laboratory exercises, but it would not be correct to classify it virtual because it includes elements of real processes and objects. Typical electronic means, which are used in industrial process control are applied. The specific part is that the images are being multiplied on several work places, allowing normal operation of more students. In this sense, the term semi-virtual exercise is introduced, which means it is not purely virtual because students attend it and at the same time they make a review of real objects by virtual means.

Students' opinion regarding the introduction of this type of exercise is very positive. The submitted electronic reports showed better understanding and presentation of the results.

Acknowledgement

The research was carried out in the framework of Contract No. ДУНК-01/3/2010.

References

[1] Prasad Singh, Beyond AOI - SMT Quality Control SMT September, 2005, http://smt.pennnet.com/

[2] Titus T. Suck, International Product Manager and European Marketing Manager, Orbotech S.A. Controlling the Process: Post-Reflow AOI (Automated Optical Inspection) to Ascertain Machineand Process Capability http://www.advprecision.com/pdf/AOI_Process_Control.pdf 2008.

[3] Owen Sit and Joshua Petras Using AOI in the 01005 Components Assembly Process http://www.yestechinc.com/

[4] Technical Datasheet for F50380 SEOULSEMICONDUCTOR

Database Integration for the Needs of the Educational Process and its Reports

Student author: Konstantin Zaimov
Mentors: Rossen Radonov[1], Tihomir Brusev[2]

Abstract – **This paper presents the results of different databases integration for the purposes of educational process. An environment using data about students, courses, curricula and academic schedule for reporting workload of teachers and grading has been created. The environment allows for full control over the time and reduces the likelihood of mistakes. There are also elements of activities automation.**

Keywords – **education, database integration, student marks**

I. Introduction

There are different approaches to create and use databases. One can make different classifications of databases depending on the platform [1], data content (e.g. financial [2]), period of use, access [3] and others. In the field of education different databases with different orientation and accomplishment [4] are also used. The latter can be divided into two major groups - database for immediate use in educational process and databases for its managing. The approaches and implementation of the second kind are reviewed in this paper.

II. The Educational Process

Besides databases containing learning materials (materials in various scientific fields), there are data that are common to all educational processes. These are the data related to the operation, management of the process and reporting of the workload.

The central database contains information about students, curricula, courses, faculties and departments of the university. The existing University Student Information System (USIS) at the Technical University of Sofia is based on Oracle Database [3] and is a client-server windows desktop application. The system is designed to store data for university students and to provide basic references. It is designed to store data for university students and provide reference information. The system is integrated with a second system providing data from admission campaign. The system uses TCP/IP protocol over the existing intranet for connection with the database server.

A fragment of data available through this system is shown in Fig. 1. - student's personal page (Fig. 1a), schedule of an exam session (Fig. 1b).

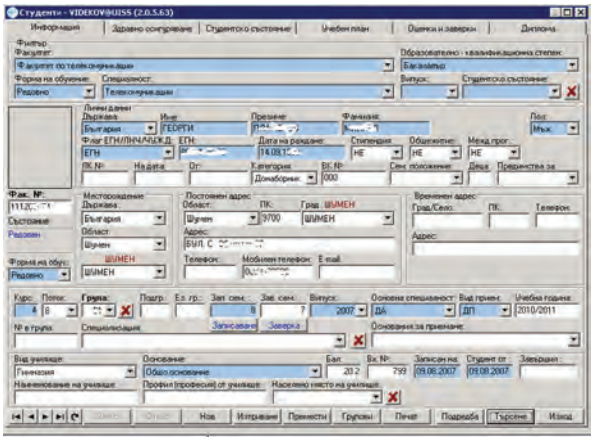

Fig. 1a. Personal page of a student with data.

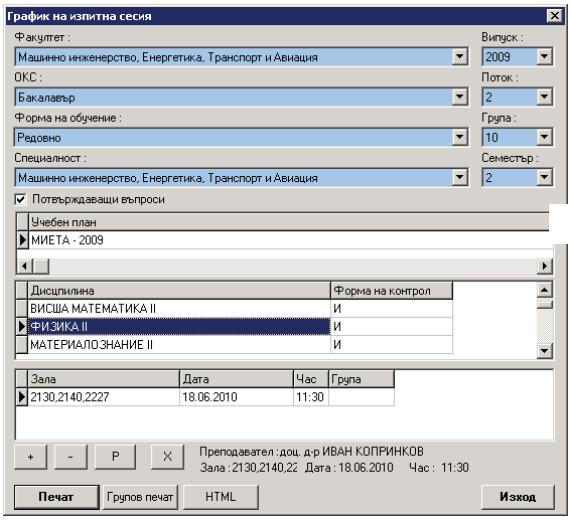

Fig. 1b. Schedule of an exam session.

The presence of a central database for the educational process allows the creation of specialized local databases in separate directions and activities. Such typical activities are the evaluation of knowledge and completion of grades reports, formation of specialized study groups, preparing reports on the progress of ongoing studies (performance report) and others.

Student author:
Konstantin Zaimov is with the Faculty of Electronics, Technical University of Sofia, 8 St. Kl. Ohridsky blvd, 1797 Sofia, Bulgaria, E-mail: Zaimov@ecad.tu-sofia.bg

Mentors:
[1]Rossen Radonov is with the Faculty of Electronics, Technical University of Sofia, 8 St. Kl. Ohridsky blvd, 1797 Sofia, Bulgaria, E-mail: Rossen.Radonov@ecad.tu-sofia.bg
[2]Tihomir Brusev is with the Faculty of Telecommunications, Technical University of Sofia, 8 St. Kl. Ohridsky blvd, 1797 Sofia, Bulgaria, E-mail: brusev@ecad.tu-sofia.bg

III. THE TASK

The accelerating and facilitating the grading, reporting the workload and other activities, which are being carried out by the teacher are of particular interest. At the same time securing the necessary identification data in respect to the origin and timing performance is needed.

In connection with the above digital certificates were generated for the teachers at the Technical University of Sofia for the purposes of the educational process. The certificates can be used for identification and completion of relevant data. The electronic report system was created first. It is used for completion of grades in students' data records by the teachers without the participation of student offices. One of student offices' tasks is to generate the examination reports, which could be accessed by the teachers through that system - Fig.2.

Fig. 2. Examination reports for a teacher.

A teacher can choose an examination report, examine the data, fill in some or all grades and review old completed reports. After completing the grades they are being automatically transferred to students' data records within one hour, and the students can see them. The reports have a deadline for completion, after which they are locked. A verification procedure, which identifies students who failed or did not attend exams is carried out. The system automatically generates examination reports for those students. Those reports are available for the teachers without the intervention of student offices.

All grades in students' data record are being identified in respect of time of completion, reason for grading (examination protocol number) or an officer from student office, who has filled it in.

The second system which is linked with the central database is the one for reporting the workload of teachers. It is also being accessed through identification by digital certificates. A teacher logs on and selects the relevant classes, which are being retrieved from the central database. A fragment of such selection is shown in Fig. 3.

Fig. 3. Completion of a workload report.

The completion of records in a database consistent with a single central database system allows to make summaries for various sections and to monitor implementation of the curriculum in real time A summary of workload reports is shown in Fig. 4.

Fig. 4. Summary of workload reports.

IV. CONCLUSION

The approach that is described in this paper, related to the integration of different databases with a central one allows more flexible data usage at different levels of management while maintaining the unity of information. The application of digital certificates for accessing the databases increases the accuracy of information and improves mobility in the deployment and use. The system was tested with completion of over 80000 grades and over 48000 monthly workload reports.

ACKNOWLEDGEMENT

The research was carried out in the framework of Contract No. ДУНК-01/3/2010.

REFERENCES

[1] Oracle Database - http://www.oracle.com
[2] Business navigator - http://www.cfinance.bg/new609.html
[3] Kroenke, David M. Database Processing: Fundamentals, Design, and Implementation (1997), Prentice-Hall, Inc.
[4] OnLineMath & Sciences - http://telearn.tu-sofia.bg/math&science

Optical Control of Laser Cut Stencils

Student authors: Aleksey Stratev, Georgi Farkov
Mentor: Valentin Videkov

Abstract – **The report explores the preparation of stencils for the needs of the surface mounting, and the application of optical control with their qualification. Cases of control after the technological preparation and after additional finish processing are considered. Possibilities are discussed for examination of the surface of the stencil and the vertical edge after cutting. For some cases, destructive control methods are used. Experimentally achieved results are presented**

Keywords – **optical control, laser cutting, stencil, SMD.**

I. Introduction

In surface mounting, the printing application through a metal mask could be adopted as a classic method for application of solder paste [1]. There are two main technologies for preparation of such masks: through chemical etching [2] and through laser cutting [3]. With chemically etched stencils, different profiles of the apertures can be obtained depending of the mode used, as well as stencils for application of paste with various thickness. With the laser cut stencils, a more vertical edge is obtained, and there is practically no change in the designed size of the aperture. In fig. 1, vertical profiles of a chemically etched and a laser cut stencil are shown.

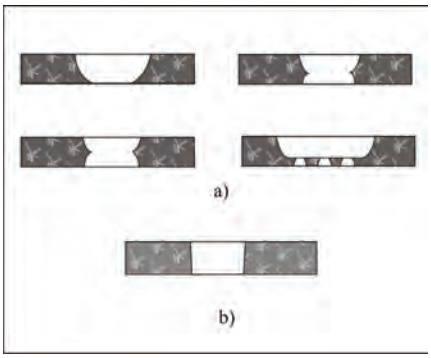

Fig .1. Profiles of stencils prepared through etching a) and cutting b).

Student autors:
[1]Aleksey Stratev is with the Faculty of Electronics, 8 St. Kl. Ohridsky blvd. Technical University of Sofia, 1797 Sofia Bulgaria, E-mail: astratev@ivastech.com.
[2]Georgi Farkov is with the Faculty of Electronics, 8 St. Kl. Ohridsky blvd. Technical University of Sofia, 1797 Sofia Bulgaria, E-mail: georgi@farkov.net

Mentor:
Valentin Videkov is with the Faculty of Electronics, 8 St. Kl. Ohridsky blvd. Technical University of Sofia, 1797 Sofia Bulgaria, E-mail: videkov@ecad.tu-sofia.bg.

A definite difficulty with both methods of preparation is the obtaining of extra small apertures for application of fine-step imprints. In these cases, a technology for electrochemical growing of stencils can be used [4].

II. Optical Control

The optical control is the main and the most widespread method with the surface mounting. It is widely applied at all stages of the production cycle. The optical control itself can be applied with visual assessment of the process by an operator (manual optical control), or through usage of technical vision systems, the so-called automatic optical control [5]. The standard optical control is used as non-destructive control of the processes: application of solder paste, position of elements, quality of the solder joints. On fig. 2, result of optical monitoring of a defect with soldered components is shown.

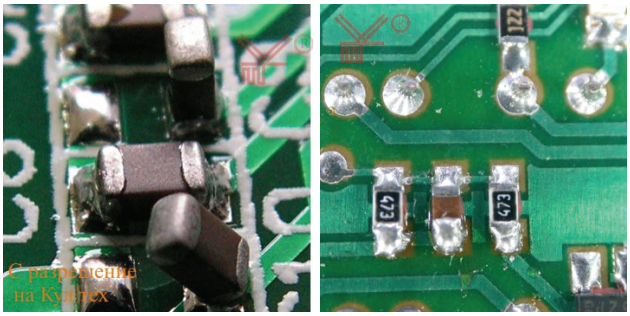

Fig .2. Optical control of soldered components.

The optical systems can also be applied with automated position of elements [6] (for identification of the coordinates) – fig. 3, as well as with size measurements.

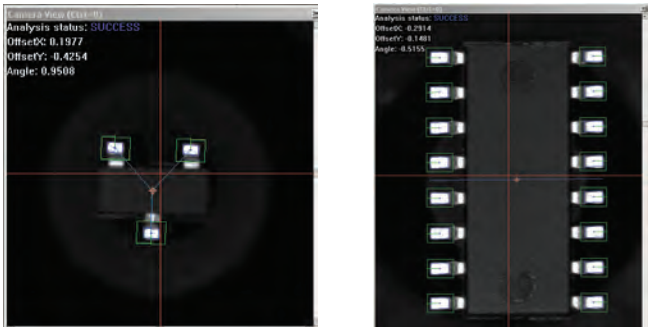

Fig .3. Defining coordinates through a technical vision system.

The optical control can also be used as a destructive control.

Its most typical application is for qualification of the solder joints and examination of the intermetallic phases.

III. Stensils Preparation

There are two main processes for preparation of stencils. The photolithographic method uses one-sided or two-sided application of photoresist (lamination of dry photoresist), exposing and development for formation of the topology of the stencil and subsequent chemical etching. During this process, special attention should be paid to the following elements:

- Precise coordination of the photo patterns for two-sided etching
- Evenness of the etching process throughout the whole area
- Recognizing the change of size as a result of the underetching.

The first element of coordination can be controlled optically still in the process of preparation of masks. The second element is harder to control during the process itself. The third element is usually defined experimentally, and presents a technological tolerance. For the quality preparation of stencils, optical control is needed at each of the stages.

On fig. 4 a result of optical control of the evenness of etching of a stencil through the photoresistent mask is shown. Shown is uneven etching , etched apertures with non-removed photoresist.

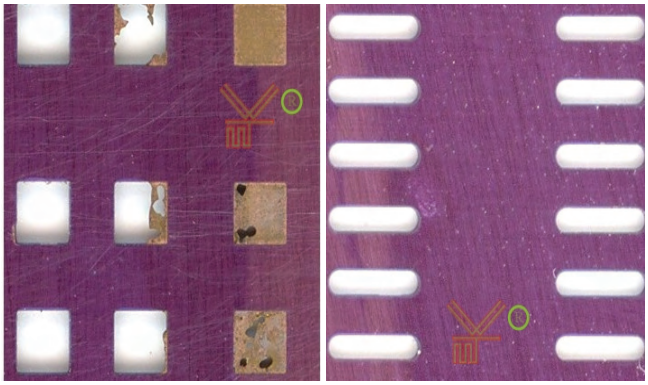

Fig .4. Optical control of the etching during the preparation of a stencil.

When monitoring with high zooming, the underetching, the evenness of etching along the aperture, and, in some cases, the dislocation of the patterns can be defined. Such control is carried out through monitoring by microscope and the respective size measurements. On fig. 5, a fragment of a chemically etched aperture with underetched section and visible displacement of the mask for both sides is shown. The underetched contour 1 is seen through the photoresist, and the displacement 2 is outside the contour of the photoresist.

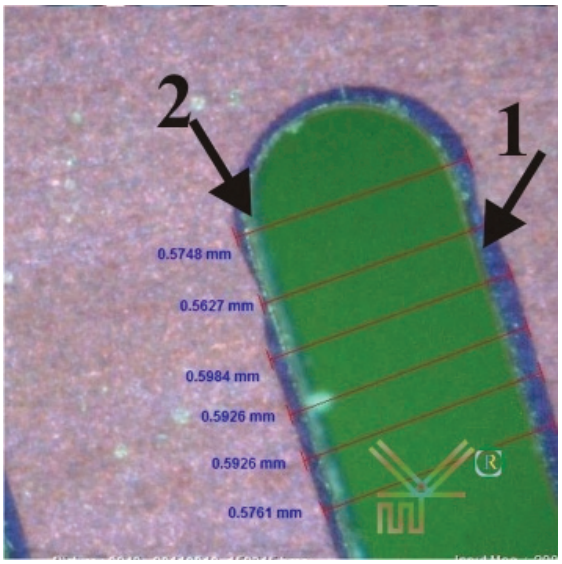

Fig. 5.Underetching of a stencil.

In spite of the relatively easy finding of size changes and lack of coordination, the optical monitoring of the surface cannot provide complete information for the process of etching. For this purpose, destructive control is applied through preparation of thin sections. On fig. 6, examples of the vertical profile of stencils obtained through etching are shown.

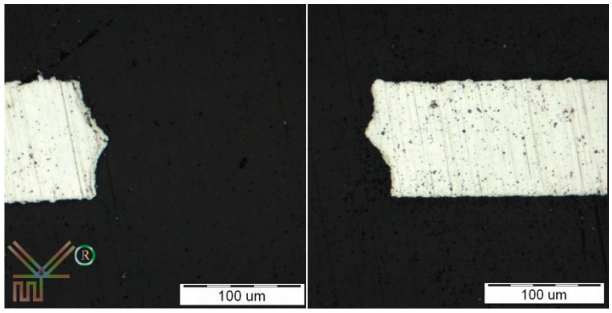

Fig. 6. Left and right profile of an etched aperture.

Depending on the mode of etching and the solutions used, both the profile and the surface can change. These results are shown on fig.7.

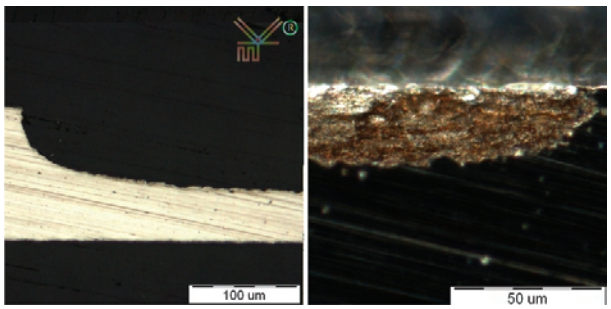

Fig. 7. Profile and surface with one-sided etching of a stencil.

In laser cut stencils the three elements which should be controlled for the chemically etched stencils are practically missing. With them, through the laser beam the aperture is cut immediately by the contour, and thus there is no need to coordinate patterns, the cutting is all the same throughout the whole area and there is no underetching. The optical control of the surface can provide an answer for the size of the aperture. With high zooming the spatters of molten metal can also be found. Such are shown on fig.8.

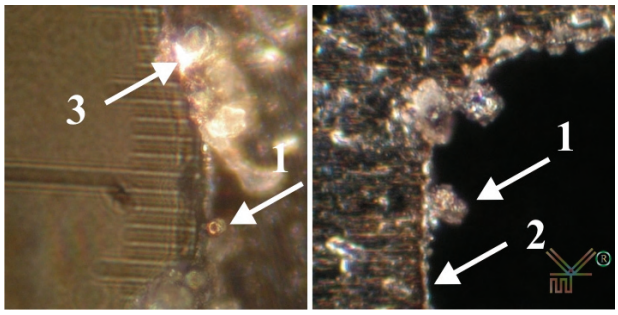

Fig. 8. Spatters of metal in laser cut stencils. 1 – spatters of metal, 2 cut contour, 3 big spatter.

The removal of these defects requires additional processing of the surface. It is carried out mechanically, and then again optical control of the surface follows. On fig. 9, depiction of processed and non-processes part is shown.

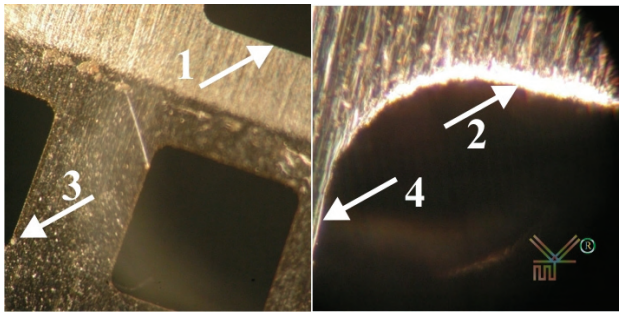

Fig. 9 Surface of a laser cut stencil after mechanical processing: 1 - processed edge front side, 2 – processed edge back side, 3 – spatter of metal, 4 – edge in the direction of the processing.

In this case the surface monitoring also cannot provide a full picture of the process. The presence of glare (2 on fig. 9) shows that in vertical direction changes are also monitored. On fig. 10a and 10b, vertical profiles of laser cut stencils are shown before and after mechanical processing. It is seen that as a result of the processing, rounding of the edge is obtained, a result both of the position of the edge towards the direction of processing and the pressure from the system.

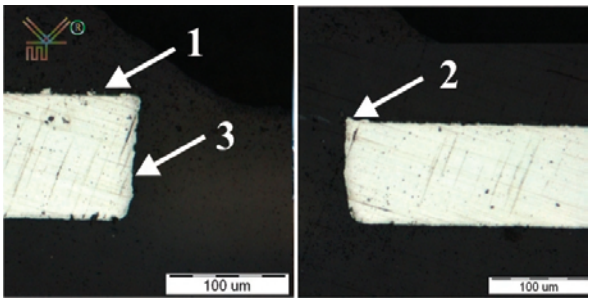

Fig. 10.a. Non-processed stencil.

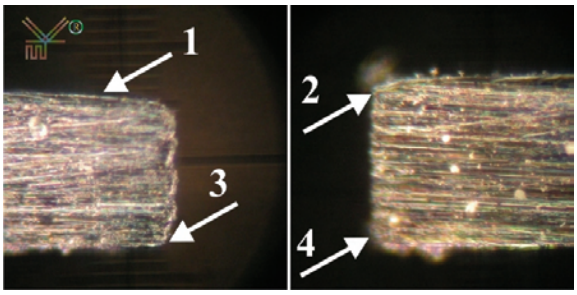

Fig. 10.b. Mechanically processed stencil.

The monitoring of the edge with high zooming enables monitoring both of the traces of the laser beam and internal remainders of the melt – fig. 11.

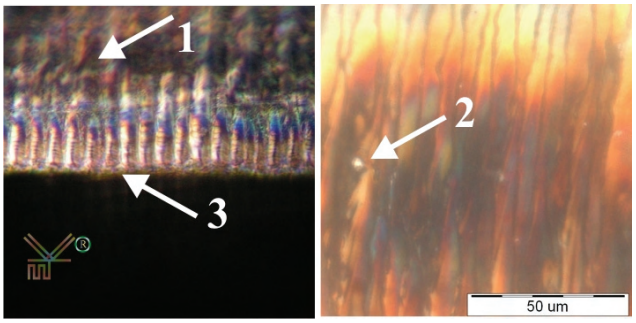

Fig. 11. Profile of laser cut stencil.

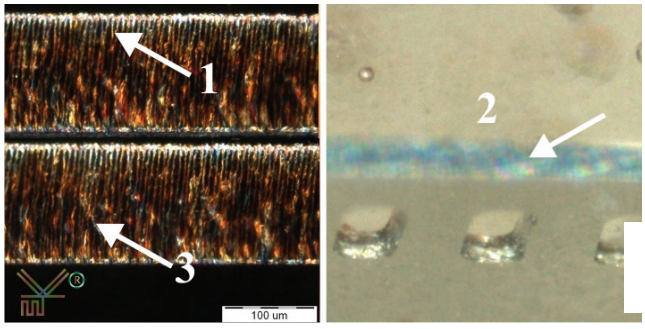

Fig. 12. Profiles of stencils with various optical monitoring.

On fig. 12, comparison of different areas of a laser cut stencil is shown. While on the surface there is regularity of the profile, in depth the surface has statistically random profile.

III. CONCLUSION

The experimental results carried out by monitoring and qualification of stencils showed that their complete characterization requires monitoring both of the surface and the vertical profile of the stencil. With the surface monitoring, assessments can be given for sizes, evenness, repeating of the apertures made, but we have no information for the profile. Such an assessment can be made through destructive control and making cuts on the stencils. These cuts can be monitored immediately or through cross-sections. The experimental results are obtained through studying stencils produced by different companies in Bulgaria. The laser cut stencils are made in IVAS TEH OOD , with G 6060 machine, and the micro-sections are examined in FESTO Production EOOD, within the PhD studies of the authors.

REFERENCES

[1] Ray P. Prasad, Surface mount technology: principles and practice, Second Edition, 1997, ISBN-10: 9780412129216

[2] http://www.stencilsunlimited.com/photo_chemical_etching.php

[3] http://www.thinmetalparts.com/documents/TMPStencilOverview.pdf

[4] D. Manessis at all, Technological advancements in Lead-free Wafer Bumping using Stencil Printing Technology, EMPC 2005, June 12-15, pp 427-433

[5] Fredrik Mattson et al, "PCB Design and Assembly Process Study of 01005 Size Passive Components Using Lead-Free Solder, SMTAI, September 2004

[6] Industrial Vision & Automation Systems PLM2000 Pick & Place http://www.ivastech.com/ 2011

Session SS II:

STUDENT SESSION II

Behavioral VHDL-AMS Model for Monolithic Voltage-Controlled Amplifier

Student authors: Marieta Kovacheva[1], Dimo Martev[2] and *Mentor:* Ivailo Pandiev[3]

Abstract – **This paper presents behavioral VHDL-AMS model for monolithic voltage-controlled amplifier (VCA). The proposed model is independent of actual technical realizations and is based upon compromises regarding the representation of exact circuit structures in the model. For creating the model, simplification and build-up techniques known from macro-modeling operational amplifiers have been adapted. The model accurately reflects input impedance, transfer function (amplifier gain versus control voltage), small-signal frequency response, CMRR versus frequency, large-signal pulse response, output characteristic (voltage and current limitations) and output resistance. Model parameters are extracted for the monolithic voltage-controlled amplifier VCA810 from Texas Instruments as an example. The verification check of the model is performed by comparison of the simulation results with the manufacturer's data and with the results obtained by simulation of the PSpice macro-model supplied from Texas I. To confirm the workability of the proposed VCA model some practical electronically controllable analog circuits are investigated. The basic parameters obtained by simulations are compared with the results of the circuits using a valid PSpice macro-model and theoretically calculated parameters.**

Keywords – **Programmable analog circuits, Voltage-controlled amplifiers, Behavioral models, VHDL-AMS, Mixed-signal simulation.**

I. Introduction

The monolithic voltage controlled amplifiers (VCAs) are basic elements of contemporary analog-digital (mixed) circuits and systems. They have an analog signal input, an analog signal output and a digital control of the voltage amplification. Internally, the VCA is based on voltage-controlled two-quadrant analog multiplier. The gain-control sub-circuit converts the controlling voltage to a current. This current varies the transconductance g_m of the current mirror, which specifies the bias currents of the differential stage. Therefore the bias currents variation alters the transconductance g_m of the differential transistor pair. As a result the voltage gain of the amplifier is modified in the specified range. In addition, the most of the VCAs contain input and output voltage follower [1-3].

Testing the workability of electronic circuits with VCAs is done usually using SPICE (Simulation Program with Integrated Circuit Emphasis) based programs. A variety of SPICE macro-models for the VCAs, is available in the literature [4-8]. The majority of published macro-models contains extensive number of active and passive elements. Furthermore, testing complete mixed-signal systems with large number of elements is an extremely difficult process and may often become infeasible due to the limitation of simulation capacity.

One method to decrease simulation time and improve the convergence, without a significant losses of information, is by using behavioral modeling technique. Nowadays one of the most effective techniques for behavioral modeling of mixed-signal electronic circuits is by using VHDL-AMS. The literature survey reveals that behavioral models for the VCAs have not been available yet. Without any doubt behavioral models for basic types of VCAs are necessary for simulating mixed-signal circuits and systems. The goal of this paper therefore is to develop a behavioral VHDL-AMS model that accurately simulates the basic electrical characteristics of most common VCAs based on two-quadrant analog multiplier.

II. A Practical Approach to Generate Behavioral Models

In this section is presented a specific practical approach for generation of behavioral models of complex analog and mixed systems. The proposed design approach is based on the methodology for generating behavioral models of A/D systems and a practical approach for managing simulation projects given in [10-12]. The design approach diagram is shown in Fig. 1.

The presented approach has two basic branches. The left

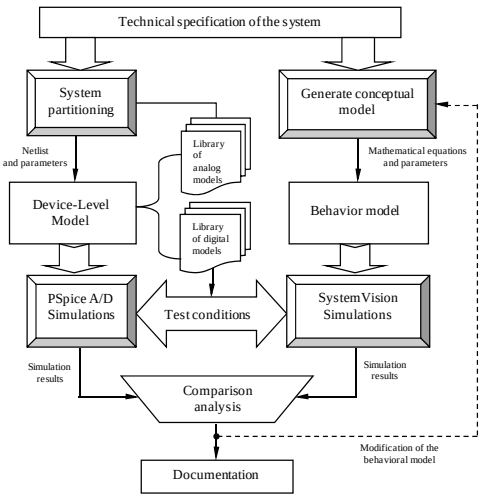

Fig. 1. A practical approach to generate behavioral models.

Student authors:
[1]Marieta Kovacheva is with the Faculty of Electronics, Kl. Ohridski 8, 1000 Sofia, Bulgaria, E-mail: marieta_fnm@yahoo.com.
[2]Dimo Martev is with the Faculty of Electronics, TU-Sofia, Kl. Ohridski 8, 1000 Sofia, Bulgaria, E-mail: dsmartev@yahoo.com
Mentor:
[3]Ivailo Pandiev is with the Faculty of Electronics, TU-Sofia, Kl. Ohridski 8, 1000 Sofia, Bulgaria, E-mail: ipandiev@tu-sofia.bg.

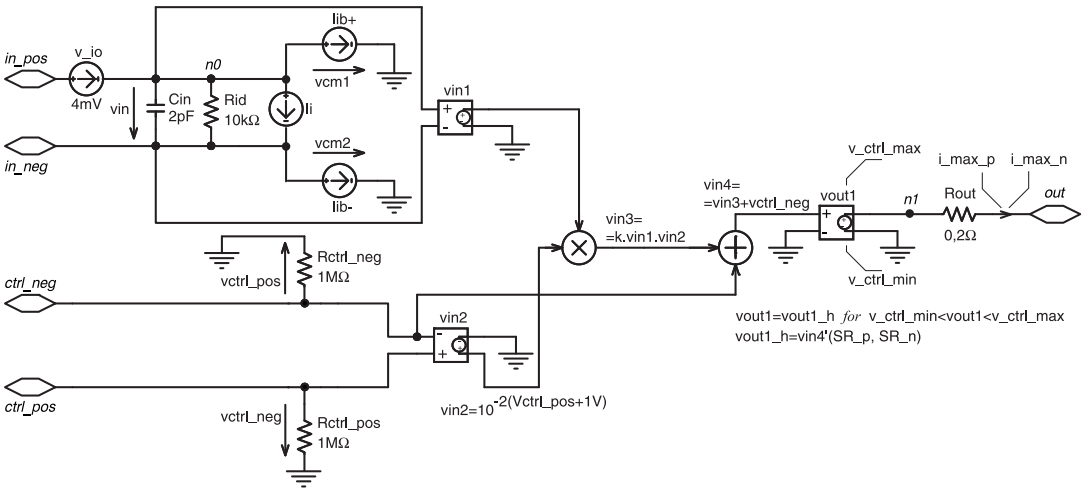

Fig. 2. Circuit diagram for the behavioral voltage-controlled amplifier model.

one is related to generation of a device-level model from actual device and the right one is the procedure for generating the behavioral model. The *device-level model* called *micromodel*, reflects most electrical parameters of the actual device. The *conceptual model* is a mathematical and logical representation of the actual device and the *behavioral computerized model* is the conceptual model implemented on a computer. The conceptual model is developed through an *analysis phase* and the computerized model is developed through a *computer programming* and *implementation phase*.

Once the models are created the comparison analysis is performed. The purpose of comparison analysis is to guarantee the correct behavior of each element in the developed model. In this process each element is tested to ensure that, firstly, they behave in the manner intended by the model code and, secondly, that their behavior is representative of the actual device.

In case the computer model, does not respond fully to the technical specifications, modification and optimization of the structure and the mathematical equations are needed.

Finally, the documentation of the behavioral model should include the conceptual model (critical for the future reuse of the model), a detailed description of the computer model and simulation results for the included electrical parameters.

III. BEHAVIORAL MODELING WITH VHDL-AMS

The technical requirement for effective models is generally agreed when the simplest possible model is developed. Simple models have a number of advantages. They can be developed faster, are more flexible, require less data, run faster and it is easier to interpret the results since the structure of the model is better understood. As the complexity increases, these advantages are lost [10].

The created behavioral model of the VCA is developed following the design approach given in Fig. 1 by using a style combining structural and mathematical description. The structural description is the netlist of the model and the behavioral description consists of simultaneous statements to describe the continuous behavior. An object of research and modeling is a monolithic voltage-controlled amplifier VCA810 from Texas I. [12]. The internal structure of the VCA810 is based on voltage-controlled two-quadrant analog multiplier, which has differential input and single output. The gain control voltage V_c for VCA810 will adjust the gain from $-40dB$ $(0{,}01)$ at $V_c = 0V$ to $+40dB$ (100) at $V_c = -2V$.

The review of the available technical documentation for mixed-signal ICs showed that VCA810 is a typical representative of the base structure used for implementation of controllable amplifiers.

A. A behavioral language: VHDL-AMS

VHDL-AMS is a comparatively new standard 1076.1 of VHDL that supports hierarchical description and simulation of analog, digital and mixed-signal applications with conservative and non-conservative equations [13, 14]. On the mixed-signal side a variety of abstraction levels is supported. The VHDL-AMS modeling is not restricted to mixed-signal applications but also supports thermal and mechatronic systems.

B. A voltage-controlled amp behavioral VHDL-AMS model

The proposed model of the VCA is built using the results obtained by analyses of the SPICE based macro-model for VCA in [8] and by using the results for the behavioral models presented in [9]. The circuit diagram of the VCA behavioral model is shown in Fig. 2, where the different stages are presented with controlled sources and passive RC components. The model includes the following elements and parameters with numerical values: $r_{id} = 10k\Omega$ and $c_{in} = 2\,pF$ – input resistance and capacitance; $V_{io} = 4mV$ – input offset voltage; $I_{io} = 100nA$ – input offset current; $I_{ib} = 6\mu A$ –input bias current; $f_{pi} = \omega_{pi} / 2\pi = 30MHz$ – the $-3dB$ pole frequency; $f_{cm} = 2MHz$ – the $-3dB$ common mode pole frequency; $rctrl\_pos = rctrl\_neg = 1M\Omega$ – positive and negative resistance of the voltage controlled source; $CMRR$ – Common-Mode Rejection Ratio; A_{d0} is differential dc gain and can be defined using equation $A_{d0} = 10^{-2(Vc+1)}$ and A_{cm} is CM gain;

$SR\_p = -SR\_n = 350V/\mu s$ – positive and negative SR; $v\_\sup ply\_p = 3{,}2V$ ($v\_\sup ply\_n = -3{,}2V$) – positive and negative voltage drops for the output voltage

```
library IEEE;
use IEEE.MATH_REAL.all;
use IEEE.electrical_systems.all;
entity vca_810 is
     generic (
   --generic parameters here);
   port (terminal in_pos, in_neg, ctrl_pos, ctrl_neg, output, nvdd, nvss :electrical);
end entity vca_810;
architecture default of vca_810 is
   -- inner terminals
   terminal  n0, n1 : electrical;
   -- branch quantities
   quantity v_io across i_io through in_pos to n0;
   quantity vin across iin , icin, ii through n0 to in_neg;
   quantity vdd across nvdd;
   quantity vss across nvss;
   quantity icc through nvdd to ELECTRICAL_REF;
   quantity iee through nvss to ELECTRICAL_REF;
   quantity vcm1 across iib1 through n0 to ELECTRICAL_REF;
   quantity vcm2 across iib2 through in_neg to ELECTRICAL_REF;
   quantity vctrl_pos across ictrl_pos through ctrl_pos to ELECTRICAL_REF;
   quantity vctrl_neg across ictrl_neg through ctrl_neg to ELECTRICAL_REF;
   quantity vout1 across iout1 through n1 to ELECTRICAL_REF;
   quantity vrout across irout through n1 to output;
   quantity vout across output to ELECTRICAL_REF;
  -- free quantities
    quantity vin1 : real;
    quantity vin2 : real;
    quantity vin3 : real;
    quantity vin4 : real;
    quantity vcm :voltage;
    quantity vmid :voltage;
    quantity irout_h : current;
    quantity vout1_h : voltage;
  -- constants declarations here
begin
   --***input stage***--
    v_io == vio;
    ii == iio / 2.0;
    iib1 == iib;
    iib2 == iib;
    icc == pos_s_c;
    iee == neg_s_c;
    iin  == vin / rid;
    icin == cin*vin'dot;
    vcm  == ((vcm1+vcm2)/2.0);
    vmid == (vdd+vss)/2.0;
    vin1 == vin'ltf(num_p, den_p) + (1.0/cmrr)*vcm'ltf(num_cm, den_cm) + vmid;
  --***control stage***--
    ictrl_pos  == vctrl_pos / rctrl_pos;
    ictrl_neg  == vctrl_neg / rctrl_neg;
  --gain vs control voltage—
 if vctrl_pos'above(v_ctrl_min)       use  vin2 == 0.0001;
    elsif not vctrl_pos'above(v_ctrl_max)  and vctrl_pos'above(-2.5) use  vin2 == 100.0;
    elsif not vctrl_pos'above(-2.5) use vin2 == 1.0;
    else vin2 == (10.0) ** (-2.0*(vctrl_pos+1.0));
 end use;
  --***intermediate stage***--
    vin3 == k*vin1 * vin2;
    vin4 == vin3 + vctrl_neg;
  --***output stage***--
    vout1_h == vin4'slew(SR_p,SR_n);
    irout_h == vrout/rout;
 if vout1_h'above(vdd - v_supply_p)         use  vout1 == vdd - v_supply_p;
   elsif not vout1_h'above(vss - v_supply_n) use  vout1 == vss - v_supply_n;
   else vout1 == vout1_h;
 end use;
 if irout_h'above(i_max_p) use   irout == i_max_p;
  elsif not irout_h'above(i_max_n) use    irout == i_max_n;
  else irout == irout_h;
 end use;
end architecture default;
```

Fig. 3. A VCA behavioural VHDL-AMS model.

limitation; $i\_\max\_p = -i\_\max\_n = 60mA$ – maximum output currents; $r_{out} = 0{,}2\Omega$ – output resistance.

The proposed model includes small- and large-signal effects such as (1) input impedance, (2) transfer function (amplifier gain versus control voltage), (3) small-signal frequency response, (4) CMRR versus frequency, (5) large-signal pulse response, (6) output characteristic (voltage and current limitations) and (7) output resistance. The mathematical equations that describe the model can be given as

$$i_{in} = v_{in}\left(\frac{1}{r_{id}} + sc_{in}\right) \tag{1}$$

$$v_{cm} = (v_{cm1} + v_{cm2})/2 \tag{2}$$

$$v_{mid} = (v_{ss} + v_{dd})/2 \tag{3}$$

$$v_{in1} = \frac{\omega_p}{s+\omega_p} v_{in} + \frac{1}{CMRR} v_{cm} \frac{s+\omega_{cm}}{\omega_{cm}} + v_{mid} \tag{4}$$

$$i_{ctrl\_pos} = v_{ctrl\_pos} / r_{ctrl\_pos} \tag{5}$$

$$i_{ctrl\_neg} = v_{ctrl\_neg} / r_{ctrl\_neg} \tag{6}$$

$$v_{in2} = \begin{cases} 0{,}0001, & v_{ctrl\_pos} > 0{,}15V \\ 10^{-2(v_{ctrl\_pos}+1)}, & -2V < v_{ctrl\_pos} < 0{,}15V \\ 100, & -2{,}5V < v_{ctrl\_pos} < -2V \\ 1, & v_{ctrl\_pos} < -2{,}5V \end{cases} \tag{7}$$

$$v_{in3} = k v_{in1}.v_{in2} \tag{8}$$

$$v_{in4} = v_{in3} + v_{ctrl\_neg} \tag{9}$$

$$SR = dv_{in4}/dt \tag{10}$$

$$v_{out1\_h} = v_{in4} \tag{11}$$

(12)

$$v_o = \begin{cases} v_{dd} - v\_\sup ply\_p - i_{rout\_h}.r_{out}, & v_{in4} \geq v_{dd} - v\_\sup ply\_p \\ v_{in4} - i_{rout\_h}.r_{out}, & v_{dd} - v\_\sup ply\_p < v_{in4} < v_{ss} - v\_\sup ply\_n \\ v_{ss} - v_{\sup ply\_n} - i_{rout\_h}.r_{out}, & v_{in4} \leq v_{ss} - v_{\sup ply\_n} \end{cases}$$

Fig. 3 shows the behavioral VHDL-AMS model of VCA. Library clause and the use clause make all declarations in the packages math_real and electrical_systems visible in the model. This is necessary because the model uses nature electrical and constant math_2_pi for the value of 2π from packages. The proposed model is composed by an e*ntity* and an *architecture*, where bold text indicates reserved words and upper-case text indicates predefined concepts. The entity declares the generic model parameters and specifies seven interface terminals of nature electrical. The proposed model includes the following electrical terminals: in_neg, in_pos – inverting and non-inverting inputs, ctrl_neg, ctrl_pos – inverting and non-inverting inputs of the voltage-controlled source, output – output, nvdd, nvss – positive and negative supply voltage

terminals. Furthermore, the model has two inner terminals: `n0` and `n1`. They are used to specify the voltages `v_io` and `vout1` respectively.

The architecture is subdivided into four parts according to the functions of the different elements: *input*, *control*, *intermediate* and *output stage*. It contains the implementation of the model. The architecture is coded by using behavioral description that consists simultaneous statements.

IV. Model Performance

The verification of the proposed behavioral model shown in Fig. 3, is performed by comparing simulation results with the manufacturer's data and with the results obtained by simulation of the PSpice macro-model supplied from Texas I. The simulation modeling of the behavioral model was implemented within simulation program SystemVision (from Mentor Graphics). Based on the simulation results, conclusions for value of relative error are made. The value of the average relative error ε_{av} is not higher than $4{,}5\%$. Compared with PSpice macro-model, the proposed model is more precise (the average error for the PSpice model is $\approx 15\%$). Moreover, the CMRR vs. frequency and the limitations in transfer function are not included in the PSpice macro-model.

For validation check of the proposed model, simulation of first-order low-pass filter shown in Fig. 4 was carried out for both the aforementioned model and the macro-model given by Texas I. in the PSpice library. The simulation results are shown in Fig. 5 and Fig. 6. Comparison with theoretically calculated parameters (for the pass-band gain and the pole frequency) shows the advantages of the proposed model ($\varepsilon_{av} = 9\%$) over the macro-model ($\varepsilon_{av} = 12\%$).

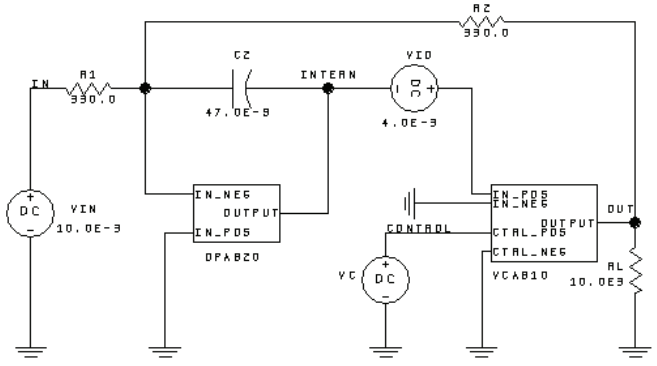

Fig. 4. A VCA behavioral VHDL-AMS model.

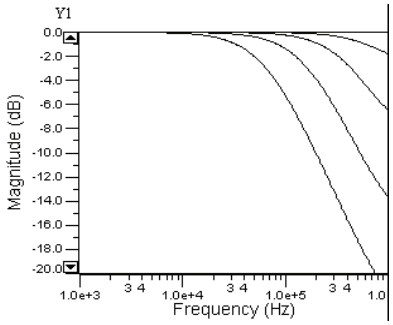

Fig. 5. The simulated response of the low-pass filter shown in Fig. 4 for the proposed VHDL-AMS model.

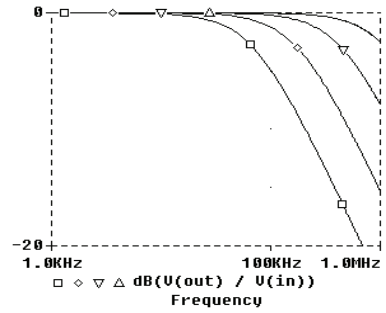

Fig. 6. The simulated response of the low-pass filter shown in Fig. 4 for the VCA810/BB.

V. Conclusion

In this paper a generalized behavioral VHDL-AMS model of monolithic VCA based on two-quadrant analog multiplier has been presented. The proposed model accurately simulates the actual performance of typical VCA for a wide range of frequencies. To achieve simplicity of the mathematical equations describing the model, it neglects several second-order effects found in the VCAs, such as the noise, the temperature effects and the PSRR. The efficiency of the model was proved by comparison between the datasheet parameters of the monolithic controllable amplifier VCA810 and simulation results.

Acknowledgement

This paper is part of a project, which is sponsored by the research program of the TU-Sofia, Bulgaria.

References

[1] M. Seifart, *Analoge Schaltungen. 6 Auflage*. Verlag Technik Berlin, 2003 (in German).
[2] W. Jung, W. *Op amp applications*. Analog Devices, MA, 2002.
[3] J. Siegl, *Schaltungstechnik – Analog und gemischt analog/digital. 2. Auflage.* Springer-Verlag, 2005 (in German).
[4] Spice models, Analog Devices, last accessed, Feb. 16.2011.
[5] Spice models, Texas Instruments, last accessed, Feb. 16.2011.
[6] Spice macromodels, National Semiconductor, last accessed, Feb. 16.2011.
[7] PSpice library list, Release 9.2, Cadence Design Systems, 2000.
[8] I. Pandiev, P. Yakimov, T. Todorov, "Macromodeling of programmable gain amplifiers". E+E, No 7-8, pp. 69-76, 2009.
[9] M. Kovacheva, "Development of behavioral VHDL-AMS models for VCAs", *Diploma Thesis*, Faculty of Electronics, TU-Sofia, 2011 (in Bulgarian).
[10] S. Robinson, *Successful simulation. A practical approach to simulation projects*. McGraw-Hill, New York, 1999.
[11] R. Sarget, "Some approaches and paradigms for verifying and validating simulation models", Proceedings of Winter Simulation Conference, pp. 106-114, 2001.
[12] High Gain Adjust Range, Wideband, Voltage-Controlled Amplifier VCA810 (Rev. F) – Datasheet, Texas I., Dec. 2010.
[13] E. Christen, K. Bakalar, "VHDL-AMS – A hardware description language for analog and mixed-signal applications, IEEE Trans. on cir. and syst. – II, vol. 46 (10), pp. 1263-1272, 1999.
[14] *Definition of analog and mixed signal extensions to IEEE standard VHDL*, IEEE Standard 1076.1, 1999.

Instantaneous Power Dissipation in Class B Stage, Operating with Complex Load Impedance

Student author: Hristo Zhivomirov[1]
Mentors: Ekaterinoslav Sirakov[2] and Boris Nikolov[3]

Abstract – **The present paper describes analysis of the instantaneous power dissipated by active elements in class B push-pull amplifier stage. Both situations of operating with resistive and complex load impedance are treated. The simulation results that confirm the theoretical formulation are given using OrCAD PSpice.**

Keywords – **Instantaneous power, Dissipation, Class B, Complex load.**

I. INTRODUCTION

The study of power parameters and characteristics of the power amplifier stages is a major task in the analysis and design of amplifiers. In this paper, because of the restriction volume the focus is primarily on the instantaneous power dissipated by the active elements in amplifiers operating in class B with complex load impedance.

II. ANALYSIS

The functional circuit of the power amplifier stage working in class B with bipolar transistors is given in Fig. 1.

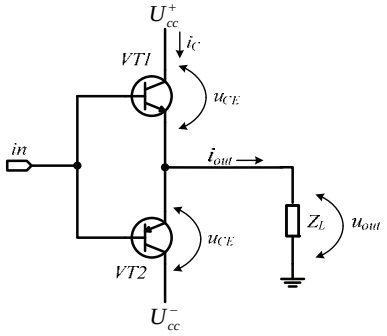

Fig.1. Functional circuit of the power amplifier stage working in class B

Student author:
[1]Hristo Zhivomirov is with the Technical University-Varna, Studentska Street 1, Varna 9010, Bulgaria.
E-mail: hristo_car@abv.bg

Mentors:
[2]Assoc. Prof. Ekaterinoslav Sirakov is with the Technical University-Varna, Studentska Street 1, Varna 9010, Bulgaria, E-mail: katiosirakov@abv.bg
[3]Asst. Boris Nikolov is with the Technical University-Varna, Studentska Street 1, Varna 9010, Bulgaria, E-mail: boris84@abv.bg

The output voltage and current of the amplifier when sinusoidal signal is applied can be described as [1]:

$$u_{out} = U_{out\,m} \sin(2\pi t / T), \text{ V} \quad (1)$$

$$i_{out} = \frac{U_{out\,m} \sin(2\pi t / T)}{Z_L}, \text{ A} \quad (2)$$

where: $U_{out\,m}$ – amplitude of the output voltage, V;
Z_L – impedance of the load, Ω;
T – period of the signal, s.

For the time $0 \le t \le T/2$, works the transistor that is connected to a positive voltage supply rail U_{cc}^{+}, and the voltage drop on transistor is $u_{CE} = U_{cc}^{+} - u_{out}$. Similarly for the time $T/2 \le t \le T$, works the lower arm and the voltage drop on the transistor working in it is $u_{CE} = \left| U_{cc}^{-} - u_{out} \right| = u_{out} - U_{cc}^{-}$. Usually $U_{cc} = U_{cc}^{+} = U_{cc}^{-}$ [1].

Instantaneous power dissipation with resistive load

The power dissipated by each transistor can be represented as a product between the voltage drop u_{CE} and the current through it $i_C = i_{out}$. Thus for the instantaneous power dissipated by transistors with resistive load is obtained the expression [1], [2]:

$$P_{D(inst)} = \left[U_{cc} - U_{out\,m} \sin\left(\frac{2\pi t}{T} \right) \right] . \frac{U_{out\,m}}{R_L} \sin\left(\frac{2\pi t}{T} \right), \text{ W} \quad (3)$$

If the coefficient of effective use of supply voltage is assumed to be $\xi = \frac{U_{out\,m}}{U_{cc}}$ [3], the latter expression can be written as:

$$P_{D(inst)} = \frac{U_{cc}^2}{R_L} \left[\xi \sin\left(\frac{2\pi t}{T} \right) - \xi^2 \sin^2\left(\frac{2\pi t}{T} \right) \right], \text{ W} \quad (4)$$

Since $\frac{2\pi t}{T} = 2\pi ft = \omega t = \alpha$, rad [4], then:

$$P_{D(inst)} = \frac{U_{cc}^2}{R_L} \left(\xi \sin\alpha - \xi^2 \sin^2 \alpha \right), \text{ W} \quad (5)$$

Instantaneous power dissipation with complex load

A complex load means load that has impedance, composed of resistance and reactive (reactance) capacitive (capacitance) or inductive (inductance) component, according [4]:

$$\dot{Z}_L = R_L \pm jX_L = \left|\dot{Z}_L\right|.e^{j\varphi} = Z_L \angle \varphi \text{ , } \Omega \qquad (6)$$

$$\left|\dot{Z}_L\right| = \sqrt{R_L^2 + X_L^{\ 2}} \text{ , } \Omega; \ \varphi = arctg\left(\frac{X_L}{R_L}\right) \text{, rad} \qquad (7)$$

Further in this paper will be assumed $Z_L = const$.

If the phase shift between current i_C and voltage u_{CE} is denoted as φ, then from Eqs. (3) and (5) for the instantaneous power dissipation with complex load can be recorded:

$$P_{D(inst)} = \frac{U_{cc}^2}{Z_L}\left[\xi \sin\alpha - \xi^2 \sin(\alpha+\varphi)\sin\alpha\right] \text{, W} \qquad (8)$$

Fig. 2 presents an analysis of the expression for ξ = 1 and different load phase angles φ. It can be seen that the peak of $P_{D(inst)}$ could be about 6,4 times more than average power dissipation when resistive load is applied to the amplifier.

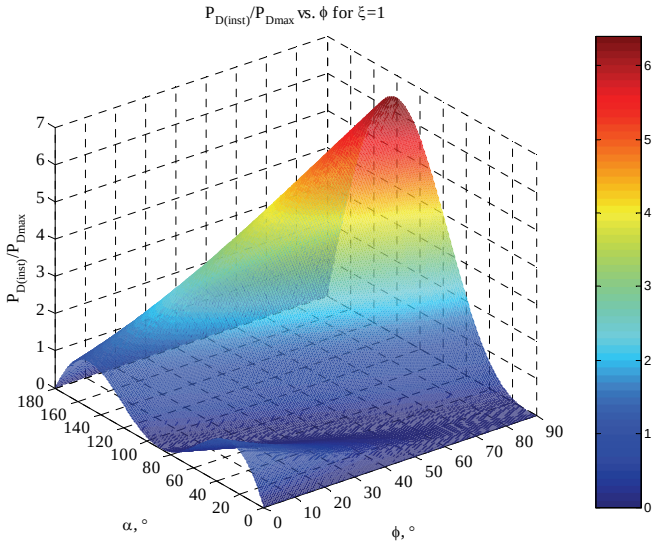

Fig. 2. Instantaneous power dissipation $P_{D(inst)}$ for ξ = 1 as a function of phase shift φ, with complex load

Fig. 3 presents the analysis of Eq. (8) for phase shift angle φ = 90 ° and different values of ξ.

The instantaneous power dissipation when resistive load is applied, i.e. when phase shift φ = 0°, is shown in Fig. 4 as a function of the coefficient ξ. It can be noted, that the peak of $P_{D(inst)}$ in that case is about 1,23 times more than the average power dissipated by active elements.

The instantaneous power is rated to a maximum average power dissipation of both active devices for resistive load P_{Dmax}. The last one can be described when $\xi = 2/\pi$, as [1], [5]

$$P_{Dmax} = \frac{2U_{cc}^2}{\pi^2 R_L} \text{ , W} \qquad (9)$$

In Fig. 5 and Fig. 6 the peak instantaneous power dissipation $P_{D(inst)peak}$ as a function of the coefficient ξ, with parameter phase shift angle φ is presented.

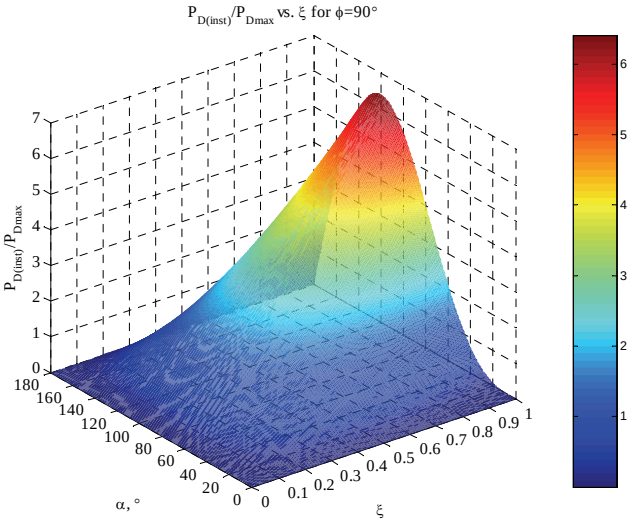

Fig. 3. Instantaneous power dissipation $P_{D(inst)}$ for φ = 90° as a function of the coefficient ξ when reactive (inductive) load is applied

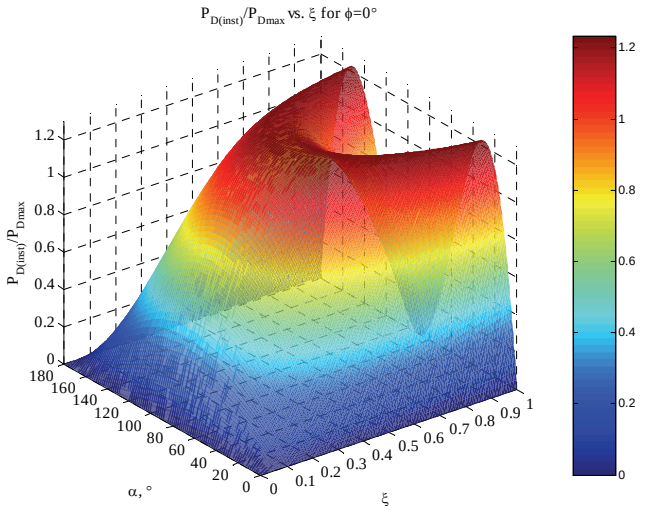

Fig. 4. Instantaneous power dissipation $P_{D(inst)}$ for φ = 0° as a function of the coefficient ξ when resistive load is applied

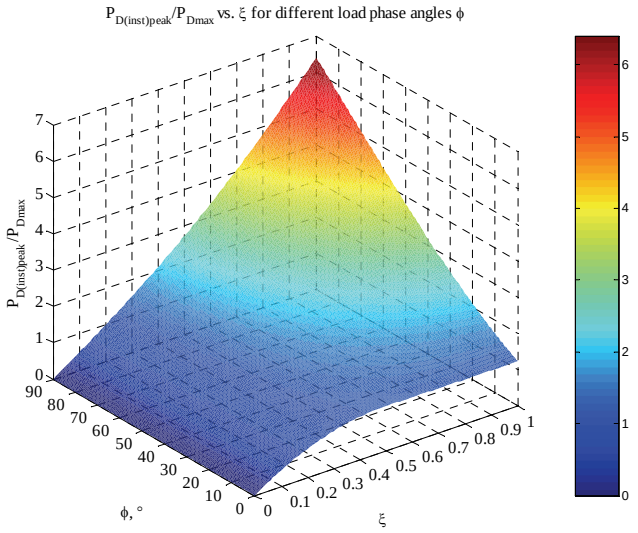

Fig. 5. Peak instantaneous power dissipation $P_{D(inst)peak}$ as a function of the coefficient ξ, and parameter phase shift φ (3D expression)

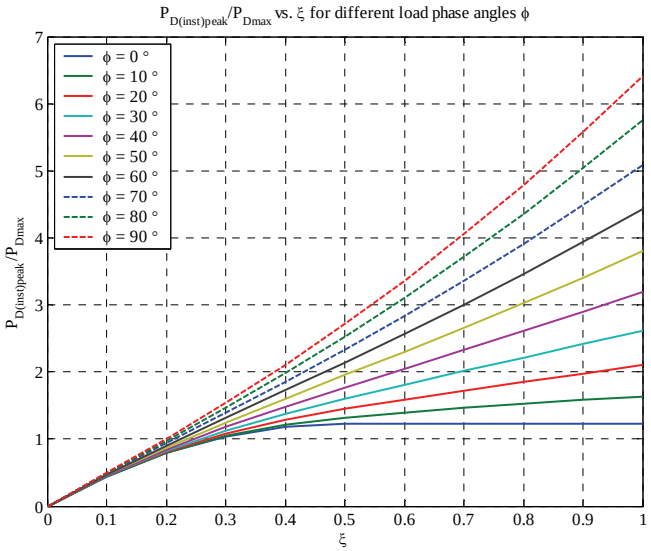

Fig. 6. Peak instantaneous power dissipation $P_{D(inst)peak}$ as a function of the coefficient ξ, and parameter phase shift φ

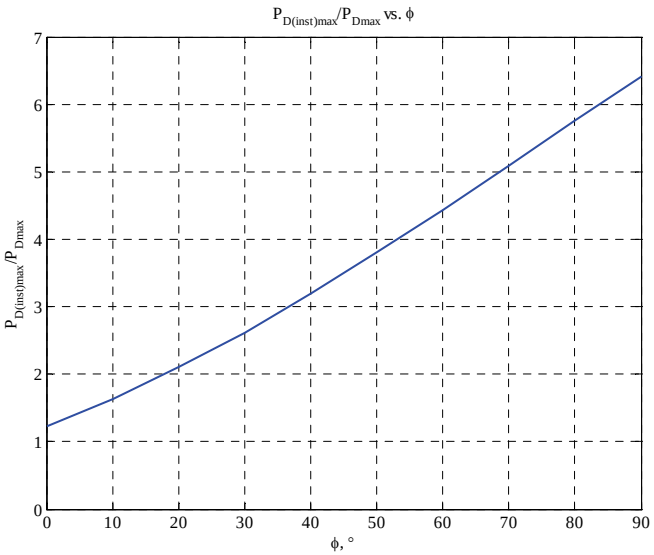

Fig. 7. Absolute maximum value of $P_{D(inst)peak\ max}$, as function of phase shift φ

It can be seen (Fig. 2) that the absolute maximum value $P_{D(inst)peak\ max}$, which can reach the instantaneous peak power dissipation with phase shift angle φ is obtained when the full phase of the signal is:

$$\begin{aligned} \omega t = \alpha &= 30° + \frac{\varphi}{3}, ° \\ &= 0,5236 + \frac{\varphi}{3}, rad \end{aligned} \quad , \qquad (10)$$

if the current anticipates the voltage, i.e. the voltage lags the current (capacitive load) [†] and:

$$\begin{aligned} \omega t = \alpha &= 180° - \left(30° + \frac{\varphi}{3}\right), ° \\ &= \pi - \left(0,5236 + \frac{\varphi}{3}\right), rad \end{aligned} \quad , \qquad (11)$$

if the current lags the voltage (inductive load)[†] and can be found if substituting the value for α obtained by Eqs. (10) and (11) in Eq. (8)· Derived expressions do not match those in [2]. Such an analysis is made in [3], where the resulting expression is essentially different from Eqs. (10) and (11), but gives an equivalent result.

The dependence given with Eqs. (10) and (11) is presented graphically in Fig. 7 again rated to P_{Dmax}. The problem has been solved with the use of numerical methods and the graphical form is identical to that obtained from the analytic solution so that demonstrates the consistency of the displayed dependence. The same result is shown in [2].

[†] The starting point (α = 0) is the point at which current passes through it's zero value.

III. Computer Simulations

At the following figures are shown the computer simulations made with OrCAD PSpice 9.1 (Cadence Design Systems). The Transient analysis in the time domain of the load voltage, the current through one of transistors and it's instantaneous power dissipation as product between collector current and collector-emitter voltage drop are presented. All simulations were carried out with coefficient ξ = 1. Similar results are shown in [6].

Fig. 8 shows the test circuit for simulation of instantaneous power dissipation with a resistive load R_L = 8 Ω. Fig. 9 shows the results from the simulation (transient analysis), in the time domain.

From Fig. 9, $P_{D(inst)peak}$ = 7 W when P_{Dmax} = 5,7 W, i.e. $\frac{P_{D(inst)peak}}{P_{Dmax}} = 1,23$, in agreement with Eq. (5) and Fig. 6.

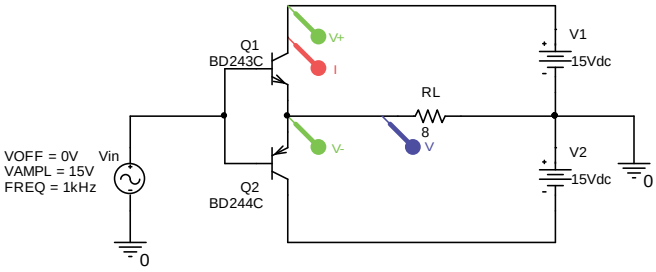

Fig. 8. Test circuit for simulation of the instantaneous power dissipation when a resistive load is applied

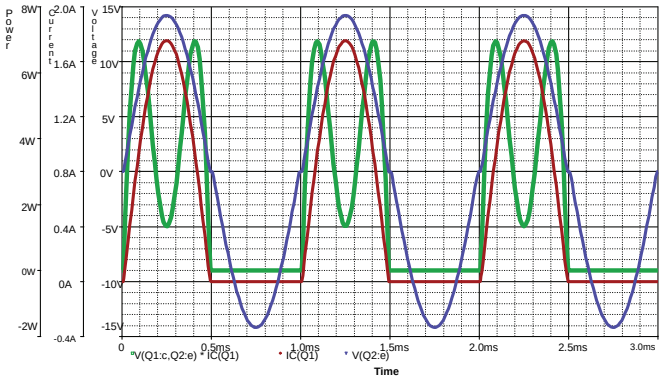

Fig. 9. Signals in the time domain for the simulated circuit in Fig. 8

Fig. 10 shows the simulation circuit for instantaneous power dissipation in case of a complex load $Z_L \angle \varphi = 8 \angle 90° \, \Omega$. Fig. 11 shows the results from simulation. From Fig. 11, $P_{D(inst)peak} \approx 37$ W when $P_{Dmax} = 5{,}7$ W, i.e. $\frac{P_{D(inst)\,peak}}{P_{Dmax}} = 6{,}5$, in agreement with Eqs. (11), (8) and Fig. 6.

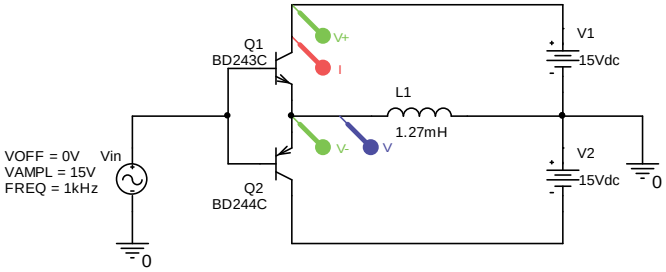

Fig. 10. Test circuit for simulation of the instantaneous power dissipation when a complex load (reactance) is applied

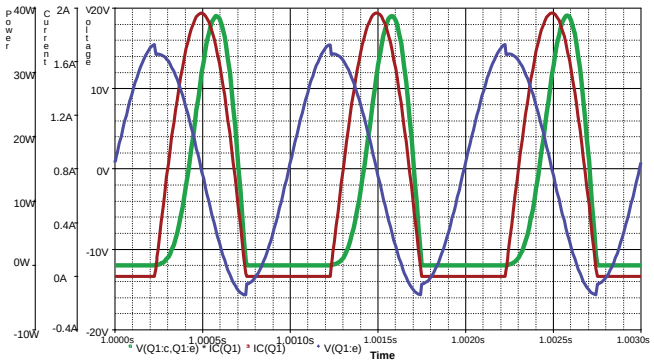

Fig. 11. Signals in the time domain for the simulated circuit in Fig. 10

IV. Conclusion

An examination of the instantaneous power dissipation by the active elements in Class B amplifiers with a complex load is presented. The affected subject is of particular importance for the design and analysis of power amplifiers, especially in the low-frequency applications. The statement concerns the work of all active components, no matter the type – integrated or discrete, solid state or vacuum. Conducted computer simulations demonstrate unequivocally the reliability of the theoretical formulation. In the statement Eqs. (5) and (8) and Figs. 3, 5 and 6 are originally presented, and Eqs. (10) and (11) are original contribution.

This work can serve the design and improvement of amplifier equipment, and theoretical analysis of amplifiers.

Consideration of the theme will continue with finding the necessary power parameters that are required to have active components operating in the class B amplifiers, with a complex load.

Acknowledgement

This paper was developed in the frames of a scientific research project “Multi-dimensional Computer Analysis in Communications”, sponsored by Ministry of Education, Youth and Science, Bulgaria, 2011.

References

[1] W. Marshall Leach, Jr., *Introduction to Electroacoustics and Audio Amplifier Design*, Dubuque, Iowa, Kendall/Hunt Publishing, 2003.

[2] E. Benjamin, “Audio Power Amplifiers for Loudspeaker Loads, Journal of the Audio Engineering Society”, Vol. 42, No. 9, pp. 670 - 683, Sept., 1994.

[3] E. S. Sirakov, “Instantaneous and Average Output Dissipated by an Output Stage Operating in Class AB”, ICEST 2002 Conference Proceedings, pp. 93-96, Nis, Serbia & Montenegro, 2002.

[4] R. L. Boylestad, *Introductory Circuit Analysis*, Upper Saddle River, New Jersey, Prentice Hall, 2010.

[5] A. Sedra, K. Smith, *Microelectronic Circuits*, Oxford, Oxford University Press, 2004.

[6] D. Self, *Audio Power Amplifier Design Handbook*, Oxford, Focal Press, 2009.

Inspection of Topography of Cracks Using Scanning Acoustic Microscopy

Student authors: Endre Harkai[1], Tamás Hurtony[2]
Mentor: Péter Gordon[3]

Abstract – **Scanning acoustic microscopy is an analysis tool mainly used for detecting inhomogeneities inside the inspected samples, but it is also capable for measuring the thickness of a given layer. A standard method for thickness measurements is based on observing a so called A-mode echo signal. In this paper the authors present pilot results of a method for thickness measurements based on analyzing the grayscale value of the C-mode image. The method can be used only under certain circumstances, but has the advantage to estimate the thickness of a layer using only the C-mode image.**

Keywords – **Scanning Acoustic Microscopy, measuring thickness, grayscale image processing**

I. Introduction

Scanning acoustic microscopy (SAM) is a commonly used non destructive inspection method in electronic failure analysis. One major advantage of this method is that with the help of ultrasonic signals it is capable to detect cracks or delaminations inside the sample under test.

In case of using SAM in a reflexive mode the so called A-mode signal gives the fundamental information about the inner structure of the inspected sample. The A-mode signal is an oscilloscope type signal which displays the reflected echoes as a function of time. The amplitude of the main peaks in the reflected signal provides information about the inner interfaces of the sample as follows [1]:

$$R = \frac{Z_2 - Z_1}{Z_2 + Z_1} \qquad (1)$$

where R is the fraction of the reflected amplitude from an interface, Z_1 and Z_2 are the acoustic impedances of the primary and secondary materials of the given interface, respectively. Acoustic impedance values of materials mentioned in this paper are summarized in Table I.

Measuring the time elapsed between the main peaks gives the possibility to estimate the thickness of the given layer:

$$d = \frac{v \cdot t}{2} \qquad (2)$$

where d is thickness of the layer, v is the velocity of the ultrasonic signal in the layer and t is the time elapsed between the appearance of the main peaks.

The accuracy of measuring the elapsed time between the adequate peaks determines the accuracy of the thickness measurement. In case the peaks are too close to each other the measurement of the thickness of the layer becomes inaccurate; in case of overlapping peaks the measurement is not performable. By applying transducers with higher operational frequencies higher depth resolution can be achieved because of the shorter wavelengths, however the penetration depth into the given material will decrease.

In this paper we present the results of the pilot measurements of a method which uses the value of a specific amplitude of the reflected signal, that is the grayscale value of the C-mode image for predicting the thickness of the given layer. The principles of the method are as follows: the value of the acoustic impedance of air is approximately 0, thus when the inspection signal reaches a crack or delamination filled with air the total amount of the incident wave will be reflected according to Eq. (1). If during the inspection the ultrasonic wave propagates though only one material before reaching the air-gap then the attenuation of the signal will be proportional with the thickness of this inspected material. Thus the thickness of the layer above the air-gap can be estimated from the grayscale value of the C-scan image.

TABLE I
ACOUSTIC IMPEDANCE VALUES USED (@ 25 °C)

Material	**Z ($kg \cdot s^{-1} \cdot m^{-2} \cdot 10^6$)**	**Reference**
Air	0.00041	[2]
Water	1.49	[2]
Aluminum	17	[3]
Copper	42	[3]

II. Experimental Setup

Measurements were performed by a scanning acoustic microscope Sonix HS1000 equipped with a transducer of operational frequency of 50 MHz.

Authors are with the Department of Electronics Technology, Budapest University of Technology and Economics, Goldmann György tér 3., 1111 Budapest, Hungary

Student authors:
[1]E-mail: harkai@ett.bme.hu
[2]E-mail: hurtony@ett.bme.hu

Mentor:
[3]E-mail: gordon@ett.bme.hu

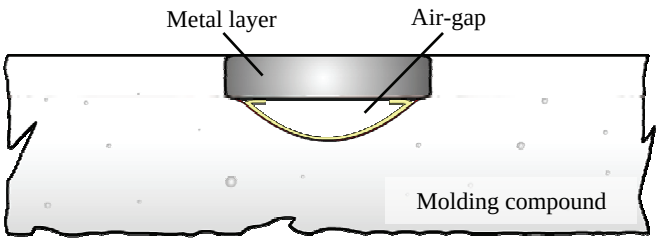

Fig. 1: Virtual cross-section of a sample

Aluminum and copper samples of different thicknesses were used for measurements. The thickness value of the inspected samples was formed by grinding the base material.

On the back of the inspected samples air-gaps were formed using a paper spacer and foil. After that the samples were molded into a two component acrylic compound. The mold compound gave a mechanical stability to the samples, and prevented the air-gaps from filling with water during the inspections. A virtual cross-section image of one sample is shown in Fig. 1.

From samples with the same composition the thickest one was measured firstly. The transducer was focused to the air-gap under the sample, then the value of the gain of the acoustic microscope was set in such a way that the amplitude of the reflected peak from the sample – air-gap interface would not overdrive the evaluation system during the C-scan imaging. All other samples with the same composition were measured using the same value of gain and focusing the transducer to the sample – air-gap interface. In these cases the ultrasonic wave was propagated though a higher thickness of water and a smaller thickness of metal, thus the attenuation of the wave was higher and these samples appeared darker in the C-scan images.

III. Results and Discussion

Results of measuring the aluminum samples are shown in Fig. 2. It can be seen that by decreasing the thickness of the samples the grayscale value of the C-scan images is linearly decreases. The attenuation of the ultrasonic signal in case of any material should be exponential, however in case of such a narrow thickness interval the linear approximation can be acceptable. Determining the slope of the approximation line gives the possibility to estimate the thickness of any layer of the same composition above an air-gap if using the same value of gain. Additional limitations are that the thickness of the layer must be lower that the penetration depth of the inspection wave, but also should be high enough to significantly attenuate the propagating wave.

Fig. 3 shows the results of measuring the copper samples. In contrast to aluminum samples there is no significant difference among the grayscale values of the measured copper samples. This result possibly can be explained by the higher acoustic impedance of copper according to aluminum. The propagating signal was not able to significantly attenuate in the sample because of the relatively high wavelength of the transducer.

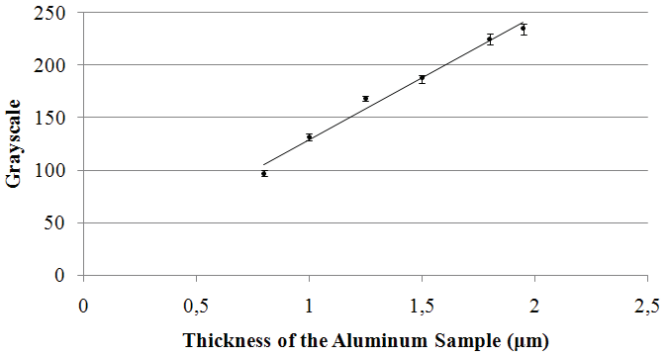

Fig. 2: Results of measuring the aluminum samples

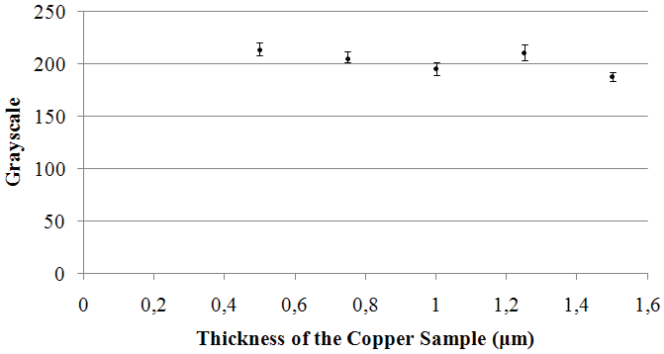

Fig. 2: Results of measuring the copper samples

IV. Conclusion

This paper presents the results of the pilot measurements of a method which estimates the thickness of a given material above an air filled crack or delamination by the grayscale value of the C-mode image.

Results show that under certain circumstances it is possible to estimate the thickness value of a material by the grayscale value, however the inspection frequency of the transducer significantly limits the available interval and accuracy of the thickness measurement similarly to measuring the thickness from the A-mode signal.

The main advantage of this method could be that thickness measurements can be done without the A-mode echoes by applying simple image processing steps. The generalization of the method and revealing its limits are the following tasks of the authors.

References

[1] Perry L. Martin: Electronic Failure Analysis Handbook, McGraw-Hill Handbooks, pp: 7.1-7.22, 1999.

[2] G. A. D. Briggs, O. V. Kolosov: Acoustic Microscopy 2nd Ed., Oxford University Press, Oxford, 2010.

[3] Louis Cartz: Nondestructive Testing: radiography, ultrasonics, liquid penetrant, magnetic particle, eddy current, ASM International, 1995.

Effect of Solder Pad Symmetry on Evolution of Sn-Cu Intermetallic Compounds

Student authors: Tamás Hurtony, Endre Harkai,
Mentor: Péter Gordon

Abstract – **The effect of symmetry of the solder pad on the evolution of Sn-Cu intermetallic compounds (IMCs) in laser reflowed solder joints was investigated. A Q-switched, frequency tripled Nd:YAG laser was applied in order to precisely control the exposing energy. The microstructure of the solder joint was analyzed with SEM, and Optical Microscopy (OM) on cross-section samples. The composing elements were identified by SEM-EDS. The amount and the distribution of dissolved IMC were investigated during soldering onto square, triangle and circular pads. The results showed that the symmetrical condition of the geometry of the solder pad has no significant influence on the amount of the developed mass fractions of IMCs inside the solder bulk**

Keywords – **Laser heat treatment, Intermetallic compound, geometric conditions.**

I. INTRODUCTION

Laser beam soldering is one of the most emerging selective joining technologies, because some of its big advantages – like the concentrated heat effected zone or the high energy density – cannot be obtained by any other conventional joining technology (e.g. IR reflow or soldering iron). But on the other hand due to the rapid temperature rise and drop unexpected phenomena can be occurred which could alternate the microstructure of the solder causing the modification of the mechanical properties [1-2]. The high temperature gradients significantly influence the diffusion processes so as the natural heat convection in the molten solder [3]. Applying the same processing parameter on different pad shapes the temperature distribution in the solder might be diverse [4]. Alternating the geometry will have effect on the temperature distribution, and the surface of the molten solder created by the wetting reaction. The aim of this paper is to compare the microstructure of the lead free solder alloy soldered under three different symmetrical conditions.

II. MATERIALS AND METHODS

For our soldering experiments we applied FR4 glass-fiber reinforced epoxy single sided Printed Circuit Board (PCB) with 35 μm thick copper conducting layer. We used non solder mask defined structure, and galvanic tin surface finishing. The pads were organized on the PCB into three groups according to their geometric shapes. The number and the orientation of the pads were designed in order to be compatible with the cross sectioning preparation method of our department.

Three kinds of regular mathematical objects were chosen. The area of the rectangular, triangular, and circular pads were equal, in order to have the same amount of solder paste on each of them. The lead free solder paste (Sn96.5Ag3.0Cu0.5) was deposited onto the pads with 110 μm thick nickel stencil, through adequately sized laser cut apertures.
During the heat treatment process we used a laser diode pumped, Q-switched, frequency tripled Nd:YAG laser (Coherent Avia 4500-355).

Since the wavelength of the laser is in the near UV region (355 nm) the optical properties of the pure matt tin determine the laser material interaction mainly. The tin solder balls mixed with flux gel absorb this wavelength very well. Due to the multiple reflections between the individual balls, we consider that the major part of the energy of the laser beam is absorbed by the solder paste. This is a very important assumption, since the most significant influencing technological parameters, are the average power (P_a), and the heat processing time (t_s). The multiplication of these two parameters gives the coupled energy, which turns into heat in the solder, rising the temperature of the flux and solder balls above melting point.

In order not to ablate either the flux or the solder balls a defocusing was applied. Instead of rising up the scanning head of the laser, the sample was raised 60 mm above the focal plane. This way, after the solid-liquid phase transition, as the convergent laser beam reaches the surface it won't be scattered so intensive. Since the optical properties of the molten solder are considerably different than the solder paste this reflected beam can serve feedback of the melting fact. In order to have more homogenous energy coupling the defocused laser spot was scanned along a circular path which was 0,4 mm in diameter.

A special two-stage heating process was applied. First we used 2 W of average power to activate the flux, and melt the solder paste (7,5 s), than the power was reduced to 1W (further 70 s of heat treatment). The laser was operating in Q-switched mode, so in order to reach a rapid power reduction the pulse repetition frequency was raised twice of the original 30 kHz, to 60 kHz. During normal operation the rapid change of the repetition frequency of the laser would yield to the deterioration of the laser mode, but applying a significant

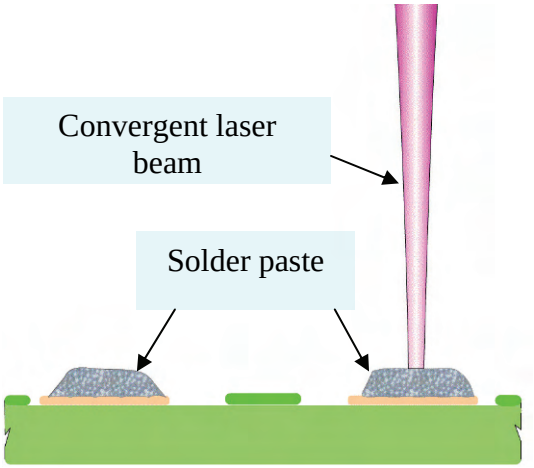

Fig. 1. The solder paste was directly illuminated by defocused laser beam

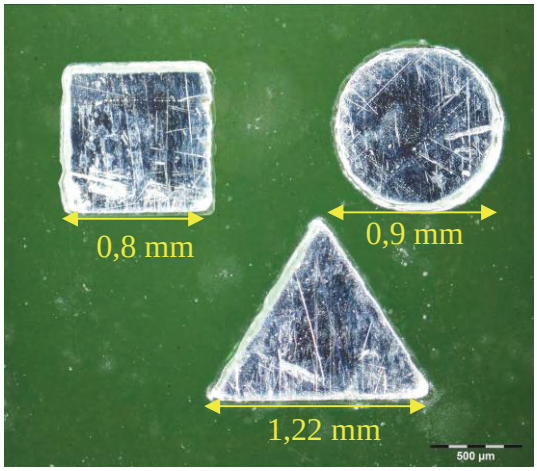

Fig. 2. The area of the different pads were the same, which was 0,64 mm^2

defocusing this effect does not have any influence on the experiment. The samples were cooled down by natural heat transition to room temperature.

The metallographic preparation was the following. First the samples were embedded in acryl based (Technovit 4006) resin. We applied active oxide polishing suspension (Struers OP-S) for surface finishing. The optical microscopic images were taken by an Olympus BX51 upright microscope. SEM analysis was done by a FEI Inspect S50 scanning electron microscope with a Bruker Quantax EDX (energy dispersive X-ray analysis) system.

III. Results

The primary objective was to examine the difference of the microstructures of the different pad shapes. In our investigation we focused on the properties of the intermetallic layer (IML) between the copper and the solder, and the intermetallic compounds (IMC) that were dissolved into the bulk material.

The average thickness of the IML was measured by an automated script developed in MATLAB. The measured values can be seen in Fig. 3. The average values were based on the measurement of 10 pads per each geometrical shape. On each image the thickness of the IML was measured at 20 points randomly chosen by the algorithm. The reason of the relatively big deviation is not caused by the inaccuracy of the algorithm. It is due to the differently shaped scallops of the IML. The resolution of the images limited the accuracy but since 12 megapixel photos had been taken the uncertainty of the measurement was limited by the theoretical resolution of the optical microscope.

Since the mechanical properties of the IMC differs a lot compared to the mechanical properties of the solder or the copper, the IMC content of the solder bulk has to be investigated [5]. That is the reason why the amount and the distribution of the IMC dissolved into the bulk material were also observed. Thanks to the OP-S surface finishing the composing elements of the microstructure were not only polished, but selectively etched a little bit. Since the IMCs are more brittle than the solder they are etched less, by the etchant. The difference between the structure of the IMC crystallites and the solder affects their optical properties which makes possible to distinguish them from each other. In Fig. 5 the Sn_6Cu_5 (η-phase) appears slightly darker. This consideration was verified by SEM-EDX. Based on the hue differences of the composing zones a MATLAB script was developed in order to determine the ratio of the solder and the IMC dissolved in the solder bulk. The uneven illumination was compensated by adaptive histogram equalizer. The

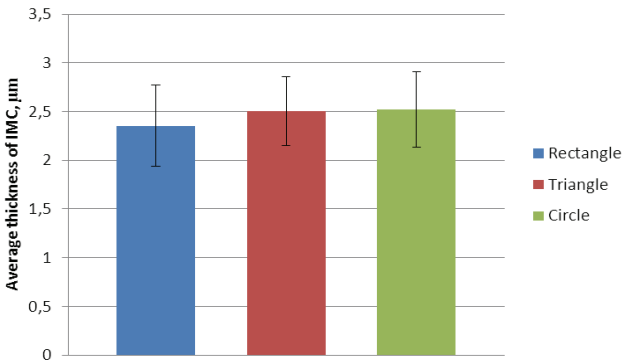

Fig. 3. The average thickness of the IML does not depend of the shape of the pad

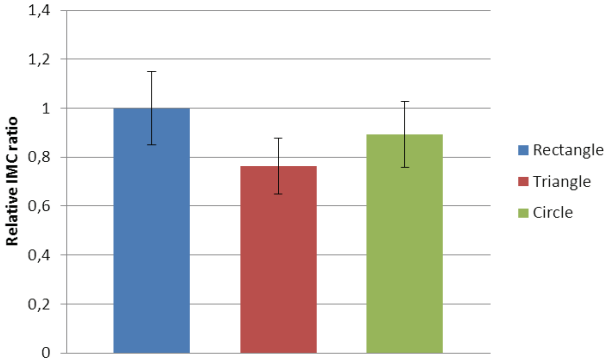

Fig. 4. The IMC-solder ratios were normalized to the highest absolute value. which was measured in rectangular case

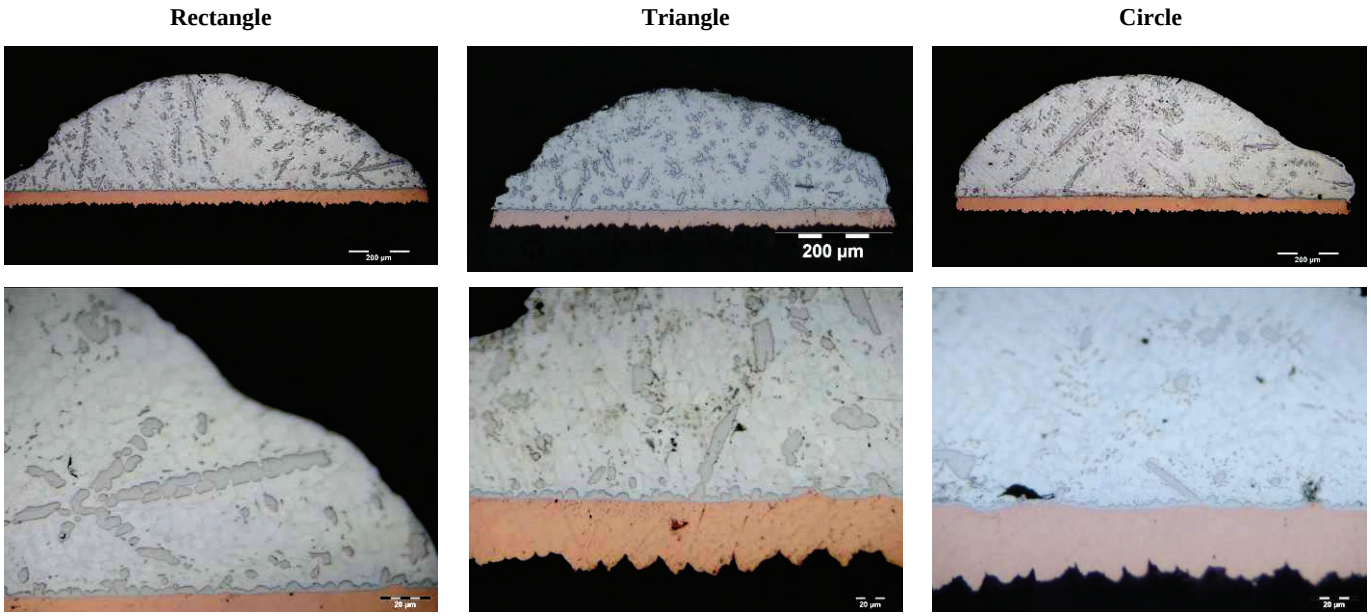

Fig. 5. The distribution of the dissolved IMC in the solder bulk was slightly different.

highest contrast difference was obtained from the red channel of the images, because the copper substrate is more saturated in this channel. The threshold for the binarization was also adaptively determined, and the binarized images were morphologically filtered.

After the filtering process the total area of the solder bump was calculated for each image, because the cross sectioning plane was not the same in every cases. The source of the noise during the image analysis process can be originated of the presence of the polishing suspension fractals (they were coming from the voids that were formed during either the wetting reaction or the cooling reaction).

IV. Discussion

The differences between the average thicknesses of the IML in the case of different shapes of pads are not significant. The deviation is in the range of the standard deviation of the measurement. So we can say that the geometry itself does not have significant influence on the average thickness of the IML. Since the volume of the printed solder paste were the same in each cases, the heat capacitance, which determines the temperature of the molten solder, should have been almost the same. Concluding the Kinetic Analysis model of Flux-Driven Ripening of IMCs developed by Kim [1] the average radius of the IMC scallops can be described by the following equation:

$$R = \sqrt[3]{\left(\frac{9}{2}\frac{n}{n_i}\frac{D(C^b - C^e)}{C_i}\right)} \qquad (1)$$

,where $\boldsymbol{n_i}$: atomic density in IMC; $\boldsymbol{n}$: atomic density in the solder bulk; **D**: Diffusion Coefficient; $\mathbf{C^e}$: The equilibrium concentration of η-phase; $\mathbf{C^b}$: The equilibrium concentration of Cu-phase; $\boldsymbol{C_i}$: atomic fraction of Cu (6/11) in η-phase; $\boldsymbol{\delta}$: the width of the channel between the scallops through which the Cu support comes.

The temperature has effect on the average radius through the temperature dependence of the diffusion coefficient and the equilibrium concentration. The volume of the solder was the same in every cases so the ratio of $\boldsymbol{n}$ and $\boldsymbol{n_i}$ can be considered unique. However, the characteristics of the scallops were slightly different. The average radius of the curvatures of the scallops was the smallest in the case of the triangle pads, while it was approximately the same applying either rectangular, or circle pads.

It can be seen in Fig 5, that the surface of the solder is not even stretched surface, which can be expected in a wetting reaction. This phenomenon indicates that the solidification of the molten solder was a rapid process, and it was definitely not an equilibrium reaction. After switching off the laser beam the whole structure freeze immediately, and it is conserving the actual microstructure.

The average grain size of the solidified solder depends on the tangent of the cooling profile. The bigger the gradient the smaller the grain size should be [6]. The area of the pads was the same, through which some heat flux could be leaked. The heat capacitance of the solder was the same so as the heating profiles and the soldering time, but the surface of the solder was different. Different surface means different boundary condition in the differential equations of the heat transfer. The smallest surface belongs to the circular pads, so the solder bump on circular pads should be cooled down the slowest way. Thus the average grain size should be the biggest on circle pads and the smallest using triangle pads. The validation of this assumption needs further investigation.

It is interesting to note that in some cases small voids appeared at the interface. In spite of the fact of the relatively long time-above-liquidus the voids that were formed during the beginning of the wetting reaction did not leave the structure.

The dissolved IMC solidifies together with the solder and may form dendrites (Fig. 6.), since the rod-like structure tends to minimize the surface energy [8].
Investigating the microstructure on cross section samples might be misleading, because one cannot be sure whether a rod like shape or the cross section of a flake can be seen in the picture. In a cylindrical symmetric situation one can expect, that the extension of the structure will be the same along the third coordinate, because of the cylindrical symmetry of the boundary conditions. But in the case of other symmetries we have to validate our observation.
We electrochemically etched the tin from the solder bulk, the etched surface was observed with SEM. Since the electrochemical potential of the IMC differs from the potential of the pure tin, electrochemical etching has a high selectivity to tin. Fig. 7. shows a SEM image of the spatial dimension of a rod-like IMC that can be seen in Fig 6. It can be seen that dendrite-like formations are truly rod like structures, rather than cross-sectioned flakes.

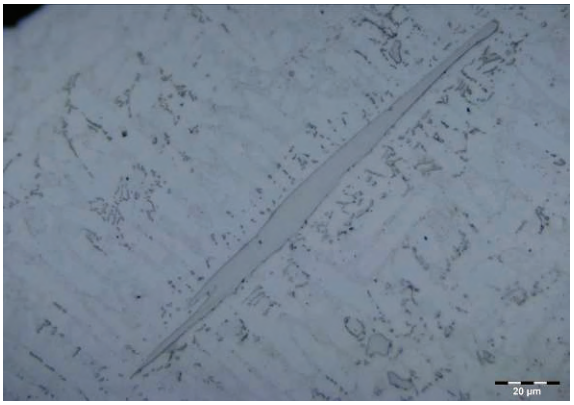

Fig. 6. The rod-like IMC can cause anisotropic mechanical properties of the solder joint

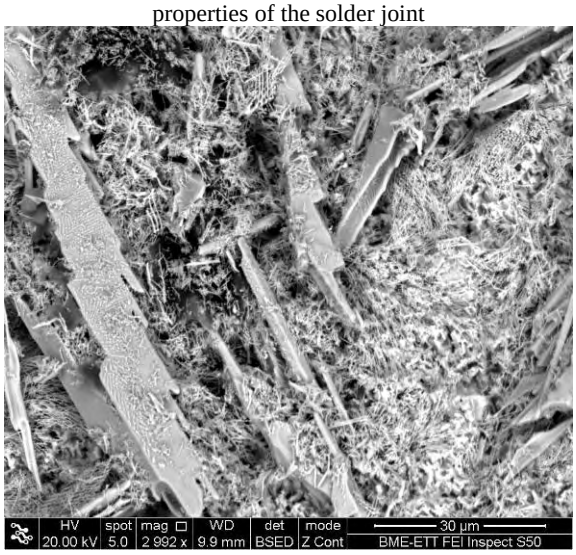

Fig. 7. The dendrite-like η-phase has sharp edges. The submicron Ag_3Sn particles are likely to be deposited onto the boundaries of the IMC.

The Sn96.5Ag3.0Cu0.5 alloy also contains Sn-Ag intermetallic compounds. The volume of the η-phase Ag_3Sn is very small compared to the Sn-phase. The structure consists of rod-like phases, situated at the boundaries of the Sn crystallite grains (Fig. 7). We have found several Ag3Sn segregation at the surface of the IMC fractions (Fig 6.) which is in good correlation with the observation of D.Q. Yu et al. in [2]. The porous material was identified as Ag_3Sn intermetallic compound. As the tin was electrochemically etched from the solder bulk, the Ag_3Sn skeleton remained on the surface.

V. Conclusion

The effect of the symmetry of the solder pad on the evolution of Sn-Cu intermetallic compounds (IMCs) in laser reflowed solder joints was investigated. With our Q-switched, frequency tripled Nd:YAG laser we applied two-stage heat treatment.
We found that the average thickness of the IML does not depend on the applied pad shape; however the scallop type can be slightly different. The amount of the dissolved IMC into the solder bulk was approximately the same in all situations, but the distribution and the characteristics was quite different. The most even structure was the triangle one, where no dendrite like fraction was found in the bulk. The microstructure of solder bumps, soldered onto circular, and rectangular pads was very similar to each other.

References

[1] P K.S. Kim, S.H. Huh, K. Suganuma, “Effects of cooling speed on microstructure and tensile properties of Sn–Ag–Cu alloys”, Materials Science and Engineering, A333, pp. 106–114, 2002.

[2] Schaefer, M, Laub, W., M. Sabee, J., A. Fournelle, R. A “Numerical Method for Predicting Intermetallic Layer Thickness Developed During the Formation of Solder Joints”, Journal of Electronic Materials, Volume 25, Issue 6, pp. 992-1003, 1996.

[3] Jeong-Won Yoon, Sang-Won Kim, Seung-Boo Jung, “Effects of reflow and cooling conditions on interfacial reaction and IMC morphology of Sn–Cu/Ni solder joint“, Journal of Alloys and Compounds 415, pp. 56–61, 2006.

[4] C.K. Wong, J.H.L. Pang, J.W. Tew, B.K. Lok, H.J. Lu, F.L. Ng, Y.F. Sun, “The influence of solder volume and pad area on Sn–3.8Ag–0.7Cu and Ni UBM reaction in reflow soldering and isothermal aging“, Microelectronics Reliability 48, pp. 611–621, 2008.

[5] Ping-Feng Yang, Yi-Shao Lai, Sheng-Rui Jian, Jiunn Chen, Rong-Sheng Chen, “Nanoindentation identifications of mechanical properties of Cu6Sn5,Cu3Sn, and Ni3Sn4 intermetallic compounds derived by diffusion couples”, Materials Science and Engineering A 485, pp. 305–310, 2008.

[6] Jeong-Won Yoon, Sang-Won Kim, Seung-Boo Jung, „Effects of reflow and cooling conditions on interfacial reaction and IMC morphology of Sn–Cu/Ni solder joint”, Journal of Alloys and Compounds 415, pp. 56–60, 2006.

[7] Yu, D.Q.; Wu, C.M.L.; Law, C.M.T.; L.Wang, J.K.L. Lai “Intermetallic compounds growth between Sn–3.5Ag lead-free solder and Cu substrate by dipping method, Journal of Alloys and Compounds”, 392(1-2), pp. 192-199. 2005.

[8] W. Yang, L.E. Felton, Messler, R.W., Jr., Proc. “The effect of soldering process variables on the microstructure and mechanical properties of eutectic Sn-Ag/Cu solder joints”, Journal of Electronic Materials, 24(10), pp. 1465-1472. 1995.

Using IR-Light for Proximity Detecting

Student author: Stanislav D. Yanov[1]
Mentor: Plamen Angelov

Abstract – **In a few words – If you interested in a method how IR-Detectors or Proximity Detectors work , send and receive data using IR-Light. How it work, through communication between transmitter and receiver ,and what scheme to use**

Keywords – **Proximity Detector, IR-Detector, Ir-LED**

I. Task of the Article

A. Introduction

In this article I will show method from communication between simple IR-LED (Transmitter) and receiver from TSOPxxxx from Vishay Smiconductors, specified frequencies and timings of pulses to be received correctly from receiver and decoded true.

B. Ir-Emiters and Receivers

Some technical examples of the IR receivers and transmitters are shown to the fig.1 and fig.2.

Fig.1. IR-Receivers

Fig.2. IR-Emitters

Different TSOPxxxx – Frequences is shows in table.1. [1]

Student autors:
[1]Stanislav D. Yanov Student of Burgas Free University Degreed Computer Systems and Technologies studding Computer's Telecommunications and Networks.
E-mail: kukata86@gmail.com
Mentor:
Assprofessor Plamen A. Angelov, Faculty of Computer Science and Engineering, Burgras Free University, 62 San Stefano Str., Burrgas-8001, Bulgaria, E-mail: pangelov@bfu.bg

TSOP1830 30kHz	TSOP1833 33kHz
TSOP1836 36kHz	TSOP1837 37kHz
TSOP1838 38kHz	TSOP1840 40kHz
TSOP1856 56kHz	

Last two digits show the carrier frequency of the TSOP receiver.

C. Important notes for correct work of receiver or setting the transmitter.

- Carrier frequency must be close up like recommended from supplier.
- An important requirement is Gap Time on the chip, which establishes stable operation of the receiver. It is compulsory to leave the chip to cease work -Gap Time* after the sequence of pulses (information)
  Minimum 6 pulses (to start work)/ 9 pulses break (e.g. 90ms / 15ms)
  GAP-Time is needed for the chip so it can "receive" the information and to "recover" for a new on. Reducing the time sharply reduces its sensitivity.
- Practical suggestion – sensitivity is on the account of the transmitted frequency/speed

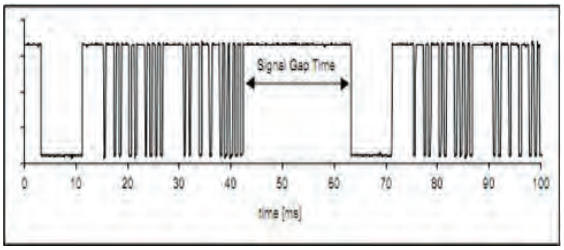

Fig.3. Gap time diagram

General Block scheme of an IR receiver is shown on fig.4.

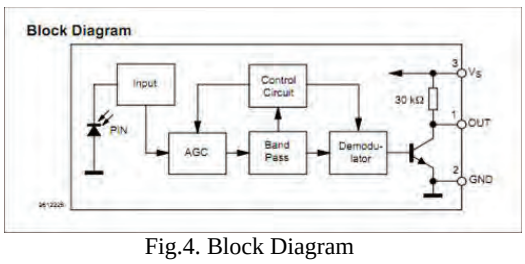

Fig.4. Block Diagram

Advantage of the using method:

- protection from interference caused by other electrical equipment (like halogen lamp);

- Internal automatic gain control (AGC) system - allows precise control the output level;
- Internal Band Pass filter reduce all output noise;
- used demodulator achieves very good separation between the carrier signal and the useful digital signal;
- Power supply 5V compatible with TTL IC'S.

D. Schematic of transmitter

Shown schematic is implemented with a timer LM555 [2], which is a necessary condition for the two desired frequencies. By serial connection of two bipolar (BJT) transistors achieve the necessary modulation of the output digital signal. But in the practical development has proved that - direct control of the powerful transistor (Q6) cause unacceptable smoothing the fronts of pulses. This cause the driver circuit (transistors Q1, Q4 and Q5) which provides precise control of the power stage. The simulation schematic is shown in fig.5.

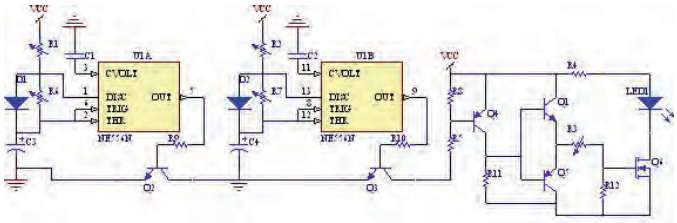

Fig.5. The simulation schematic

E. Alternative methods of miming

It can be used simple NAND in astable multivibrator mode only with two passive components one resistor and one capacitor. Examples of technical solutions such schemes are shown in fig.6.

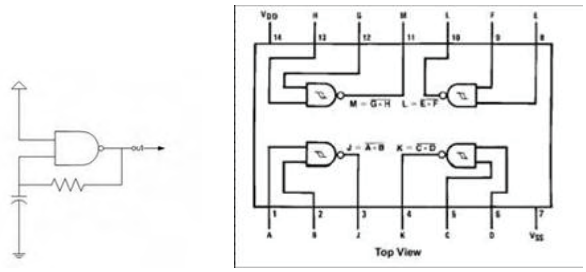

Fig.6. Example connection of the NAND inverter

F. Simulation on Proteus 7

The results of the simulation program are shown in fig.7 and fig.8.

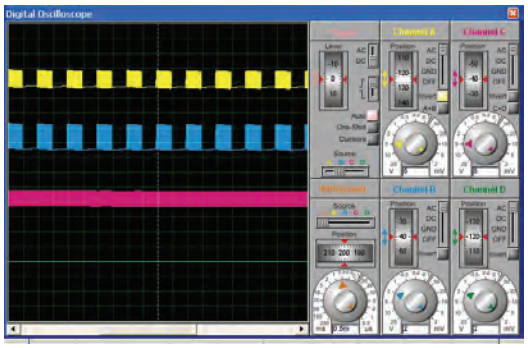

Fig.7. Result of the program simulation in observing the packet of information

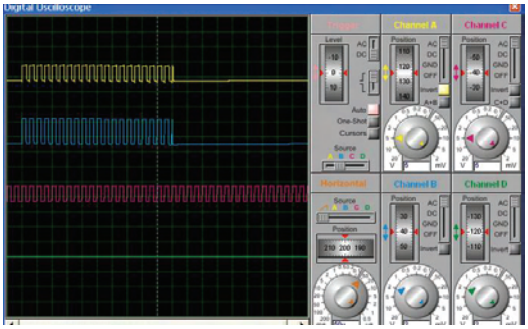

Fig.8. Result of the program simulation in observing the content of the digital package

G. Picture of working board

Some pictures from the practical implementation are shown in fig.9.

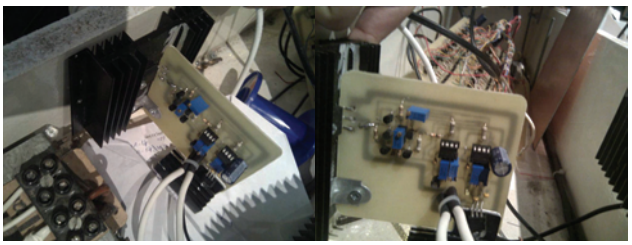

Fig.9. Pictures from the practical implementation

II. CONCLUSIONS

- Manage the power stage must be done using the driver circuit;
- The specificity of the used driver is reducing the level of control signal.

REFERENCES

[1] Photo Modules for PCM Remote Control Systems, Document Number 82047, Rev. 13, 13-Sep-00.
[2] LM555 Timer, 2006 National Semiconductor Corporation DS00785.

Comparison of RFID Systems from Aspect of the Operating Frequencies and One Practical Implementation

Student author: Aleksandar Gosic
Mentor: Milun Jevtic

Abstract – **In this paper the description of RFID systems and their comparison from aspect of the operating frequencies are presented. There are several different operating frequency bands which affects cost, size, reading range and performance of RFID systems. An overview of these characteristics and one concrete realization of RFID system for access control are given, too.**

Keywords – **RFID Systems, Operating Frequencies, Access Control.**

I. Introduction

RFID (Radio Frequency Identification) is a technology that uses communication via radio waves to exchange data for purpose of identification, tracking and many other applications. An RFID system is always made up of minimum two components, which are represented in Fig. 1, and that are:

- the transponder or tag, that carries information;
- and the interogator or reader, which, depending on design and technology used may be read or read/write device.

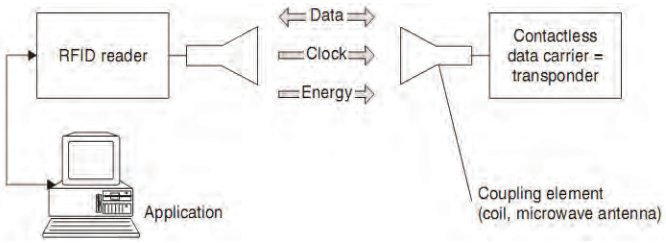

Fig. 1. The reader and transponder are the main components of every RFID system

RFID systems exist in countless variants, produced by an almost equaly high number of manufacturers. If we want to maintain an overview of RFID systems we must seek out features that can be used to differentiate one RFID system from another. In Fig. 2 features which can be used for comparing RFID system are given. One of the most important features of RFID systems is the operating frequency range of the system. Accordingly, in this paper attention to comparison of RFID systems depending on operating frequency ranges is devoted. After that, one practical realization of RFID system for access control is given.

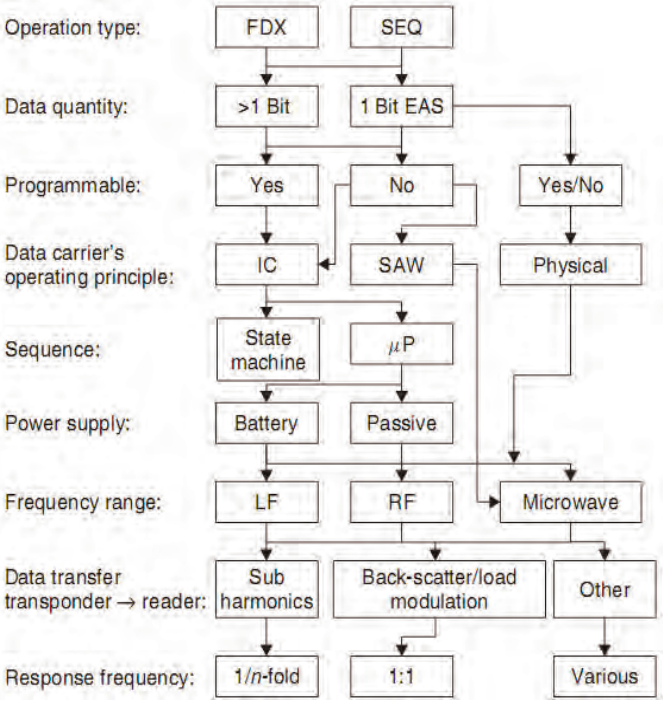

Fig. 2. The various features of RFID systems

II. Operating Frequency Ranges of RFID Systems

The frequency of an RFID system defines the relationship between the tag and the reader, and impacts on many other characteristics of RFID system like reading range, data transmission speed, cost, size and others. In accordance with the previous, there is differences in the typical uses of RFID systems some of which are access control and security, logistics, animal ID and tracking, electronic article surveillance, moving vehicle toll and many others.

There is no global public body that governs the frequencies used for RFID. In principle, every country can set its own rules for this. Because of that, today we have RFID systems which operates at widely different frequencies. But, these various operating frequencies are generally considered to be organized into four main frequency bands which are commonly used:

- 125 – 134kHz low frequency band (LF);
- 13.56MHz high frequency band (HF);

Student autor:
Aleksandar Gosic is with the Faculty of Electronic Engineering, Aleksandra Medvedeva 14,18000 Nis,Serbia,
E-mail: gosa46@yahoo.com.

Mentor:
Prof. dr Milun Jevtic is with the Faculty of Electronic Engineering, Aleksandra Medvedeva 14,18000 Nis,Serbia,
E-mail: milun.jevtic@elfak.ni.ac.rs.

- 860 – 960MHz ultrahigh frequency band (UHF);
- 2.45GHz – 5.8GHz microwave band.

III. Comparison of RFID Systems Depending on Operating Frequency Ranges

Before we make comparison of RFID systems depending on operating frequency ranges it is important to notice that there are difference in energy supply of transponders. Here we distinguish between passive, active and semi-passive transponders. This also affects size, cost, lifetime and reading range of transponder. Passive transponders do not have any power supply. All the energy required for operating the transponder is provided by magnetic or electromagnetic field produced by the reader and because of that their lifetime is not limited. In contrary, active transponders have their own energy supply, usually in form of a battery and their lifetime is limited to a maximum of 10 years. Semi-passive transponders also use battery to power the digital logic on the chip, but still use harvested power for communication, and have limited lifetime, too. Actual cost of passive tags start at $0.05 each and for special tags go to $5, that also depending on operating frequency, in the contrary to the cost of active tags which can go up to $100.

Further, more attention will be devoted to RFID systems that using passive transponders because of their characteristics and ease of use.

A. Low frequency band

Low frequency RFID systems are typically 125 KHz, though there are systems operating at 134 KHz as well. This frequency band provides a shorter read range, less than 0.5m for passive transponders, and slower read speed than the higher frequencies. This speed is typically less than 1kbps. Low frequency RFID systems have the strongest ability to read tags on objects with high water or metal content compared to any of the higher frequencies. They are suitable for working around corners and signal carried by this low frequency can pass through most objects. They are more tolerant of reflections and radiations. Low frequency tags are slightly more expensive than higher frequency tags.

The first RFID systems were implemented in this low frequency range. Typical low frequency RFID applications are access control, animal tracking, vehicle immobilizers, healthcare applications, product authentication and various point-of-sale applications.

B. High frequency band

High frequency RFID systems operate at 13.56 MHz, and have a feature of a greater read range and higher read speed than low frequency systems. Read speed or data transfer rate goes to approximately 25kbps. Also, the price of the tags is among the lowest of all RFID tags. Typical read range is up to 1.5 meters for passive transponders, and the ability to read tags on objects with high water or metal content is not as good as low frequency systems but stronger than ultrahigh frequency systems.

Applications include smart cards and smart shelves for item level tracking, and are also currently used to track library books, healthcare patients, product authentication and airline baggage. Another common application is maintenance data logging for sensitive equipment that needs regular checking such as fire suppression systems.

C. Ultrahigh frequency band

Ultrahigh frequency RFID utilizes the 860 to 960MHz band typically 868 MHz in Europe and 915 MHz in North America. Ultrahigh frequency tags typically cost about the same as high frequency tags. Read range is up to 8 meters with passive transponders and the data transfer rate is faster than high frequency systems, though still lower than microwave based RFID systems discussed next. Data transfer rates in this frequency band can have very different values that range from a few tens of kbps up to 800kbps. One drawback of ultrahigh frequency systems is a limited ability to read tags on objects with or surrounded by high water or metal content. Also, they are less resistant to reflections that occur due to the existence of obstacles than lower frequency RFID systems.

This is typically the frequency recommended for distribution and logistics applications. The primary rationale for utilizing this frequency in the supply chain is the greater read range it offers over the other frequency ranges. However, ultrahigh frequency RFID systems is also widely used for electronic toll collection systems on highways, manufacturing applications and parking lot access based on the greater range provided by the frequency.

D. Microwavwe band

The final frequency option is the microwave band, either 2.45GHz or 5.8GHz. Though microwave based RFID systems offer the highest data read rates which can go over 1Mbps. They are the most expensive systems although the tags are small and cheap to produce. RFID systems in this operating frequency band have a read range of up to 15m when using passive transponders. Additionally, microwave based systems are not able to penetrate objects with high water or metal content which makes it unsuitable for many applications. These RFID systems are the least resistant of reflections and other disturbances caused by presence of obstacle. The advantage of these RFID systems and systems operating in the ultrahigh band is the ability to read multiple tags simultaneously because of high data reading rate, which increase operating speed of RFID system.

At this time, microwave is constrained to specialized applications such as tracking airline baggage or electronic toll collection. Though it could be used for some supply chain applications with high data content, the inability to penetrate water or metal combined with the higher cost will limit its deployments in this realm.

IV. RFID Standards

As previously mentioned, there is no globally accepted universal standard for RFID systems. But, on the other side, there are several standards bodies that make effort in the development and definition of RFID technology standards, including:

- International Organisation of Standardisation (ISO);
- EPCglobal Inc;
- European Telecommunications Standards Institute (ETSI);
- Federal Communications Commission (FCC) and many other less important.

The ISO (International Standards Organization) and EPCglobal are leading figures in RFID standardisation. They developed many standards in this field, that are mutually incompatible in some sections, but they are commonly in use worldwide. Some of this standards, that are mostly used, as well as other previously discussed characteristics are given in Table I.

TABLE I
RFID CHARACTERISTICS OVERVIEW

Band	LF band	HF band	UHF band	Microwave band
Typical RFID Frequencies	125 – 134kHz	13.56 MHz	860 – 960 MHz	2.45 – 5.8MHz
Approximate read range	less than 0.5m	up to 1.5m	up to 8m	over 15m
Data transfer rate	less than 1kbps	25 kbps	up to 800 kbps	over 1Mbps
Applied standards: ISO	ISO 11784 ISO/IEC 18000-2A ISO/IEC 18000-2B	ISO/IEC 14443 ISO/IEC 15693 ISO 18000-3	ISO 18000-6A ISO 18000-6B ISO 18000-6C	ISO 18000-4 ISO/IEC 24730-2
EPCglobal			EPC: Class 0 Class 1 Class 1 Gen 2	

V. Practical Realization and Implementation of RFID System

For the purposes of the Digital Electronics Laboratory at the Faculty of Electronic Engineering, University of Nis, a system that performs control and track access to lab computers is developed. The system is composed of hardware terminal for interaction with users and software package on the server's side [6]. This hardware terminal is the primary focus throughout this paper.

For the design of hardware was used microcontroller from PIC18F family, that is the main part of hardware terminal in which appropriate firmware is embedded. This microcontroller performs overall operations of the hardware terminal. Other system components are graphic LCD display 128x64 dots with touch panel and RFID transceiver for interaction with users and their identification. For communication with the server via TCP/IP network, Ethernet controller ENC28J60 is used. RFID reader is selected to work at 125kHz operating frequency band because of several reasons. Some of them are: price, availability, ease of implementation and use of standard instrumentation without expensive tools for the design of high frequency system. Block diagram of described hardware terminal is given in Fig. 3.

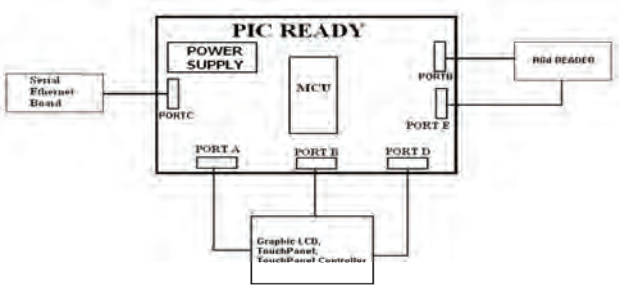

Fig. 3. Hardware terminal block dagram

VI. How System Works

The system works as following. While the inclusion of the system, on the display appears the message "PLEASE WAIT WHILE CONNECTION IS ESTABLISHED...", where assigning address from a DHCP server is checked.

After address is assigned to the terminal system and mutual communication with server is established, display gets following look, Fig. 4.

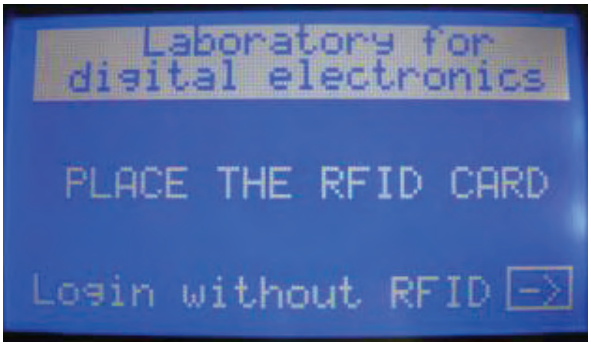

Fig. 4. The appearance of the initial screen

User logs in using RFID tags or, in case if there is no tag access enabled, directly through the touchscreen, and using PIN code that is entered via the keypad that appears on the touchscreen, as can be seen in Fig. 5.

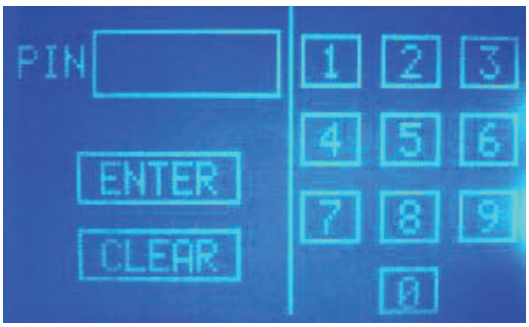

Fig. 5. The screen for entering the PIN code

If user enters a wrong PIN code or the number of RFID tag is not valid, following message will be displayed on the screen: “NOT VALID RFID OR PIN”.

If entered PIN code and RFID tag code (if RFID tag is used for accessing) matches with the values from the database on server, next picture will be displayed on screen, Fig. 6, allowing the user to select a free computer on which wants to work.

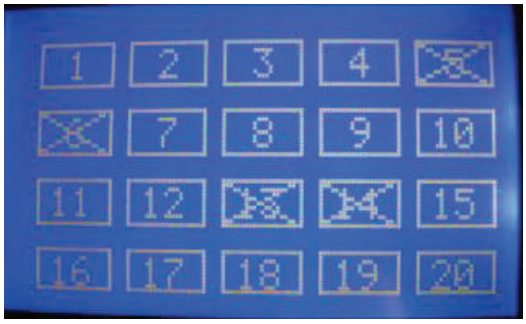

Fig. 6. Selection computer screen

If a crossed square with the computer numbers inside appears on the screen, it means that corresponding computer is busy and the user can not select it, while others are free to use. When the user selects the desired computer, the message of successful login to the computer is displayed on the screen, and then the system returns to the initial state where it waits for next user and previously selected computer starts with adequate access.

In case of losing communication with server, stoppage of packets receiving from it for defined time, the messages “BAD ETHERNET LINK” appears on the screen and than terminal retries to renew address from DHCP and restore communication with server. In this way the system is prevented from getting stuck.

This system is designed to be user friendly and easy to use. The system is very reliable and great attention to reducing in power consumption and increasing in speed is payed. Also, there is no possibility for system to stuck. Possible number of system users and computers, that system controls, is large enough and can be easy changed, which makes the system flexible for use. Look-out of assembled system is shown in Fig. 11.

Fig. 11. Look-out assembled system

VII. Conclusion

In this paper the description of RFID systems and their comparison from aspect of the operating frequencies are presented. An overview of characteristics of various RFID systems depending on operating frequency band and one concrete realization of RFID system for access control are given, too.

Lower frequency RFID systems use a larger-sized antenna to obtain the best transmission range and therefore occupy larger surface than the higher frequency RFID systems, that is disadvantage of lower frequency systems. Their speed of data transmission is quite slower and reading range is smaller in contrast to the higher frequency RFID systems, which is another disadvantage of lower frequency systems. They have advantages to work well in the presence of obstacles, as well as lower prices as opposed to high frequency system. Another advantage of lower frequency RFID systems is easier way of development and implementation, contrary to high frequency systems.

On the other side, described system for access control is successfully realized and implemented in Digital Electronics Laboratory at the Faculty of Electronic Engineering, University of Nis.

References

[1] K. Finkenzeller, “RFID Handbook – Fundamentals and Applications in Contactless Smart Cards and Radio Frequency Identification and Near-Field Communication”, 3rd edition, Wiley, 2010, ISBN: 978-0-470-69506-7.

[2] M. Ward, R. van Kranenburg, G. Backhousee, “RFID: Frequency, standards, adoption and innovation”, JISC Technology and Standards Watch, 2006.

[3] “Understanding RFID and Associated Application”, Psion Teklogix, Inc. 2004.

[4] Advanced, comprehensive C compiler for PIC MCUs, http://www.mikroe.com/en/compilers/mikroc/pic/.

[5] M. Verle, “PIC microcontrollers”, Mikroelektronika, Belgrade, Serbia, 2005, ISBN: 978-86-84417-14-7.

[6] A. Gosic, A. Lakicevic, M. Obradovic, M. Milivojevic, “Digital electronic laboratory access control system”, Proc. IEEESTEC, 2nd Student projects conference, pp. 55-58, Nis, Serbia, 2009, ISBN 978-86-6125-001-9.

Impact of Document Spectral Hue Intensity on Fax Compression Ratio

Student authors: Vladimir R. Ristić[1], Nemanja J. Mitić[1] and Dušan S. Marjanović[1]
Mentors: Radomir S. Stanković[2] and Dušan B. Gajić[2]

Abstract - **This paper presents the results of a student research done on analysis of impact of grey colour presence on the efficiency of the one-dimensional fax compression. The objective of analysis is to validate the implementation of advanced compression methods. Through performing a simulation of the modified Huffman compression, using a C++ software implementation, various experimental results were gathered. For example, after analysis of results a strong dependency of middle intensity spectral hue area coverage on compression ratio is detected. The implementation has solid real-world performance, but it was primarily developed with educational purposes in mind.**

Keywords - **One-dimension fax compression, modified Huffman compression, fax compression methods.**

I. INTRODUCTION

The main intention of the research leading to this paper was to obtain practical knowledge about the significance of advanced compression methods. The methodology rests upon simulation of real environment conditions using representative document patterns. Architecture of dialog based MFC application used for this research is simple. Input document image is a BMP file. Access to the bits that encode document image pixels is enabled using *dynamic_bitset* class [5] from the Boost C++ Libraries [4]. Application is developed in Microsoft Visual Studio 2010 IDE. Results are gathered manually and processed by Microsoft Excel 2007. More complex pattern sets require further aplication version to be featured with automatically gathering and graphically presenting the results through its own GUI.

A. Fax standards

ITU-T, former Comité Consultatif International Téléphonique et Télégraphique is a part of the International Telecommunications Union. Although this body declares its acts as "Recommandations", international standards are mandatory in a form of national laws of countries which adopted them.

Standard T.3 (Group 3 fax) introduced digital devices using analog lines for data transmission and was first to consider the image data compression standardization. Standard T.4 involves significant compression algorithm improvement and T.6 standard (Group 4 fax) is implying digital telecommunication lines (for example ISDN) [2].

B. Data compression

Data compression algorithms can be lossy or lossless [1]. If we consider data as a coded entity from real world, and information as useful data then even lossy compression algorithms save the actually desired information. Lossless compression saves all the data, useful at the present moment but also data that might be useful later. Fax data compression is saving all data, so the lossless compression is implemented.

C. Facsimile compression

Result of scanning process is a monochrome bit mapped file, which is to be send to destination fax. Compression is performed to remove data redundancy, thus decreasing the file size to reduce the file transferring time. **Modified Huffman (MH) compression** method is used, a run-length codebook based statistical algorithm [2]. Statistically, there will be more white areas on document than black ones, so codebook contains shorter words for white pixel sequences. MH algorithm takes into count most common pixel sequences which are 2-4 of black and 2-7 of white, so they are coded with shortest codes. Here is the main compression problem. White area is represented with white pixels and black area is represented with black ones. When middle intensity spectral hue is scanned, optical scanning system generates alternating sequence of black and white pixels. As the single pixel sequence is rare it will be coded with word longer than one bit [1]. It means that those sequences will deteriorate the compression. Determining the rate of this impact is the primary goal of this work. Method described above is the so called **one-dimension fax compression** [1]. It is used for T.3 Recommendation standard implementation. Advanced T.4 standard is based on Modified Read (MR) which is known as two-dimension fax compression. This method initializes encoding in the manner of MH method for the first scanned line on page, but second line is then compared to the first one and differences are encoded. Every next line is compared to the previous one as reference to encode the further

Student authors:
[1]Vladimir R. Ristić, Nemanja J. Mitić and Dušan S. Marjanović are with the University of Niš, Faculty of Electronic Engineering, Aleksandra Medvedeva 14, 18000 Niš, Serbia, E-mails: nemanja.mitic@elfak.rs, studentristicvladimir@gmail.com, dusan.marjanovic@elfak.rs.
Mentors:
[2]Radomir S. Stanković and Dušan B. Gajić are with the University of Niš, Faculty of Electronic Engineering, Aleksandra Medvedeva 14, 18000 Niš, Serbia, E-mails: radomir.stankovic@gmail.com, dusan.gajic@elfak.ni.ac.rs.

differences. This method is especially effective when differences are small or none. Bad side of MR method is that data transition error propagates through the whole page. T.4 standard does not provide correction of errors, but provides number limitation of lines encoded by MR between the lines encoded by MH method. T.6 Recommendation standard allows more MR encoded lines between MH encoded lines due to improvement of reliability of digital lines [1].

D. ITU-T document patterns

In developing code for T.3 standard, ITU-T took eight representative documents as statistical patterns. Optimal codebook was efficiently derived through counting all black and white pixel sequences. As those documents are copyrighted by ITU-T they cannot be used as experimental material [1]. So, new reference document set is created.

II. Algorithm of Choice for Compression

Crucial moment during the development process is **fax compression method** choice. Properly selected algorithm must meet both the requirements for high rate lossless compression and for high efficiency, resulting in short image processing time. As those requirements are in contradiction, the primary goal is finding an optimal solution.

Total fax device costs, C_t consists of initial costs C_i (device price) and operating costs C_o (including phone bills):

$$C_t = C_i + C_o \quad (1)$$

$$C_t = f'_{ci}(A_c) + f''_{tt}(A_c) \quad (2)$$

Initial costs (blue curve in Figure 1.) directly depend on compression algorithm complexity and operating costs (red curve) directly depend on compression ratio, i.e. operating costs indirectly depend on compression algorithm complexity. In this case, sum of two opposite depending functions of the same argument (green curve) has a local minimum. Projection of the local minimum onto the axe of compression algorithm complexity indicates an optimal algorithm.

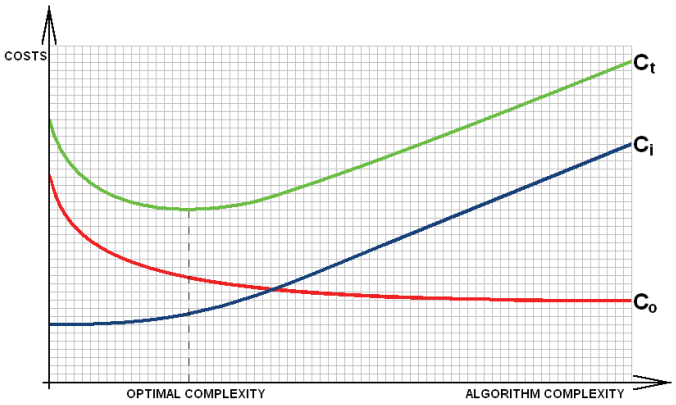

Fig. 1. Fax device costs dependencies on algorithm complexity.

Factors, additionally influencing this optimum, can be classified into two groups: as environmental and as implementational. A fax device development doesn't set the environmental factors (quality of telecommunication infrastructure, payment rates etc.), but must consider them. What development sets are implementational factors (device resolution, modulation type, data transmission rate etc.). From the standpoint of economy, key feature of cost effective device exploitation, is implemented compression algorithm.

If some document property has a huge negative impact on fax compression rate using conventional methods, advanced compression methods should be implemented to solve this problem.

III. Reference Document Set

For this research, the original reference was unavailable, but the document description was available. As the focus of experimental work was on compression rate deterioration, caused by incensement of middle intensity spectral hue coverage, reference document set was modified. Facsimile optical system converts any document image into monochromatic file. More intense hue document is converted into a bit map that contains more dense black pixels among white pixels, and vice versa. Half intensity hue is converted in alternating black and white pixel sequence.

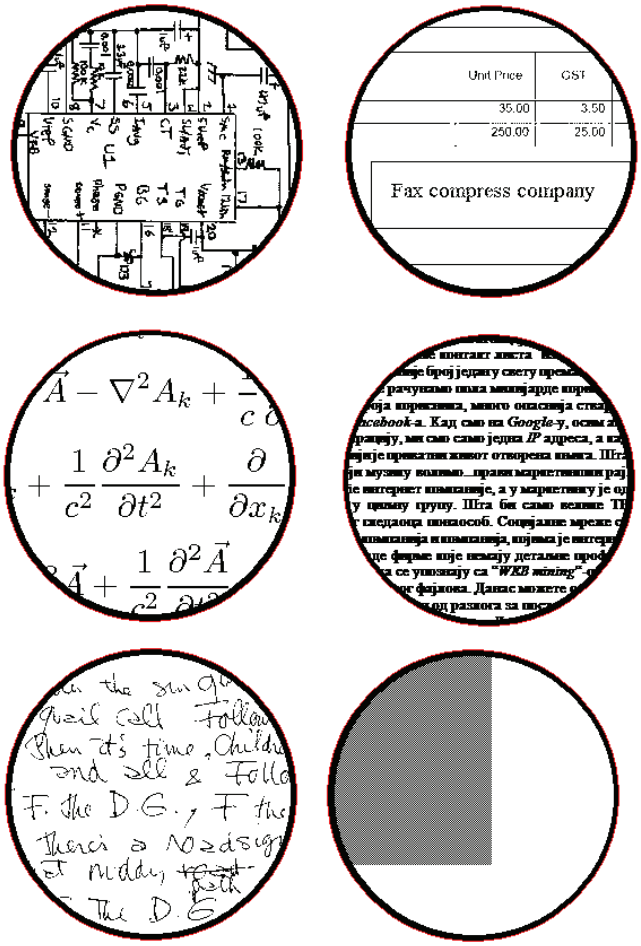

Fig. 2. Reference document parts.

In order to simulate documents with middle intensity hue, a series of BMP files was created containing various area percentage of alternating black and white pixels. Modified reference set consists of seven representative document images, one image file completely filled with black pixels, and four files with 6%, 13%, 25% and 50% of area filled with half-intense gray hue in form of alternating B/W pixels.

Figure 2. shows parts of image files used to simulate representative documents. Obviously, invoice document image (second circle part) contains longest sequences of black or white pixels, while dense document image (fourth circle part) consists of very short sequences of the same color pixels, not counting the last circle with alternating area. It is expected in experiments to get the result set that is in accordance with this note, i.e. best compression ratio for invoice image, and worst in case of dense document or document with alternating black and white.

IV. Software Simulation

Main dialog of graphic user interface is shown in Figure 3.

Fig. 3. Software simulation user interface.

Reason for choosing C++ rather than some other program languages was its high speed and performance of executive code, as well as its bit manipulation capabilities. Application is a simulation of one-dimension fax compression.

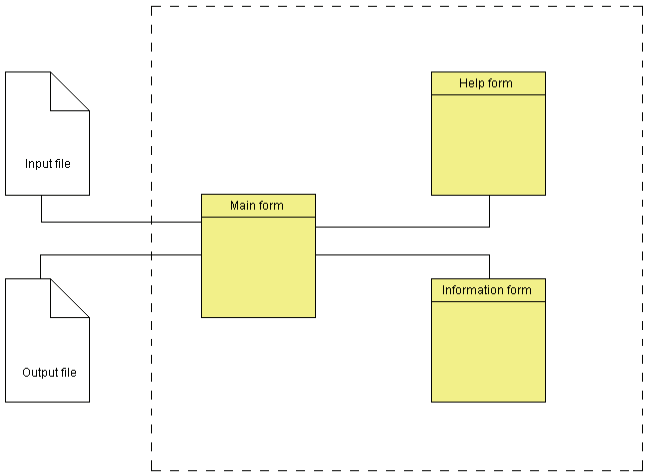

Fig. 4. Simulation program architecture.

Codebook is realized as a bit array vector. Input bitmap file is processed row by row, loading the bitset vector and counting the same color pixels in sequence within. Code words are written into a binary file. Decompression is not implemented, as it is not relevant for compression ratio data set.

V. Results and Analysis

As expected, the experimental results confirmed the theory. As Table I shows, there is a huge compression efficiency variation caused by document properties.

TABLE I
COMPRESSION RATIO AND TIME

No.	Document type	In (B)	Out (B)	Ratio (%)	Time (ms)
1	Business letter	109416	84819	77	31
2	Electric circuit	104960	95922	91	47
3	Invoice	83412	27722	33	16
4	Dense report	100032	108400	108	47
5	Equations	65604	44534	67	15
6	Dense document	108600	122288	112	46
7	Handwritings	54450	37594	69	16
8	Black area 100%	75000	2900	3	16
9	Gray area 50%	75000	327643	436	94
10	Gray area 25%	75000	170227	226	47
11	Gray area 13%	75000	86429	115	31
12	Gray area 6%	75000	48394	64	15

We can note that very dense documents have negative compression ratio. Average pixel sequence length is close to one. This effectively approaches to negative impact of gray

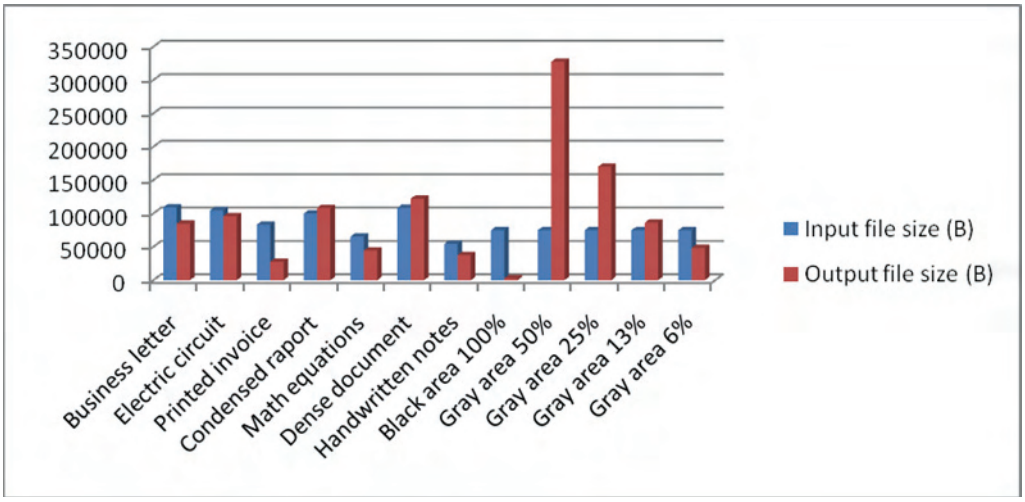

Fig. 5. Input file size variations.

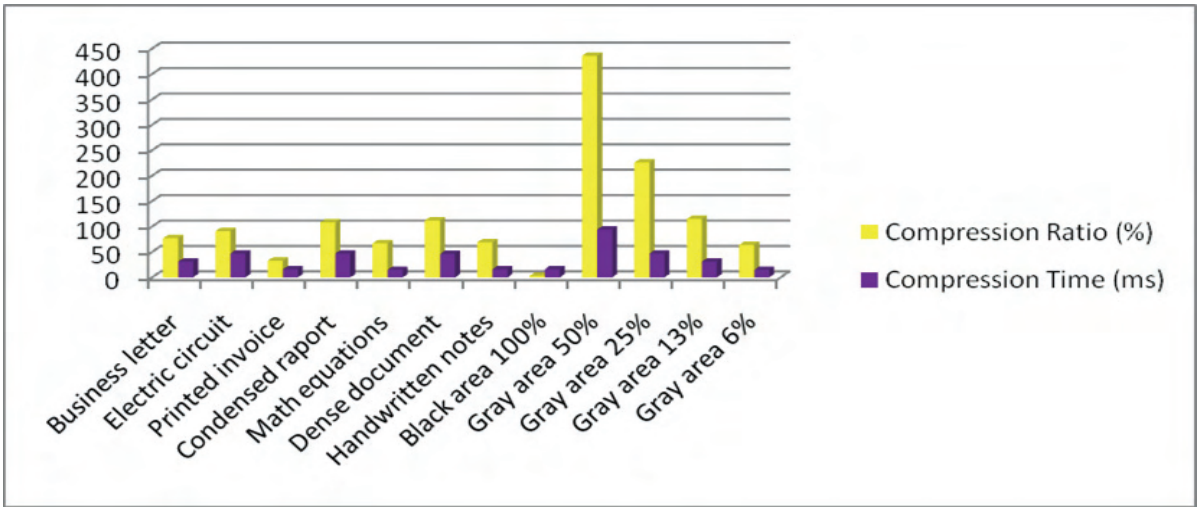

Fig. 6. Compression ratio and time variations.

hues on compression ratio. Invoice has huge white area coverage, resulting in high compression ratio.

The minimal rate of compression minimal is 3%. This is also theoretical minimum due to contextual data in coded file.

Strong compression ratio and compression time dependencies on percentage of middle spectral hue coverage on document are very notable facts. For turning compression rate into negative value, it is enough that the document contains more than 10% of this area. Still, facsimile is prevalent use for documents with high contrast degree rather than with middle intensity spectral hues.

VI. Conclusion

The programming implementation is able to execute both the task of image compression and of compression ratio measuring. It was found appearance of hues of middle intensity has strong negative impact on compression ratio. Experimental results in conjunction with the starting assumption lead us to conclusion that advanced compression methods application is conditionally sustainable. This stands under the assumption that the telecommunication infrastructure is of high quality which provides low data transmission error rate.

Device implementation environment is a key factor to be considered when implementing two-dimension facsimile compression method. In digital infrastructure environment this is method of choice.

References

[1] David Salomon, *Data Compression: The Complete Reference*, 3rd edition, Springer, 2004. (ISBN 0-387-40697-2)
[2] http://en.wikipedia.org/wiki/Fax, 23. 12. 2010, 18:00.
[3] http://en.wikipedia.org/wiki/Data_compression, 24. 12. 2010, 16:00.
[4] http://www.boost.org, 14. 11. 2010, 9:00.
[5] http://www.boost.org/doc/libs/1_45_0/libs/dynamic_bitset/dynamic_bitset.html, 14. 11. 2010, 13:00.
[6] http://www.britannica.com/EBchecked/topic/199972/fax, 27.12.2010, 20:00.

Critical Analyses of International Standards for Non-ionizing Radiation

Student authors: Liliya Zh. Petrova[1]
Mentor: Plamen Angelov

Abstract: ***In the article we will present a comparison between the international norms for non-ionizing radiation and comparative analysis with the norms of Bulgaria.***

Keywords – Non-ionizing radiation, European standard

I. TASK OF THE ARTICLE

A .Introduction:

The concept in this paper is to show the limit emission levels for non-ionizing radiation. In order to make comparison is necessary to define the tasks that be conducted. In the first part will be compared between non-ionizing radiation in industrial sector and the general population. The second part is for the rules adopted by the EU and Bulgaria. The article finishes with conducting a numerical experiment to determine the maximum level of non-ionizing radiation.

B. Comparison of European standards for non-ionizing radiation. Analysis for the values between industrial conditions and the general population.

Following a comparison of the values presented in Tables 1 and 2 it can be seen that the values at industrial conditions are significantly higher - as well as the frequency range within 8Hz ÷ 1MHz is divided into four. In the second table the same frequency range is divided into five parts. Since there are such differences it will be able to be shown the different influence of frequencies.
International Commission ICNIRP (Commission for Non-Ionizing Radiation Protection) proposes to introduce levels of control under production conditions. In 1999 it provides recommended levels which are marked in Table 1 and Table 2
It is best to make a separate table for the range of 400 ÷ 2000MHz because various standards fall in this range. Table 3 was made according to rules announced by the ICNIRP - International Organization for Non-Ionizing Radiation Protection. By the table it is noted that there is a difference of 54.2 percent of the electric field in the protection of the population while the strength of the electric field is 53.8%. There are also differences in the magnetic induction which is 54% and the power of density has a difference of 60%.

C. Comparison with the European standards adopted in Bulgaria.

Confirmation of rules paste in table 3 using published in 2008, "Directive 2004/40/EC of the European Parliament and Council, as the last change made with M3 under Regulation (EC) N 1137/2008 of the European Parliament and Council [1].
The frequency range considered in Table 3 is for types of production limitations in the range of 400 ÷ 2000MHz. The ordinance which is used in Bulgaria for regulation levels of Non-Ionizing Radiation is - N9 [2].

To be conducted comparisons is necessary to adjust the parameters which will be compared because different values are adopted for the equivalent. In Bulgaria the values of the Ordinance are $S = 10\mu W / sm^2$ which is within the frequency range of $f = 0{,}3 \div 30GHz$. To make the transformation is necessary to use the next calculations:

$$S = 10\mu W / sm^2 \Rightarrow S = \frac{10}{10^{-4}}\mu W / m^2 \Rightarrow S = 10^5 \mu W / m^2 = 100mW / m^2 = 0{,}1W / m^2 \quad (1)$$

The ordinance does not clearly defined frequency range of the network and there is no defined distance and distinction for the production environment. The graphical comparison between European (ICNIR), U.S. (FCC) and Bulgarian standards is shown in fig.1 and fig.2. Frequency range of analysis is chosen to include WiFi networks. The returnees result shows clearly the low value of the exposure that was accepted in Bulgaria to the rest of the world's recommendations.On the other side to implement the research on wifi networks is necessary to know that the power density depends on the distance measurement which is raised to the second degree [4]:

$$S = \frac{PG}{4\pi r^2} \quad (2)$$

where: P - transmitted power; G – gain (factor on amplification) of the antenna and r - distance measurement.

Student autors:
[1]Liliya Zh. Petrova Student of Burgas Free University Degreed Computer Systems and Technologies studding Computer Systems and Technologies. E-mail: lily_burgas@yahoo.com

Mentor:
Assprofessor Plamen A. Angelov, Faculty of Computer Science and Engineering, Burgras Free University, 62 San Stefano Str., Burrgas-8001, Bulgaria, E-mail: pangelov@bfu.bg

D. Alternative methods of miming

From data obtained (Fig. 3) it is clear that the limit rates for non-ionizing radiation are met after crossing the border of 15m. This is due to the high output power embedded in the testing set. Practically the value of 250mW can be achieved only by changing the Firmware of the router. The reason of such change is to increase the operating range of the router or changing the speed of communication for distance users. But whatever the reason is the limi t of 250mW remains real and must be complied with WiFi networks.

II. CONCLUSIONS

1. There are significantly lower levels in Bulgaria than the recommended standards of ICNIR and FCC. The only addition may be the defined distance measurement and control.

2. After a numerical simulation we can see that the running router with radiated power of 250mW has the limit distance of 15m. Practically the power of the broadcast router is variable and rarely reaches this limit level.

REFERENCES

[1] Директива 2004/40/ЕО на европейския парламент и на съвета относно минималните изисквания за здраве и безопасност, свързани с експозицията на работниците на рискове, дължащи се на физически агенти (електромагнитни полета)(осемнадесета специална директива по смисъла на член 16, параграф 1 на Директива 89/391/ЕИО. Официален вестник L3113/стр.1./21.11.2008

[2] Наредба № 9 от 1991 г. за пределно допустими нива на ЕМП в населени територии и определяне на хигиенно защитните зони около излъчващи обекти (Обн. ДВ. бр.35 от 3 май 1991г., попр. ДВ. бр.38 от 14 май 1991г., изм. ДВ. бр.8 от 22 януари 2002 г.)

[3] GUIDELINES FOR LIMITING EXPOSURE TO TIME-VARYING ELECTRIC, MAGNETIC, AND ELECTROMAGNETIC FIELDS (UP TO 300 GHz) International Commission on Non-Ionizing Radiation Protection, 1999 Health Physics Society

[4] Neubauer, G., Roosli, M., Feychting, M., Hamnerius, Y., Kheifets, L., Kuster, N., Ruiz, I., Schuz, J., Uberbacher, R., Wiart, J.Study on the Feasibility of Epidemiological Studies on Health Effects of Mobile Telephone Base Stations – Final Report March 2005 Copy No. 1 ARC-IT—0124

[5] International Commission on Non-Ionizing Radiation Protection GUIDELINES FOR LIMITING EXPOSURE TO TIME-VARYING ELECTRIC, MAGNETIC, AND ELECTROMAGNETIC FIELDS (UP TO 300 GHz)

TABLE.1. REFERENCE LEVELS FOR OCCUPATIONAL EXPOSURE TO TIME-VARYING ELECTRIC AND MAGNETIC FIELDS [5]

Frequency range	Electric field strength E (V/m)	Magnetic field strength H (A/m)	Magnetic flux density B (μT)	Equivalent plane wave power density Seq (W/m2)
0 ÷ 1Hz	-	1,63.105	2.105	-
1 ÷ 8Hz	20000	1,63.105/f2	2.105/f2	-
8 ÷ 25Hz	20000	2.104/f	2,5.104/f	-
0,025÷0,82kHz	500/f	20/f	25/f	-
0,82÷65kHz	610	24,4	30,7	-
0,065 ÷ 1 MHz	610	1,6/f	2,0/f	-
1÷10MHz	610/f	1,6/f	2,0/f	-
10÷400MHz	61	0,16	0,2	10
400÷2000MHz	3.f1/2	0,008.f1/2	0,01.f1/2	f /40
2÷300GHz	137	0,36	0,45	50

TABLE.2. REFERENCE LEVELS FOR GENERAL PUBLIC EXPOSURE TO TIME-VARYING ELECTRIC AND MAGNETIC FIELDS [5]

Frequency range	Electric field strength E(V/m)	Magnetic field strength H (A/m)	Magnetic flux density B (μT)	Equivalent plane wave power density Seq (W/m2)
0 ÷ 1Hz	-	3,4.104	4.104	-
1 ÷ 8Hz	10000	3,4.104/f2	4.104/f2	-
8 ÷ 25Hz	10000	4000/f	5000/f	-
0,025÷0,8kHz	250/f	4/f	5/f	-
0,8 ÷ 3 kHz	250/f	5	6,25	-
3 ÷ 150kHz	87	5	6,25	-
0,15÷1MHz	87	0,73/f	0,92/f	-
1÷10MHz	87/f1/2	0,73/f	0,92/f	-
10÷400MHz	28	0,073	0,092	2
400÷2000MHz	1,375. f1/2	0,0037. f1/2	0,0046. f1/2	f /200
2÷300GHz	61	0,16	0,20	10

TABLE.3. COMPARATIVE ANALYSES OF THE REFERENCE LEVELS

Exposure limit for	Frequency range MHz	Electric field strength E (V/m)	Magnetic field strength H (A/m)	Magnetic flux density B (μT)	Equivalent plane wave power density Seq (W/m2)
Occupational exposure	400÷2000	$3.f^{1/2}$	$0{,}008.f^{1/2}$	$0{,}01.f^{1/2}$	f /40
Public exposure limit	400÷2000	$1{,}375.\ f^{1/2}$	$0{,}0037.\ f^{1/2}$	$0{,}0046.\ f^{1/2}$	f /200

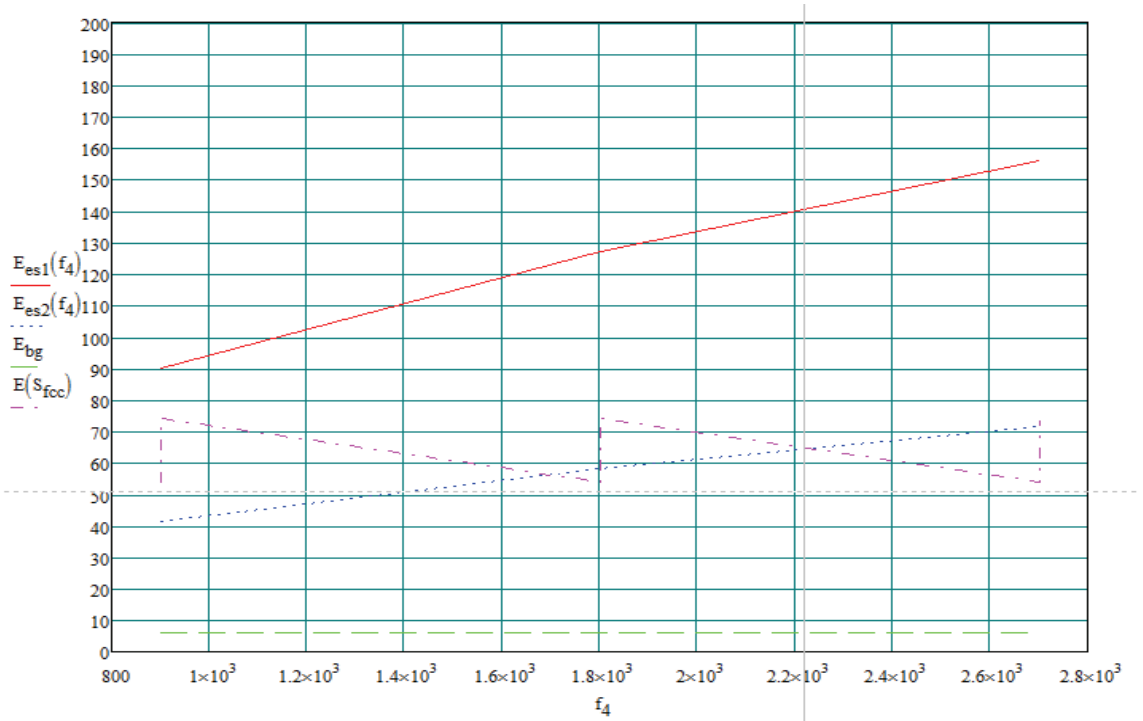

Fig.1. Comparison of Electric field strength in the range of 800MHz ÷ 2800 MHz and accepted standards for electric fields E

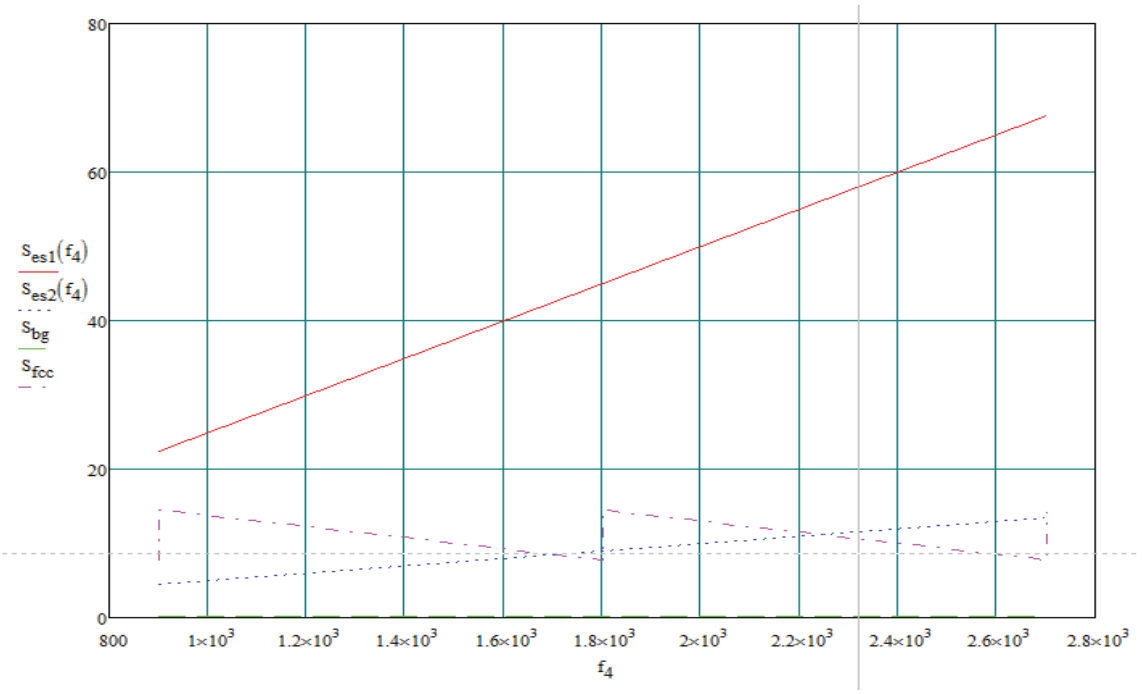

Fig.2. Comparison of accepted standards in the frequency range of 800 MHz ÷ 2800 MHz for the power density S

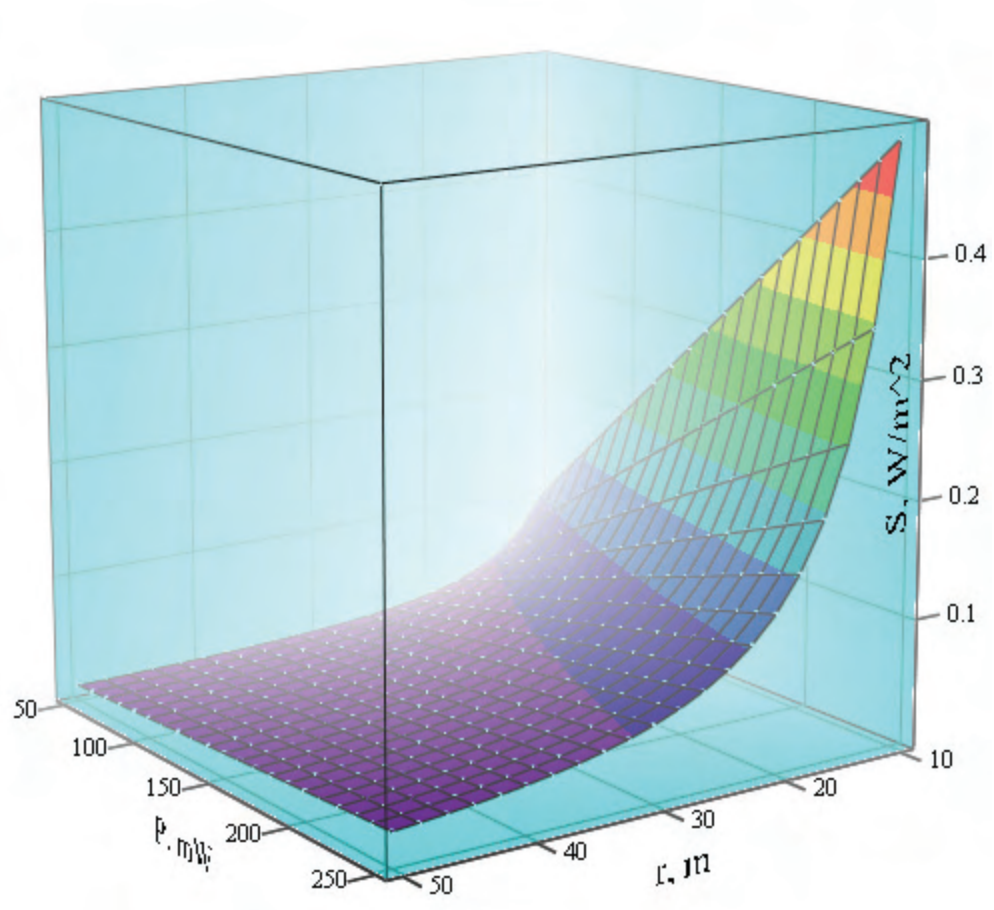

Fig.3. Amendment of the power density S, the modification of transmitter power P = 50 ÷ 250mW, distance r = 10 ÷ 50m and G = 2,5

Investigation of Localization Accuracy in Wireless Sensor Networks

Student authors: Vasil Dimitrov, Georgi Georgiev
Mentor: Rozalina Dimova

***Abstract* – The paper presents results from some sensor network challenges investigations – accuracy of localization techniques. Critical demand in wireless sensor networks (WSN) introducing in industry is to be localized with high precision. Our investigations purpose is to present localization sensor nodes in one area with minimal error. The statistical results from MatLab 7.9 simulations show the dependence of mean square error and the limit of Cramer-Rao in unknown sensor nodes localization, using anchors.**

***Keywords* – Localization, wireless sensor.**

I. INTRODUCTION

Wireless sensor networks are new technology, which atracts appreciable investigation interest through the last few years. The last developments in this area have made the sendor nodes small, inteligent and running many functions [1]. There are many interesting applications of the sensor networks like watching the environment, tracing orders and etc.These new applications require placing many sensor nodes in big geometric areas, as the benefit of them depends on the automatic and certain evaluation of their location. This would lead to correct indentifying of important places, when some event happens. Moreover, the certain location may be helpful for processing information, tasks, requests [2].

In the distributed localization is necessary to have a number of nodes,which coordinates are known. These nodes are ususally named anchors. The locations of the nodes is unknown, exept of the anchors. Due of the limits of the power, the communication between the nodes is restricted do local neighbours. The sensor nodes have the opportunity to measure the distance and the angle of the location to neighboring nodes [3]. Based on evaluation like that, they must define their spaced placement, by geometric techniques named: Trilateration and triangulation [4].

The method localization must be with good accuracy,and no matter of the space, the error should be reasonably slight.

Student autors:
[1]V.Dimitrov is with the Technical University of Varna, ul. Studentska 1, 9010 Varna, Bulgaria (phone: +359-52-383350; e-mail: v_1986@abv.bg).
[2]G.Georgiev, is now with the Technical University of Varna, ul. Studentska 1, 9010 Varna, Bulgaria; (phone: +359-52-383350, e-mail: georgi_ygeorgiev@yahoo.com)

Mentor:
Dr. R.Dimova is with the Technical University of Varna, ul. Studentska 1, 9010 Varna, Bulgaria; (phone: +359-52-383350, e-mail: rdim@abv.bg)

II. MEASUREMENT ACCURACY POSITIONING

To be able to make a realistic assessment of the accuracy in localization, we test already approved in practice mathematical methods.

A. Mean square error - MSE

Mean square error (MSE) of estimator quantify the difference between estimator and true value of quantify being estimated [5]. MSE measure average of square of error. The error is the sum with which estimator differs from quantity to be estimated. The MSE of estimator $\hat{\theta}$ with respect to estimated parameter θ can be presented as:

$$MSE(\hat{\theta}) = E\left((\hat{\theta}-\theta)^2\right) \quad (1)$$

The MSE is equal to sum of variance and squared bias of estimator

$$MSE(\hat{\theta}) = Var(\hat{\theta}) + \left(Bias(\hat{\theta},\theta)\right)^2 \quad (2)$$

In other words, the more precisely estimated location of unknown node is equal to less MSE [6].

B. Cramer-Rao lower bound (CRLB)

Cramer-Rao bound define the ultimate accuracy of any estimation procedure [7]. This lower bound is intimately related to the maximum likelihood estimator. If I_θ is the Fisher information matrix (FIM), for unknown parameter $p(z \mid \theta)$.

$$I_\theta = E\left\{\frac{\partial \log p(z\mid\theta)}{\partial\theta}\left(\frac{\partial \log p(z\mid\theta)}{\partial\theta}\right)^T\right\} \quad (3)$$

then CRLB can be presented as:

$$E\{(\hat{\theta}-\theta)(\hat{\theta}-\theta)^T\} \geq I_\theta^{-1} \quad (4)$$

where θ is unbiased estimate of θ and I_θ is the FIM.

One of easy way to compare different positioning algorithms is with their MSE. When MSE is lower bounded by the CRLB the result is minimum mean-square error (MMSE). The last one can be presented as:

$$MSE \triangleq E\left\{\left\|\hat{\theta}-\theta\right\|^2\right\} = trace\left[E\left\{(\hat{\theta}-\theta)(\hat{\theta}-\theta)^T\right\}\right] \geq \ldots$$

$$\ldots \geq trace[I_\theta^{-1}] \triangleq MMSE \quad (5)$$

MMSE for RSS-based positioning system [8] is:

$$MMSE_{RSS} = \left(\frac{\ln 10}{10n}\right)^2 \frac{\sum_{i=1}^{Nm}\sigma_{sh,i}^{-2}d_i^{-2}}{\sum_{i=1}^{N_m}\sum_{j=1}^{i-1}\sigma_{sh,i}^{-2}\sigma_{sh,j}^{-2}d_i^{-2}d_j^{-2}\sin^2(\psi_i-\psi_j)} \quad (6)$$

where n is the path lost exponent, $\sigma^2_{sh,i}$ is the variance of the log-normal shadowing for the ith measurement and

$$d_i = \sqrt{(x - x_i)^2 + (y - y_i)^2} \quad (7)$$

is the distance between unknown node and ith known node. The accuracy of RSS-based positioning depend on channel parameters and estimates at all nodes [9].

III. Numerical Results and Analysis of the Sensor Network

In order to evaluate the described approaches to sensor network localization, many numerical tests were performed. We performed a variety of simulation experiments to cover a wide range of network system configurations including the size of the network (number of nodes), the number of anchor nodes, anchor nodes deployment, the radio range, the distance measurement error and computation time. The key metric for evaluating all listed measurement was the accuracy of the location.

A. Description of the system

Let us consider L anchors, with coordinates (x_i , y_i) where i=1,...,L, are random placed in two-dimensional (2D) plane with size (x_{max} , y_{max}). The coordinates of the anchors are known. During the each of K simulations the positions of anchors are static. In this plane are random placed also LL unknown nodes, with coordinates (x_{0i} , y_{0i}) i=1,...,LL. From the propagation point of view the measurement are assumed to be made under line of sight condition. The true distance between one anchor and one unknow node is d_i and can be determine like:

$$d_i = \sqrt{(x_0 - x_i)^2 + (y_0 - y_i)^2} \quad (8)$$

The measured distance is:

$$r_{d_i} = d_i + \varepsilon_i \quad (9)$$

where ε_i ~N(0, σ_i^2) is the zero mean Gaussian noise with variance σ_i^2.

B. Examined parameters of the system

We examined the impact of the following parameters over localization in sensor network:

- Number of anchors - L
- Number of unknown nodes -LL
- Noise level - ε (represented as Gaussian random variable with normal distribution with mean 0 and standard deviation σ^2)
- Speed - v (v_x - speed in direction x, v_y - speed in direction y)
- Number of simulations - K
- Iterations to update estimates - S

C. Investigating the precision of localization of one and more unknown nodes

In one real network the number of unknown nodes usually is more than one. When one unknown node is with determined position based on fixed anchors, after that it can be use like fixed anchor for other unknown nodes. In this case the number of anchors increase, respectively MSE decrease, which mean more accuracy.

Whole algorithm consists of 4 steps:

- Step 1: determine positions of each unknown node based on the fixed anchors.
- Step 2: for all unknown positions determine distance between nodes

for node $i : \left(\hat{x}^0_{(i)}, \hat{y}^0_{(i)}\right)$,

for node $j : \left(\hat{x}^0_{(j)}, \hat{y}^0_{(j)}\right)$

$$\hat{d}^0_{i,j} = \sqrt{(\hat{x}^0_{(i)} - \hat{x}^0_{(j)})^2 + (\hat{y}^0_{(i)} - \hat{y}^0_{(j)})^2} + noise^0_{i,j} \quad (10)$$

- Step 3: determine distance to L and distances to LL
  d – for fixed anchors
  $d^{(0)}_{i,j}$ - for unknown nodes
- Step 4: repeat Step 2-3 S times - iterations to update estimate

$$\hat{d}^{\alpha}_{i,j} = \sqrt{(\hat{x}^{\alpha}_{(i)} - \hat{x}^{\alpha}_{(j)})^2 + (\hat{y}^{\alpha}_{(i)} - \hat{y}^{\alpha}_{(j)})^2} + noise^{(\alpha)}_{i,j} \quad (11)$$

In this case MSE for node i is

$$MSE_i = \frac{1}{K}\sum_{j=1}^{K}\left[\left(x_0 - \hat{x}_0^{(i,j)}\right)^2 + \left(y_0 - \hat{y}_0^{(i,j)}\right)^2\right] \quad (12)$$

MSE is:

$$MSE = \frac{1}{LL}\sum_{m=1}^{LL+1} MSE_j \quad (13)$$

The Cramer-Rao bound in this case will be:

$$CRB = \frac{4\sigma^2}{L + LL} \quad (14)$$

As can be seen in Figure 1. with increasing the number of anchors MSE decrease. Interesting of this picture is that, when assume unknown node to fixed anchors the minimum bound of MSE decrease. Respectively the accuracy on the system can increase. CRB and CRB(L+LL) are not parallel, and with increasing the number of anchors they stay closer and closer. Other interesting in this picture is that, when change *S*, the accuracy of the system does not increase. This mean the system work sufficiently good with only one estimation of the position of unknown nodes.

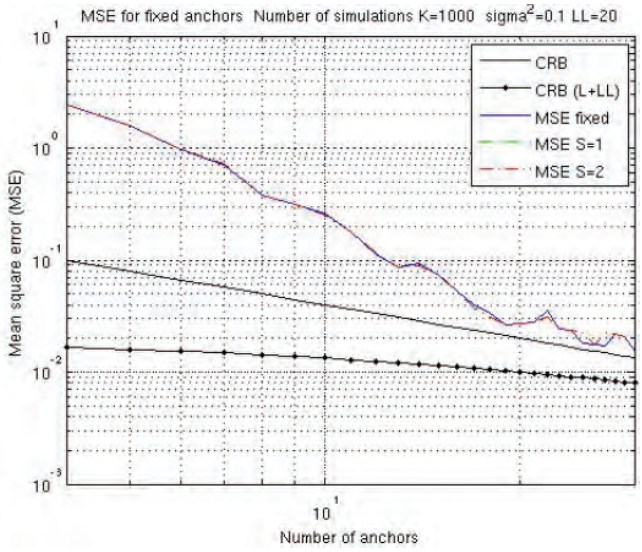

Fig. 1. Dependence between MSE and L for σ^2 =10^{-1}

Figure 2. shows the dependency between MSE and number of unknown nodes, which became anchors. The trend to decrease MSE with increasing the number of anchors holds true here.

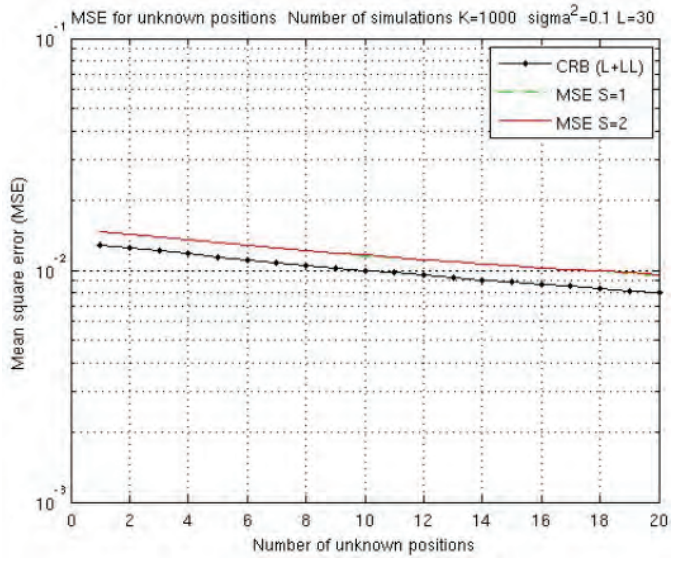

Fig. 2. Dependence between MSE and LL for σ^2 =10^{-1}

In Figure 3. shown the case, when the anchors are not sufficiently for good estimation of unknown nodes. As can be seen MSE increase with increasing number of unknown nodes, which are assumed to anchors.

Also with increasing the number of iteration to update estimates, MSE increase. This is called error propagation. On this example the number of unknown nodes does not matter for accuracy and MSE. They can not be used like anchors, because their positions can not be established sufficiently good.

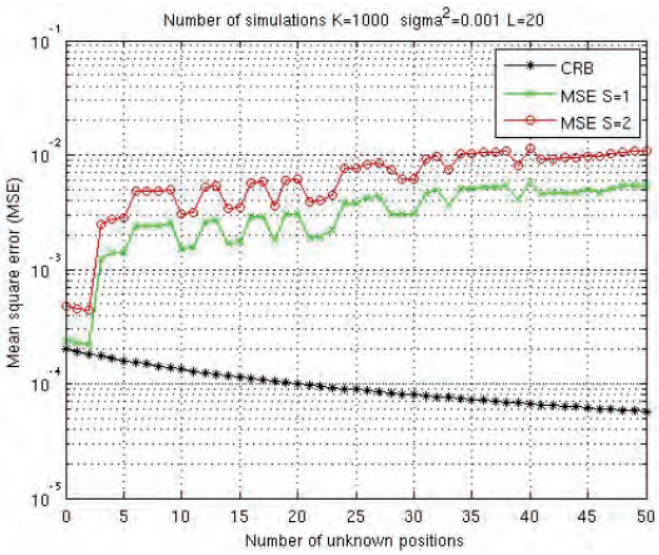

Fig. 3. Error propagation

D. Position tracking

In all up to now observed scenarios the unknown node does not change its position at the time of one simulation. In the real life the unknown node (most often human) change its position. The movement can be divide in three case: movement with constant speed, random walk and combination of both. The movement can be divided to ten steps (t=1,...,10). The first position is t=1. Then each new step can be presented as:

$$x(t+1) = x(t) + v_x T \text{ и } y(t+1) = y(t) + v_y T,$$

where $v_x T$ and $v_y T$ are the speed in direction x and the speed in direction y. According $v_x T$ and $v_y T$ movement is divided into three types:

• constant speed - $v_x T$ =const and $v_y T$ =const

• random walk - $v_x T$ =random and $v_y T$ =random

• constant speed and random walk - $v_x T$ =const+random and $v_y T$ = const + random

Therefore estimated position will be:

$$\hat{x}(t),\ \hat{x}(t+1),\ \ldots,\ \hat{x}(t+10),$$
$$\hat{y}(t),\ \hat{y}(t+1),\ \ldots,\ \hat{y}(t+10)$$

The next step can be predicted. In this case the speed for next step can be determine with these equals:

$$\hat{v}_x T(i) = \frac{1}{i}\sum_{i=1}^{i}(\hat{x}(i) - \hat{x}(i-1)) \quad (15)$$

$$\hat{v}_y T(i) = \frac{1}{i}\sum_{i=1}^{i}(\hat{y}(i) - \hat{y}(i-1)) \quad (16)$$

which use to predict next position of unknown node $\tilde{x}(i+1)$ and $\tilde{y}(i+1)$

$$\tilde{x}(i+1) = \tilde{x}(i) + \hat{v}_x T(i) \quad (17)$$

$$\tilde{y}(i+1) = \tilde{y}(i) + \hat{v}_y T(i) \quad (18)$$

So next step may be predict with determined accuracy. This algorithm can improve the performance of steepest descent algorithm and also accuracy of the system.

In the three cases the dependence between MSE and the speed is the same and it is show in Figure 4. As can be seen the MSE vary very little between 10^{-5} and 10^{-1}. After 10^{-1} MSE increased significantly.

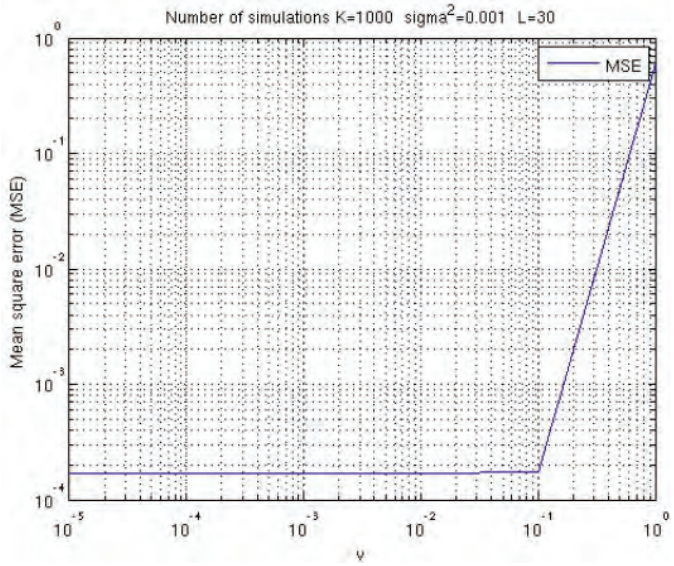

Fig. 4. Dependence between MSE and the speed

Dependence between MSE and σ^2, shown in Figure 5. When σ^2 increase, MSE increase linear.

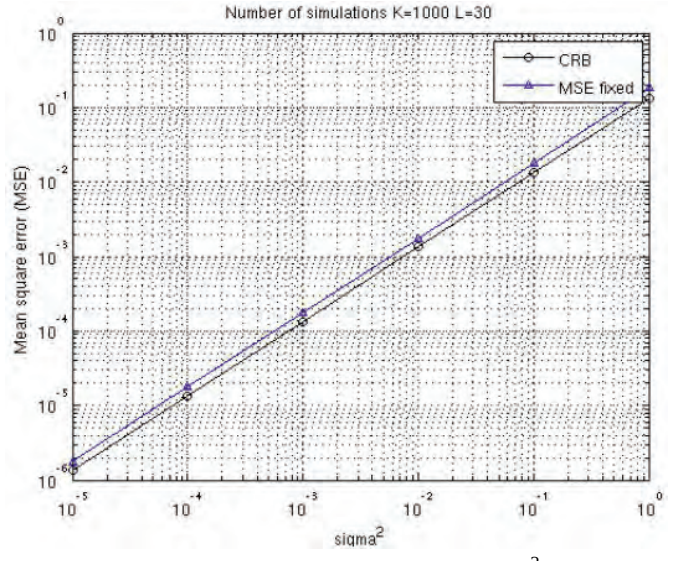

Fig. 5. Dependence between MSE and σ^2

IV. Conclusion

Finding the location of the sensor nodes is from substantially matter for building sensor networks.

To evaluate the accuracy in localization of the sensor nodes in the space,we use mean square error and the limit of Cramer-Rao.

From research done can be seen that with geometric techniques for determining the position we can accomplish relatively good lokalization. The results of the sumitaion are these:

- MSE increase linear with increasing σ^2.
- the number of anchors for sufficiently accuracy is more than theoretical number.
- increase the number of iterations to update estimates can not improve accuracy.
- unknown node can be use like anchors only if anchors are more than few times theoretical number.
- the algorithm of predicting can be applied to improve the localization of the unknown nodes.

Based on the wrought researches in future may be improved the communication between the rest of the sensor nodes and to be relegated the cost price of the system.

Acknowledgement

This paper was developed in the frames of the research project № DVU01/0109 “Research on Cross Layer Optimization of Telecommunication Resource Allocation“ in the frames of FNI, Ministry of Education, Bulgaria .

References

[1] D. Estrin, L. Girod, G. Pottie, M. Srivastava, “Instrumenting the world with wireless sensor networks,” *In Proceedings of the International Conference on Acoustics, Speech and Signal Processing (ICASSP 2001)*, Salt Lake City, Utah, May 2001.

[2] C.-Y. Chong and S. P. Kumar, "Sensor networks: evolution,opportunities, and challenges," Proceedings of the IEEE, vol. 91, pp.1247-1256, 2003.

[3] D. Braginsky and D. Estrin, “Rumor Routing Algorithm For Sensor Networks,” Under submission to International Conference on Distributed Computing Systems, Novemb. 2001.

[4] H. Bulusu, D. Estrin, L. Girod and J. Heidemann, “Scalable Coordination for wireless sensor networks: Self-Configuring Localization Systems,” *In Proceedings of the Sixth International Symposium on Communication Theory and Applications*, Ambleside, Lake District,UK, July 2001.

[5] Z H. Cramer, *Mathematical Methods of Statistics*. Princeton, NJ: Princeton Univ. Press, 1946.

[6] Y. C. Eldar, A. Ben-Tal, and A. Nemirovski, “Robust mean-squared error estimation in the presence of model uncertainties,” IEEE Trans. Signal Process., vol. 53, pp. 168–181, Jan. 2005.

[7] C. R. Rao, Linear Statistical Inference and Its Applications, second ed. New York: Wiley, 1973.

[8] Hongchi Shi, Xiaoli Li, Yi Shang, Dianfu Ma ”Cramer-Rao Bound Analysis of Quantized RSSI Based Localization in Wireless Sensor Networks” Proceedings of the IEEE, vol. 2, pp. 32-36, 1521-9097, July 2005

[9] Y. C. Eldar, “Minimum variance in biased estimation: Bounds and asymptotically optimal estimators,” IEEE Trans. Signal Process., vol. 52, pp. 1915–1930, Jul. 2004.

Sensitivity of Impulse Response Measurements with Maximum Length Sequences and Sweeps

Student authors: Marko Ličanin, Ana Đorđević, Marko Jelenković
Mentor: Dejan Ćirić

Abstract – **Measurement of room impulse response can be affected by different disturbances appearing in the measured or measurement system. Thus, depending on the applied measurement technique, the disturbances such as noise and nonlinearity can cause certain degradation of the results. In this paper, sensitivity of the room impulse response measurement by two most widely used techniques (maximum length sequence and swept sine) is studied. The emphasis is given to certain imperfections of the measurement system causing time invariance in the reproduction of the excitation and recording of the response. The latency, repeatability and validity of the extracted impulse responses are analysed.**

Keywords – **Impulse response, MLS, swept sine, sensitivity.**

I. INTRODUCTION

An impulse response (IR) describes behavior of a linear time-invariant system. By definition, the IR is a response of a system when it is excited by the Dirac delta function [1]. In modern acoustics and its sub-areas, such as room acoustics, IR has become the only descriptor of the acoustic characteristics of a room since all acoustic parameters can be determined based on the room impulse response (RIR).

It is of great significance to select an adequate excitation signal for the measurement, which then implies the deconvolution technique for impulse response extraction. The most widely used excitation signals recently are maximum length sequence (MLS) and sine whose frequency varies in time (swept sine or sweep) [2-4]. The mentioned signals are stretched out in time enabling greater energy of the excitation and greater signal-to-noise ratio of the measured RIR.

In RIR measurement, some common problems, such as noise, nonlinearity and time variance limit the quality of the results including obtainable dynamic range of the extracted RIR. Thus, the achieved ranged can be insufficient for certain applications. This problem can be overcome applying adequate procedures for dynamic range increase including the averaging of RIRs measured in the repeated measurements [6-8]. However, if the measurement repeatability is too low, the averaging does not yield any improvement of the dynamic range. One of the reasons that can affect the repeatability is the latency present in the measurement. It can be caused by applied hardware or software [5]. In addition, the measurement results can be degraded due to sensitivity of a RIR measurement technique to certain factors.

The sensitivity of two RIR measurement techniques, MLS and swept sine technique, to hardware imperfections is investigated in this paper. These imperfections are related to lack of adequate synchronization and latency between reproduction of the excitation and recording of the response. For the purpose of investigation, several hardware configurations are applied for the measurements. Special attention is paid to the repeatability and latency of the estimated IRs.

II. IMPULSE RESPONSE MEASUREMENT

MLS technique represents a technique that has been widely used in various acoustical measurements. This technique uses a special type of white pseudo-random noise (MLS) as an excitation signal. MLS has a number of advantages in comparison to other excitation signals: it can be easily generated using shift register, it is stretched out in time enabling great excitation energy, its temporal content is known so that it can be precisely repeated, etc [2]. However, MLS technique has also certain drawbacks including sensitivity to time-variance and non-linearity that can severely degraded the obtained results.

Swept sine technique has been recently introduced in acoustic measurements [3,4]. The excitation signal used in this technique is so called swept sine or sweep. It represents a sine signal with frequency varying in time, e.g. linearly (linear sweep) or exponentially (logarithmic sweep). Swept sine technique is considered to be immune to some disturbances such as time variance or non-linearity [3,4]. Also, one of its advantages is that precise synchronization between the clock of signal generating (reproducing) and recording during the measurement is not required [4].

III. METHODS OF ANALYSIS

The sensitivity of MLS and swept sine technique on hardware imperfections is investigated performing a number of impulse response measurements. In that regard, the impulse responses of pure electrical and acoustical system are measured applying both mentioned techniques on several diferent measurement configurations (systems). Here, a part of

Student authors:
Marko Ličanin, Ana Đorđević and Marko Jelenković are with the Faculty of Electronic Engineering, University of Niš, Aleksandra Medvedeva 14, 18000 Nis, Serbia, E-mail: lichanin@elfak.rs, ana_djordjevic88@yahoo.com, virtus@elfak.rs

Mentor:
Ass. Prof. Dejan Ćirić is with the Faculty of Electronic Engineering, University of Niš, Aleksandra Medvedeva 14, 18000 Niš, Serbia, E-mail: dejan.ciric@elfak.ni.ac.rs

the measurement system consisting of a PC with the sound board (internal or external) represents the tested electrical system. The measurements on this system are carried out linking the output and input of the sound board. On the other hand, the measurements on the acoustical system (room in this case - one of the laboratories of the Faculty of Electronic Engineering in Niš) are performed using the whole measurement system including the acoustic transducers (dodecahedral omni-directional loudspeaker and condenser microphone B&K type 4144), Fig. 1. Different desktop and laptop computers with integrated sound board or with external sound board (M-Audio ProFire 610) are used as a central part of the measurement system.

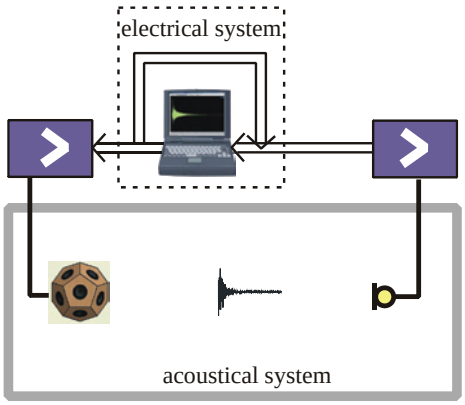

Fig. 1. Measurement of IR of electrical and acoustical system

The excitation signals, both MLS and logarithmic sweep of duration of 20 s, are generated by the developed MATLAB software module, used also for processing of the recorded responses. The analysis is based on determination of the latency and repeatability of the estimated IRs. Latency is determined in an automated procedure that requires starting point of the IR to be detemined. Repeatability is analysed observing and comparing the patterns of the obtained IRs. For each measurement configuration, the measurement is repeated 20 times in a series under the same conditions.

IV. Results

A. Latency

The extracted IRs of the electrical system measured with external sound board are presented in Fig. 2. The responses are grouped so that all twenty responses presented are not visible, but only seven of them. Besides, there is certain shift between them representing the latency. It has the smallest value among all other hardware configurations, but even in this case where specialised hardware component for reproduction and recording is used there is certain latency.

The latency has even greater values for the rest of hardware configurations. Some of the results are given in Fig. 3. While the measured IRs can be delayed for less than 50 samples (or about 1 ms for the sampling frequency of 44100 Hz) in Fig. 2, the IRs are delayed for a few hundreds of samples (several ms) in Fig. 3. The delay can be even greater in some other cases (not presented), e.g. it can be greater than a few thousands of samples (several tenths of ms).

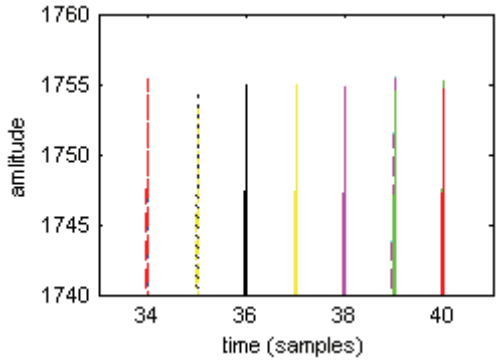

Figure 2. Zoom on the peaks of the IRs of electrical system measured with external sound board using *swept sine* technique

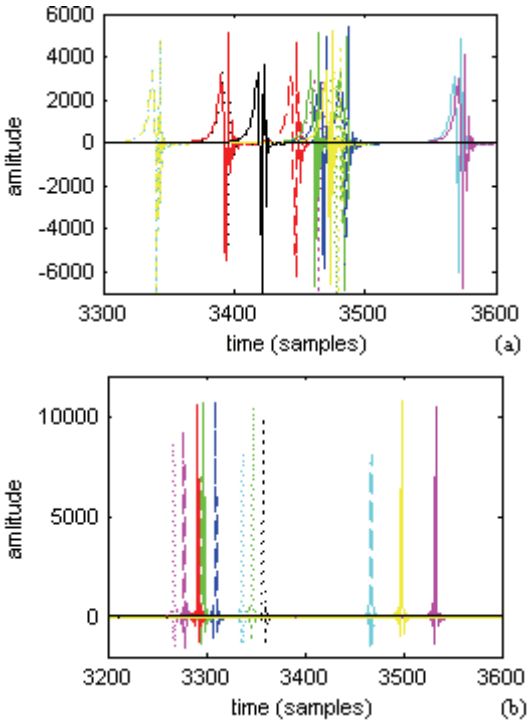

Figure 3. IRs of the electrical system measured with desktop (a) and laptop (b) computer using *swept sine* technique

The IRs of the acoustical system (room) are of much longer duration. However, the trend found in the electrical system exists also here. This is illustrated in Fig. 4. Thus, the extracted IRs are also delayed for certain variable time in relation to each other.

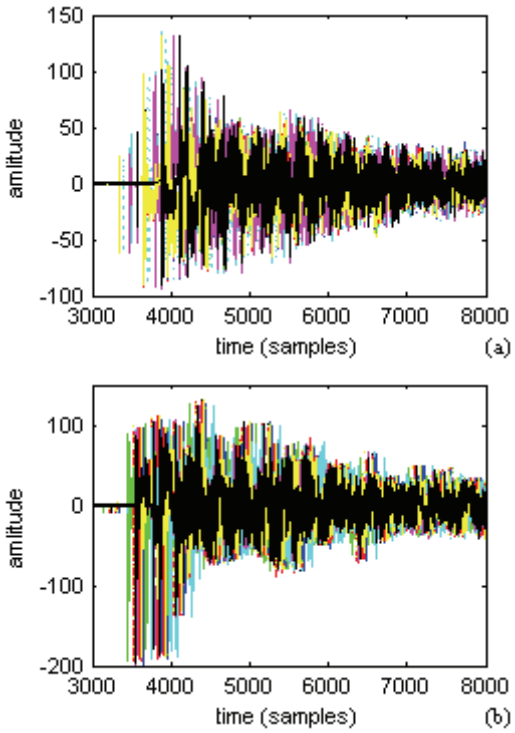

Figure 4. IRs of the acoustical system measured with desktop (a) and laptop (b) computer using *swept sine* technique

The latency does not depend on the applied measurement technique, so similar results are obtained for MLS technique independently on the measured system, Fig. 5.

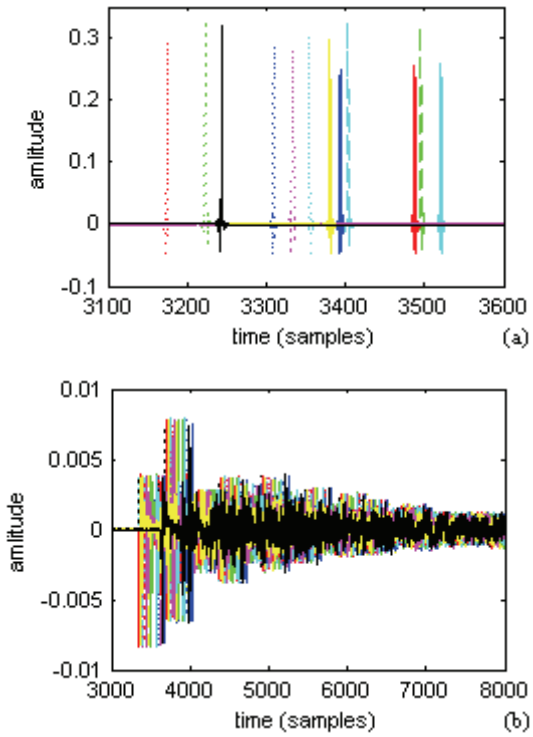

Figure 5. IRs of the electrical (a) and acoustical (b) system measured with laptop computer using *MLS* technique

B. Repeatability

The repeatability is tested so that a shift of the impulse responses caused by the latency is removed. In this way, all the responses begin in the same time point. Then, the responses measured with the same measurement technique and the same hardware configurations are compared first. Some of the results can be seen in Fig. 6. The IRs shown in this figure are without latency between them, so that their pattern can be compared. There is significant difference between the mentioned patterns for both electrical, Fig. 6(a) and acoustical system, Fig. 6(b). This difference is somewhat greater in the part of the response with greater amplitude, Fig. 6(c), and they can be even about 70 % of the maximum IR amplitude. Normalization of the IR amplitude does not reduce the difference between the IR amplitudes.

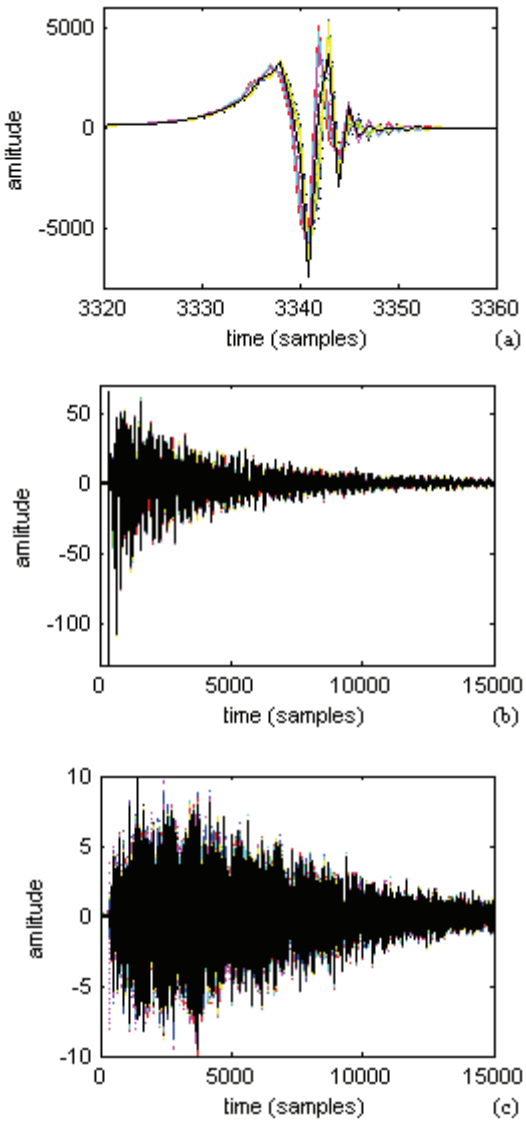

Figure 6. IRs (with removed latency) of the electrical system measured using *swept sine* technique applied on the desktop computer (a) and of the acoustical system measured with external sound board (b) together with the differences of the latter IRs (c)

The same analysis is carried out for the IRs measured using other hardware configurations and also another technique (MLS technique). The results are similar with the presented ones. Moreover, when the IRs of particular measured system (acoustical system) obtained by different hardware configurations are compared, the differences of the patterns are further increased. The same is observed when two measurement techniques are included in the comparison.

C. Sensitivity

Comparison of the results obtained by MLS and swept sine technique shows that MLS technique can be more vulnerable to some problems, which is not the case with swept sine technique. Thus, lack of synchronization between reproduction and recording as well as instability of sampling clock can cause significant degradation of the extracted impulse responses. In the extreme cases, especially when the response duration is relatively short, such as the case with the measured electrical system, the IRs can not be recovered at all. In less extreme cases the temporal shape of the extracted response is disturbed, and in further cases the dynamic range of the response is reduced. The representative examples are given in Fig. 7. The temporal shape of the IRs of the electrical system is completely degraded, Fig. 7(a), and it is completely useless. On the other hand, the dynamic range of the acoustical system IRs is significantly reduced, Fig. 7(b).

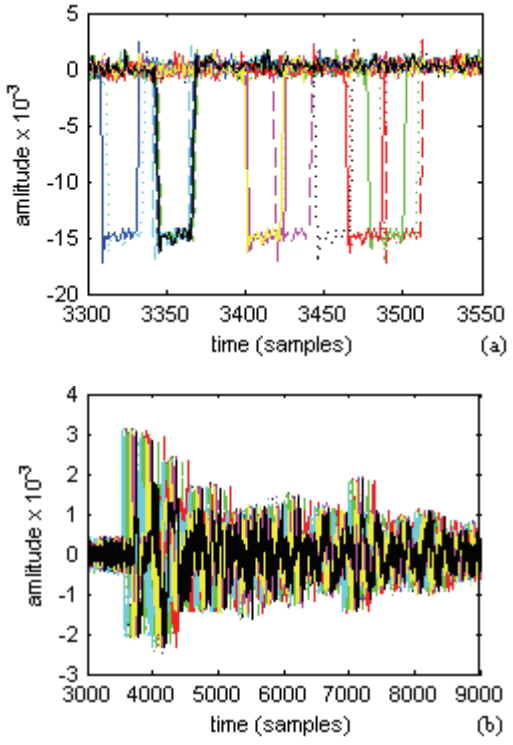

Figure 7. IRs of the electrical system (a) and acoustical system (b) measured whit desktop computer using *MLS* technique

V. Conclusion

Based on the results shown in this paper, it can be concluded that latency of the measured responses caused by the measuring system depends on system quality itself. However, it exists in all obtained results. What is even worse, this latency is variable and causes certain shift of the measured responses. In this way, direct averaging of responses is not possible, or the result of averaging would not lead to the dynamic range improvement. The latency can not be predicted. However, its effects can be minimized by additional processing.

Repeatability of the measured IRs is smaller than expected, especially when a hardware configuration of lower quality is used. The pattern of the IRs is usually kept, but the differences of the IR amplitude can be significant. The repeatability will be further explored in the future research.

MLS technique has shown some drawbacks compared to swept sine technique including vulnerability to certain imperfections of the measurement system. As a consequence, in some cases it can be even impossible to extract the IR.

Acknowledgement

This research is supported by the Ministry of Science and Technological Development of Serbia through the project No. 44009.

References

[1] D. Ćirić, *Contribution to Development of Measurement and Processing of Room Impulse Response in Determination of Acoustical Quantities* (in Serbian), Ph.D. dissertation, Faculty of Electronic Engineering, University of Niš, Serbia, 2006.

[2] G.-B. Stan, J.-J. Embrechts, and D. Archambeau, “Comparison of Different Impulse Response Measurement Techniques”, J. Audio Eng. Soc., vol. 50, no. 4, pp. 249–262, 2002.

[3] A. Farina, “Simultaneous Measurement of Impulse Response and Distrortion with a Swept-sine Technique”, 108th Convention Audio Eng. Soc., abstract in J. Audio Eng. Soc., vol. 48, no. 4, p. 350, 2000.

[4] S. Müller and P. Massarani, “Transfer-Function Measurement with Sweeps,” J. Audio Eng. Soc., vol. 49, no. 6, pp. 443–471, 2001.

[5] A. Đorđević, M. Jelenković and M. Ličanin, “Research of Latency in Measurement of Impulse Response of Room as Acoustical System”, 3rd Student projects Conference. IEEESTEC, pp.81-85, Niš, 2010.

[6] M. Milošević and D. Ćirić, “Averaging in Various Methods for Reverberation Time Measurement,” 4th Int. Conf. Telsiks 99, Confernce Proceedings, pp.649-652, Niš, 1999.

[7] F. Kawakami, K. Yamaguchi, “Space-ensamble Average of Reverberation Decay Curves,” J. Acoust Soc. Am., vol. 70, no. 4, pp. 1071–1082, 1981.

[8] W. T. Chu, “Comparison of Reverberation Measurements Using Schroeder’s Impulse Method and Decay-curve Averaging Method,” J. Acoust Soc. Am., vol. 63, no. 5, pp. 1444–1450, 1978.

AUTHOR INDEX